Measurement of Effective Diffusivity: Chromatographic Method (Pellets & Monoliths)

Zhang, Runtong

Award date:
2013

Awarding institution:
University of Bath

Measurement of Effective Diffusivity: Chromatographic Method (Pellets & Monoliths)

Runtong Zhang

A thesis is submitted for the degree of Doctor of Philosophy

University of Bath

Department of Chemical Engineering

October 2013

Abstract

This thesis aims to find out the effective diffusivity (D_{eff}) of a porous material – γ-alumina, using an unsteady state method with two inert gases at ambient condition with no reactions. For porous materials, D_{eff} is important because it determines the amount of reactants that transfers to the surface of pores. When D_{eff} is known, the apparent tortuosity factor of γ-alumina is calculated using the parallel pore model. The apparent tortuosity factor is important because: (a) it can be used to back-calculate D_{eff} at reacting conditions; (b) once D_{eff} with reactions is known, the Thiele modulus can be calculated and hence the global reaction rate can be found; (c) apparent tortuosity factor is also important for modelling purposes (e.g. modelling a packed-bed column or a catalytic combustion reactor packed with porous γ-alumina in various shapes and monoliths).

Experimental measurements were performed to determine the effective diffusivity of a binary pair of non-reacting gases (He in N_2, and N_2 in He) in spherical γ-alumina pellets (1 mm diameter), and in γ-alumina washcoated monoliths (washcoat thickness 20 to 60 μm, on 400 cpsi (cells per square inch) cordierite support). The method used is based on the chromatographic technique, where a gas flows through a tube, which is packed with the sample to be tested. A pulse of tracer gas is injected (e.g. using sample loops: 0.1, 0.2, 0.5 ml) and by using an on-line mass spectrometer the response in the outlet of the packed bed is monitored over time. For the spherical pellets, the tube i.d. = 13.8 mm and the packed bed depths were 200 and 400 mm. For monoliths the tube i.d. = 7 mm and the packed lengths were 500 and 1000 mm. When the chromatographic technique was applied to the monoliths, it was observed that experimental errors can be significant, and it is very difficult to interpret the data.

However, the technique worked well with the spherical pellets, and the effective diffusivity of He in N_2 was 0.75 – 1.38 $\times 10^{-7}$ m^2 s^{-1}, and for N_2 in He was 1.81 – 3.10 $\times 10^{-7}$ m^2 s^{-1}. Using the parallel pore model to back-calculate the apparent tortuosity factor, then a value between 5 to 9.5 was found for the pellets.

Acknowledgement

I would like to express my sincere gratitude to the people who helped and supported me during my PhD study from 2009 – 2013.

First and foremost, I would like to thank my supervisor, **Prof. Stan Kolaczkowski**, for his guidance and support that made this thesis possible. Prof. Stan was also my undergraduate tutor at University of Bath from 2005 – 2008. Knowing him for seven years, he was a great academic, lecturer, tutor, supervisor and most of all – a great friend. I learnt a lot from him and this has been helping me grow both professionally and personally.

Special thanks to the following people:

- Dr. Serpil Awdry and Dr. Yeow Hong Yap, for helping me with COMSOL modelling and Matlab.
- Dr. Dinh Chien Le, for helping me get familiar with MS.
- Mr. Euan A. Spence, for the helpful discussions on numerical methods and convolution theorem.
- Mr Fernando Acosta, John Bishop, Robert Brain and Mrs Marianne Harkins for their technical supports.
- Mr Merv Newnes, for providing the IT supports and facilities.
- Miss Charlotte Wilkes and Miss Amy Phillips for the administration work.
- Dr. Shifei Ye and Dr. Firas AL Badran, for the helpful suggestions and discussions.
- David Mcclymont, Ben Firth, Chen Zhao for many valuable discussions and funs.

Last but not least, all other friends and colleagues at University of Bath for their help on numerous occasions.

Table of Contents

Nomenclature

Alphabetical

A	cross-sectional area of a linear pore, m^2 (used in Chapter 1)
A	cross-sectional area of the packed bed, m^2 (used in Chapters 1 and 3)
A	constant in Antoine equation in Chapter 2
A	tracer gas A in tracer-carrier gas pair $A - B$ in Chapter 3
A	area under the fitted curve by a Gaussian area function, m^2 (used in Chapter 3 and Appendix 4)
A	constant used for axial dispersion coefficient equation in Chapters 3 and 4
A	surface area of the pore, $m^2\ g^{-1}$ (used in Chapter 2)
$A_{1,2}$	cross-sectional area of the tortuous pores, m^2 (used in in Chapter 1)
$A_{0,1,2,3,4}$	system-found baseline constants, used in peak fitting with Gaussian area function in Chapter 3 and Appendix 4
A_p	BJH cumulative pore area, $m^2\ g^{-1}$
$A_{tortuous}$	the cross-sectional area available for diffusion in the porous pellet, m^2
a	particle shape factor, a =1 (slab), a = 2 (cylindrical), a = 3 (sphere)
a	constant used in Dirac delta function or pulse injection function
a	constant used in Gaussian function in Chapter 3
a_0	interfacial area per unit bed volume, m^{-1}
B	constant used in the Antoine equation in Chapter 2
B	carrier gas B in tracer-carrier gas pair $A - B$
B	constant in Antoine equation in Chapter 2
B	constant used for axial dispersion coefficient equation in Chapters 3 and 4
$B_{0,1,2,3,4}$	user-defined baseline constants, used in peak fitting with Gaussian area function in Chapter 3 and Appendix 4
b	constant used in Gaussian function in Chapter 3
C	constant in Antoine equation in Chapter 2
C or C_A	concentration of the tracer gas (A) in the fluid phase or in the interparticle space, mol m^{-3}_{fluid} (used in Chapters 1 and 3)

$\bar{C}(x, s)$	concentration function curve in Laplace form, i.e. $L[C(x, t)]$
C_{As}^{s}	concentration of the tracer gas A at the external surface of the particle, mol m_{fluid}^{-3} (used in Chapters 1 and 3)
C_{As}	concentration of the tracer gas A in the solid particle, mol m_{solid}^{-3}, same as C_{μ} (used in Chapters 1 and 3)
C_i or C_s	concentration of the tracer gas in the pore structure of the particle (adsorbent), mol m_{pore}^{-3} (used in Chapter 1 and in Particle Models 1 and 2 in Chapter 3)
C_{μ}	adsorbed tracer gas concentration, mol m_{solid}^{-3}, same as C_{As} (used in Particle Model 3 in Chapter 3)
$C(t)$	pulse response curve, or tracer concentration curve, known as C-curve, mol m^{-3}
$C_0(t)$	initial concentration of the tracer pulse at the column inlet, mol m^{-3}
$C_1(t)$	square wave or Dirac delta pulse input, mol m^{-3}
$C_2(t)$	response to square wave or Dirac delta pulse input, mol m^{-3}
c	average energy of adsorption, dimensionless (used in BET equation in Chapter 2)
c	constant used in Gaussian function in Chapter 3
D	difference in two consecutive pore diameters for the computation of pore size distribution (PSD) using the BJH model, m
$\bar{D}$	average composite local diffusivity, $m^2\ s^{-1}$
D_{AB}	bulk diffusivity or bulk diffusion coefficient, same as the molecular diffusivity, D_m, $m^2\ s^{-1}$
D_{ax} (or E)	axial dispersion coefficient, $m^2\ s^{-1}$
D_B	hydraulic diameter of the packed-bed, m
D_{eff} (or D_e)	effective diffusivity or effective intraparticle diffusion coefficient, $m^2\ s^{-1}$
D_K (or $D_{K(rp)}$)	Knudsen diffusivity or Knudsen diffusion coefficient, $m^2\ s^{-1}$
D_m	molecular diffusivity or molecular diffusion coefficient, same as the bulk diffusivity, D_{AB}, $m^2\ s^{-1}$
D_C	composite diffusivity or local diffusivity, same as the pore diffusivity, D_p, $m^2\ s^{-1}$

D_p	pore diffusivity or pore diffusion coefficient, same as the composite diffusivity, D_C, $m^2\ s^{-1}$ (used in Chapters 1 and 3)
D_p	particle diameter, m (used in Chapters 1, 3 and 4)
$\bar{D_p}$	average pore diameter, m (used in the BJH model for the computation of PSD in Chapter 2)
D_t	tube internal diameter (i.d.), m
D_μ	diffusion coefficient in the mesopores of the particle, $m^2\ s^{-1}$
D_M	diffusion coefficient in the macropores of the particle, $m^2\ s^{-1}$
d	monolith height, m (used in Chapters 1, 2 and 5)
d (or d_p)	diameter of the γ-alumina bead, m (used in Chapter 3)
d_{i+1}, d_i	cumulative pore diameter, m
d_{pore}	pore diameter, m (used in Chapters 1 and 3)
d_p	pore diameter, m (used in Chapter 2)
$d_{molecule}$	gas molecule diameter, m (used in Chapter 1)
E_z	axial dispersion coefficient in the interparticle region of the packed-bed, $m^2\ s^{-1}$
$E_{r,z}$	dispersion coefficient in the r, z – directions, $cm\ s^{-1}$
$E(t)$	exit age distribution curve, or the normalisation curve, known as *E*-curve, s^{-1}
$E(\alpha)$	Residence Time Distribution (RTD) function or age distribution function; e.g. $E_1(\alpha_1)$ and $E_2(\alpha_2)$
f	correction factor between effective diffusivity, D_{eff} and composite diffusivity, D_C, dimensionless
F_1, F_2	carrier gas flowrates, $cm^3 min^{-1}$ (used in Chapter 1)
G	constant used for non-linear curve fit in Chapter 3 and 4
ΔH_A	heat of adsorption, $J\ mol^{-1}$
ΔH_L	heat of liquefaction, $J\ mol^{-1}$
h (h_1, h_2)	time intervals selected on the response peak curve for numerical integrating (Simpson's rule) the peak area, s
$I(t)$	pulse response curve, or tracer intensity curve, known as *I*-curve, torr
J_K	flux due to Knudsen diffusion, $mol\ m^{-2}\ s^{-1}$
$J\|_R$	mass transfer rate into the particle per unit interfacial surface area, $mol\ m^{-2}\ s^{-1}$

K	adsorption equilibrium constant, with or without unit depends on which Particle Model used
K_a	adsorption equilibrium constant, dimensionless (used in Cases 1 and 5)
K_A	adsorption equilibrium constant, $cm^3_{pore}\ g^{-1}$ (used in Case 2)
K_A^c	adsorption equilibrium constant, $cm^3_{pore}\ g^{-1}$ (used in Case 2c)
$K_A{}'$	dimensionless adsorption equilibrium constant (used in Particle Model 2)
K_h	Henry's law adsorption equilibrium constant or Henry's law constant defined in terms of sorbate pressure, molecule /(cavity torr)
K_H	dimensionless adsorption equilibrium constant or Henry's law constant (used in Cases 3, 4 and 6)
K_s	adsorption equilibrium constant, $cm^3_{pore}\ g^{-1}$ (defined in this thesis)
k	geometry parameter and depends on the pore type, dimensionless (used in the Kelvin equation in Chapter 2)
k_f	external mass transfer coefficient, $m\ s^{-1}$
k_s	reaction rate constant, $m^3_{fluid}\ m^{-2}_{solid}\ s^{-1}$ (used in Chapter 1)
k_m	mass transfer coefficient, $m^3_{fluid}\ m^{-2}_{solid}\ s^{-1}$ (used in Chapter 1)
k_0	overall rate constant in Chapter 1, $m^3_{fluid}\ m^{-2}_{solid}\ s^{-1}$ (used in Chapter 1)
k_{ads}	adsorption rate constant, s^{-1} or $cm^3\ g^{-1}\ s^{-1}$
k^1_{ads}	adsorption rate constant, $cm^3_{pore}\ g^{-1}\ s^{-1}$
k_{des}	desorption rate constant, s^{-1} or $cm^3\ g^{-1}\ s^{-1}$
k^1_{des}	adsorption rate constant, $cm^3_{pore}\ g^{-1}\ s^{-1}$
k_m	mass transfer coefficient, $m\ s^{-1}$
L	length of the fictitious bed, m (used in Chapter 4 for glass and γ-alumina beads)
L_c	length of the fictitious bed packed with monoliths, m
L_t	glass tube column length, m
l	the thickness of external film, m (used in Chapter 1)
l	monolith length, m (used in Chapters 1, 2 and 5)
l_p	pore length, m
M or m	mass of a γ-alumina bead, g (used in Chapter 2)

M	molecular weight of the tracer gas, g mol^{-1} (used in Knudsen diffusivity expression, D_K in Chapter 3)
M_A and M_B	molar mass of species *A* and *B*, same as $\tilde{M}_1$ and $\tilde{M}_2$, g mol^{-1}
$\tilde{M}_1$ and $\tilde{M}_2$	molar mass of species 1 and 2, same as M_A and M_B, g mol^{-1}
M_{pellet}	packing weight, or the total weight of the γ-alumina beads packed in the column, g
M_{solid}	mass of the sample, g
M_v	gram molecular volume, m^3 mol^{-1}
m	molecular weight of adsorbent (nitrogen), g mol^{-1} (used in the BET surface area equation in Chapter 2)
m_{pellet}	mass of a γ-alumina bead, g
m_n	*n*-th moment, s^n
m_0	zero order moment, dimensionless
N	number of data points selected for numerical integrating the peak area: Simpson's rule
N	moles of tracer injected as a Dirac pulse, mole (used in Chapter 3)
N_A	the amount (in moles) of gases transfer onto the porous surface at steady state when $r^s_{As} = N_A$, mol m^{-2}_{solid} s^{-1} (used in Chapter 1)
N_A	Avogadro constant, 6.023 $\times 10^{23}$ molecule per mole (used in Chapter 2)
N_{diff}	difference between the total number of packed and re-packed monoliths in the same SPSC column
N_i	the amount of gas molecules diffuses through a linear pore, mol m^{-2}_{pore} s^{-1} (used in Chapter 1)
N_i	molar flux from fluid in pore to catalyst surface, based on unit void volume of catalyst pellet, mol m^{-3}_{pore} s^{-1} (used in Chapter 3)
$(N_i)_{tortuous}$	the amount of gas molecules diffuses through the tortuous path in the pore, mol m^{-2}_{pore} s^{-1}
N_{WS}	number of washcoated monoliths packed inside a column
n_A	concentration of the adsorbed tracer A per unit void volume of catalyst pellet, mol m^{-3}_{pore}
n, n_m	specific amount adsorbed and the BET monolayer capacity, used in the classification of adsorption isotherm in Chapter 2

P	vapour pressure, bar (used in the Antoine equation in Chapter 2)
P	equilibrium vapour pressure, Pa (used in the BET equation in Chapter 2)
P	applied pressure in mercury porosimeter, Nm^{-2} (used in the Young-Laplace equation in Chapter 2)
P	pressure, Pascal or bar (used in the empirical correlation for bulk diffusivity, D_{AB} for a binary gas mixture in Chapters 3 and 4)
P_0	saturation vapour pressure, Pa (used in the BET equation in Chapter 2)
p	partial pressure, Pascal
Pe	Péclet number, dimensionless
Q	gas or fluid flowrate, $m^3\ s^{-1}$
q_s	total number of sites per unit weight or volume of adsorbent
r_e	equivalent pore radius, m
R	channel equivalent radius for washcoated ceramic cordierite monolith, m (used in Chapter 2)
R	particle radius, m (used in Chapters 3 and 4)
R or R_g	universal gas constant, 8.314 J mol^{-1} K^{-1}
R_p	equivalent particle radius, m
r	radial coordinate in cylindrical or spherical coordinate system, m
r_1 and r_2	mutually perpendicular pore radii in the cylindrical coordinate system, m
r_p	pore radius, m
r_k (or r_c)	Kelvin radius also known as core radius, m
r_n	radius of the neck of the ink-bottle pore, m
r_w	radius of the wide body of the ink-bottle pore, m
Re (or Re_p)	Reynolds number of the packed-bed, same as the Reynolds number of the particle, dimensionless
Re_H	Reynolds number of the packed-bed, calculated with hydraulic diameter, D_B, dimensionless
S_w	BET surface area or mass specific area, $m^2\ g^{-1}$
Sc	Schmidt number, dimensionless
S	slope of the linear plot for adsorption equilibrium constant calculation
S_i	sticking coefficient of species i onto the active sites, dimensionless
S_p	incremental pore area or BJH incremental pore area, $m^2\ g^{-1}$

s	time domain, t in Laplace form, i.e. s-domain.
T	absolute temperature, K
T	liquid nitrogen temperature, 77.3 K (used in the Kelvin equation in Chapter 2)
t	time, s
t_{bead}	peak elution time for column packed with γ-alumina beads, s
t_d (or t_{d1}, t_{d2})	peak elution time difference between the blank and washcoated monoliths, s (used in Chapter 5)
t_{glass}	peak elution time for column packed with glass beads, s
t_{mean} (or t_m)	mean residence time, same as the first moment, μ_1, s
t	thickness of the film layers on the pore surfaces formed by condensed vapour, m (used in the Kelvin equation in Chapter 2)
t_0	tracer pulse injection duration time, s
u_i	interstitial carrier gas velocity in the axial direction (x – direction), m s^{-1}
u_0	superficial carrier gas velocity in the axial direction (x – direction), m s^{-1}
U_1	dimensionless first moment or dimensionless mean residence time
V	volume of gas adsorbed, cm^3 g^{-1} (used in the BET equation in Chapter 2)
V_{column}	the volume of the packed-bed column, m^3
V_i or v_i	diffusion volumes of gas molecules for species 1 and 2, or A and B
V_L	molar volume of the condensed liquid nitrogen, 34.6×10^{-6} m^3 mol^{-1} (used in the Kelvin equation in Chapter 2)
V_m	monolayer capacity (volume of one layer of gas), cm^3 g^{-1}
V_p	incremental pore volume or BJH incremental pore volume, cm^3 g^{-1}
V_{pellet}	volume of a spherical γ-alumina bead, m^3
V_{solid}	volume of the sample not including voids, m^3
V_{total}	combined volume of the voids and the sample, m^3
V_{void}	volume of the voids in the sample, m^3 (used in Chapter 2)
V_{void}	total volume of the voids (or empty space) in the interparticle region of the packed-bed, m^3 (used in Chapter 3)
v_p	BJH cumulative pore volume, cm^3 g^{-1}
w	monolith width, m (used in Chapters 1, 2 and 5)

w	real constant in the Gaussian area function
w	concentration of the adsorbed gas per unit weight of adsorbent, mol $g^{-1}_{adsorbent}$ (used in Particle Model 2 in Chapter 3)
y	variable depends on x, e.g. for a linear function, $y = f(x) + c$
y_0	baseline constant, defined in the Gaussian area function in Chapter 3
x	independent variable, e.g. for a linear function, $y = f(x) + c$
x	relative pressure (from 0 – 1), dimensionless
x	coordinate in the Cartesian system, m
x	relative pressure, i.e. $x = P/P_0$, dimensionless (used in the Kelvin equation in Chapter 2)
x_A	relative pressure $(P/P_0)_A$ for adsorption process in the pore, dimensionless
x_c	real constant in the Gaussian area function
x_D	relative pressure $(P/P_0)_D$ for desorption process in the pore, dimensionless
y	coordinate in the Cartesian system, m
z	axial coordinate in cylindrical coordinate system, m

Greek symbols

α	independent variable – time, s
γ	surface tension of pure mercury, 0.485 N m^{-1} at 25 ℃
γ_{LV}	interfacial surface tension, suffixes referring to liquid-vapour (LV), 8.85×10^{-3} N m^{-1} (used in the Kelvin equation in Chapter 2)
γ_1, γ_2	defined in Equations (4.16) and (4.17) in Chapter 4
ε	particle porosity, dimensionless
ε_b	bed porosity or column void fraction, dimensionless
ε_L	bed porosity of the SPSC column packed with monoliths, dimensionless
ε_p	intraparticle void fraction or particle porosity, dimensionless (used in Chapters 1 and 3)
$\varepsilon_{particle}$	porosity of the sample, same as ε_p, dimensionless (used in Chapter 2)

ε_μ	particle micropore (or mesopore) porosity, dimensionless
ε_M	particle macropore porosity, dimensionless
ε_1, ε_2, ε_3	γ-alumina bead porosity calculated based on skeletal and bulk densities values from pycnometer, mass to volume ratio (m/V) and mercury porosimeter, dimensionless
$\delta(t)$	Dirac impulse function or unit impulse function
$\delta_a(t)$	Dirac delta function
$f_a(t)$	pulse injection function (defined in this thesis)
μ	dynamic viscosity of the fluid, Pa s
μ_n	n-th absolute moment or the n-th normalised moment, s^n
μ_n'	n-th central moment, s^n
μ_1	first moment, same as the mean residence time, t_{mean}, s
$\Delta\mu_1$	difference in first moment, s
$(\mu_1)_{ads}$	first moment for adsorption run, evaluated from experimental response curve, s
$(\mu_1)_0$	first moment for blank run, calculated from a theoretical expression in Equations (3.59) and (3.60) in Chapter 3, s
$(\mu_1)_{inert}$	first moment for inert run, evaluated from experimental response curve, s
μ_2'	second central moment, same as the variance, σ^2, s^2
$(\mu_2')_{ads}$	second central moment for adsorption run, evaluated from experimental response curve, s^2
μ_{1d}, μ_{2d}	delay or 'dead' volume first moment and second central moment for a short blank tube experiment, s and s^2 (used in Appendix 7)
λ	the mean free path of gas molecules in pore, m (used in Chapters 1 and 3)
Θ	fraction coverage: fraction of the surface sites occupied by the adsorbate molecule, dimensionless
θ	cordierite thickness or monolith wall thickness, m (used in Chapter 2)
θ	wetting angle used in the Kelvin equation in Chapter 2, taken as 0^o
θ	mercury-solid-vacuum contact angle in mercury porosimetry system
θ	dimensionless time i.e. $\theta = t / t_m$
ρ	density of the fluid, g cm^{-3}

ρ_{bulk} or ρ_b	bulk density or apparent density, g cm^{-3}
$\rho_{skeletal}$ or ρ_s	skeletal density or true density, g cm^{-3}
ρ_p	apparent density of the adsorbent particle, same as ρ_{bulk} or ρ_b, g $cm^{-3}_{particle}$
σ	area occupied by one adsorbate molecule, usually taken as 16.2 $\times 10^{-20}$ m^2 for nitrogen at 77.3 K (used in Chapter 2)
σ	standard deviation or standard error, s
σ_c	constriction factor, $\sigma_c = f(\beta)$, is a function of the ratio of maximum to minimum pore areas, dimensionless
σ^2	variance, same as the second central moment, μ_2', s^2
σ_θ^2	dimensionless second central moment or dimensionless variance
ξ_1	total resistance, s (defined in Equations (3.101), (A6.4) and (A7.4))
ξ_a	adsorption resistance, s (defined in Equations (3.102), (A7.5) and (A9.6))
ξ_e (or ξ_f)	external mass transfer resistance, s (defined in Equations (3.106), (A6.5), (A7.7), (A8.17) and (A9.7))
ξ_i (or ξ_M)	intraparticle diffusion resistance, s (defined in Equations (3.105), (A6.6), (A7.6), (A8.18) and (A9.8))
ξ_d	axial dispersion resistance, s (defined in Equations (3.103), (A8.16) and (A9.5))
ξ_0	resistance parameter, s (defined in Equations (3.104), (A6.3), (A7.3), (A8.15) and (A9.4))
τ	time lag, s (used in Chapter 3)
τ	time constant or the system's theoretical residence time, s, same as t_m or μ_1 (used in Chapter 3)
τ	tortuosity, dimensionless (used in Chapters 3 and 4)
τ_d	delay time or 'dead' volume time, s
τ_p	tortuosity factor, dimensionless
τ_1	the delay time in the lines to the column, s
τ_2	the delay time in the lines to the MS, s
ν	kinematic viscosity of the fluid, m^2 s^{-1}

φ	interfacial area per unit bed volume, m^{-1}

Subscript

ads	adsorption
des	desorption
b	bed (bulk)
i	component *i*
f	fictitious bed
LV	liquid-vapour
μ	mesopores (or mesoporous)
r,z	radial (*r*) and axial (*z*) directions
WS (or *WC*)	washcoat, or washcoated

Abbreviations

ASAP2020	Micromeritics Accelerated Surface Area and Porosimetry System 2020
Ave.	Average
amu	atomic mass unit
BET	Brunauer, Emmett and Teller
BJH	Barrett, Joyner and Halenda
cpsi	Cells per square inch
DFT	Density Function Theory
DOC	Diesel Oxidation Catalyst
FS	Free-space
FWHM	Full Width at Half Maximum
HETP	Height Equivalent to a Theoretical Plate
HDS	Hydrodesulfurization
I.D (or i.d.)	Inner diameter
IUPAC	International Union of Pure and Applied Chemistry
QIC	Quartz Inert Capillary

MS	Mass Spectrometer
MID	Multiple Ion Detection
NIST	National Institute of Standards and Technology
O.D (or o.d.)	Outer diameter
ODEs	Ordinary Differential Equations
PDEs	Partial Differential Equations
PTFE	Polytetrafluoroethylene, $(C_2F_4)n$
PSD	Pore size distribution
PFR	Plug Flow Reactor
psia	Pounds per square inch absolute
ppb	Parts per billion (1 in 10^9)
ppm	Parts per million (1 in 10^6)
RTD	Residence time distribution
RSQ	R-square or R^2 value
SQRT	Square root of
SEM	Scanning Electron Microscope
SEM	Second Electron Multiplier
SPSC	Single Pellet String Column
SPSR	Single Pellet String Reactor
STP	Standard temperature and pressure
STD (or Std)	Standard deviation
UHV	Ultra-high vacuum

1 Introduction

The main focus of the work in this thesis builds on a technique described in Zhang *et al.* (2004), where experimental techniques were used to evaluate the effective diffusivity of a binary pair of gases, in a γ-alumina material. In combination with information on pore size and porosity, and data from diffusivity experiments, the parallel pore model was used to back-calculate the apparent tortuosity factor for that material. This then enabled sufficient information to have been acquired to apply that model to determine the effective diffusivity of other gases at different temperatures and pressures. The effective diffusivity was evaluated using a steady-state technique in Zhang *et al*. (2004), whereas in this work, an unsteady-state technique i.e. gas chromatographic method was used.

One engineering application for this work would be in the modelling of catalytic converters, which reduce emissions of CO, HCs and NOx from vehicles. In that application, the quantification of:

- the diffusion of reactants through the layer containing the catalyst, and/or
- the diffusion of reaction products though that catalytic layer back into the gas phase,

are important in reactor modelling.

Besides, similar to the use of γ-alumina in catalytic converters or catalytic combustion reactors, it is also used as a catalyst support for many industrial catalysts, such as in Hydrodesulfurization (HDS) and some Ziegler-Natta polymerisations (Gary and Handwerk, 2001; Hoff and Mathers, 2010).

So this introduction starts with a brief description of catalytic converters to identify the location and function of the washcoat in such a converter, and then explains the terms: diffusion in porous materials and effective diffusivity.

This then leads to a brief introduction to experimental techniques that have been used, and the particular challenges to be tackled in this thesis are highlighted.

1.1 General background

The catalytic pellet packed bed reactor, and the catalytic monolith reactor have and are still used in catalytic combustion applications, many of which are related to pollution control e.g. cars and power plants (Hayes and Kolaczkowski, 2000). When used to control emissions from a vehicle, such a device is known as a catalytic converter, and the monolith support structure is usually used.

On a vehicle, the catalytic converter reduces emissions from vehicles, by converting components in the exhaust gas (e.g. carbon monoxide (CO), hydrocarbons (HC) and oxides of nitrogen (NO_x)), into less harmful gases (e.g. carbon dioxide (CO_2), water vapour (H_2O), and nitrogen (N_2)). There are two main types of catalytic converter:

(a) Three-way catalytic converter; and
(b) Two-way catalytic converter (e.g. Diesel Oxidation Catalyst (DOC)).

The difference between these two converters is the NO_x reduction. In three-way catalytic converter, NOx is reduced to nitrogen with rhodium catalyst, whereas in two-way catalytic converter, with Rh absent, the catalytic reduction of NOx is carried out by Selective Catalytic Reduction (SCR) with hydrocarbons (i.e. HC react with NOx). However, the problem with SCR by hydrocarbons is that it can occur to a limited extent over a narrow temperature window because Pt-based catalysts tend to operate at relatively low temperature. Another problem is that the popular Pt/Al_2O_3 favours the formation of N_2O over N_2 at relatively low temperatures (Pollington *et al.*, 2003).

Depending on the overall design of the exhaust system, a modern exhaust system to control emissions from a diesel engine could contain the following (Wörner and Sigel, 2005):

(a) Diesel oxidation catalytic converter (a core component);
(b) De-NO_x converter (a supplementary component);
(c) Particulate filter (a supplementary component);
(d) Selective Catalytic Reduction (SCR) converter (a supplementary component).

Based on information in Nijhuis *et al.* (2001), a typical Diesel Oxidation Catalyst (DOC) consists of:

a) **Blank monolith substrate or uncoated cordierite (i.e. the catalyst support):** this could be in a cylindrical shape and is usually made from a ceramic material with a honeycomb structure. The honeycomb structure provides:
   - a large geometric surface area,
   - offers a lower pressure drop than a packed bed, and
   - the ceramic catalyst support (or substrate) is able to withstand high operating temperatures and has a low level of thermal expansion.

   The surface of the cordierite is also porous and the pore size is usually in the macroporous range.

b) **Washcoat:** this is often a mixture of alumina and silica, has a high surface area (BET surface area for γ-Al_2O_3 is around 100 – 200 m^2/g), and can be coated onto the surface of a blank monolith. This washcoat provides a porous surface (pore size in mesopore range) into which noble metals with catalytic properties are deposited and dispersed, creating an active catalytic layer.

c) **The catalyst (i.e. the noble metals):** this could be from a group of precious metals consisting of:
   - platinum (Pt) and palladium (Pd): acting as oxidation catalysts; and
   - rhodium (Rh): acting as a reduction catalyst.

   In a DOC, the catalyst Pt is mainly used because of its high performance when compared with other noble metals.

When considering the physical properties of the washcoat such as: density, BET surface area, and pore size, then based on the measurements in Yap (2011):

(i) washcoats with the Pt catalyst, and
(ii) washcoats without the Pt catalyst,

were found to exhibit very similar physical properties which had an impact on the measurement of effective diffusivity. This was an interesting observation, as it enables the transport properties which are related to these parameters (i.e. diffusion in the washcoat) to be

studied in a non-catalytic washcoat. This eliminates some of the complexities of using a catalytically active washcoat.

A scanning electron microscope (SEM) image is presented of a monolith (Figure 1.1) which has been washcoated. In Figure 1.2, a schematic is presented which shows a cross-sectional view through a layer of the washcoat. The structure is complex, with:

(a) many of the pores having dead-ends,
(b) pores present in the washcoat that are isolated from their neighbours,
(c) and pores which interconnect with one another.

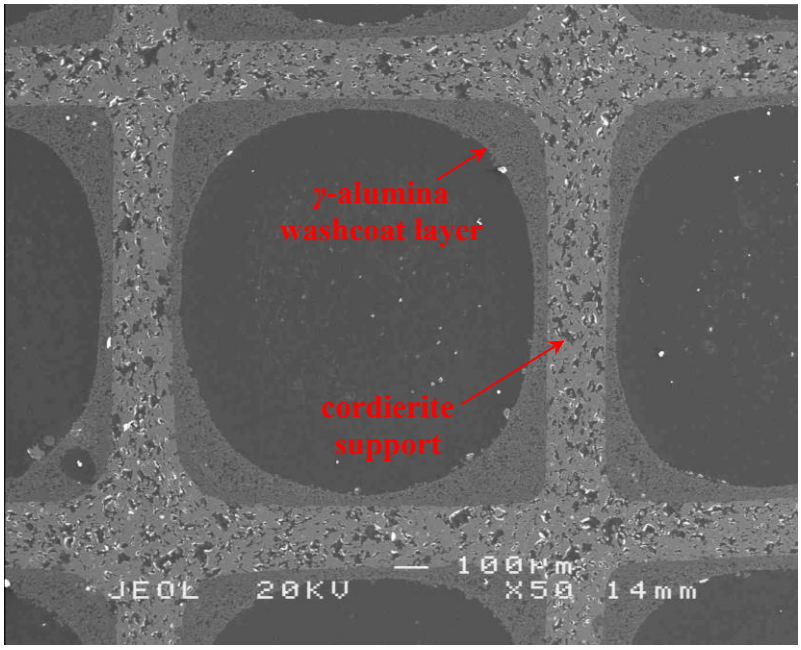

Figure 1.1: SEM image with 50 ×magnification for washcoated monolith channels (adapted from Yap (2011), with permission).

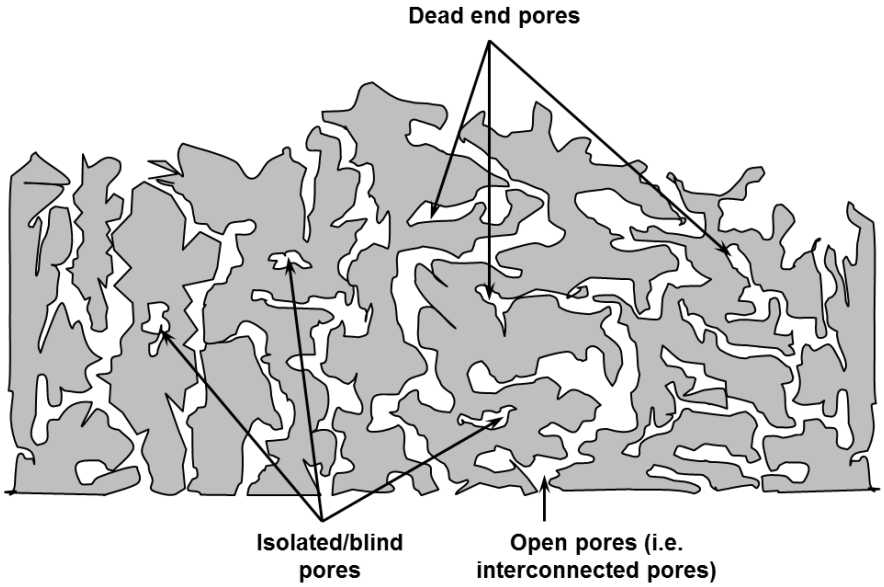

Figure 1.2: Cross-sectional view of the tortuous pathways representing the porous washcoat layer (adapted from Yap (2011), with permission).

1.2 Mass transfer and diffusion mechanism

In a DOC, the reactants (e.g. CO, HCs, O_2) need to be transported from the bulk gas phase to the catalytically active sites in the washcoat layer. So in the sections that follow, this process is briefly described.

1.2.1 Transport process in heterogeneous catalysis

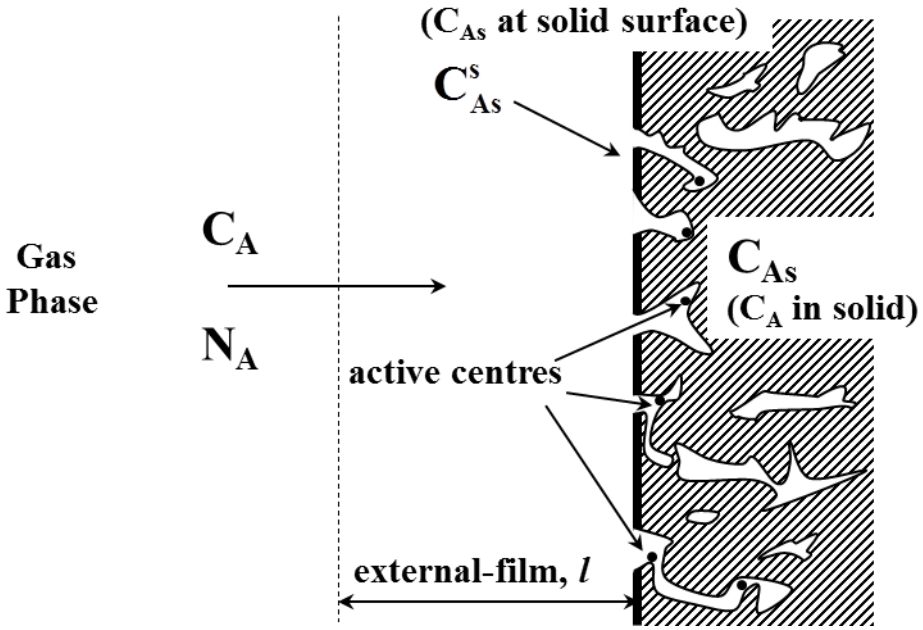

Figure 1.3: Transport and reaction mechanism on a catalyst surface and inside catalyst (adapted from Bird *et al.* (1960))

Based on a description in Atkins *et al.* (2006), the following simplified description is provided of what might take place in a DOC. Considering the schematic in Figure 1.3, reactions at the catalyst surface have two limiting cases:

i. For rapid mass transfer: the reaction rate constant, k_s, is negligible compared with mass transfer coefficient, k_m, which means that the overall rate constant, k_o, is equal to k_s, hence the overall process is reaction rate controlled.

ii. For rapid reaction: the mass transfer coefficient, k_m, is negligible compare to the reaction rate constant, k_s, which means that the overall rate constant, k_o, is equal to k_m, hence the overall process is diffusion controlled.

For the measurement of the effective diffusivity in a catalyst, two inert gases (or non-reacting gases with the catalyst) are used.

1.2.2 Intraparticle gradient effects – pore diffusion

The reaction rate k_s of a catalyst shown in Figure 1.3 is proportional to the surface area of the catalyst (assuming uniform catalyst activity). This can be maintained high by dispersing the catalyst throughout a high surface area support, e.g. γ-alumina, which has a surface area of e.g. 100 – 200 m^2/g (Hayes and Kolaczkowski, 2000), whereas for a low surface area material such as the blank uncoated monolith then this is less than 1 m^2/g (Jarrah *et al.*, 2003). A high surface area is achieved by having a highly porous structure with small pores, and this creates a high ratio of [surface area]: [volume].

From Figure 1.2 it is also clear that pore shape varies, pore size is not uniform, and a pore size distribution (PSD) exists. PSD is measured by nitrogen adsorption analysis (ASAP 2020) or mercury porosimetry. There are two types of PSD:

(a) Bimodal distribution of pore sizes;
(b) Unimodal distribution of pore sizes.

The samples to be studied in this thesis are likely to have a bimodal PSD. This initial assumption is supported by Hayes and Kolaczkowski (1997). As mention in their book, the pore size distribution provides information on the distribution of mesopores (range: 2 – 50 nm) and macropores (> 50 nm) in the catalyst structure. According to Gregg and Sing (1982), this classification for mesopores and macropores had been adopted by the International Union of Pure and Applied Chemistry (IUPAC). To have a catalyst with a large internal surface area, a porous material with many small pores is required. When a catalyst pellet is formed by pressing smaller particles together, or a monolith is coated with a washcoat (consisting of small particles), a plot of pore size distribution is likely to show two peaks representative of a biomodal pore size distribution. The first peak represents the ‘micropores’ or ‘mesopores’ in the particles, and the second peak represents the ‘macropore’ between the particles.

For gas diffusion through a single cylindrical pore, the ratio of pore diameter (d_{pore}) to the mean free path of the gas (λ) will determine whether or not the pore wall affects the diffusion.

As described in Malek and Coppens (2003a) and Schirmer (1995), three different situations can exist:

Situation 1

(i) $d_{pore} >> \lambda$: molecule diffusion dominates, i.e. Fickian diffusion.

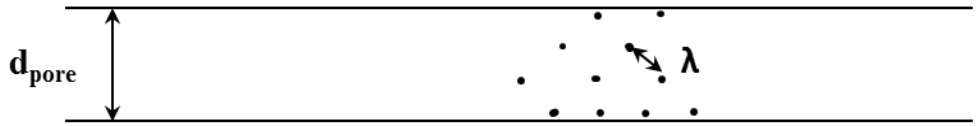

Figure 1.4: Gas molecules in a cylindrical pore: $d_{pore} >> \lambda$

Situation 2

(ii) $d_{pore} << \lambda$, and $d_{molecule} < d_{pore}$: molecule interactions with the pore wall dominate, diffusion known as Knudsen diffusion.

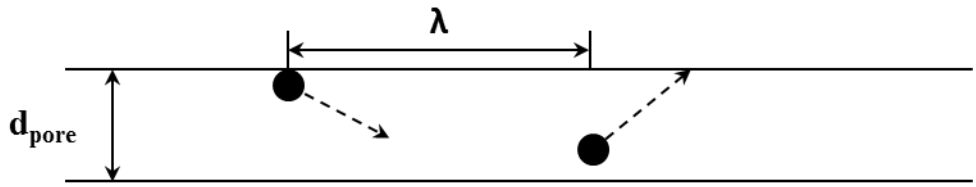

Figure 1.5: Gas molecules in a cylindrical pore: $d_{pore} << \lambda$ and $d_{molecule} < d_{pore}$

Situation 3

(iii) $d_{pore} << \lambda$, and $d_{molecule} \sim d_{pore}$: complex interaction of diffusing molecules with the force-fields of molecules making up the wall, referred to as configurational diffusion and very difficult to predict (e.g. very large hydrocarbon molecules – petroleum desulpurisation; or very small size pores such as diffusion within zeolites crystals, or through biological cell walls).

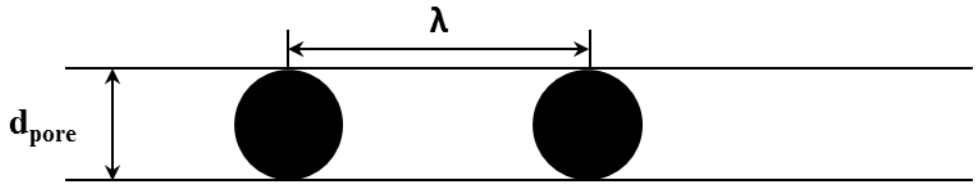

Figure 1.6: Gas molecules in a cylindrical pore: $d_{pore} << \lambda$ and $d_{molecule} \sim d_{pore}$

For non-zeolite catalysts, both molecular and Knudsen diffusion dominate. The pore diffusion coefficient, D_p will be a function of D_m and D_k. The molecular diffusion coefficient D_m in some literature is also known as the bulk phase diffusion coefficient, D_{AB}. Likewise, pore diffusion coefficient is recognised as composite diffusivity, D_C.

The following information is obtained from a number of different sources (e.g. Pollard and Present (1948), Mason and Malinauskas (1983)):

The Bosanquet formula can be used to approximate the D_p term:

$$\frac{1}{D_p} = \frac{1}{D_m} + \frac{1}{D_k} \tag{1.1}$$

From D_p, an effective diffusion coefficient, D_{eff} is added to account for the complex pore structure of the catalyst. An approximation of D_{eff}, which is often adequate for design purposes, is given by (Wheeler, 1955):

$$D_{eff} = \frac{\varepsilon_p D_p}{\tau_p} \tag{1.2}$$

where: – ε_p is the intraparticle void fraction or particle porosity;
– τ_p is the tortuosity factor.

Therefore a comparison between the diffusion in a single pore and diffusion in a porous pellet is shown in Figure 1.7. The terms tortuosity, τ, and tortuosity factor, τ_p, express two different characteristics of a material. Tortuosity is the ratio of actual distance travelled between two points to the minimum distance between the same two points in a porous pellet. A tortuosity factor is commonly used in the area of heterogeneous catalysis and is the ratio of tortuosity to constriction, where constriction is a function of the ratio of maximum to minimum pore areas as shown in part (a) of Figure 1.8. According to the discussion in Satterfield (1981), the constriction σ and tortuosity τ can be treated as one factor– tortuosity factor, τ_p and it is set equal to:

$$\tau_p = \frac{\tau}{\sigma_c} \tag{1.3}$$

According to Fogler (2004), when the two areas, A_1 and A_2, are equal, β = 1, and the constriction factor is unity. When β = 10, and $A_2 = 10 \times A_1$, then the constriction factor is

approximately 0.5. Hence, the constriction factor σ_c is generally treated as 1 in the literature for the purpose of calculating the effective diffusivity.

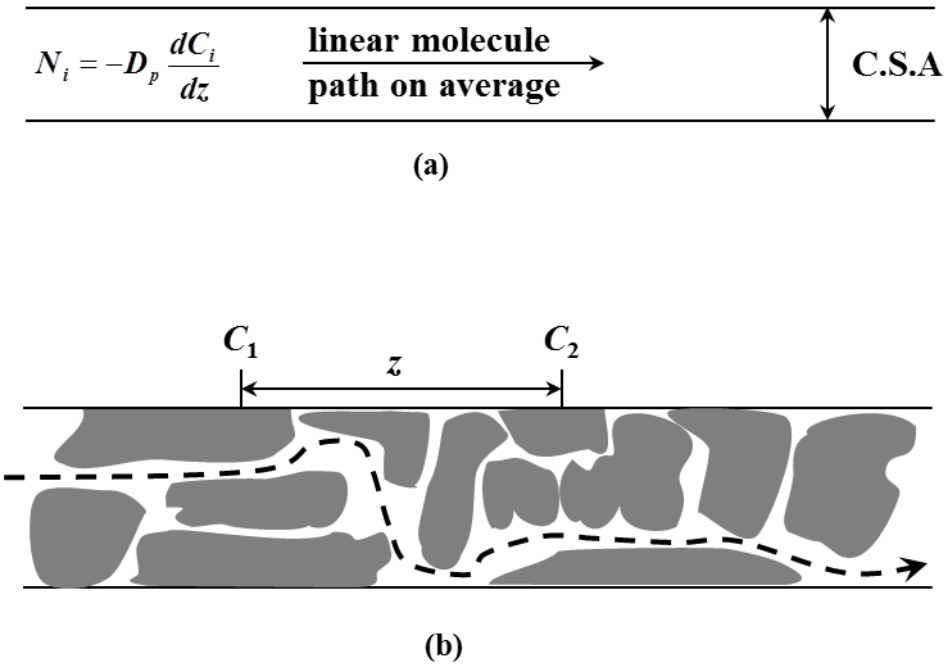

Figure 1.7: Comparison of (a) diffusion in a single pore with (b) diffusion in a porous pellet.

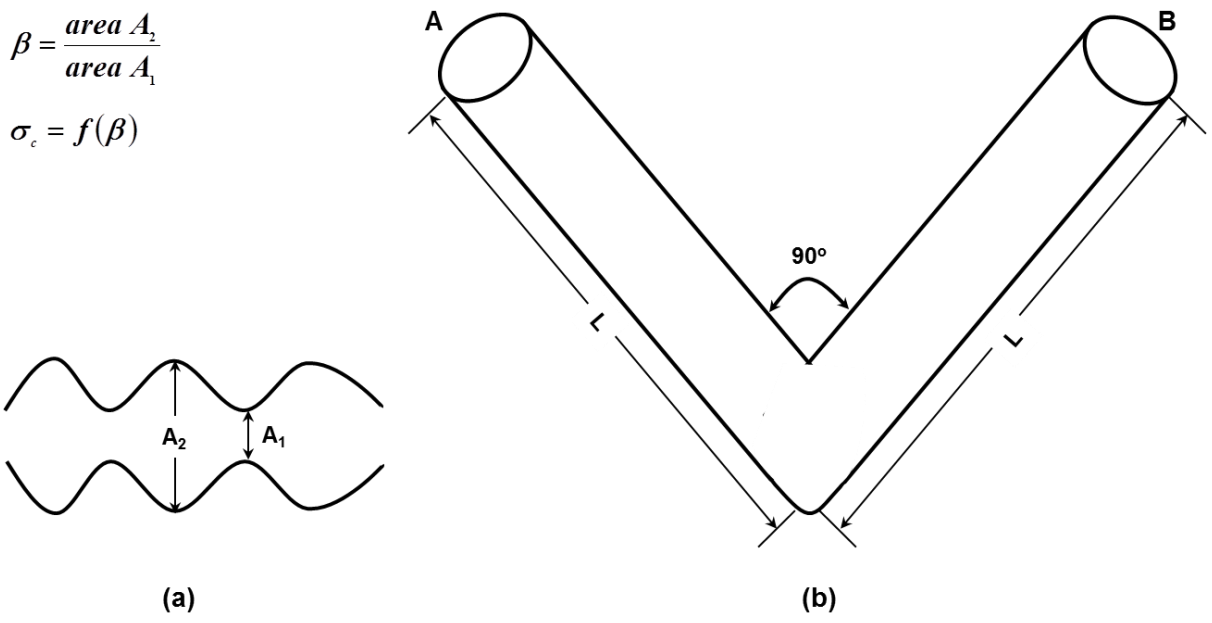

Figure 1.8: Pore characteristics: (a) pore constriction; (b) pore tortuosity, (adapted from Fogler (2004)).

As described in Webb (2001), the tortuosity factor characterises the efficiency of diffusion of fluids through a porous media. It is particularly important for diffusion-controlled processes where the solid support usually contains a pore network with pores ranging from micropores to macropores. The interconnected behaviour of these pores has a profound influence on the accessibility of reactants to the active sites and on the removal of products. The cross-sectional area available for diffusion in the porous pellet is:

$$A_{\text{tortuous}} = A\varepsilon_p \tag{1.4}$$

Therefore, the amount transferred in a porous pellet $(N_i)_{\text{tortuous}}$ is smaller than the amount transferred in a linear pore N_i. The amount of gas molecules which diffuses through the tortuous path is:

$$(N_i)_{\text{tortuous}} = \frac{-\varepsilon_p D_p}{\tau_p}\frac{dC_i}{dz} \tag{1.5}$$

where: – C_i is the gas concentration in the pores and has units: mol m_{pore}^{-3};

– $(N_i)_{\text{tortuous}}$ is the molar flux and with units: mol m_{pore}^{-2} s^{-1}.

Mass transfer inside various porous catalysts and absorbents is often quantified in terms of effective diffusivity, D_{eff}. However, the effective diffusivity cannot be interpreted as correcting bulk phase diffusivity (D_{AB}) by the reduction of the cross-sectional area because of the porous solid phase. The important reasons to prove this simple approach invalid are:

(a) interconnections within the pore structure, the tortuous character of individual pores and variations in cross-section area along the pore length make the diffusion become difficult, and

(b) one or more of several diffusion mechanisms may be responsible for the mass transfer process (Armatas *et al.*, 2005).

A large number of techniques have been employed to measure the effective diffusivity in porous solids. These techniques can be divided into two groups:

(i) steady-state methods; and

(ii) unsteady-state methods.

Steady-state methods: In the literature, these are mainly based on the classic Wicke-Kallenbach cell, and the effective diffusivity can be calculated according to the random pore model developed by Wakao and Smith (1962). According to Smith (1981), when adding up the various parallel contributions (i.e. diffusion in the mesopores and macropores), the following equation can be obtained:

$$D_{eff} = \varepsilon_M^2 D_M + \frac{\varepsilon_\mu^2 (1+3\varepsilon_M)}{1-\varepsilon_M} D_\mu \tag{1.6}$$

where:
- ε_μ and ε_M are the micropore (or mesopore) and macropore porosity respectively,
- the diffusion coefficients in the mesopores D_μ, and in the macropores D_M are a combination of the bulk and Knudsen diffusivities (Hayes and Kolaczkowski, 2000).

However, it should be emphasised that the data analysis from the Wicke-Kallenbach cell does not depend on the diffusion model (i.e. either random pore or parallel pore model). The mathematical models and equations used for steady-state method can be found in Hayes and Kolaczkowski (2000) and Zhang *et al.* (2004). In these papers, the effective diffusivity value calculated by random pore model was treated as a simple approximation and was used to compare with the D_{eff} result obtained by steady-state method.

The steady-state method suffers from some drawbacks i.e. the mounting procedures may restrict access to pores, and the diffusion reflects only those pores that allow passages of gas from one side of the pellet to the other (open pores). However, the dead-end pores as illustrated in Figure 1.2 are neglected (Guangsuo *et al.*, 2000).

Unsteady-state methods: These are generally based on the principle of chromatography. The chromatographic method for the evaluation of the effective diffusion coefficients in porous materials is well established (Schneider and Smith, 1968b; Haynes, 1988). Effective diffusivities are evaluated from the chromatographic response signal from a column packed with particles of the porous material to be tested. Porous particles with cylindrical or spherical shapes can be packed into the column in two types of configurations:

(i) Packed-bed arrangement (tube to particle diameter ratio = 15, and tube length to particle diameter ratio > 50 are often used);
(ii) Single Pellet String Column (SPSC): with a tube to particle diameter ratios from 1.1 to 1.7.

In Table 1.1 the results of a literature review are provided, illustrating: different column arrangements; column dimensions and ratios; carrier gas flowrates and tracer gas sample volumes. This information helps to select conditions which will be used in this thesis.

Table 1.1: Literature data for two column arrangements: packed-bed and SPSC.

	Column type	**Column internal diameter (i.d.) & Length (mm)**	**Particle diameter (mm)**	**Carrier gas flowrate (cm^3min^{-1})**	**Tracer gas pulse volume (cm^3)**	**Tube to particle diameter ratio (D_t / D_P)**	**Tube length to particle diameter ratio (L_t / D_P)**
Star ý *et al.* (2006)	S.P.S.C	i.d. = 8; L = 500	4.3 ×5.9 ×3	30 – 200 (Nitrogen)	0.273 (Argon, Helium)	1.4	85
		i.d. = 8; L = 1000					170
Armatas *et al.* (2005)	Packed bed	i.d. = 2	0.25	5 – 45 (Nitrogen)	0.1 (Helium)	8	440
		L = 110					
Guangsuo *et al.* (2000)	S.P.S.C	i.d. = 6	i.d. = 5.422	10 – 90 (He / N_2)	0.2 (N_2 / He)	1.1-1.4	123
		L = 668	L = 4.327				
Santos *et al.* (1996)	Packed bed	i.d. = 10.7	4 – 5	102 – 1020	0.5	27 / 21	1090 – 872
		L = 4360					
Garc á-Ochoa and Santos (1994)	Packed bed	i.d. = 10.7	4.5 – 5.7	80 – 900	0.5	2.4 / 1.9	271 – 214
		L = 1220					
Tang *et al.* (1987)	S.P.S.C	i.d. = 4; L = 395	3.18	N/A	0.2	1.26	124
		i.d. = 5; L = 600	4.76			1.05	126
		i.d. = 6; L = 900	4.85			1.24	186
Baiker *et al.* (1982)	S.P.S.C	i.d. = 5.8	4.9	$8.5 < F_1 < 26.5$ $9.0 < F_2 < 21.0$	0.15	1.1 – 1.7	82
		L = 400					

The chromatographic method is an unsteady-state method, which utilizes a pulse input, or a step change of a tracer gas of a known concentration, and injects this tracer gas into the carrier gas stream which flows at a constant flow through the column. The tracer concentration *versus* time curve (or the chromatographic response curve) is measured at the column outlet. For the step change method, the response curve follows either an upward increase in concentration (for an up-ward step input), or a downward decrease in concentration (downward step input). Various laboratory instruments could be used to measure the gas concentration, for example:

(i) **Gas chromatograph (GC):** experimental results using a GC are often reported in the literature.
(ii) **Mass spectrometer (MS):** this could be used, but experimental results using an MS for the purpose of measuring effective diffusivity using the chromatographic method have not been noticed in the literature.

In this thesis, a Hiden HPR-20 QIC Mass Spectrometer gas analyzer is used and this is shown in Figure 1.9. The chromatographic method of analysis was used based on the following experimental configuration:

(a) The packed-bed columns were designed and mounted individually.
(b) A Valco VICI 6-port injection valve with an electric actuator was used to create the pulse which was injected (this is similar to the injector on a GC).
(c) Small lines and fittings were used to minimize lags, and in-line back-mixing.

The chromatographic response of tracer gas (or the concentration of tracer gas over a time period) is monitored by a Secondary Electron Multiplier (SEM) detector connected to the RC interface unit shown in Figure 1.9. The SEM detector is chosen rather than a Faraday detector because of its high sensitivity (e.g. the typical scan range for SEM detector is between 10^{-13} – 10^{-7} torr, which is in the Ultra-high vacuum regime (UHV)).

In the MASsoft program, MID scans were selected. This means that the Multiple Ion Detection mode monitors a series of masses (or auxiliary inputs, or total pressure) and plots the signal intensity with respect to time. The vertical axis displays partial pressure and the horizontal axis displays time. Hence, raw experimental data (i.e. signal intensity *versus* time) in peak shapes are recorded. The concentration *versus* time data is calculated by analysing the

peak areas and correlating these with the total number of moles in the tracer sample. Based on the technical literature for the HPR-20 QIC gas analysis system, it has the following important features:

- A compact bench-top piece of analytical kit;
- Is capable of being operated at atmospheric pressure;
- Is robust, flexible, heated (up to 200 ℃) Quartz Inert Capillary (QIC);
- Has a direct capillary inlet (QIC) for less than 500 ms response to gases / vapours;
- Has a continuous sampling of 1 – 20 cm^3/min from 10 mbar to 2 bar;
- Has an automated flow control interface for constant ion source pressure;
- Has a high sensitivity (to 5 ppb), and a mass range to 510 amu (Atomic Mass unit);
- Is stable (less than ±0.5% height variation over 24 h).

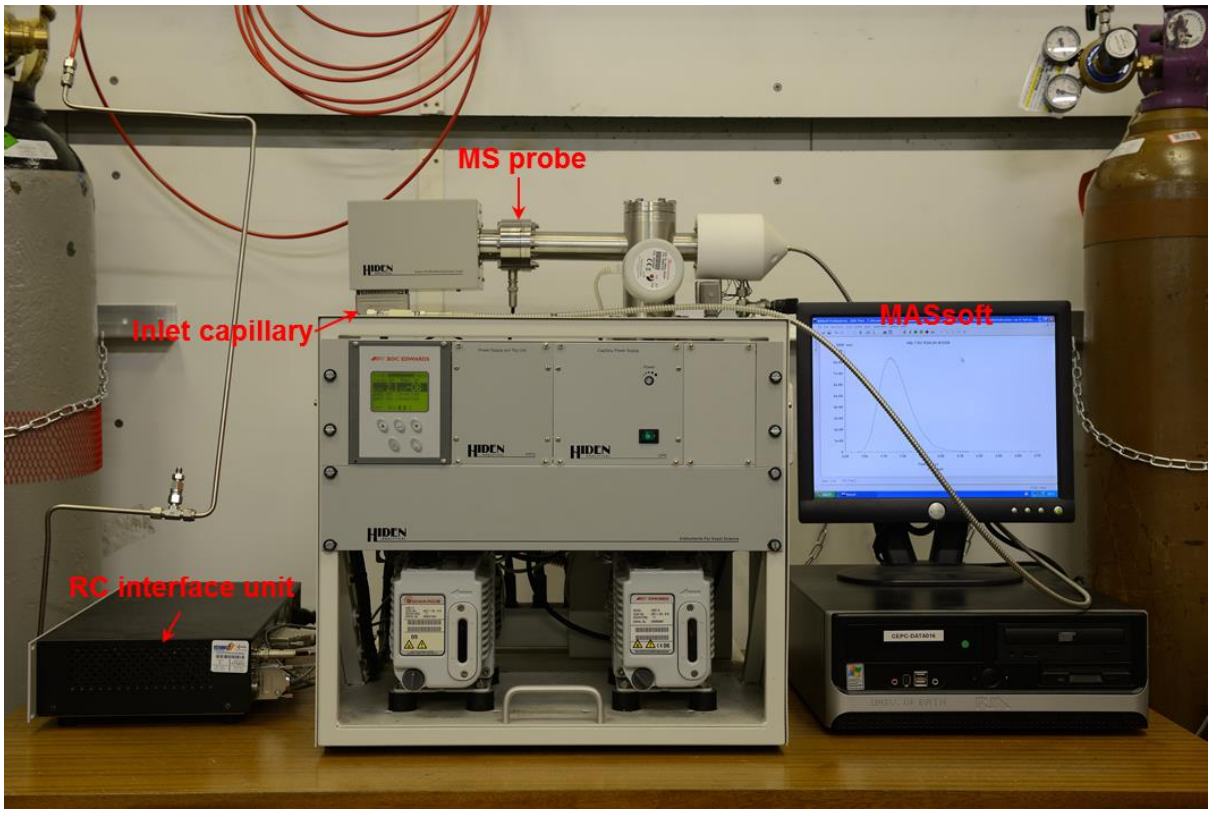

Figure 1.9: Mass spectrometer: a Hiden HPR-20 QIC gas analyzer connected with MASsoft.

1.3 Motivation for the research

Work on monoliths

(a) In the literature much work has been done on the measurement of effective diffusivity in pellets, but there have been very few studies performed on monoliths. The reason being that measurements on monoliths are difficult; because the layer of washcoat is very thin e.g. 20 to 100 μm (e.g. Sideris (1998) and Holder (2008))

(b) In a review paper by Kolaczkowski (2003), it was proposed that the viability of using the chromatographic technique should be explored further, as a method of measuring the effective diffusivity in catalytic monoliths. It was proposed that a number of monoliths could be mounted inside a single tube, such that the channels in the monoliths were aligned along the axis of the tube, see Figure 1.10.

(c) This suggestion led to the work described in Starý *et al.* (2006), in which the chromatographic technique was used to measure the effective diffusivity in catalytic monoliths. However, they did not align the monoliths as suggested in Kolaczkowski (2003), instead they packed cut sections of monolith in a random manner (see Figure 1.11). Unfortunately, there is a lack of information in Starý *et al.* (2006), to check exactly how the data was interpreted, and the extent of experimental errors in their method. At the University of Bath, Yap (2011) tried the chromatographic technique (using the configuration in Figure 1.10), but did not find it easy to apply it to a monolith, without encountering significant experimental errors. Therefore in this thesis, it was decided to have a closer look at the technique described in Starý *et al.* (2006).

Work on spherical pellets

Although there is much published work on spherical pellets, in most of that work, after the differential equations were derived, then the Laplace transformation methods were used to arrive at analytical solutions. The main motivation to include a study of pellets in this thesis was to understand the difficulties of applying the chromatographic technique. However, as will be found when reading this thesis, this involved a considerable amount of work to understand what had been published in the past, and then to apply this information to freshly acquired data in this thesis.

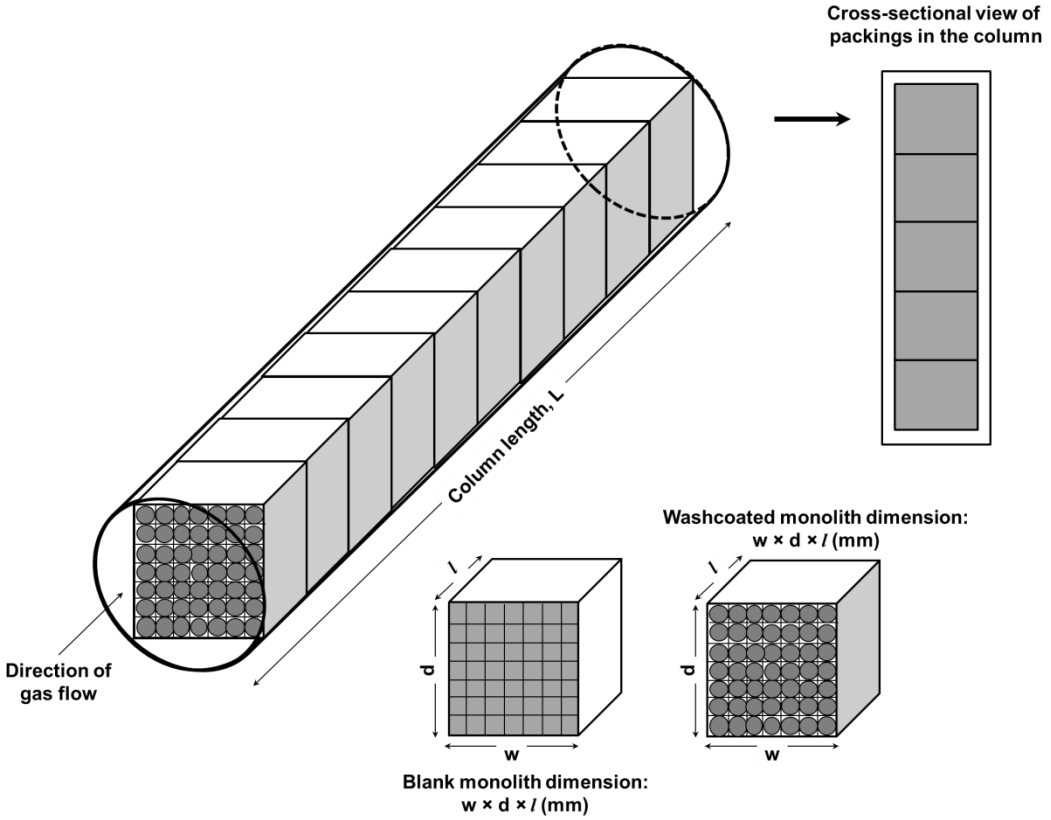

Figure 1.10: Schematic illustrating the positioning of monoliths for a chromatographic experiment (adapted from Kolaczkowski (2003)).

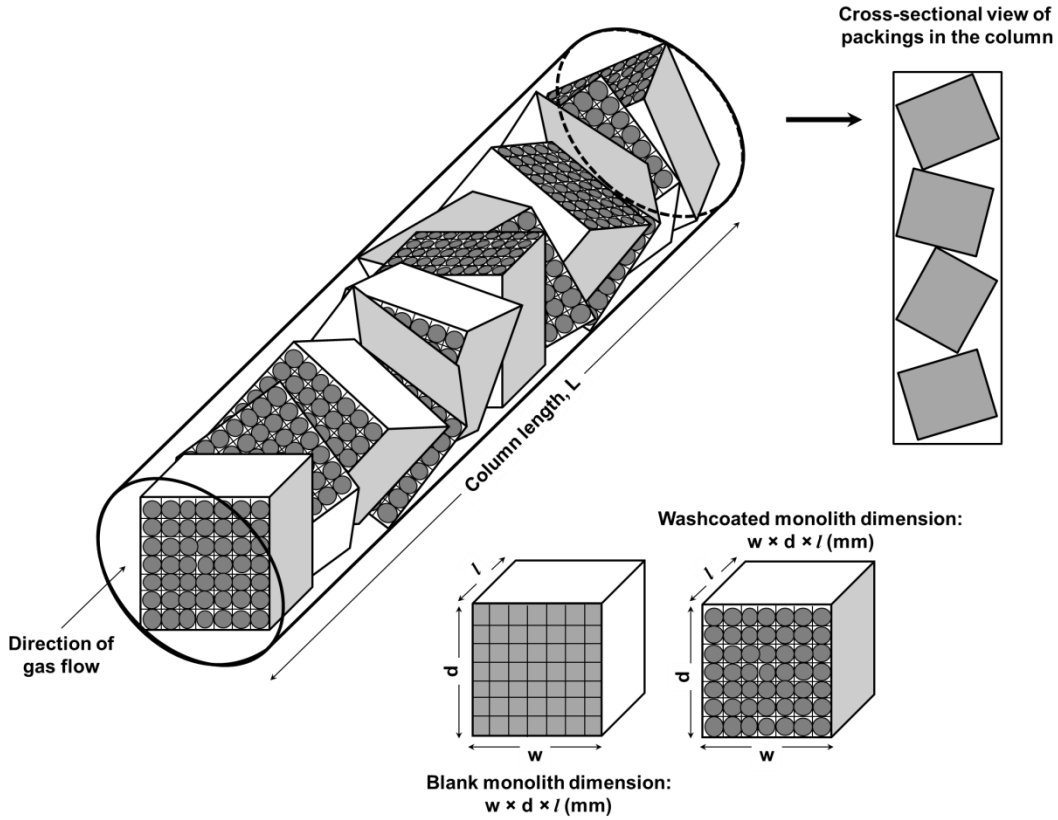

Figure 1.11: Schematic illustrating the positioning of monoliths for a chromatographic experiment (adapted from Staráý *et al.* (2006)).

1.4 Novelties in this work

At the start of this project, the novelty was focusing on application of apply chromatographic method on monoliths packed in the column. To study this, using the chromatographic technique is novel because only one paper was on this subject (i.e. Stará *et al.* (2006)). However, despite the fact that this paper had been published on Chemical Engineering Science Journal, there were concerns whether these claims were correct. So an important novelty aspect of this work is to explore this paper and investigate the gas chromatographic method in more details. As a results, from the main findings of this work on applying chromatographic method to cordierite and washcoated monoliths, using the same conditions as described in Stará *et al.* (2006) (i.e. Chapter 5), the author of this thesis concluded that the technique does not work as described in this paper. Hence, this is a novel observation and the author has quantified why it doesn't work.

In terms of this thesis, additional novel components come in because the detailed studies the author has done to the chromatographic technique on spherical γ-alumina beads. A lot of works had been published on measuring effective diffusivity of slab/cylindrical/spherical shape porous materials packed inside the column. However, many of these works were done between 1960 to 2004, some of them were difficult to follow, and some were lack of information. Besides, different mathematical models and equations were used. Among these works, there were no comparisons of these methods on the same set of experimental system. As a results, another important novelty of this work is that, the author has done detailed studies on comparing many of the well-documented methods using a consistent set of experimental results. This provides a comprehensive comparison of different methods & experimental techniques, and thereby the shortcomings of certain methods have been more clearly identified. In addition, new combinations of mathematical models were made and the results were satisfactory.

And to come back to the topic on monolith, in order to have confidence to criticize that work (i.e. Stará *et al.* (2006)). The knowledge on how the chromatographic method works on pellets is crucial.

1.5 Structure of this thesis

The overall structure of this thesis is illustrated in Figure 1.12, which shows the links between the chapters. It was decided to perform experiments on γ-alumina beads, glass beads, blank uncoated cordierite monolith, and γ-alumina washcoated monolith.

In **Chapter 2** physical properties are measured and also gathered on spherical pellets and monoliths studied, which are necessary to interpret the experimental results in the chapters that follow.

In **Chapter 3** the chromatographic technique is applied to measure residence time distribution (RTD) and moments are determined. These are used to evaluate equilibrium adsorption constants.

In **Chapter 4** the effective diffusivity of He in N_2, and N_2 in He, in spherical γ-alumina pellets is determined. To quantify axial dispersion terms in such packed beds, experiments were also performed with glass beads in the bed. External mass transfer coefficients are also determined. Making use of information on physical properties obtained in Chapter 2, the tortuosity factor is then calculated (using moment analysis, and analytical solutions based on Laplace transforms).

In **Chapter 5** the chromatographic technique is applied to measure the RTD of He in N_2, and N_2 in He, in washcoated and uncoated monoliths. Experiments were also performed with sections of monolith in two different orientations:

(a) channels aligned, as illustrated in Figure 1.10.
(b) random packing as illustrated in Figure 1.11 (this was referred to as a 'Single Particle String Column' in Staňý *et al.* (2006)).

This leads to some interesting observations, which relate to experimental errors (and limitations) with the application of this technique to monoliths.

Finally in **Chapter 6** conclusions are summarized and recommendations are presented for further work.

Note: All of the experimental work and modelling work described in this thesis, was performed by the author of this thesis. No other student was involved in the experimental work, or the development or execution of the calculations described in this thesis.

The author also constructed the experimental apparatus that was used for the chromatographic experiments.

However, help with the initial use of the analytical equipment, the MS and equipment to measure pore size and volume (etc), was obtained from colleagues. Also, the information on the physical properties of the monoliths was obtained from Yap (2011).

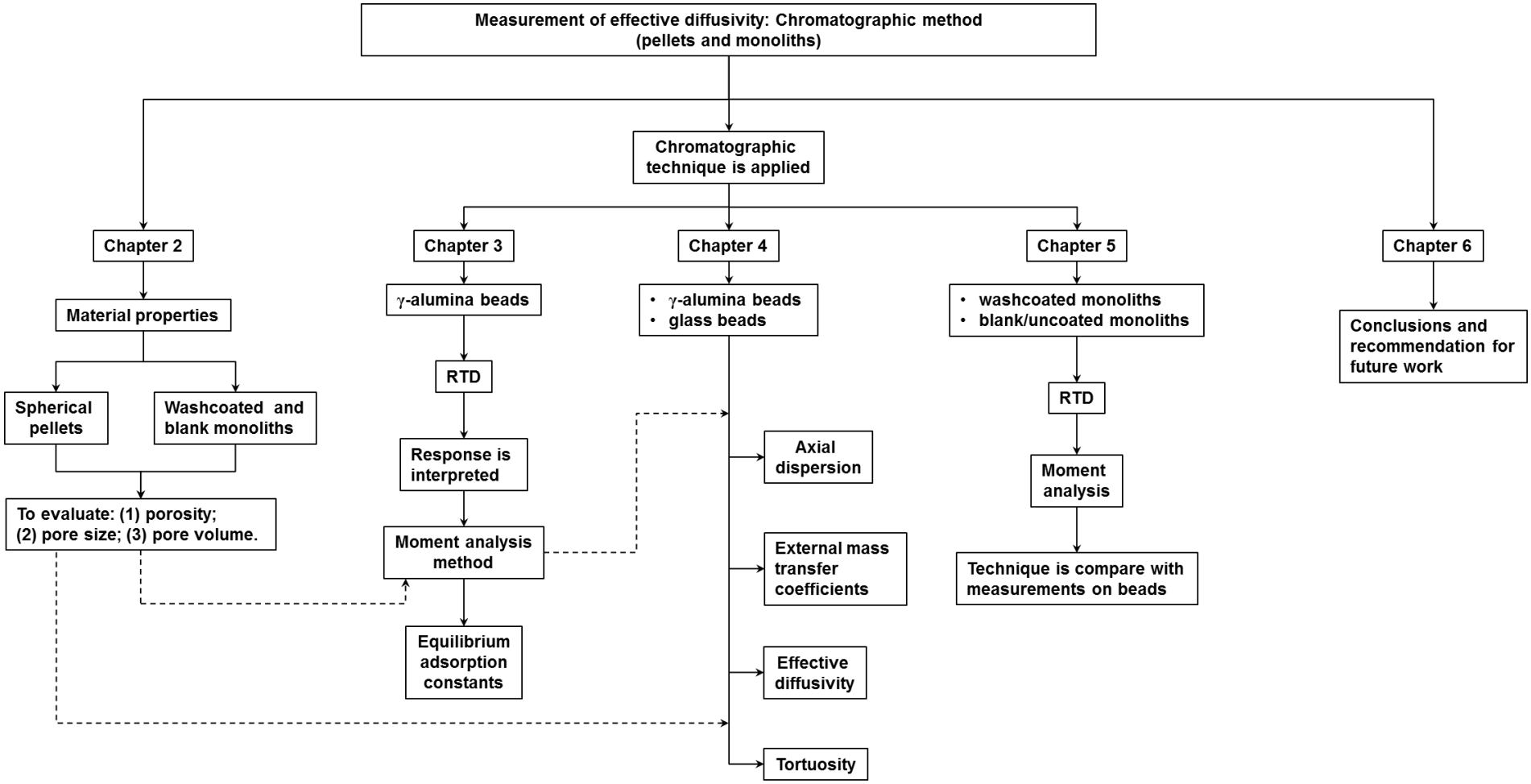

Figure 1.12: Simplified structure of the thesis and links between chapters

References

Armatas, G., Petrakis, D. & Pomonis, P., 2005. Estimation of diffusion parameters in functionalized silicas with modulated porosity: Part I: Chromatographic studies. *Journal of Chromatography A,* 1074, pp. 53-59.

Atkins, William, P. & De Paula, J., 2006. *Atkins' Physical Chemistry.* Oxford University Press.

Baiker, A., New, M. & Richarz, W., 1982. Determination of intraparticle diffusion coefficients in catalyst pellets: a comparative study of measuring methods. *Chemical Engineering Science,* 37, pp. 643-656.

Bird, R.B., Stewart, W.E. & Lightfoot, E.N., 1960. *Transport phenomena.* Wiley New York.

Fogler, H.S., 2004. *Elements of Chemical Reaction Engineering.* Pearson Education.

Garc á-Ochoa, F. & Santos, A., 1994. Effective diffusivity under inert and reaction conditions. *Chemical Engineering Science,* 49, pp. 3091-3102.

Gary, J.H. & Handwerk, G.E., 2001. *Petroleum Refining: Technology and Economics.* CRC Press.

Gregg, S. & Sing, K., 1982. Adsorption, Surface Area and Porosity Academic. *New York,* pp. 242-245.

Guangsuo, Y., Jianguo, Y. & Zunhong, Y., 2000. The measurement of effective diffusivity for sulfur-tolerant methanation catalyst. *Chemical Engineering Journal,* 78, pp. 141-146.

Hayes, R.E. & Kolaczkowski, S.T., 1997. *Introduction to catalytic combustion.* Gordon and Breach.

Hayes, R.E. & Kolaczkowski, S.T., 2000. Evaluating the effective diffusivity of methane in the washcoat of a honeycomb monolith. *Applied Catalysis B: Environmental,* 25, pp. 93-104.

Haynes, H.W., 1988. The experimental evaluation of catalyst effective diffusivity. *Catalysis Review-Science and Engineering,* 30, pp. 363–627.

Hoff, R.E. & Mathers, R.T., 2010. *Handbook of transition metal polymerization catalysts.* Wiley Online Library.

Holder, R., 2008. *A Global Reaction Mechanism for Transient Simulations of Three-Way Catalytic Converters.* Cuvillier Verlag.

Jarrah, N., van Ommen, J.G. & Lefferts, L., 2003. Development of monolith with a carbon-nanofiber-washcoat as a structured catalyst support in liquid phase. *Catalysis Today,* 79–80, pp. 29-33.

Kolaczkowski, S.T., 2003. Measurement of effective diffusivity in catalyst-coated monoliths. *Catalysis Today,* 83, pp. 85-95.

Malek, K. & Coppens, M.-O., 2003. Knudsen self-and Fickian diffusion in rough nanoporous media. *The Journal of chemical physics,* 119, p. 2801.

Mason, E.A. & Malinauskas, A., 1983. *Gas transport in porous media: the dusty-gas model.* Elsevier Amsterdam.

Nijhuis, T.A., Beers, A.E.W., Vergunst, T., Hoek, I., Kapteijn, F. & Moulijn, J.A., 2001. Preparation of monolithic catalysts. *Catalysis Reviews,* 43, pp. 345-380.

Pollard, W. & Present, R., 1948. On gaseous self-diffusion in long capillary tubes. *Physical Review,* 73, p. 762.

Pollington, S., Poulston, S., Torbati, R. & Rajaram, R.R., 2003. Exhaust system including hydrocarbon SCR catalyst. WO Patent 2,003,033,118.

Santos, A., Bahamonde, A., Avila, P. & Garcia-Ochoa, F., 1996. Measurement of the effective diffusivity for a vanadia-tungsta-titania/sepiolite catalyst for SCR of NO_x. *Applied Catalysis B: Environmental,* 8, pp. 299-314.

Satterfield, C.N., 1981. *Mass transfer in heterogeneous catalysis.* RE Krieger Publishing Company.

Schirmer, W., 1995. Molecular Transport and Reaction in Zeolites—Design and Application of Shape Selective Catalysis. *Zeitschrift für Physikalische Chemie,* 191, pp. 282-282.

Schneider, P. & Smith, J.M., 1968. Adsorption rate constants from chromatography. *AIChE Journal,* 14, pp. 762-771.

Sideris, M., 1998. *Methods for monitoring and diagnosing the efficiency of catalytic converters: a patent-oriented survey.* Elsevier Science.

Smith, J.M., 1981. *Chemical engineering kinetics.* McGraw-Hill.

Starý, T., Solcová, O., Schneider, P. & Marek, M., 2006. Effective diffusivities and pore-transport characteristics of washcoated ceramic monolith for automotive catalytic converter. *Chemical Engineering Science,* 61, pp. 5934-5943.

Tang, G.H.Y., Trimm, D.L. & Wainwright, M.S., 1987. Effective diffusivity in cylindrical catalyst pellets. *Chemical engineering in Australia,* 12, pp. 9-12.

Wörner, S. & Sigel, U., 2005. Exhaust gas system. U.S. Patent No. 6,938,729. Washington, DC: U.S. Patent and Trademark Office.

Wakao, N. & Smith, J.M., 1962. Diffusion in catalyst pellets. *Chemical Engineering Science,* 17, pp. 825-834.

Webb, P.A., 2001. An introduction to the physical characterization of materials by mercury intrusion porosimetry with emphasis on reduction and presentation of experimental data. Micromertics Instrument Corp.

Wheeler, A., 1955. Reaction rates and selectivity in catalyst pores. *Catalysis,* 2, pp. 105-165.

Yap, Y., 2011. *On-line and on-engine catalyst characterisation – effective diffusion and reaction mechanisms.* Phd, University of Bath.

Zhang, F., Hayes, R. & Kolaczkowski, S., 2004. A new technique to measure the effective diffusivity in a catalytic monolith washcoat. *Chemical Engineering Research and Design*, 82, pp. 481-489.

2 Material properties

In this chapter, information is gathered on the following samples:

- Ceramic monoliths (400 cpsi without any washcoat).
- Ceramic monoliths (400 cpsi with γ-alumina washcoat).
- Spherical γ-alumina beads (1 mm diameter).

The physical properties of beads and monoliths are important because this information was expected to be necessary to support the analysis in the chapters that follow. The work done in this chapter is summarised in Figure 2.1.

Some of the information on physical properties was obtained in order to compare the characteristics of the γ-alumina material in the washcoat *versus* its bead form.

Other information was obtained as it was expected to be required to support the analysis of data from the chromatographic analysis experiments in the chapters that follow.

Much of the information on the physical properties of the washcoated monoliths was already available in Yap (2011). However, measurements had to be performed on the γ-alumina beads. As these measurements were done by the author of this thesis, the theory that supports these measurements had to be understood, and so this is included in the descriptions that follow providing also a record of the decisions made.

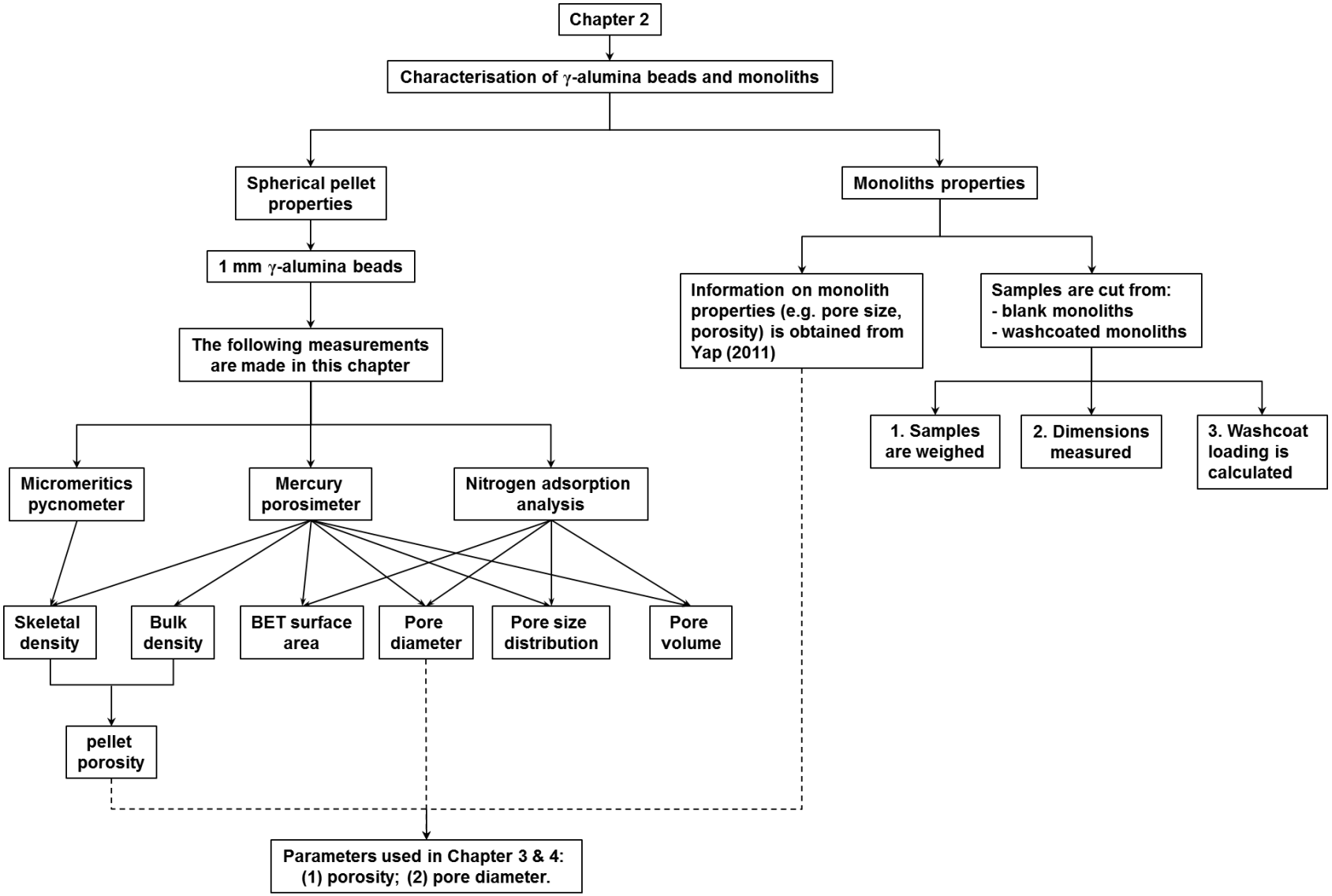

Figure 2.1: Structure of Chapter 2 and links with other chapters

2.1 Properties of the monolith samples

For a different project on the performance of a Diesel Oxidation Catalyst (DOC), samples were supplied by Johnson Matthey (UK). From that set of samples, a blank cordierite monolith (DOC-JM-B) with 400 cpsi (cells per square inch) and a washcoated cordierite monolith (DOC-JM-WC) were used. A picture showing the difference between these two monoliths is shown in Figure 2.2.

Much of the information on the samples of monolith that will be used, had already been measured by Yap (2011), this is summarised in Table 2.1.

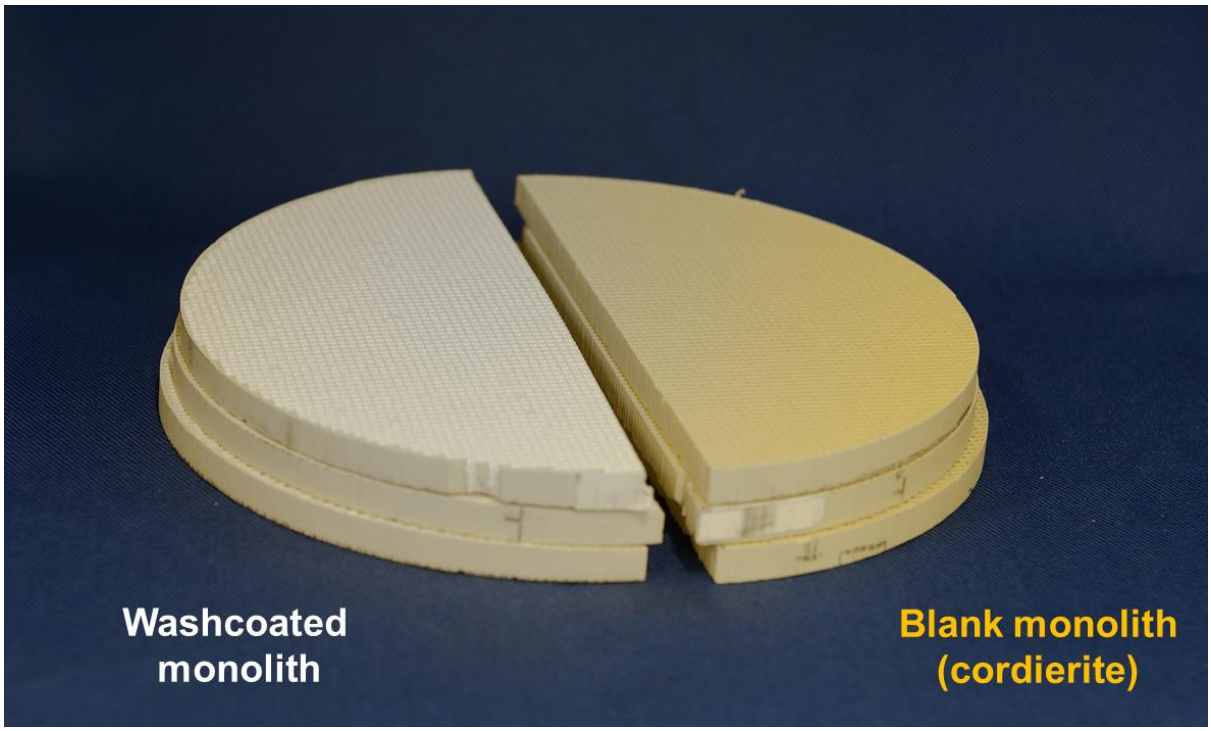

Figure 2.2: Comparison between washcoated and blank monoliths manufactured by Johnson Matthey (UK). Each slice has a thickness of 5.0 mm and was cut from monolith blocks.

Table 2.1: Information on monolith properties obtained from Yap (2011).

Physical properties		**Measured properties of cordierite uncoated monolith**	**Calculated properties of γ-alumina washcoat** [(a)]
Bulk density (g cm^{-3})		1.1123 ± 0.1363	0.8924
Skeletal density (g cm^{-3})		2.4539 ± 0.2306	2.1553
Porosity		0.5467	0.5860
Pore diameter (nm)		2000 – 5000	11.056
Washcoat BET surface area (m^2 g^{-1})		N/A	168.157
Pore volume (cm^3 g^{-1})		0.233	0.5653
Dimensions	**cell density**	400 cpsi	400 cpsi
	cell size (mm)	1 mm × 1 mm	N/A
	cell wall thickness (μm)	175.403 ± 5.209	175.403 ± 5.209
	washcoat thickness (μm)	0	28.74 to 201.25

Note: (*a*): Values of the properties of the washcoated were calculated from measurements taken on uncoated cordierite and washcoated cordierite monolith samples.

2.1.1 Monolith sample weight and dimensions

From the monolith slices shown in Figure 2.2, square shaped samples were cut (i.e. 4 cells in a row × 3 cells in a column, 12 cells in total). Examples of the square shaped samples (i.e. washcoated and blank) are shown from Figure 2.3 to Figure 2.5. As reported in Yap (2011), the thickness of the washcoat can vary depending on the position from which the sample is taken from the monolith block (see Table 2.2).

Table 2.2: Monolith catalyst information obtained from Yap (2011).

Sample	**Cordierite thickness, θ (mm)**	**Channel width (mm)**	**Washcoat thickness [(a)] (mm)**	**Channel equiv. radius, R [(a)] (mm)**
Cordierite/Blank monolith	0.1754	1.0 × 1.0	N/A	N/A
Washcoated monolith (Entrance)	0.1754	1.0 × 1.0	0.0287	0.6044
Washcoated monolith (Quarter)	0.1754	1.0 × 1.0	0.0865	0.5367
Washcoated monolith (Middle)	0.1754	1.0 × 1.0	0.2013	0.3931
Washcoated monolith (Average)	0.1754	1.0 × 1.0	0.1055 ± 0.0878	0.5189 ± 0.1079

Note: (*a*) The washcoat thickness and channel equivalent radius were measured optically using scan electron microscopy (SEM).

In this thesis, samples were cut from sections that had a thin layer of washcoat (see Figure 2.3) and also from sections which had a thicker layer (Figure 2.4). This is reflected in the data presented in Table 2.3. As the samples used were from different parts of the monoliths, average values were calculated.

The schematic diagrams showing the cordierite thickness θ for blank monolith, and the channel equivalent radius, R, for the washcoated monolith are shown in Figures 2.6 and 2.7 respectively.

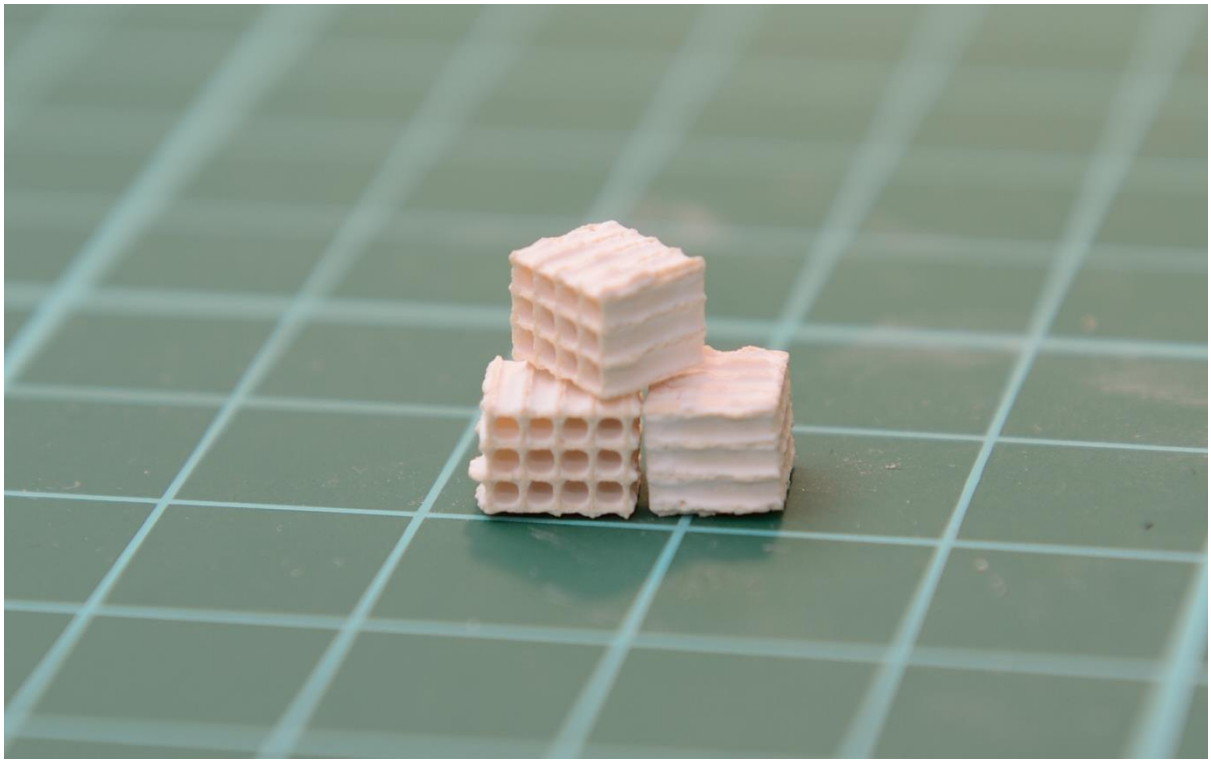

Figure 2.3: Square shaped washcoated (thin) monoliths.

Figure 2.4: Square shaped washcoated (thick) monoliths.

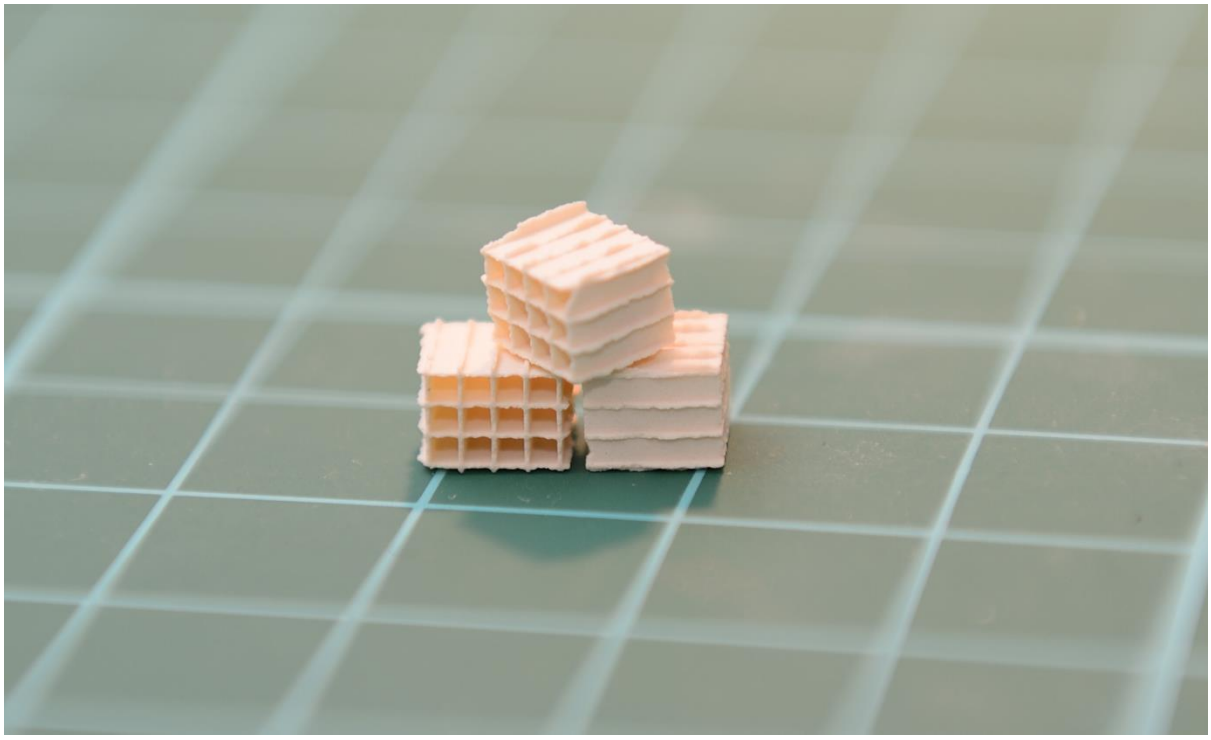

Figure 2.5: Square shaped blank monoliths (cordierite).

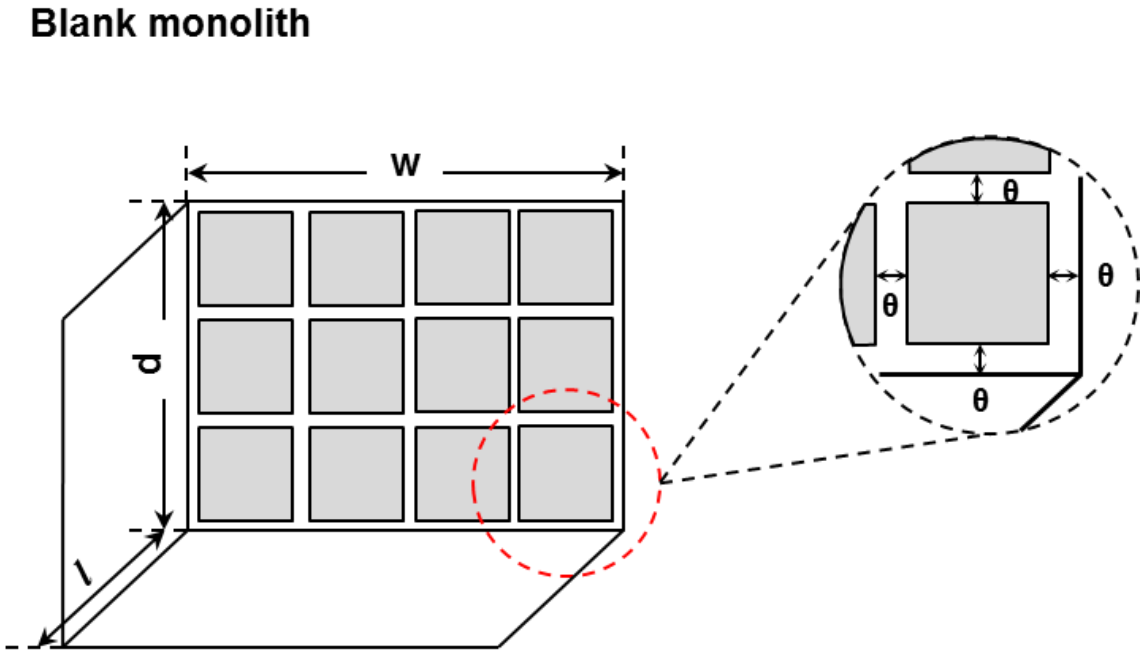

Figure 2.6: Schematic diagram shows a blank monolith with specified dimensions (w × d × *l*) and cordierite thickness *θ*.

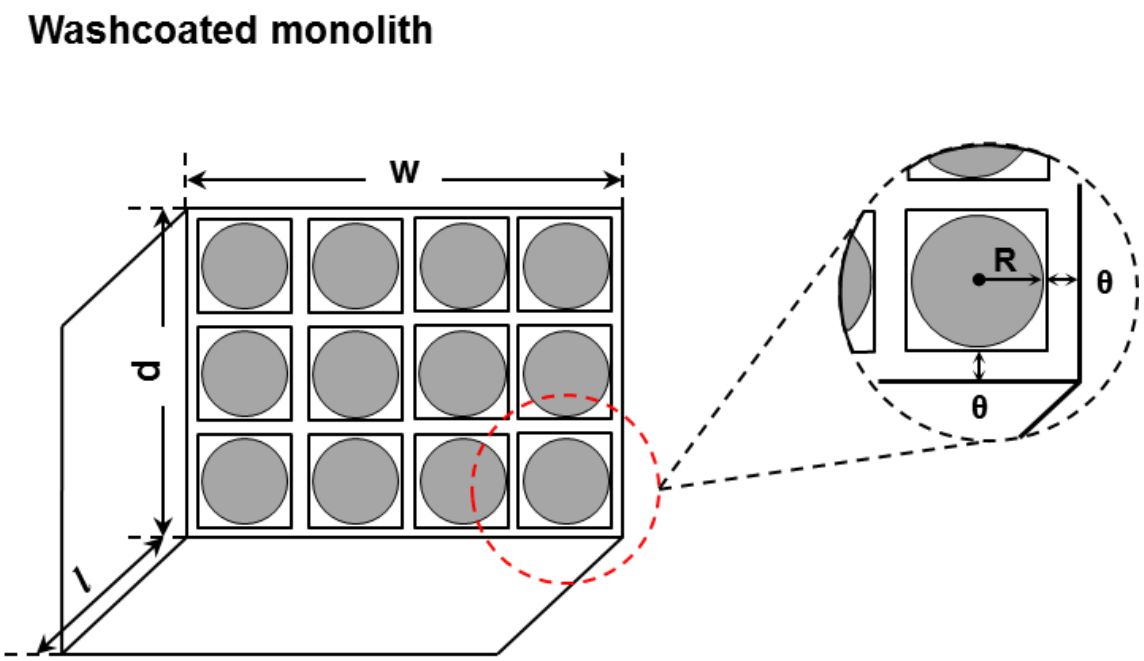

Figure 2.7: Schematic diagram shows a washcoated monolith with dimensions (w × d × *l*), cordierite thickness *θ* and channel equivalent radius *R*.

Table 2.3: Monoliths: weight and dimensions measured (12 cells per sample).

Sample		Weight (g)	Dimension (w × d × *l*) (mm)	Monolith volume including channels (cm^3)
Cordierite/ Blank monolith	**1**	0.0622	6.09 × 4.80 × 5.30	0.1549
	2	0.0598	5.96 × 4.55 × 5.26	0.1426
	3	0.0598	5.82 × 4.74 × 5.22	0.1440
	Ave.	**0.0606 ± 0.0011**	**5.96 × 4.70 × 5.26**	**0.1472 ± 0.0055**
Washcoated monolith (thin)	**1**	0.0770	5.70 × 4.76 × 4.92	0.1335
	2	0.0768	5.55 × 4.79 × 4.96	0.1319
	3	0.0747	5.73 × 4.55 × 4.76	0.1241
Washcoated monolith (thick)	**1**	0.0989	5.80 × 4.72 × 5.21	0.1426
	2	0.1010	6.30 × 4.79 × 5.21	0.1572
	3	0.1052	6.10 × 4.93 × 5.23	0.1573
Washcoated monolith (average)	**1**	0.0880	5.75 × 4.74 × 5.07	0.1381
	2	0.0889	5.93 × 4.79 × 5.09	0.1443
	3	0.0899	5.92 × 4.74 × 5.00	0.1401
	Ave.	**0.0889 ± 0.0008**	**5.87 × 4.76 × 5.05**	**0.1408 ± 0.0026**

Note: The abbreviation 'Ave.' stands for 'Average'.

The skeletal volumes of blank and washcoated monoliths used in this thesis (i.e. exclude the total volume of empty channel cells but contains the volume of pore voids) are calculated and the results are summarised in Table 2.4.

Table 2.4: Monolith volume excluding the volume of channels.

Sample		**Monolith length (mm)**	**Total volume of 12 channels (cm^3)**	**Monolith volume excluding channels (cm^3)**
Cordierite/ Blank monolith	**1**	5.30	0.0636	0.0913
	2	5.26	0.0631	0.0795
	3	5.22	0.0626	0.0814
	Ave.	**5.26 ± 0.03**	**0.0631 ± 0.0004**	**0.0841 ± 0.0052**

Sample		**Monolith length (mm)**	**Channel equivalent radius, *R* (mm)**	**Total volume of 12 channels (cm^3)**	**Monolith volume excluding channels (cm^3)**
Washcoated monolith (thin)	**1**	4.92	0.5705 [(a)]	0.0604	0.0731
	2	4.96	0.5705 [(a)]	0.0609	0.0710
	3	4.76	0.5705 [(a)]	0.0584	0.0657
Washcoated monolith (thick)	**1**	5.21	0.3931	0.0304	0.1123
	2	5.21	0.3931	0.0304	0.1269
	3	5.23	0.3931	0.0305	0.1268
Washcoated monolith (average)	**1**	5.07	0.5189	0.0514	0.0866
	2	5.09	0.5189	0.0516	0.0927
	3	5.00	0.5189	0.0507	0.0893
	Ave.	**5.05 ± 0.04**	**0.5189 ± 0.1079**	**0.0513 ± 0.0004**	**0.0896 ± 0.0025**

Note: (*a*): The channel equivalent radius for washcoated monolith (thin) is calculated by averaging the channel equivalent radii (Entrance and Quarter) shown in Table 2.2 for washcoated monoliths.

2.2 Properties of the spherical pellets

A picture of the 1 mm γ-alumina beads used in this thesis is shown in Figure 2.8, and this can be compared with samples of non-porous glass beads shown in Figure 2.9.

Figure 2.8: SASOL alumina beads diameter: 1.0 mm with 98% Al_2O_3, and with porous surface area of 157 m^2 g^{-1} (manufacturer data).

Figure 2.9: Non-porous glass beads (diameter: 1 mm).

2.2.1 Pellet weight and bulk volume

The results of measurements are summarised in Table 2.5.

Table 2.5: General physical properties of γ-alumina beads.

Labware type	Tare weight (g)	Pellet quantity	Net weight (g)	Pellet volume (cm^3)	Single pellet weight (g)
Plastic cup	2.0147	21	2.0326	5.236×10^{-4}	0.00085
Plastic vial	1.0160	10	1.0240	5.236×10^{-4}	0.00080
Glass beaker	13.6347	38	13.6681	5.236×10^{-4}	0.00088
None	0.0000	20	0.0158	5.236×10^{-4}	0.00079
				Average	0.00083 ± 0.00004

2.2.2 Pellet density and porosity

The skeletal density of the γ-alumina beads can be measured by:

(i) Micromeritics Accupyc 1330 Pycnometer;

(ii) Micromeritics Autopore III Mercury Porosimeter.

The bulk density can also be obtained from mercury porosimeter but not the pycnometer. Other textural properties of the alumina sample as provided by the manufacturer SASOL are shown in Table 2.6.

Table 2.6: Textural properties of γ-alumina beads (SASOL, 2009).

γ-alumina beads			
Surface area ($m^2\ g^{-1}$)	157	Median diameter (mm)	1.03
Packed bulk density ($g\ cm^{-3}$)	0.77 – 0.81	*Si* – content (ppm)	64
Side crushing strength (N)	52	*Fe* – content (ppm)	107
Al_2O_3 – content (%)	97.7	*Ti* – content (ppm)	15

According to Webb (2001):

a) **Bulk volume** (as applied to a collection of pieces): is the sum of the volumes of the solids in each piece, the voids within the pieces and the voids among the pieces.
b) **Envelope volume** (as applied to a single piece): is the volume of a particle or monolith as would be obtained by tightly shrinking a film around it. In other words, it is the sum of volumes of the solid components, the open and closed pores within each piece, and the voids between the surface features of the material and the close-fitting imaginary film that surrounds the piece.
c) **Bulk density:** is equal to the total material mass divided by the bulk volume or envelope volume.
d) **Skeletal volume** (as applied to discrete pieces of solid material): is the sum of the volumes of the solid material in the pieces and the volume of closed pores within the pieces.
e) **True volume**: is the volume only of the solid material, excluding the volume of open pores and closed pores.
f) **Skeletal density**: is equal to the total material mass divided by the skeletal volume or true volume.

The skeletal volume as determined by mercury porosimetry and helium pycnometry may differ because mercury cannot intrude into small micropores (i.e. pore diameters equal to or less than 0.002 μm or 2 nm). Hence, for porous particles with pore diameter between microporous (< 2 nm) and mesopore ($2 < d_p < 50$ nm) range (Gregg and Sing, 1982), the skeletal density measured by pycnometer is always higher than mercury porosimeter data.

The skeletal density and bulk density are calculated as follows:

$$\text{Skeletal density} = \frac{\text{Mass of sample}}{\text{Volume of sample (not including voids)}} \tag{2.1}$$

$$\text{Bulk density} = \frac{\text{Mass of sample}}{\text{Volume of sample (including voids)}} \tag{2.2}$$

The mathematical forms of Equations (2.1) and (2.2) are:

$$\rho_{skeletal} = \frac{M_{solid}}{V_{solid}} \tag{2.3}$$

$$\rho_{bulk} = \frac{M_{solid}}{V_{total}} \tag{2.4}$$

where M_{solid} is the mass of the sample, V_{solid} is the volume of sample not including voids and V_{total} is the volume of sample including voids.

The porosity of a sample is deduced according the following equations:

$$\varepsilon_{particle} = \frac{V_{void}}{V_{void} + V_{solid}} \tag{2.5}$$

$$V_{void} = V_{total} - V_{solid} \tag{2.6}$$

Substitute Equation (2.6) into Equation (2.5)

$$\varepsilon_{particle} = \frac{V_{total} - V_{solid}}{V_{total}} \tag{2.7}$$

Combining Equation (2.7) with Equations (2.3) and (2.4)

$$\varepsilon_{particle} = \frac{\left[\frac{M_{solid}}{\rho_{bulk}} - \frac{M_{solid}}{\rho_{skeletal}}\right]}{\left(\frac{M_{solid}}{\rho_{bulk}}\right)} = 1 - \frac{M_{solid}}{\rho_{skeletal}} \times \frac{\rho_{bulk}}{M_{solid}} = \frac{\rho_{skeletal} - \rho_{bulk}}{\rho_{skeletal}} \tag{2.8}$$

where:
- $\varepsilon_{particle}$ is the porosity of the sample,
- V_{void} is the volume of the voids in the sample,
- V_{total} is the combined volume of the voids and the sample,
- $\rho_{skeletal}$ is the skeletal density or true density, and
- ρ_{bulk} is the bulk density.

Experimental and preparation procedures for pycnometer

To measure the skeletal density using the pycnometer, alumina spheres are pre-treated in an oven at a constant temperature of 200 ^{o}C for one hour before inserting into the cell chamber. The pycnometer cell volume is checked and calibrated for every experimental run. Experiments with pycnometer were repeated at least three times to ensure the reliability of results.

The skeletal densities obtained from the pycnometer, the calculated bulk densities based on mass to volume ratio (*m*/*V*), and the calculated porosity for the γ-alumina beads are summarised in Table 2.7.

Table 2.7: Skeletal and bulk density of γ-alumina beads (obtained from pycnometer and *m*/*V* ratio).

γ-alumina beads	**Skeletal density, $\rho_{skeletal}$ (g cm^{-3})**	**Bulk density, ρ_{bulk} (g cm^{-3})**	**Porosity, ε**
Exp. run 1	3.3885 ± 0.0029	1.5852 [(a)]	0.5322
Exp. run 2	3.3810 ± 0.0030	1.5852 [(a)]	0.5311
Average	3.3848 ± 0.0038	1.5852 [(a)]	0.5317 ± 0.0006

Note: (*a*): Bulk density of γ-alumina beads is calculated based on the single pellet weight and volume listed in Table 2.5.

2.2.3 Nitrogen adsorption measurements

2.2.3.1 Introduction

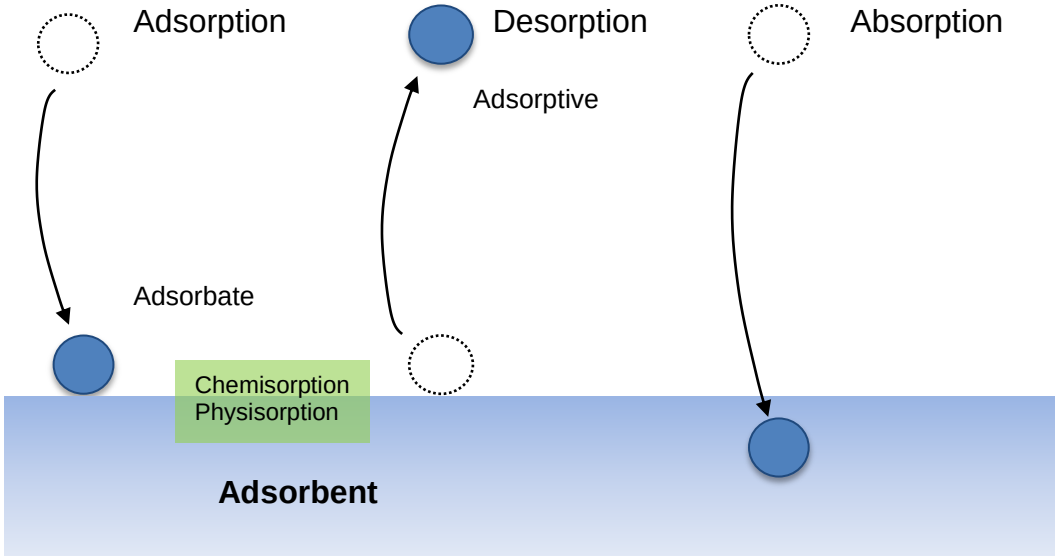

Figure 2.10: A visualisation of adsorption, desorption and absorption (adapted and redrawn from *Seminar on Adsorption*, BEL JAPAN).

According to Rouquerol *et al.* (1999), there are two types of adsorption methods to characterise the surface area and pore size of a solid material. The first one is physical adsorption or physisorption, known as bonding between molecules and the surface by weak Van der Waals forces. The second one is chemical adsorption or chemisorption, which means a chemical bond is formed between molecules and the surface during the adsorption process.

The explanations that follow are based on description in Anderson and Pratt (1985), Imelik and Vedrine (1994), and Micromeritics (2011). For physisorption, gas adsorption measurements are widely used to determine the surface area and pore size distribution of different solid material. The Micromeritics Accelerated Surface Area and Porosity System (ASAP) 2020 was used to characterise the γ-alumina beads in this thesis. The ASAP system uses N_2 (or H_2, CO_2, Ar and Kr) gas adsorption at a liquid nitrogen temperature (77.3 K) to obtain: the adsorption-desorption isotherms, and surface area and pore size distribution of solid material. The adsorptive gas is dosed and admitted to the sample flask with accuracy, while the adsorbent (solid sample) uptakes the analysis gas at specific relative pressures and temperature. The amount adsorbed, V (cm^3 g^{-1} STP), are measured in equilibrium and plotted

against relative pressure to give the adsorption isotherm. The relative pressure, P/P_0, is the adsorptive gas pressure P divided by the vapour pressure P_0 of N_2 at the relative temperature.

Experimental and preparation procedures for ASAP 2020

Full adsorption/desorption micro/mesoporous analysis is performed on γ-alumina beads. The following experimental steps were involved (Micromeritics, 2011):

1. Before starting the nitrogen adsorption measurements, the sample is degased in-situ at 150 ^{o}C for 480 minutes.
2. After degasing, the sample container is cooled and the dry mass of absorbent is calculated.
3. For the full adsorption-desorption analysis, adsorptive gas nitrogen at 77.3 K is dosed in low pressure (incremental dose mode at 3 cm^3 g^{-1} STP), and the amount of N_2 adsorbed by the adsorbent is measured at equilibrium with an equilibration interval of 45 s, and the applied relative pressure ranges from P/P_0 = 0.00001 to P/P_0 = 0.995.
4. The maximum applied pressure is the vapour saturated pressure of nitrogen at 1 atm. The vapour pressure of N_2 (P_0) is calculated at each elevated temperature and pressure for gas adsorption/desorption for two reasons: firstly, to prevent condensation in the chamber due to over-pressure, and secondly, to enable the calculation of the relative pressure P/P_0 at the sample.
5. The vapour pressure is calculated according to Antoine equation shown in Equation (2.9).
6. After reaching the maximum relative pressure P/P_0 = 1, the procedure is repeated the other way around (desorption). The surface area and pore size analysis is performed using this volumetric method, which is based on the amount of N_2 gas adsorbed and desorbed.
7. The assessment of physisorption data for gas/solid system is in accordance to IUPAC recommendation (Sing *et al.*, 1985). A *T*-plot method was used to access the microporosity of the γ-alumina sample. The micropore volume recorded was 0.004284 cm^3 g^{-1}, which is almost negligible compared to the volume adsorbed: 284.8831 cm^3 g^{-1} STP. Therefore micropore analysis was ignored.

According to Antoine equation (Boubl ƙ *et al.*, 1984):

$$\log_{10} P = A - \frac{B}{T + C} \tag{2.9}$$

where: – P is the vapour pressure in bar
– T is temperature in Kelvin
– A, B and C are constants

The Antoine equation is a vapour pressure equation and describes the relation between vapour pressure and temperature for pure components. The Antoine equation is derived from the Clausius-Clapeyron relation and the assumptions for Equation (2.9) are:

(a) the vapour is an ideal gas;
(b) the molar volume of the vapour is much greater than the molar volume of the saturated liquid;
(c) heat of vaporization is independent of temperature.

The National Institute of Standards and Technology (NIST) has calculated the values for constant *A*, *B* and *C* according to the data obtained from Moussa *et al.* (1966) and Edejer and Thodos (1967):

Table 2.8: The coefficients *A*, *B* and *C* determined from experimental data for liquid nitrogen.

Temperature (K)	***A***	***B***	***C***	**Reference**
63.14 – 126.0	3.7362	264.651	-6.788	Edejer and Thodos (1967)
63.14 – 78.0	3.6379	257.877	-6.344	Moussa *et al.* (1966)

2.2.3.2 Calculating free-space values for micropore analysis

Although the results from full adsorption/desorption micro/mesoporous analysis report showed that the micropore volume is almost negligible compared to the amount that was adsorbed, it is recommended in the ASAP 2020 operation manual (Micromeritics, 2011) to perform a blank test using empty tubes that will be employed later for the sample analysis. The blank test uses microporous analysis but only uses one relative pressure point at P/P_0 = 0.01 to work out the cold and warm free-space volumes. The measured free-space data can be used thereafter on every analysis performed on these sample tubes. The differences of using or not using the cold and warm free-space volume for full micro/mesoporous analysis are shown in the adsorption-desorption isotherm, BET and pore size distribution (PSD) plots in this chapter.

2.2.3.3 International Union of Pure and Applied Chemistry (IUPAC): classification of pore size and adsorption isotherms

According to Gregg and Sing (1982), pores are classified based on the size of pore diameter, d_p (Hayes and Kolaczkowski, 1997):

Micropores: $d_p < 20$ Å (1 angstrom = 1×10^{-10} m), equivalent to 2 nm,

Mesopores: $20 < d_p < 500$ Å (2 and 50 nm), and

Macropores: $d_p > 500$ Å (50 nm).

Figure 2.11 shows the classification of adsorption isotherms defined by IUPAC, according to Sing *et al.* (1985) and Rouquerol *et al.* (1999). Different isotherm types correspond to different pore sizes:

Type I isotherm are given by microporous materials having relatively small external surfaces (e.g. zeolite and activated carbon).

Type II isotherm is usually seen in non-porous materials (e.g. non-porous alumina and silica). Point B means the starting point of the almost linear middle section of the isotherm, which associates the meaning of the stage at which monolayer coverage is complete and multilayer adsorption about to begin.

Type III isotherm is often exhibited by non-porous materials and materials which have the weak interaction between the adsorbate and adsorbent (e.g. graphite/water).

Type IV isotherm has a special feature – hysteresis loop, which is exhibited by mesopores in the material, due to capillary condensation (e.g. mesoporous alumina and silica).

Type V isotherm is related to porous materials and materials that have weak interaction between the adsorbate and adsorbent (e.g. activated carbon/water).

Type VI isotherm is represented by homogeneous or uniform non-porous surface materials (e.g. graphite/Kr and NaCl/Kr).

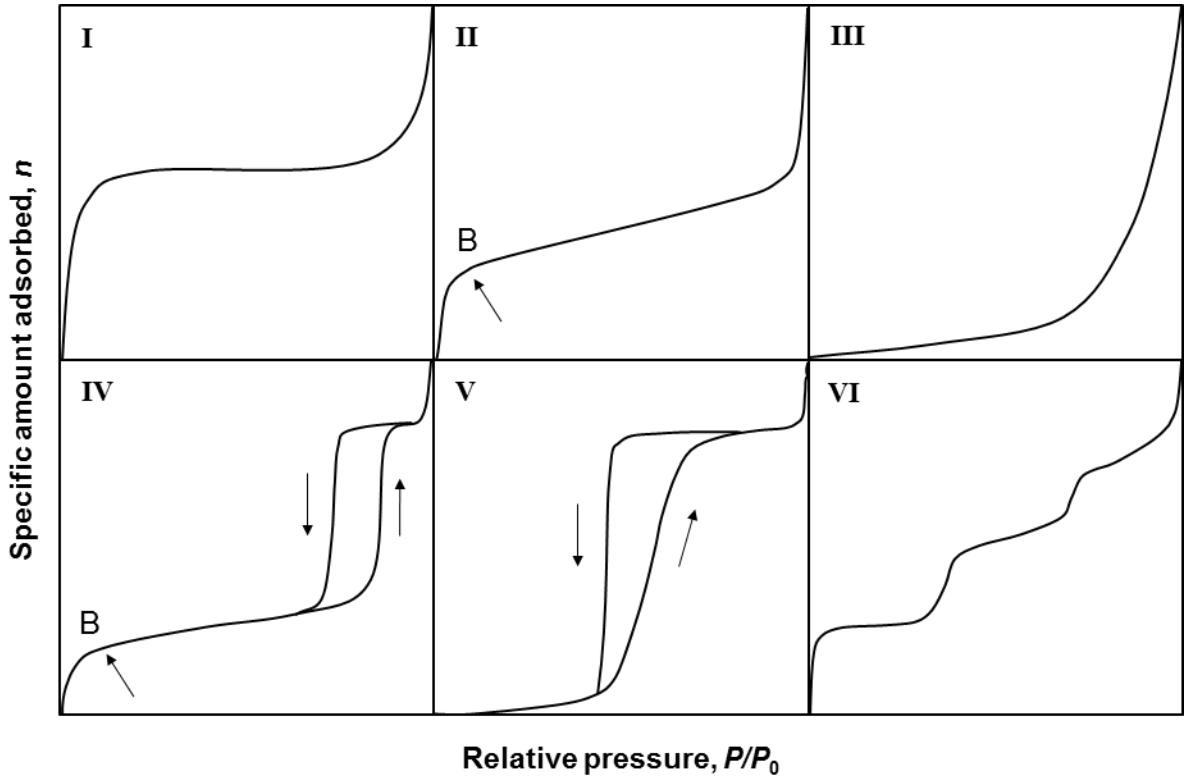

Figure 2.11: The classification of adsorption isotherms defined by IUPAC (picture redrawn and adapted from Sing *et al.* (1985)).

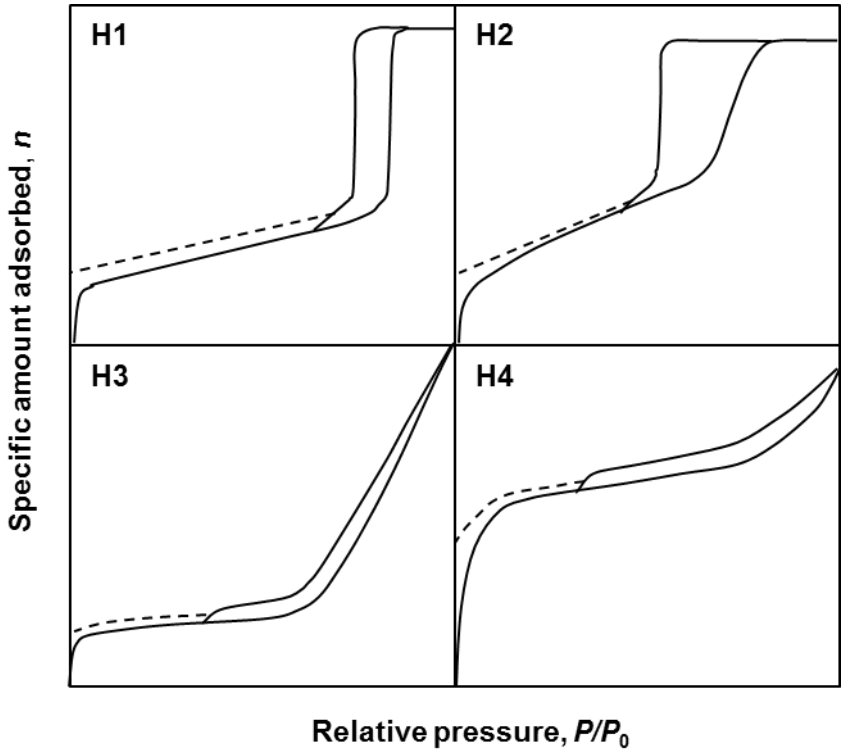

Figure 2.12: The classification of adsorption isotherms with hysteresis loop (picture redrawn and adapted from Sing *et al.* (1985)).

Point B in Figure 2.11 means the changeover from monolayer to multilayer adsorption, which occurs at the beginning of the middle, nearly linear, section of the isotherm (Sing *et al.*, 1985). The theoretical support for this proposal is the publication of the Brunauer-Emmett-Teller (BET) theory, where the uptake at Point B was found to be in good agreement with the BET monolayer capacity, n_m (Sing, 2001).

Hysteresis loop is usually associated with capillary condensation, which appears in the multilayer of physisorption in mesopore structures. Figure 2.12 shows the hysteresis loops with different shapes exhibited by adsorption isotherms. The former branches, Type H1 and H2, are almost vertical at certain relative pressure point and become parallel after a sufficient amount of gas is adsorbed. The latter two branches: Type H3 and H4, can be regarded as the intermediate between the two extremes, H1 and H2 (Sing *et al.*, 1985).

Materials with different porous structures exhibit different shapes of hysteresis loops. Type H1 is often associated with porous materials that consist of agglomerates, or uniform spheres, which have a narrow distribution of pore sizes. The situation in a Type H2 hysteresis loop is quite complicated because materials tend to have a distribution of pore size and shape, and these are not well defined. Type H3 and H4 hysteresis loop are often associated with slit-shape pores and microporous materials (Sing *et al.*, 1985).

2.2.3.4 Adsorption-desorption isotherm at 77.3 K for γ-alumina beads

The adsorption-desorption isotherms which relate the amount of adsorptive adsorbed, V ($cm^3\ g^{-1}$ STP), and the relative pressure, P/P_0, for the γ-alumina beads at 77.3 K are shown in Figures 2.13 and 2.14. Hysteresis occurs when the adsorption curve and desorption curve deviate from each other (Sing *et al.*, 1985). This physisorption phenomena suggests that multilayer adsorption and capillary condensation occurs in the sample. At point B, monolayer adsorption switched into multilayer adsorption. The initial part of the isotherm is attributed to monolayer and multilayer adsorption. The multilayer adsorption region provides information regarding the surface area (BET method), and the hysteresis region, which is associated with capillary condensation in pores, provides information on pore size.

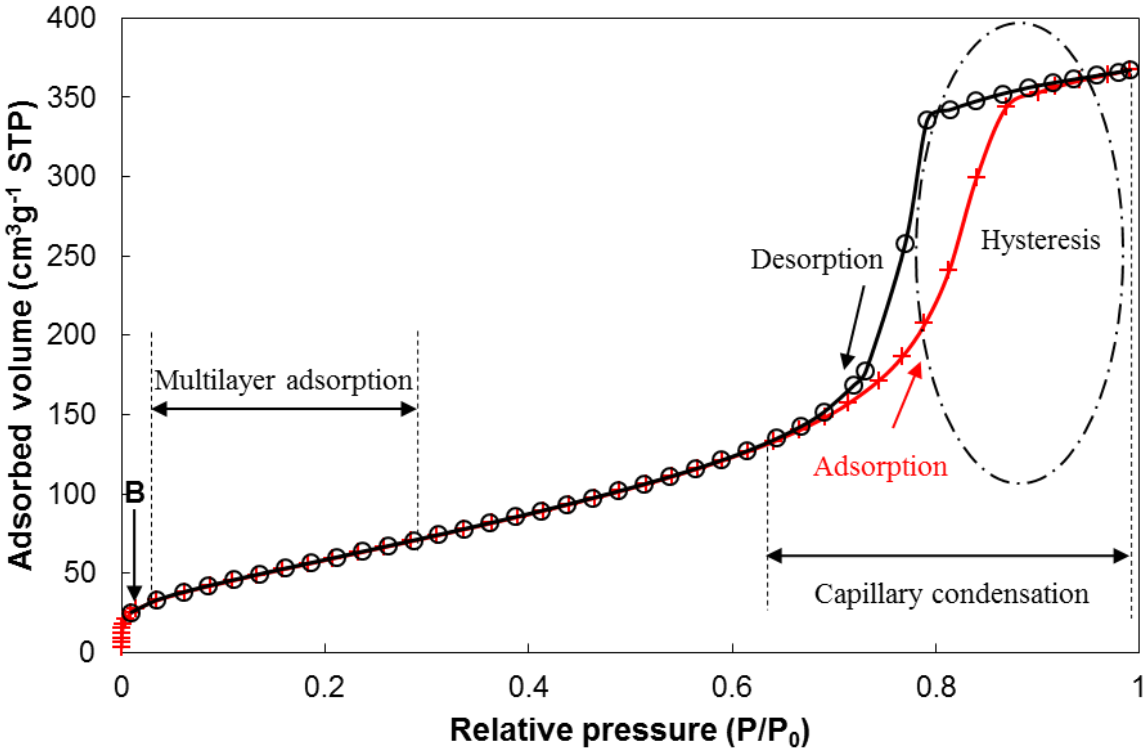

Figure 2.13: Nitrogen adsorption-desorption isotherm for the γ-alumina beads without "free-space" analysis.

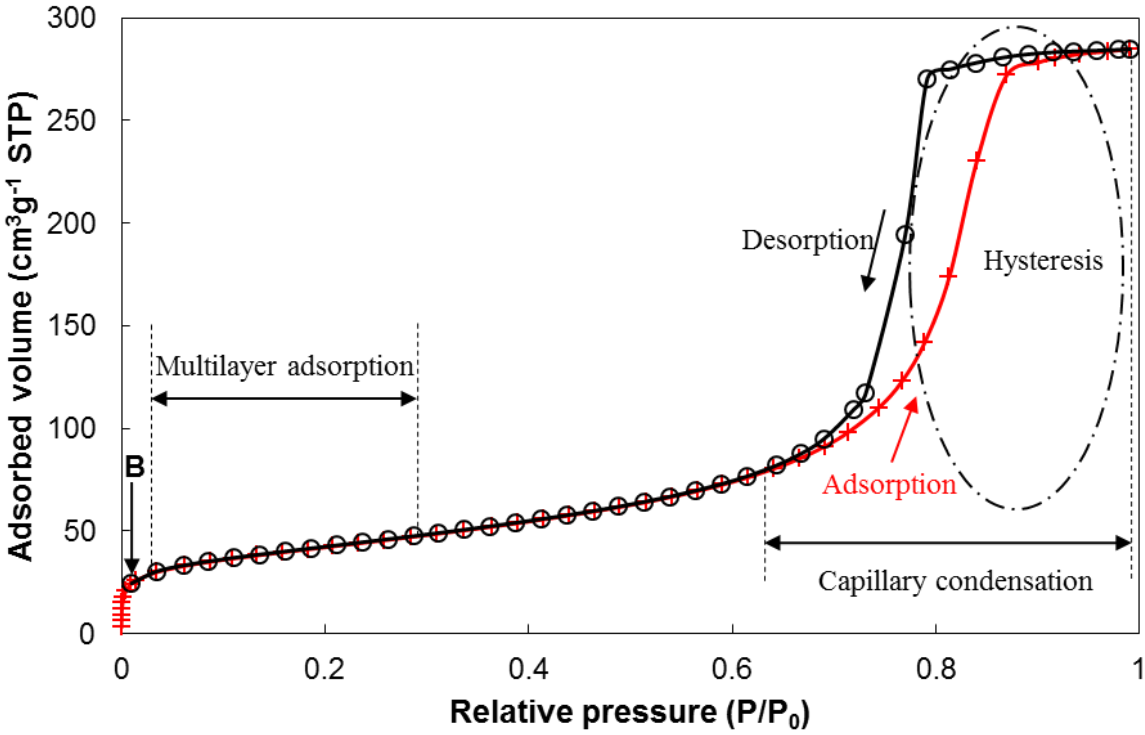

Figure 2.14: Nitrogen adsorption-desorption isotherm for the γ-alumina beads with "free-space" analysis; cold free-space: 27.6910 cm^3; warm free-space: 86.5955 cm^3.

According to classification of adsorption isotherms defined by IUPAC, the following conclusions are made based on the adsorption isotherms shown in Figures 2.13 and 2.14:

1. This is a Type IV isotherm according to the IUPAC classification.
2. The observed hysteresis loop in Figures 2.13 and 2.14 resemble a Type H1 hysteresis loop. The plateau at high P/P_0 was clear and obvious for the adsorption isotherm of the sample with free-space analysis in Figure 2.14, as compared to the isotherm without free-space analysis in Figure 2.13.
3. According to Thommes (2010), a Type IV isotherm with a Type H1 hysteresis loop suggests that the γ-alumina sample tested has a narrow distribution of relatively uniform (cylindrical-like) pores in the mesoporous range
4. There are very few macropores present. Sing *et al.* (1985) stated that if a solid contains no macropores, the isotherm remains nearly horizontal over a range of relative pressure close to unity, and this is the case in Figures 2.13 and 2.14.

2.2.3.5 Brunauer, Emmett and Teller (BET) surface area of γ-alumina beads

Isotherms interpretation

Base on explanations in Urbonaite (2008), for a comparison of different materials, quantitative interpretation is needed and such interpretation for isotherms is not straightforward. The interpretation of adsorption isotherms in micropores is difficult, when compared to mesopores and macropores. Generally speaking, the extraction of information is usually done by applying mathematical models to the isotherm data. The most popular methods are Brunauer-Emmett-Teller (BET) and Dubinin-Radushkevich (D-R) together with its modifications, *t* and *α*-plots, and Density Functional Theory (DFT). The D-R method is widely used in microporous analysis.

2.2.3.6 BET method

The BET equation is:

$$\frac{P}{V(P_0 - P)} = \frac{1}{V_m c} + \frac{c-1}{V_m c} P / P_0 \qquad (2.10)$$

where:
- V is the volume of gas adsorbed ($cm^3\ g^{-1}$) at STP or in molar amount (mmol/g),
- V_m is the volume of gas ($cm^3\ g^{-1}$) that is required for a monolayer at STP or in molar amount (mmol/g),
- P is the equilibrium vapour pressure (Pa),
- P_0 is the saturation vapour pressure (Pa),
- c is the average energy of adsorption ($c = e^{[(\Delta H_A - \Delta H_L)/RT]}$),
- ΔH_A is the heat of adsorption, and
- ΔH_L is the heat liquefaction.

Equation (2.10) can be rewritten as:

$$\frac{1}{V\left(P_0 / P - 1\right)} = \frac{c-1}{V_m c}\left(\frac{P}{P_0}\right) + \frac{1}{V_m c} \qquad (2.11)$$

The BET method is based on several assumptions (Pierotti and Rouquerol, 1985):

(a) the surface is flat;
(b) all the surface sites have uniform energy, molecules in the first layer act as sites for molecules in the second and higher layers;
(c) the condensation and evaporation properties of all layers above the first are similar to liquid adsorptive properties;
(d) there is no interaction between adsorbed molecules;
(e) the number of layers is unlimited (Kruk and Jaroniec, 2001).

Surface areas are determined by physical adsorption also known as physisorption. The most common procedure to determine surface area is to measure how much N_2 is adsorbed onto a certain amount of material. The uptake is measure at constant low pressure (i.e. 77.3 K) as a function of N_2 pressure (or relative pressure P/P_0), and is described by the Brunauer-Emmett-

Teller (BET) isotherm (Niemantsverdriet, 2008). After determining the number of N_2 molecules that form a monolayer on the support, one obtains the total area by setting the area of a single N_2 molecule to 0.16 nm^2 (Anderson and Garcia, 2005).

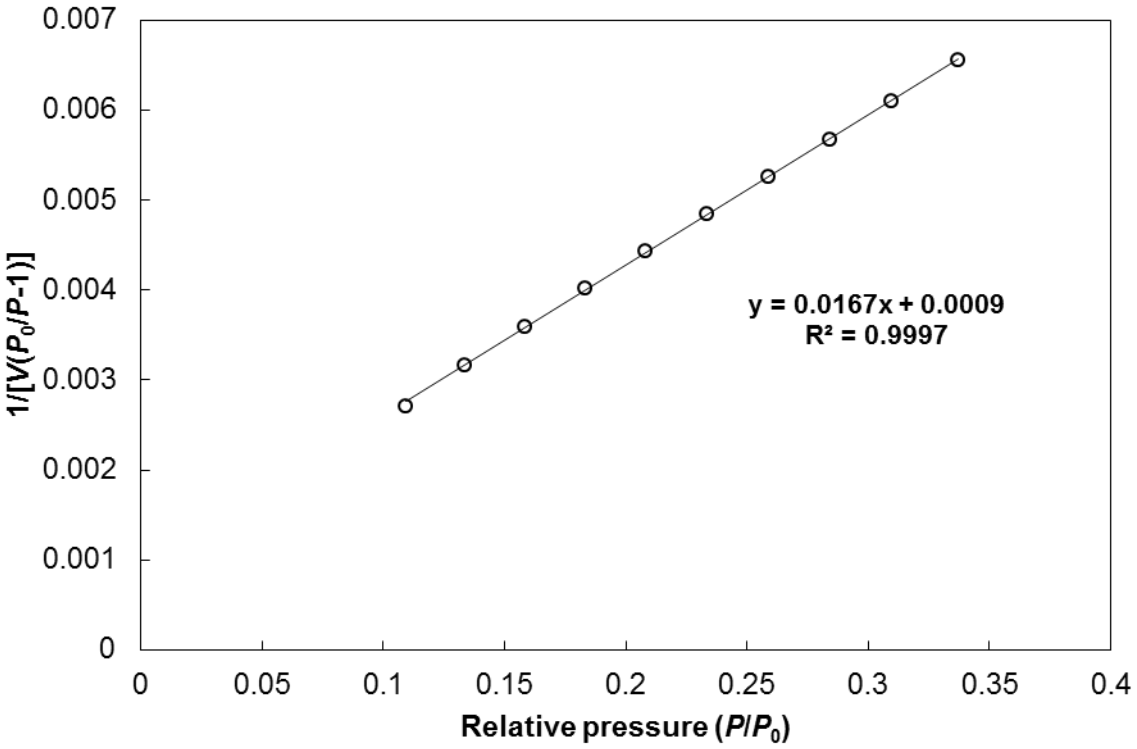

Figure 2.15: BET plot for γ-alumina beads without free-space analysis.

Figures 2.15 and 2.16 show the BET plots for the γ-alumina sample with and without free-space analysis. According to Equation (2.13), the BET equation assumes a linear relationship between $1/[V(P_0/P - 1)]$ and P/P_0. A plot of $1/[V(P_0/P - 1)]$ against P/P_0 yields a line of slope $(c - 1)/(V_m c)$ and intercept $1/(V_m c)$. The range of linearity is restricted to a limited part of the isotherm, that is in Figures 2.13 and 2.14, the isotherm region which relative pressure P/P_0 is within the range of 0.05 – 0.35. There has been a general agreement on this 'linear range' in the literature (Condon, 2006). Hence, in this work, linear trendlines within this region are plotted with RSQ values bigger than 0.99 (RSQ means the goodness of fit, RSQ = 1 implies perfect straight line) are found between $1/[V(P_0/P - 1)]$ and P/P_0. The gradient and the intercept on *y*-axis on this linear plot will provide information on monolayer capacity, V_m, and the adsorption energy, c.

Therefore, extracting this information from the BET plots yields the following results:

For the sample without free-space analysis:

$$\frac{c-1}{V_m c} = 0.0167\,;\ \frac{1}{V_m c} = 0.0009\ \text{g cm}^{-3} \tag{2.12}$$

V_m = 56.8182 cm^3 g^{-1}, c = 19.5556 at STP for γ-alumina beads.

For the sample with free-space analysis:

$$\frac{c-1}{V_m c} = 0.0295\,;\ \frac{1}{V_m c} = 8\times10^{-5}\ \text{g cm}^{-3} \tag{2.13}$$

V_m = 33.8066 cm^3 g^{-1}, c = 369.75 at STP for γ-alumina beads.

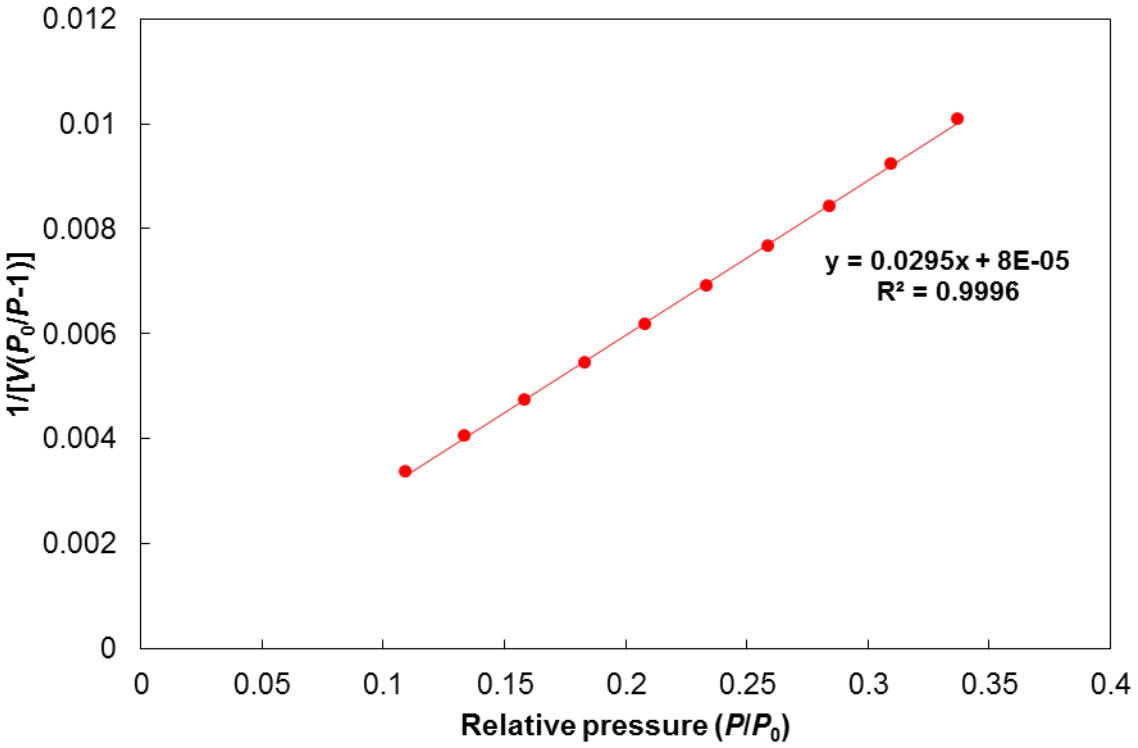

Figure 2.16: BET plot for γ-alumina beads with free-space analysis; cold free-space: 27.6910 cm^3; warm free-space: 86.5955 cm^3.

Sing *et al.* (1985) explain that, according to the BET theory, c is related exponentially to the enthalpy (heat) of adsorption in the first adsorbed layer. The adsorption energy constant, c, is used to characterise the shape of the isotherm in the BET range ($0.05 < P/P_0 < 0.30$) except that, the constant itself doesn't give a quantitative measure of enthalpy of adsorption but

merely acts as an indicator of the order of magnitude of the adsorbent-adsorbate interaction energy.

According to Sing *et al.* (1985), a high value of *c* (~ 100) corresponds to a sharp knee in the isotherm, which enables one to visualise the uptake at Point B (i.e. shown in Figures 2.11, 2.13 and 2.14, meaning the changeover from monolayer adsorption to multilayer adsorption). The over one-hundred *c*-value that was calculated from the BET plots for the sample with free-space analysis was: $c = 369.75$. Moreover, point B seems to be well located (as shown in Figure 2.14), therefore, the calculation of monolayer capacity should be trustworthy (i.e. $V_m = 33.8066$ cm^3 g^{-1}). To relate the monolayer capacity to surface area it is necessary to know the area occupied by one molecule, σ.

The surface area, or the BET surface area is calculated from the monolayer capacity using the following relationship (Allen, 1997):

$$S_w = \frac{N_A \sigma V_m}{M_v} \tag{2.14}$$

where:
- S_w is the mass specific area or BET surface area per unit mass of adsorbate, m^2 g^{-1};
- N_A is the Avogadro constant, 6.023×10^{23} molecules per mole;
- σ is the area occupied by one adsorbate molecule, usually taken as 16.2×10^{-20} m^2 for nitrogen at 77.3 K;
- V_m is the monolayer capacity (cm^3 per gram of adsorbent);
- M_v is the gram molecular volume ($M_v = m/\rho$, where m is the molecular weight of the adsorbate, nitrogen, 28.013 g mol^{-1}; and ρ is the density of the adsorbate, nitrogen, 1.25×10^{-3} g cm^{-3}; $M_v = 0.02241$ m^3 mol^{-1}).

Equation (2.14) is based on the assumption that (Westermarck, 2000):

(a) the first adsorbed layer involves adsorbate/adsorbent energies;
(b) and the following layers the energies of the adsorbate/adsorbate interaction.

Therefore for nitrogen gas at liquid nitrogen temperature:

$$S_w = \frac{(6.023\times10^{23})(16.2\times10^{-20})}{0.02241} V_m \tag{2.15}$$

$$S_w = 4353975.9 V_m \tag{2.16}$$

$$S_w = 147.2\ \mathrm{m^2 g^{-1}} \tag{2.17}$$

The BET surface area given by the built-in software in Micromeritics ASAP 2020 for the γ-alumina beads with free-space analysis is 141.9265 m^2 g^{-1}. This value is slightly different from the BET surface area calculated using Equation (2.17). The surface area reported in Antonyuk *et al*. (2006) for γ-alumina beads (SASOL, 97.9% γ-Al_2O_3) is 145 m^2 g^{-1}.

2.2.3.7 Pore size distribution – physical adsorption

As mentioned in Allen (1997), in order to calculate a pore size distribution, one must decide (a) which pore model to study; and (b) which branch of the isotherm to use. In general, there are three types of pore model: (1) Cylindrical pore; (2) Parallel plate (slit shape) or wedge shaped pore; (3) Ink-bottle pore. Their graphical interpretations are shown from Figure 2.17 to Figure 2.19.

(a) Cylindrical pore model – Kelvin equation

Figure 2.17 is a cylindrical pore with open ends and pore radius, r_p. In the cylindrical pore model, the classic Kelvin equation is described as (Sing *et al.*, 1985; Allen, 1997):

$$RT \ln x = \frac{-k\gamma_{LV} V_L \cos\theta}{r_k} \text{ ; where } r_k = r_c = r_p - t \qquad (2.18)$$

where:
- γ is the interfacial surface tension, suffixes referring to liquid-vapor (LV), 8.85×10^{-3} N m^{-1};
- θ is the wetting angle which is taken as zero or 0^o;
- V_L is the molar volume of the condensed liquid nitrogen, 34.6×10^{-6} m^3 mol^{-1};
- R is the universal gas constant, 8.314 J mol^{-1} K^{-1};
- T is the liquid nitrogen temperature, 77.3 K;
- x is the relative pressure, i.e. P/P_0;
- For geometry factor k, the following are used for adsorption process (Condon, 2006):
  - k = 1 for slit-shaped pores;
  - k = 2 for cylindrical-shaped pores.
- r_k is the Kelvin radius also known as the core radius, r_c.

According to Allen (1997) and Sing *et al*. (1985), for non-cylindrical pores, having mutually perpendicular radii, r_1 and r_2 as shown in Figure 2.17, Equation (2.18) has become:

$$RT \ln x = -\gamma_{LV} V_L \cos\theta \left[\frac{1}{r_1} + \frac{1}{r_2} \right] \qquad (2.19)$$

During adsorption, condensed vapour in the pores, formed film layers on both pore surfaces, with a thickness *t*. Therefore, as shown in Figure 2.17, for an adsorption process, where $r_1 = r_c$ and $r_2 = \infty$, substituting these conditions into Equation (2.19) yields:

$$RT \ln x_A = \frac{-\gamma_{LV} V_L \cos\theta}{r_c} \tag{2.20}$$

where x_A is the relative pressure $(P/P_0)_A$ for adsorption process. During desorption, the radii r_1, r_2 and r_c are equal. Hence, Equation (2.19) becomes:

$$RT \ln x_D = \frac{-2\gamma_{LV} V_L \cos\theta}{r_c} \tag{2.21}$$

where x_D is the relative pressure $(P/P_0)_D$ for desorption process.

Hence, from Equations (2.20) and (2.21), the following relation holds for x_A and x_D:

$$(x_A)^2 = x_D \tag{2.22}$$

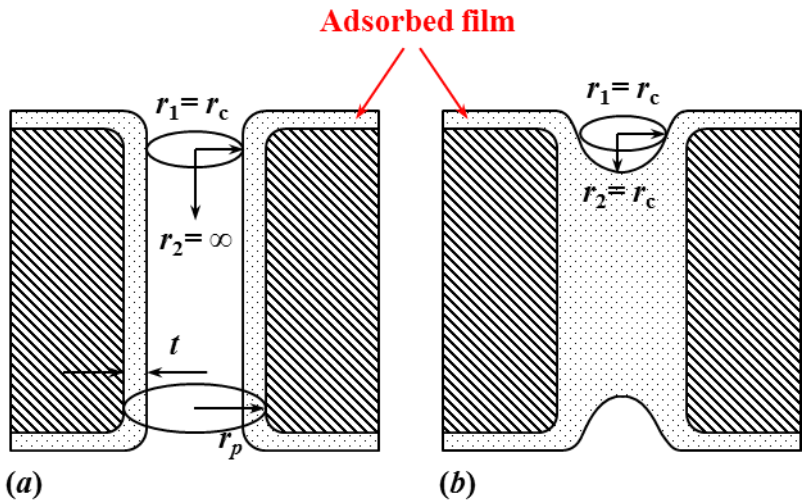

Figure 2.17: Cylindrical pore model shows: (a) adsorption; and (b) desorption processes (adapted and redrawn from Allen (1997)).

The Kelvin equation is dependent upon the thermodynamic principles and does not allude to the specific properties of materials. With nitrogen adsorption, only open pores are determined and the cylindrical pore model is assumed in the pore size distribution measurement (Allen, 1997). Therefore, the assumptions for Equation (2.18) are (Wei *et al.*, 2001):

(i) open-ended pores;

(ii) pore networks are absence or the pore connectivity is neglected;

(iii) the adsorbent surface is assumed to be chemically homogeneous;

(iv) the vapour phase is assumed to be an ideal gas.

(b) Ink-bottle pore model– Kelvin equation

For an ink-bottle pore, wide close body and open short neck are the obvious features of this pore, as shown in Figure 2.18, where $r_w \leq 2r_n$. Therefore, according to Allen (1997), the necks are filled, when the Kelvin radius corresponds to $r_n/2$, but it is only at a relative pressure corresponding to $r_w/2$ that the whole capillary is filled. Desorption or emptying of the pore takes place at a relative pressure corresponding to a Kelvin radius equal to r_n. Hence, from the Kelvin equation (Equation (2.18)):

For adsorption

$$P = P_0 \exp\left(\frac{\gamma_{LV} V_L \cos\theta}{RTr_w}\right) \tag{2.23}$$

For desorption

$$P = P_0 \exp\left(\frac{2\gamma_{LV} V_L \cos\theta}{RTr_n}\right) \tag{2.24}$$

Conditions are:

$$\ln\left(\frac{P}{P_0}\right)_A = \ln(x_A);\ r_k = r_w/2 \text{ at full adsorption} \tag{2.25}$$

$$\ln\left(\frac{P}{P_0}\right)_D = \ln(x_D);\ r_k = r_n \text{ for desorption at the neck} \tag{2.26}$$

Desorption at the neck can be expressed by substituting Equation (2.26) into Equation (2.24), resulting in:

$$\ln x_D = \frac{2\gamma_{LV} V_L \cos\theta}{RTr_n} \tag{2.27}$$

For full capillary adsorption in the ink-bottle pore, substituting Equation (2.25) into Equation (2.23) yields:

$$\frac{P}{P_0} = \exp\left[\left(\frac{\gamma_{LV} V_L \cos\theta}{RTr_k}\right) \times \frac{1}{2}\right]$$
$$\Rightarrow 2\ln\left(\frac{P}{P_0}\right)_A = \frac{\gamma_{LV} V_L \cos\theta}{RTr_k} \Rightarrow \ln(x_A)^2 = \frac{\gamma_{LV} V_L \cos\theta}{RTr_k} \quad (2.28)$$

Hence, according to Allen (1997), for adsorption at the neck, the Kelvin radius has the correlation $r_k = r_n/2$, hence Equation (2.28) has become:

$$\ln(x_A)^2 = \frac{2\gamma_{LV} V_L \cos\theta}{RTr_n} \quad (2.29)$$

Therefore, by correlating the adsorption and desorption at the neck of the ink-bottle pore, the following relationship holds (Allen, 1997):

$$RT \ln x_D = \frac{2\gamma_{LV} V_L \cos\theta}{r_n}; \text{ where } x_D = x_A{}^2 \quad (2.30)$$

The derivation of the Kelvin equation for the ink-bottle pore model is shown in this thesis because these steps the author wished to verify as they were not clearly explained in the literature.

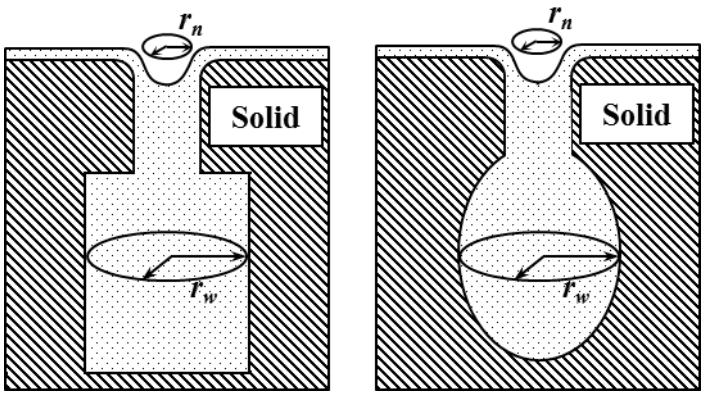

Figure 2.18: Ink-bottle pores; with r_n representing the radius of neck, and r_w represents the radius of the wide body (adapted and redrawn from Allen (1997)).

The reasons why ink-bottle pore model or ink-bottle shaped pores are important are explained in Section 2.2.4 of this chapter.

(c) Parallel plate model

In contrast to the cylindrical and ink-bottle pore models, a meniscus cannot be formed during adsorption due to hysteresis, but a cylindrical meniscus is present during desorption as shown in Figure 2.19 (Allen, 1997). As a consequence, this pore model would not be suitable for the sample studied in this chapter, because hysteresis loops occurred:

(a) during adsorption-desorption transition phase at high P/P_0; and

(b) during desorption phase at high P/P_0 as shown in Figures 2.13 and 2.14, but not during adsorption phase at the beginning (i.e. low P/P_0).

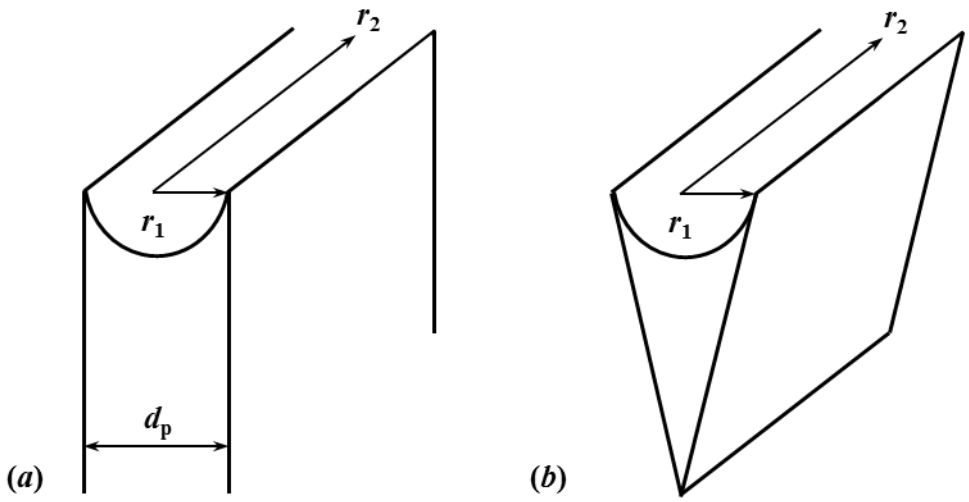

Figure 2.19: A meniscus cylindrical shape form during desorption from: (a) parallel plate (slit), and (b) wedge shaped pores. Such shapes cannot be formed during adsorption due to hysteresis; where d_p is the pore diameter, r_1 and r_2 represent the cylindrical coordinates in the *r-z* direction (adapted and redrawn from Allen (1997)).

2.2.3.8 Mesopore size distribution: the Barrett, Joyner and Halenda (BJH) computational method

To study the pore size distribution of a sample catalyst, there are two key factors that need to be considered:

(a) which branch of isotherm to study; and
(b) which pore model to use.

Allen (1997) stated that the desorption branch is preferred for the determination of pore size distribution (PSD), because the desorption branch is thermodynamically more stable than the adsorption branch. However, Sing *et al.* (1985) suggested that if a pore blocking effect occurs, the pore size distribution curve derived from the desorption branch tends to be unreliable because it only reflects the distribution of the narrower channels rather than the actual distribution of the pores. Therefore, the adsorption branches were used for calculation of the PSD in this thesis.

To choose which pore model to study and its related mathematical method, the Barrett, Joyner and Halenda (1951) method (abbreviation: BJH) based on the cylindrical pore model is the most popular one among many "classical" computational methods that rely on the Kelvin equation, which still remains in current use. Hence in this thesis, the BJH model is used for the pore size distribution study from nitrogen adsorption isotherms. According to Barrett *et al.* (1951), the BJH model provides a practical basis for the computation of pore volume distributions with respect to pore radii, and it depends on two fundamental assumptions:

(i) the pores are cylindrical, and
(ii) the amount of adsorbate in equilibrium with the gas phase is retained by the adsorbent by two mechanisms:
    (a) physical adsorption on the pore walls; and
    (b) capillary condensation in the inner capillary volume.

According to the BJH model, for the computation of the mesopore size distribution, the relation between pore volume and pore dimension is presented either in the form of:

(a) a cumulative plot of pore volume against mean pore size (i.e. v_p *versus* $\bar{D}_p$); or

(b) as a probability density function (or frequency curve), *dV*/*dD versus* $\bar{D}_p$,

where D and $\bar{D}_p$ represent the difference in two consecutive pore diameters and average pore diameter respectively; and v_p and V_p represent the cumulative and incremental pore volume correspondingly. In this thesis, the latter expression, (b), is used and the PSDs for the sample are expressed in Figures 2.21 and 2.22. The BJH adsorption average pore diameter also known as the hydraulic diameter or the mean pore diameter is calculated from the volume-to-surface area ratio (Rouquerol *et al.*, 1999):

$$\bar{D}_p = \frac{4 \times \text{BJH cumulative pore volume}}{\text{BJH cumulative pore area}} = \frac{4v_p}{A_p} \tag{2.31}$$

The necessary assumptions made for the computations of mesopore size distribution are, according to Rouquerol *et al.* (1999):

(i) The Kelvin equation is applicable over the complete mesopore range (2 – 50 nm);

(ii) The meniscus curvature is controlled by the pore size and shape and $\theta = 0^o$;

(iii) The pores are rigid and of well-defined shape (cylindrical pores for BJH model);

(iv) The distribution is restricted to the mesopore range only, micropore range are overridden in this case;

(v) The filling (or emptying) of each pore does not depend on its location within the network;

(vi) The adsorption on the pore walls proceeds in exactly the same way as on the corresponding open surface.

In Figure 2.17, capillary condensation occurs as multi-layer adsorption builds up. The volume adsorbed as pressure increases is made up of two parts: (a) the volume that filled the capillary cores; (b) the volume which increases the thickness of adsorbed layers on the unfilled pores. Therefore, the pore radius of a cylindrical pore is:

$$r_p = r_c + t \tag{2.32}$$

The thickness of the adsorbed film, *t*, in Figure 2.20 may be represented by two empirical equations of Harkins and Jura type as follows (Whittemore Jr and Sipe, 1974):

Empirical formula I:

$$t = \left[\frac{0.1399}{0.034 - \log x}\right]^{\frac{1}{2}}; \text{ For } 0 < x = P/P_0 < 0.8 \text{ (or } 0.75) \tag{2.33}$$

Empirical formula II:

$$\log x = -\frac{0.1611}{t^2} + 0.1682\exp\left(-1.137t\right); \text{ For } 0.4 < x = P/P_0 < 0.96 \tag{2.34}$$

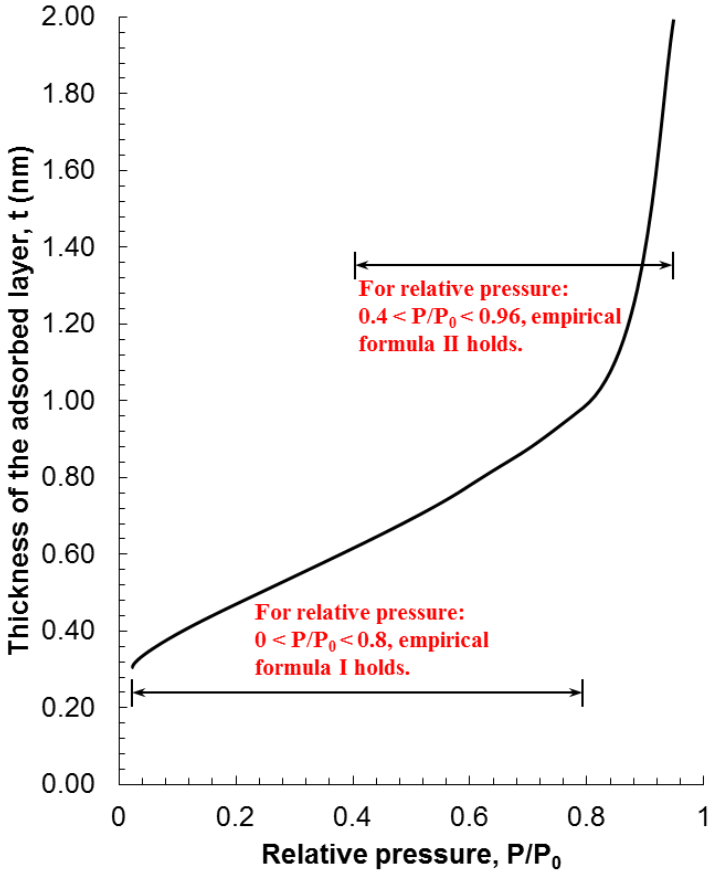

Figure 2.20: The common *t*-curve of de Boer, produced from the published tables of *t* against *x* (i.e. P/P_0) in Lippens and de Boer (1965) representing the thickness of the adsorbed layer *t* as a function of relative pressure, *x*.

2.2.3.9 Results summary from Micromeritics ASAP 2020 for pore size distribution of γ-alumina beads

The results are shown in Tables 2.9 and 2.10. Columns (1), (2) and (3) are data generated by the micromeritics ASAP 2020. Data in Columns (4) to (8) are values calculated based on the data in Columns (1) to (3).

The average pore diameter $\overline{D}_p$ is calculated using:

$$\overline{D}_p = \frac{4V_p}{S_p} \tag{2.35}$$

where V_p and S_p are the incremental pore volume and incremental surface area in Columns (2) and (3). Equation (2.35) is based on the assumption of cylindrical shape of pores open at ends.

The differential pore volume, dV/dD (i.e. Column (5)), is computed by dividing the incremental pore volume in Column (2) by the difference in pore diameter in Column (1) (i.e. Column (7)). The differential pore volume in term of logarithm of pore diameter $dV/(d\log D)$ (i.e. Column (6)), is calculated by dividing the incremental pore volume in Column (2) by Column (8).

Consequently, by plotting Column (5) *versus* Column (4), or Column (6) *versus* Column (4), yields adsorption pore diameter density function curves as shown in Figures 2.21 and 2.22. The adsorption pore diameter density function curve (or pore size distribution curve) for free-space analysis shows that the γ-alumina beads have pores in the mesopore range (2 – 50 nm), with the modal pore size around 12 nm.

The average pore diameters and pore volume reported in the literature are:

1. The mean mesopore diameter reported in the pore size distribution curve in Tang *et al.* (1987) for γ-alumina pellet is around 8.3 nm using nitrogen adsorption and mercury porosimetry;
2. The pore volume reported in Chu *et al.* (2007) for γ-alumina beads (SASOL Puralox, 98% γ-Al_2O_3) is 0.477 $cm^3\ g^{-1}$;
3. In Klose *et al.* (2007), the $\overline{D}_p$ measured for γ-alumina beads (SASOL, purity > 97%) is 12 nm.

Table 2.9: Data generated by Micromeritics ASAP 2020 for γ-alumina beads without free-space analysis.

Pore Diameter Range, d_p (Å)	**Incremental pore volume,** V_p ($cm^3\ g^{-1}$)	**Incremental pore area,** S_p ($m^2\ g^{-1}$)	**Average pore diameter,** $\overline{D}_p$ (Å)	**Differential pore volume** dV/dD ($cm^3\ g^{-1}\ Å^{-1}$)	**Differential pore volume** $dV/(d\log D)$ ($cm^3\ g^{-1}\ Å^{-1}$)	**Difference in diameter,** D (Å)	**Log difference in diameter,** $\log D$ (Å)
2128.6 - 656.1	0.004961	0.255	778.019	0.000003691	0.009706059	1472.5	0.511124020
656.1 - 343.5	0.006514	0.638	408.194	0.000020838	0.023177923	312.6	0.281043296
343.5 - 245.3	0.007419	1.069	277.702	0.000075550	0.050735423	98.2	0.146229193
245.3 - 203.6	0.006715	1.219	220.352	0.000161031	0.082983424	41.7	0.080919775
203.6 - 155.3	0.017238	3.993	172.66	0.000356894	0.146573758	48.3	0.117606318
155.3 - 127.0	0.089464	25.906	138.135	0.003161272	1.023993586	28.3	0.087367735
127.0 - 108.5	0.121206	41.727	116.189	0.006551676	1.772691821	18.5	0.068373983
108.5 - 96.0	0.068299	26.933	101.434	0.005463920	1.284817920	12.5	0.053158505
96.0 - 86.6	0.041711	18.382	90.7636	0.0044373	0.9320198	9.4	0.0447533
…	…	…	…	…	…	…	…
…	…	…	…	…	…	…	…
27.0 - 25.3	0.005838	8.95	26.0898	0.0034341	0.2067043	1.7	0.0282432
25.3 - 23.8	0.005714	9.325	24.5113	0.003809333	0.215268755	1.5	0.026543564
23.8 - 22.4	0.005226	9.068	23.0533	0.003732857	0.198488821	1.4	0.026328939
22.4 - 21.1	0.004948	9.12	21.7035	0.003806154	0.190560089	1.3	0.025965563
21.1 - 19.8	0.004765	9.337	20.4142	0.003665385	0.172536998	1.3	0.027617265
19.8 - 18.6	0.004415	9.21	19.1746	0.003679167	0.162601650	1.2	0.027152246
18.6 - 17.4	0.004106	9.138	17.9725	0.003421667	0.141763676	1.2	0.028963696

Table 2.10: Data generated by Micromeritics ASAP 2020 for γ-alumina beads with free-space analysis. Volume entered: cold free-space: 27.6910 cm^3; warm free-space: 86.5955 cm^3.

Pore diameter Range, d_p (Å)	**Incremental pore volume,** V_p ($cm^3\ g^{-1}$)	**Incremental pore area,** S_p ($m^2\ g^{-1}$)	**Average pore diameter,** $\overline{D}_p$ (Å)	**Differential pore volume** dV/dD ($cm^3\ g^{-1}\ Å^{-1}$)	**Differential pore volume** $dV/(d\log D)$ ($cm^3\ g^{-1}\ Å^{-1}$)	**Difference in diameter,** D (Å)	**Log difference in diameter,** $\log D$ (Å)
2129.9 - 657.4	0.001873	0.096	779.355	0.000001270	0.003668740	1472.5	0.510529514
657.4 - 344.8	0.00227	0.222	409.53	0.000007260	0.008099551	312.6	0.280262443
344.8 - 246.6	0.003759	0.539	279.038	0.000038300	0.025821886	98.2	0.145574185
246.6 - 204.9	0.004059	0.732	221.688	0.000097300	0.050452999	41.7	0.080451114
204.9 - 156.6	0.012375	2.845	173.997	0.000256211	0.105995535	48.3	0.116750201
156.6 - 128.3	0.086341	24.762	139.472	0.003050919	0.997411181	28.3	0.086565101
128.3 - 109.8	0.119434	40.65	117.525	0.006455892	1.766139853	18.5	0.067624316
109.8 - 97.4	0.065976	25.679	102.77	0.005320645	1.267711588	12.4	0.052043383
97.4 - 87.9	0.038998	16.937	92.1002	0.0041050	0.8749816	9.5	0.0520434
…	…	…	…	…	…	…	…
…	…	…	…	…	…	…	…
28.3 - 26.7	0.000863	1.259	27.4264	0.0005394	0.0341442	1.6	0.0252752
26.7 - 25.1	0.000712	1.103	25.848	0.000445000	0.026530002	1.6	0.026837540
25.1 - 23.7	0.000555	0.91	24.3899	0.000396429	0.022266465	1.4	0.024925375
23.7 - 22.4	0.000387	0.672	23.0401	0.000297692	0.015795707	1.3	0.024500328
22.4 - 21.2	0.000327	0.601	21.7508	0.000272500	0.013675052	1.2	0.023912157
21.2 - 19.9	0.000135	0.264	20.5112	0.000103846	0.004912166	1.3	0.027482785
19.9 - 18.8	0.000017	0.036	19.3091	0.000015500	0.000688392	1.1	0.024695227

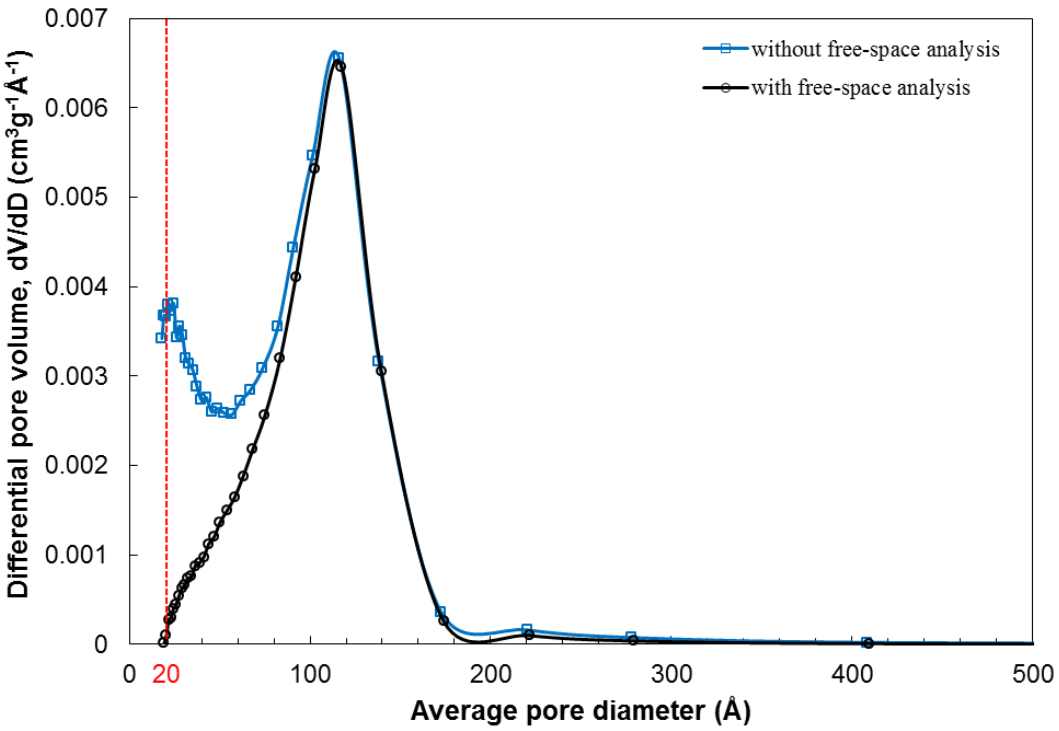

Figure 2.21: Pore size distribution (*dV*/*dD versus* $\bar{D}_p$) using BJH adsorption method: (a) without free-space analysis; and (b) with free-space analysis. Volume entered: cold free-space: 27.6910 cm^3; warm free-space: 86.5955 cm^3.

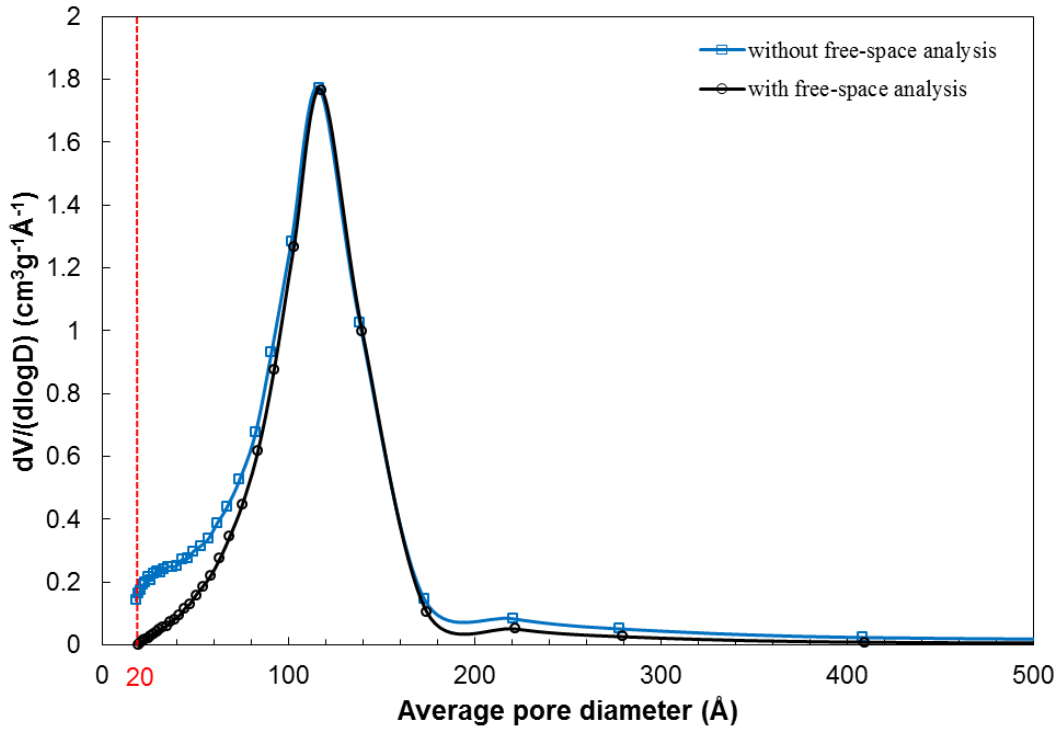

Figure 2.22: Pore size distribution (*dV*/(*d*log*D*) *versus* $\bar{D}_p$) using BJH adsorption method: (a) without free-space analysis; and (b) with free-space analysis. Volume entered: cold free-space: 27.6910 cm^3; warm free-space: 86.5955 cm^3.

2.2.4 Mercury porosimetry measurements

2.2.4.1 Introduction

Mercury intrusion porosimetry is another important technique that can be used to characterise the physical properties based upon the behaviour of non-wetting liquids in capillaries. Mercury penetration or intrusion covers a pore diameter range of mesopore to macropore i.e. 3 nm to 360 μm (Webb, 2001), compared to nitrogen adsorption analysis which covers a micropore to mesopore range between 0.3 – 300 nm (Westermarck, 2000). Mercury porosimetry can be used to determine the surface area and particle size distribution and to study the tortuosity, permeability, fraction dimension and compressibility of porous materials similar to nitrogen adsorption analysis (Neimark *et al.*, 2008), besides, this technique also provides information on skeletal and bulk densities.

Unlike nitrogen adsorption analysis, in which information on pores is extracted from wetting the pore walls by capillary condensation (i.e. contact angle < 90^o), in mercury porosimetry a non-wetting process is used by forcing mercury (i.e. contact angle: θ = 130^o > 90^o) into the pores at high pressures. For high pressure porosimetry analysis in this thesis, a Micromeritics Autopore III mercury porosimeter was used, starting from atmospheric pressure (14.7 psia, 1.013 bar(a)) to 60,000 psia (i.e. 4140 bar(a)). The relationship between applied pressure and pore radius is described by the Young-Laplace equation for a cylindrical pore:

$$\pi r_p^2 P = -2\pi r_p \gamma \cos\theta \Rightarrow \boxed{r_p = -\left(\frac{2\gamma}{P}\right)\cos\theta} \tag{2.36}$$

where:
- γ is the surface tension of the pure mercury, 0.485 N m^{-1} at 25 ^{o}C,
- θ is the mercury-solid-vacuum contact angle,
- P is the applied pressure, N m^{-2}, and
- r_p is the pore radius, m.

In Equation (2.36), the pores are assumed to be cylindrical in shape.

The characterization of the γ-alumina beads was performed using a Micromeritics Autopore III mercury porosimeter. The steps involved were as follows:

(i) Choose the right penetrometer and write down the series number and constant in the analysing software;

(ii) A blank run analysis is done with an empty penetrometer so that the penetrometer volume is calibrated;

(iii) The sample is weighed and should not fill above half of the bulb volume on the penetrometer;

(iv) Grease both the stem end, and the bulb edge on the penetrometer;

(v) Insert the penetrometer into the low pressure analysis port, where the sample is evacuated to remove air and moisture. The penetrometer's cup (or known as bulb) and capillary stem are then automatically backfilled with mercury;

(vi) After low pressure analysis, the penetrometer filled with mercury is transferred to the high pressure analysis port for full intrusion-extrusion analysis with mercury;

(vii) The pressure in the high pressure analysis can go up to or above 60,000 psia (4140 bar(a));

(viii) When the analysis is finished, the vacuum pump decreases the pressure in small steps back to ambient;

(ix) Health and safety issues are taken seriously when operating with mercury porosimeter. Sodium hydroxide was used to wash out the mercury residues in the penetrometer;

(x) The experiment was repeated using γ-alumina beads.

2.2.4.2 The cumulative pore volume intrusion-extrusion curve for γ-alumina beads

Figure 2.23 show the intrusion-extrusion cycle for the γ-alumina beads at different pressures. The intrusion volume points (interpreted as points A, B and C) on a mercury intrusion plot are critical in the determination of volume and density:

(a) Point A is used to determine the bulk or envelope volume.
(b) Points A and B: determine interparticle void volume.
(c) Points A and C: determine skeletal volume.

The maximum intrusion pressure in Figure 2.23 is about 413 MPa or 4,126 bar(a).

According to Neimark *et al.* (2008), the following interpretations from the intrusion-extrusion curves can be made:

(i) The small and near constant cumulative pore volume in Region I corresponds to rearrangement of particles within the penetrometer cup followed by intrusion of the interparticle voids;
(ii) Region II represents the filling of the pores;
(iii) Region III represents the plateau where the maximum pressure is reached therefore this means the maximum pore volume intruded;
(iv) A hysteresis loop is observed and extrusion starts: i.e. Region IV;
(v) On completion of the intrusion-extrusion cycle, some mercury is always retained by the sample which prevents the loop from closing;
(vi) The transition point on the intrusion curve means the shift from low pressure to high pressure analysis in the porosimeter;
(vii) The effective pore volume for the γ-alumina beads is calculated by subtracting the cumulative volume achieved just before the pore filling starts (i.e. Region I) from the maximum volume of mercury intruded (i.e. Region III).

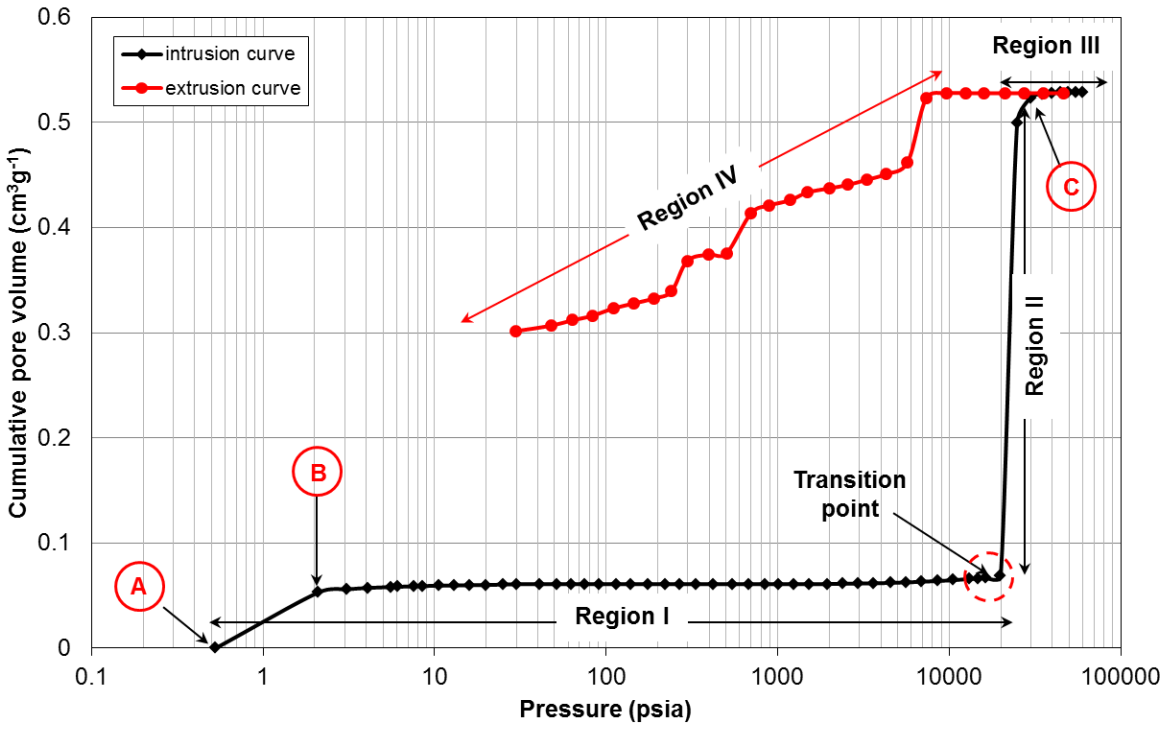

Figure 2.23: Cumulative pore volume plot at different intrusion and extrusion pressures for γ-alumina beads in solid form.

2.2.4.3 Pore size distribution – mercury penetration

Pore size distribution curve for the γ-alumina beads in term of mercury intrusion method can be plotted by:

(a) differential pore volume (dV/dD) *versus* average pore diameter $\bar{D}_p$, or

(b) differential pore volume ($dV/(d\log D)$) *versus* average pore diameter $\bar{D}_p$.

The data obtained from the mercury porosimeter are shown in Columns (1) to (4) in Table 2.12. In Column (1), for intrusion pressures < 1535 psia, the incremental pore volumes and pore areas were zero. The average pore diameter in Column (5) was calculated based on Equation (2.35). The difference in pore diameter was calculated based on the pore diameter range, d_p in Column (2):

$$D = d_{i+1} - d_i \tag{2.37}$$

The pore size distribution curves (Figures 2.24 and 2.25) for γ-alumina beads show that the pore diameter is in the mesopore range around 8.2 nm. The pore diameter obtained from the mercury porosimeter was slightly lower than in the nitrogen adsorption analysis (12 nm), but close to the manufacturer's value (8.8 nm, which claimed to have used both mercury penetration and nitrogen adsorption methods). The difference in pore size results between mercury porosimetry and nitrogen adsorption analysis is reasonable, because mercury cannot enter some of the small pores which nitrogen can.

Besides, as mentioned in Westermarck (2000), mercury porosity overestimates the volume of the smallest pores and this is due to ink-bottle shaped pores and interconnected pores that shift the volume pore size distribution towards smaller pores. The diameter of the pore opening into the surface the sample determines when mercury is intruded into the sample. Large pores with a small opening are thus filled at high pressures, and detected as smaller pores than they actually are.

For a γ-alumina washcoat or various shape pellets with surface area 100 – 200 m^2 g^{-1}, the average pore diameter, $\bar{D}_p$ described in the literature are:

(i) The average pore diameter $\bar{D}_p$ reported in Chu *et al.* (2007) for γ-alumina beads (SASOL Puralox, 98% γ-Al_2O_3) is 8.3 nm.

(ii) In Davidová (1990), the mean mesopore diameter is 5 nm with pore volume 0.344 cm^3 g^{-1} using mercury porosimetry.

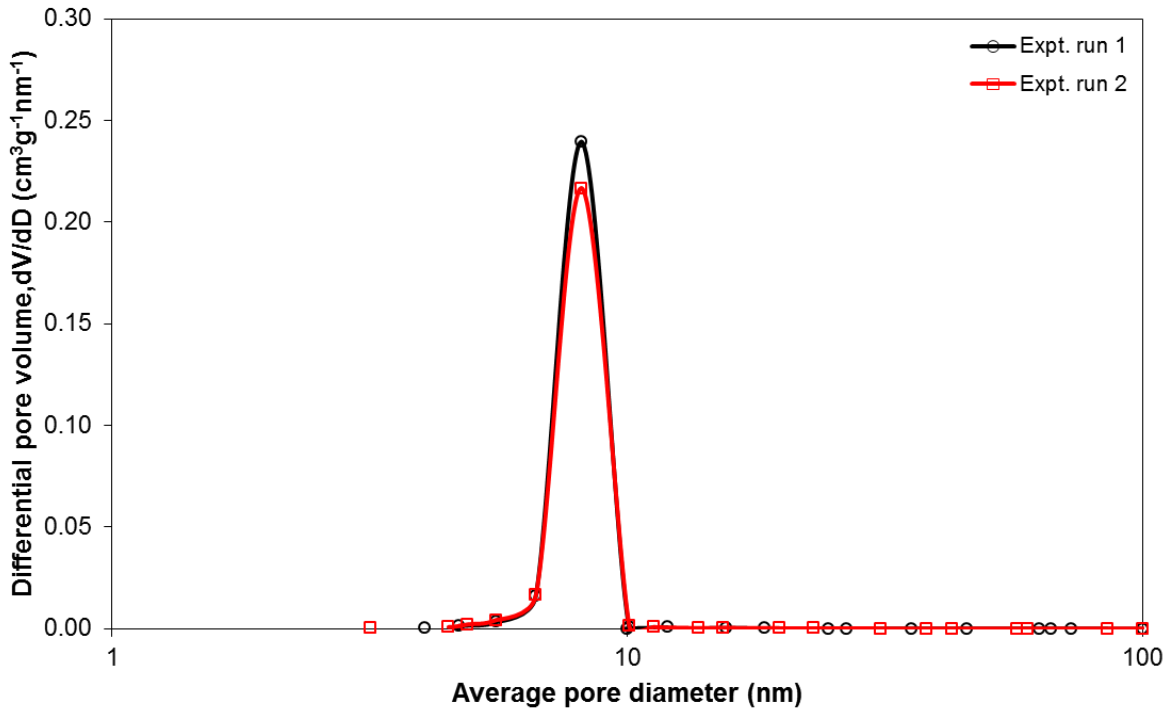

Figure 2.24: Pore size distribution (dV/dD *versus* $\bar{D}_p$) for γ-alumina beads based on the intrusion curve.

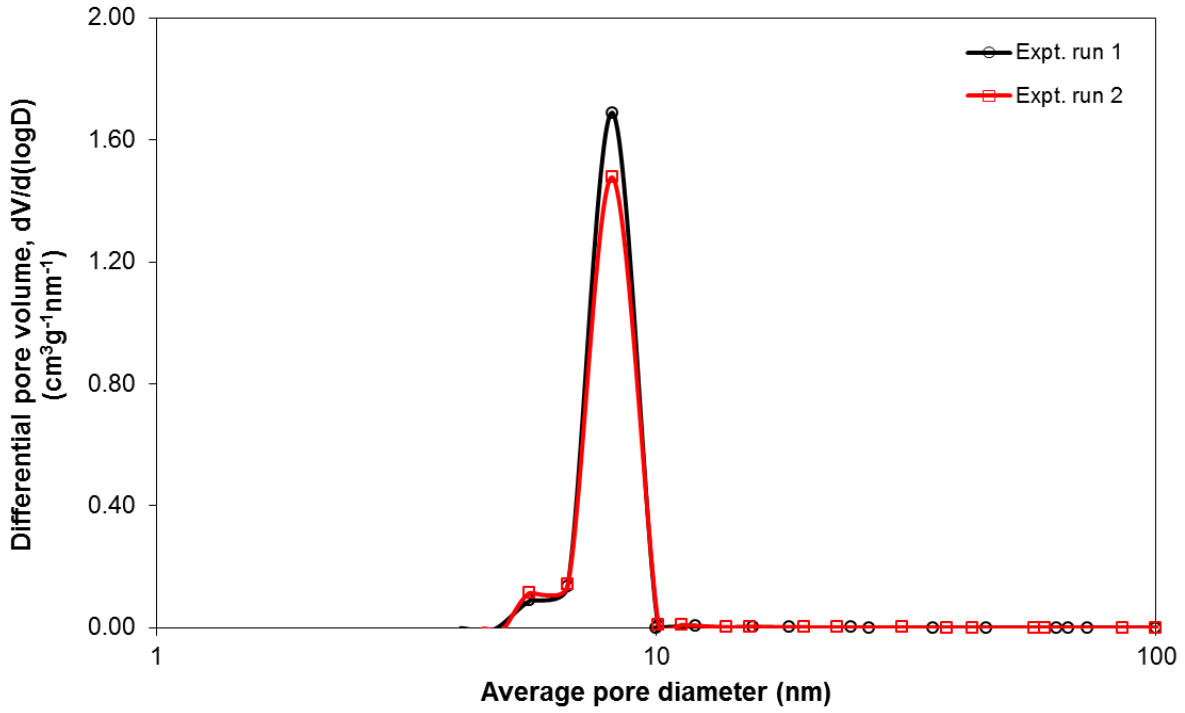

Figure 2.25: Pore size distribution ($dV/(d\log D)$ *versus* $\bar{D}_p$) for γ-alumina beads based on the intrusion curve.

Table 2.11: Summary of surface area and pore volume of γ-alumina beads in solid form using the mercury porosimeter.

γ-alumina bead	**Surface area (m^2 g^{-1})**	**Cumulative volume before pore filling (cm^3 g^{-1})**	**Total volume intruded (cm^3 g^{-1})**	**Effective pore volume (cm^3 g^{-1})**	**Average pore diameter (nm)**
1	231.01	0.0684	0.5284	0.4600	8.1672
2	224.54	0.0676	0.5110	0.4434	8.1662
Average	227.775 ± 3.2350	0.0680 ± 0.0004	0.5197 ± 0.0087	0.4517 ± 0.0083	8.1667 ± 0.0005

Table 2.12: Data generated by the Micromeritics Autopore III Mercury Porosimeter for the γ-alumina beads (Experimental run 1).

Intrusion pressure, P (psia)	**Pore diameter range, d_p (nm)**	**Incremental pore volume, V_p ($m^3\ g^{-1}$)**	**Incremental pore area, S_p ($m^2\ g^{-1}$)**	**Average pore diameter, $\bar{D}_p$ (nm)**	**Difference in pore diameter, D (nm)**	**Differential pore volume, dV/dD ($cm^3\ g^{-1}\ nm^{-1}$)**	**Differential pore volume. $dV/d(\log D)$ ($cm^3\ g^{-1}\ nm^{-1}$)**
1535	161.3 – 131.3	1.0×10^{-10}	0.004	100.0	30.0	3.3×10^{-6}	6.8×10^{-5}
1950	131.3 – 105.3	1.0×10^{-10}	0.004	100.0	26.2	3.8×10^{-6}	7.1×10^{-5}
2403	105.3 – 84.0	2.0×10^{-10}	0.011	72.7	21.3	9.4×10^{-6}	1.5×10^{-4}
2935	84.0 – 68.4	2.0×10^{-10}	0.012	66.7	15.6	1.3×10^{-5}	1.7×10^{-4}
3643	68.4 – 55.6	3.0×10^{-10}	0.019	63.2	12.8	2.3×10^{-5}	2.7×10^{-4}
4560	55.6 – 44.7	4.0×10^{-10}	0.035	45.7	10.9	3.7×10^{-5}	3.9×10^{-4}
5594	44.7 – 36.0	5.0×10^{-10}	0.056	35.7	8.7	5.7×10^{-5}	5.3×10^{-4}
6889	36.0 – 29.3	5.0×10^{-10}	0.075	26.7	6.7	7.5×10^{-5}	6.1×10^{-4}
8614	29.3 – 23.6	7.0×10^{-10}	0.114	24.6	5.7	1.2×10^{-4}	9.3×10^{-4}
10561	23.6 – 19.1	8.0×10^{-10}	0.173	18.5	4.5	1.8×10^{-4}	1.2×10^{-3}
13154	19.1 – 15.4	1.2×10^{-9}	0.308	15.6	3.7	3.2×10^{-4}	2.1×10^{-3}
14748	15.4 – 13.0	1.0×10^{-10}	0.040	10.0	2.4	4.2×10^{-5}	2.6×10^{-4}
16396	13.0 – 11.6	1.0×10^{-9}	0.334	12.0	1.4	7.1×10^{-4}	6.8×10^{-3}
19952	11.6 – 10.0	1.4×10^{-9}	0.555	10.1	1.6	8.8×10^{-4}	6.9×10^{-3}
24883	10.0 – 8.2	4.3×10^{-7}	211.088	8.2	1.8	2.4×10^{-1}	1.7
29879	8.2 – 6.7	2.4×10^{-8}	14.489	6.7	1.5	1.6×10^{-2}	1.4×10^{-1}
34919	6.7 – 5.6	3.7×10^{-9}	2.648	5.6	1.1	3.4×10^{-3}	8.9×10^{-2}
39911	5.6 – 4.9	1.0×10^{-9}	0.847	4.7	0.7	1.4×10^{-3}	-6.5×10^{-3}
44937	4.9 – 4.3	2.0×10^{-10}	0.197	4.1	0.6	3.3×10^{-4}	-9.0×10^{-4}
49796	4.3 – 3.8	0.0	0.000	N/A	0.5	0.0	0.0
54898	3.8 – 3.5	0.0	0.000	N/A	0.3	0.0	0.0
59842	3.5 – 3.2	0.0	0.000	N/A	0.3	0.0	0.0

2.2.4.4 Skeletal and bulk density – mercury penetration

From the mercury porosimeter, information was also obtained on skeletal and bulk densities. This information is presented in Table 2.13, and the results are compared with earlier measurements using the pycnometer.

Table 2.13: Results summary for skeletal and bulk densities for the γ-alumina beads (measured with pycnometer and mercury porosimeter).

γ-alumina beads	Skeletal density, $\rho_{skeletal}$ (g cm^{-3})		Bulk density, ρ_{bulk} (g cm^{-3})	
	From pycnometer	From mercury porosimeter	From *m*/*V* ratio (*a*)	From mercury porosimeter
Exp. run 1	3.3885 ± 0.0029	2.7751	1.5852	1.1251
Exp. run 2	3.3810 ± 0.0030	3.0320	1.5852	1.1893
Average	3.3848 ± 0.0038	2.9036 ± 0.1285	1.5852	1.1572 ± 0.0321

γ-alumina beads	Porosity, ε_1 (*b*)	Porosity, ε_2 (*c*)	Porosity, ε_3 (*d*)
Exp. run 1	0.5322	0.6680	0.5946
Exp. run 2	0.5311	0.6482	0.6078
Average	0.5317	0.6581	0.6012

Notes: (*a*): Bulk density calculated from mass to volume ratio based on data provided in Table 2.5.

(*b*): For ε_1, skeletal density was obtained from pycnometer and bulk density from mass to volume ratio.

(*c*): For ε_2, skeletal density was obtained from pycnometer and bulk density from porosimeter;

(*d*): For ε_3, both densities were obtained from mercury porosimeter.

For a γ-alumina washcoat, or various shaped pellets, with surface areas 100 – 200 $m^2 g^{-1}$, the bulk densities or apparent densities, ρ_{bulk} or ρ_b, described in the literature are:

(a) The bulk density reported in Hayes and Kolaczkowski (2000) was between 1.307 – 1.414 g cm^{-3};

(b) In Antonyuk *et al.* (2006), the bulk density reported for γ-alumina beads (SASOL, 97.9% γ-Al_2O_3) was 1.04 g cm^{-3};

(c) Further supporting literature can be found in Sharma *et al.* (1991) with the bulk density ranging between 1.16 – 1.42 g cm^{-3}, and surface area between 96.5 – 171 $m^2 g^{-1}$;

(d) In Davidová (1990), the apparent density (bulk density) reported was between 0.811 – 1.195 g cm^{-3} for γ-alumina Raschig rings (cylindrical shape) with a BET surface area of 218 $m^2 g^{-1}$.

In this thesis, the bulk density obtained for the powder form of γ-alumina beads using mercury porosimeter is 0.6276 g cm^{-3} which is very similar to the manufacturer's data (i.e. SASOL (2009): 0.77 – 0.81 g cm^{-3}). However, the internal porous structure of the γ-alumina beads is destroyed when using powder as a testing material. Hence, results with powder are not shown in the thesis because its general properties are not relevant to the works done in other chapters.

Tests on the solid form of γ-alumina beads with the mercury porosimeter show that the average bulk density is 1.1572 $\pm$ 0.0321 g cm^{-3}. Whereas, the apparent density calculated for γ-alumina beads based on the mass to volume ratio is 1.5852 g cm^{-3}, which is above the range in literature data. Therefore, the solid form of the γ-alumina bulk density from the mercury porosimeter was used, i.e. 1.1251 g cm^{-3}.

The skeletal densities, or true densities, $\rho_{skeletal}$ or ρ_s, reported in the literature for a γ-alumina washcoat, or various shaped pellets, with a surface area: 100 – 200 $m^2 g^{-1}$, are:

1. In Antonyuk *et al*. (2006), the skeletal density reported for γ-alumina beads (SASOL, 97.9% γ-Al_2O_3) was 3.23 g cm^{-3};
2. In Tang *et al.* (1987), the skeletal density reported for γ-alumina and silica-alumina (with surface area around 100 $m^2 g^{-1}$) was 3.393 and 2.310 g cm^{-3} respectively;
3. In Davidová (1990), the true density reported for cylindrical shaped γ-alumina was 3.174 $\pm$ 0.015 g cm^{-3} using pycnometer.

In this thesis, the average skeletal density found for γ-alumina beads using the pycnometer was 3.3848 ± 0.0038 g cm^{-3}, compared with 2.9036 ± 0.1285 g cm^{-3} obtained from the mercury porosimeter. These results support the statement made previously that for a porous material with a pore diameter within the microporous to mesoporous range, the true densities obtained from pycnometer will always be higher than from mercury penetration, because the mercury cannot enter pore diameters ≤ 2 nm, but small gas molecules (i.e. helium) can. In this work, the skeletal density from mercury porosimeter was used, i.e. 2.7751 g cm^{-3}.

The reason behind choosing the mercury porosimetry data for skeletal and bulk densities is that:

(a) the standard error for both densities are almost in the same range: 2.8 – 4.4%, whereas the standard error for pycnometer is 0.11% (calculated from Table 2.13), and

(b) for the porosity calculation, it is important that the density data used has the same standard error.

Hence, the skeletal and bulk densities used for porosity calculations with same standard error are:

(i) $\rho_{skeletal}$ from pycnometer and ρ_{bulk} from m/V ratio;

(ii) $\rho_{skeletal}$ and ρ_{bulk} from mercury porosimeter.

The porosities reported in the literature for the γ-alumina washcoat, or various shaped pellets are:

(a) the porosity calculated for the γ-alumina beads (SASOL, 97.9% γ-Al_2O_3) in Antonyuk *et al*. (2006) was 0.678;

(b) the porosities for γ-alumina and silica-alumina measured by Tang *et al.* (1987) were 0.592 and 0.596 respectively;

(c) the porosities for γ-alumina catalysts reported by Davidová (1990) were from 0.624 to 0.747.

From Table 2.7, the γ-alumina bead porosity calculated using the pycnometer and the mass to volume ratio was 0.5317 ± 0.0006, comparing to 0.6012 ± 0.0066 obtained from the mercury porosimeter. In conclusion, the porosity calculated using the mercury porosimeter data is more trustworthy. Therefore, in this work, the porosity for γ-alumina beads was 0.5946.

2.3 Summary of pellet properties

Table 2.14: General properties of the γ-alumina beads studied.

Physical properties										
Mass of a γ-alumina bead based on container type, *M* (g):	**Plastic cup**		**Plastic vial**		**Glass beaker**		**None**		**Average ± Std**	
	0.00085		0.00080		0.00088		0.00079		0.00083 ± 0.00004	
Bulk density, ρ_b (g cm^{-3}):	**From manufacturer**		**From mercury porosimeter**				**From mass over volume measured**			
	0.77		1.1572 ± 0.0321 [(a)]		0.6276 [(b)]		1.5852			
Skeletal density, ρ_s (g cm^{-3}):	**From pycnometer**						**From mercury porosimeter**			
	3.3848 ± 0.0038						2.9036 ± 0.1285			
Porosity, ε_p:	**ρ_s from pycnometer and ρ_b from mass over volume**						**ρ_s and ρ_b from mercury porosimeter**			
	0.5317 ± 0.0006						0.6012 ± 0.0066			
Surface area, *A* (m^2 g^{-1}):	**Surface area from nitrogen adsorption analysis**						**Surface area from mercury porosimetry**			
	BET with free-space		*BET without free-space*							
	141.9		244.2				227.775 ± 3.235			
Pore volume, V_p (cm^3 g^{-1}):	**From nitrogen adsorption**						**From mercury porosimetry**			
	BJH with free-space		*BJH without free-space*				*Max. pore volume intrude*		*Effective pore volume*	
	0.4441		0.5749				0.5197 ± 0.0087		0.4517 ± 0.0083	
Pore diameter, d_p (nm):	**From nitrogen adsorption**				**From manufacture data**		**From mercury porosimetry**			
	12 (with FS) [(c)]		12 (without FS) [(c)]		8.8		8.1667 ± 0.0005 [(a)]		8.1621 [(b)]	

Notes: (a) The average bulk density and pore diameter of γ-alumina beads in solid form.

(b) The average bulk density and pore diameter of γ-alumina beads in powder form.

(c) The abbreviation term 'FS' stands for 'free-space'.

2.4 Summary on key properties

By referring to earlier work described by Yap (2011) on washcoated and uncoated monoliths, this helped with the selection of appropriate techniques to interpret many of the experimental measurements described in this chapter. Nevertheless, the measurement of these physical properties was a very time consuming activity, and care had to be taken with these techniques. Sometimes the analytical equipment was not available as it required maintenance, or it was used by others and a time had to be scheduled for its use.

Based on the results of measurements in this chapter, the γ-alumina beads in solid form have very similar properties to the γ-alumina washcoat used on the monolith. For example:

- **Surface area:** washcoat: 168.157 m^2 g^{-1};
  beads: 147.2 m^2g^{-1} (BET surface area, nitrogen adsorption);
  227.775 ± 3.235 m^2 g^{-1} (mercury porosimeter).
- **Pore volume:** washcoat: 0.5653 cm^3 g^{-1};
  beads: 0.4441 cm^3 g^{-1} (nitrogen adsorption);
  0.4517 ± 0.0083 cm^3 g^{-1} (mercury porosimeter).
- **Pore diameter:** washcoat: 11.056 nm;
  beads: 12 nm (nitrogen adsorption);
  8.1667 ± 0.0005 nm (mercury porosimeter).
- **Skeletal density:** washcoat: 2.1553 g cm^{-3};
  beads: 3.3848 ± 0.0038 g cm^{-3} (pycnometer);
  2.9036 ± 0.1285 g cm^{-3} (mercury porosimeter).
- **Bulk density;** washcoat: 0.8924 g cm^{-3};
  beads: 1.5852 g cm^{-3} (mass to volume ratio);
  1.1572 ± 0.0321 g cm^{-3} (mercury porosimeter).
- **Porosity:** washcoat: 0.5860;
  beads: 0.5317 ± 0.0006 (ρ_s from pycnometer and ρ_b from m/V ratio)
  0.6012 ± 0.0066 (ρ_s, ρ_b from mercury porosimeter).

This is not surprising and was expected, however, this is a useful check on these two materials, and on the measurement techniques and how the data was interpreted in this chapter. It will now be interesting to compare in the chapters that follow, the value of effective diffusivity when it is:

(i) measured in beads;
(ii) measured in the washcoated monolith,
(iii) compared with published data in the literature.

and how this would translate into an 'apparent tortuosity', when used in the parallel pore model.

Base on the data and discussions presented in this chapter, the following physical properties will be used in the chapters that follow:

Cordierite monolith

(a) The pore size distribution from Yap (2011) shows that the pore diameter for cordierite monolith is about 2 to 5 μm.
(b) The pore volume of cordierite monolith is 0.233 $cm^3\ g^{-1}$.
(c) The wall thickness of the channel is 175.403 ± 5.209 μm.
(d) The cell size of a single channel is 1.0 mm × 1.0 mm.
(e) The average bulk volume of a cut sample with 12 cells (4 cells in a row × 3 cells in a column) of cordierite monolith used in this thesis is: 0.1472 ± 0.0055 cm^3.
(f) The average skeletal volume of a cut sample with 12 cells (4 cells in a row × 3 cells in a column) of cordierite monolith used in this thesis is: 0.0841 ± 0.0052 cm^3.
(g) The average mass of a cut sample with 12 cells (4 cells in a row × 3 cells in a column) of cordierite monolith used in this thesis is: 0.0606 ± 0.0011 g.

Washcoated monolith

(a) The pore size distribution from Yap (2011) shows that the pore diameter for washcoated monolith is about 10 nm.
(b) The pore volume of the washcoated monolith is 0.5653 $cm^3\ g^{-1}$.
(c) The wall thickness of the channel is 175.403 ± 5.209 μm.
(d) The average channel equivalent radius: 0.5189 ± 0.1079 mm.

(e) The average washcoat thickness: 0.1055 ± 0.0878 mm.

(f) The average bulk volume of a cut sample with 12 cells (4 cells in a row × 3 cells in a column) of washcoated monolith used in this thesis is: 0.1408 ± 0.0026 cm^3.

(g) The average skeletal volume of a cut sample with 12 cells (4 cells in a row × 3 cells in a column) of washcoated monolith used in this thesis is: 0.0896 ± 0.0025 cm^3.

(h) The average mass of a cut sample with 12 cells (4 cells in a row × 3 cells in a column) of washcoated monolith used in this thesis is: 0.0889 ± 0.0008 g

γ-alumina washcoat

(a) The pore diameter of γ-alumina washcoat is assumed to be the same as the pore diameter of washcoated monolith in Yap (2011), i.e. 10 nm.

(b) The pore volume of the γ-alumina washcoat is 0.5653 $cm^3\ g^{-1}$.

(c) The average washcoat thickness: 0.1055 ± 0.0878 mm.

(d) The average bulk density of the γ-alumina washcoat is 0.8924 g cm^{-3}.

(e) The average skeletal density of the γ-alumina washcoat is 2.1553 g cm^{-3}.

(f) The porosity for the γ-alumina washcoat: 0.5860.

1.0 mm γ-alumina beads

(a) From the pore size distribution curves for the γ-alumina beads measured in this thesis, the average pore diameter is 8.2 with mercury porosimetry and 12 nm with nitrogen adsorption.

(b) The BET surface area measured in this thesis for γ-alumina beads is 147.2 $m^2\ g^{-1}$ with nitrogen adsorption. The surface area measured with mercury porosimetry is: 227.775 ± 3.235 $m^2\ g^{-1}$.

(c) The pore volume measured in this thesis for γ-alumina beads are 0.4441 and 0.4517 ± 0.0083 $cm^3\ g^{-1}$ with nitrogen adsorption and mercury porosimetry.

(d) For γ-alumina beads, the skeletal density preferred to use is 2.7751 g cm^{-3} from mercury porosimetry.

(e) For γ-alumina beads, the preferred bulk density is 1.1251 g cm^{-3}, obtained from the mercury porosimetry.

(f) The preferred porosity for γ-alumina beads is 0.5946, which was calculated from mercury porosimetry data.

References

Allen, T., 1997. *Particle Size Measurement Volume 2: Surface Area and Pore Size Determination.* Springer.

Anderson, J.A. & Garcia, M.F., 2005. *Supported Metals in Catalysis.* London: Imperial College Press.

Anderson, J.R. & Pratt, K.C., 1985. *Introduction to characterization and testing of catalysts.* Academic Press Sydney.

Antonyuk, S., Khanal, M., Tomas, J., Heinrich, S. & Mörl, L., 2006. Impact breakage of spherical granules: experimental study and DEM simulation. *Chemical Engineering and Processing: Process Intensification,* 45, pp. 838-856.

Barrett, E., Joyner, L. & Halenda, P., 1951. The Determination of Pore Volume and Area Distributions in Porous Substances. I. Computations from Nitrogen Isotherms. *Journal of the American Chemical Society,* 73, pp. 373-380.

BEL JAPAN. *Seminar on Adsorption: What is adsorption?* [Online]. Available: http://www.nippon-bel.co.jp/tech/seminar01_e.html [Accessed: 06 January 2012].

Boublík, T., Fried, V. & Hála, E., 1984. *The vapour pressures of pure substances.* United States: Elsevier Science Pub. Co., Inc., New York, NY.

Chu, W., Chernavskii, P.A., Gengembre, L., Pankina, G.A., Fongarland, P. & Khodakov, A.Y., 2007. Cobalt species in promoted cobalt alumina-supported Fischer–Tropsch catalysts. *Journal of Catalysis,* 252, pp. 215-230.

Condon, J.B., 2006. *Surface area and porosity determinations by physisorption: measurements and theory.* Elsevier Science.

Davidová, H., 1990. Chromatographic determination of effective diffusivities of Raschig ring-shaped catalyst: Radial anisotropy of pellets. *Applied catalysis,* 66, pp. 167-179.

Edejer, M.P. & Thodos, G., 1967. Vapor Pressures of Liquid Nitrogen Between the Triple and Critical Points. *J. Chem. Eng. Data,* 12, pp. 206-209.

Gregg, S. & Sing, K., 1982. Adsorption, Surface Area and Porosity Academic. *New York,* pp. 242-245.

Hayes, R.E. & Kolaczkowski, S.T., 1997. *Introduction to catalytic combustion.* Gordon and Breach.

Hayes, R.E. & Kolaczkowski, S.T., 2000. Evaluating the effective diffusivity of methane in the washcoat of a honeycomb monolith. *Applied Catalysis B: Environmental,* 25, pp. 93-104.

Imelik, B. & Vedrine, J.C. 1994. Catalyst characterization: physical techniques for solid materials. *In:* Imelik & Védrine (eds.). New York Plenum Press.

Klose, F., Wolff, T., Lorenz, H., Seidel-Morgenstern, A., Suchorski, Y., Piórkowska, M. & Weiss, H., 2007. Active species on γ-alumina-supported vanadia catalysts: Nature and reducibility. *Journal of Catalysis,* 247, pp. 176-193.

Kruk, M. & Jaroniec, M., 2001. Gas Adsorption Characterization of Ordered Organic−Inorganic Nanocomposite Materials. *Chemistry of Materials,* 13(10), pp. 3169-3183.

Lippens, B.C. & de Boer, J.H., 1965. Studies on pore systems in catalysts: V. The t method. *Journal of Catalysis,* 4, pp. 319-323.

Micromeritics, 2011. ASAP 2020. Accelerated Surface Area and Porosimetry System. Operator's Manual.

Moussa, M.R., Muijlwijk, R. & van Dijk, H., 1966. The vapour pressure of liquid nitrogen. *Physica (Amsterdam),* 32, pp. 900-912.

Neimark, A.V., Sing, K.S. & Thommes, M., 2008. Mercury Porosimetry in Surface Area and Porosity. *Handbook of Heterogeneous Catalysis*.

Niemantsverdriet, J.W., 2008. *Spectroscopy in Catalysis: An Introduction.* John Wiley & Sons.

Pierotti, R. & Rouquerol, J., 1985. Reporting physisorption data for gas/solid systems with special reference to the determination of surface area and porosity.

Rouquerol, F., Rouquerol, J. & Sing, K., 1999. *Adsorption by Powders and Porous Solids: Principles, Methodology and Applications.* London: Academic Press.

SASOL, 2009. Spheres & Extruate Presentation [Online]. Available: http://www.sasolgermany.de/fileadmin/doc/alumina/Sasol_Spheres_and_Extrudates-Dec2009_web.pdf [Accessed 08 February 2012].

Sharma, R.K., Cresswell, D.L. & Newson, E.J., 1991. Effective diffusion coefficients and tortuosity factors for commercial catalysts. *Industrial & Engineering Chemistry Research,* 30, pp. 1428-1433.

Sing, K., 2001. The use of nitrogen adsorption for the characterisation of porous materials. *Colloids and Surfaces A: Physicochemical and Engineering Aspects,* 187–188, pp. 3-9.

Sing, K.S.W., Everett, D.H., Haul, R.A.W., Moscou, L., Pierotti, R.A., Rouquerol, J. & Siemieniewska, T., 1985. Reporting physisorption data for gas/solid systems with special reference to the determination of surface area and porosity (Recommendations 1984). *Pure and Applied Chemistry*, 57, pp. 603-619.

Tang, G.H.Y., Trimm, D.L. & Wainwright, M.S., 1987. Effective diffusivity in cylindrical catalyst pellets. *Chemical engineering in Australia,* 12, pp. 9-12.

Thommes, M., 2010. Physical Adsorption Characterization of Nanoporous Materials. *Chemie Ingenieur Technik,* 82, pp. 1059-1073.

Urbonaite, S., 2008. *Synthesis and characterisation of carbide derived carbons.* Department of Physical, Inorganic and Structural Chemistry, Stockholm University.

Webb, P.A., 2001. An introduction to the physical characterization of materials by mercury intrusion porosimetry with emphasis on reduction and presentation of experimental data. Micromertics Instrument Corp.

Wei, J., Denn, M.M., Seinfeld, J.H., Chakraborty, A., Ying, J., Peppas, N. & Stephanopoulos, G., 2001. *Molecular modeling and theory in chemical engineering.* Access Online via Elsevier.

Westermarck, S., 2000. *Use of mercury porosimetry and nitrogen adsorption in characterisation of the pore structure of mannitol and microcrystalline cellulose powders, granules and tablets.* Helsinki, Finland: University of Helsinki

Whittemore Jr, O.J. & Sipe, J.J., 1974. Pore growth during the initial stages of sintering ceramics. *Powder Technology,* 9, pp. 159-164.

Yap, Y. 2011. *On-line and on-engine catalyst characterisation – effective diffusion and reaction mechanisms.* Phd, University of Bath.

3 Chromatographic methods and moment analysis

In this chapter experiments are performed on the γ-alumina beads, and the following key themes are covered:

- **Different forms of diffusion:** a description of molecular, Knudsen and surface diffusion is provided. This then leads to an explanation of the effective diffusivity term.

- **Chromatographic experiments:** a description is provided of how residence time distribution (RTD) analysis is used to interpret the results of chromatographic experiments. This leads to an explanation of how the 1^{st} moment and 2^{nd} central moment can be evaluated from experimental data.

- **Experimental chromatographic technique:** the design of the experimental apparatus is described and the modifications that had to be made in order to improve the technique. The apparatus is then used and the response of packed columns to a pulse input under different flow conditions is discussed. Experiments are performed with 1 mm γ-alumina beads in 200 mm and 400 mm long packed beds.

- **Moment analysis:** this is considered in more detail, looking at the choice of 'Peak' and 'Base-line' options and their impact on the final solution. Simpson's rule is used to integrate peak areas, and this method is compared with the use of a proprietary peak analysis tool known as OriginPro 8.6. Different material balance models are then considered and from there the adsorption equilibrium constant, K is determined.

The work done in this chapter is summarised in Figure 3.1:

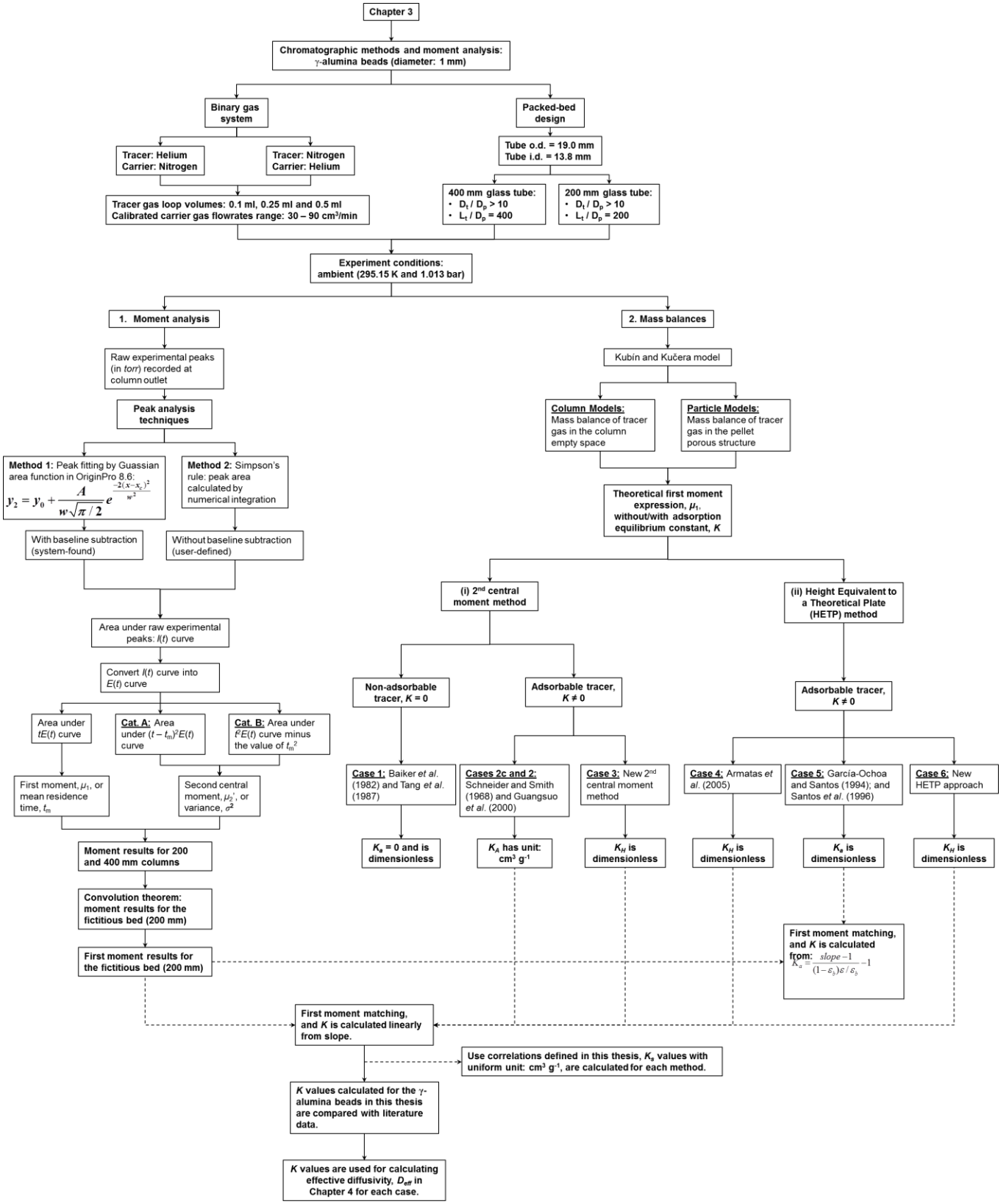

Figure 3.1: Structure of Chapter 3 and links with other chapters.

3.1 Types of diffusion

3.1.1 Mass transport and diffusion mechanism

Diffusion effects, gas transport and diffusion mechanism inside a packed-bed column containing porous pellets are shown in Figure 3.2.

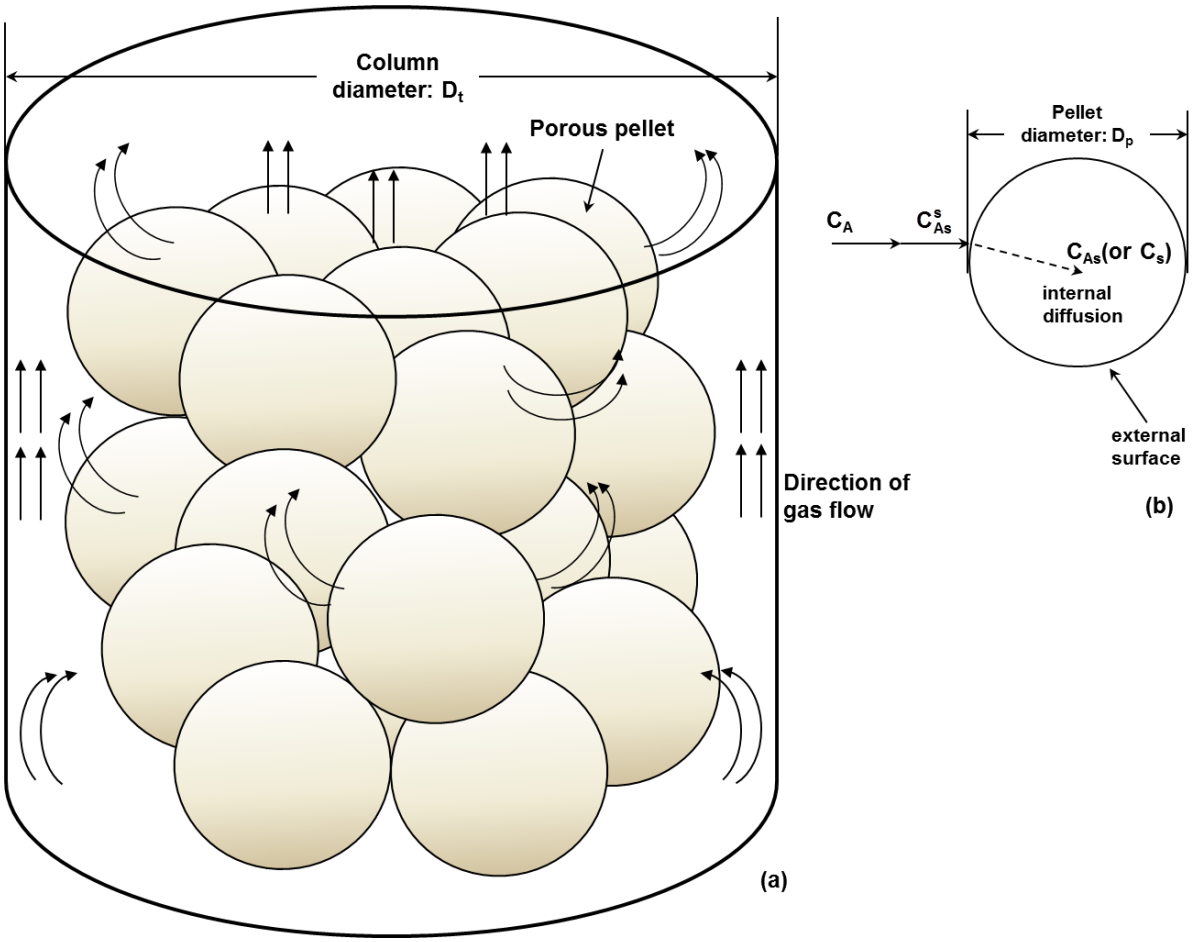

Figure 3.2: A schematic showing: (a) gas transport in the column free-space of a packed-bed column and (b) the external mass transport of tracer gas *A* in the column free space to the external surface of the particle (i.e. C_A to C^s_{As}); and the internal transport, or diffusion of tracer gas *A* in the pore structure of a particle (i.e. C^s_{As} to C_{As}, or C^s_{As} to C_s).

Note: The difference between C_{As} and C_s is the definition of units. The detail can be found in the Nomenclature, and in Sections 3.8.4 and 3.8.6.

There are three types of diffusion in catalyst pores, and these are illustrated in Figure 3.3:

(a) Molecular diffusion (or bulk diffusion);

(b) Knudsen diffusion;

(c) Surface diffusion.

Molecular or bulk diffusion occurs when the mean free path is relatively short compared to the pore size (Hosticka *et al.*, 1998). Knudsen diffusion occurs when the mean free path λ is longer than the pore size, d_{pore}, so the molecules collide frequently with the pore wall. Knudsen diffusion is dominant for pores that range in diameter between 2 and 50 nm (Malek and Coppens, 2003b). Surface diffusion occurs when solutes adsorb on the surface of the pore and hop from one site to another through interactions between the surface and molecules, and it can also be regarded as pore diffusion (Jaguste and Bhatia, 1995). For most of the catalysts used in industrial practice, the most important mechanisms are Knudsen diffusion and bulk diffusion. The surface diffusion is only taken into consideration when adsorption is important.

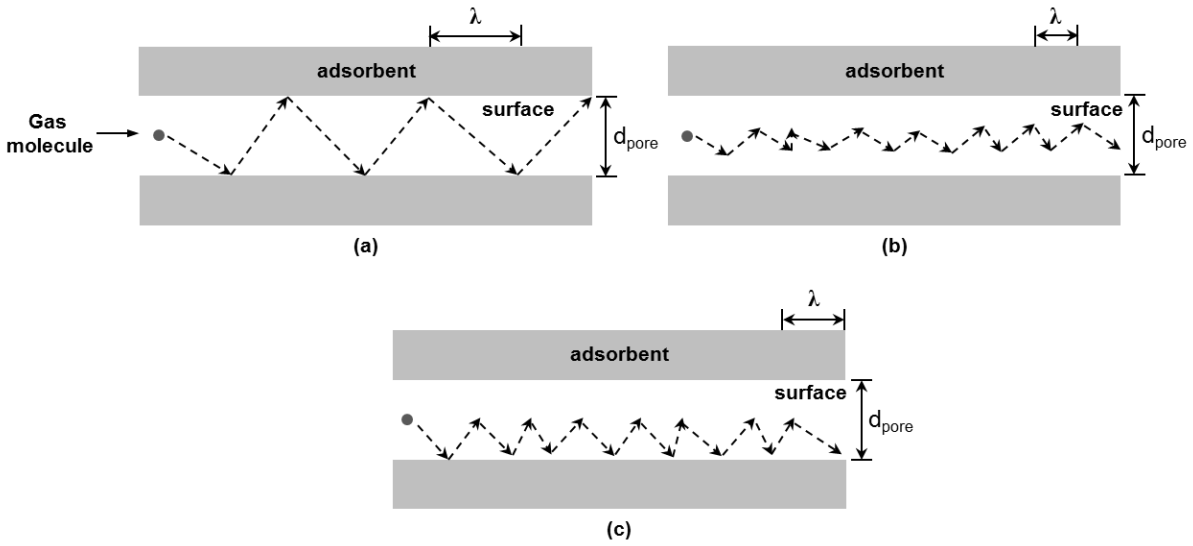

Figure 3.3: Different types of diffusion mechanisms: (a) Knudsen diffusion; (b) Molecular diffusion; (c) Surface diffusion

Mass transport inside a porous particle is shown in Figure 3.2(b) has been usually described according to the hypothesis of a pseudo-homogeneous media, where Fick's equation can be applied through effective diffusivity (Garcı́a-Ochoa and Santos, 1994):

$$N_i = -D_e \left. \frac{dC_i}{dr} \right|_{r=R} \tag{3.1}$$

where:
- R is the radius of the porous pellet;
- N_i is the molar flux;
- C_i is the concentration of tracer gas in the pore structure of the particle (same as C_s, with units mol m^{-3}_{pore});
- D_e is the effective diffusivity.

Effective diffusivity, D_e (or D_{eff}), is usually defined as:

$$D_e = \bar{D} f \tag{3.2}$$

where:
- $\bar{D}$ is the average composite local diffusivity;
- f is a correction factor.

The advantage of this correction factor is that it does not depend on operational conditions, but only on the solid structure considered. For the simplest models, parallel pore and cross-linking pore models, the factor f is usually calculated as (Satterfield, 1981):

$$f = \frac{\varepsilon}{\tau} \tag{3.3}$$

where:
- ε is the particle porosity;
- τ is the apparent tortuosity factor.

3.1.2 Bulk, Knudsen and Composite diffusivity

In Hayes and Kolaczkowski (1997, 2000) theoretical expressions and example calculations for diffusion terms have been provided from which the following information has been obtained.

3.1.2.1 Bulk diffusion coefficient

In Hayes and Kolaczkowski (1997), the empirical correlation for bulk diffusivity, D_{AB} for a binary gas mixture developed by Fuller *et al.* (1966) gives the following expression:

$$D_{AB} = \frac{1.013\times10^{-2}T^{1.75}\left(\frac{1}{M_A}+\frac{1}{M_B}\right)^{\frac{1}{2}}}{P\left[\left(\sum v_i\right)_A^{1/3}+\left(\sum v_i\right)_B^{1/3}\right]^2} \tag{3.4}$$

where:
- D_{AB} is the diffusion coefficient, $m^2\ s^{-1}$;
- T is the absolute temperature, K;
- P is the pressure, Pascal;
- M_A and M_B are the molecular weights of the gas pair A and B, $g\ mol^{-1}$;
- $(v_i)_A$ and $(v_i)_B$ are the diffusion volumes of gas molecules.

Besides, a similar expression to Equation (3.4) was given in Cussler (2009), which has the following form:

$$D_{AB} = 10^{-3}\frac{T^{1.75}\left(1/\tilde{M}_1+1/\tilde{M}_2\right)^{\frac{1}{2}}}{P\left[\left(\sum_i V_{i1}\right)^{1/3}+\left(\sum_i V_{i2}\right)^{1/3}\right]^2} \tag{3.5}$$

where:
- D_{AB} is the diffusion coefficient, $cm^2\ s^{-1}$;
- T is the absolute temperature, K;
- P is in atmospheres, bar;
- $\tilde{M}_1$ and $\tilde{M}_2$ are the molecular weights of the gas pair 1 and 2, $g\ mol^{-1}$;
- V_{i1} and V_{i2} are the diffusion volumes of gas molecules.

Equations (3.4) and (3.5) are effectively the same apart from the difference in unit for D_{AB} and P. The diffusion volumes of gas molecules can be found in Reid *et al.* (1987). Therefore, in this thesis, Equations (3.4) was used to calculate the bulk diffusivity, D_{AB}.

3.1.2.2 Knudsen diffusion coefficient

The Knudsen diffusivity in a pore radius r_p and length l_p where $l_p >> r_p$, is defined as (Satterfield, 1981):

$$J_K = -D_K \frac{dC}{dx} = -\frac{2}{3} r_p \sqrt{\frac{8R_g T}{\pi M}} \frac{dC}{dx} \tag{3.6}$$

$$D_{K(r_p)} = -\frac{2}{3} r_p \sqrt{\frac{8R_g T}{\pi M}} = 97 r_p \sqrt{\frac{T}{M}} \tag{3.7}$$

where: – the $D_{K(rp)}$ is given in $m^2\ s^{-1}$;

– R_g is the universal gas constant;

– T the temperature in K and M is the molecular weight of tracer gas.

3.1.2.3 Composite or local diffusion coefficient

For diffusion of gases in porous solids, with very fine pores and for low concentration of diffused component within the particle, the composite diffusivity is a combination of Knudsen and Bulk diffusivity, D_C is given by (Zhu, 1981; Santos *et al.*, 1996):

$$D_C = \int_0^{\infty} \left(\frac{1}{D_{AB}} + \frac{1}{D_{K(r_p)}} \right)^{-1} f(r_p) dr_p \tag{3.8}$$

where: – $D_{K(rp)}$ is the Knudsen diffusivity in a pore of radius r_p;

– $f(r_p)$ is the pore size density function.

As described in example calculations in Hayes and Kolaczkowski (1997), Equation (3.8) can be simplified as:

$$D_C = \frac{1}{D_{AB}} + \frac{1}{D_K} \tag{3.9}$$

3.1.2.4 Effective diffusivity and composite diffusivity

The effective diffusivity D_{eff} is related to the composite diffusivity D_C by the expression, which is required to match the predictions to experimental data (Johnson and Stewart, 1965; Satterfield and Cadle, 1968; Feng and Stewart, 1973):

$$\frac{D_{eff}}{D_C} = \frac{\varepsilon}{\tau_p} \tag{3.10}$$

where: – ε is the particle porosity;

– τ_p is the tortuosity factor.

This equation is similar to the effective diffusivity equation for a parallel pore model described by Fogler (2004):

$$D_{eff} = \varepsilon \frac{D_{AB}\sigma_c}{\tau} \tag{3.11}$$

The constriction factor is generally treated as 1 and hence the tortuosity factor τ_p in Equation (3.10) is equivalent to the tortuosity τ define in Equation (3.11). The tortuosity factor calculated in this thesis is determined from Equation (3.10), rather than Equation (3.11), because the Knudsen diffusivity is an important factor that one cannot simply neglect.

3.2 Review of methods measuring effective diffusivity

The effective diffusivity can be determined from measurement under inert conditions, or at the same conditions when a chemical reaction is taking place inside the catalyst particle (Garcá-Ochoa and Santos, 1994). In other words, these can be regarded as physical and chemical techniques of evaluating effective diffusivity. The measurement methods under inert conditions (i.e. using a carrier gas and tracer gas; such as Nitrogen and Helium) can be classified into two groups:

1. Steady-state measurement method;
2. Unsteady-state or transient measurement method.

The steady-state method usually employs a Wicke-Kallenbach type of cell, where a catalyst pellet is mounted in a diffusion cell. One major disadvantages of the steady-state method is that diffusion reflects only those pores that allow passage of gas from one side of the pellet to the other (i.e. open pores or cross-link pores).

The unsteady-state method (i.e. gas chromatographic method) will detect diffusion in the dead-end pores, and the diffusion measured reflect both close-end and continuous pores. This fact led to the debate that the effective diffusivities obtained more closely reflect diffusivities in a reacting system (Westermarck, 2000; Zhang, 2005). Besides, the advantages of chromatographic method are (Biswas *et al.*, 1987; Garcá-Ochoa and Santos, 1994; Do, 1998):

(a) easy to set up and collection of data, conveniently used over wide range of temperatures and pressures;
(b) multiple pellets employed, can be used with commercial catalyst particles;
(c) can be used even under reaction conditions;
(d) quick if only affinity constant is required.

The disadvantages of chromatographic method are:

(a) data analysis is quite cumbersome, the response used to measure D_{ax} and D_{eff} is a function of many factors;
(b) complicated mathematical model;
(c) nonisothermal operation.

3.3 The unsteady-state method – gas chromatographic technique

This technique is already well described in many publications (e.g. Schneider and Smith, 1968; Baiker *et al*., 1982; Tang *et al*., 1987; Garc ń-Ochoa and Santos, 1994; Santos *et al*., 1996; Guangsuo *et al*., 2000; Armatas *et al*., 2005). In simple terms, the sample to be tested is packed into a column through which an inert gas (carrier stream) flows. A pulse of tracer gas is injected, and at the outlet of the column, the concentration of that tracer gas is monitored as a function of time. The packed-bed geometries used in the literature are summarised as follows:

1. **A packed-bed column**: it is suggested in many papers/books (Rase and Holmes, 1977; Froment *et al.*, 1990; Idem *et al.*, 1997; Hayes and Kolaczkowski, 1997; Aboudheir *et al.*, 2006) that, to obtain isothermal reactor operation and to minimise channelling, conditions for designing a packed-bed column that allow plug flow to be approached inside the column are:
   (a) the ratio of bed height to particle size $L_t / D_p > 50$; and
   (b) the ratio of internal diameter of the column to the particle size, $D_t / D_p > 10$. Although in some literature, $D_t / D_p > 15$ is used.
2. **A Single Particle String Column (SPSC) or Single Pellet String Reactor (SPSR)**: the internal column diameter (D_t) to particle size (D_p) ratio proposed by Baiker *et al.* (1982), Tang *et al*. (1987) and Guangsuo *et al.* (2000), are $D_t / D_p = 1.05$ to 1.7. The ratio of $L_t / D_p > 50$ is also recommended.

The flow inside such a column is usually assumed to be isobaric and isothermal. An example of a packed-bed model is known as the Kub ń and Kučera model (Kub ń, 1965; Kučera, 1965) and this model was used in this thesis to describe the transport of tracer gas inside the porous particles, and in the column free space in the packed-bed. The five parameters considered in the Kub ń-Kučera model are:

i) The adsorption equilibrium constant, K;
ii) The adsorption rate constant: k_{ads} (since the tracer concentration is small, the physical adsorption rate is assumed to be first order);
iii) The external mass transfer coefficient: k_f;
iv) The intraparticle diffusivity: D_{eff};
v) The axial dispersion coefficient: D_{ax}.

Applying Laplace transformation to the differential equations (i.e. the mass transport of tracer gas in the bulk gas phase and in the pores), Kub ń and Kučera showed that these parameters are determinable from theoretical moment expressions. Therefore, by matching the moments obtained from experimental response curves, with the theoretical moment expressions, then the intraparticle diffusivity, or the effective diffusivity of tracer gas in the porous structure could be calculated.

In this chapter, experiments are performed on such a column that is packed with spherical 1.0 mm beads. As an illustration, a schematic of what the response may look like is presented in Figure 3.4.

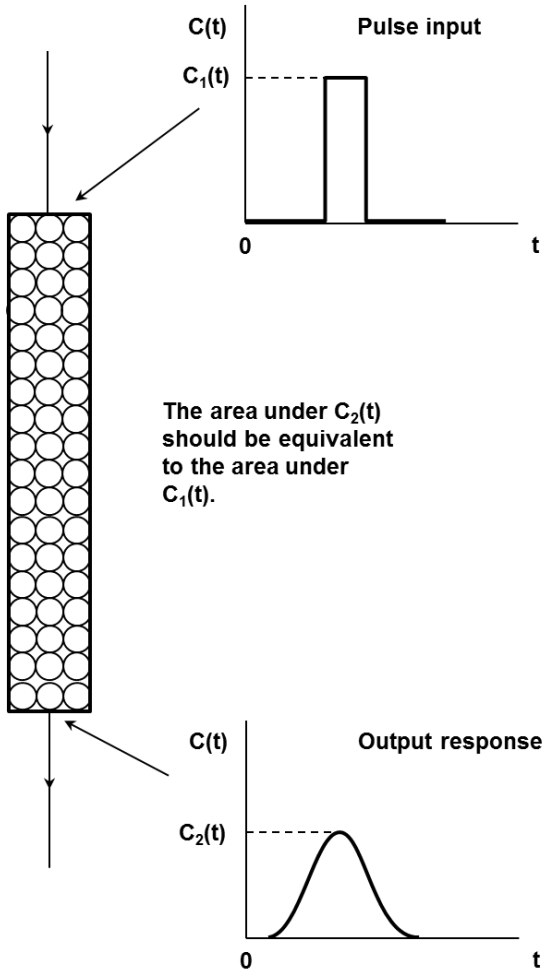

Figure 3.4: Schematic illustrating how the chromatographic method works, where $C_1(t)$ is the input pulse concentration curve, and $C_2(t)$ is the output concentration curve.

According to Tang *et al.* (1987), the effective diffusivities measured by the unsteady-state method are likely to be larger than those determined by steady-state method because of dead-end pores.

3.4 Residence-Time Distribution (RTD) analysis and modelling

The analysis of the response obtained in Figure 3.4 requires an understanding of RTD techniques and so these are briefly described in this section.

3.4.1 Ideal models: plug flow and perfect mixer

There are two simple ideal flow patterns, plug flow and well-mixed flow (perfect mixing), although in real equipment, the real flow patterns deviate from these ideals. In plug flow, it is assumed that matter flows without any dispersion or diffusion in the axial direction with a flat velocity profile. A Dirac injection is therefore transported without any deformation and shifted by a time-lag τ. A mathematical expression for the residence time distribution (RTD) function of the plug flow model is:

$$E(t) = \delta(t - \tau) \tag{3.12}$$

where δ is the Dirac impulse function, and this is shown in Figure 3.5. $E(t)$ on the y-axis is the residence time distribution (RTD) function at the measurement point. The plug flow model assumes no axial dispersion but only convective flow. Therefore, all of the tracer leaves the column at the same time.

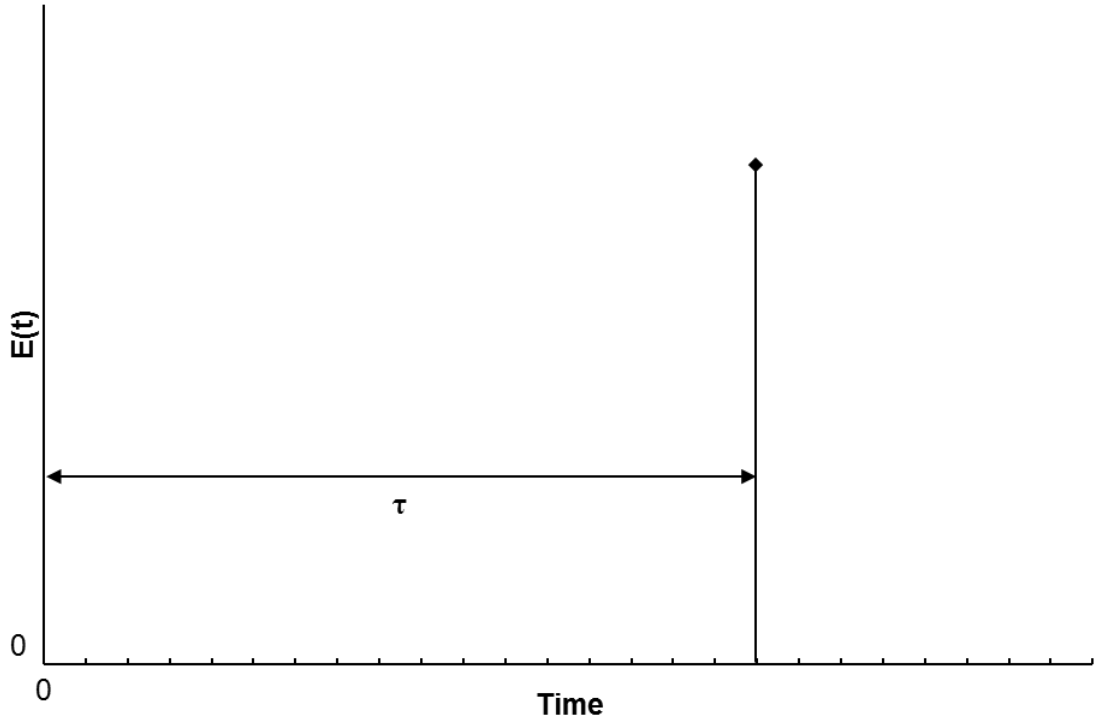

Figure 3.5: Ideal Plug Flow model (IAEA, 2008)

The RTD function for the well-mixed model is shown in Figure 3.6. The tracer is assumed to be mixed instantaneously and uniformly in the whole volume of the system. A mathematical expression for this model is:

$$E(t) = \frac{1}{\tau}\exp\left(-\frac{t}{\tau}\right) \tag{3.13}$$

The first moment about the origin gives the mean residence time, which is denoted as t_{mean} or τ. The second central moment gives the variance and is denoted as σ^2.

Plug flow and well-mixed models can be seen as two extreme cases, where mixing is either non-existent, or complete and instantaneous.

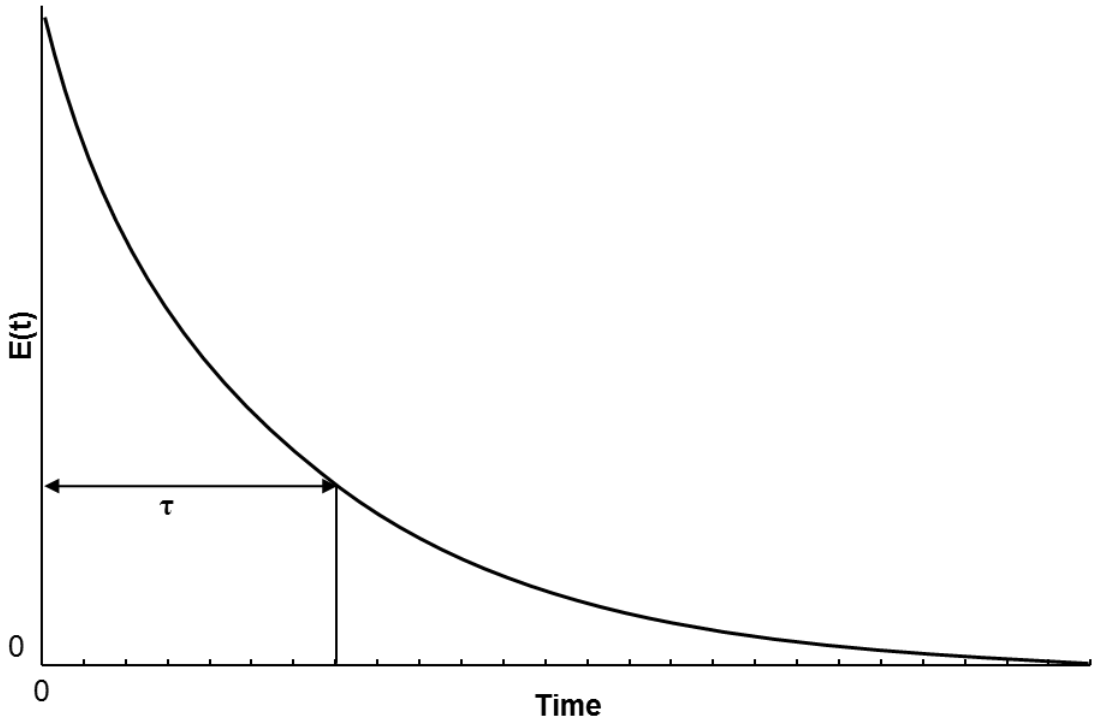

Figure 3.6: Well-mixed model (IAEA, 2008)

The Dirac impulse function $\delta(t)$, or unit impulse function, belongs to the special case of a Dirac delta function. For a small positive constant a, then the function $\delta_a(t)$ is defined in Mathews and Howell (2010) as:

$$\delta_a(t) = \begin{cases} \dfrac{1}{a} & \text{for } 0 < t < a, \\ 0 & \text{otherwise} \end{cases} \tag{3.14}$$

The unit impulse function is obtained by letting the time interval in Equation (3.14) go to zero:

$$\delta(t) = \lim_{a \to 0} \delta_a(t) \tag{3.15}$$

To illustrate the physical meaning, in this thesis, when a pulse injection of 0.25 ml is applied from a sample loop, a pulse injection function $f_a(t)$ is used. Figure 3.7 shows the graph of $y = f_a(t)$ at carrier gas flowrates of 30, 50 and 70 cm^3/min.

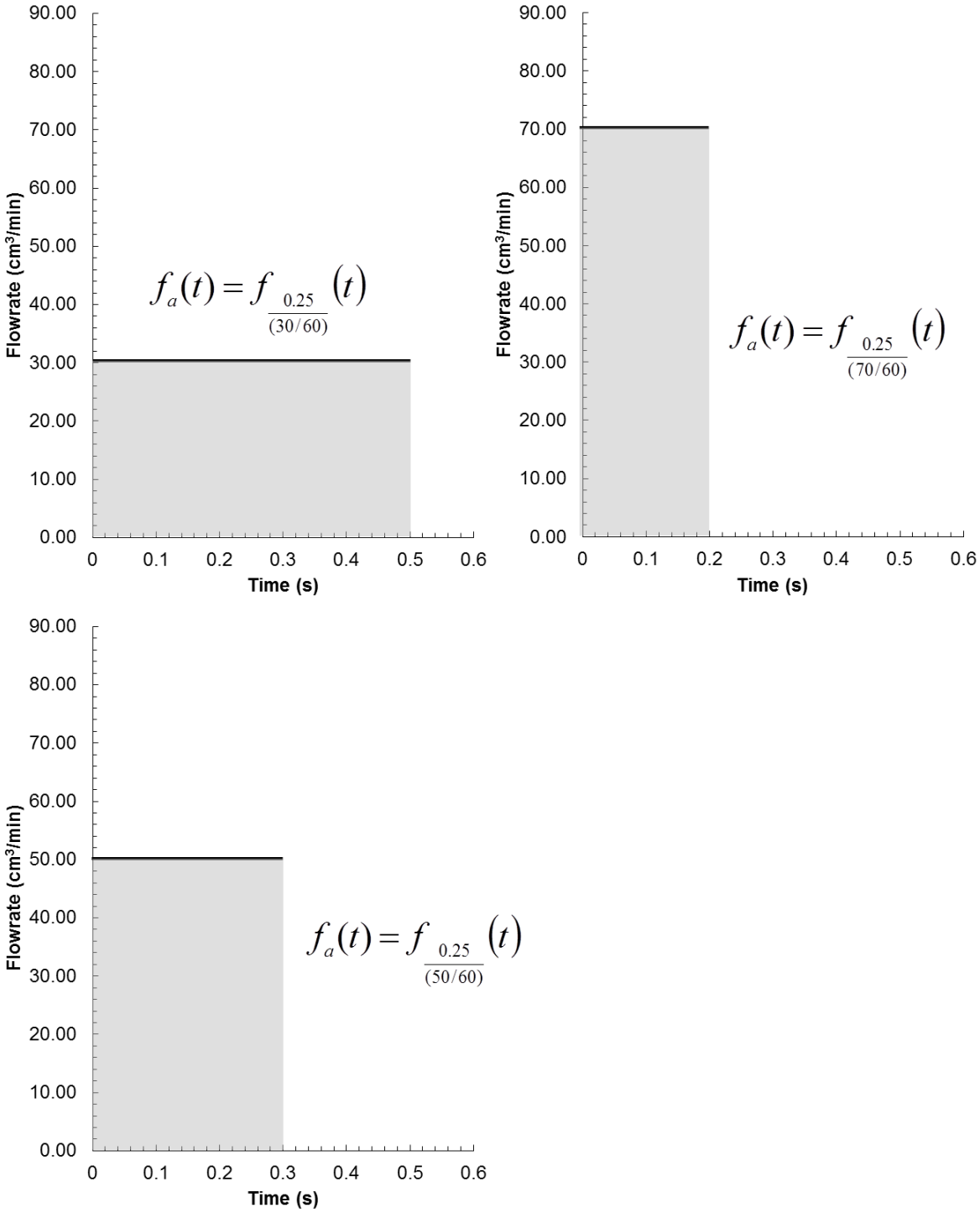

Figure 3.7: Graphs for $y = f_a(t)$ for a = 30, 50 and 70 (idea adapted from Mathews and Howell (2010)).

3.4.2 Non-ideal flow models

For the packed-bed of pellets illustrated in Figure 3.4, if the pellets were non-porous (e.g. glass beads), then a one dimensional axial dispersion model could be used, which would consist of an accumulation term, a convection term and a dispersion term (IAEA, 2008):

$$\varepsilon_b \frac{\partial C_A}{\partial t} + u_0 \frac{\partial C_A}{\partial x} = D_{ax} \frac{\partial^2 C_A}{\partial x^2} \tag{3.16}$$

where: – C_A is the concentration of tracer gas in the column free space, mol m^{-3};

– u_0 is the superficial carrier gas velocity in axial direction (x – direction), m s^{-1}.

Equation (3.16) can be expressed in non-dimensional form in terms of two parameters:

(a) Time constant or the mean residence time, τ is:

$$\tau = \frac{\varepsilon_b L}{u_0} \tag{3.17}$$

where L is the length of the system and ε_b is the bed porosity or the column void fraction.

(b) Non-dimensional Péclet number, *Pe*, can be expressed as:

$$Pe = \frac{u_i L}{D_{ax}} \tag{3.18}$$

where u_i is the interstitial carrier gas velocity, and it is related to the superficial carrier gas velocity, u_0 as:

$$u_i = \frac{u_0}{\varepsilon_b} \tag{3.19}$$

Pe number represents the ratio of convective to dispersive effects. Note that as the Péclet number becomes very small, the flow tends to be perfectly mixed and dispersion is predominant (e.g. with a small u_i or large D_{ax}). As the Péclet number tends to infinity (e.g. with a large u_i or small D_{ax}), the flow tends to plug flow and dispersion is negligible (Hayes and Mmbaga, 2012).

A common analytical solution that describes the tracer concentration field as a function of time and distance, when N moles of tracer are injected as a Dirac pulse (at $x = 0$, $t = 0$) and dispersion is allowed at both ends of the domain (or known as "open-open" boundary conditions) is:

$$C_A(x,t) = \frac{N}{\sqrt{4\pi D_{ax} t}} \exp\left(- \frac{(x - u_i t)^2}{4 D_{ax} t} \right) \tag{3.20}$$

Equation (3.20) is the dimensional form of the Gaussian curve. As mentioned in Hayes and Mmbaga (2012), when the Péclet number becomes increasingly large, the shape of the output curve (normalized RTD function) tends toward a symmetrical curve (Gaussian distribution). Therefore, Equation (3.20) is valid under the assumption that when $Pe > 100$, an injection of an idealized pulse of tracer into the feed of the vessel gives a nearly symmetrical output curve. However, it is important to note that Equation (3.20) is derived from Equation (3.16) with dispersion, convective and accumulation terms involved in the material balance. Apart from the terms shown in Equation (3.16), for much complicated cases where diffusion, adsorption and reaction terms are involved, the above assumptions made for symmetrical response curve (or Gaussian curve) may not be valid. Therefore, to calculate the Pe and axial dispersion (D_{ax}) of a packed-bed column, it recommended to use non-porous materials such as glass beads or sand with uniform shape where the diffusion and reaction terms can be ignored.

3.4.3 The Residence-Time Distribution (RTD) measurement

The RTD is determined experimentally by injecting an inert chemical, molecule or atom, called a tracer into the reactor at some time $t = 0$ and then measuring the tracer concentration, C in the effluent stream as a function of time. The two most used methods of injection are pulse input and step input.

The RTD describes how elements of fluid take different routes through the reactor and this behaviour causes the length of time to pass through the vessel to be different. This behaviour is illustrated in Figure 3.8.

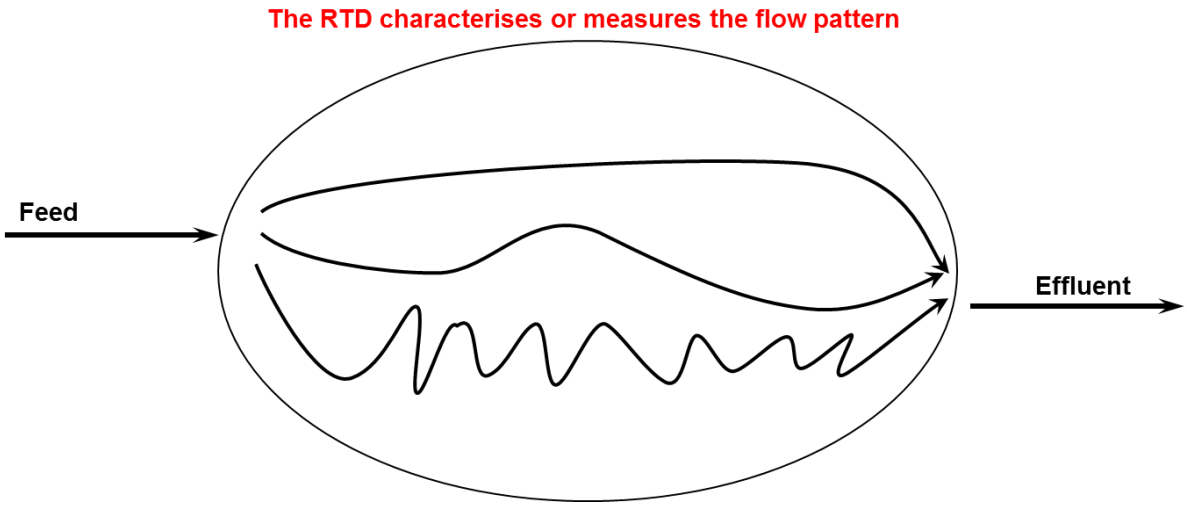

Figure 3.8: The characterisation of residence-time distribution of fluids or gases flowing in an arbitrary reactor with single feed and effluent streams (adapted from Rawlings and Ekerdt (2002)).

The distribution of these times for the stream of fluid leaving the vessel is called the exit age distribution E. The term "age" for an element of the exit stream refers to the time spent by that element in the vessel (Levenspiel, 1998). E has units of time^{-1}. It is convenient to represent the RTD in such a way that the area under the curve is unity:

$$\int_0^\infty E(t)d(t) = 1 \tag{3.21}$$

This procedure is called the normalization of distribution, or normalization of the area of the experimental tracer curve. In other words, the tracer concentration as a function of time curve (i.e. *C*-curve) is converted into an *E*-curve. This operation has several benefits (IAEA, 2008):

(a) The influence of all the factors that affect the area of the curves but not their shape (injected activity, friction effects by column walls) is eliminated.
(b) The calculation of moments is easier with area-normalized data.
(c) Area normalization curves are in certain cases RTD curves that have a precise meaning in terms of fluid population balance.

3.4.4 Gaussian area function

Area normalization can be done by using suitable software. The tracer concentration *C*-curve is normalized by dividing each data point by the area under the curve:

$$E(t) = \frac{C(t)}{\int_0^\infty C(t)dt} \tag{3.22}$$

where: – $C(t)$ is the tracer concentration at any given time;

– $E(t)$ is the residence time distribution (RTD) function.

According to Levenspiel (1998), the response peak for a tracer gas pulse input is symmetrical and Gaussian at any instant as shown in Figure 3.9. This statement is only true for large Péclet number (technically only for $Pe = \infty$). The outlet response curve or the RTD function curve approaches Gaussian as $Pe \rightarrow \infty$. Practically the outlet curve is Gaussian or near Gaussian-shaped for $Pe \geq 100$ (Hayes and Mmbaga, 2012).

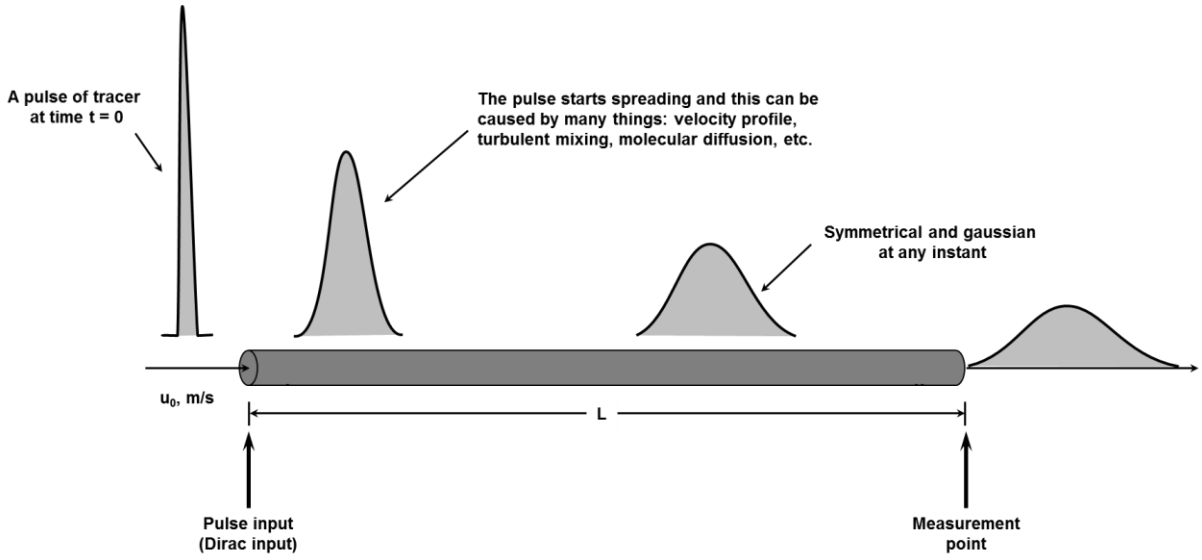

Figure 3.9: The spreading of tracer according to the dispersion model (adapted and redrawn from Levenspiel (1998)).

Apart from calculating the area of the *C*-curve manually by numerical integration (e.g. Simpson's rule), software programs such as: MATLAB code "Peak Fitter" or OriginPro 8.6 are both powerful analysis tools for peak fitting. This thesis uses the latter one for peak analysis because:

(a) when the response peak is not Gaussian-shaped, by choosing the "Integrate Peaks" option under "Peak and Baseline" analysis in OriginPro 8.6, the peak area is integrated numerically by Simpson's rule;

(b) when the response peak is near Gaussian-shaped, the software will fit the peak with a Gaussian area function. If the fit was successful, a fit converged dialogue will emerge and the number of iterations done during the peak fitting process, together with a tolerance value will be given. The area calculated using the Gaussian fit curve is shown along with a standard error. Besides, a R-square (RSQ) value is also provided which indicates the goodness of fit;

(c) when the outlet curve is Gaussian-shaped, the software will perform the exact same procedures as shown in (b). The differences are that with the successful peak fit assured, the number of iterations done, the tolerance value and the standard error will be much smaller than the near Gaussian-shaped curve. Besides, a higher RSQ value is guaranteed (e.g. For near Gaussian or Gaussian-shaped curves, RSQ values equivalent to or larger than 0.95 are recommended);

(d) OriginPro 8.6 provides comprehensive studies, useful gadgets and various options on peak analysis which MATLAB code "Peak Fitter" cannot.

In mathematics, a Gaussian function is of the form:

$$f(x) = ae^{\frac{-(x-b)^2}{2c^2}} \tag{3.23}$$

Parameters *a*, *b* and *c* are real constants. A plot of this function (Figures 3.10 and 3.11) has a characteristic symmetric "bell curve" shape that quickly falls off towards plus/minus infinity ($\pm \infty$), *a* is the height of the curve's peak, *b* is the position of the centre of the peak and *c* controls the width of the "bell". The parameter *c* is related to the Full Width at Half Maximum (FWHM) of the peak as:

$$\text{FWHM} = 2\sqrt{2\ln 2}c \approx 2.35482c \tag{3.24}$$

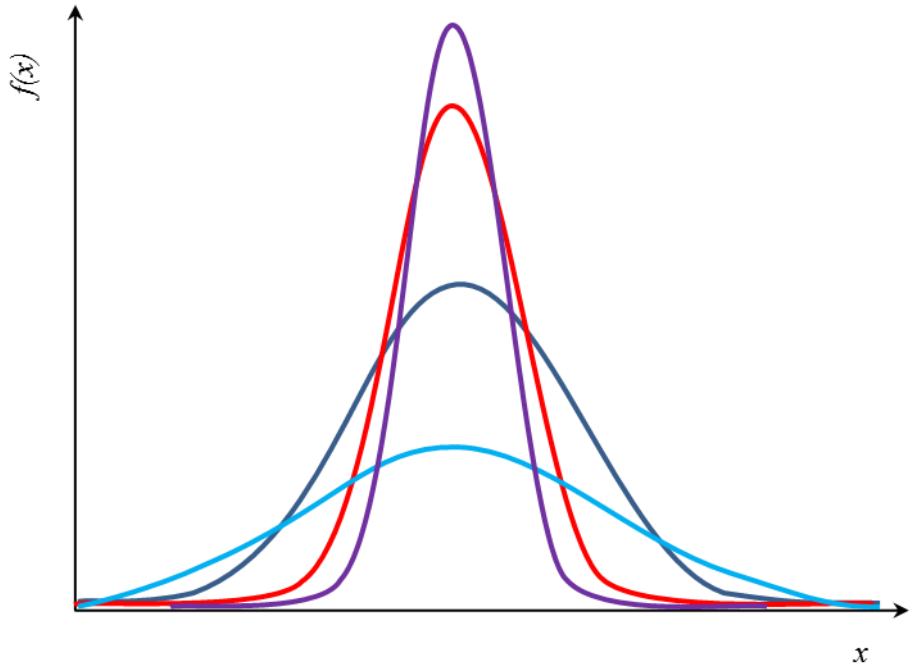

Figure 3.10: Typical Gaussian curves with "bell curve" shape.

For peaking fitting in OriginPro 8.6, because of the baseline effect (explained in later sections), an improved formula – Gaussian area function is used instead of Equation (3.23):

$$y = y_0 + \frac{A}{w\sqrt{\pi/2}} e^{\frac{-2(x-x_c)^2}{w^2}} \tag{3.25}$$

where y_0 is the baseline constant, A is the area under the fitted curve, x_c and w are real constants and their relationships are interpreted in Figure 3.11.

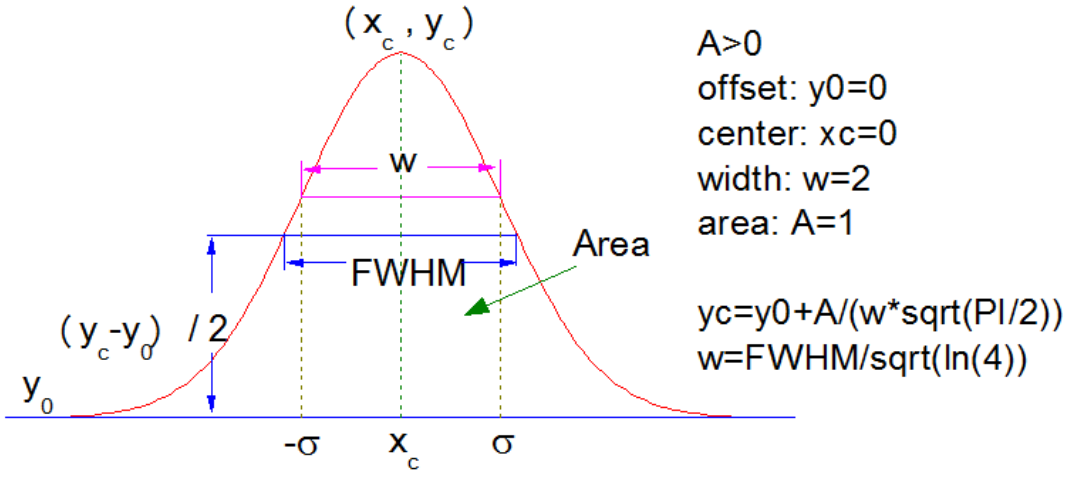

Figure 3.11: Non-linear curve fitting with a Gaussian area function (figure adapted from OriginPro 8.6).

Returning to Equation (3.20), the RTD at the output of the system ($x = L$) can be deduced from the solution as follows:

$$E(t) = \frac{1}{2}\left(\frac{Pe}{t\pi\tau}\right)^{\frac{1}{2}} \exp\left(-\frac{Pe(\tau - t)^2}{4t\tau}\right) \tag{3.26}$$

This simple axial dispersion flow model has two parameters: τ and Pe. The mean residence time (first moment) is equal to τ and the variance (second central moment) $\sigma^2 = 2\tau^2 / Pe$.

The effect of varying Pe on the pulse response curve $E(t)$ is illustrated in Figure 3.12 using Equation (3.26). The curves get shaper and sharper when Pe number increases. For each pulse response curve, there was always one single peak and the peak height and tail length is correlated. In Figure 3.12, the tail of the pulse response curve is short when the peak is sharp (when Pe number is big); and the tail of the pulse response curve is long when the peak is wide (when Pe number is small).

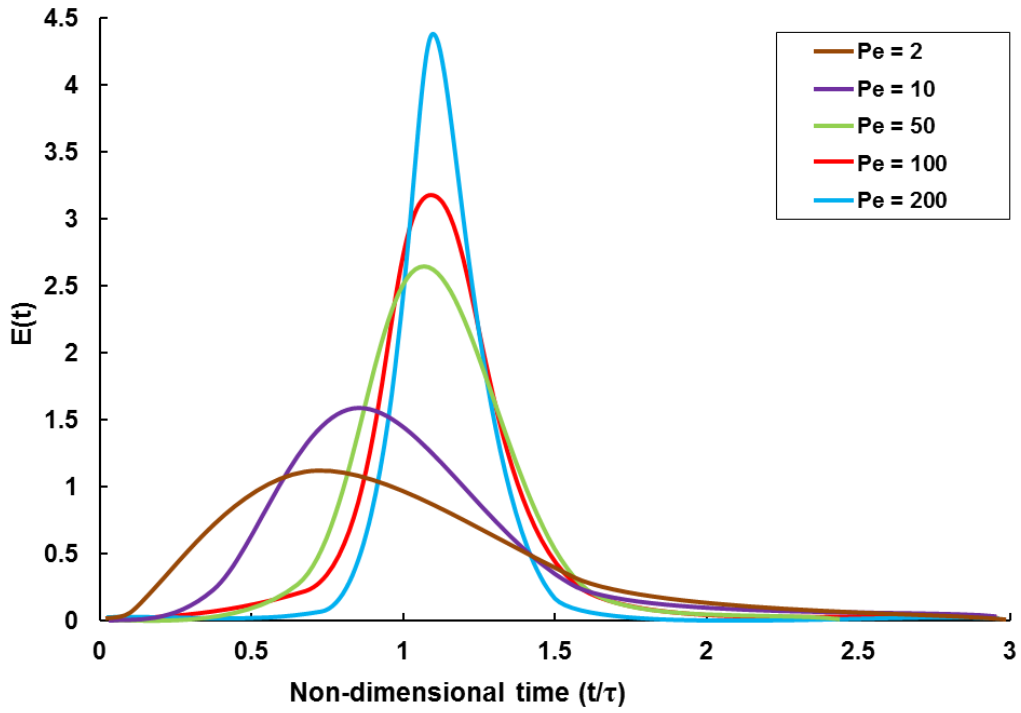

Figure 3.12: Axially dispersed flow model as a function of the Péclet number *Pe* (adapted from IAEA (2008)).

3.4.5 Experimental first moment μ_1 and second central moment μ_2'

In chromatographic experiments, for a pulse of tracer input, the first moment (i.e. mean residence time μ_1) and the second central moment (i.e. variance μ_2' which measures the spread of a curve) of a chromatographic response curve could be calculated according to the definition (Levenspiel, 1998):

First moment:

$$\mu_1 = t_{mean} = \frac{\int_0^\infty tCdt}{\int_0^\infty Cdt} \cong \frac{\sum_i t_i C_i \Delta t_i}{\sum_i C_i \Delta t_i} \tag{3.27}$$

Second central moment:

$$\mu_2' = \sigma^2 = \frac{\int_0^\infty (t-\mu_1)^2 Cdt}{\int_0^\infty Cdt} \cong \frac{\sum_i (t_i-\mu_1)^2 C_i \Delta t_i}{\sum_i C_i \Delta t_i} \tag{3.28}$$

Similarly, an alternative way to find the experimental moments is to transform $C(t)$ into $E(t)$, and this process is called "Normalization" which is shown schematically in Figure 3.14. In Figure 3.15, the first moment is found by calculating the area under curve $tE(t)$ *versus* t, and the second central moment μ_2' is equivalent to the area under the $t^2E(t)$ curve minus the value of t_m^2. Alternatively, the second moment is obtained by calculating the area under $(t - t_m^2)E(t)$ curve. The mathematical expressions are shown as follows (Fogler, 2004):

First moment:

$$\mu_1 = t_m = \int_0^\infty tE(t)dt \tag{3.29}$$

Second central moment:

$$\mu_2' = \int_0^\infty (t-t_m)^2 E(t)dt = \int_0^\infty t^2 E(t)dt - t_m^2 \tag{3.30}$$

The equations for Simpson's rule (known as trapezoidal rule method) and how they can be applied for numerical integration of curves is explained in Appendix 1 and Figures 3.13 to 3.15.

Figure 3.13 shows how Simpson's rule is applied for calculating the area of a *C*-curve. First, the area under the *C*-curve is divided into a number of intervals (in this case 18 intervals, 19 data points) with equal interval length, *h*. The total area under the chromatographic response curve in Figure 3.13 can be calculated as:

$$\int_{t_0}^{t_{18}} C(t)dt = \int_{t_0}^{t_{14}} C(t)dt + \int_{t_{14}}^{t_{18}} C(t)dt \tag{3.31}$$

For most of the moment calculation done in this thesis, the peak fitting method in OriginPro 8.6 was used, in which the area of the response peaks are fitted with a Gaussian area function i.e. Equation (3.25).

Besides, from Equations (3.29) and (3.30), and the corresponding graphical interpretations from Figure 3.13 to Figure 3.15, the concentration data $C_i(t)$ on the C-curve doesn't have to be in mol m^{-3} because of the normalization process from $C_i(t)$ (unit: mol m^{-3}) to $E_i(t)$ (unit: s^{-1}) for each data point. Therefore, for the mass spectrometer employed in this thesis, raw data on the experimental response peaks generated by the MID scans are used i.e. pressure, I (unit: torr) as a function of time, t, or known as the intensity curve $I(t)$.

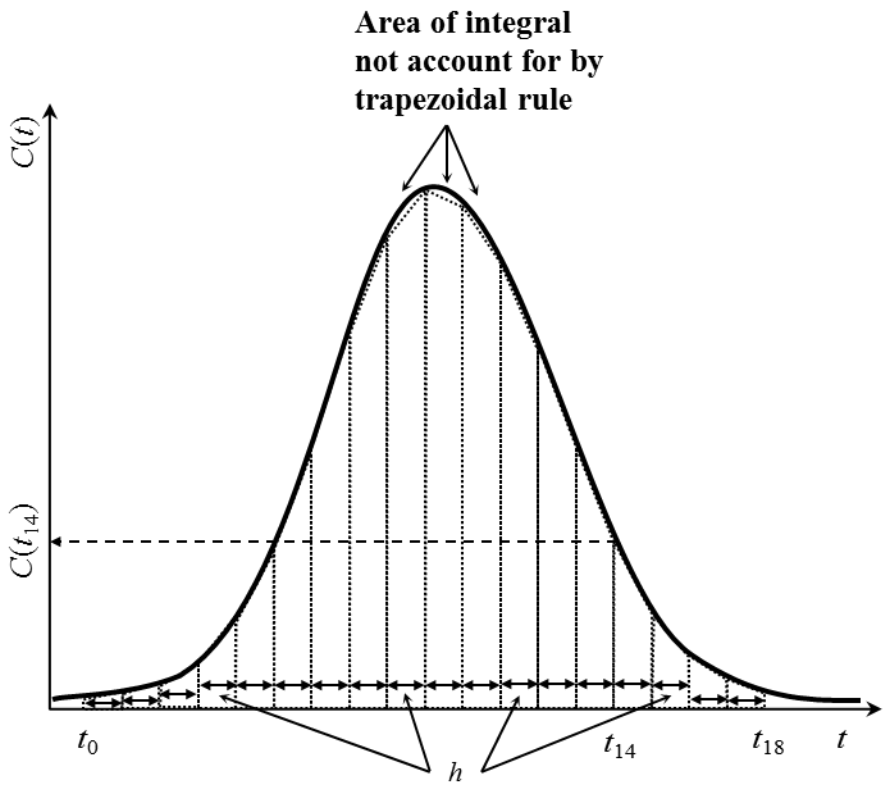

Figure 3.13: Numerically integration of the chromatographic response curve using Simpson's rule.

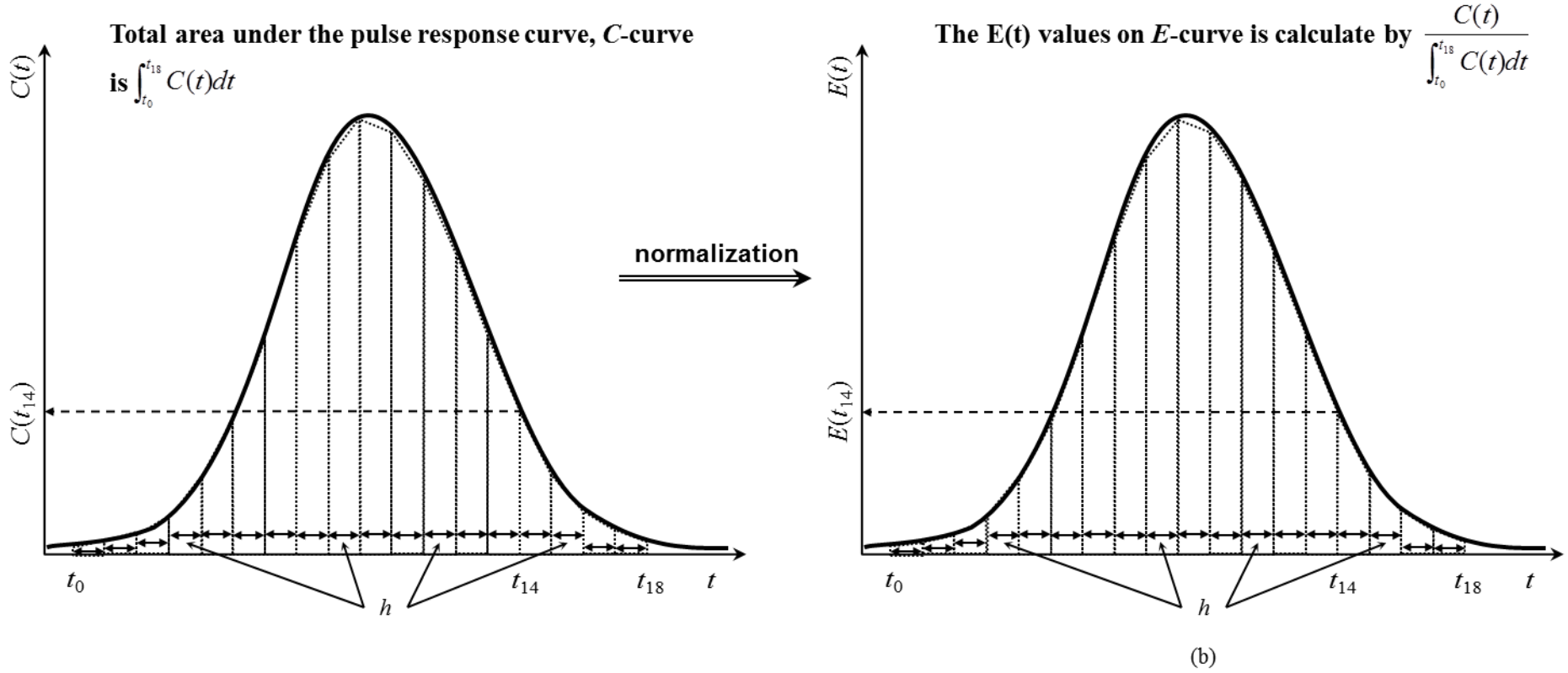

Figure 3.14: Normalization of *C*-curve into *E*-curve: (a) pulse response curve; (b) *E*-curve: the area under the curve is equal to unity, i.e. $\int_{t_0}^{t_{18}} E(t)dt = 1$.

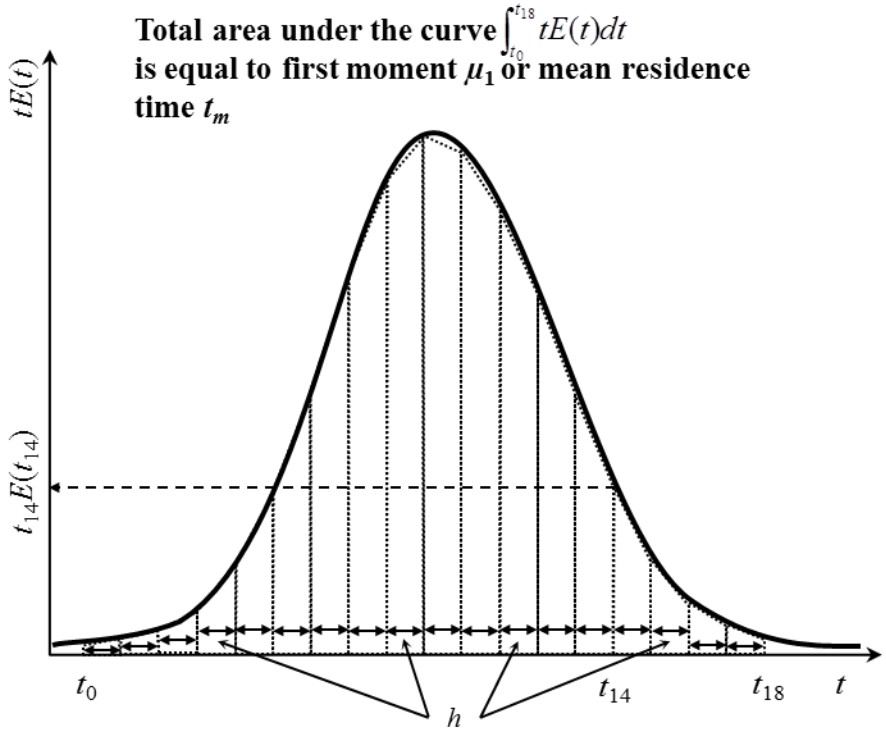

(a)

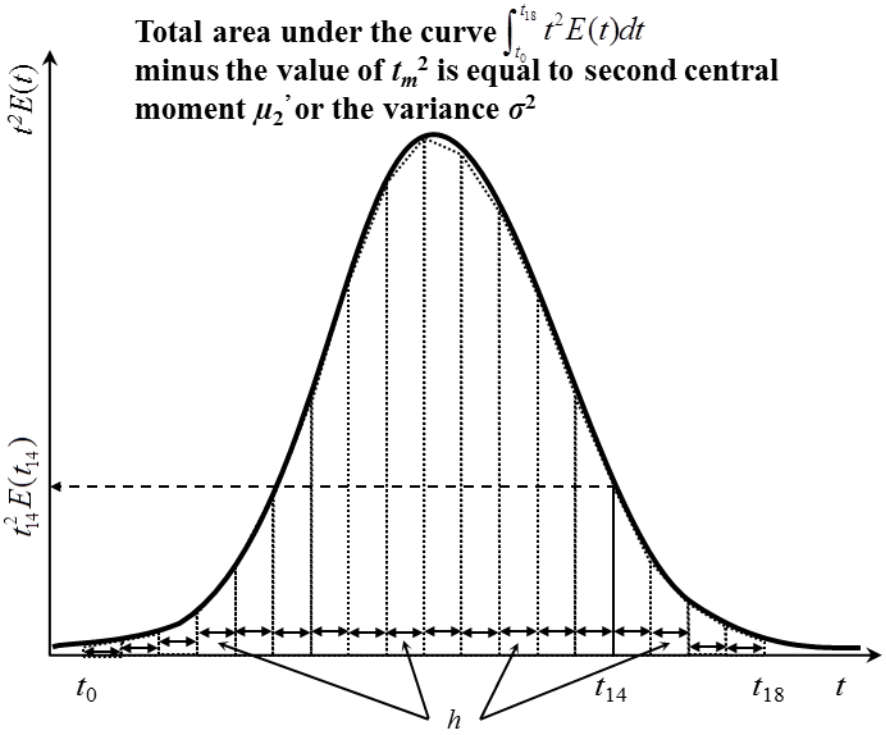

(b)

Figure 3.15: Experimental moment calculation using Simpson's rule: (a) the area under $tE(t)$ *versus t* curve is first moment, or known as t_m; (b) the area under $t^2E(t)$ curve minus the value of t_m^2 is equal to the second central moment.

3.4.6 The correlation of dimensionless second central moment (σ_θ^2) with Péclet number (*Pe*) for the 1D axial dispersion model

As mentioned in Haynes and Mmbaga (2012), the dispersion model for flow in a tube (not packed-bed) can be viewed as plug flow with a superimposed dispersion. For the transient flow of a non-reacting tracer, the mole balance equation is:

$$D_{ax}\frac{\partial^2 C}{\partial x^2}-u_0\frac{\partial C}{\partial x}=\frac{\partial C}{\partial t} \tag{3.32}$$

where the dimensionless terms in Equation (3.32) are:

$$x^*=\frac{x}{L};\ \theta=\frac{t}{t_m};\ C^*=\frac{C}{C_0}.$$

Therefore, the dimensionless equation after substituting the terms above is:

$$\left(\frac{D_{ax}}{u_0 L}\right)\frac{\partial^2 C^*}{\partial x^{*2}}-\frac{\partial C^*}{\partial x^*}=\frac{\partial C^*}{\partial \theta}\Rightarrow\left(\frac{1}{Pe}\right)\frac{\partial^2 C^*}{\partial x^{*2}}-\frac{\partial C^*}{\partial x^*}=\frac{\partial C^*}{\partial \theta} \tag{3.33}$$

The density function for the two cases (i.e. Equations (3.29) and (3.30)) are related by:

$$f(\theta)d\theta=E(t)dt \tag{3.34}$$

The moments about the origin and the central moments for the normalised RTD function are:

$$\mu_n=\int_0^\infty \theta^n f(\theta)d\theta \tag{3.35}$$

$$\mu_n^{'}=\int_0^\infty (\theta-1)^n f(\theta)d\theta=\int_0^\infty (\theta)^n f(\theta)d\theta-t_m^n=\frac{\mu_n^{'}}{t_m^n} \tag{3.36}$$

Therefore, the **dimensionless** first moment U_1 and second central moment σ_θ^2 are:

$$U_1=\int_0^\infty\left(\frac{t}{t_m}\right)E(t)dt \tag{3.37}$$

$$\sigma_\theta^2=\int_0^\infty\left(\frac{t}{t_m}-1\right)^2 E(t)dt \text{ or } \sigma_\theta^2=\int_0^\infty\left(\frac{t}{t_m}\right)^2 E(t)dt-t_m^2 \tag{3.38}$$

The Péclet number can be found experimentally using a pulse injection into the tube inlet and finding the RTD function. According to Levenspiel and Smith (1957), the Péclet number depends on the variance of the normalized RTD function as (i.e. for plug flow in an empty tube):

$$\sigma_\theta^2 = \frac{2}{Pe} - \frac{2}{Pe^2}\left[1 - \exp(-Pe)\right] \tag{3.39}$$

When the extent of axial dispersion is relatively small, i.e. when Péclet number is greater than about 100, Equation (3.39) can be approximated by the form (Hayes and Mmbaga, 2012):

$$\sigma_\theta^2 = \frac{2}{Pe} \tag{3.40}$$

The relationships of Péclet number and Gaussian-shaped curves are explained in Chapter 4 Section 4.1.2 using moments results obtained from packed-bed experiments in this thesis.

3.5 Determination of moments from experimental data

To test the feasibility of the moment analysis method, γ-alumina pellets (d: 1.0 mm) were packed inside glass tubes with two different tube lengths: 200 mm and 400 mm. The tracer-carrier gas system used in this thesis contained two inert gas pairs:

a) Nitrogen (Tracer) – Helium (Carrier) gas system;
b) Helium (Tracer) – Nitrogen (Carrier) gas system.

For trial run experiments, a tracer gas pulse with a known concentration in the sample loop (using sample loop volumes = 0.1 ml, 0.25 ml and 0.5 ml) was injected into the column (i.e. Prototype design I, shown in Figure 3.16). The pulse response peaks at the top and bottom sampling ports were recorded. The elution (retention) time of the tracer gas sample was delayed due to dispersion and diffusion effects in the column.

The experimental apparatus consisted of:

1. Two glass tubes with the same tube diameters (O.D 19.0 mm and I.D 13.8 mm) but with different tube lengths: i.e. 200 mm and 400 mm were used. A photograph of γ-alumina beads packed inside a 400 mm glass tube is shown in Figure 3.16.
2. Stainless steel fittings and tubes were used for connections between the six-port injection valve and the glass tube packed with γ-alumina beads. PTFE ferrules were used in the glass tube fittings instead of stainless steel ferrules.
3. Pure nitrogen and helium gases from gas cylinders were used, with inlet pressure monitored by gas regulators. The experimental layout is shown schematically in Figure 3.17.
4. A Valco instrument – VICI E60-AL a six-port injection valve was actuated automatically with an electric actuator for pulse input. A picture of the VICI E60-AL is shown in Figure 3.18. The injection and loading sequence of VICI E60-AL is shown schematically in Figure 3.19.
5. The volumes of pulse injection of tracer gas loops used were: 0.1 ml, 0.25 ml and 0.5 ml, mounted on a six-port injection valve. According to Wei and Kaufman (1976), the maximum sample volume that can be injected into the column for chromatographic experiment without degrading the resolution of its separation is 1 ml.
6. Carrier gas flowrate was monitored by two MPB long series 1200 BVL flowmeters with flowrate ranges between (25 – 200 cm^3/min). According to Guiochon and

Guillemin (1988), for sample loop volume exceed 0.1 ml, the recommended values are 3 L/hr (i.e. 50 cm^3/min) for carrier gas flowrate.

7. The rotameter flowrates were calibrated using a Hewlett-Packard soap film flowmeter. The calibration graphs for Nitrogen and Helium are shown in Figure 3.20 and Figure 3.21 respectively.
8. A mass spectrometer: Hiden HPR-20 QIC gas analyzer with high sensitivity Secondary Electron Multiplier (SEM) detector was used for the chromatographic experiments (see Figure 1.9).
9. Response peaks at the sampling ports are recorded by Multiple Ion Detection (MID) scan mode in MASsoft (mass spectrometer analysis software). The raw data collected from the response peak curves is in pressure (torr) term at relevant time *t*.

In this thesis, chromatographic experiments were carried out at ambient conditions (i.e. 295.15 K and 1.013 bar) with 1 mm beads packed inside the columns. The packed-bed column characteristics are summarised as follows:

- Spherical 1 mm beads packed inside a 400 mm glass tube (O.D: 19 mm and I.D: 13.8 mm) with $D_t / D_p = 13.8$ and $L_t / D_p = 400$;

- Spherical 1 mm beads packed inside a 200 mm glass tube (O.D: 19 mm and I.D: 13.8 mm) with $D_t / D_p = 13.8$ and $L_t / D_p = 200$.

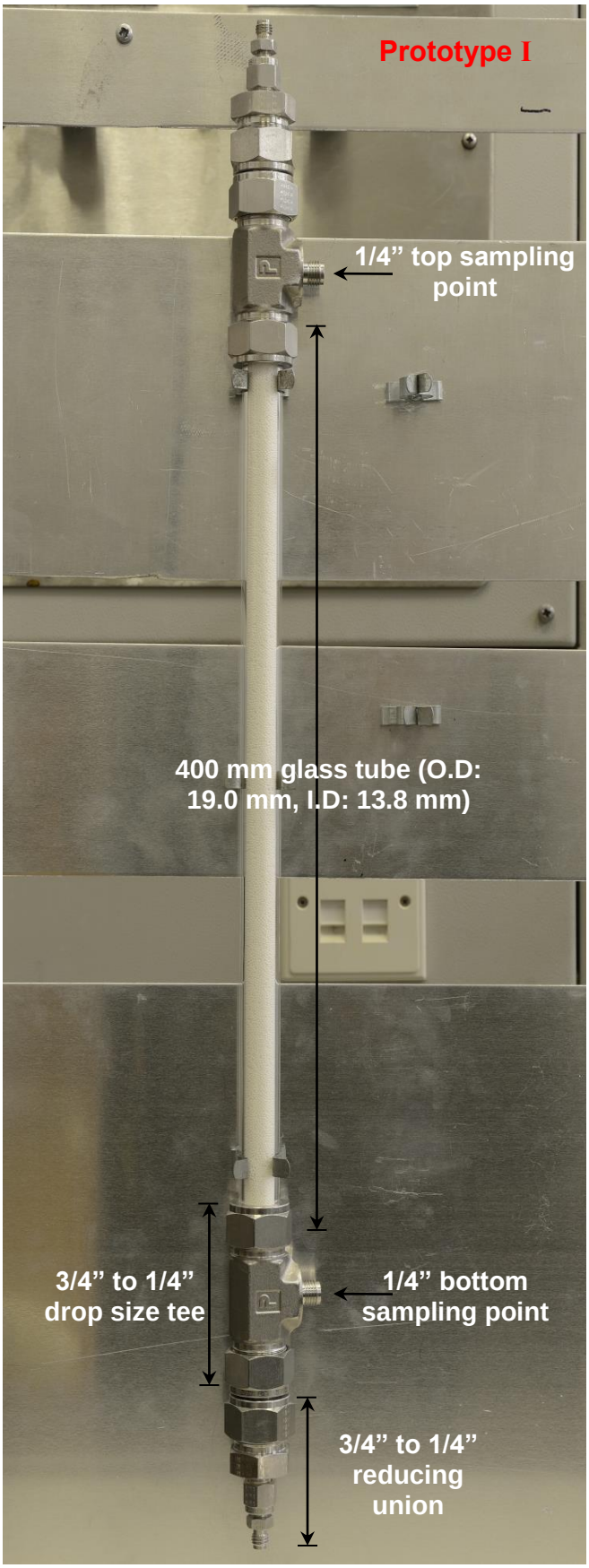

Figure 3.16: Prototype I design: column packed with γ-alumina beads (d: 1.0 mm).

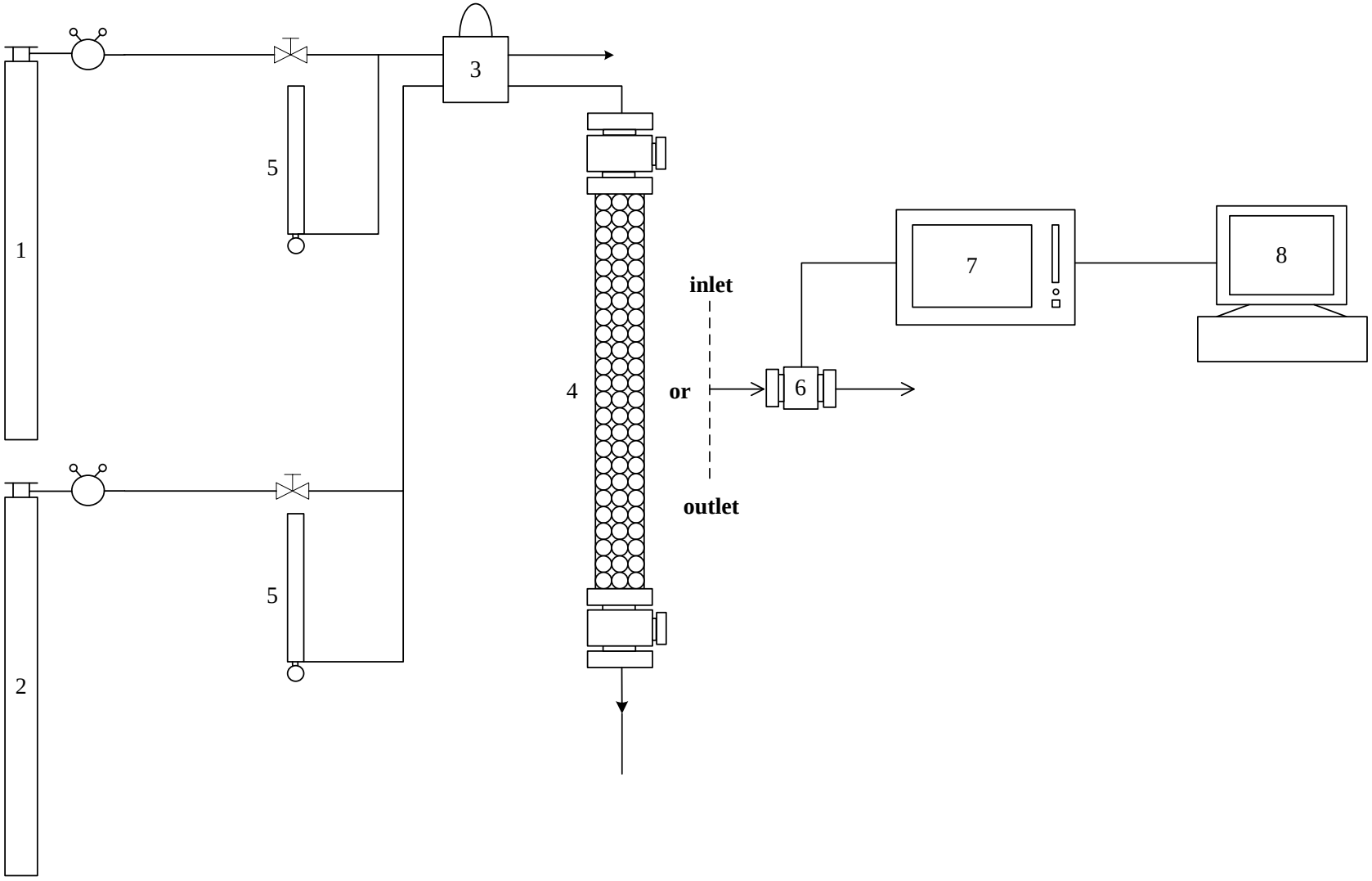

Figure 3.17: Schematic showing the chromatographic experimental set-up: (1) tracer gas cylinder; (2) carrier gas cylinder; (3) VALCO six-port injection valve; (4) column packed with γ-alumina beads; (5) MPB long series 1200 BVL flowmeter; (6) MS inlet capillary to make design more flexible to cover prototype I & II; (7) Hiden HPR-20 QIC gas analyzer; (8) MID scan mode in MASsoft.

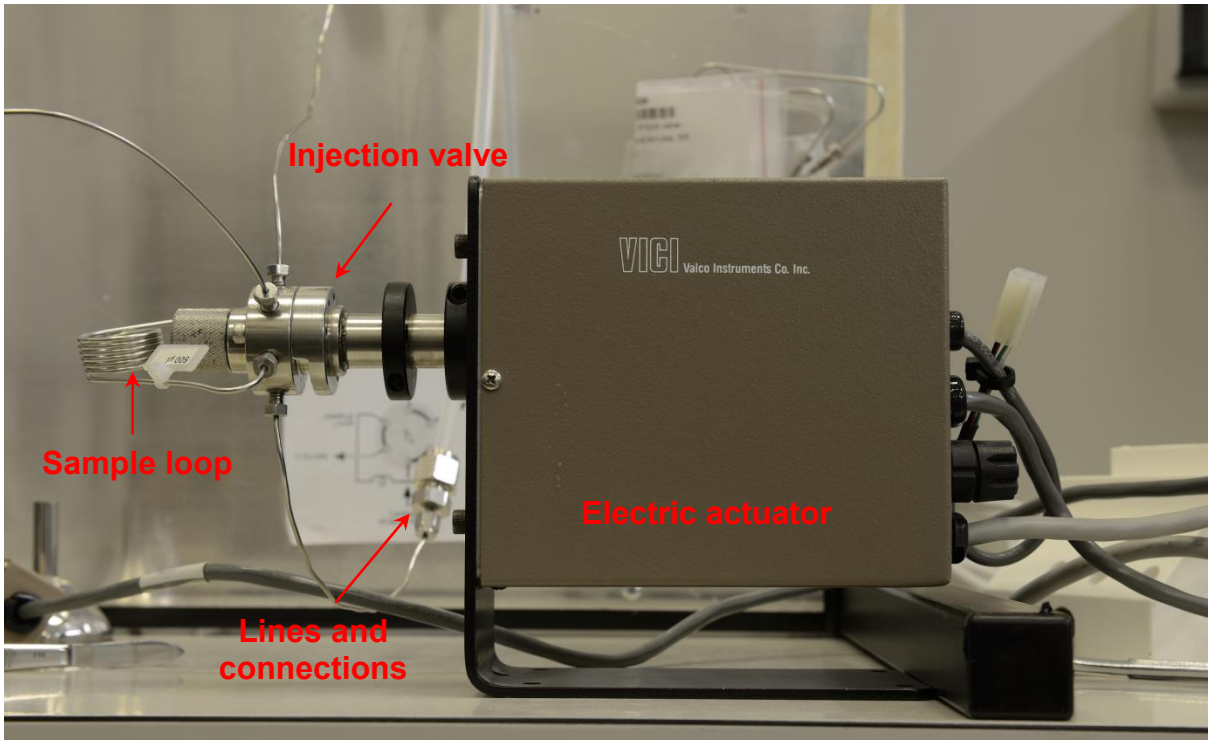

Figure 3.18: A VALCO six-port injection valve mounted on an electric actuator.

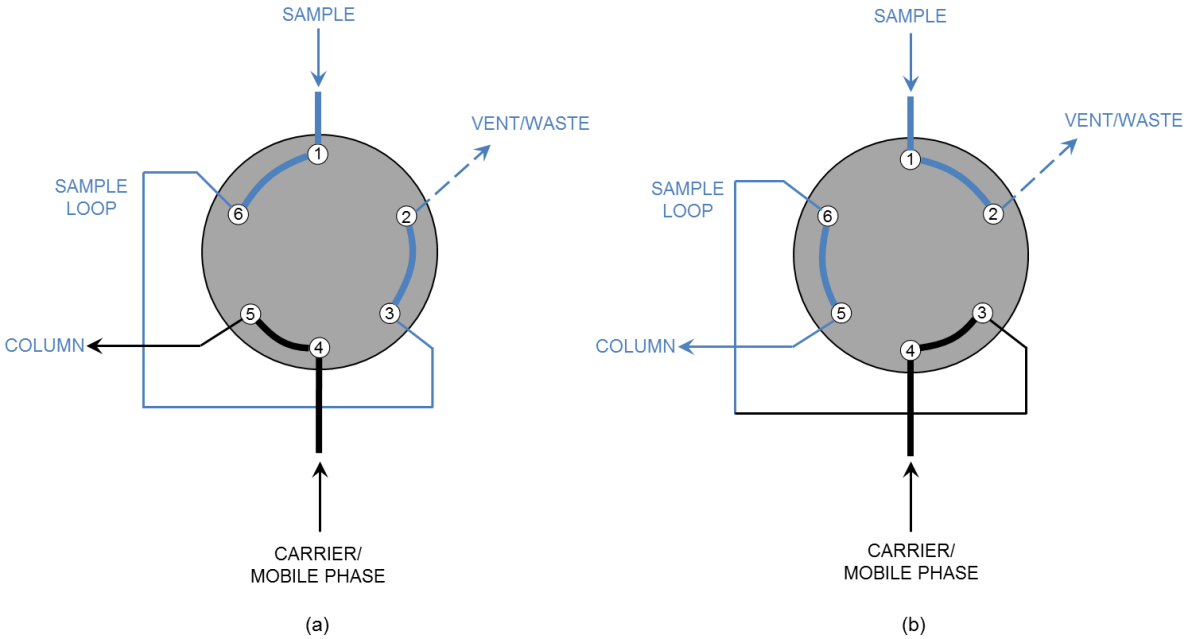

Figure 3.19: Schematic diagram shows injection valve viewed from the preload end: (a) loading phase; (b) injection phase (adapted and redrawn from VICI Valco Instruments Co. Inc. Technical Note 203).

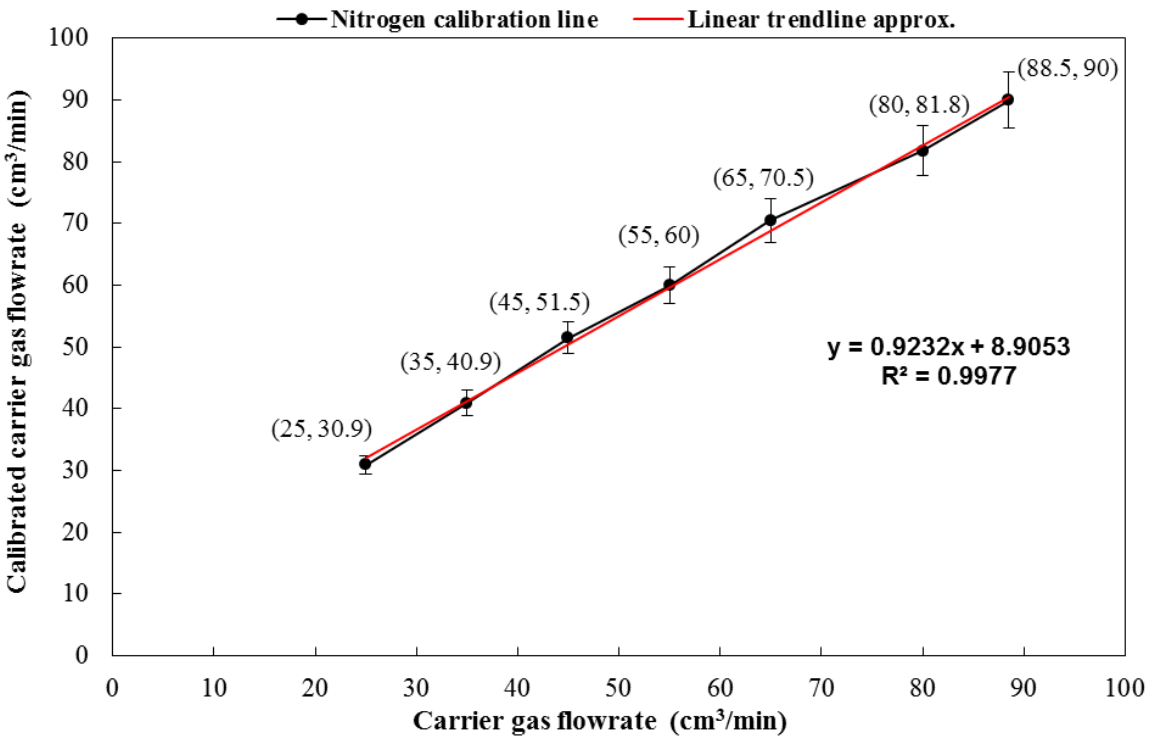

Figure 3.20: Calibration graph for nitrogen gas flow in the flowmeter.

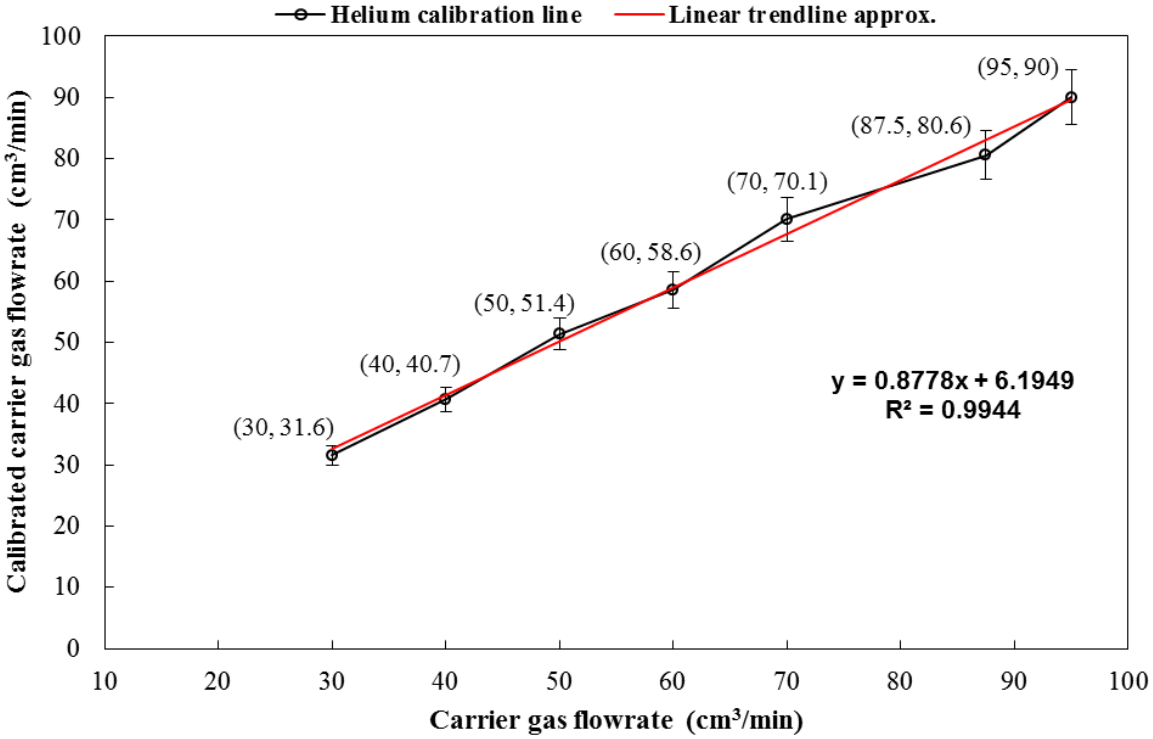

Figure 3.21: Calibration graph for helium gas flow in the flowmeter.

3.5.1 Preliminary experiments

Using the experimental apparatus illustrated in Figure 3.16, pulse input experiments were performed and the concentration profiles at the inlet and outlet of the column were measured. In these preliminary experiments, the concentration profile at the inlet to the column did not resemble a pulse input, and after much work, various modifications were implemented which eventually resulted in the achievement of a sharp pulse-shaped input peak.

The modifications consisted of:

- Selecting a fast acting valve.
- Reducing the internal diameter of the lines to and from the column.
- Reducing the complexity of the fittings at the top and bottom of the column – replacing the T-pieces (i.e. drop size tees), with reducing unions (3/4 inch to 1/4 inch), to eliminate back-mixing in the side branch of the T-piece.
- Use of a Plasticine moulding inside the reducing union fittings at the top and bottom of the column (to reduce dead-space and minimize back-mixing in the fittings).
- Rather than sampling from the side port of a T-piece, the gas was sampled directly from a reducing union:
  (a) from the top of the column, by temporarily removing the column and connecting it directly to the MS sampling probe; and
  (b) from the bottom of the column, by connecting it directly to the MS sampling probe.

These modifications finally led to a design labelled as Prototype II, and an example of response peaks is shown in Figure 3.22 with Peak 1 showing the input, and Peak 2 showing the output. Having established that a pulse-shaped input signal was being obtained, it was only necessary to monitor the output signal from this column.

The experimental conditions in Figure 3.22 are:

(1) N_2 (carrier) – He (tracer) gas system;
(2) tracer gas sample loop 0.25 ml;
(3) calibrated carrier gas flowrate 50 cm^3/min.

For the peak area in the output (Peak 2), a total number of 414 data points were recorded using SEM detector as compared to 7 data points for Peak 1. The reasons for choosing the SEM detector rather than the Faraday detector are given in Appendix 2. As compared to a Dirac impulse in an ideal PFR shown in Figure 3.5, it is reasonable to assume the response peak at the top sampling point is a good representation of a Dirac pulse input. This assumption was validated using peak fitting with OriginPro 8.6. The response peak area (Peak 2 area) at the bottom sampling point is 3.7870×10^{-7} torr s, which is almost the same as the area at top (Peak 1 area): 3.7214×10^{-7} torr s.

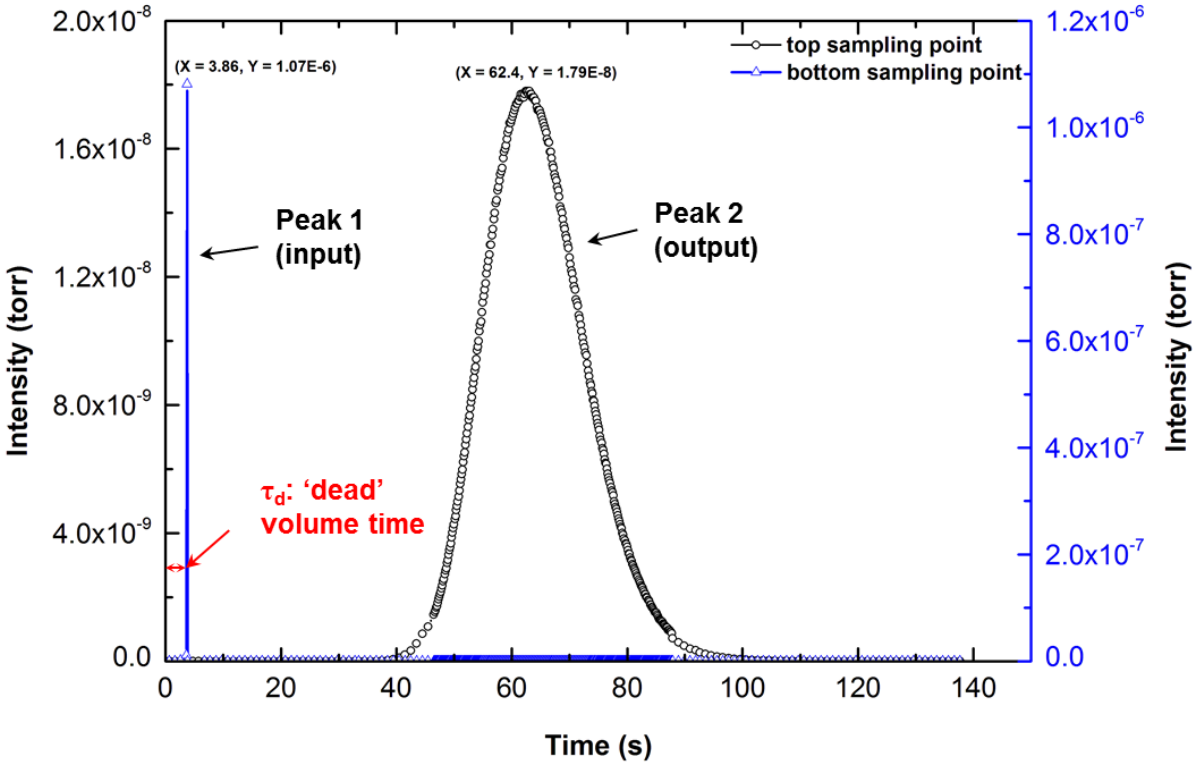

	Value	Adj. R^2	Standard Error
Peak 1 (Gaussian) Area	3.72143E-7	0.99989	2.39331E-7

	Value	Adj. R^2	Standard Error
Peak 2 (Gaussian) Area	3.78701E-7	0.98411	2.05638E-9

Figure 3.22: Response peaks recorded at top input and bottom output sampling points with Prototype II design.

In Figure 3.22, the delay time, τ_d, at the top measuring point before the pulse entered the column (in the lines and fittings) was estimated as 1.32 s.

Figure 3.23: Prototype II design: column packed with γ-alumina beads (d: 1.0 mm).

3.5.2 Column upstream and downstream processes – 'dead' volume time, τ_d

From the gas loop to the column, there is a delay time, τ_1. From the base of the column to the MS there is a delay time, τ_2 = 2.29 s. This was calculated from an experiment. The MS sampling rate is the same for all carrier gas flowrates. Therefore, the total delay time is:

$$\tau_d = \tau_1 + \tau_2 = \tau_1 + 2.29\,\text{s} \tag{3.41}$$

and this is shown in Figure 3.24 and in Table 3.1.

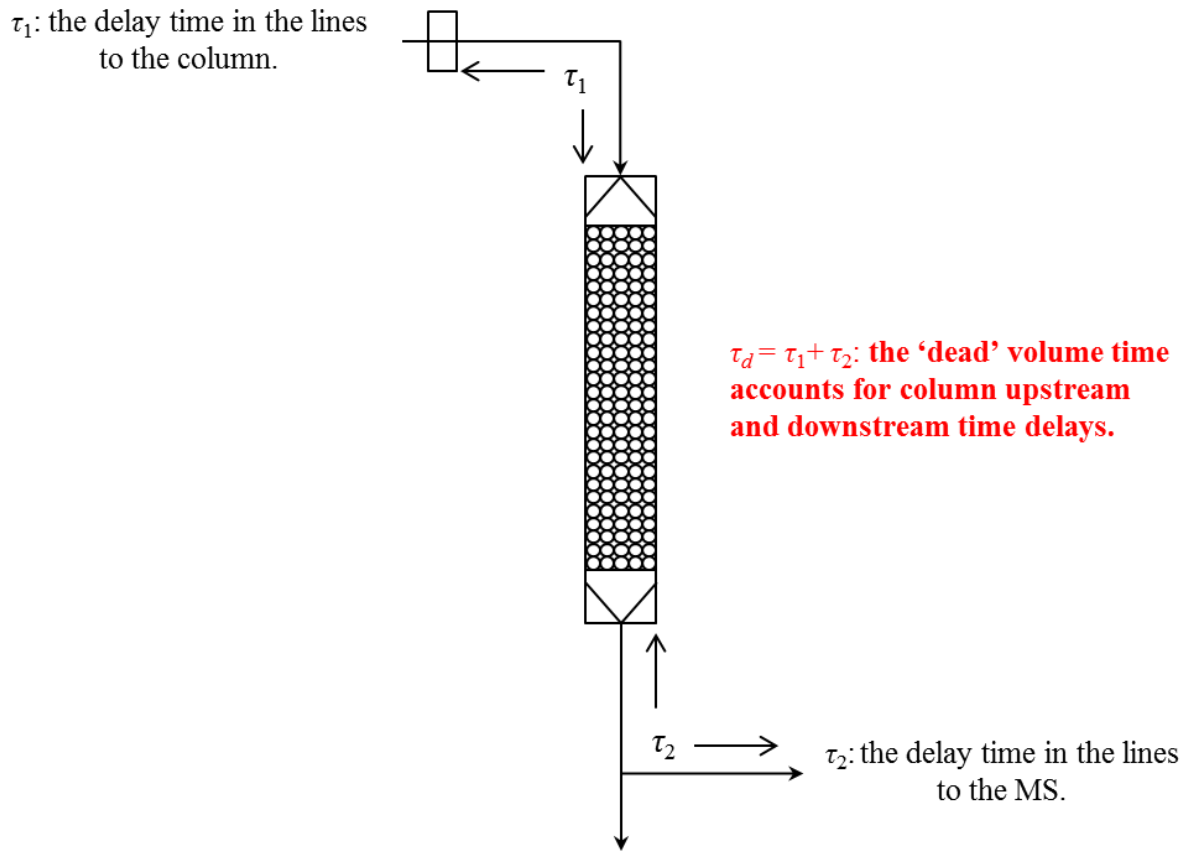

Figure 3.24: The 'dead' volume time, τ_d, of the packed bed column.

Table 3.1: The delay time of tracer, τ_d, at different carrier gas flowrates.

Carrier gas flowrate (cm^3/min)	**Calculated τ_1 (s)**	**Calculated τ_2 (s)**	**Delay time, τ_d (s)**
30	2.20	2.29	4.49
40	1.65	2.29	3.94
50	1.32	2.29	3.61 (measured)
60	1.10	2.29	3.39
70	0.94	2.29	3.23
80	0.83	2.29	3.12
90	0.73	2.29	3.02

In conclusion, the experiment moments obtained in this thesis at different carrier gas flowrates would need to be corrected by the delay time, τ_d shown in Table 3.1.

3.5.3 Summary of experimental conditions

The following bed properties and experimental conditions are used in the moment analysis studies, and for the calculation of the adsorption equilibrium constant, *K*, described in this chapter:

1. Size of packing material:
   a) γ-alumina beads (diameter: 1 mm), with pore size diameter d_p = 8.8 nm and porosity ε_p = 0.5946;
   b) glass beads (diameter: 1 mm), non-porous material used for measuring the axial dispersion effect (i.e. D_{ax} or E) in the packed-bed column.
2. Packed-bed geometry:
   i) 400 mm long glass tube (O.D 19 mm and I.D 13.8 mm);
   ii) 200 mm long glass tube (O.D 19 mm and I.D 13.8 mm).
3. The packing porosity, or packed-bed void fraction (i.e. bed voidage), ε_b, of a packed glass tube column was calculated from:

$$\varepsilon_b = \frac{V_{void}}{V_{column}} = \frac{V_{column} - \dfrac{M_{pellet}}{m_{pellet}} \times V_{pellet}}{V_{column}} \tag{3.42}$$

   where: – V_{void} is the total volume of the voids (or the empty space) in the interparticle region of the packed-bed, m^3;
   – V_{column} is the volume of the packed-bed column, m^3;
   – M_{pellet} is the total weight of the γ-alumina beads packed in the column, g;
   – m_{pellet} is the mass of a γ-alumina bead, g;
   – V_{pellet} is the volume of a spherical γ-alumina bead, m^3.

   Note: For column packed with alumina pellets, $(\varepsilon_b)_1$ = 0.4446;

   For column packed with glass beads, $(\varepsilon_b)_2$ = 0.4446.
4. Tracer gas sample loop volumes used: 0.1 ml, 0.25 ml and 0.5 ml.
5. Tracer – carrier gas systems:
   i) He (tracer) – N_2 (carrier), and ii) N_2 (tracer) – He (carrier) gas systems.
6. Calibrated carrier gas flowrate used: 30 – 90 cm^3/min.
7. Experimental temperature and pressure: 295.15 K and 1.013 bar.
8. The weight of a single γ-alumina pellet, skeletal density, bulk density, pellet pore diameter and pellet porosity, the values used are as determined in Chapter 2.

3.6 Moment analysis for γ-alumina beads: peak fitting method

In this section, peak area is determined using a numerical integration method by Simpson's rule, and peak area is also calculated using Gaussian area function in OriginPro 8.6.

Note: However, the delay time τ_d has not been deducted from the moments calculated. The reason is explained in the sections that follow.

3.6.1 Moment calculations using Simpson's rule

Example calculations were performed on the results of experiments with γ-alumina beads (diameter: 1.0 mm) packed inside a 400 mm long glass tube and these are presented in Appendix 3. The experimental conditions were:

(a) Prototype II design was used.
(b) N_2 (carrier) – He (tracer) gas system.
(c) Tracer sample loop volume: 0.25 ml, with calibrated carrier gas flowrate: 50 cm^3/min.
(d) The maximum intake pressure on the SEM detector is maintained constantly at 1.8 × 10^{-6} torr (Ultra high vacuum pressure).

Note: when the MID scan starts, a buffer time (around 30 s) is allowed before each sample injection sequence. The data in the buffer time is excluded from the peak analysis.

Calculations were performed with a time step of h_1 = 4 s and h_2 = 5 s. The results from this analysis are presented in Table 3.2, and the following observations were made:

(a) The area under the *I*-curve at the two time intervals (h_1 = 4 s and h_2 = 5 s) is almost the same.
(b) Areas under the *E*-curve match well.
(c) The average first moment, μ_1, is: 64.439 ± 0.0075 s.
(d) The average second central moment, μ_2', calculated from the area under $(t - t_m)^2E(t)$ curve: 77.155 ± 0.0855 s^2.
(e) The average second central moment μ_2' calculated from the area under $t^2E(t)$ curve deducting t_m^2 value is: 77.162 ± 0.0695 s^2.

Table 3.2: Area calculations with different time intervals.

Parameters	**Time interval, *h* (s)**		
	4	**5**	**Average**
Area under $I(t)$ curve (torr.s)	3.7710×10^{-7}	3.8082×10^{-7}	$3.7896 \times 10^{-7} \pm 1.86 \times 10^{-9}$
Area under $E(t)$ curve	0.9999	1.0000	$0.9995 \pm 5.00 \times 10^{-5}$
Area under $tE(t)$ curve: μ_1 or t_m (s)	64.446	64.431	64.439 ± 0.008
Area under $(t - t_m)^2 E(t)$ curve: μ_2' or σ^2 (s^2)	77.240	77.069	77.155 ± 0.086
Area under $t^2E(t)$ curve deducting t_m^2: μ_2' or variance σ^2 (s^2)	77.231	77.092	77.162 ± 0.070

Ideally, the response peak should have a symmetrical and Gaussian shape (Levenspiel, 1998). In other words, the beginning and the tail of the response peak should have a 'sharp in' and 'sharp out' shape. However, for some response peaks shown in this thesis, the peak-end baseline concentration is always slightly higher than the baseline concentration at peak-beginning, and this is called 'Long tail' effect. This problem was also reported in IAEA (2008) as shown in Figure 3.12. Except that the 'Long tail' effect is weaker at higher carrier gas flowrate. The chromatographic response peak obtained using helium tracer at two different flowrates is illustrated in Figure 3.25.

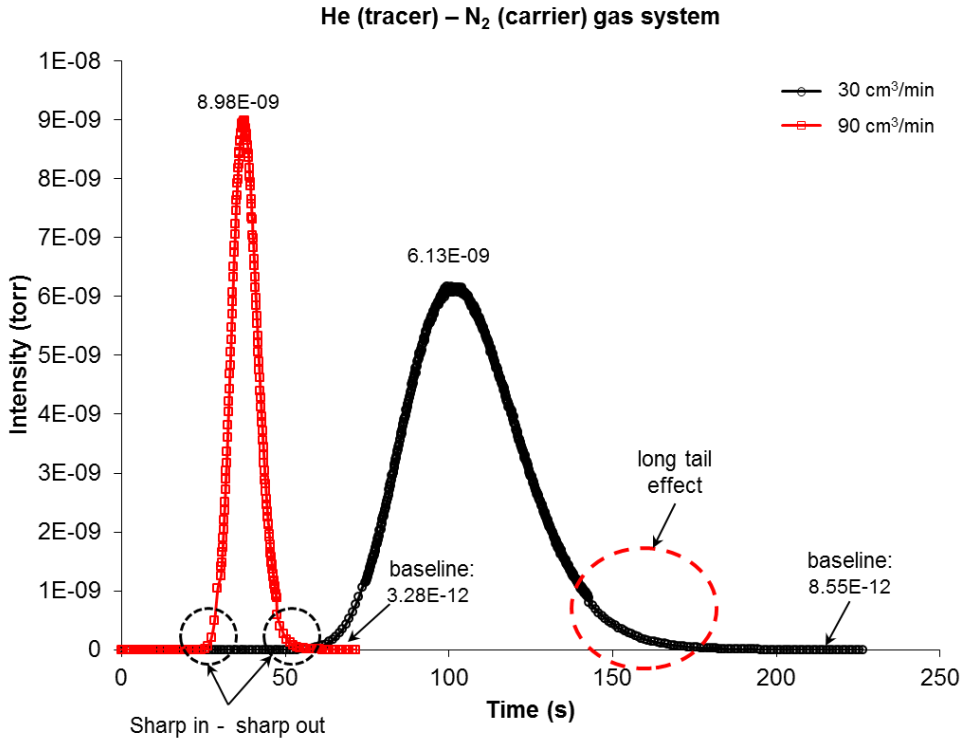

Figure 3.25: Experimental response peak obtained using 0.1 ml sample loop and carrier gas flowrates at 30 and 90 cm^3/min respectively.

In contrast to the helium tracer, whose baseline concentration is around 10^{-12} to 10^{-13} torr, in experiments with nitrogen as tracer, it was found that even though the baseline was calibrated using only carrier gas (helium) flow at 70 cm^3/min for at least one hour, it was difficult to bring down the baseline close to 10^{-12} or 10^{-13} torr. The baseline concentration remained 10^{-10} to 10^{-9} torr. However, the baseline did drop at high carrier gas flowrates (above 50 cm^3/min). This is illustrated in Figure 3.26 and Figure 3.27.

Therefore, this brings the question of whether or not to ignore this baseline value, or must it be subtracted from the experimental data points. This question is investigated in the next section using a peak fitting method with and also without baseline subtraction.

One explanation for the 'Long tail' effect could be that the Péclet number is equivalent or smaller than 100. This is because 'Long tail' means that RTD curve is not Gaussian-shaped and therefore according to Hayes and Mmbaga (2012), a non-Gaussian peak has $Pe < 100$. However, this is only limited to the dispersion model with diffusion absent (i.e. Equation (3.16)). The simple dispersion model is not suitable for porous γ-alumina beads packed bed.

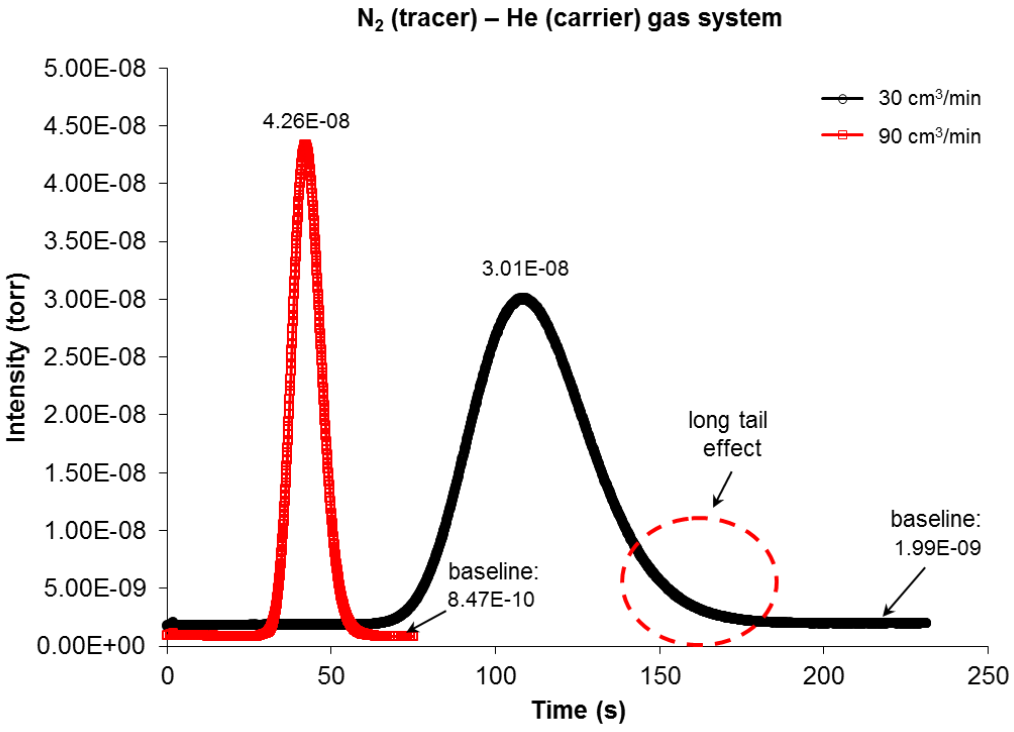

Figure 3.26: Experimental response peaks obtained using 0.1 ml sample loop and carrier gas flowrates at 30 and 90 cm^3/min respectively.

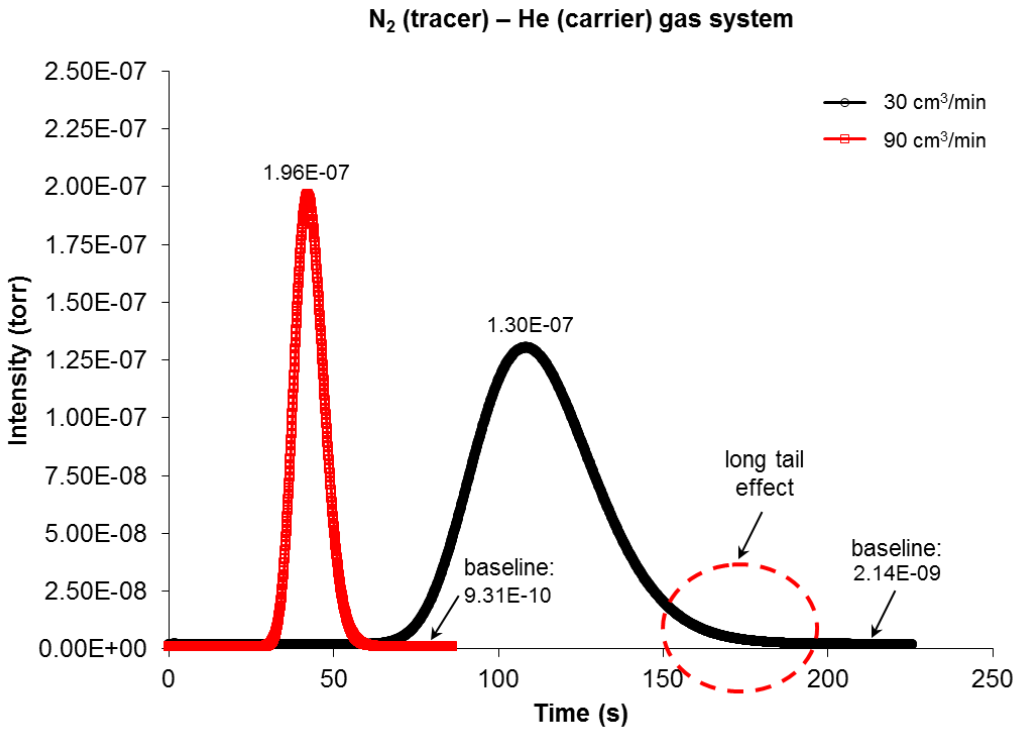

Figure 3.27: Experimental response peaks obtained using 0.5 ml sample loop and carrier gas flowrates at 30 and 90 cm^3/min respectively.

3.6.2 Moment calculations using peak fitting with a Gaussian area function

OriginaPro 8.6 was used as a peak analysing tool which offers a range of helpful features: (a) peak fitting; (b) surface fitting; (c) statistics; (d) signal processing; (e) gadgets; and (f) image handling.

Using OriginPro 8.6, the peak areas were calculated for the conditions described at the start of Section 3.6.1, and the results from the various options explored are presented in Appendix 4, and a summary is provided in Table 3.3.

The experimental response curve used for peak fitting example shown in this section is exactly the same curve used for peak analysis with Simpson's rule (Section 3.6.1), which is obtained under the following experimental conditions:

(a) Helium tracer sample loop volume: 0.25 ml;
(b) Nitrogen carrier gas flowrate: 50 cm^3/min;
(c) 400 mm column packed with γ-alumina beads;
(d) Maximum intake pressure for the SEM detector is maintained at 1.8×10^{-6} torr.

Table 3.3: Moment analysis parameters obtained by peak fitting with different baseline rules.

Parameters	1. System-found baseline *without* baseline subtraction	2. System-found baseline *with* baseline subtraction	3. User-defined baseline *without* baseline subtraction	4. User-defined baseline *with* baseline subtraction
		***I*-curve**		
Baselines, A_0 / B_0 (torr) *(a)*	3.49375×10^{-13}	**0** *(b)*	6.03397×10^{-12}	0 *(b)*
Gaussian Fit Peak Area (torr.s) *(a)*	3.7957×10^{-7} $\pm1.4395\times10^{-9}$	**3.7847×10^{-7} $\pm2.3591\times10^{-9}$**	3.7821×10^{-7} $\pm2.3567\times10^{-9}$	3.7821×10^{-7} $\pm2.3567\times10^{-9}$
		***E*-curve**		
Baselines, A_1 / B_1 (s^{-1}) *(a)*	9.20459×10^{-7}	**0** *(b)*	1.59539×10^{-5}	0 *(b)*
Gaussian Fit Peak Area	0.9971 ± 0.0062	**1 ± 0.0062**	1 ± 0.0062	1 ± 0.0062
		***tE*(*t*) curve**		
Baselines, A_2 / B_2 *(a)*	0	**0** *(b)*	5.81853×10^{-4}	0 *(b)*
μ_1: Gaussian Fit Peak Area (s)	64.157 ± 0.444	**64.341 ± 0.446**	64.361 ± 0.446	64.340 ± 0.445
		$(t-t_m)^2E(t)$ curve *(c)*		
Baselines, A_3 / B_3 (s) *(a)*	1.59294×10^{-5}	**0** *(b)*	0.01241	0 *(b)*
μ_2': Gaussian Fit Peak Area (s^2)	72.327 ± 0.660	**72.204 ± 0.659**	71.904 ± 0.586	72.364 ± 0.582
		$t^2E(t)$ curve		
Baselines, A_4 / B_4 (s) *(a)*	0	**0** *(b)*	0.02122	0 *(b)*
Gaussian Fit Peak Area (s^2)	4203.285 ± 52.505	**4218.935 ± 30.621**	4221.85 ± 28.836	4218.70 ± 30.562
		$\int t^2E(t)dt - t_m^2$ *(d)*		
μ_2'	87.115 ± 77.476	**79.042 ± 65.050**	79.550 ± 64.245	79.035 ± 64.908

Note: (*a*): A_0, A_1, A_2, A_3 and A_4 are baseline symbols used for both **system-found** baseline *with and without* baseline subtraction; whereas B_0, B_1, B_2, B_3 and B_4 are baseline symbols used for both **user-defined** baseline *with and without* baseline subtraction.

(*b*): The baseline values subtracted in Column 2 and 4 are the baseline values defined in Column 1 and 3. However, this subtraction is only needed for the data points on the raw experimental response peak i.e. *I*-curve. Then, the follow-up moment calculations, such as: peak fitting for *E*(*t*) curve will use subtracted data from previous curve *I*(*t*) divided by the peak area calculated by subtracted data i.e.

$\int_0^t I(t)dt$. And same applies for $tE(t)$ curve from $E(t)$ curve, $(t - t_m)^2E(t)$ curve from $E(t)$ curve.

(*c*): The areas under $(t - t_m)^2E(t)$ curve with standard errors using different baseline rules were presented in Table 3.3. The **addition and subtraction of values with standard deviation rule** was used to calculate these standard errors. The definition of addition and subtraction of values with standard deviation is that: for two or multiple values with independent uncertainties, the square of the uncertainty in the sum or difference of two numbers is the sum of the squares of individual absolute errors (Taylor, 1997). For example, in Column 2 from Table 3.3, the data used to calculated the area under $(t - t_m)^2E(t)$ curve was shown in Appendix A4.2, Table A4.2. There are two peaks in the $(t - t_m)^2E(t)$ curve and each peak has an individual standard error. Hence, the addition and subtraction rule can be applied:

$$\int_0^t (t-t_m)^2 E(t)dt = (31.889 + 40.315) \pm \text{sqrt}\ ((0.426)^2 + (0.503)^2) = 72.204 \pm 0.659\ \text{s}^2$$

(*d*): The error analysis for $\int t^2E(t)dt - t_m^2$ uses two different rules: **(i) the exponents or the power rule**; **(ii) the subtraction rule**. Unlike the multiplication and division rule, where the uncertainties of two or multiple values are independent of each other. The exponent rule means that the error on each value is mostly correlated (Taylor, 1997). The general formula for power rule is:

$$Z = X^n$$

Then the uncertainty of the product is:

$$\Delta Z = nX^{(n-1)}\Delta X$$

For example, t_m^2 with standard error in Column 2 Table 3.3, was calculated by:

$t_m^2 = (64.341)^2 \pm 2 \times 64.341 \times 0.446 = 4139.893 \pm 57.392\ \text{s}^2$

Therefore, using the subtraction rule, the value of $\int t^2E(t)dt - t_m^2$ with standard error is:

$$\int_0^t t^2E(t)dt - t_m^2 = (4218.935 - 4139.893) \pm \text{sqrt}\ ((30.621)^2 + (57.392)^2) = 79.042 \pm 65.050\ \text{s}^2$$

From this analysis, the following observations are made:

The system found baseline for *I*-curve: $A_0 = 3.49375 \times 10^{-13}$ torr, is located automatically by searching the minimum values on *I*-curve, in this case at time $t_1 = 22.758$ s and $t_2 = 30.771$ s. The system found baseline for *E*-curve: $A_1 = 9.20459 \times 10^{-7}$ s^{-1}, is calculated based on Equation (3.22) (i.e. system found baseline A_0 is divided by the area of *I*-curve). Similarly, baseline A_2, A_3 and A_4 are calculated at time $t_1 = 22.758$ s and $t_2 = 30.771$ s. With baseline subtraction means that all data points are subtracted by the fixed baseline defined in the corresponding peaks.

The user-defined baseline: $B_0 = 6.03397 \times 10^{-12}$ torr at time $t = 36.47$ s, is the same constant used in the numerical integration method for calculating peak area shown in Section 3.6.1. Hence, the user-defined baseline: B_1, B_2, B_3 and B_4 are calculated at time $t = 36.47$ s. However, $B_0 = 6.03397 \times 10^{-12}$ torr is not the lowest baseline for the experimental response curve i.e. $I(t)$ curve. Instead it is chosen in Section 3.6.1 for numerical integration because from that point onward, it is easy to allocate other data points and besides, it is relatively the lowest intensity data that can be found at the peak-beginning.

General comparison:

(a) In general, the areas under the *I*-curve, *E*-curve, $tE(t)$ curve and $(t - t_m)^2E(t)$ curve, all show good agreements with different baseline methods. However, the peaking fitting result for μ_2' using the area of $t^2E(t)$ curve minus the value of t_m^2 with system found baseline (without baseline subtraction) is quite different from other baseline rules.

(b) From the results of peak fitting, for both system-found and user-defined baseline *with* baseline subtraction, the moment analysis results are almost identical. More importantly, moment analysis results from peak fitting agree well with results from numerical integration for the first moment μ_1.

(c) The second central moment results shown in Table 3.4, disagree with second central moment expressions in Equation (3.30). For Gaussian peak fitting method with baseline subtraction, the peak area under $(t - t_m)^2E(t)$ curve is 72 s^2, comparing to 79 s^2 from the area of $t^2E(t)$ curve minus t_m^2.

(d) In addition, differences are also observed when comparing the μ_2' results obtained using peak fitting in Table 3.4 with the results obtained using Simpson's rule in Table 3.2 (e.g. For Simpson's rule, μ_2' is around 77 s^2 using both expressions in Equation (3.30)).

Table 3.4: Average values and standard deviation calculated based on results in Table 3.3.

Parameters	**Peaking fitting**	
	Column 1 and 3 in Table 3.3 (*a*)	**Column 2 and 4 in Table 3.3 (*b*)**
	Average	**Average**
Area under $I(t)$ curve (torr.s)	$3.7889\times10^{-7} \pm 1.3808\times10^{-9}$	$3.7834\times10^{-7} \pm 1.6673\times10^{-9}$
Area under $E(t)$ curve	0.9986 ± 0.0044	1.0000 ± 0.0044
Area under $tE(t)$ curve: μ_1 or t_m (s)	64.260 ± 0.315	64.341 ± 0.315
Area under $(t - t_m)^2 E(t)$ curve: μ_2' or σ^2 (s^2)	72.115 ± 0.441	72.284 ± 0.440
Area under $t^2E(t)$ curve deducting t_m^2: μ_2' or variance σ^2 (s^2)	83.332 ± 50.324	79.039 ± 45.947

Note: (*a*): Average values and standard deviation for peak fitting without baseline subtraction;

(*b*): Average values and standard deviation for peak fitting with baseline subtraction.

(*a*) and (*b*): The error analysis in Table 3.4 used the **multiplication by a constant with standard deviation rule** followed by the **addition of values with standard deviation rule**. The multiplication by a constant with standard deviation rule means that when an uncertain quantity is multiplied by a constant, the absolute error on the product is the constant times the absolute error of the original quantity (Taylor, 1997). For example, for calculating the standard error of the average area under $tE(t)$ curve between Column 1 and 3 in Table 3.3, it can be treated as the data in each column is multiplied by a constant of value equals to 0.5 and then follow by the addition of values:

$$\underline{\text{Column 1:}} \left(\int_0^t tE(t)dt\right)_1 = \frac{64.157}{2} \pm \frac{0.444}{2} = 32.079 \pm 0.222 \text{ s}$$

$$\underline{\text{Column 3:}} \left(\int_0^t tE(t)dt\right)_3 = \frac{64.361}{2} \pm \frac{0.446}{2} = 32.181 \pm 0.223 \text{ s}$$

The addition and subtraction of values with standard deviation means that the square of the uncertainty in the sum or difference of two numbers is the sum of the squares of individual absolute errors. Therefore, the standard error or uncertainty in the average area under $tE(t)$ curve between Column 1 and 3 is calculated as:

$$\left(\int_0^t tE(t)dt \right)_{AV} = (32.079 + 32.181) \pm \text{sqrt}\,((0.222)^2 + (0.223)^2) = 64.260 \pm 0.315 \text{ s}$$

For moment analysis using numerical integration (Simpson's rule), there is no particular point chosen for the baseline, because the integration is carried out at a user-defined point (e.g. 6.03397×10^{-12} torr at the beginning of the peak was chosen as shown in Figure A3.1 in Appendix 3). This baseline constant is not subtracted from the data points on the response curve.

From the size of standard errors in Table 3.4, peak fitting results with baseline subtraction are more reliable than without subtraction.

In conclusion: **Peak fitting with a system found baseline with baseline subtraction** (Column 2 in Table 3.3) is chosen as the main peak fitting method used in this thesis.

3.7 The use of chromatographic method for packed-bed applications

According to Do (1998), in the chromatographic method particles of a uniform size, or narrow particle size distribution are packed in a cylindrical column. An inert gas is then introduced into the column until the column is stabilised, which means that there are no variation in the signal at the exit of the column. This is registered as the baseline. Once this baseline has been set, a pulse of tracer, is introduced at the inlet of the column. If the tracer is non-adsorbing, it will exit the column at the mean retention of the systems. However, if the tracer is an adsorbing solute or gas, its movement down the column is delayed due to the attraction between the tracer and particle, and this speed of propagation depends on the magnitude of this affinity. The stronger the attraction, the longer it takes for the tracer to exit the column. The response curve usually exhibits a bell shape with the mean retention time (i.e. first moment or mean residence time) being proportional to the affinity between the two phases. The spread of the curve (i.e. second central moment or variance) is a complex function of all dispersion forces in the system.

These dispersive forces are (Do, 1998):

a) axial dispersion;
b) film resistance;
c) all resistances within the particle: (i) pore diffusion resistance in macropore; (ii) micropore diffusional resistance; (iii) finite adsorption resistance

3.7.1 The initial condition

The initial state of the column can be one of the following two situations (Do, 1998):

(a) the column is initially free of any tracer molecule, or
(b) the column is initially equilibrated with a tracer of concentration C^*.

The first situation is the initial condition which is used in the chromatographic experiments conducted in this thesis. The inlet capillary on the mass spectrometer was calibrated with a carrier gas which flowed through the column, until the baseline was stable, and once this was stabilised, a tracer was injected into the column with a concentration of $C_0(t)$ at the inlet. The concentration was chosen such that the adsorption isotherm of this tracer towards the solid packing is linear. This results in a set of linear equations which permit the use of Laplace

transforms to obtain the solution analytically. Knowing the solution in the Laplace domain, the solution in real time can be obtained by an inversion procedure. However, the moment analysis method can be utilised to obtain moments from the Laplace solutions directly without the tedious process of inversion.

3.7.2 The moment method

For either the pulse or square injection, the moments can be obtained experimentally from the response of the exit concentration *versus* time. The *n*-th moment is defined as follow (Schneider and Smith, 1968a):

$$m_n = \int_0^\infty t^n C(x,t)dt \tag{3.43}$$

and the normalised moment scaled against the zero order moment is defined as:

$$\mu_n = \frac{m_n}{m_0} \tag{3.44}$$

The *n*-th central moment is defined as the moment relative to the centre of gravity of the chromatographic curve:

$$\mu_n' = \frac{1}{m_0}\int_0^\infty (t-\mu_1)^n C(x,t)dt \tag{3.45}$$

The set of governing linear equations are solved by the method of Laplace transform. The transform is defined as:

$$\overline{C} = \int_0^\infty e^{-st} C(x,t)dt \tag{3.46}$$

If the solution in the Laplace domain is known, the *n*-th order moment can be readily obtained by taking the *n*-th derivative of $\overline{C}$:

$$m_n = (-1)^n \frac{d^n \overline{C}(s)}{ds^n}\bigg|_{s=0} \tag{3.47}$$

By matching the theoretical moments give in Equation (3.47) with the experimental moments, system parameters can be obtained.

3.7.3 Convolution theorem for γ-alumina beads experiment

3.7.3.1 RTD for combinations of non-interacting regions

From Froment *et al.* (1990), if an impulse input is used at the beginning of a combination of independent regions, such that the RTD of any one region is unaffected by the presence of the others, the combination RTD is given by the convolution formula as:

$$E(\alpha) = \int_0^{\alpha} E_1(\alpha_1) E_2(\alpha - \alpha_1) d\alpha_1 \tag{3.48}$$

where $E(\alpha)$ is the normalised RTD function or age distribution function, and α is the time, an independent variable (same as t). The impulse input term is used mathematically to derive the convolution integral (Equation (3.48)) from partial differential equations (Himmelblau and Bischoff, 1968). For engineering practise and industrial process, impulse input is very difficult to achieve because of dispersion effects. Therefore, the pulse input can be any kind of inputs and impulse is a special case (Stará *et al.*, 2006; IAEA, 2008).

From Equation (3.48), if $E_1(\alpha)$ and $E_2(\alpha)$ are normalized, so is $E(\alpha)$:

$$\int_0^{\infty} E(\alpha) d\alpha = \int_0^{\infty} d\alpha \int_0^{\alpha} d\alpha_1 E_1(\alpha_1) E_2(\alpha - \alpha_1) \tag{3.49}$$

From Equation (3.21), the area of the normalized curve, $E(\alpha)$ is 1. Therefore, a new variable α_2 is defined as: $\alpha_2 \equiv \alpha - \alpha_1$, changing the order of integration in Equation (3.49) yields:

$$\begin{aligned} &\int_0^{\infty} E(\alpha) d\alpha = \int_0^{\infty} d\alpha_1 E_1(\alpha_1) \int_0^{\infty} d\alpha_2 E_2(\alpha_2) \\ &\int_0^{\infty} E(\alpha) d\alpha = 1 \times 1 = 1 \end{aligned} \tag{3.50}$$

The overall mean residence time or the first moment is found by:

$$\begin{aligned} &\tau = \int_0^{\infty} \alpha d\alpha \int_0^{\alpha} d\alpha_1 E_1(\alpha_1) E_2(\alpha - \alpha_1) \\ &\tau = \int_0^{\infty} d\alpha_1 E_1(\alpha_1) \left[\int_0^{\infty} \alpha_2 d\alpha_2 E_2(\alpha_2) + \alpha_1 \int_0^{\infty} d\alpha_2 E_2(\alpha_2) \right] \\ &\tau = \tau_2 + \tau_1 \end{aligned} \tag{3.51}$$

where the same procedure was utilized.

Finally, the same procedure was carried out for the variance or the second central moment gives:

$$\sigma_\alpha^2 = \int_0^\infty (\alpha - \tau)^2 E(\alpha) d\alpha$$
$$\sigma_\alpha^2 = \sigma_{\alpha,1}^2 + \sigma_{\alpha,2}^2 \tag{3.52}$$

This can be put into the dimensionless form for consideration of the width of the overall RTD:

$$\sigma^2 = \frac{\sigma_\alpha^2}{\tau^2} \tag{3.53}$$

By consecutively repeating these manipulations for multiple region convolutions, the moments would be:

$$\tau = \sum_i \tau_i \qquad\qquad \sigma_\alpha^2 = \sum_i \sigma_{\alpha,i}^2 \tag{3.54}$$

The conclusion for mean residence time and second central moment in Equation (3.54) from Froment *et al*. (1990) is very important for the moment analysis results in the sections that follow on γ-alumina and also on glass beads.

3.7.3.2 The first moment and second central moment for a fictitious bed packed with γ-alumina beads

To allow for delay time, τ_d ($\tau_d = \tau_1 + \tau_2$), and other column end effects (at the inlet and outlet of the column), a fictitious bed of length 200 mm is considered (see Figure 3.28). This fictitious bed has no end effects.

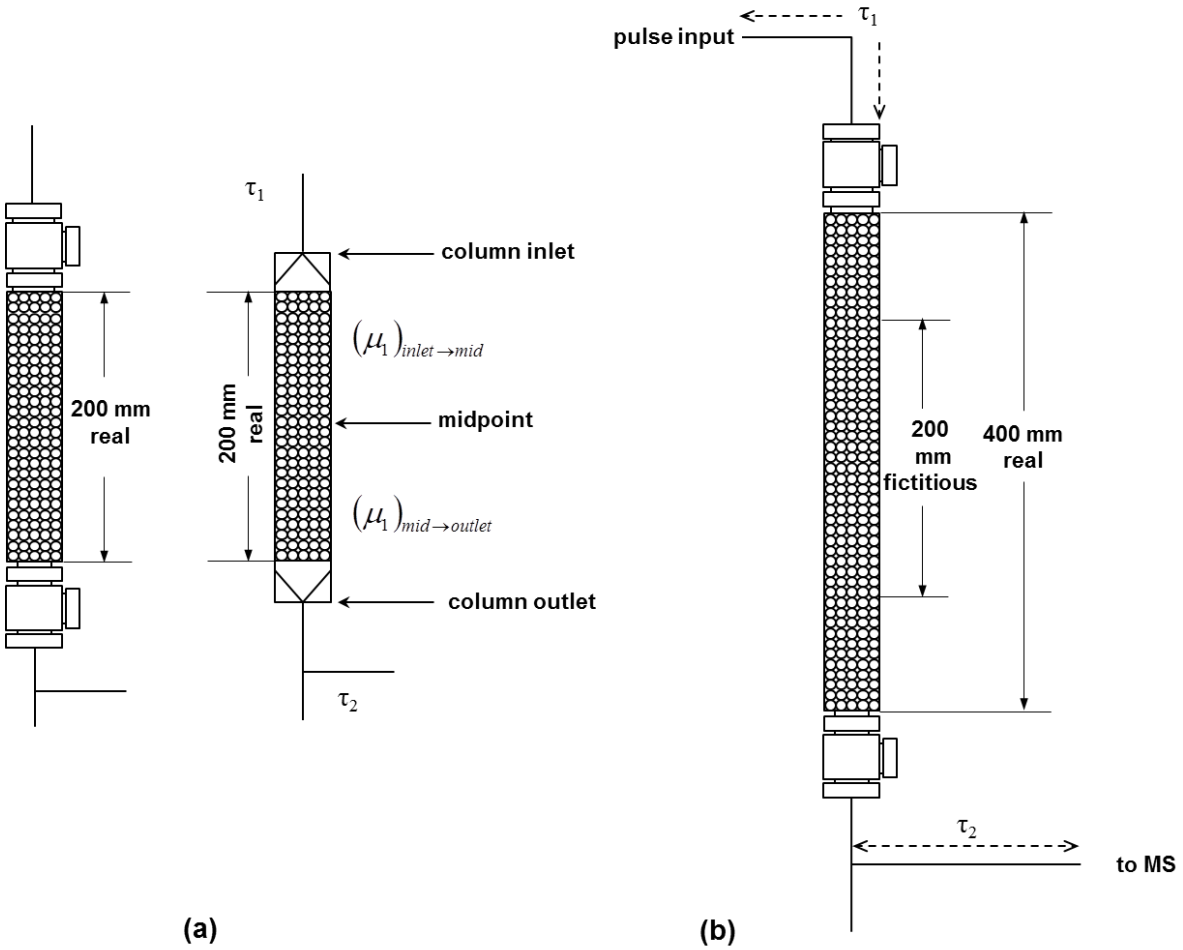

Figure 3.28: Schematic illustration of the real columns and the fictitious bed.

According to Equation (3.54), assuming the convolution theorem can be applied to this combination of independent regions shown in Figure 3.28 (Froment *et al*., 1990). Then:

$$(\mu_1)_{400} = (\mu_1)_{200} + (\mu_1)_{f,200} \tag{3.55}$$

where the mean residence time of a 200 mm column (real) consists of:

$$(\mu_1)_{200} = \tau_1 + (\mu_1)_{\text{inlet}\rightarrow\text{mid}} + (\mu_1)_{\text{mid}\rightarrow\text{outlet}} + \tau_2 \tag{3.56}$$

Hence, the mean residence time, $(\mu_1)_{f,\,200}$, of a fictitious 200 mm bed (without column end effects) is:

$$(\mu_1)_{f,200} = (\mu_1)_{400} - (\mu_1)_{200} \tag{3.57}$$

and for the variance, $\mu_2^{'}$ is:

$$(\mu_2^{'})_{f,200} = (\mu_2^{'})_{400} - (\mu_2^{'})_{200} \tag{3.58}$$

A plot for the fictitious bed (200 mm) deduced from the experimental first moment and second central moment for the two 'real' columns using convolution theorem is shown in Figure 3.29.

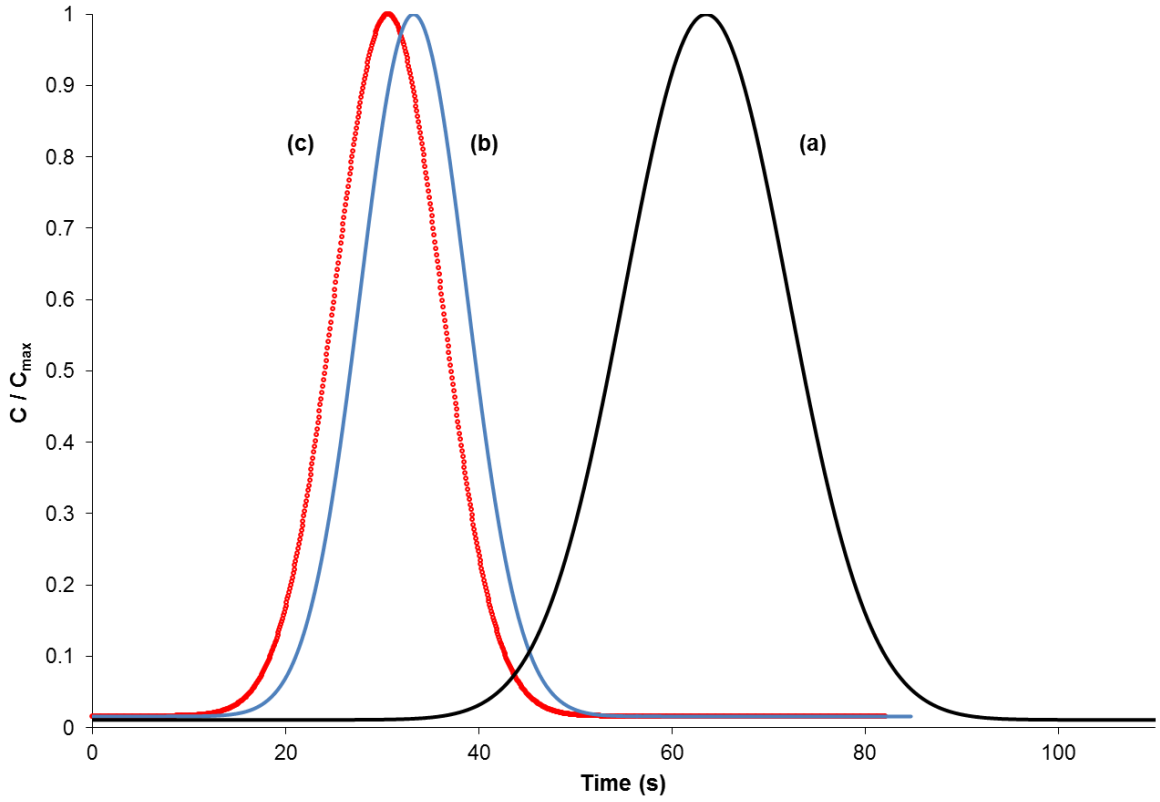

Figure 3.29: Example of output response and calculation for the fictitious bed: (a) 400 mm real column, (b) 200 mm real column, and (c) 200 mm fictitious bed.

3.7.4 Results for moment analysis

The results of moment analysis performed on the experimental response curves for the γ-alumina beads using two different column lengths (200 and 400 mm), and the moment results calculated for the fictitious bed (200 mm) are presented in Appendix 5. The following points are emphasised:

(a) The response peak generated by the 0.1 ml tracer pulse is not smooth (i.e. contains noise), and sometimes the scan range of SEM detector needs to be re-adjusted in order to obtain a smooth peak but with less data points;

(b) The response peak generated by injecting a 0.25 or a 0.5 ml tracer pulse is smooth.

(c) The average R-square (goodness of fit) for peak fitting was above 0.96. Simpson's rule for peak area calculation was only applied to the results for the 400 mm column, in order to check the peak fitting values obtained using OriginPro 8.6, but not for the 200 mm column.

(d) When adsorption equilibrium constant, $K = 0$, the theoretical first moment $(\mu_1)_0$ for a blank run, or in some literature (e.g. Guangsuo *et al*. (2000)), it refers to a theoretical first moment expression for an inert run $(\mu_1)_{inert}$, are:

$$\left(\mu_1\right)_0 = \frac{L\varepsilon_b}{u_0}\left[1+\frac{\left(1-\varepsilon_b\right)\varepsilon}{\varepsilon_b}\right]; \qquad \left(\mu_1\right)_{inert} = \frac{L}{u_i}\left[1+\frac{\left(1-\varepsilon_b\right)\varepsilon}{\varepsilon_b}\right] \tag{3.59}$$

$$\left(\mu_1\right)_0 = \frac{L\varepsilon_b}{u_0}\left[1+\frac{\left(1-\varepsilon_b\right)\varepsilon}{\varepsilon_b}\right]+\frac{t_0}{2}; \quad \left(\mu_1\right)_{inert} = \frac{L}{u_i}\left[1+\frac{\left(1-\varepsilon_b\right)\varepsilon}{\varepsilon_b}\right]+\frac{t_0}{2} \tag{3.60}$$

where u_0 is the superficial carrier gas velocity, and u_i is the interstitial carrier gas velocity. The interstitial velocity, u_i is equal to superficial velocity, u_0 divided by bed porosity, ε_b. This is explained in the later session.

(e) For $(\mu_1)_0$ and $(\mu_1)_{inert}$, the difference between the two is that the former is a theoretical expression used in the calculation, whereas the latter one, $(\mu_1)_{inert}$ is evaluated from the experimental response curves, $tE(t)$ curve of runs with carrier gas. Equations (3.59) and (3.60) are used later for calculating the adsorption equilibrium constant.

(f) Equations (3.59) and (3.60) can be used when the pulse input is a square-wave or dirac pulse (Schneider, 1986; Do, 1998).

(g) For 2nd central moment analysis, $\mu_2^{'}$, although the mathematical derivation showed that two different $\mu_2^{'}$ expression in Equation (3.30) should yield the same results, the difference in variance, σ^2 is quite significant at low carrier gas flowrate. Therefore,

moment analysis by peak fitting for second central moment, μ_2', is divided into two categories:

Cat. A: Gaussian peak fitting with second central moment, μ_2', equal to the area under the $(t - t_m^2)\,E(t)$ curve;

Cat. B: Gaussian peak fitting with second central moment, μ_2', equal to the area of the $t^2E(t)$ curve minus t_m^2.

The issue with 2nd central moment difference between **Cat. A** and **Cat. B** will be addressed in Chapter 4, whereas in this chapter, only the first moment is needed for calculating *K*.

(h) The moment results for the fictitious bed (length: 200 mm) are shown in Table 3.5 to Table 3.8 and these were carried out at the following conditions:

i) 0.25 ml sample loop at carrier gas flowrate 30 – 90 cm^3/min, at 295.15 K and 1.013 bar;

ii) He (tracer) – N_2 (carrier) and N_2 (tracer) – He (carrier) gas systems;

iii) 2nd central moment for both real columns are obtained from **Cat. A** and **Cat. B**.

(i) The error analysis for first moments and second central moments of the fictitious bed (200 mm) shown in Table 3.5 to Table 3.8 follows: (a) **the addition and subtraction of values**, and (b) **the exponent or power of values with standard deviation rules**. The interpretations are given as follows: for error analysis rule (a), if A = 2.23 ± 0.05 and B = 1.56 ± 0.23, then the standard deviation dX of X = A + B or X = A – B is calculated by: dX = sqrt ($(0.05)^2$ + $(0.23)^2$) = 0.24. For rule (b), the standard deviation dX of $X = A^n$, is calculated by $dX = n \times 2.23^{(n-1)} \times 0.05$, where *n* can be any real number, not just an integer.

(j) The response curves obtained from the 0.25 ml sample loop were re-run for repeatability checks at each carrier gas flowrate, same was done for the 0.1 ml and 0.5 ml sample loops. Nevertheless, although experimental response curves generated by the 0.25 and 0.5 ml sample loops are smooth (compared to 0.1 ml), this doesn't mean that the moment analysis results from the 0.1 ml is useless. For values of *K* shown in this chapter, average values (plus standard error) were used from the moment analysis results for 0.1, 0.25 and 0.5 ml sample loops.

Table 3.5: Moment analysis results **(He tracer)** for the **fictitious bed** (**200 mm)** packed with γ-alumina beads, and 2nd central moment is obtained from **Cat. A**.

N_2(carrier) - He(tracer)	**γ-alumina beads (0.25 ml sample loop)**					
	Flowrate (cm^3/min)	**1st moment, μ_1 (s) (a)**	**2nd central moment, μ_2' (s^2) (b)**	**$(\mu_1)_0$ for blank run (Equation (3.59)) (s)**	**$(\mu_1)_0$ for blank run (Equation (3.60)) (s)**	**Injection time, t_0 (s)**
bot01	30	51.133 ± 0.676	177.832 ± 2.041	46.356	46.456	0.50
bot03	40	38.859 ± 0.648	77.669 ± 1.241	34.767	34.842	0.38
bot06	50	30.368 ± 0.524	40.237 ± 0.721	27.814	27.874	0.30
bot08	60	25.778 ± 0.463	24.968 ± 0.533	23.178	23.228	0.25
bot10	70	22.307 ± 0.385	17.070 ± 0.374	19.867	19.910	0.21
bot13	80	19.202 ± 0.427	11.429 ± 0.304	17.384	17.421	0.19
bot16	90	17.375 ± 0.419	8.791 ± 0.203	15.452	15.485	0.17

Note: (*a*): The error analysis for the first moments of the fictitious bed follows the addition and subtraction of values with standard deviation rule. For example, in "**bot06**", the first moment for the 400 mm real column with standard error is (Table 3.3):

$(\mu_1)_{400} = 64.341 \pm 0.446$ s

and the first moment for the 200 mm real column with standard error is:

$(\mu_1)_{200} = 33.973 \pm 0.275$ s

Applying the **subtraction of values with standard deviation rule**, the first moment for the fictitious bed with standard error is:

$(\mu_1)_{fictitious,200} = (64.341 - 33.973) \pm \text{sqrt}\,((0.446)^2 + (0.275)^2) = 30.368 \pm 0.524$ s

(*b*): Similarly, the second central moments (Cat. A) with standard errors for the 200 and 400 mm real columns follow the same error analysis as shown in (*a*). From Appendix A4.2 and Table A4.2, the $(t - t_m)^2E(t)$ curve has two peak areas (i.e. Peak 1 and 2), and therefore, using the **addition of values with standard deviation rule** yields:

$(\mu_2')_{400} = (31.889 + 40.315) \pm \text{sqrt}\,((0.426)^2 + (0.503)^2)\ s^2 = 72.204 \pm 0.659\ s^2$

and the second central moment (Cat. A) for the 200 mm real column is:

$(\mu_2')_{200} = (14.014 + 17.953) \pm \text{sqrt}\,((0.183)^2 + (0.227)^2)\ s^2 = 31.967 \pm 0.292\ s^2$

Applying the **subtraction of values with standard deviation rule**, the second central moment (Cat. A) for the fictitious bed with standard error is:

$(\mu_2')_{fictitious,200} = (70.204 - 31.967) \pm \text{sqrt}\,((0.659)^2 + (0.292)^2) = 40.237 \pm 0.721\ s^2$

Table 3.6: Moment analysis results **(N_2 tracer)** for the **fictitious bed** (**200 mm)** packed with γ-alumina beads, and 2nd central moment is obtained from **Cat. A**.

He(carrier) - N_2(tracer)	**γ-alumina beads (0.25 ml sample loop)**					
	Flowrate (cm^3/min)	**1st moment, μ_1 (s)**	**2nd central moment, μ_2' (s^2)**	**$(\mu_1)_0$ for blank run (Equation (3.59)) (s)**	**$(\mu_1)_0$ for blank run (Equation (3.60)) (s)**	**Injection time, t_0 (s)**
bot01	30	52.142 ± 0.421	197.016 ± 4.560	46.356	46.456	0.50
bot03	40	39.086 ± 0.298	70.886 ± 0.943	34.767	34.842	0.38
bot05	50	34.359 ± 0.250	48.670 ± 0.630	27.814	27.874	0.30
bot07	60	30.708 ± 0.231	34.685 ± 0.457	23.178	23.228	0.25
bot09	70	25.499 ± 0.180	19.791 ± 0.342	19.867	19.910	0.21
bot12	80	22.247 ± 0.164	13.128 ± 0.205	17.384	17.421	0.19
bot14	90	19.708 ± 0.169	9.722 ± 0.211	15.452	15.485	0.17

Table 3.7: Moment analysis results **(He tracer)** for the **fictitious bed** (**200 mm)** packed with γ-alumina beads, and 2nd central moment is obtained from **Cat. B**.

N_2(carrier) - He(tracer)	γ-alumina beads (0.25 ml sample loop)					
	Flowrate (cm^3/min)	**1st moment, μ_1 (s) (a)**	**2nd central moment, μ_2' (s^2) (b)**	**$(\mu_1)_0$ for blank run (Equation (3.59)) (s)**	**$(\mu_1)_0$ for blank run (Equation (3.60)) (s)**	**Injection time, t_0 (s)**
bot01	30	51.133 ± 0.676	189.429 ± 133.029	46.356	46.456	0.50
bot03	40	38.859 ± 0.648	91.962 ± 101.106	34.767	34.842	0.38
bot06	50	30.368 ± 0.524	46.619 ± 68.409	27.814	27.874	0.30
bot08	60	25.778 ± 0.463	31.052 ± 46.694	23.178	23.228	0.25
bot10	70	22.307 ± 0.463	15.213 ± 37.207	19.867	19.910	0.21
bot13	80	19.202 ± 0.427	16.153 ± 35.386	17.384	17.421	0.19
bot16	90	17.375 ± 0.419	12.867 ± 32.139	15.452	15.485	0.17

Note: (*a*): The first moments with standard errors shown in Tables 3.7 and 3.8 are exactly the same as in Tables 3.5 and 3.6 for He and N_2 tracer respectively.

(*b*): The error analysis for second central moments (Cat. B) in Table 3.7 for He tracer is different from second central moments (Cat. A) in the Table 3.5 (as well as second central moments shown in Table 3.8 and Table 3.6 for N_2 tracer). The reason being that the error analysis in second central moment (Cat. B) uses not only the **addition/subtraction of values with standard deviation rule**, but also the **exponent or power of values with standard deviation rule**. For example in "**bot06**", from Table A4.2 in Appendix A4.2, the area under the $t^2E(t)$ curve with standard error for the 400 mm real column is:

$$\left(\int_0^t t^2 E(t)dt\right)_{400} = 4218.935 \pm 30.621 \text{ s}^2$$

From Table A4.2, using the **power of values with standard deviation rule**, the square of first moment with standard error for the 400 mm real column is:

$(t_m^2)_{400} = (64.341)^2 \pm 2 \times 64.341 \times 0.446 = 4139.893 \pm 57.392 \text{ s}^2$

Hence, the second central moment (Cat. B) with standard error is:

$(\mu_2')_{400} = (4218.935 - 4139.893) \pm \text{sqrt}\,((30.621)^2 + (57.392)^2) = 79.042 \pm 65.050 \text{ s}^2$

Applying the same rules yield the second central moment (Cat. B) with standard error for the 200 mm real column:

$(\mu_2')_{200} = (1186.556 - 1154.133) \pm \text{sqrt}\,((10.189)^2 + (18.701)^2) = 32.423 \pm 21.296 \text{ s}^2$

Finally, using the **subtraction rule**, the second central moment (Cat. B) with standard error for the fictitious bed is:

$(\mu_2')_{fictitious,200} = (79.042 - 32.423) \pm \text{sqrt}((65.050)^2 + (21.296)^2) = 46.619 \pm 68.409 \text{ s}^2$

Table 3.8: Moment analysis results **(N_2 tracer)** for the **fictitious bed** (**200 mm)** packed with γ-alumina beads, and 2nd central moment is obtained from **Cat. B**.

He(carrier) - N_2(tracer)	**γ-alumina beads (0.25 ml sample loop)**					
	Flowrate (cm^3/min)	**1st moment, μ_1 (s)**	**2nd central moment, μ_2' (s^2)**	**$(\mu_1)_0$ for blank run (Equation (3.59)) (s)**	**$(\mu_1)_0$ for blank run (Equation (3.60)) (s)**	**Injection time, t_0 (s)**
bot01	30	52.142 ± 0.421	227.316 ± 91.848	46.356	46.456	0.50
bot03	40	39.086 ± 0.298	79.775 ± 48.899	34.767	34.842	0.38
bot05	50	34.359 ± 0.250	50.493 ± 35.494	27.814	27.874	0.30
bot07	60	30.708 ± 0.231	45.315 ± 29.344	23.178	23.228	0.25
bot09	70	25.499 ± 0.180	14.387 ± 19.262	19.867	19.910	0.21
bot12	80	22.247 ± 0.164	12.373 ± 14.554	17.384	17.421	0.19
bot14	90	19.708 ± 0.169	11.253 ± 13.581	15.452	15.485	0.17

In Tables 3.5 to 3.8:

(i) The first column or Column (1) in each table is the run name and number created in the MID scans, starts with 'bot' which implies the column outlet.

(ii) Column (2) is the calibrated carrier gas flowrate applied for each run.

(iii) Column (3) is the first moment, μ_1, for the fictitious bed (200 mm), obtained from the difference between first moment results from 200 and 400 mm columns (real). The first moment results of the real columns were evaluated from experimental response curves using Equation (3.29) with peak fitting method (details in Appendix 4).

(iv) Column (4) is the second central moment, μ_2', for the fictitious bed (200 mm), obtained from the difference between second central moment results from 200 and 400 mm columns (real). The second central moment results of the real columns were evaluated from experimental response curve using Equation (3.30) with peak fitting method (details in Appendix 4).

(v) Column (5) is the first moment for blank run, $(\mu_1)_0$, calculated from theoretical first moment expression shown in Equation (3.59).

(vi) Column (6) is the first moment for blank run, $(\mu_1)_0$, calculated from theoretical first moment expression shown in Equation (3.60).

(vii) Column (7) is the injection duration time, t_0 of the pulse tracer, which is calculated from: [sample loop volume / carrier gas flow].

Looking at the moment results for the fictitious bed in Tables 3.5 to 3.8, the following observations are made:

(a) According to Do (1998), a correlation between degree of the spread and the carrier gas velocity can be interpreted as illustrated in Figure 3.30(a). From Figure 3.30(a), as u_0 increases, then the degree of spread of a pulse response curve decreases and then increases, while the pore diffusion effect increases, and the axial dispersion effect in the column decreases.

(b) The combined dispersion and diffusion effects plot of the fictitious 200 mm bed is shown in Figure 3.30(b). For the packed-bed experiments with γ-alumina beads in this thesis, the combined effect lies in the range of the optimum velocity region in Figure 3.30(a).

(c) In Columns (3) and (4) (Tables 3.5 to 3.8), the mean residence time and variance for He and N_2 tracer are both inversely proportional to flow.

(d) In Columns (5), (6) and (7), the first moment for the blank runs, $(\mu_1)_0$, is calculated using two different first moment expressions (Equation (3.59) and (3.60) when $K = 0$), and these are almost identical. Therefore, the injection time term, $t_0/2$ and $t_0^2/12$, used in the theoretical first moment and second central moment expression is negligible and can be ignored.

In conclusion: data have now been obtained on first moments, μ_1, of a fictitious bed: 200 mm without entrance and exit effects, which is calculated from the difference between first moment results evaluated from the experimental response curves of the 400 and 200 mm columns (real). The μ_1 results for the fictitious bed in Tables 3.5 to 3.8 for the 0.25 ml sample loop, along with the first moment results from 0.1 and 0.5 ml sample loops, will be used in Section 3.8.6 to determine the average adsorption equilibrium constant, K.

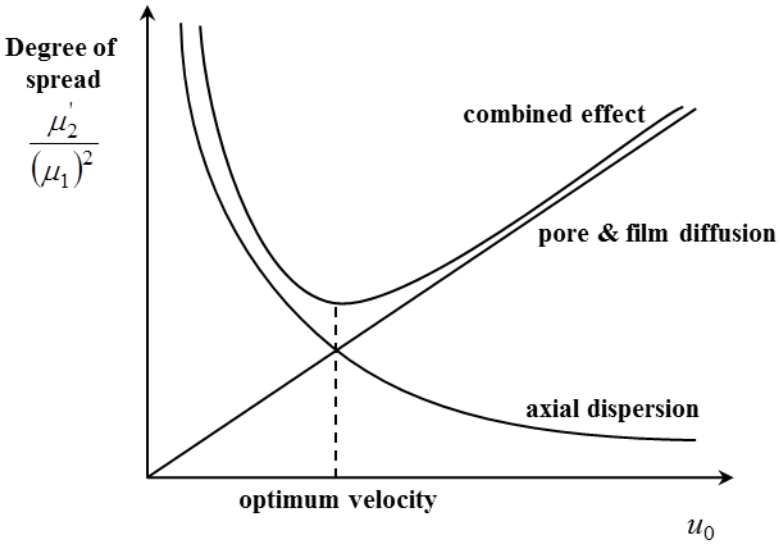

(a) Theoretical plot adapted and redrawn from Do (1998).

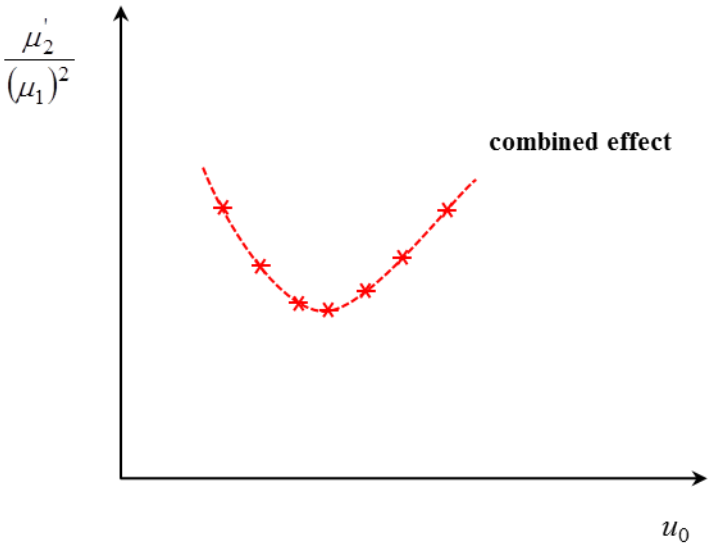

(b) Plot for the fictitious 200 mm bed

Figure 3.30: Degree of spread μ_2'/μ_1 *versus* superficial carrier gas velocity u_0.

3.8 Moment matching to determine equilibrium constant, *K*

3.8.1 The derivations of adsorption equilibrium constant, *K* and Henry's law constant, K_h

The following descriptions are based on explanations provided in a number of textbooks (Hayes and Kolaczkowski, 1997; Ruthven, 1984):

One of the most commonly used models in catalysis is known as the Langmuir adsorption model. If the exchange of molecules between adsorbed and gaseous phases is considered, then the rate of adsorption is

$$\underline{\textbf{Rate of adsorption:}}\ k_{ads}p(1-\Theta) \tag{3.61}$$

where:
- Θ is the fraction coverage, it means that for adsorbate molecule *A*, Θ is the fraction of surface sites occupied by *A*. Therefore, $(1 - \Theta)$ means the number of vacant sites available for *A* to adsorb (Hayes and Kolaczkowski, 1997);
- k_{ads} is the adsorption rate constant (units in s^{-1},or $cm^3g^{-1}s^{-1}$ in the literature);
- *p* is the partial pressure; according to idea gas law, concentration, C_i or C_s can be used instead of partial pressure, *p*, representing the concentration of tracer gas *A* in the particle pores.

The rate of desorption is:

$$\underline{\textbf{Rate of desorption:}}\ k_{des}\Theta \tag{3.62}$$

where:
- k_{des} is the desorption rate constant (units in s^{-1}, or $cm^3g^{-1}s^{-1}$ in the literature).

According to Ruthven (1984), the fraction coverage Θ is:

$$\Theta = \frac{q}{q_s} \tag{3.63}$$

where:
- q_s is the total number of sites per unit weight or volume of adsorbent.

At equilibrium, the net rate of adsorption is zero, so combing Equations (3.61) and (3.62) yields:

$$k_{ads}p(1-\Theta) = k_{des}\Theta \tag{3.64}$$

Therefore, from Equation (3.64), the adsorption equilibrium term, K is defined as:

$$\frac{\Theta}{1-\Theta} = \frac{k_{ads}}{k_{des}} p = K \times p \tag{3.65}$$

Rearranging Equation (3.65) yields:

$$\Theta = \frac{q}{p} = \frac{K \times q_s}{1 + K \times p} \tag{3.66}$$

At low sorbate partial pressure (i.e. low sorbate concentration), as $p \rightarrow 0$, Henry's law is approached:

$$\lim_{p \to 0} \left(\frac{q}{p} \right) = K \times q_s = K_h \tag{3.67}$$

where: – K_h is the Henry's law adsorption equilibrium constant or Henry's law constant defined in terms of sorbate pressure, unit: molecule /(cavity torr).

Moment matching or moment analysis based on linearization, or non-linearization method can be classified as follows:

(a) **Without dimensionless adsorption equilibrium constant K_a:** Baiker *et al*. (1982) and Tang *et al*. (1987);

(b) **With adsorption equilibrium constant K_A^c, K_A (cm^3 g^{-1}):** Schneider and Smith (1968) and Guangsuo *et al*. (2000);

(c) **With dimensionless adsorption equilibrium constant, K_a:** Garc á-Ochoa and Santos (1994) and Santos *et al.* (1996).

(d) **With dimensionless Henry's law constant, K_H:** Do (1998) and Armatas *et al*. (2005).

Examples of techniques to determine K and D_{eff} values with non-reacting tracer are summarised in Table 3.9. The theoretical moment expressions and resistance parameters are all based on the Kub ń and Kučera model, but with slight differences between one and another. It should be emphasised that in Garc á-Ochoa and Santos (1994) and Santos *et al.* (1996), moment matching for D_{eff} calculation using non-linear method: a so-called "Finite difference alogrithmn curve fitting method" was briefly mentioned but with no explanations whatsoever. Therefore, in this thesis, this non-linear method was tested using the non-linear curve fitting in OriginPro 8.6 and the results were found to be satisfactory.

Table 3.9: Examples of techniques in the literature to determine K and D_{eff} values with no reaction.

	Literature (inert tracer)	Equilibrium constant	Method of analysis	Effective diffusivity, D_{eff} determined from	Method of analysis D_{eff}
1	**Baiker *et al*. (1982) and Tang *et al*. (1987)**	No	N/A	**2nd central moment method** (matching of experimental 2nd central moment with theoretical μ_2'	Linear (D_{eff} from intercept)
2	**Schneider and Smith (1968) and**	Yes	Linear (K_A^c, from slope)	**2nd central moment method** (same as 1)	Linear (D_{eff} from intercept)
3	**Guangsuo *et al*. (2000)**	Yes	Linear (K_A from slope)	**2nd central moment method** (same as 1)	Linear (D_{eff} from intercept)
4	**Garc ́a-Ochoa and Santos (1994); Santos *et al.* (1996).**	Yes	Linear (K_a, from slope)	**HETP method** (matching of experimental 1st moment and 2nd central moment with HETP expression)	Non-linear (D_{eff} from constant G)
5	**Armatas *et al*. (2005)**	Yes	Linear (K_H, from slope)	**HETP method** (same as 4)	Linear (D_{eff} from slope)

3.8.2 The general formulation of the material balance equation

The moment analysis method involves the formulation of material balance equations describing the concentration distribution of tracer in two systems:

(a) The material balance of tracer gas *A*, in the column free space (the bulk phase), and

(b) The material balance of tracer gas *A*, in the porous structure of a particle (i.e. intraparticle material balance).

In the sections that follow, different approaches are described and used to interpret the experimental data obtained.

3.8.3 The material balance for the tracer gas in the column free space (Kub ń, 1965; Kučera, 1965):

Column Model:

$$\underbrace{\frac{D_{ax}}{\varepsilon_b}\frac{\partial^2 C}{\partial x^2}}_{\text{axial dispersion term}} - \underbrace{\frac{\partial C}{\partial t}}_{\text{accumulation term}} - \underbrace{u_i \frac{\partial C}{\partial x}}_{\text{convection term}} - \underbrace{\frac{a}{R}\frac{1-\varepsilon_b}{\varepsilon_b}\left(D_e \left.\frac{\partial C_s}{\partial r}\right|_R\right)}_{\text{mass transfer from fluid phase to porous particle}} = 0 \qquad (3.68)$$

where:
- *x*, *r* correlate to change of tracer concentration in axial and radial direction;
- C is the tracer gas concentration in the fluid phase, mol m^{-3};
- C_s is the tracer gas concentration in the porous structure of particles (adsorbent), mol m^{-3};
- u_i is the interstitial carrier gas velocity, cm s^{-1};
- ε_b is the column void fraction or packed bed porosity;
- R is the particle radius, m;
- D_{ax} is the axial dispersion coefficient, cm^2 s^{-1};
- D_e is the effective intraparticle diffusion coefficient, cm^2 s^{-1};
- a is the particle shape factor; $a = 1$ for slab shaped particle, $a = 2$ for cylindrical shaped and $a = 3$ for spherical shaped particle.

The equation describing the external mass transfer through the film surrounding the adsorbent particles is:

$$D_e \left.\frac{\partial C_s}{\partial r}\right|_R = k_f \left(C - C_s\right) \tag{3.69}$$

where: – k_f is the external mass transfer coefficient, cm s^{-1}.

Equation (3.68) was chosen to be the most representative of describing the material balance of tracer gas in the column free space (Schneider and Smith, 1968a). This is because as explained in the following paragraphs, many different forms of the material balance equation have been used in the literature, and the terms and their units are not always explained clearly.

Column models with different forms have been used in the literature, the author has checked these equations, and some of them turned out to be the same as Equation (3.68), others were wrong and misleading. For example, in Suzuki and Smith (1971), the material conservation of *A* in the gas phase in the bed leads to:

$$E_z \frac{\partial^2 C}{\partial x^2} - \frac{\partial C}{\partial t} - u_i \frac{\partial C}{\partial x} - \frac{a}{R}\frac{\left(1-\varepsilon_b\right)}{\varepsilon_b} N_0 = 0 \tag{3.70}$$

where: – E_z is the axial dispersion coefficient in the interparticle region of the bed.

– N_0 is the molar flux from the fluid to particle in the bed, mol cm^{-2} s^{-1}. N_0 is the same as the diffusion term in Equation (3.68) described by Fick's Law.

The E_z (column free space – interparticle region) term is equal to axial dispersion coefficient, D_{ax} in the general axial direction (*x*-axis) of the packed bed divided by the bed porosity term, ε_b, as follows:

$$E_z = \frac{D_{ax}}{\varepsilon_b} \tag{3.71}$$

This also means that E_z is always higher than D_{ax} and is closely related to the interstitial velocity, u_i.

In Equation (3.70), this is also a link between interstitial velocity, u_i, and superficial velocity, u_0, as follows:

$$u_i = \frac{u_0}{\varepsilon_b} \quad \text{where: } u_0 = \frac{\text{gas or fluid flow through the bed, } Q}{\text{packed bed cross-sectional area (C.S.A), } A} \tag{3.72}$$

In another example, in Do (1998), the column model has the following form:

$$D_{ax}\frac{\partial^2 C}{\partial x^2} - \varepsilon_b \frac{\partial C}{\partial t} - u_0 \frac{\partial C}{\partial x} - \varphi J\big|_R = 0 \tag{3.73}$$

where:
- u_0 is the superficial carrier gas velocity, cm s^{-1};
- J_R is the diffusion flux and the unit is: mol cm^2 s^{-1}, so it is the same as Equation (3.68) described by Fick's Law.
- φ is the interfacial area per unit bed volume and is defined as (Do, 1998):

$$\varphi = \frac{a(1-\varepsilon_b)}{R} \tag{3.74}$$

Therefore, substituting Equation (3.72) into Equation (3.73) yields the same material balance equation as shown in Equation (3.68).

The symbols in Equations (3.70) and (3.73) are not the same symbols as used in the publications. In this thesis, an attempt has been made to use consistent symbols and definitions in order to check the derivations in the literature. In some of the publications, the terms in some of the equations, are incorrectly defined and this made it very difficult to progress forward, as careful check had to be made.

3.8.4 The material balance for the tracer gas in the porous structure (Kub ń, 1965; Kučera, 1965):

Particle Model 1 (for adsorbable/non-adsorbable tracer):

$$\frac{D_e}{\varepsilon}\left(\frac{\partial^2 C_i}{\partial r^2}+\frac{(a-1)}{r}\frac{\partial C_i}{\partial r}\right)-\frac{\partial C_i}{\partial t}-N_i=0 \tag{3.75}$$

where:
- C_i is the concentration of reactant in intraparticle pore space (i.e. total volumes of the pores), mol cm^{-3}_{pore};
- ε is the particle porosity, with unit: cm^3_{pore} / $cm^3_{particle}$;
- N_i is the molar flux from fluid in pore to catalyst surface, based on unit void volume of catalyst pellet, mol cm^{-3}_{pore} s^{-1}.

$$N_i = k_{ads}\left(C_i-\frac{n_A}{K_a}\right) \tag{3.76}$$

where:
- k_{ads} is the adsorption rate constant and has unit: s^{-1};
- n_A is the concentration of adsorbed tracer A per unit void volume of catalyst pellet, mol cm^{-3}_{pore};
- K_a is the adsorption equilibrium constant and it is dimensionless.

To check the form of Equation (3.76), the forward adsorption rate of tracer gas concentration, C_i is:

Forward rate = $k_{ads}C_i$ (3.77)

The reverse rate of adsorbed tracer concentration, n_A into the gas phase in the particle pores is:

Reverse rate = $k_{des}n_A$ (3.78)

At equilibrium, Equation (3.77) is equal to Equation (3.78), and the net flux is:

Net flux = Forward rate – Reverse rate (3.79)

Substituting Equations (3.77) and (3.78) into (3.79), and combining with Equation (3.65) yields:

$$N_i = k_{ads}C_i - k_{des}n_A = k_{ads}C_i - \frac{k_{ads}}{k_{des}}n_A = k_{ads}\left(C_i-\frac{n_A}{K_a}\right) \tag{3.80}$$

The unit balance check on Equation (3.76) is:

$$\frac{\text{mol}}{\text{cm}^3_{\text{pore}}\text{s}} = \frac{1}{\text{s}}\left(\frac{\text{mol}}{\text{cm}^3_{\text{pore}}} - \frac{\text{mol}}{\text{cm}^3_{\text{pore}}}\right) \tag{3.81}$$

Based on the definition of units, this makes K_a dimensionless.

Similar to the external mass transfer equation in Equation (3.69), Equation (3.76) can be re-written as:

$$\frac{\partial n_A}{\partial t} = k_{ads}\left(C_i - \frac{n_A}{K_a}\right) \tag{3.82}$$

Finally, Equation (3.75) has now become:

$$D_e\left(\frac{\partial^2 C_i}{\partial r^2} + \frac{(a-1)}{r}\frac{\partial C_i}{\partial r}\right) - \varepsilon\frac{\partial C_i}{\partial t} - \varepsilon\frac{\partial n_A}{\partial t} = 0 \tag{3.83}$$

The unit balance check on Equation (3.83) is:

$$\begin{aligned}\varepsilon\frac{\partial C_i}{\partial t} &= \frac{\text{cm}^3_{\text{pore}}}{\text{cm}^3_{\text{particle}}} \times \frac{\text{mol}}{\text{cm}^3_{\text{pore}}} \times \frac{1}{\text{s}} = \frac{\text{mol}}{\text{cm}^3_{\text{particle}}\text{s}} \\ \varepsilon\frac{\partial n_A}{\partial t} &= \frac{\text{cm}^3_{\text{pore}}}{\text{cm}^3_{\text{particle}}} \times \frac{\text{mol}}{\text{cm}^3_{\text{pore}}} \times \frac{1}{\text{s}} = \frac{\text{mol}}{\text{cm}^3_{\text{particle}}\text{s}}\end{aligned} \tag{3.84}$$

Particle Model 1 was first mentioned in Suzuki and Smith (1971), and was used in Baiker *et al*. (1982) and Tang *et al*. (1987) for the derivation of theoretical moment expressions and resistance parameters when $K_a = 0$. It was also used in the Garc á-Ochoa and Santos (1994), and Santos *et al*. (1996) when $K_a \neq 0$.

Particle Model 2 (for adsorbable/non-adsorbable tracer):

$$D_e\left(\frac{\partial^2 C_s}{\partial r^2}+\frac{(a-1)}{r}\frac{\partial C_s}{\partial r}\right)-\underbrace{\varepsilon\frac{\partial C_s}{\partial t}}_{\frac{\text{cm}^3_{\text{pore}}}{\text{cm}^3_{\text{particle}}}\times\frac{\text{mol}}{\text{cm}^3_{\text{pore}}\text{s}}}-\underbrace{\rho_p\frac{\partial w}{\partial t}}_{\frac{\text{g}}{\text{cm}^3_{\text{particle}}}\frac{\text{mol}}{\text{g s}}}=0 \tag{3.85}$$

where:
- C_s is the concentration of the adsorbable gas in the pore space (total volume of the pores), mol cm^{-3}_{pore};
- ρ_p is the apparent density of the adsorbent particle, g $cm^{-3}_{particle}$;
- w is the concentration of the adsorbed gas per unit weight of adsorbent, mol g^{-1}.

For linear adsorption, the follow relationship holds:

$$\frac{\partial w}{\partial t}=k^1_{ads}\left[C_s-\frac{w}{K_A}\right] \tag{3.86}$$

where:
- k^1_{ads} is the adsorption rate constant for tracer gas A, cm^3_{pore} g^{-1} s^{-1};
- K_A is the adsorption equilibrium constant for tracer gas, cm^3_{pore} g^{-1}.

The derivations done for Equation (3.86) are similar to the steps in Equations (3.77) to (3.80) for **Particle Model 1**, but with different units for the adsorption rate constants (k^1_{ads} and k^1_{des}, both in cm^3_{pore} g^{-1} s^{-1}), adsorbed tracer gas concentration, w (in mol g^{-1}) and adsorption equilibrium constant, K_A (in cm^3_{pore} g^{-1}). The unit balance check on Equation (3.86) is:

$$\frac{\text{mol}}{\text{g s}}=\frac{\text{cm}^3_{\text{pore}}}{\text{g s}}\left(\frac{\text{mol}}{\text{cm}^3_{\text{pore}}}-\frac{\text{mol}}{\text{g}}\times\frac{\text{g}}{\text{cm}^3_{\text{pore}}}\right) \tag{3.87}$$

According to Schneider (1984, 1986), K_A in Equation (3.86) was converted into a dimensionless number, K_A', which has the following form:

$$\frac{\partial w}{\partial t}=k^1_{ads}\left[C_s-\frac{\rho_p}{\varepsilon}\left(\frac{w}{K_A'}\right)\right] \tag{3.88}$$

The unit balance check on Equation (3.88) is:

$$\frac{\text{mol}}{\text{g s}} = \frac{\text{cm}^3_{\text{pore}}}{\text{g s}} \times \left(\frac{\text{mol}}{\text{cm}^3_{\text{pore}}} - \frac{\text{mol}}{\text{g}}_{w} \times \underbrace{\frac{\text{g}}{\text{cm}^3_{\text{particle}}}}_{\rho_p} \times \underbrace{\frac{\text{cm}^3_{\text{particle}}}{\text{cm}^3_{\text{pore}}}}_{\varepsilon} \div 1 \right) \tag{3.89}$$

By comparing Equations (3.86) and (3.88), the following applies:

$$K_A^{'} = \frac{\rho_p}{\varepsilon} K_A \tag{3.90}$$

From Equation (3.85), the balance for the consumption term of adsorbed tracer gas is:

$$\rho_p \frac{\partial w}{\partial t} = \rho_p k_{ads}^1 \left[C_s - \frac{w}{K_A} \right] \tag{3.91}$$

The unit balance check on Equation (3.91) is:

$$\text{LHS} = \frac{\text{g}}{\text{cm}^3_{\text{particle}}} \frac{\text{mol}}{\text{g s}} = \frac{\text{mol}}{\text{cm}^3_{\text{particle}}\text{s}} \qquad \text{RHS} = \frac{\text{mol}}{\text{cm}^3_{\text{particle}}\text{s}} \tag{3.92}$$

According to Equations (3.81) and (3.92), the dimensionless adsorption equilibrium constant, K_a in Equation (3.76) for **Particle model 1** is linked to the adsorption equilibrium constant, K_A (unit: $\text{cm}^3_{\text{pore}}\ \text{g}^{-1}$) in **Particle model 2** as indicated:

$$K_a = \frac{\rho_p}{\varepsilon} K_A \Rightarrow \begin{cases} \text{LHS: } 1 \\ \text{RHS: } \dfrac{\text{g}}{\text{cm}^3_{\text{particle}}} \times \dfrac{\text{cm}^3_{\text{particle}}}{\text{cm}^3_{\text{pore}}} \times \dfrac{\text{cm}^3_{\text{pore}}}{\text{g}} = 1 \end{cases} \tag{3.93}$$

Particle model 2 in Equation (3.85) was used in Schneider and Smith (1968) and Guangsuo *et al*. (2000) for the derivation of theoretical moment expressions and resistance parameters when K_A (or K_A^c) $\neq 0$. The difference between K_A^c (used in Schneider and Smith (1968)) and K_A (used in Guangsuo *et al*. (2000)) is explained in the Section 3.8.5.

Particle Model 3 (for adsorbable/non-adsorbable tracer):

$$D_e\left(\frac{\partial^2 C_s}{\partial r^2}+\frac{(a-1)}{r}\frac{\partial C_s}{\partial r}\right)-\varepsilon\frac{\partial C_s}{\partial t}-(1-\varepsilon)\frac{\partial C_\mu}{\partial t}=0 \tag{3.94}$$

where: – term $(1-\varepsilon)$ is skeletal volume fraction of the particle, cm^3_{solid} / $cm^3_{particle}$);

– C_μ is the adsorbed concentration, mol cm^{-3}_{solid}.

Check on units in Equation (3.94):

$$\begin{aligned}\varepsilon\frac{\partial C_s}{\partial t}&=\frac{cm^3_{pore}}{cm^3_{particle}}\times\frac{mol}{cm^3_{pore}}\times\frac{1}{s}=\frac{mol}{cm^3_{particle}s}\\(1-\varepsilon)\frac{\partial C_\mu}{\partial t}&=\frac{cm^3_{solid}}{cm^3_{particle}}\times\frac{mol}{cm^3_{solid}}\times\frac{1}{s}=\frac{mol}{cm^3_{particle}s}\end{aligned} \tag{3.95}$$

In Do (1998), in the pore diffusion model with linear adsorption kinetics, the following relationship holds:

$$\frac{\partial C_\mu}{\partial t}=k_{ads}\left[C_s-\frac{C_\mu}{K_H}\right] \tag{3.96}$$

where: – K_H is the Henry's law constant and as defined in Do (1998) it is dimensionless.

Note: However, a check on the units in Equation (3.96) reveals an inconsistency:

$$\frac{mol}{cm^3_{solid}s}=\frac{1}{s}\left[\frac{mol}{cm^3_{pore}}-\frac{mol}{cm^3_{solid}}\right] \tag{3.97}$$

Particle model 3 in Equation (3.94) was adopted from Do (1998), and used in Armatas *et al.* (2005) for the derivation of theoretical moment expressions and resistance parameters when $K_H \neq 0$. Equation (3.94) was also used in the new 2nd central moment and new HETP approach for the derivation of theoretical moment expressions and resistance parameters.

To summarise, by converting the partial differential equations (PDEs) in the **Column Model** and the **Particle Model** into ordinary differential equations (ODEs) in Laplace form, the general solutions in Laplace form, $\bar{C}(x, s)$ can be obtained. Then, after lengthy algebra and applying Equation (3.47) to the general solutions $\bar{C}(x, s)$, the theoretical moments expressions (μ_1 and μ_2') and resistance parameters(e.g. ξ_f and ξ_M) can be derived (Schneider, 1986).

3.8.5 Six cases based on different material balance equations and methods of analysis

Using different combinations of the column and particle models, the following six cases are considered in more detail.

Cases 1, 2, 4 and 5: These are based on techniques described in the literature and hence many of the steps were checked and are presented in the Appendices 6, 7, 8 and 9 respectively.

Cases 3 and 6: result from refinements made to some of these models by the author of this thesis and these are therefore shown in more detail in the respective sections.

Experimental moment results: the moments (i.e. the first moment and second central moment) results from the fictitious bed (200 mm) were used for all six cases.

<u>Case 1:</u> Column Model, Particle Model 1 and dimensionless adsorption equilibrium constant, K_a = 0 (Baiker *et al*., 1982; Tang *et al*., 1987):

For non-adsorbable tracer, the theoretical moment equations and resistance parameters **are presented in Appendix 6,** and the following is emphasised:

(i) For carrier gas flows 30 – 90 cm^3/min and tracer gas sample loops 0.1, 0.25 and 0.5 ml, by matching experimental second central moment obtained from moment analysis with second central moment expression, μ_2', in Equation (A6.8), D_{eff} can be obtained from the intercept by linearization method.

<u>Case 2:</u> Column Model, Particle Model 2 and adsorption equilibrium constant, $K_A \neq 0$ (unit: $cm^3_{pore}\ g^{-1}$) (Guangsuo *et al*., 2000):

For adsorbable tracer but with no reaction, the theoretical moment equations and resistance parameters **are presented in Appendix 7**, and the following is emphasised:

(i) For carrier gas flows 30 – 90 cm^3/min and tracer gas sample loops 0.1, 0.25 and 0.5 ml, K_A is evaluated from a linear regression plot of difference in experimental first moments $\Delta\mu_1$, as a function of interstitial velocity term $1/u_i$ (Equation (A7.11)). Term $\Delta\mu_1$ is the difference between the first moments of adsorption runs, $(\mu_1)_{ads}$ and inert runs, $(\mu_1)_{inert}$. The first moment for an adsorption run, $(\mu_1)_{ads}$, is the first moment calculated from experimental response curve using *A* (tracer gas) for a *A* (tracer) – *B* (carrier) gas system. Whereas the first moment for an inert run, $(\mu_1)_{inert}$, is evaluated from experimental response curves using *B* (tracer gas) for a *B* (tracer) – *A* (carrier) gas system.

(ii) For carrier gas flowrates 30 – 90 cm^3/min and tracer gas sample loops 0.1, 0.25 and 0.5 ml, by matching the experimental second central moment obtained from moment analysis, with the second central moment expression, $\mu_2^{'}$, in Equation (A7.13), D_{eff} can be obtained from the intercept by a linearization method.

(iii) Besides, the difference in D_{eff} by adding or not adding the external mass transfer coefficient term, k_f, is compared. k_f is calculated according to:

$$\frac{2k_f R}{D_{AB}} = 2.00 + 1.45\,\mathrm{Re_p}^{1/2}\,\mathrm{Sc}^{1/3} \qquad \text{For Re} < 100 \qquad (3.98)$$

Equation (3.98) was proposed by Wakao *et al*. (1958). The external mass transfer coefficient, k_f is related to particle Reynolds (Re_p) and Schmidt number (Sc). According to Hayes and Kolaczkowski (1997), the particle Reynolds number Re_p is equivalent to the Reynolds number of the packed-bed column, Re. The reason being that Reynolds number in a packed bed is usually defined in terms of the particle diameter, d_p.

The effective diffusivity D_{eff} results calculated for Case 2 are classified as: **Case 2a** (without k_f) and **Case 2b** (with k_f). The superficial velocity, u_0, used in the theoretical moment expressions and resistance parameters in Guangsuo *et al*. (2000) appear to be wrong, as this should be the interstitial velocity, u_i. A corrected set of equations are presented in Equations (A7.1) to (A7.7).

Besides, apart from the misinterpretation of interstitial and superficial velocity, the theoretical moment expressions and moment parameters in Guangsuo *et al*. (2000) were exactly the same as Schneider and Smith (1968a). For K_A calculations, unlike Guangsuo *et al*. (2000), Schneider and Smith (1968) used the first moment for blank run, $(\mu_1)_0$ in Equation (3.59) instead of evaluating the first moment from the inert runs, $(\mu_1)_{\text{inert}}$. Because of the similarities in these two papers, the only difference between them is in the use of $(\mu_1)_{\text{inert}}$ and $(\mu_1)_0$, therefore, Schneider and Smith (1968) is denoted as **Case 2c** in this thesis, and the adsorption equilibrium constant, K_A, is replaced by K_A^c for Case 2c.

It is worth mentioning that in Schneider and Smith (1968), a set of experiments was carried out with active adsorbable gases (hydrocarbons) as tracer, and helium as carrier. This was tested over three different porous pellets (silica) with a radius R = 0.50, 0.39 and 0.11 mm (in a packed bed column). Their experiment results with the strong adsorbable tracer show that, when the pellet radius R = 0.5 mm, the adsorption resistance, ξ_a in Equation (A7.5) contributes for 1 to 4% of the total resistance, ξ_1, (ξ_1 is defined in the theoretical second central moment expression in Equation (A7.2) and in Equation (A7.4)). The intraparticle diffusion resistance, ξ_i accounts for 95.0 to 95.9% of the total resistance and the rest is external mass transfer resistance, ξ_e. This explains why in the literature on the chromatographic method with inert or weak adsorbable gases (i.e. helium, argon or nitrogen), the adsorption resistance, ξ_a is generally ignored, or not even mentioned.

<u>Case 3:</u> Column Model, Particle Model 3 and dimensionless adsorption equilibrium constant, $K_H \neq 0$ (New 2nd central moment method):

Comparing Baiker *et al*. (1982), Tang *et al*. (1987) and Guangsuo *et al*. (2000), the following differences are distinguishable:

(i) The use of adsorption equilibrium constant *K*: in Baiker *et al*. (1982) and Tang *et al*. (1987), $K_a = 0$, and corresponds to non-adsorbable tracer. Whereas in Guangsuo *et al*. (2000), for adsorbable tracer but with no reactions on adsorbent particles, the adsorption resistance term ξ_a is neglected, but adsorption equilibrium constant $K_A \neq 0$.

(ii) The material balance of tracer gas *A* in the porous structure of particles: in Baiker *et al*. (1982) and Tang *et al*. (1987), the intraparticle material balance of tracer was based on Suzuki and Smith (1971). Whereas, in Guangsuo *et al*. (2000), the intraparticle material balance based on Schneider and Smith (1968) was used. Despite the differences, both equations were derived from the Kubń and Kučera model, except that, the adsorbed concentration n_A is correlated with particle porosity, ε, in Equation (3.83), whereas w is correlated with apparent density, ρ_p, in Equation (3.85). The reason for this is because the K_a used in the molar flux term, N_i in Equation (3.76) is dimensionless, whereas K_A in Equation (3.86) has unit: $\text{cm}^3_{\text{pore}}\ \text{g}^{-1}$. Therefore, the intraparticle material balances are similar, and they have different definitions for the adsorption equilibrium constant (details in Section 3.8.4).

In this thesis, this analysis is taken one step further, and a new approach is proposed. In this D_{eff} is calculated by matching second central moment (obtained from experimental response curves) with the second moment expression, μ_2', (derived from the material balance equations). In the moment expressions, the linear adsorption kinetics and resistance parameters from Do (1998) are used (Equations (3.99) to (3.106)):

$$\mu_1 = \frac{L\varepsilon_b}{u_0}(1+\xi_0) \tag{3.99}$$

$$\mu_2' = \frac{L\varepsilon_b}{u_0}\left[\xi_1 + \xi_d\right] \tag{3.100}$$

$$\xi_1 = \xi_i + \xi_a + \xi_e \tag{3.101}$$

$$\xi_a = \left(\frac{1-\varepsilon_b}{\varepsilon_b}\,\varepsilon\right)\frac{(1-\varepsilon)\,K_H^2}{\varepsilon k_{ads}} \tag{3.102}$$

$$\xi_d = \frac{D_{ax}}{\varepsilon_b}(1+\xi_0)^2\left(\frac{\varepsilon_b}{u_0}\right)^2 \tag{3.103}$$

$$\xi_0 = \frac{1-\varepsilon_b}{\varepsilon_b}\varepsilon\left(1+\frac{(1-\varepsilon)K_H}{\varepsilon}\right) \tag{3.104}$$

$$\xi_i = \left(\frac{1-\varepsilon_b}{\varepsilon_b}\varepsilon\right)\left(1+\frac{(1-\varepsilon)K_H}{\varepsilon}\right)^2\frac{R^2\varepsilon}{a(a+2)D_{eff}} \tag{3.105}$$

$$\xi_e = \left(\frac{1-\varepsilon_b}{\varepsilon_b}\varepsilon\right)\frac{R^2\varepsilon}{a(a+2)}\left(1+\frac{(1-\varepsilon)K_H}{\varepsilon}\right)^2\frac{(a+2)}{k_f R} \tag{3.106}$$

For an inert run, the adsorption equilibrium constant, K_H is 0, and Equation (3.99) is simplified as:

$$(\mu_1)_{inert} = \frac{L\varepsilon_b}{u_0}\left[1+\frac{(1-\varepsilon_b)\varepsilon}{\varepsilon_b}\right] \tag{3.107}$$

The first moment for an inert run, $(\mu_1)_{\text{inert}}$ in Equation (3.107) is the same as the first moment for a blank run, $(\mu_1)_0$, in Equation (3.59). Both first moments were obtained from theoretical first moment expression when $K_H = 0$. Whereas, in Guangsuo *et al*. (2000) as well as in this thesis, $(\mu_1)_{\text{inert}}$ was not calculated from Equation (3.107), but was obtained from the experimental response curve by using the carrier gas as an inert tracer. This is explained as follows: for an adsorption run, He (tracer) – N_2 (tracer) gas system was used, $(\mu_1)_{\text{ads}}$ is the first moment calculated from the experimental response curve using helium tracer, then the corresponding first moment for inert run, $(\mu_1)_{\text{inert}}$ was calculated from the response curve using nitrogen tracer in a N_2 (tracer) – He (carrier) gas system.

For an adsorption run, the adsorption equilibrium constant $K_H \neq 0$, and Equation (3.99) becomes:

$$(\mu_1)_{ads} = \frac{L\varepsilon_b}{u_0}\left[1+\frac{(1-\varepsilon_b)\varepsilon}{\varepsilon_b}\left(1+\frac{(1-\varepsilon)K_H}{\varepsilon}\right)\right] \tag{3.108}$$

The adsorption equilibrium constant K_H was evaluated from the linear regression plot of the difference in the first moment as a function of superficial velocity u_0:

$$\Delta\mu_1 = (\mu_1)_{ads} - (\mu_1)_{inert} = \frac{L(1-\varepsilon_b)(1-\varepsilon)}{u_0}K_H \tag{3.109}$$

Hence, the second central moment expression μ_2' with the new method should be:

$$\left(\mu_2^{'}\right)_{ads} = \frac{2L\varepsilon_b}{u_0}\left[\xi_1 + \frac{\varepsilon_b D_{ax}\left(1+\xi_0\right)^2}{u_0^2}\right] \tag{3.110}$$

$$\frac{\left(\mu_2^{'}\right)_{ads}}{2L/u_0} = \varepsilon_b\xi_1 + \frac{\varepsilon_b^2 D_{ax}\left(1+\xi_0\right)^2}{u_0^2} \tag{3.111}$$

In addition, effective diffusivity D_{eff} was calculated under two conditions:

(i) without external mass transfer resistance ξ_e term, and

(ii) with external mass transfer resistance, ξ_e.

For adsorbable tracer with no reaction, the theoretical moment equations and resistance parameters are presented in Equations (3.99) to (3.106), and the following is emphasised:

(i) For carrier gas flows 30 – 90 cm^3/min and tracer gas sample loops 0.1, 0.25 and 0.5 ml, K_H was evaluated from a linear regression plot of the difference in experimental first moments $\Delta\mu_1$ as a function of superficial velocity $1/u_0$ (Equation (3.109)). The first moment for the inert run, $(\mu_1)_{\text{inert}}$ was calculated from the moment analysis results for the experimental response curves. Whereas $(\mu_1)_{\text{ads}}$ was obtained from moment analysis results from the experimental response curves for the corresponding tracer gas used.

(ii) For carrier gas flows 30 – 90 cm^3/min and tracer gas sample loops 0.1, 0.25 and 0.5 ml, by matching the experimental second central moment obtained from moment analysis, with the second central moment expression, $\mu_2^{'}$, in Equation (3.111), D_{eff} was obtained from the intercept by a linearization method.

(iii) The D_{eff} results are compared for: **Case 3a** (without k_f) and **Case 3b** (with k_f), and k_f was calculated according to:

$$\frac{k_f(2R_p)}{D_{AB}} = 2 + 1.1\left(\frac{u_0 2R_p\rho}{\mu}\right)^{0.6}\left(\frac{\nu}{D_{AB}}\right)^{\frac{1}{3}} \tag{3.112}$$

Equation (3.112) was proposed by Do (1998), and ρ is the density of the fluid, R_p is the equivalent particle radius, μ and ν is the dynamic and kinematic viscosity of the fluid respectively.

<u>Case 4:</u> Column Model, Particle model 3 and dimensionless adsorption equilibrium constant, $K_H \neq 0$ (Armatas *et al*., 2005):

For adsorbable tracer with no reaction, the theoretical moment equations and resistance parameters are presented in Appendix 8, and the following is emphasised:

(i) For carrier gas flows 30 – 90 cm^3/min and tracer gas sample loops 0.1, 0.25 and 0.5 ml, K_H was evaluated from the same equation used in Case 3. Except that in Armatas *et al*. (2005), $(\mu_1)_{inert}$ in Equation (3.109) was replaced by the first moment for a blank run, $(\mu_1)_0$, and becomes:

$$\frac{(\mu_1)_{ads} - (\mu_1)_0}{L(1-\varepsilon_b)(1-\varepsilon)} = K_H \frac{1}{u_0} \tag{3.113}$$

where $(\mu_1)_0$ is calculated from a theoretical expression in Equation (3.107) and not from moment analysis.

(ii) For carrier gas flows 30 – 90 cm^3/min and tracer gas sample loops 0.1, 0.25 and 0.5 ml, by matching the experimental first moment and second central moment with the Height Equivalent to a Theoretical Plate (HETP) expression in Equation (A8.32), then D_{eff} was obtained from the slope by the linearization method. However, as will be discussed further in Chapter 4, the D_{eff} calculated from the linearization of HETP is around 10 times (or more) smaller than in the other method, which leads to a huge tortuosity factor. Hence, this linearization method as used for HETP is not reliable.

In Armatas *et al*. (2005), the intraparticle resistance parameter, ξ_M presented in their paper is incorrect, as a particle porosity term, ε is missing. The correct form for ξ_M is given in Equation (A8.18). The reason being that Armatas *et al*. (2005) misinterpreted the difference between the pore diffusivity, D_p, and the effective diffusivity, D_{eff}, given by Do (1998), and treated them as the same. Whereas the definition of D_p in Do (1998) is:

$$D_{eff} = \varepsilon \times D_p \tag{3.114}$$

<u>Case 5:</u> Column Model, Particle model 1 and dimensionless adsorption equilibrium constant, $K_a \neq 0$ (Garc á-Ochoa and Santos, 1994; Santos *et al*.,1996):

For adsorbable tracer with no reaction, the theoretical moment equations and resistance parameters are presented in Appendix 9, and the following is emphasised:

(i) For carrier gas flows 30 – 90 cm^3/min and tracer gas sample loops 0.1, 0.25 and 0.5 ml, K_a was evaluated from a linear plot of experimental first moments μ_1 as a function of L/u_i (Equation (A9.2)). K_a is then calculated from the slope of the linear plot from:

$$K_a = \frac{slope - 1}{(1-\varepsilon_b)\varepsilon / \varepsilon_b} - 1 \tag{3.115}$$

where *slope* is obtained from the linear plot of μ_1 *versus* L/u_i, and it is always > 1.

(ii) For carrier gas flows 30 – 90 cm^3/min and tracer gas sample loops 0.1, 0.25 and 0.5 ml, when comparing with Case 4, D_{eff} was obtained from the HETP expression (Equation (A9.11)) using a non-linear curve fitting method.

(iii) The equation used for calculating the external mass transfer coefficient, k_f, is presented in Equation (3.98), which leads to the calculation of the external mass transfer resistance, ξ_f in Equation (A9.7). The difference in D_{eff} values without, and with this ξ_f term is < 2%, which explains why in the literature, the external mass transfer resistance, ξ_f, is generally ignored in D_{eff} calculations.

As shown in Equation (A9.11), a small mistake was found when checking the HETP expression given in Garc á-Ochoa and Santos (1994). The bed porosity, ε_b, is missing from the axial dispersion term in their paper. The derivation of the HETP expression in Case 5 is shown in the next section.

<u>Case 6:</u> Column Model, Particle model 3 and dimensionless adsorption equilibrium constant, $K_H \neq 0$ (New HETP approach):

From Garcá-Ochoa and Santos (1994), Santos *et al.* (1996) and Armatas *et al*. (2004), the following differences are distinguishable:

(i) Moment expressions and resistance parameters were deduced from different intraparticle material balance equations (i.e. Particle Models).

(ii) Methods for D_{eff} evaluation are different: in Armatas *et al*. (2005), a linearization method was used between HETP and u_0 to evaluate D_{eff}, whereas in Garcá-Ochoa and Santos (1994) and Santos *et al.* (1996), they briefly mentioned that Equation (A9.11) was solved by a finite difference algorithmn for curve fitting method introduced in Marquardt (1963) but the details of the procedures were not shown.

(iii) In Armatas *et al*. (2005), in order to using the linearization method, the axial dispersion coefficient, D_{ax}, was neglected, which is very inappropriate. Besides, external mass transfer resistance ξ_f was also neglected. The D_{eff} results for the γ-alumina beads obtained from this method are around 10 times (or more) smaller than other literature methods (discussed further in Chapter 4).

As a consequence, in this thesis, theoretical moment expressions and resistance parameters used for the new HETP approach are the same as those listed in Appendix 8 (Armatas *et al*., 2005). However, to evaluate D_{eff} by matching the first moment and second central moment from experimental response curves with the new HETP approach, the axial dispersion term D_{ax} and the external mass transfer resistance ξ_f were retained, and this has the following form:

HETP is a measure of the degree of spread multiplied by column length. i.e. $\mu_2' L/(\mu_1)^2$. Therefore, substituting Equations (A8.15) to (A8.18) into Equations (A8.13) and (A8.14) yields:

$$\mathrm{HETP} = \underbrace{2\frac{D_{ax}}{u_0}}_{(a)} + \underbrace{\left(\frac{\dfrac{(1-\varepsilon_b)\varepsilon}{\varepsilon_b}\left(1+\dfrac{(1-\varepsilon)K_H}{\varepsilon}\right)^2 \dfrac{R^2\varepsilon}{a(a+2)D_{eff}}}{(1+\xi_0)^2} + \frac{\dfrac{(1-\varepsilon_b)\varepsilon}{\varepsilon_b}\left(1+\dfrac{(1-\varepsilon)K_H}{\varepsilon}\right)^2 \dfrac{R\varepsilon}{ak_f}}{(1+\xi_0)^2} \right)}_{(b):\ \frac{(\xi_M+\xi_f)}{(1+\xi_0)^2}} \frac{2u_0}{\varepsilon_b} \quad (3.116)$$

Part (a) (in Equation (3.116)) of the HETP expression given in García-Ochoa and Santos (1994) was shown to be wrong, because they used u_i and not u_0.

In Equation (3.116), a is the shape factor and a = 3 for a sphere. In part (b) of Equation (3.116), divide the whole section by ξ_0^2, hence the intraparticle diffusion resistance ξ_M can be expressed as:

$$\frac{\xi_M / \xi_0^2}{(1+\xi_0)^2 / \xi_0^2} = \frac{\overbrace{\frac{(1-\varepsilon_b)}{\varepsilon_b}\left(1+\frac{(1-\varepsilon)K_H}{\varepsilon}\right)^2 \frac{R^2}{15D_{eff}}}^{\xi_M} \times \overbrace{\frac{\varepsilon_b^{1}}{\varepsilon^{2}(1-\varepsilon_b)^{1}}\left(1+\frac{(1-\varepsilon)K_H}{\varepsilon}\right)^{-2}}^{1/\xi_0^2}}{\frac{1}{\xi_0^2}+\frac{2}{\xi_0}+1}$$

$$\frac{\xi_M / \xi_0^2}{(1+\xi_0)^2 / \xi_0^2} = \frac{\frac{R^2}{15D_{eff}}\frac{\varepsilon_b}{(1-\varepsilon_b)}}{\left(1+\frac{1}{\xi_0}\right)^2} \tag{3.117}$$

Then the external mass transfer resistance ξ_f becomes:

$$\frac{\xi_f / \xi_0^2}{(1+\xi_0)^2 / \xi_0^2} = \frac{\overbrace{\frac{(1-\varepsilon_b)}{\varepsilon_b}\left(1+\frac{(1-\varepsilon)K_H}{\varepsilon}\right)^2 \frac{R}{3k_f}}^{\xi_f} \times \overbrace{\frac{\varepsilon_b^{1}}{\varepsilon^{2}(1-\varepsilon_b)^{1}}\left(1+\frac{(1-\varepsilon)K_H}{\varepsilon}\right)^{-2}}^{1/\xi_0^2}}{\frac{1}{\xi_0^2}+\frac{2}{\xi_0}+1}$$

$$\frac{\xi_f / \xi_0^2}{(1+\xi_0)^2 / \xi_0^2} = \frac{\frac{R}{3k_f}\frac{\varepsilon_b}{(1-\varepsilon_b)}}{\left(1+\frac{1}{\xi_0}\right)^2} \tag{3.118}$$

Combining Equations (3.117) and (3.118) yields:

$$\text{HETP} = 2\frac{D_{ax}}{u_0} + \frac{\frac{R^2}{15D_{eff}}\frac{\varepsilon_b}{(1-\varepsilon_b)}}{\left(1+\frac{1}{\xi_0}\right)^2}\frac{2u_0}{\varepsilon_b} + \frac{\frac{R}{3k_f}\frac{\varepsilon_b}{(1-\varepsilon_b)}}{\left(1+\frac{1}{\xi_0}\right)^2}\frac{2u_0}{\varepsilon_b} \tag{3.119}$$

which can be simplified as:

$$\text{HETP} = \frac{\mu_2' L}{(\mu_1)^2} = 2\frac{D_{ax}}{u_0} + \left\{ \frac{\frac{2}{15}\frac{R^2}{(1-\varepsilon_b)}}{\left(1+\frac{1}{\xi_0}\right)^2} \left(\frac{1}{D_{eff}} + \frac{5}{k_f R} \right) \right\} u_0 \tag{3.120}$$

In this thesis, Equation (3.120) was compiled sucessfully in the 'Fitting Function Builder' in OriginPro 8.6 (this technique was also applied for D_{eff} evaluation when using the Santos *et al.* (1996) method) as:

$$\text{HETP} = \frac{A}{u_0} + B + Gu_0 \tag{3.121}$$

Therefore, by non-linear curve fitting (that is by plotting HETP results calculated from moment analysis of experimental curves *versus* u_0 in OriginPro 8.6), the data were fitted with the compiled function (i.e. Equation (3.121)). Results of *A*, *B* and *G* are obtained with an R-square value indicating the goodness of fit. Consequently, D_{eff} can be calculated from the constant *G* when k_f is known.

For adsorbable tracer with no reaction, the same theoretical moment equations and resistance parameters were used as in Case 4, and the following are emphasised:

(i) For carrier gas flows 30 – 90 cm^3/min and tracer gas sample loops 0.1, 0.25 and 0.5 ml, K_H was evaluated from the same equation (i.e. Equation (3.113)) used in Case 4.

(ii) For carrier gas flows 30 – 90 cm^3/min and tracer gas sample loops 0.1, 0.25 and 0.5 ml, moment matching for HETP is the same as Case 4 (i.e. Equation (A8.31)), except that instead of using a linearization method, non-linear curve fitting in OriginPro 8.6 was used.

(iii) The external mass transfer resistance, ξ_f, was included in the new HETP method, and was calculated from:

$$\xi_f = \frac{(1-\varepsilon_b)}{\varepsilon_b}\left(1+\frac{(1-\varepsilon)K_H}{\varepsilon}\right)^2 \frac{R\varepsilon^2}{ak_f} \tag{3.122}$$

The external mass transfer coefficient, k_f, was calculated using Equation (3.112), which was from Do (1998) and is also the same equation used in Case 3.

3.8.6 Summary of values for the adsorption equilibrium constant

In summary, for the γ-alumina beads, the adsorption equilibrium constant for the six different cases was calculated using moment analysis results for the fictitious bed (i.e. 200 mm 'imaginary' column without entrance and exit effects), and the results are summarised in Table 3.10. These values are close to the values described in the literature (see Table 3.12), which indicates that the adsorption of He and N_2 on porous γ-alumina beads is weak. Therefore, the whole process is diffusion limited.

However, in the literature, in some cases, a dimensionless adsorption equilibrium constant was used, and in other cases, the adsorption equilibrium constant was assigned units. From this chapter, the author found that this is all linked to the intraparticle material balance (i.e. Particle Model) that was used. To be more precise, it is closely correlated to the units used for the adsorbed tracer concentration, in the terms: n_A, or C_μ, or w. In general, all particle models used the linear adsorption kinetics correlation shown in Equations (3.76), (3.86) and (3.96), but because of different interpretations of the adsorbed tracer concentration, units varied, i.e. n_A in units of mol cm^{-3}_{pore}, or C_μ in mol cm^{-3}_{solid}, whereas, w was based on mol $g^{-1}_{adsorbent}$.

Furthermore, apart from comparing adsorption equilibrium constant values using literature data, a uniform unit in $\mathbf{cm^3_{pore}\ g^{-1}_{adsorbent}}$ was used to calculate $\boldsymbol{K_s}$ in each case so that it is easier to compare the values. The results are summarised in Table 3.11.

The earlier check on units in Equation (3.96) for **Particle Model 3** did not explain why the adsorption equilibrium constants, K_H was claimed to be dimensionless. Besides, according to the explanations in Section 3.8.1, K_H in Equation (3.96) is not Henry's law constant, but an adsorption equilibrium constant without units. Assuming that the following conversions may be applied, then let:

$$K_s = \frac{\varepsilon}{\rho_p} K_a \tag{3.123}$$

$$K_s = K_A;\ K_s = K_A^c \tag{3.124}$$

Table 3.10: Adsorption equilibrium constant calculated from a **fictitious bed** (200 mm) packed with γ-alumina beads using different methods.

Fictitious bed (200 mm) (μ_1 from peak fitting)		**Adsorption equilibrium constant (Helium as tracer)**	***RSQ*** [(a)] ***(Helium as tracer)***	**Adsorption equilibrium constant (Nitrogen as tracer)**	***RSQ*** [(a)] ***(Nitrogen as tracer)***
Case 1	**Baiker *et al*. (1982) and Tang *et al*. (1987)**	N/A	*N/A*	N/A	*N/A*
Case 2	**Guangsuo *et al*. (2000)**	K_A = 0.3161 ± 0.0602 (cm^3/g)	*0.8375 ± 0.0958*	K_A = 0.3161 ± 0.1090 (cm^3/g)	*0.8375 ± 0.0958*
Case 2c	**Schneider and Smith (1968)**	K_A^c = 0.1048 ± 0.0141 (cm^3/g)	*0.8762 ± 0.0584*	K_A^c = 0.3763 ± 0.0602 (cm^3/g)	*0.8075 ± 0.1224*
Case 3	**New 2nd central moment method**	K_H = 0.8773 ± 0.1672	*0.8375 ± 0.0958*	K_H = 0.8773 ± 0.1672	*0.8375 ± 0.0958*
Case 4	**Armatas *et al*. (2005)**	K_H = 0.2909 ± 0.0391	*0.8762 ± 0.0584*	K_H = 1.2762 ± 0.0759	*0.9088 ± 0.0864*
Case 5	**García-Ochoa and Santos (1994) and Santos *et al*. (1996)**	K_a = 0.1983 ± 0.0267	*0.9992 ± 0.0004*	K_a = 0.1382 ± 0.0771	*0.9899 ± 0.0015*
Case 6	**New HETP approach**	K_H = 0.2909 ± 0.0391	*0.8762 ± 0.0584*	K_H = 1.2762 ± 0.0759	*0.9088 ± 0.0864*

Note: (*a*) RSQ means the R-square value. e.g RSQ = 0 implies that data is non-linear at all, where RSQ = 1 means a perfect linear line.

Table 3.11: Adsorption equilibrium constants, K_s with uniform unit: $cm^3_{pore}\ g^{-1}_{adsorbent}$, calculated for γ-alumina beads packed inside a **fictitious bed** (200 mm).

Fictitious bed (200 mm) (μ_1 from peak fitting)		**K_s, ($cm^3\ g^{-1}$) (Helium as tracer)**	***RSQ* *(Helium as tracer)***	**K_s, ($cm^3\ g^{-1}$) (Nitrogen as tracer)**	**RSQ (Nitrogen as tracer)**
Case 1	**Baiker *et al*. (1982) and Tang *et al*. (1987)**	N/A	*N/A*	N/A	*N/A*
Case 2	**Guangsuo *et al*. (2000)**	0.3161 ± 0.0602	*0.8375 ± 0.0958*	0.3161 ± 0.0602	*0.8375 ± 0.0958*
Case 2c	**Schneider and Smith (1968)**	0.1048 ± 0.0141	*0.8762 ± 0.0584*	0.3763 ± 0.0602	*0.8075 ± 0.1224*
Case 3	**New 2nd central moment method**	see [1]			
Case 4	**Armatas *et al*. (2005)**	see [1]			
Case 5	**García-Ochoa and Santos (1994) and Santos *et al*. (1996)**	0.1048 ± 0.0141	*0.9992 ± 0.0004*	0.0730 ± 0.0407	*0.9899 ± 0.0015*
Case 6	**New HETP approach**	see [1]			

Note [1]: The value calculated has not been converted to K_s in unit of $cm^3\ g^{-1}$, because of an uncertainty as to the units of K_H in Particle Model 3.

Table 3.12: Examples of adsorption equilibrium constant values found in the literature.

	Sample studied	**Temperature (*K*)**	**Tracer**	**Adsorption equilibrium constant**	***Correlation coefficient (RSQ)***	**Adsorption strength**
Schneider and Smith (1968)	Silica	323	Ethane, propane and n-butane	14.6, 65.4 and 311 ($cm^3\ g^{-1}$)	*N/A*	Intermediate – strong
Guangsuo *et al*. (2000)	Sulfur-tolerant (metal oxides)	313 – 383	He and N_2	0.065 – 0.043 ($cm^3\ g^{-1}$)	*0.8 – 0.9*	weak
García-Ochoa and Santos (1994)	Silica-alumina	298	N_2 and Ar	0.53 – 1.05	*N/A*	light
Santos *et al*. (1996)	De-NOx catalyst	298, 473	He and Ar	1.3	*N/A*	light
Armatas *et al*. (2005)	Silica oxides	303	He	38 – 41 (see Note 1)	*0.99*	Weak

Note 1: The K_H values reported in Armatas *et al*. (2005) are most probably a print error. Because: (a) in their abstract and the main body of their paper, the authors had mentioned twice that: "the low values of the Henry law constants found indicated that the adsorption of He on the porous surface of the solid is weak", and (b), helium is an inert gas.

3.8.7 Concluding remarks on the adsorption equilibrium constant

Methods for calculating the constant by matching first moments can be categorized in three ways:

(i) **<u>Scenario 1 (Case 2, 2c and 3):</u>** For each sample loop volume injected, K_A and K_A^c in $cm^3\ g^{-1}$, and K_H (a dimensionless constant) were evaluated from the slope of the linear plot. As shown in Figure 3.31 and Figure 3.32, for Cases 2 and 2c, K_A and K_A^c were evaluated by plotting the difference in first moments ($\Delta\mu_1$) between adsorption runs $(\mu_1)_{ads}$ and inert runs $(\mu_1)_{inert}$ (blank run $(\mu_1)_0$ for Case 2c) at corresponding flows *versus* interstitial velocity, u_i.

Whereas for Case 3, as shown in Figure 3.33, the difference between the adsorption runs and the inert runs ($\Delta\mu_1$) was plotted against superficial velocity, u_0. The first moment for inert runs, $(\mu_1)_{inert}$, is the moment from the experimental response curves with the opposite tracer-carrier gas system to that used in the adsorption run, $(\mu_1)_{ads}$.

Advantage: K_A (or K_H) values are consistent for the two tracer-carrier gas systems used (i.e. Cases 2 and 3, but not Case 2c).

Disadvantage: moderate correlation coefficient, that is moderate R-square value (0.8 ~ 0.9).

(ii) **<u>Scenario 2 (Case 4 and 6):</u>** For each sample loop volume injected, K_H was evaluated from the slope of a linear plot of the difference in first moments between adsorption runs, $(\mu_1)_{ads}$, and the first moment from blank runs, $(\mu_1)_0$ at corresponding flows *versus* superficial carrier gas velocity, u_0, as shown in Figure 3.34. The first moment of the blank run, $(\mu_1)_0$ was calculated using Equation (3.59).

Advantage: K_H values have a good correlation coefficient: R values around 0.8 ~ 0.9 with different sample loops used.

Disadvantage: K_H values are inconsistent for the two tracer-carrier gas systems used.

(iii) **Scenario 3 (Case 5):** For each sample loop volume injected, K_a was evaluated indirectly by plotting the first moments from experimental moment analysis, $(\mu_1)_{ads}$, at corresponding flows *versus* interstitial velocity, u_i, as shown in Figure 3.35, and then calculated according to Equation (3.115).

Advantages: consistent K_a values and extremely good correlation coefficient (i.e. ultra high R-square value (≥ 0.99)).

Disadvantages: Indirect correlation between first moment, μ_1 and K_a. The direct correlations of first moment and adsorption equilibrium constant, K, as found in Case 2, 2c and Case 4 are:

Case 2 and 2c:

$$\text{Case 2: } (\mu_1)_{ads} - (\mu_1)_{inert} = \frac{L}{u_i}\left[1+\frac{(1-\varepsilon_b)\varepsilon}{\varepsilon_b}\left[1+\rho_p K_A\right]\right] - \frac{L}{u_i}\left[1+\frac{(1-\varepsilon_b)\varepsilon}{\varepsilon_b}\right] \quad (3.125)$$

$$\Rightarrow \Delta\mu_1 = \frac{L}{u_i}\frac{(1-\varepsilon_b)(1-\varepsilon)}{\varepsilon_b}\rho_p K_A$$

$$\text{Case 2c: } (\mu_1)_{ads} - (\mu_1)_0 = \frac{L}{u_i}\left[1+\frac{(1-\varepsilon_b)\varepsilon}{\varepsilon_b}\left[1+\rho_p K_A^c\right]\right] - \frac{L}{u_i}\left[1+\frac{(1-\varepsilon_b)\varepsilon}{\varepsilon_b}\right] \quad (3.126)$$

$$\Rightarrow \Delta\mu_1 = \frac{L}{u_i}\frac{(1-\varepsilon_b)(1-\varepsilon)}{\varepsilon_b}\rho_p K_A^c$$

Case 4:

$$(\mu_1)_{ads} - (\mu_1)_0 = \frac{L\varepsilon_b}{u_0}\left[1+\frac{(1-\varepsilon_b)\varepsilon}{\varepsilon_b}\left[1+\frac{(1-\varepsilon)}{\varepsilon}K_H\right]\right] - \frac{L\varepsilon_b}{u_0}\left[1+\frac{(1-\varepsilon_b)\varepsilon}{\varepsilon_b}\right] \quad (3.127)$$

$$\Rightarrow \Delta\mu_1 = \frac{L\varepsilon_b}{u_0}\frac{(1-\varepsilon_b)(1-\varepsilon)}{\varepsilon_b}K_H$$

In this thesis, the adsorption equilibrium constant, K from **Cases 2 and 3** in **Scenario 1** is chosen although RSQ value is moderate, because Equation (3.125) and Equation (3.109) consider the adsorption strength of both tracer and carrier gases (i.e. both first moment for adsorption and inert runs were obtained from the experimental response curves).

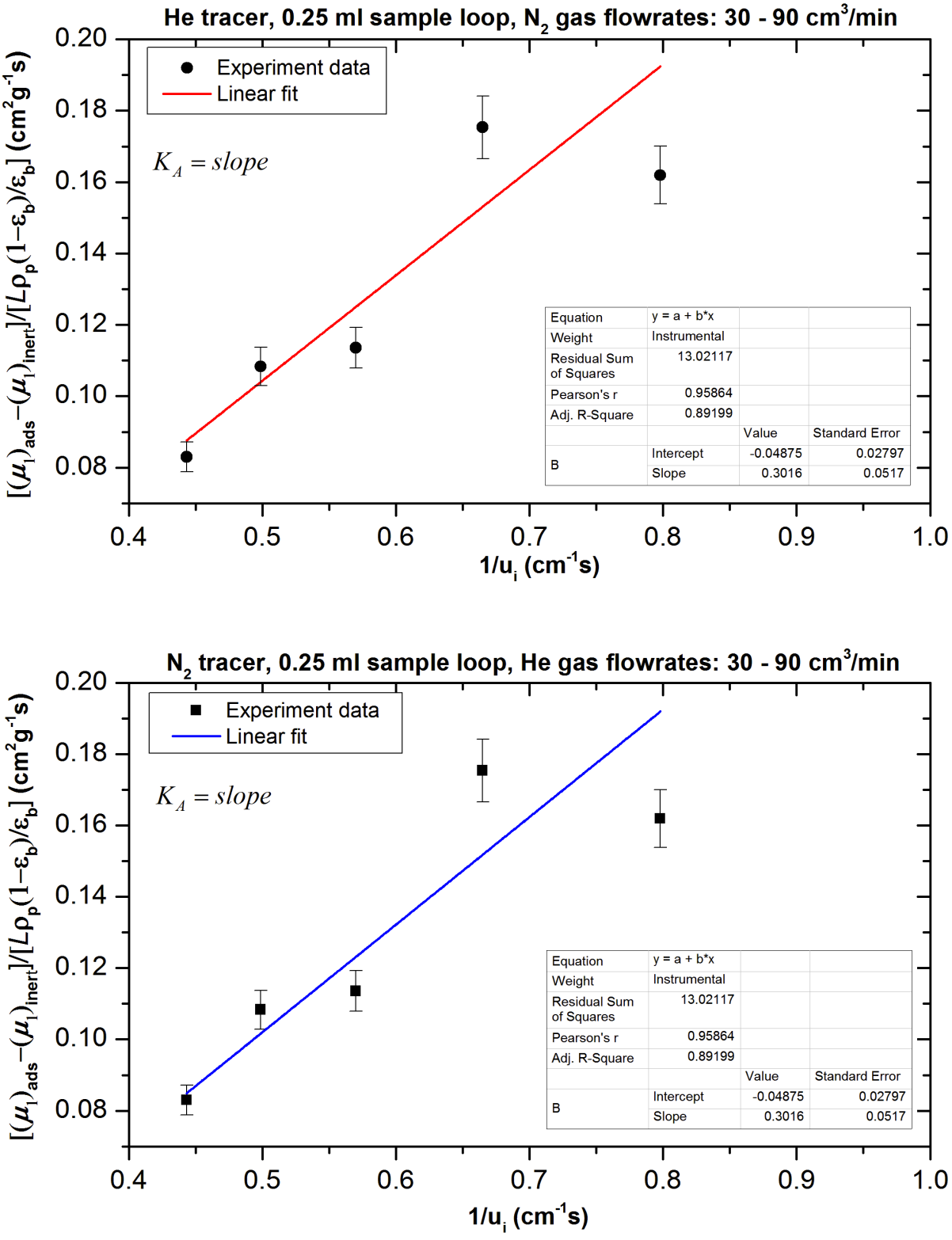

Figure 3.31: Scenario 1, Case 2 (Guangsuo *et al.*, 2000): K_A values for γ-alumina beads experiments using two different tracers obtained from the slope of a linear plot (Equation (3.125)), and first moment results of the fictitious bed (200 mm) were used.

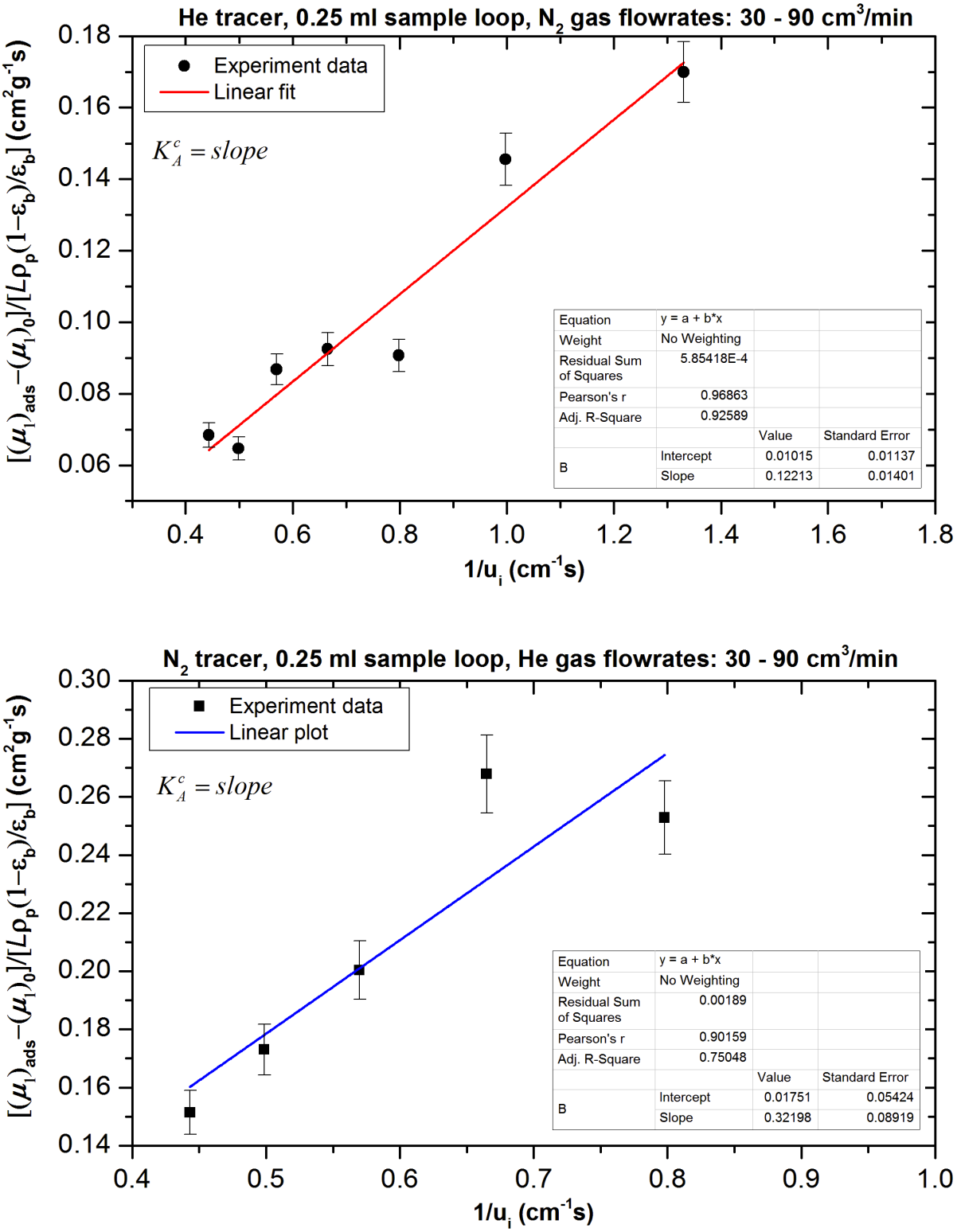

Figure 3.32: Scenario 1, Case 2c (Schneider and Smith, 1968a): K_A^c values for γ-alumina beads experiments using two different tracers obtained from the slope of a linear plot (Equation (3.126)), and first moment results of the fictitious bed (200 mm) were used.

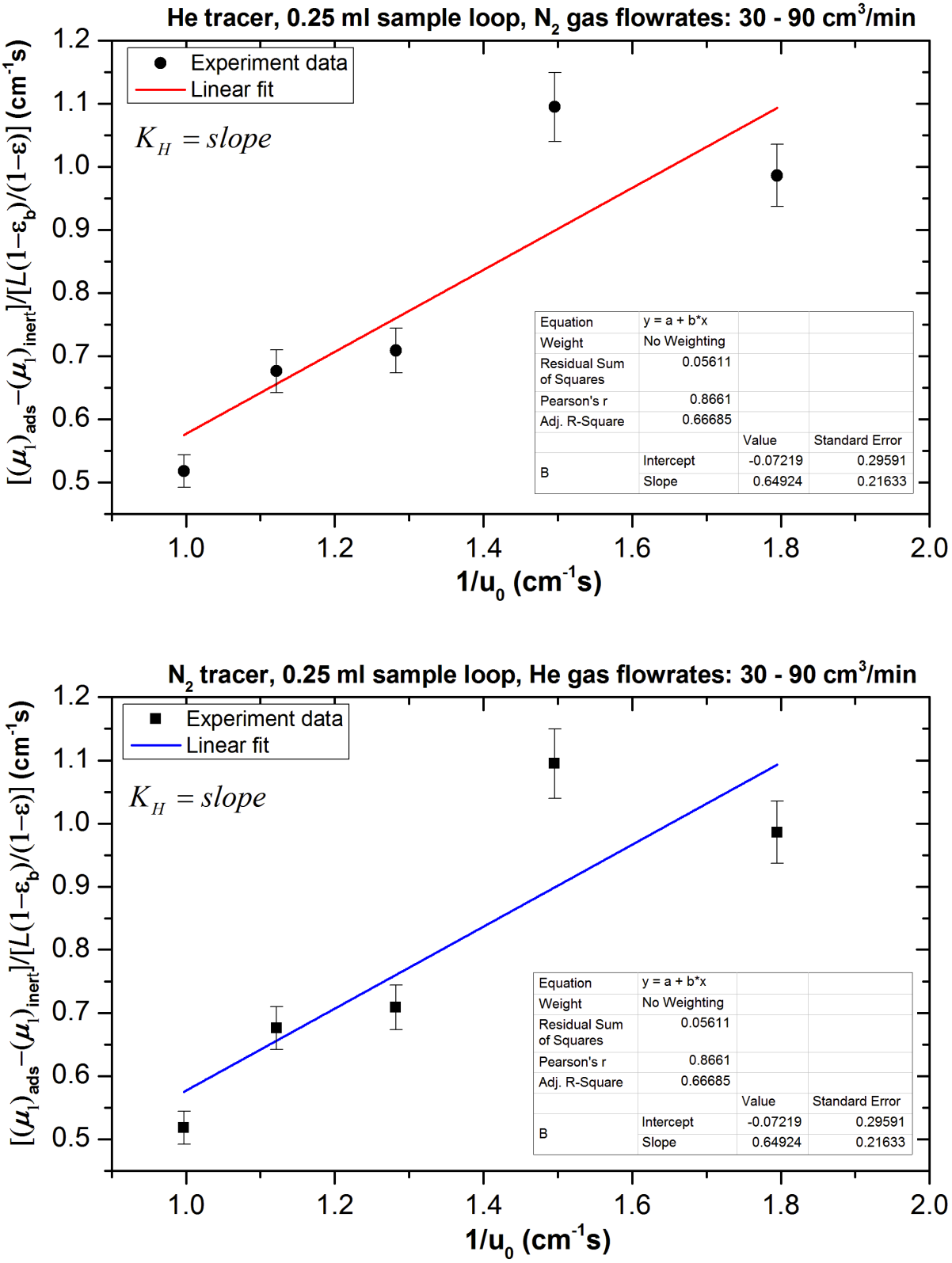

Figure 3.33: Scenario 1, Case 3 (New 2nd central moment method): Dimensionless K_H values for γ-alumina beads experiments using two different tracers obtained from the slope of a linear plot (Equation (3.109)), and first moment results of the fictitious bed (200 mm) were used.

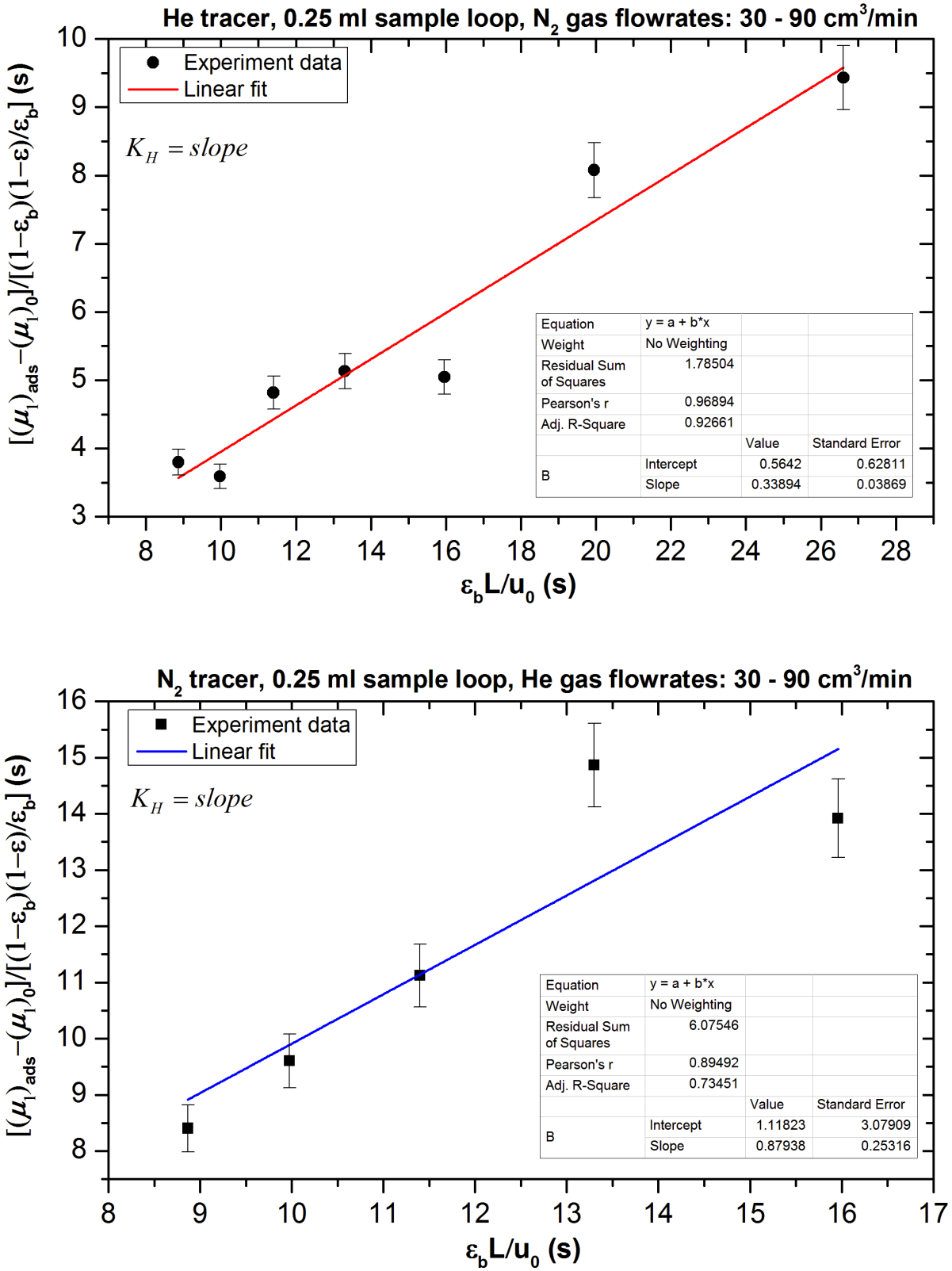

Figure 3.34: Scenario 2, Cases 4 and 6 (Armatas *et al.* (2005) and New HETP method): Dimensionless K_H values for γ-alumina beads experiments using two different tracers obtained from the slope of a linear plot (Equation (A8.23)), and first moment results of the fictitious bed (200 mm) were used.

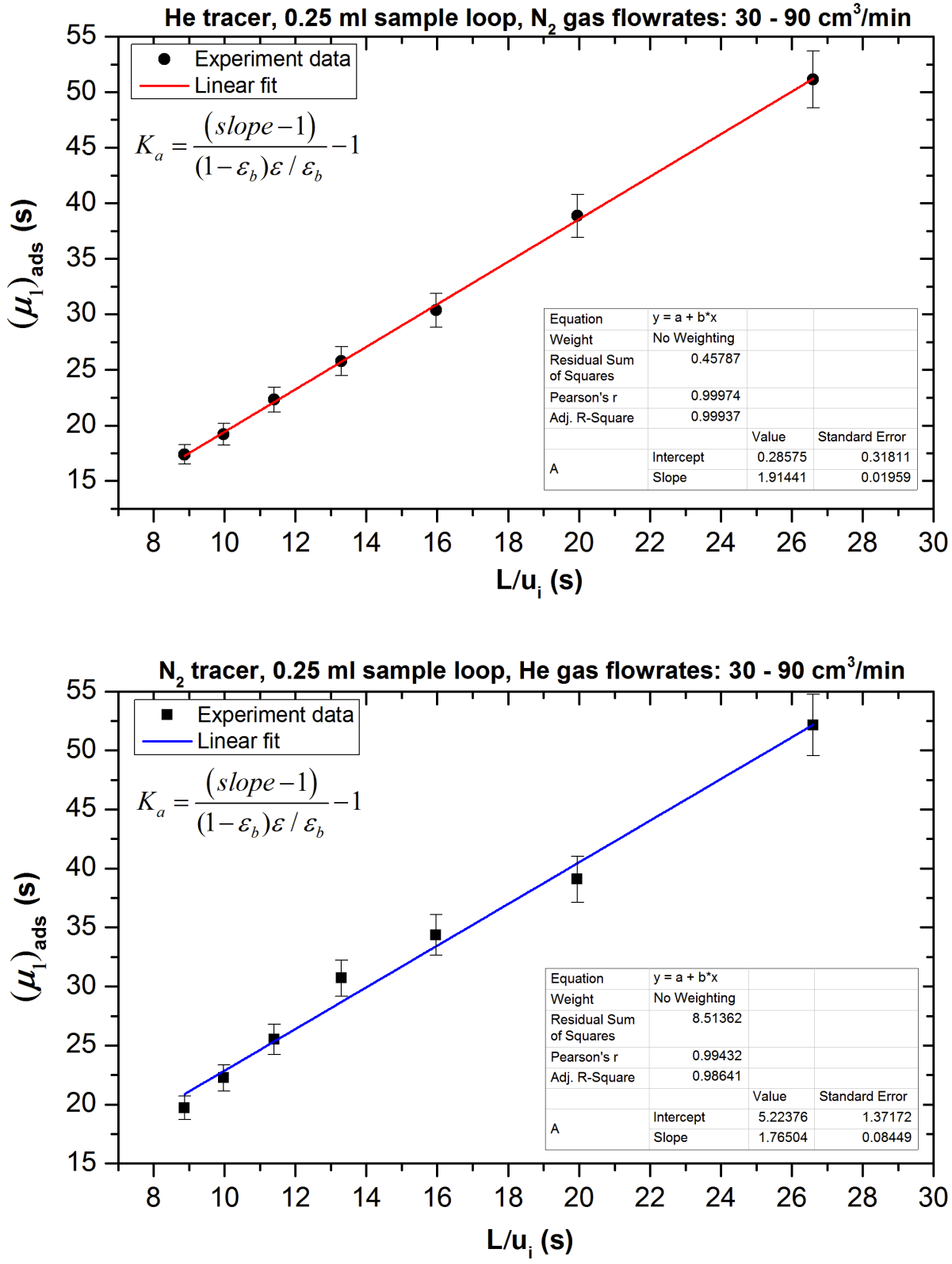

Figure 3.35: Scenario 3, Case 5 (Garcá-Ochoa and Santos, 1994; Santos *et al.*, 1996): Dimensionless K_a values for γ-alumina beads experiments using two different tracers obtained indirectly from the slope of a linear plot (Equation (A9.2)), and first moment results of the fictitious bed (200 mm) were used.

3.9 Conclusions

- **Column design:** By making modifications to the design of the inlet and outlet sections to the column, and eliminating T-pieces (which created back-mixing), and using Plasticine to minimise dead-volume at the entrance to the packed section in the fittings, it was possible to generate a sharp pulse-shaped input into the column using a fast acting valve.

- **Response peak measurement:** After injecting a short Dirac pulse at the inlet, the use of the mass spectrometer with the SEM detector is a suitable method to measure the response at the column outlet. The repeatability of the experiments was good with peak height variation less than $\pm 0.5\%$ over 24 h.

- **Two inert tracer-carrier gas systems:** Both He (tracer) – N_2 (carrier) and N_2 (tracer) – He (carrier) gas systems were used. From moment analysis results in Section 3.7.4, there is a difference between the mean residence time of He and N_2 gases when used as tracer. In general, N_2 gas eluted from the packed bed slower than the He gas, and this leads to a bigger variance than with He. The reason for using two inert gas system is that, in calculations to determine the adsorption equilibrium constant, K_A and K_H (in Case 2 and Case 3), the first moment for the inert run, $(\mu_1)_{\text{inert}}$, is evaluated from the experimental response curve using carrier gas as tracer.

- **Sample loop volume:** although experiments were performed with 0.1, 0.25 and 0.5 ml sample-loop volumes, the results from the 0.25 ml and the 0.5 ml sample-loops were more reliable (less signal noise).

- **Peak fitting:** Based on an analysis of the results of calculations using a variety of peak fitting methods, it was decided to use a system that found the baseline and then applied baseline subtraction (in OriginPro 8.6).

- **Peak area:** Although Simpson's rule provides a good method of calculating the area, it was decided to use the method in OriginPro 8.6, which was based on the use of a Gaussian area function term.

- **'Dead' volume time, τ_d:** The delay time, τ_d, caused by delays in inlet and outlet lines was quantified.

- **First moment, μ_1 or mean residence time, t_m:** To allow for the delay time, τ_d, and column inlet and exit effects, convolution theorem was applied and results for a fictitious bed (200 mm) were generated using data from real 200 and 400 mm columns.

- **First moment for blank run, $(\mu_1)_0$ and first moment for inert run, $(\mu_1)_{inert}$:** The first moment for a blank run, $(\mu_1)_0$ was used in Cases 2c, 4 and 6. The advantage of using $(\mu_1)_0$ is that a high linear correlation coefficient was obtained (0.8 ~ 0.9), therefore the K results were more accurate. However, the disadvantage of $(\mu_1)_0$ is that in one of the calculation steps (Case 4) the adsorption strength of the carrier gas is not considered. So, instead of performing a blank run experiment (i.e. run with carrier gas as tracer), $(\mu_1)_0$ is assumed equal to the result calculated from Equation (3.59), which is derived from the theoretical first moment expression when $K = 0$. Whereas $(\mu_1)_{inert}$ (used in Cases 2 and 3) considers the adsorption strength of the carrier gas for adsorption equilibrium constant calculation, because it is evaluated from the experimental response curve, but the linear correlation coefficient is rather weak (0.7 ~ 0.8).

- **Adsorption equilibrium constant**: A variety of different methods were explored for the evaluation of this constant. The values determined in Cases 2 and 3 were preferred as the adsorption strength of the tracer and also the carrier gas were considered. The calculated values (from experiments) confirmed that the level of adsorption was weak, and this was consistent with literature and expectations.

- **Second central moment, μ_2' or variance, σ^2:** For moment analysis with the peak fitting method, μ_2' is calculated using two different expressions: Cat. A and Cat. B. Experiments were performed on 200 and 400 mm columns packed with γ-alumina beads. Then, the second central moment of the fictitious 200 mm bed was calculated. These values are then used in Chapter 4.

References

Aboudheir, A., Akande, A., Idem, R. & Dalai, A., 2006. Experimental studies and comprehensive reactor modeling of hydrogen production by the catalytic reforming of crude ethanol in a packed bed tubular reactor over a Ni/Al_2O_3 catalyst. *International Journal of Hydrogen Energy,* 31, pp. 752-761.

Armatas, G., Petrakis, D. & Pomonis, P., 2005. Estimation of diffusion parameters in functionalized silicas with modulated porosity: Part I: Chromatographic studies. *Journal of Chromatography A,* 1074, pp. 53-59.

Baiker, A., New, M. & Richarz, W., 1982. Determination of intraparticle diffusion coefficients in catalyst pellets: a comparative study of measuring methods. *Chemical Engineering Science,* 37, pp. 643-656.

Biswas, J., Do, D.D., Greenfield, P.F. & Smith, J.M., 1987. Evaluation of bidisperse transport properties of a reforming catalyst using a diffusion cell I. Theoretical development. *Applied catalysis,* 32, pp. 217-234.

Cussler, E.L., 2009. *Diffusion: mass transfer in fluid systems.* Cambridge university press.

Do, D.D., 1998. *Adsorption Analysis: Equilibria and Kinetics.* Imperial College Press.

Feng, C. & Stewart, W.E., 1973. Practical Models for Isothermal Diffusion and Flow of Gases in Porous Solids. *Industrial & Engineering Chemistry Fundamentals,* 12, pp. 143-147.

Fogler, H.S., 2004. *Elements of Chemical Reaction Engineering.* Pearson Education.

Froment, G.F., Bischoff, K.B. & De Wilde, J., 1990. *Chemical reactor analysis and design.* Wiley New York.

Fuller, E.N., Schettler, P.D. & Giddings, J.C., 1966. New method for prediction of binary gas-phase diffusion coefficients. *Industrial & Engineering Chemistry,* 58, pp. 18-27.

Garc á-Ochoa, F. & Santos, A., 1994. Effective diffusivity under inert and reaction conditions. *Chemical Engineering Science,* 49, pp. 3091-3102.

Guangsuo, Y., Jianguo, Y. & Zunhong, Y., 2000. The measurement of effective diffusivity for sulfur-tolerant methanation catalyst. *Chemical Engineering Journal,* 78, pp. 141-146.

Guiochon, G. & Guillemin, C.L., 1988. *Quantitative Gas Chromatography for Laboratory Analyses and On-Line Process Control.* Elsevier.

Hayes, R.E. & Kolaczkowski, S.T., 1997. *Introduction to catalytic combustion.* Gordon and Breach.

Hayes, R.E. & Kolaczkowski, S.T., 2000. Evaluating the effective diffusivity of methane in the washcoat of a honeycomb monolith. *Applied Catalysis B: Environmental,* 25, pp. 93-104.

Hayes, R.E. & Mmbaga, J., 2012. *Introduction to Chemical Reactor Analysis.* CRC Press.

Himmelblau, D.M. & Bischoff, K.B., 1968. *Process analysis and simulation: deterministic systems.* Wiley.

Hosticka, B., Norris, P.M., Brenizer, J.S. & Daitch, C.E., 1998. Gas flow through aerogels. *Journal of Non-Crystalline Solids,* 225, pp. 293-297.

IAEA, 2008. Radiotracer Residence Time Distribution Method for Industrial and Environmental Applications. *Training Course Series 31.*

Idem, R.O., Katikaneni, S.P.R. & Bakhshi, N.N., 1997. Catalytic conversion of canola oil to fuels and chemicals: roles of catalyst acidity, basicity and shape selectivity on product distribution. *Fuel Processing Technology,* 51, pp. 101-125.

Jaguste, D.N. & Bhatia, S.K., 1995. Combined Surface and Viscous-Flow of Condensable Vapor in Porous-Media. *Chemical Engineering Science,* 50, pp. 167-182.

Johnson, M.F.L. & Stewart, W.E., 1965. Pore structure and gaseous diffusion in solid catalysts. *Journal of Catalysis,* 4, pp. 248-252.

Kubń, M., 1965. Beitrag zur Theorie der Chromatographie. *Collection of Czechoslovak Chemical Communications,* 30, pp. 1104-1118.

Kučera, E., 1965. Contribution of the theory of chromatography: linear non-equilibrium elution chromatography. *Journal of Chromatography* 19, pp. 23-248.

Levenspiel, O., 1998. *Chemical Reaction Engineering; 3rd Edition.* John Wiley & Sons.

Levenspiel, O. & Smith, W., 1957. Notes on the diffusion-type model for the longitudinal mixing of fluids in flow. *Chemical Engineering Science,* 6, pp. 227-235.

Malek, K. & Coppens, M.O., 2003. Knudsen self-and Fickian diffusion in rough nanoporous media. . *Journal of Chemical Physics,* 119, pp. 2801-2811.

Marquardt, D., 1963. Finite difference algorithm for curve fitting. *Society for Industrial and Applied Mathematics,* 11, pp. 431-441.

Mathews, J. & Howell, R., 2010. *Complex analysis for mathematics and engineering.* Jones & Bartlett Publishers.

Rase, H.F. & Holmes, J.R., 1977. Chemical reactor design for process plants.

Rawlings, J.B. & Ekerdt, J.G., 2002. *Chemical reactor analysis and design fundamentals.* Nob Hill Pub.

Reid, R.C., Prausnitz, J.M. & Poling, B.E., 1987. *The Properties of Gases & Liquids.* New York: McGraw-Hill.

Ruthven, D.M., 1984. *Principles of Adsorption and Adsorption Processes.* John Wiley & Sons Inc.

Santos, A., Bahamonde, A., Avila, P. & Garcia-Ochoa, F., 1996. Measurement of the effective diffusivity for a vanadia-tungsta-titania/sepiolite catalyst for SCR of NO_x. *Applied Catalysis B: Environmental,* 8, pp. 299-314.

Satterfield, C.N., 1981. *Mass transfer in heterogeneous catalysis.* RE Krieger Publishing Company.

Satterfield, C.N. & Cadle, P.J., 1968. Diffusion in Commercially Manufactured Pelleted Catalysts. *Industrial & Engineering Chemistry Process Design and Development,* 7, pp. 256-260.

Schneider, P., 1984. Time-domain expression for impulse response (chromatographic) curve for the Kubín-Kučera model of adsorption column. *Chemical Engineering Science,* 39, pp. 927-929.

Schneider, P., 1986. Determination of effective diffusion coefficients for porous packings with an impermeable centre from peak moments. *Chemical Engineering Science,* 41, pp. 1759-1764.

Schneider, P. & Smith, J., 1968. Adsorption rate constants from chromatography. *AIChE Journal,* 14, pp. 762-771.

Starý, T., Solcová, O., Schneider, P. & Marek, M., 2006. Effective diffusivities and pore-transport characteristics of washcoated ceramic monolith for automotive catalytic converter. *Chemical Engineering Science,* 61, pp. 5934-5943.

Suzuki, M. & Smith, J., 1971. Kinetic studies by chromatography. *Chemical Engineering Science,* 26, pp. 221-235.

Tang, G.H.Y., Trimm, D.L. & Wainwright, M.S., 1987. Effective diffusivity in cylindrical catalyst pellets. *Chemical engineering in Australia,* 12, pp. 9-12.

Taylor, J.R., 1997. *An introduction to error analysis: the study of uncertainties in physical measurements.* University science books.

Wakao, N., Oshima, T. & Yagi, S., 1958. Mass transfer from packed beds of particles to a fluid. *Chemical Engineering of Japan,* 22, pp. 780-785.

Wei, L. & Kaufman, M., 1976. Gaseous sample compression as a means of increasing sensitivity in gas chromatographic analysis. *Analytical Chemistry,* 48, pp. 2029-2030.

Westermarck, S., 2000. *Use of mercury porosimetry and nitrogen adsorption in characterisation of the pore structure of mannitol and microcrystalline cellulose powders, granules and tablets.* Helsinki, Finland: University of Helsinki

Zhang, F., 2005. *Measurement of the effective diffusivity of carbon monoxide in commercial catalytic monolith converters.* Phd, University of Bath.

Zhu, B.C., 1981. *Inorganic Chemical Reaction Engineering.* Chemical Industry Press, Beijing

4 Chromatographic methods – axial dispersion and effective diffusivity

This chapter consists of the following main sections:

- **Axial dispersion coefficient, D_{ax} in a bed packed with 1 mm glass beads:** D_{ax} is calculated for the packed beds using: (a) 2nd central moment; and (b) HETP method.

- **Axial dispersion coefficient, D_{ax} in packed bed with γ-alumina beads:** is calculated for Cases 1, 2, 3, 4, 5 and 6 listed in Chapter 3.

- **Effective Diffusivity, D_{eff} without and with adsorption equilibrium constant, K:** making use of the information on porosity and pore size (obtained in Chapter 2), and the moment analysis results for a fictitious bed (Chapter 3), these are then used in moment matching with the 2nd central moment and HETP methods to evaluate the effective diffusivity and apparent tortuosity of the γ-alumina beads. Values of D_{eff} are calculated without, and also with an allowance for external mass transfer resistance, ξ_e.

The work done in this chapter is summarized in Figure 4.1.

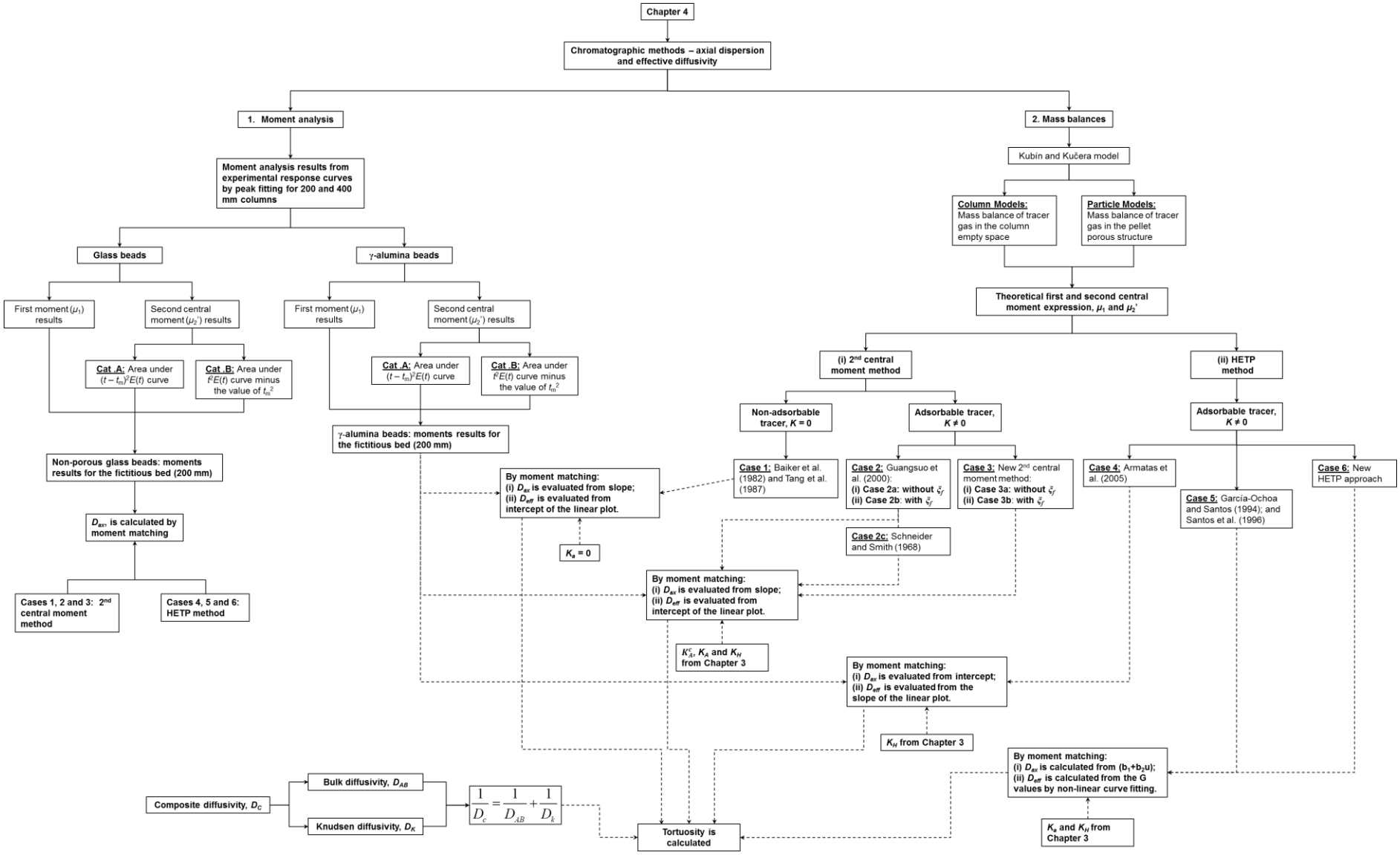

Figure 4.1: Structure of Chapter 4 and links with other chapters.

4.1 Moment matching to determine axial dispersion coefficient, D_{ax}

4.1.1 Non-porous glass beads experiment

By performing an experiment using glass beads (diameter: 1 mm) under the same set of experimental conditions as for the γ-alumina pellets, then it is possible to evaluate the axial dispersion coefficient, D_{ax}. The experimental columns used are shown in Figure 4.2.

In summary experimental conditions were as follows:

(i) **Column fittings and tubings:** the same fitting and lines were used;

(ii) **Column void fraction (bed porosity):** the diameter of glass bead is 1.0 mm, therefore the bed porosity is the same as for the γ-alumina beads i.e. $\varepsilon_b = 0.4446$;

(iii) **Column length:** 200 and 400 mm columns with tube O.D: 19.0 mm and tube I.D: 13.8 mm;

(iv) **Two inert gases**: He (tracer) – N_2 (carrier) and N_2 (tracer) – He (carrier) gas systems;

(v) **Tracer gas sample loop volumes:** 0.1, 0.25 and 0.5 ml;

(vi) **Carrier gas flowrates:** 30 cm^3/min – 90 cm^3/min;

(vii) **Temperature and pressure:** 295.15 K and 1.013 bar.

The experimental response curves recorded at the outlet of a 400 mm column packed with non-porous glass beads (0.25 ml of He tracer pulse, carrier gas N_2 flows = 30, 60 and 90 cm^3/min) are shown in Figure 4.3. On the same figure, the experimental response curves obtained earlier with the porous γ-alumina beads are shown for comparison.

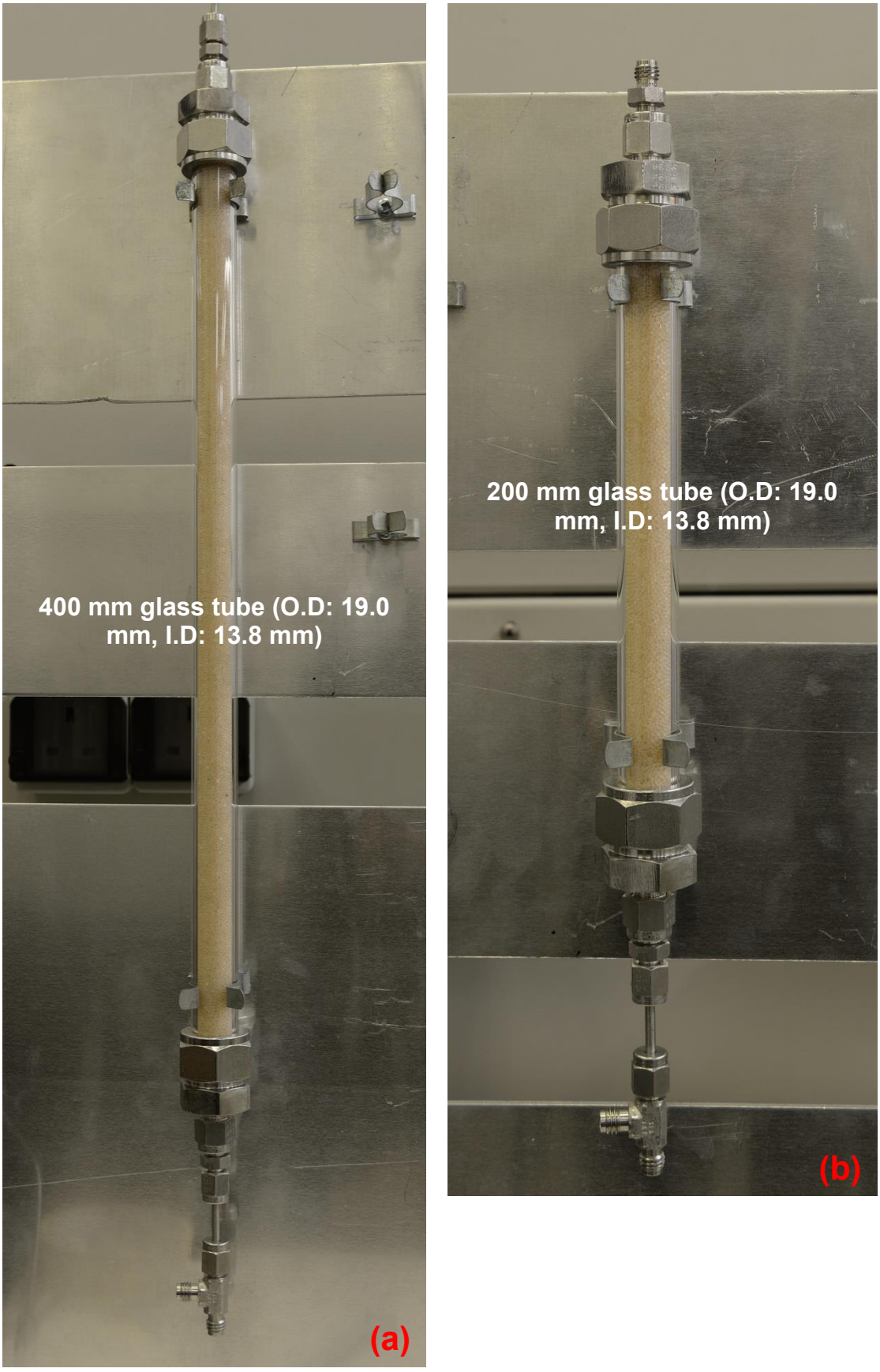

Figure 4.2: Prototype II design: column packed with non-porous glass beads: (a) 400 mm; (b) 200 mm.

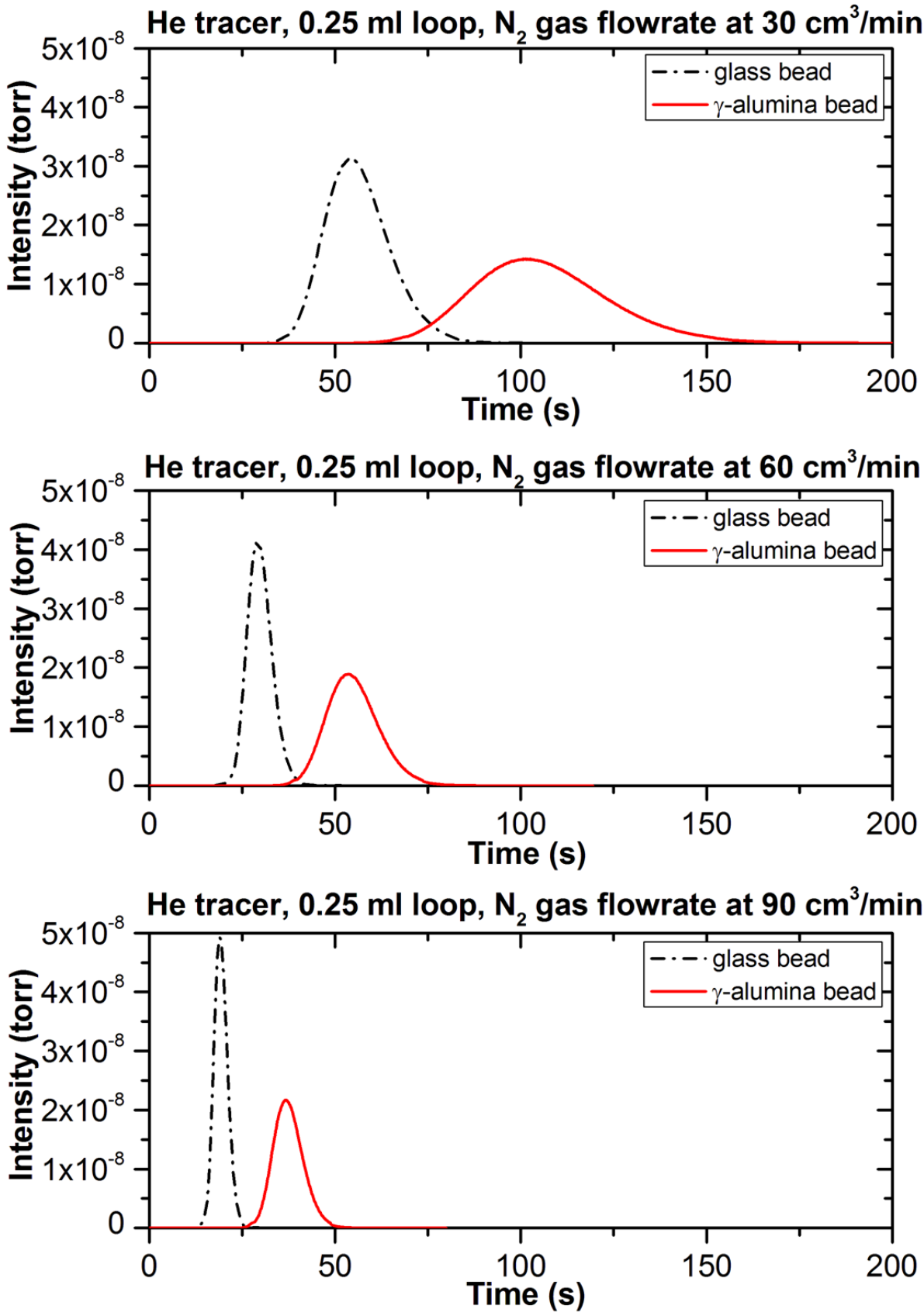

Figure 4.3: Experimental response curves obtained for glass beads and γ-alumina pellet experiment with 0.25 ml He tracer, and N_2 carrier gas flows at 30, 60 and 90 cm^3/min.

From Figure 4.3, for the glass beads, the peak elution time, t_{glass} is significantly faster than when porous γ-alumina beads, t_{bead}, are positioned in the bed. For example, the peak elution times for t_{glass} and t_{bead} are summarized in Table 4.1.

Table 4.1: The peak elution time for glass bead and γ-alumina pellet experiments

Carrier gas flow (cm^3/min)	**t_{glass} (s)**	**t_{bead} (s)**
30	54.096	101.298
60	29.040	53.721
90	19.041	36.738

One of the main feature of the Gaussian peak is that, when the peak shape is symmetrical, then the peak elution time (i.e. at the highest peak concentration, or the maximum peak height) is equivalent to the mean residence time, t_m. Therefore, by comparing t_{glass} and t_{bead}, when the time delays, τ_d, for both experiments are the same because the exact same lines and fittings were used, the dispersion and diffusion effects are dominant in porous γ-alumina beads.

Although experiments on glass beads were performed with 0.1, 0.25 and 0.5 ml sample loops, it was shown earlier that results with the 0.25 and 0.5 ml loops were more accurate, so the results for the 0.25 ml loop have been selected for the analysis that follows.

4.1.1.1 Results for moment analysis (glass beads) using 0.25 ml sample loop

In this chapter, moment analysis results from experimental response curves using Gaussian peak fitting method are shown in Tables 4.2 and 4.9, for the following range of experimental conditions:

(i) 0.25 ml sample loop at carrier gas flowrates 30 – 90 cm^3/min, at 295.15 K and 1.013 bar;

(ii) Two different column lengths: 200 and 400 mm;

(iii) He (tracer) – N_2 (carrier), N_2(tracer) – He (carrier) gas systems;

(iv) Second central moment, μ_2', obtained from **Cat. A** and **Cat. B** (see Equation (A3.4) in Appendix 3).

As a reminder:

Cat. A: Gaussian peak fitting with second central moment, μ_2', equal to the area under the $(t - t_m^2)\,E(t)$ curve;

Cat. B: Gaussian peak fitting with second central moment, μ_2', equal to the area of the $t^2E(t)$ curve minus t_m^2.

From Table 4.2 to Table 4.11, the error analysis follows the exactly same rules as described previously in Chapter 3 from Table 3.5 to Table 3.8, that is:

(a) The first moments or the areas under the $tE(t)$ curves for the 200 and 400 mm real columns and the 200 mm fictitious bed used the **addition and subtraction of values with standard deviation rule** for error analysis;

(b) The second central moments or the areas under the $(t - t_m)^2E(t)$ curves (Cat. A) for the 200 and 400 mm real columns and the 200 mm fictitious bed used the **addition and subtraction of values with standard deviation rule** for error analysis;

(c) The second central moments or the product of $\int t^2E(t)dt - t_m^2$ (Cat. B) for the 200 and 400 real columns and the 200 mm fictitious bed used the **exponent or power of values** followed by the **addition and subtraction of values with standard deviation rules** for error analysis.

400 mm packed bed with glass beads

Table 4.2: Moment analysis results **(He tracer)** for a **400 mm** column packed with non-porous glass beads, and 2nd central moment, μ_2' is obtained from **Cat. A**.

N_2(carrier) - He(tracer)	Glass beads (0.25 ml sample loop)			
	Flowrate (cm^3/min)	1st moment, μ_1 (s)	2nd central moment, μ_2' (s^2)	Injection time, t_0 (s)
bot01	30	56.509 ± 0.428	73.393 ± 0.646	0.50
bot03	40	42.712 ± 0.289	31.708 ± 0.341	0.38
bot06	50	34.365 ± 0.289	16.356 ± 0.240	0.30
bot08	60	29.861 ± 0.233	10.623 ± 0.155	0.25
bot10	70	25.846 ± 0.190	6.688 ± 0.104	0.21
bot13	80	22.434 ± 0.245	4.273 ± 0.068	0.19
bot16	90	19.343 ± 0.171	3.249 ± 0.064	0.17

Table 4.3: Moment analysis results **(N_2 tracer)** for a **400 mm** column packed with non-porous glass beads, and 2nd central moment, μ_2' is obtained from **Cat. A**.

He(carrier) - N_2(tracer)	Glass beads (0.25 ml sample loop)			
	Flowrate (cm^3/min)	1st moment, μ_1 (s)	2nd central moment, μ_2' (s^2)	Injection time, t_0 (s)
bot01	30	52.476 ± 0.200	60.977 ± 0.391	0.50
bot03	40	39.256 ± 0.160	25.236 ± 0.172	0.38
bot05	50	34.010 ± 0.137	16.350 ± 0.124	0.30
bot07	60	30.544 ± 0.119	11.635 ± 0.100	0.25
bot09	70	25.641 ± 0.104	6.848 ± 0.062	0.21
bot12	80	22.433 ± 0.103	4.508 ± 0.055	0.19
bot14	90	20.110 ± 0.111	3.192 ± 0.046	0.17

Table 4.4: Moment analysis results **(He tracer)** for a **400 mm** column packed with non-porous glass beads, and 2nd central moment, μ_2' is obtained from **Cat. B.**

N_2(carrier) - He(tracer)	Glass beads (0.25 ml sample loop)			
	Flowrate (cm^3/min)	**1st moment, μ_1 (s)**	**2nd central moment, μ_2' (s^2)**	**Injection time, t_0 (s)**
bot01	30	56.509 ±0.428	74.628 ±53.917	0.50
bot03	40	42.712 ±0.289	25.388 ±28.664	0.38
bot06	50	34.365 ±0.289	18.148 ±21.916	0.30
bot08	60	29.629 ±0.233	13.221 ±16.752	0.25
bot10	70	25.846 ±0.190	7.300 ±10.866	0.21
bot13	80	22.434 ±0.245	4.534 ±12.282	0.19
bot16	90	19.343 ±0.171	3.339 ±7.394	0.17

Table 4.5: Moment analysis results **(N_2 tracer)** for a **400 mm** column packed with non-porous glass beads, and 2nd central moment, μ_2' is obtained from **Cat. B**.

He(carrier) - N_2(tracer)	Glass beads (0.25 ml sample loop)			
	Flowrate (cm^3/min)	**1st moment, μ_1 (s)**	**2nd central moment, μ_2' (s^2)**	**Injection time, t_0 (s)**
bot01	30	52.476 ±0.200	61.617 ±23.443	0.50
bot03	40	39.256 ±0.160	26.657 ±13.882	0.38
bot05	50	34.010 ±0.137	20.148 ±10.214	0.30
bot07	60	30.544 ±0.119	11.840 ±8.007	0.25
bot09	70	25.641 ±0.104	8.605 ±5.836	0.21
bot12	80	22.433 ±0.103	3.596 ±5.320	0.19
bot14	90	20.110 ±0.111	3.458 ±4.933	0.17

200 mm packed bed with glass beads

Table 4.6: Moment analysis results **(He tracer)** for a **200 mm** column packed with non-porous glass beads, and 2nd central moment, μ_2' is obtained from **Cat. A.**

N_2(carrier) - He(tracer)	Glass beads (0.25 ml sample loop)			
	Flowrate (cm^3/min)	1st moment, μ_1 (s)	2nd central moment, μ_2' (s^2)	Injection time, t_o (s)
bot01	30	34.283 ±0.407	48.650 ±0.475	0.50
bot03	40	26.360 ±0.341	22.353 ±0.313	0.38
bot06	50	19.792 ±0.272	8.561 ±0.113	0.30
bot08	60	17.082 ±0.222	5.290 ±0.087	0.25
bot10	70	14.887 ±0.159	3.512 ±0.073	0.21
bot13	80	12.932 ±0.169	2.249 ±0.050	0.19
bot16	90	11.971 ±0.179	1.816 ±0.035	0.17

Table 4.7: Moment analysis results **(N_2 tracer)** for a **200 mm** column packed with non-porous glass beads, and 2nd central moment, μ_2' is obtained from **Cat. A**.

He(carrier) - N_2(tracer)	Glass beads (0.25 ml sample loop)			
	Flowrate (cm^3/min)	1st moment, μ_1 (s)	2nd central moment, μ_2' (s^2)	Injection time, t_0 (s)
bot01	30	31.495 ±0.173	41.146 ±0.486	0.50
bot03	40	24.063 ±0.137	19.352 ±0.174	0.38
bot05	50	21.012 ±0.126	13.213 ±0.113	0.30
bot07	60	18.756 ±0.123	9.676 ±0.088	0.25
bot09	70	15.839 ±0.119	6.053 ±0.064	0.21
bot12	80	14.061 ±0.115	4.367 ±0.065	0.19
bot14	90	12.457 ±0.169	3.235 ±0.064	0.17

Table 4.8: Moment analysis results **(He tracer)** for a **200 mm** column packed with non-porous glass beads, and 2nd central moment, μ_2' is obtained from **Cat. B.**

N_2(carrier) - He(tracer)	Glass beads (0.25 ml sample loop)			
	Flowrate (cm^3/min)	1st moment, μ_1 (s)	2nd central moment, μ_2' (s^2)	Injection time, t_0 (s)
bot01	30	34.283 ± 0.407	51.010 ± 32.256	0.50
bot03	40	26.360 ± 0.341	14.231 ± 20.378	0.38
bot06	50	19.792 ± 0.272	9.503 ± 12.063	0.30
bot08	60	17.082 ± 0.222	6.478 ± 8.487	0.25
bot10	70	14.887 ± 0.159	3.942 ± 5.594	0.21
bot13	80	12.932 ± 0.169	2.554 ± 5.007	0.19
bot16	90	11.971 ± 0.179	2.052 ± 4.657	0.17

Table 4.9: Moment analysis results **(N_2 tracer)** for a **200 mm** column packed with non-porous glass beads, and 2nd central moment, μ_2' is obtained from **Cat. B**.

He(carrier) - N_2(tracer)	Glass beads (0.25 ml sample loop)			
	Flowrate (cm^3/min)	1st moment, μ_1 (s)	2nd central moment, μ_2' (s^2)	Injection time, t_0 (s)
bot01	30	31.495 ± 0.173	38.690 ± 12.285	0.50
bot03	40	24.063 ± 0.137	18.263 ± 7.494	0.38
bot05	50	21.012 ± 0.126	13.576 ± 5.972	0.30
bot07	60	18.879 ± 0.123	7.277 ± 5.235	0.25
bot09	70	15.839 ± 0.119	6.092 ± 4.286	0.21
bot12	80	14.176 ± 0.115	2.976 ± 3.613	0.19
bot14	90	12.457 ± 0.169	2.779 ± 4.764	0.17

Comparing Tables 4.2 to 4.9 for the non-porous glass beads experiments, the following observation and conclusion are made:

(a) In Column (3), as in the earlier γ-alumina beads experiments, because of the column entrance and exit effect, the first moment or mean residence time, μ_1, in a 200 mm packed bed is not equal to half of the residence time of that tracer in a 400 mm packed bed for glass beads.

(b) From the 'dead' volume time, τ_d shown in Chapter 3 Section 3.5.2, for moment matching to evaluate axial dispersion coefficient, D_{ax} from glass bead experiments, the moment results of a fictitious bed (200 mm) are used. As mention in Chapter 3 Section 3.7.3 on convolution theorem, the first moment of the fictitious bed is deduced from the difference between the first moments of the two 'real' columns (400 and 200 mm), and the second central moment of the fictitious bed is calculated from the difference between the second central moment of the two 'real' columns. The moment analysis results for the fictitious bed (200 mm) are summarised in Tables 4.10 and 4.11.

In conclusion: In the analysis that follows on the glass and γ–alumina beads for D_{ax} calculation, the 0.25 ml sample loop will be used. Besides, to determine the axial dispersion coefficient, D_{ax} in the packed bed with non-porous and porous beads, the moment analysis results from the fictitious bed (200 mm) will be used i.e Tables 4.10 and 4.11 for the glass beads, and Tables 3.5 to 3.8 for the γ–alumina beads.

Table 4.10: Moment analysis results of a fictitious bed (200 mm) with 0.25 ml sample loop, and 2nd central moment is obtained using **Cat. A.**

Glass bead packed bed – fictitious (0.25ml sample loop)				
Flowrate (cm^3/min)	**First moment, μ_1 (s)**		**Second central moment, μ_2' (s^2) (Cat. A)**	
	He tracer	**N_2 tracer**	**He tracer**	**N_2 tracer**
30	22.226 ±0.591	20.982 ±0.265	24.743 ±0.802	19.831 ±0.623
40	16.353 ±0.447	15.192 ±0.211	9.355 ±0.463	5.884 ±0.245
50	14.573 ±0.397	12.997 ±0.186	7.795 ±0.266	3.137 ±0.168
60	12.779 ±0.322	11.788 ±0.171	5.332 ±0.178	1.959 ±0.133
70	10.958 ±0.248	9.802 ±0.158	3.176 ±0.127	0.795 ±0.089
80	9.502 ±0.298	8.372 ±0.154	2.024 ±0.084	0.141 ±0.085
90	7.372 ±0.248	7.653 ±0.202	1.433 ±0.073	-0.043 ±0.079

Table 4.11: Moment analysis results of a fictitious bed (200 mm) with 0.25 ml sample loop, and 2nd central moment is obtained using **Cat. B.**

Glass bead packed bed – fictitious (0.25ml sample loop)				
Flowrate (cm^3/min)	**First moment, μ_1 (s)**		**Second central moment, μ_2' (s^2) (Cat. B)**	
	He tracer	**N_2 tracer**	**He tracer**	**N_2 tracer**
30	22.226 ±0.591	20.982 ±0.265	23.618 ±62.829	22.927±26.466
40	16.355 ±0.447	15.192 ±0.211	11.157 ±35.170	8.393 ±15.775
50	14.573 ±0.397	12.997 ±0.186	8.645 ±25.017	6.573 ±11.832
60	12.546 ±0.322	11.665 ±0.171	6.743 ±18.779	4.562 ±9.567
70	10.958 ±0.248	9.802 ±0.158	3.358 ±12.221	2.512 ±7.241
80	9.502 ±0.298	8.257 ±0.154	1.980 ±13.264	0.620 ±6.431
90	7.372 ±0.248	7.653 ±0.202	1.287 ±8.738	0.679 ±6.858

4.1.1.2 Calculation of axial dispersion coefficient, D_{ax} for glass beads

Using the information obtained on moments, different methods are now explored to calculate the axial dispersion coefficient, D_{ax}. These are:

Category 1: **Part (a): 2nd central moment method (Cases 1 and 2a, 2b, 2c: linear correlation):** for calculating D_{ax} using the 2nd central moment method, as described in Cases 1 and 2, when the adsorption equilibrium constant (K_a, K_A or K_A^c) and particle porosity (ε) are zero for non-porous material, then Equations (A6.7) and (A7.13) in Cases 1 and 2 become:

$$\frac{\mu_2'}{2L/u_i} = \frac{D_{ax}}{\varepsilon_b}\left(\frac{1}{u_i^2}\right) \tag{4.1}$$

A linear relationship exist between the variance term, $\mu_2'/(2L/u_i)$ and the interstitial velocity term, $1/u_i^2$. Therefore, D_{ax} is evaluated from the slope of the linear plot as shown in Figure 4.4.

Part (b): New 2nd central moment method (Cases 3a and 3b): when $K_H = 0$ and $\varepsilon = 0$ for non-porous material, Equation (3.111) in Case 3 becomes:

$$\frac{\mu_2'}{2L/u_0} = \varepsilon_b^2 D_{ax}\left(\frac{1}{u_0^2}\right) \tag{4.2}$$

Equations (4.2) is exactly the same as Equation (4.1) because, as mentioned in Chapter 3, the superficial velocity, u_0 is equal to interstitial velocity, u_i multiply by bed porosity ε_b. Therefore, D_{ax} is evaluated from the slope of the linear plot as shown in Figure 4.4.

For a fictitious glass beads bed, the D_{ax} results for Cases 1, 2 and 3 for He and N_2 tracer (0.25 ml sample loop) are summarised in Tables 4.12 and 4.13, and the second central moment, μ_2', is obtained from **Cat. A and Cat. B**.

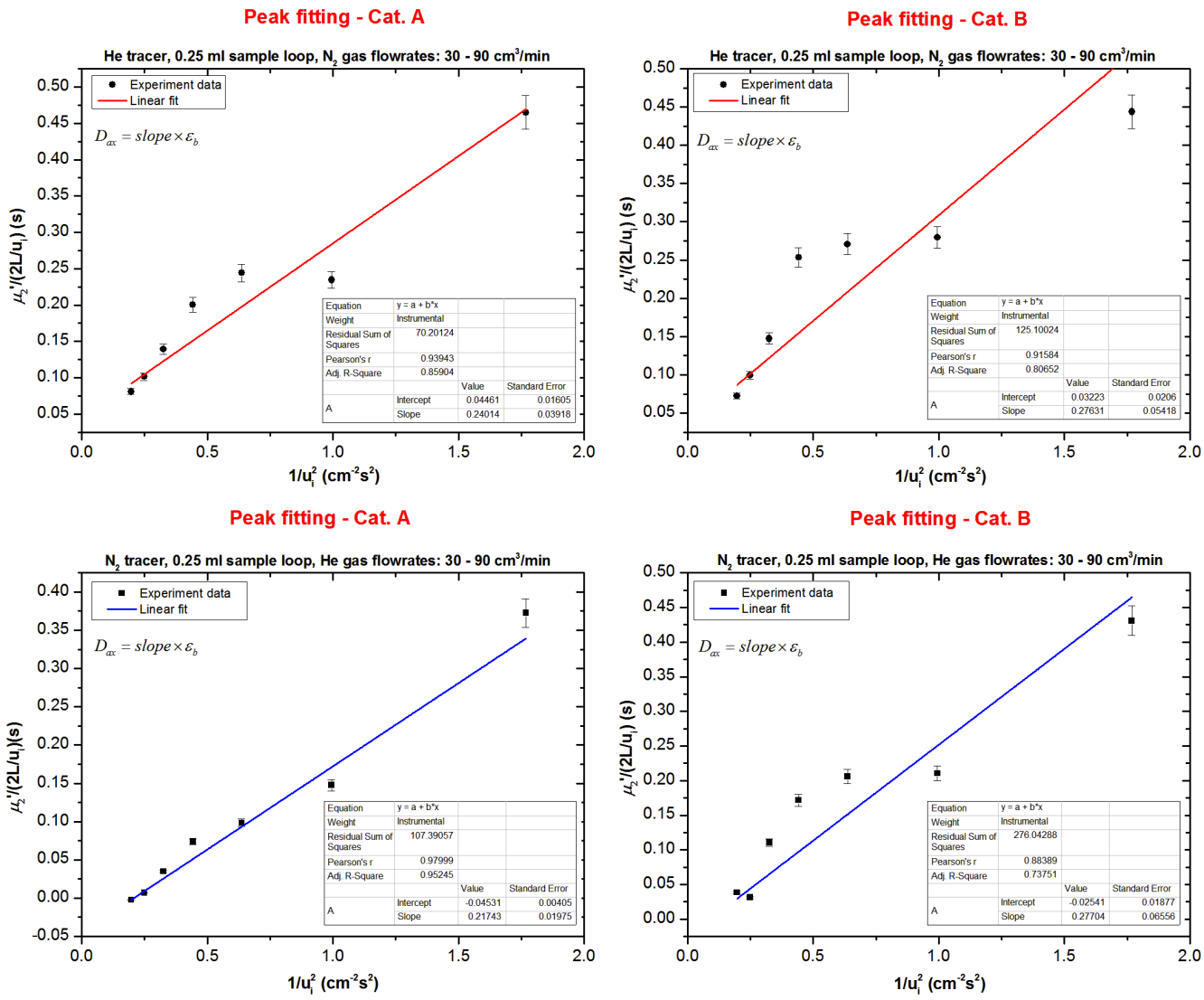

Figure 4.4: Axial dispersion coefficient, D_{ax}, for a 200 mm fictitious glass beads bed with He and N_2 tracer (0.25 ml), is obtained from the slope of the linear plot (plots shown are for **Cases 1, 2a, 2b, 2c, 3a and 3b**). **The equation for linear fit is: *y = bx + a*, where *b = slope* and *a = intercept*. This equation applies for linear fit cases for calculating D_{ax} and D_{eff}.**

Table 4.12: Axial dispersion coefficient results, D_{ax}, (He and N_2 tracer) for a **fictitious bed** (**200 mm)** packed with glass beads, and 2nd central moment is obtained from **Cat. A**.

Cases 1, 2a, 2b, 2c, 3a and 3b: glass beads (0.25 ml sample loop)								
Superficial carrier gas velocity term, $1/u_i^2$ (cm^{-2} s^2)	**$\mu_2'/(2L/u_i)$ (s)**		**Slope**		**Intercept**		**Axial dispersion coefficient, D_{ax} (cm^2 s^{-1})**	
	He	**N_2**	**He**	**N_2**	**He**	**N_2**	**He**	**N_2**
8.94847	0.465	0.373	0.2230	0.2289	0.0625	-0.463	**0.099**	**0.102**
5.03352	0.234	0.147						
3.22145	0.244	0.098						
2.23712	0.200	0.074						
1.64360	0.139	0.035						
1.25838	0.101	0.007						
0.99427	0.081	-0.002						

Table 4.13: Axial dispersion coefficient results, D_{ax}, (He and N_2 tracer) for a **fictitious bed** (**200 mm)** packed with glass beads, and 2nd central moment is obtained from **Cat. B**.

Cases 1, 2a, 2b, 2c, 3a and 3b: glass beads (0.25 ml sample loop)								
Superficial carrier gas velocity term, $1/u_i^2$ (cm^{-2} s^2)	**$\mu_2'/(2L/u_i)$ (s)**		**Slope**		**Intercept**		**Axial dispersion coefficient, D_{ax} (cm^2 s^{-1})**	
	He	**N_2**	**He**	**N_2**	**He**	**N_2**	**He**	**N_2**
8.94847	0.444	0.431	0.2133	0.2333	0.08333	0.0175	**0.095**	**0.104**
5.03352	0.280	0.210						
3.22145	0.271	0.206						
2.23712	0.254	0.172						
1.64360	0.147	0.110						
1.25838	0.099	0.031						
0.99427	0.073	0.038						

Category 2: **Part (a): HETP method (Case 4: linear correlation):** as described in Case 4; when K_H and $\varepsilon = 0$, then Equation (A8.31) becomes:

$$\text{HETP} = \frac{\mu_2^{'} L}{\left(\mu_1\right)^2} = 2\frac{D_{ax}}{u_0} \tag{4.3}$$

A linear relationship exists between $\mu_2^{'}L/(\mu_1)^2$ and $1/u_0$, and the axial dispersion coefficient D_{ax} can be obtained from the slope by moment matching in Figure 4.5.

Part (b): HETP method (Cases 5 and 6: linear and D_{ax} as a function of superficial velocity, u_0): as described in Cases 5 and 6, when K_a and $\varepsilon = 0$, the non-linear HETP equation (Equation (A9.12)) turns into a linear equation, and D_{ax} is calculated from the slope by plotting $\mu_2^{'}L/(\mu_1)^2$ as a linear function of $1/u_0$ or $1/\varepsilon_b u_i$ as:

$$\text{HETP} = \frac{\mu_2^{'} L}{\left(\mu_1\right)^2} = \frac{A}{u_0} + B \tag{4.4}$$

where D_{ax} is calculated from:

$$D_{ax} = \frac{A + Bu_0}{2} \tag{4.5}$$

This means that for D_{ax} calculations using moment results for the fictitious glass beads bed (200 mm), the HETP method for Cases 4, 5 and 6 will have the same plot but D_{ax} will be obtained in different ways. Therefore, the linear plot for HETP method in Cases 5 and 6 are also shown in Figure 4.5.

A linear relationship exists between $\mu_2^{'}L/(\mu_1)^2$ and $1/u_0$, where the constants A and B are the slope and intercept of the linear plot respectively. The axial dispersion coefficient D_{ax} can be obtained from:

(i) the slope of the linear plots shown in Figure 4.5 for Case 4; or

(ii) the slope and intercept of the linear plots in Figure 4.5 from Equation (4.5) for Cases 5 and 6.

For Cases 4, 5 and 6, the D_{ax} (He and N_2 tracer) results with 0.25 ml sample loop for a fictitious glass beads bed (200 mm) are summarised in Tables 4.14 and 4.15, and the second central moment, $\mu_2^{'}$ is obtained from **Cat. A and Cat. B**.

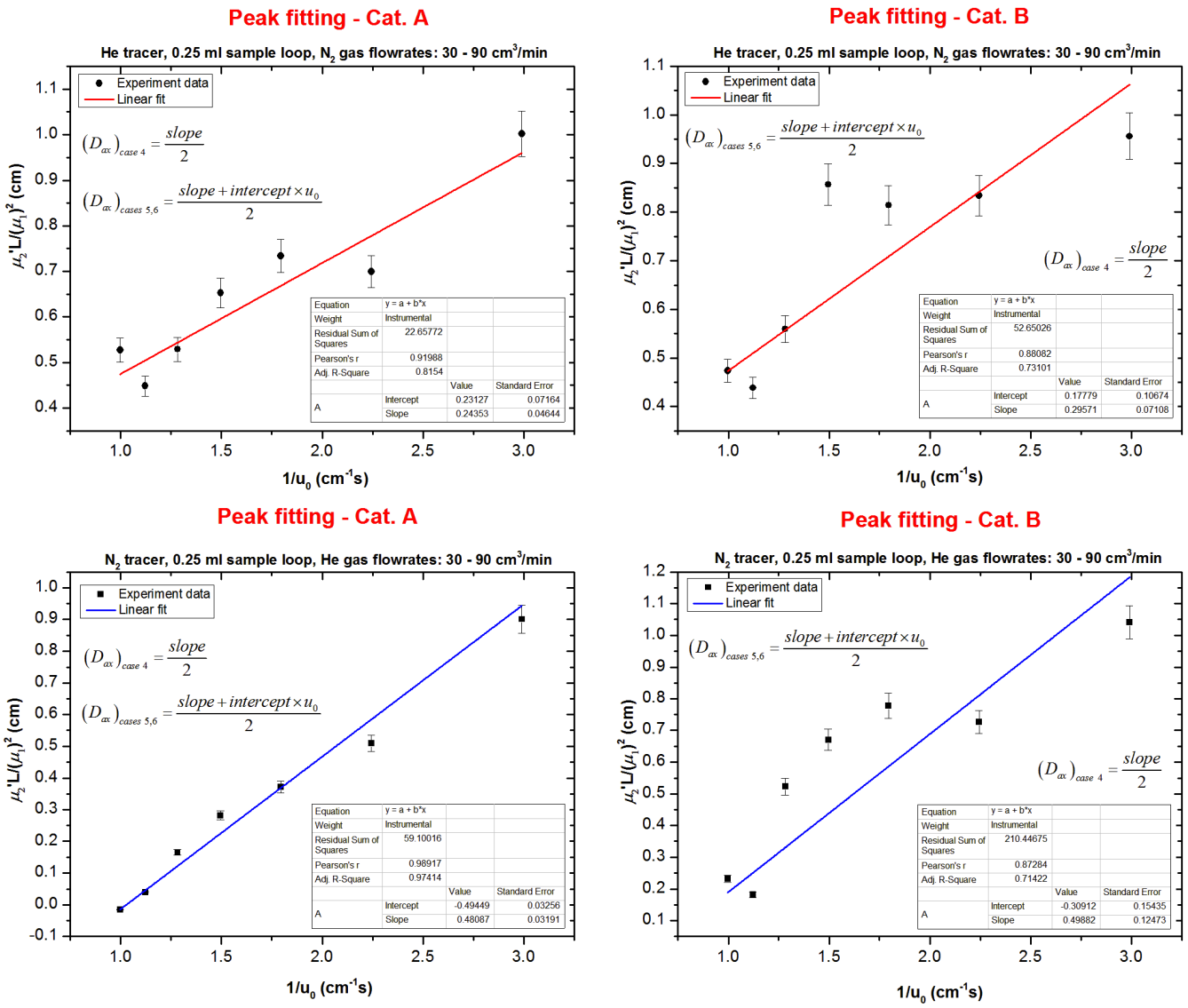

Figure 4.5: Axial dispersion coefficient, D_{ax}, for a 200 mm fictitious glass beads bed with He and N_2 tracer (0.25 ml), is obtained from the slope of the linear plot (plots shown are for **Cases 4, 5 and 6**).

Table 4.14: Axial dispersion coefficient results, D_{ax}, (He and N_2 tracer) for a **fictitious bed** (**200 mm)** packed with glass beads, and 2nd central moment is obtained from **Cat. A**.

Cases 4, 5 and 6: glass beads (0.25 ml sample loop)										
Superficial carrier gas velocity term, $1/u_0$ (cm^{-1} s)	**HETP: $\mu_2 L/(\mu_1)^2$ (cm)**		**Slope**		**Intercept**		**Axial dispersion coefficient, D_{ax} (cm^2 s^{-1})**			
							Case 5 and 6		**Case 4**	
	He	**N_2**	**He**	**N_2**	**He**	**N_2**	**He**	**N_2**	**He**	**N_2**
2.99140	1.002	0.901	0.246	0.440	0.237	-0.428	0.163	0.149	**0.123**	**0.220**
2.24355	0.700	0.510					0.176	0.125		
1.79484	0.734	0.371					0.189	0.101		
1.49570	0.653	0.282					0.202	0.077		
1.28203	0.529	0.165					0.215	0.053		
1.12178	0.448	0.040					0.229	0.029		
0.99713	0.527	-0.015					0.242	0.006		
Average, D_{ax} (cm^2 s^{-1})							**0.202**	**0.077**		

Table 4.15: Axial dispersion coefficient results, D_{ax}, (He and N_2 tracer) for a **fictitious bed** (**200 mm)** packed with glass beads, and 2nd central moment is obtained from **Cat. B**.

Cases 4, 5 and 6: glass beads (0.25 ml sample loop)										
Superficial carrier gas velocity term, $1/u_0$ (cm^{-1} s)	**HETP: $\mu_2 L/(\mu_1)^2$ (cm)**		**Slope**		**Intercept**		**Axial dispersion coefficient, D_{ax} (cm^2 s^{-1})**			
							Case 5 and 6		**Case 4**	
	He	**N_2**	**He**	**N_2**	**He**	**N_2**	**He**	**N_2**	**He**	**N_2**
2.99140	0.956	1.042	0.249	0.389	0.280	-0.070	0.171	0.183	**0.125**	**0.195**
2.24355	0.834	0.727					0.187	0.179		
1.79484	0.814	0.778					0.203	0.175		
1.49570	0.857	0.671					0.218	0.171		
1.28203	0.559	0.523					0.234	0.167		
1.12178	0.439	0.182					0.249	0.164		
0.99713	0.474	0.232					0.265	0.160		
Average, D_{ax} (cm^2 s^{-1})							**0.218**	**0.171**		

4.1.2 Investigation of dimensionless second central moment (σ_θ^2) and Péclet number (*Pe*)

The precise representative of the dispersion model for a packed-bed column is a bed packed with glass beads (i.e. Equation (3.16)). This equation is a simplified version of Equation (3.68). Since glass beads are non-porous, therefore only dispersion, convection and accumulation terms exist.

As mentioned in Hayes and Mmbaga (2012), for the dispersion model with high Péclet number, pulse response shows a near Gaussian-shaped distribution function, in this case, the Péclet number is 100. However, the dispersion model used in Hayes and Mmbaga (2012) was for plug flow in an empty column (i.e. Equation (3.32)). Whereas for plug flow in a packed-bed column described in this thesis, Equation (3.16) should be used. Therefore, the dimensionless scaling factors for Equation (3.16) are:

$$x^* = \frac{x}{L};\ \theta = \frac{t}{t_m};\ C_A^* = \frac{C_A}{C_{A0}};\ t_m = \frac{\varepsilon_b L}{u_0}.$$

Equation (3.16) becomes:

$$\frac{D_{ax}}{\varepsilon_b}\frac{\partial^2 C_A^*}{\partial x^{*2}}\frac{C_{A0}}{L^2} - \frac{u_0}{\varepsilon_b}\frac{\partial C_A^*}{\partial x^*}\frac{C_{A0}}{L} = \frac{\partial C_A^*}{\partial \theta}\frac{C_{A0}u_0}{\varepsilon_b L} \tag{4.6}$$

Rearrange Equation (4.6) yields:

$$\frac{D_{ax}}{u_0 L}\frac{\partial^2 C_A^*}{\partial x^{*2}} - \frac{\partial C_A^*}{\partial x^*} = \frac{\partial C_A^*}{\partial \theta} \tag{4.7}$$

Equation (4.7) is exactly the same as Equation (3.33) derived from Equation (3.32). Hence, Equation (3.39) which used to calculate the Péclet number of plug flow in an empty column, can now be used to calculate the Péclet number of the packed-bed column from dimensionless second central moment σ_θ^2, but with one condition. i.e. The Péclet number for plug flow in the packed-bed column is equivalent to the Péclet number calculated from Equation (3.39) divided by the bed porosity term, ε_b, as defined in Equation (3.18):

$$(Pe)_{packed-bed} = \frac{Pe}{\varepsilon_b} = \frac{u_i L}{D_{ax}} \tag{4.8}$$

The reason being that for packed-bed column, interstitial velocity u_i rather than superficial velocity u_0 is used for calculating the mean residence time and Péclet number.

To interpret the relationship of Péclet number and Gaussian-shaped curves, the first moment and second central moment results from the glass bead were used. The example calculations shown in this section used data from 0.25 ml sample loop with He tracer and N_2 carrier gas flowrates between 30 to 90 cm^3 min^{-1} for the 200 and 400 mm real columns.

Table 4.16: Dimensionless second central moment (σ_θ^2) and Péclet number (*Pe*) for 400 and 200 mm columns packed with glass beads (bed porosity: ε_b = 0.4446).

Carrier gas flowrate (cm^3/min)	**400 mm real column**		**200 mm real column**	
	Dimensionless 2nd central moment, $\sigma_\theta^{2\,(a)}$	**Péclet number, *Pe* (b)**	**Dimensionless 2nd central moment, σ_θ^2**	**Péclet number, *Pe***
30	0.0243 ± 0.0001	182.8	0.0437 ± 0.0001	100.6
40	0.0184 ± 0.0001	242.2	0.0343 ± 0.0001	128.9
50	0.0150 ± 0.0001	297.6	0.0227 ± 0.0001	195.9
60	0.0130 ± 0.0001	343.8	0.0190 ± 0.0001	234.5
70	0.0111 ± 0.0001	403.0	0.0168 ± 0.0001	265.5
80	0.0096 ± 0.0001	466.3	0.0144 ± 0.0001	310.1
90	0.0101 ± 0.0001	443.1	0.0134 ± 0.0001	333.4

Note: (*a*): The dimensionless second central moments σ_θ^2 in Table 4.16 are calculated using Cat. A:

Cat. A: $$\sigma_\theta^2 = \int_0^\infty (t/t_m - 1)^2 E(t) dt$$

and the difference between σ_θ^2 calculated by Cat. A and Cat. B is negligible.

Cat. B: $$\sigma_\theta^2 = \int_0^\infty (t/t_m)^2 E(t) dt - t_m^2$$

Therefore, σ_θ^2 results calculated by Cat. B were not shown. Besides, the peak areas (i.e. Peak 1 and 2) were calculated using peak integration in OriginPro 8.6 (i.e. numerical integration).

(*b*): Péclet number in Equation (3.39) can be solved by iteration method. For example, for the 400 mm column at carrier gas flowrate 30 cm^3/min, Equation (3.39) becomes:

$$Pe = \frac{2}{0.0243} - \frac{2}{0.0243Pe}\left[1 - \exp(-Pe)\right]$$

Let initial approximation be $(Pe)_0 = 100$, after six iteration a value of 81.3 was found. Then the Péclet number for the packed-bed column is:

$$Pe = \frac{81.3}{0.4446} = 182.8$$

Table 4.17: Péclet number (*Pe*) and axial dispersion coefficient (D_{ax}) for 400 and 200 mm columns packed with glass beads.

Interstitial carrier gas velocity (cm s^{-1})	**400 mm real column**		**200 mm real column**	
	Péclet number, *Pe*	**Axial dispersion coefficient, D_{ax} (cm^2 s^{-1})**	**Péclet number, *Pe***	**Axial dispersion coefficient, D_{ax} (cm^2 s^{-1})**
0.7519	182.8	0.165	100.6	0.149
1.0025	242.2	0.166	128.9	0.156
1.2532	297.6	0.168	195.9	0.128
1.5038	343.8	0.175	234.5	0.128
1.7544	403.0	0.174	265.5	0.132
2.0050	466.3	0.172	310.1	0.129
2.2557	443.1	0.204	333.4	0.135

From Tables 4.16 and 4.17, the following observation are made:

(i) For packed-bed experiments with γ-alumina beads and glass beads, the Péclet number from Table 4.16 shows that for both 200 and 400 mm real columns, $Pe > 100$ between the carrier gas flowrates studied. This justified the use of Gaussian area function in Peak fitting in OriginPro 8.6 and also explained the high RSQ values obtained in Peak fitting with Gaussian area function.

(ii) The axial dispersion coefficients, D_{ax} calculated for 200 and 400 columns, are similar to the D_{ax} results for the fictitious bed shown in Section 4.1.1.2. This indicates that Equation (3.39) is a good theoretical expression for calculating the Péclet number, *Pe* and the axial dispersion coefficient, D_{ax}.

4.1.3 Calculation of axial dispersion coefficient, D_{ax} for γ-alumina beads

The axial dispersion coefficient, D_{ax}, is now calculated for the fictitious bed (200 mm) packed with γ-alumina beads in the following ways:

Category 1: **Part (a): 2nd central moment method without adsorption equilibrium constant (Case 1: linear correlation)**: as described in Case 1, from moment matching, D_{ax} is evaluated linearly from the slope of Equation (A6.7), by plotting $\mu_2^{'}/(2L/u_i)$ *versus* $1/u_i^2$:

$$\frac{\mu_2^{'}}{2L/u_i} = \xi_i + \underbrace{\frac{D_{ax}}{\varepsilon_b}\left(1+\frac{(1-\varepsilon_b)\varepsilon}{\varepsilon_b}\right)^2\left(\frac{1}{u_i^2}\right)}_{\xi_d} \tag{4.9}$$

and the resistance parameter, ξ_0 is given by:

$$\xi_0 = \frac{(1-\varepsilon_b)\varepsilon}{\varepsilon_b} \tag{4.10}$$

Category 1: **Part (b): 2nd central moment method with K_A and K_A^c (Cases 2a, 2b and 2c: linear correlation):** for Cases 2a, 2b and 2c, from moment matching, D_{ax} is evaluated linearly from the slope of Equation (A7.13), by plotting $\mu_2^{'}/(2L/u_i)$ *versus* $1/u_i^2$ as shown in Figure 4.6:

$$\frac{\mu_2^{'}}{2L/u_i} = \xi_i + \frac{(D_{ax}/\varepsilon_b)(1+\xi_0)^2}{u_i^2} \tag{4.11}$$

and the resistance parameter, ξ_0 is calculated from:

$$\xi_0 = \frac{1-\varepsilon_b}{\varepsilon_b}\varepsilon\left(1+\frac{\rho_P K_A}{\varepsilon}\right) \tag{4.12}$$

where K_A is the adsorption equilibrium constant, and has units: $cm^3\ g^{-1}$.

For **Case 2c**, K_A in Equation (4.12) is replaced by K_A^c:

$$\xi_0 = \frac{1-\varepsilon_b}{\varepsilon_b}\varepsilon\left(1+\frac{\rho_P K_A^c}{\varepsilon}\right) \tag{4.13}$$

Therefore, the linear plots of variance, $\mu_2'/(2L/u_i)$ *versus* the superficial velocity, $1/u_i^2$ are shown in Figure 4.6, and the second central moment, μ_2', is obtained from **Cat. A and Cat. B**.

Experimental moment results for the fictitious γ-alumina beads bed (200 mm) are now used to determine the axial dispersion coefficient. For **Cases 1, 2a, 2b and 2c,** the D_{ax} results with He and N_2 tracer (0.25 ml sample loop) are summarised in Tables 4.18 and 4.19, and the second central moment, μ_2', is obtained from **Cat. A and Cat. B**.

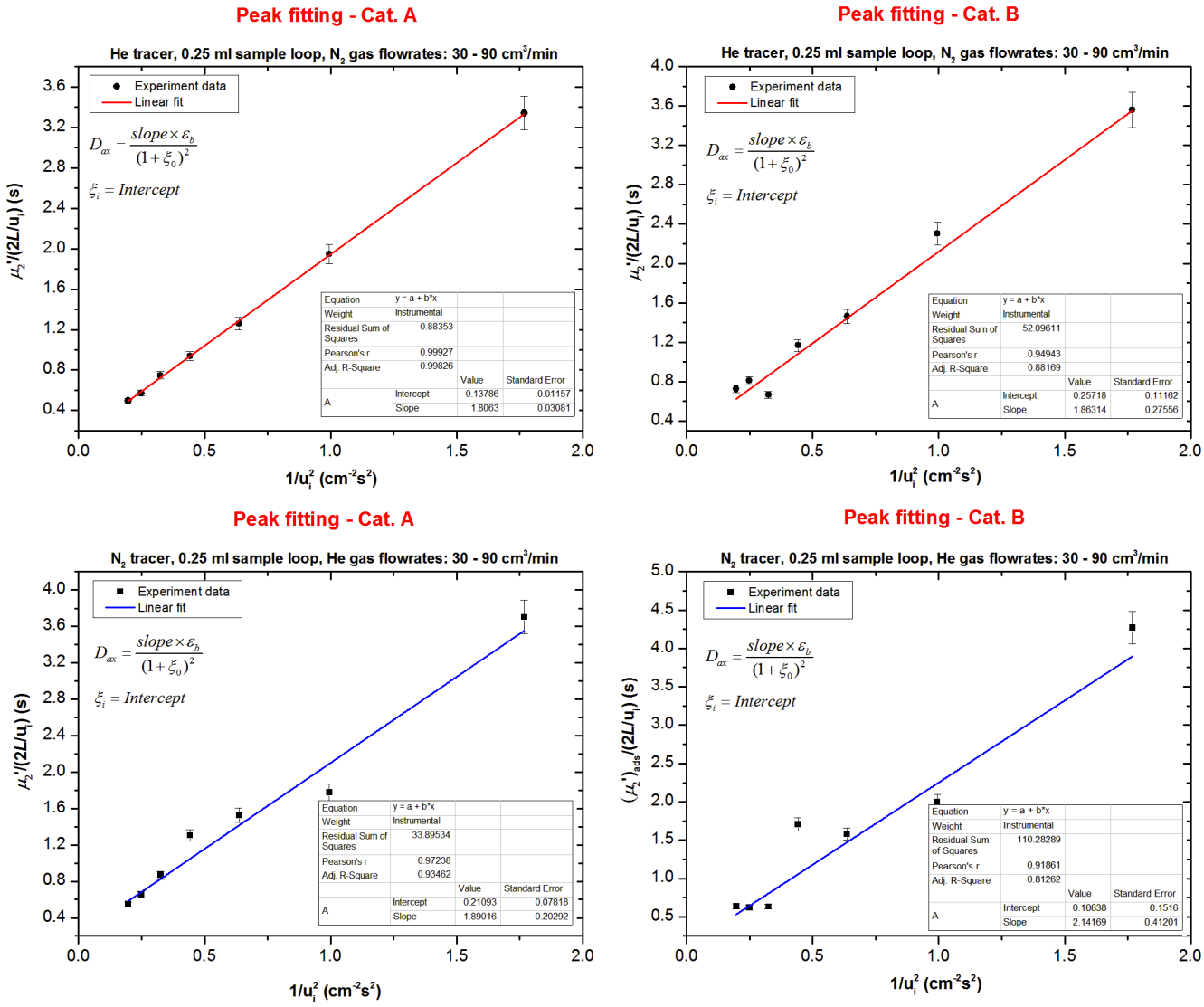

Figure 4.6: The axial dispersion coefficient, D_{ax} and the intraparticle diffusion resistance, ξ_i, for a fictitious γ-alumina beads bed (200 mm) with He and N_2 tracer (0.25 ml). These are calculated from the slope and intercept of the linear plot **(Cases 1, 2a, 2b and 2c**).

Table 4.18: Axial dispersion coefficients, D_{ax}, (He and N_2 tracer) for a **200 mm fictitious bed** packed with γ-alumina beads, and the 2nd central moment is obtained from **Cat. A**.

Cases 1, 2a, 2b and 2c: γ-alumina beads (0.25 ml sample loop)								
Interstitial velocity term, $1/u_i^2$ (cm^{-2} s^2)	**$\mu_2'/(2L/u_i)$ (s)**		**Case 1: D_{ax} (cm^2 s^{-1})**		**Case 2a and 2b: D_{ax} with K_A (cm^2 s^{-1})**		**Case 2c: D_{ax} with K_A^c (cm^2 s^{-1})**	
	He	**N_2**	**He**	**N_2**	**He**	**N_2**	**He**	**N_2**
1.76884	3.343	3.703	**0.265**	**0.342**	**0.169**	**0.229**	**0.220**	**0.230**
0.99497	1.947	1.777						
0.63678	1.261	1.525						
0.44221	0.939	1.304						
0.32489	0.749	0.868						
0.24874	0.573	0.658						
0.19654	0.496	0.548						

Table 4.19: Axial dispersion coefficients, D_{ax}, (He and N_2 tracer) for a **200 mm fictitious bed** packed with γ-alumina beads, and the 2nd central moment is obtained from **Cat. B**.

Cases 1, 2a, 2b and 2c: γ-alumina beads (0.25 ml sample loop)								
Interstitial velocity term, $1/u_i^2$ (cm^{-2} s^2)	**$\mu_2'/(2L/u_i)$ (s)**		**Case 1: D_{ax} (cm^2 s^{-1})**		**Case 2a and 2b: D_{ax} with K_A (cm^2 s^{-1})**		**Case 2c: D_{ax} with K_A^c (cm^2 s^{-1})**	
	He	**N_2**	**He**	**N_2**	**He**	**N_2**	**He**	**N_2**
1.76884	3.343	3.703	**0.276**	**0.330**	**0.171**	**0.189**	**0.248**	**0.221**
0.99497	1.947	1.777						
0.63678	1.261	1.525						
0.44221	0.939	1.304						
0.32489	0.749	0.868						
0.24874	0.573	0.658						
0.19654	0.496	0.548						

Category 2: **Part (b): 2nd central moment method with K_H (Cases 3a and 3b: linear correlation):** from moment matching, by plotting $\mu_2'/(2L/u_0)$ *versus* $1/u_0^2$ as shown in Figure 4.7, D_{ax} is evaluated linearly from the slope, which has the following form:

$$\frac{\mu_2'}{2L/u_0} = \varepsilon_b \xi_i + \frac{\varepsilon_b^2 D_{ax}\left(1+\xi_0\right)^2}{u_0^2} \tag{4.14}$$

and the resistance parameter, ξ_0 is given by:

$$\xi_0 = \frac{1-\varepsilon_b}{\varepsilon_b}\varepsilon\left(1+\frac{(1-\varepsilon)K_H}{\varepsilon}\right) \tag{4.15}$$

where K_H is the dimensionless adsorption equilibrium constant.

For **Cases 3a and 3b,** the D_{ax} results with He and N_2 tracer (0.25 ml sample loop) are summarised in Table 4.20, and the second central moment, μ_2', is obtained from **Cat. A and Cat. B**.

Table 4.20: Axial dispersion coefficients, D_{ax}, (He and N_2 tracer) for a **200 mm fictitious bed** packed with γ-alumina beads, and the 2nd central moment is obtained from **Cat. A and B**.

Cases 3a and 3b: γ-alumina beads (0.25 ml sample loop)								
Superficial velocity term, $1/u_0^2$ (cm^{-2} s^2)	**$\mu_2'/(2L/u_0)$ (s)**				**Axial dispersion coefficient, D_{ax} with K_H (cm^2 s^{-1})**			
	Cat. A		**Cat. B**		**Cat. A**		**Cat. B**	
	He	**N_2**	**He**	**N_2**	**He**	**N_2**	**He**	**N_2**
8.94847	1.486	1.647	1.583	1.900	**0.148**	**0.197**	**0.171**	**0.189**
5.03352	0.865	0.790	1.025	0.889				
3.22145	0.560	0.678	0.649	0.703				
2.23712	0.417	0.580	0.519	0.757				
1.64360	0.333	0.386	0.297	0.281				
1.25838	0.255	0.293	0.360	0.276				
0.99427	0.220	0.244	0.323	0.282				

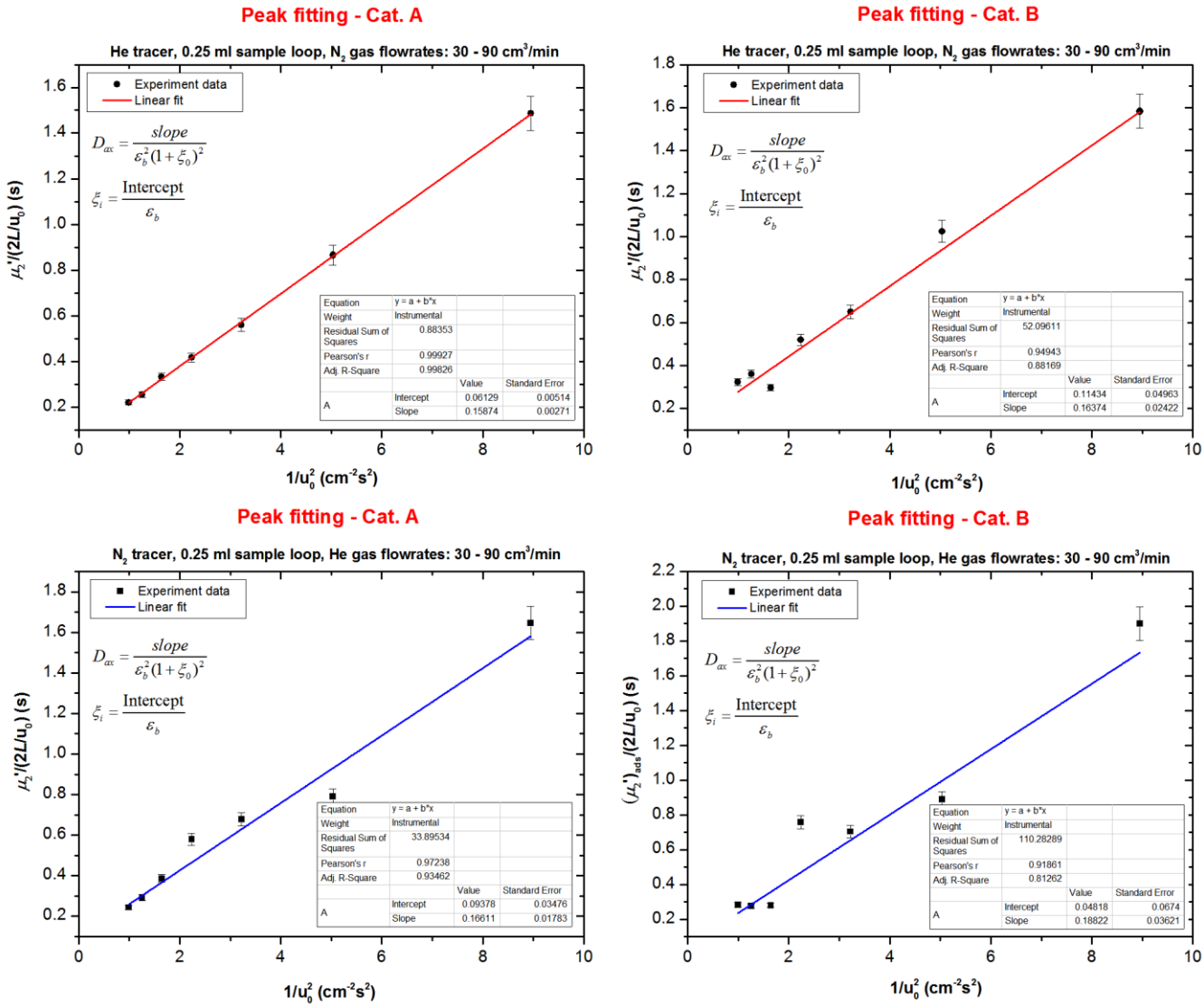

Figure 4.7: The axial dispersion coefficient, D_{ax} and the intraparticle diffusion resistance, ξ_i, for a fictitious γ-alumina beads bed (200 mm) with He and N_2 tracer (0.25 ml). These are calculated from the slope and intercept of the linear plot **(Cases 3a and 3b).**

Category 3: **HETP method, D_{ax} calculated by theoretical expression (Case 4: linear correlation):** for Case 4, D_{ax} is calculated based on the theoretical expression given by Ruthven (1984):

$$D_{ax} = \varepsilon_b \left(\gamma_1 D_{AB} + \gamma_2 2R \frac{u_0}{\varepsilon_b} \right) \tag{4.16}$$

γ_1 and γ_2 are:

$$\gamma_1 = 0.45 + 0.55\varepsilon \qquad \gamma_2 \approx 0.55 \tag{4.17}$$

Example calculations for molecular diffusivity, D_{AB}, and the Knudsen diffusivity, D_K, for He and N_2 are shown in Appendix 10. Hence, the linear plot of axial dispersion coefficient, D_{ax}, *versus* superficial carrier gas velocity, u_0, is shown in Figure 4.8.

For Case 4, the D_{ax} results calculated do not require:

(a) any moment results from the fictitious bed;

(b) any specific conditions e.g. sample loop volume, column length, etc.

The physical meaning of Equation (4.16) based on the terms used is:

(i) Assuming no interaction with pore walls (i.e. D_K is negligible), the molecular diffusivity, D_{AB}, in the intraparticle region contributes to the dispersion in the interparticle region, D_{ax}/ε_b;

(ii) The size of the particle, R in the packed bed contributes to the dispersion in the interparticle region, D_{ax}/ε_b;

(iii) Interstitial carrier gas velocity, u_i contributes to the dispersion in the interparticle region, D_{ax}/ε_b.

The D_{ax} results calculated are presented in Table 4.21.

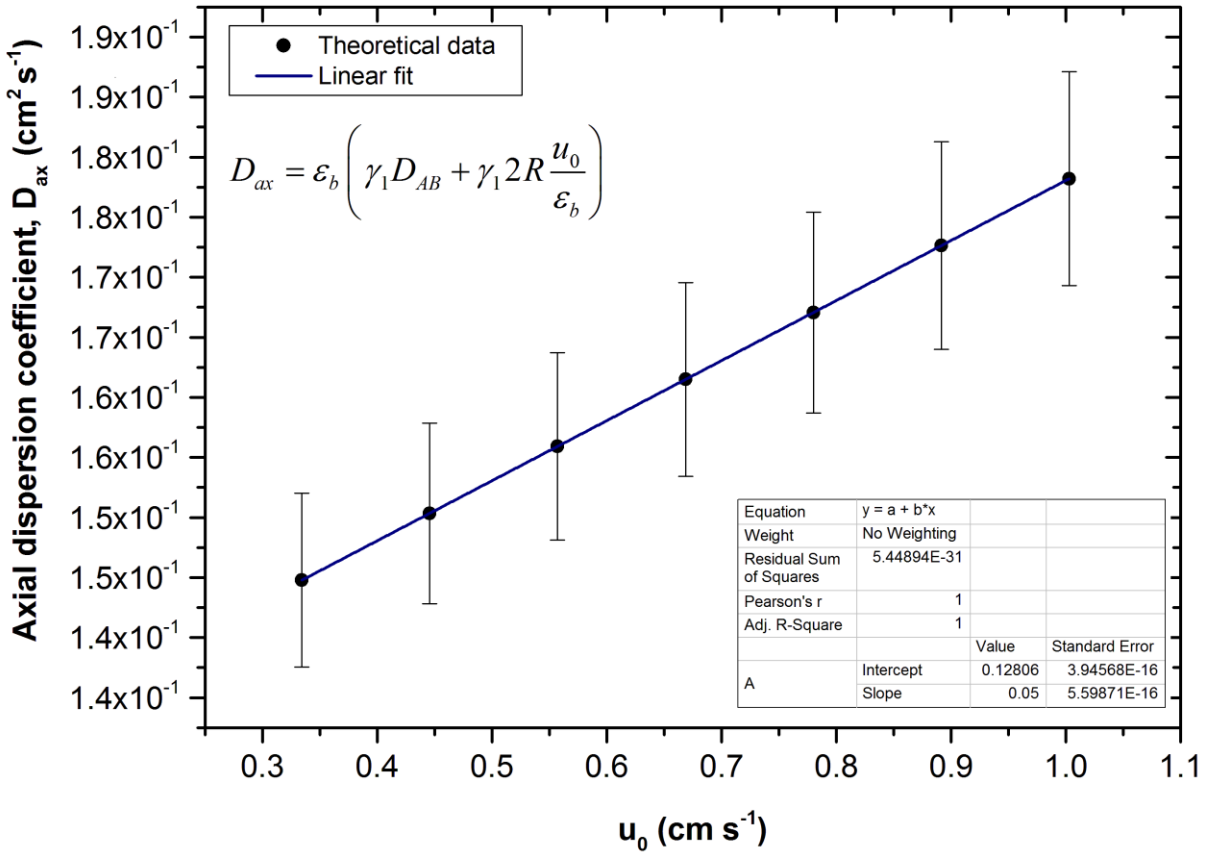

Figure 4.8: Axial dispersion coefficient, D_{ax}, as a function of u_0, was calculated from the theoretical expression given by Ruthven (1984) (plot is only applicable for **Case 4**).

Table 4.21: Axial dispersion coefficients, D_{ax}, (He and N_2 tracer) for a 200 mm fictitious bed packed with γ-alumina beads.

Case 4: γ-alumina beads (0.1, 0.25 and 0.5 ml sample loops)				
Superficial carrier gas velocity, u_0 ($cm\ s^{-1}$)	**Molecular diffusivity, D_{AB} ($m^2\ s^{-1}$)**	**γ_1**	**γ_2**	**Axial dispersion coefficient, D_{ax} ($cm^2\ s^{-1}$)**
0.33429	3.70704×10^{-5}	0.7770	0.50	0.145
0.44572				0.150
0.55715				0.156
0.66858				0.161
0.78001				0.167
0.89144				0.173
1.00287				0.178
Average axial dispersion coefficient, D_{ax} ($cm^2\ s^{-1}$)				**0.161**

Category 4: **HETP method (Case 5: Non-linear correlation)**: from moment matching, the HETP (i.e. degree of spread $\mu_2^{'}/(\mu_1)^2$ multiplied by the fictitious bed length, L), $\mu_2^{'}L/(\mu_1)^2$ is related to interstitial velocity, u_i as:

$$\text{HETP} = \frac{\mu_2^{'}L}{(\mu_1)^2} = 2\frac{D_{ax}}{\varepsilon_b u_i} + \left[\frac{\frac{2}{15}\frac{\varepsilon_b}{(1-\varepsilon_b)}R^2}{\left(1+\frac{1}{\xi_0}\right)^2}\left(\frac{1}{D_{eff}}+\frac{5}{k_f R}\right)\right]u_i \tag{4.18}$$

The resistance parameter, ξ_0 in Equation (4.18) is given as:

$$\xi_0 = \frac{(1-\varepsilon_b)\varepsilon}{\varepsilon_b}(1+K_a) \tag{4.19}$$

where K_a is a dimensionless adsorption equilibrium constant as defined in **Particle Model 1** in Chapter 3.

For non-linear curve fitting, D_{ax} is calculated from the constant A and B as:

For Case 5: $$D_{ax} = \frac{\varepsilon_b\left(A+Bu_i\right)}{2} \tag{4.20}$$

As a result, the non-linear curve plots of $\mu_2^{'}L/(\mu_1)^2$ *versus* interstitial velocity, u_i, for a fictitious γ-alumina beads bed (200 mm) are shown in Figure 4.9, and the second central moment, $\mu_2^{'}$ is obtained from **Cat. A and Cat. B**.

For a fictitious γ-alumina beads bed (200 mm), the D_{ax} results for **Case 5** with He and N_2 tracer (0.25 ml sample loop) are summarised in Tables 4.22 and 4.23, and the second central moment, $\mu_2^{'}$, is obtained from **Cat. A and Cat. B**.

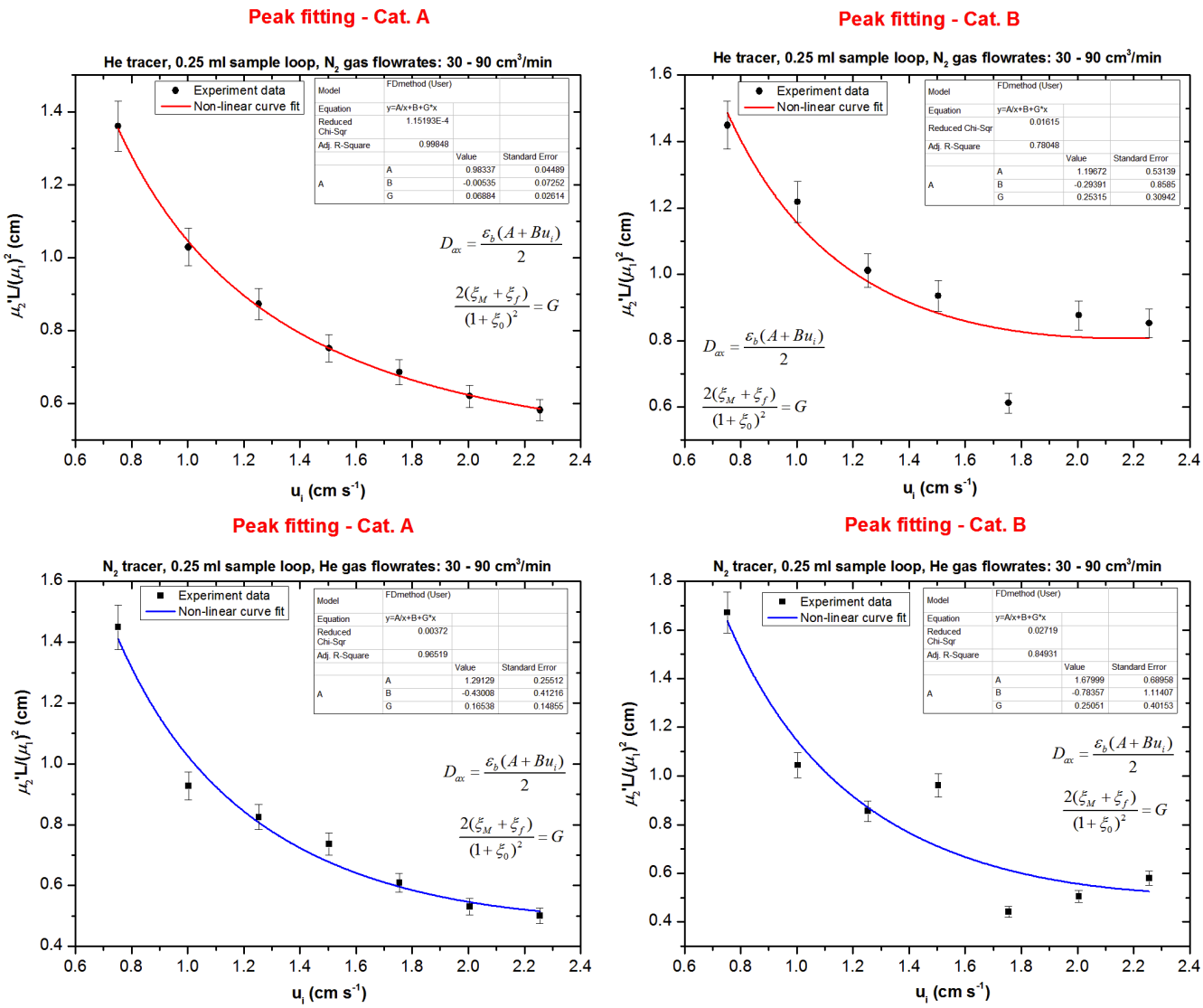

Figure 4.9: The axial dispersion coefficient, D_{ax} and the intraparticle diffusion resistance, ξ_i, for a fictitious γ-alumina beads bed (200 mm) with He and N_2 tracer (0.25 ml). These are calculated from the constants: *A*, *B* and *G* of the non-linear plot **(Case 5).**

Table 4.22: Axial dispersion coefficients, D_{ax}, (He and N_2 tracer) for a **200 mm fictitious bed** packed with γ-alumina beads, and the 2nd central moment is obtained from **Cat. A**.

Case 5: γ-alumina beads (0.25 ml sample loop)								
Interstitial carrier gas velocity, u_i (cm s^{-1})	**HETP: $\mu_2 L/(\mu_1)^2$ (cm)**		***A***		***B***		**Axial dispersion coefficient, D_{ax} (cm^2 s^{-1})**	
	He	**N_2**	**He**	**N_2**	**He**	**N_2**	**He**	**N_2**
0.75189	1.360	1.449	0.9834	1.2913	-0.0054	-0.4301	0.218	0.215
1.00252	1.029	0.928					0.217	0.191
1.25316	0.873	0.825					0.217	0.167
1.50379	0.751	0.736					0.217	0.143
1.75442	0.686	0.609					0.217	0.119
2.00505	0.620	0.530					0.216	0.095
2.25568	0.582	0.501					0.216	0.071
Average, D_{ax} (cm^2 s^{-1})							**0.217**	**0.143**

Table 4.23: Axial dispersion coefficients, D_{ax}, (He and N_2 tracer) for a **200 mm fictitious bed** packed with γ-alumina beads, and the 2nd central moment is obtained from **Cat. B**.

Case 5: γ-alumina beads (0.25 ml sample loop)								
Interstitial carrier gas velocity, u_i (cm s^{-1})	**HETP: $\mu_2 L/(\mu_1)^2$ (cm)**		***A***		***B***		**Axial dispersion coefficient, D_{ax} (cm^2 s^{-1})**	
	He	**N_2**	**He**	**N_2**	**He**	**N_2**	**He**	**N_2**
0.75189	1.449	1.672	1.1967	1.6800	-0.2939	-0.7836	0.217	0.242
1.00252	1.218	1.044					0.201	0.199
1.25316	1.011	0.855					0.184	0.155
1.50379	0.935	0.961					0.168	0.112
1.75442	0.611	0.443					0.151	0.068
2.00505	0.876	0.505					0.135	0.024
2.25568	0.852	0.579					0.119	-0.019
Average, D_{ax} (cm^2 s^{-1})							**0.168**	**0.112**

Category 5: **HETP method (Case 6: Non-linear correlation):** from moment matching, the HETP (degree of spread × fictitious bed length) i.e. $\mu_2^{'}L/(\mu_1)^2$, is related to interstitial velocity, u_0 as:

$$\text{HETP} = \frac{\mu_2^{'}L}{(\mu_1)^2} = 2\frac{D_{ax}}{u_0} + \left\{ \frac{\frac{2}{15}\frac{R^2}{(1-\varepsilon_b)}}{\left(1+\frac{1}{\xi_0}\right)^2}\left(\frac{1}{D_{eff}} + \frac{5}{k_f R}\right)\right\} u_0 \tag{4.21}$$

The resistance parameters, ξ_0 for Equation (4.21) is defined as:

$$\xi_0 = \frac{(1-\varepsilon_b)\varepsilon}{\varepsilon_b}\left(1+\frac{(1-\varepsilon)}{\varepsilon}K_H\right) \tag{4.22}$$

For non-linear curve fitting, D_{ax} for Case 6 is calculated from the constants A and B as:

For Case 6: $$D_{ax} = \frac{A+Bu_0}{2} \tag{4.23}$$

Hence, the non-linear curve plots of $\mu_2^{'}L/(\mu_1)^2$ *versus* interstitial velocity, u_0, for a fictitious γ-alumina beads bed (200 mm) are shown in Figure 4.10, and the second central moment, $\mu_2^{'}$ is obtained from **Cat. A and Cat. B**.

For a fictitious γ-alumina beads bed (200 mm), the D_{ax} results for **Case 6** with He and N_2 tracer (0.25 ml sample loop) are summarised Tables 4.24 and 4.25, and the second central moment, $\mu_2^{'}$, is obtained from **Cat. A and Cat. B**.

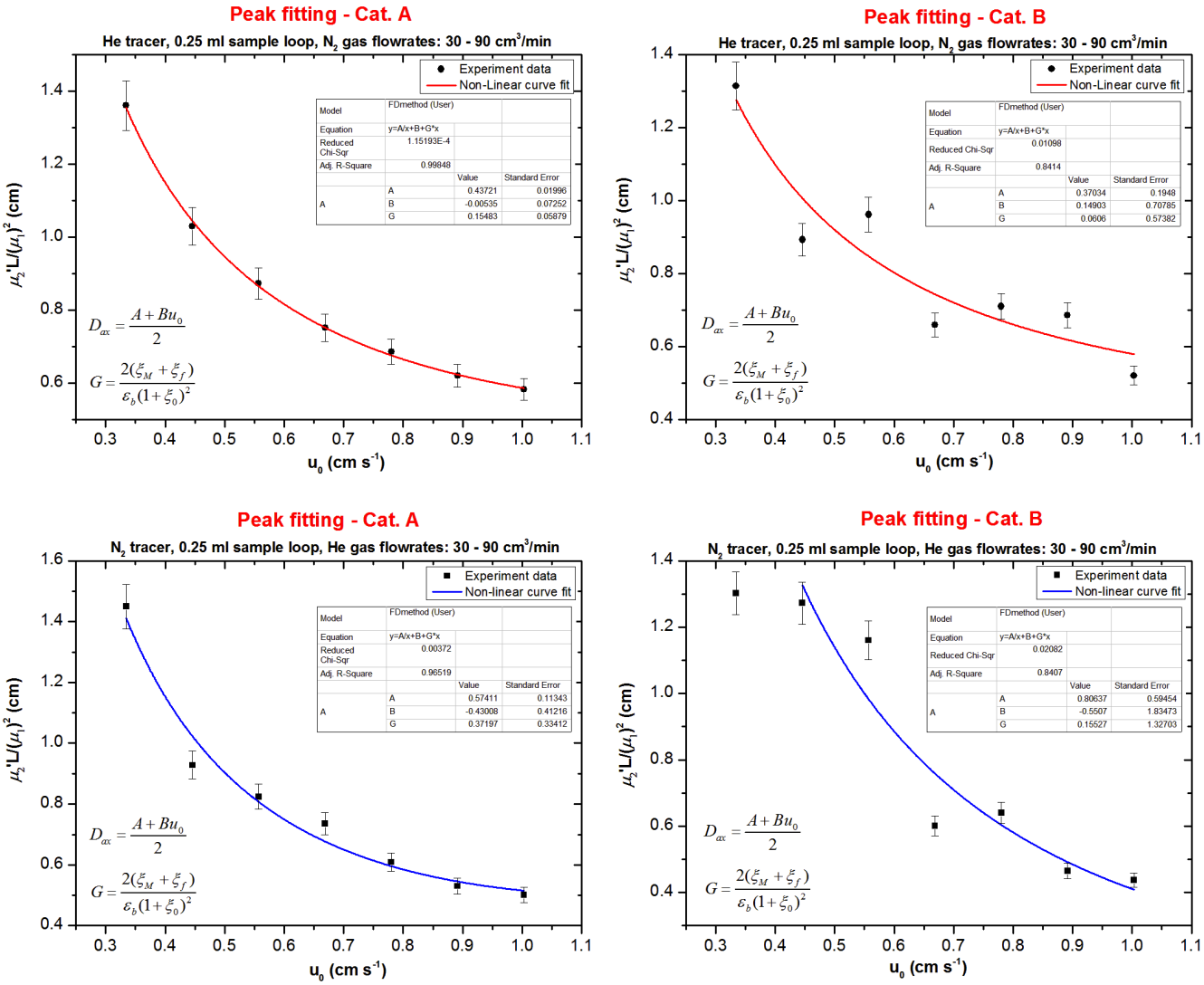

Figure 4.10: The axial dispersion coefficient, D_{ax} and the intraparticle diffusion resistance, ξ_M, for a fictitious γ-alumina beads bed (200 mm) with He and N_2 tracer (0.25 ml). These are calculated from the constants: *A*, *B* and *G* of the non-linear plot (**Case 6**).

Table 4.24: Axial dispersion coefficients, D_{ax}, (He and N_2 tracer) for a **200 mm fictitious bed** packed with γ-alumina beads, and the 2nd central moment is obtained from **Cat. A**.

Case 6: γ-alumina beads (0.25 ml sample loop)								
Superficial carrier gas velocity, u_i (cm s^{-1})	**HETP: $\mu_2 L/(\mu_1)^2$ (cm)**		***A***		***B***		**Axial dispersion coefficient, D_{ax} (cm^2 s^{-1})**	
	He	**N_2**	**He**	**N_2**	**He**	**N_2**	**He**	**N_2**
0.75189	1.360	1.449	0.4372	0.5741	-0.0054	-0.4301	0.218	0.215
1.00252	1.029	0.928					0.217	0.191
1.25316	0.873	0.825					0.217	0.167
1.50379	0.751	0.736					0.217	0.143
1.75442	0.686	0.609					0.217	0.119
2.00505	0.620	0.530					0.216	0.095
2.25568	0.582	0.501					0.216	0.071
Average, D_{ax} (cm^2 s^{-1})							**0.217**	**0.143**

Table 4.25: Axial dispersion coefficients, D_{ax}, (He and N_2 tracer) for a **200 mm fictitious bed** packed with γ-alumina beads, and the 2nd central moment is obtained from **Cat. B**.

Case 6: γ-alumina beads (0.25 ml sample loop)								
Superficial carrier gas velocity, u_i (cm s^{-1})	**HETP: $\mu_2 L/(\mu_1)^2$ (cm)**		***A***		***B***		**Axial dispersion coefficient, D_{ax} (cm^2 s^{-1})**	
	He	**N_2**	**He**	**N_2**	**He**	**N_2**	**He**	**N_2**
0.75189	1.449	1.672	0.4314	0.7469	0.1296	-0.7836	0.237	0.242
1.00252	1.218	1.044					0.245	0.199
1.25316	1.011	0.855					0.252	0.155
1.50379	0.935	0.961					0.259	0.112
1.75442	0.611	0.443					0.266	0.068
2.00505	0.876	0.505					0.273	0.024
2.25568	0.852	0.579					0.281	-0.019
Average, D_{ax} (cm^2 s^{-1})							**0.259**	**0.112**

4.1.4 Calculation of the axial dispersion coefficient: Péclet number and Reynolds number with hydraulic diameter

As described in Hayes and Kolaczkowski (1997), the dispersion coefficients in the radial and axial direction can be calculated. For a Reynolds number > 40 (which is in the turbulent region), then:

$$(Pe)_r = 10 = \frac{D_B u_0}{E_r} \tag{4.24}$$

$$(Pe)_z = 2 = \frac{D_B u_0}{E_z} \tag{4.25}$$

where D_B is the hydraulic diameter of the bed, and $E_{r,z}$ is the dispersion coefficient in the r, z – directions.

For the packed bed experiments shown in this thesis, the hydraulic diameter, D_B, of the 1 mm glass and γ-alumina beads is:

$$D_B = \frac{D_t}{1.5\left(\frac{D_t}{D_p}\right)(1-\varepsilon_b)+1} = \frac{13.8\,\text{mm}}{1.5\times\frac{13.8\,\text{mm}}{1\,\text{mm}}\times(1-0.4446)+1} = 1.104\,\text{mm} \tag{4.26}$$

and the Reynolds number, Re_H, can be calculated, using the following properties (He or N_2 gas in the bulk phase):

- Density (using ideal gas law) = 1.1567 kg m^{-3} (N_2) and 0.1653 kg m^{-3} (He);
- Dynamic viscosity = 1.8 $\times 10^{-5}$ Pa.s (N_2); 2.0 $\times 10^{-5}$ Pa.s (He) at 295.15 K;
- Superficial carrier gas velocity: 0.3343 – 1.0029 cm s^{-1}.

<u>An example calculation is provided:</u>

$$\text{Re}_H = \frac{D_B u_0 \rho}{\mu} = \frac{(1.104\times10^{-3}\ \text{m})\times\left(0.3343\times10^{-2}\,\frac{\text{m}}{\text{s}}\right)\times\left(1.1567\,\frac{\text{kg}}{\text{m}^3}\right)}{0.000018} = 0.237 \tag{4.27}$$

From Equation (4.27), the Reynolds number, would be between **0.237** to **0.712** for N_2, and between **0.031** to **0.092** for He. Therefore, Equations (4.24) and (4.25) are not suitable because the Re_H number is too low, and corresponds to the viscous flow region.

4.1.5 Summary of values for the axial dispersion coefficient, D_{ax}

Using the 0.25 ml sample loop and the moment results for the fictitious bed (200 mm), the results of the different ways in which D_{ax} has been calculated are presented in:

- Tables 4.12 to 4.15 for the glass beads, and;
- Tables 4.18 to 4.25 for the γ-alumina beads.

From these comparative results, the following additional observations are made:

D_{ax} for glass beads:

(ii) The values for Cases 1, 2a, 2b, 2c, 3a and 3b, obtained with the 2nd central moment method are the same, and the results are comparable with the values in the literature (see Table 4.29).

(iii) Cases 5 and 6 produce the same values with the HETP method. For Case 4, the values that are found with the HETP method are similar to Cases 5 and 6 (with just a slight difference). This is because in Case 4, D_{ax} is treated as a constant, whereas in Cases 5 and 6, D_{ax} is interpreted as a function of velocity.

(iv) Cat. A and B produce slightly different values, but they are of a similar order in magnitude in each case studied.

D_{ax} for γ-alumina beads:

(v) For Cases 1, 2a, 2b, 2c, 3a and 3b, with the 2nd central moment method, the difference in D_{ax} values with, or without the adsorption equilibrium constant (i.e. Case 1 and other cases) is small, and the difference between the different Particle Models (i.e. K_A for Cases 2, and K_H for Case 3) is very small.

(vi) For Case 4, the average D_{ax} value calculated (0.161 cm^2 s^{-1}) based on the theoretical expression is similar to other cases using moment matching.

(vii) The D_{ax} values are the same for Cases 5 and 6 with the HETP method.

(viii) Cat. A and B produce slightly different results, but they are of a similar order in magnitude.

Comparing glass and γ-alumina beads

(ix) In some of the cases they are similar, e.g.

Cases 4, 5 and 6 for the glass beads: 0.123 – 0.220 $cm^2\ s^{-1}$;

Cases 2 to 6 for the γ-alumina beads: 0.112 – 0.248 $cm^2\ s^{-1}$.

(x) In others they are different, e.g.

Cases 1 to 3 for the glass beads: 0.095 – 0.104 $cm^2\ s^{-1}$;

Case 1 for the γ-alumina beads: 0.265 – 0.342 $cm^2\ s^{-1}$.

In conclusion, D_{ax} is strongly correlated to velocity, as suggested by the theoretical expression in Equation (4.16).

Table 4.26: Average values of axial dispersion coefficient, D_{ax}, (He and N_2 tracer) for a **fictitious bed** (200 mm) packed with **glass beads**, and the 2nd central moment, $\mu_2^{'}$ was obtained from **Cat. A and Cat. B.**

Glass beads		**Axial dispersion coefficient, D_{ax} ($cm^2\ s^{-1}$, helium as tracer)**	***RSQ* *(Helium as tracer)***	**Axial dispersion coefficient, D_{ax} ($cm^2\ s^{-1}$, nitrogen as tracer)**	***RSQ* *(Nitrogen as tracer)***
Cat. A	**Cases 1, 2a, 2b, 2c, 3a and 3b**	$1.13 \times 10^{-1} \pm 0.0145$	*0.9495 ±0.0333*	$9.67 \times 10^{-2} \pm 0.0091$	*0.9844 ±0.0034*
	Case 4	$1.64 \times 10^{-1} \pm 0.0042$	*0.9132 ±0.0610*	$2.23 \times 10^{-1} \pm 0.0026$	*0.9890 ±0.0042*
	Cases 5 and 6	$1.70 \times 10^{-1} \pm 0.0433$	*0.9132 ±0.0610*	$7.76 \times 10^{-2} \pm 0.0030$	*0.9890 ±0.0042*
Cat. B	**Cases 1, 2a, 2b, 2c, 3a and 3b**	$1.33 \times 10^{-1} \pm 0.0274$	*0.8693 ±0.0645*	$1.35 \times 10^{-1} \pm 0.0318$	*0.9280 ±0.0229*
	Case 4	$2.36 \times 10^{-1} \pm 0.0852$	*0.7193 ±0.0047*	$3.45 \times 10^{-1} \pm 0.1741$	*0.8334 ±0.0156*
	Cases 5 and 6	$1.88 \times 10^{-1} \pm 0.0815$	*0.7193 ±0.0047*	$1.76 \times 10^{-1} \pm 0.0540$	*0.8334 ±0.0156*

Table 4.27: Average values of axial dispersion coefficient, D_{ax}, (He and N_2 tracer) for a **fictitious bed** (200 mm) packed with **γ-alumina beads**, and the 2nd central moment, $\mu_2^{'}$ was obtained from **Cat. A.**

γ-alumina beads		**Axial dispersion coefficient, D_{ax} ($cm^2\ s^{-1}$, helium as tracer)**	***RSQ* *(Helium as tracer)***	**Axial dispersion coefficient, D_{ax} ($cm^2\ s^{-1}$, nitrogen as tracer)**	***RSQ* *(Nitrogen as tracer)***
Cat. A	**Case 1 (without K_a)**	$2.67 \times 10^{-1} \pm 0.0028$	*0.9934 ± 0.0082*	$3.44 \times 10^{-1} \pm 0.0001$	*0.9616 ± 0.0118*
	Cases 2a and 2b (with K_A)	$1.70 \times 10^{-1} \pm 0.0147$	*0.9934 ± 0.0082*	$2.39 \times 10^{-1} \pm 0.0121$	*0.9616 ± 0.0118*
	Case 2c (with K_A^c)	$2.27 \times 10^{-1} \pm 0.0050$	*0.9934 ± 0.0082*	$1.94 \times 10^{-1} \pm 0.0454$	*0.9616 ± 0.0118*
	Cases 3a and 3b (with K_H)	$1.69 \times 10^{-1} \pm 0.0167$	*0.9934 ± 0.0082*	$2.19 \times 10^{-1} \pm 0.0158$	*0.9616 ± 0.0118*
	Case 4 (with D_{AB} and u_0)	$1.61 \times 10^{-1} \pm 0.0000$	*1.000 ± 0.0000*	$1.61 \times 10^{-1} \pm 0.0000$	*1.000 ± 0.0000*
	Case 5 (with K_H)	$2.68 \times 10^{-1} \pm 0.0365$	*0.9752 ± 0.0323*	$2.63 \times 10^{-1} \pm 0.0861$	*0.9853 ± 0.0145*
	Case 6 (with K_H)	$2.58 \times 10^{-1} \pm 0.0350$	*0.9947 ± 0.0052*	$2.25 \times 10^{-1} \pm 0.0654$	*0.9825 ± 0.0137*

Table 4.28: Average values of axial dispersion coefficient, D_{ax}, (He and N_2 tracer) for a **fictitious bed** (200 mm) packed with **γ-alumina beads**, and the 2nd central moment, $\mu_2^{'}$ was obtained from **Cat. B.**

γ-alumina beads		**Axial dispersion coefficient, D_{ax} ($cm^2\ s^{-1}$, helium as tracer)**	***RSQ* *(Helium as tracer)***	**Axial dispersion coefficient, D_{ax} ($cm^2\ s^{-1}$, nitrogen as tracer)**	***RSQ* *(Nitrogen as tracer)***
Cat. B	**Case 1 (without K_a)**	$2.96 \times 10^{-1} \pm 0.0538$	*0.9783 ± 0.0128*	$3.04 \times 10^{-1} \pm 0.0193$	*0.9257 ± 0.0162*
	Cases 2a and 2b (with K_A)	$2.19 \times 10^{-1} \pm 0.0327$	*0.9783 ± 0.0128*	$2.12 \times 10^{-1} \pm 0.0316$	*0.9257 ± 0.0162*
	Case 2c (with K_A^c)	$2.68 \times 10^{-1} \pm 0.0331$	*0.9783 ± 0.0128*	$2.18 \times 10^{-1} \pm 0.0246$	*0.9257 ± 0.0162*
	Cases 3a and 3b (with K_H)	$2.03 \times 10^{-1} \pm 0.0395$	*0.9783 ± 0.0128*	$1.93 \times 10^{-1} \pm 0.0040$	*0.9257 ± 0.0162*
	Case 4 (with D_{AB} and u_0)	$1.61 \times 10^{-1} \pm 0.0000$	*1.000 ± 0.0000*	$1.61 \times 10^{-1} \pm 0.0000$	*1.000 ± 0.0000*
	Case 5 (with K_H)	$1.88 \times 10^{-1} \pm 0.0331$	*0.8047 ± 0.0264*	$1.34 \times 10^{-1} \pm 0.0627$	*0.7929 ± 0.0738*
	Case 6 (with K_H)	$2.19 \times 10^{-1} \pm 0.0412$	*0.7997 ± 0.0315*	$1.51 \times 10^{-1} \pm 0.0483$	*0.7769 ± 0.0963*

Table 4.29: Examples of D_{ax} values found in the literature and the average D_{ax} calculated in this thesis.

	Particle radius (mm)	**Bed porosity**	**Particle porosity**	**Superficial carrier gas velocity (cm s^{-1})**	**Axial dispersion coefficient (cm^2 s^{-1})**
Case 1: Baiker *et al.* (1982)	1.7 – 2.45	0.320 – 0.614	0.429 – 0.458	0.42 – 1.86	0.146 – 0.325
Case 2a: Guangsuo *et al*. (2000)	2.711	0.1854	N/A	0.59 – 5.31	0.361 – 1.096
Case 2c: Schneider and Smith (1968)	R_1: 0.11	ε_{b1}: 0.378	0.486	1.2 – 15	0.103 – 0.130
	R_2: 0.39	ε_{b2}: 0.360			
	R_3: 0.5	ε_{b3}: 0.340			
This thesis	1.0	0.4446	0.5946	0.33 – 1.00	**0.078 – 0.345 (glass beads)** **0.134 – 0.344 (γ-alumina beads)**

4.2 Moment matching to determine D_{eff} and tortuosity factor τ for γ-alumina beads

4.2.1 Calculation of external mass transfer coefficient, k_f

The external mass transfer coefficient, k_f, was calculated according to the theoretical expression given in the literature (Wakao *et al.*, 1958; Do, 1998). Therefore, recalling Equations (3.98) and (3.112) in Chapter 3:

In Wakao *et al.* (1958), the external mass transfer coefficient, k_f, was obtained from:

$$\frac{2k_f R}{D_{AB}} = 2.00 + 1.45\,\mathrm{Re_p}^{1/2}\,\mathrm{Sc}^{1/3} \qquad \text{For Re} < 100 \tag{4.28}$$

where R is the particle radius. The Reynolds number, $\mathrm{Re_p}$ of the particle, is equivalent to the Reynolds number of packed bed, Re, and it is defined as:

$$\mathrm{Re_p} = \frac{D_p u_0 \rho}{\mu} \tag{4.29}$$

The Schmidt number is:

$$\mathrm{Sc} = \frac{\nu}{D_{AB}} \tag{4.30}$$

where ν is the kinematic viscosity and it is equal to dynamic viscosity divide by density of fluid or gas in the bulk phase.

A similar theoretical expression for external mass transfer coefficient, k_f is given in Do (1998) as:

$$\frac{k_f (2R_p)}{D_{AB}} = 2 + 1.1\left(\frac{u 2R_p \rho}{\mu}\right)^{0.6}\left(\frac{\nu}{D_{AB}}\right)^{\frac{1}{3}} \tag{4.31}$$

At 295.15 K and 1.013 bar, the $\mathrm{Re_p}$ of the γ-alumina beads with He and N_2 tracer are tabulated in Table 4.30. The Schmidt number for γ-alumina beads with He and N_2 tracer are: **1.7523** and **0.2253** respectively.

Therefore, the results of the mass transfer coefficient, k_f, calculated from Equations (4.28) and (4.31) at different carrier gas velocities are presented in Tables 4.31 and 4.32.

Table 4.30: The Reynolds number (295.15 K and 1.013 bar) of the γ-alumina beads calculated at different superficial carrier gas velocities.

Superficial velocity, u_0 (m s^{-1})	**Gas density, ρ at 295.15 K (kg m^{-3})**		**Dynamic viscosity, μ (kg m^{-1} s^{-1})**		**Particle Reynolds number, Re_p**	
	He	**N_2**	**He**	**N_2**	**He**	**N_2**
0.0033429	0.1567	1.1567	0.000020	0.000018	2.76×10^{-2}	2.15×10^{-1}
0.0044572					3.68×10^{-2}	2.86×10^{-1}
0.0055715					4.60×10^{-2}	3.58×10^{-1}
0.0066858					5.52×10^{-2}	4.30×10^{-1}
0.0078001					6.45×10^{-2}	5.01×10^{-1}
0.0089144					7.37×10^{-2}	5.73×10^{-1}
0.0100287					8.29×10^{-2}	6.44×10^{-1}

Table 4.31: The external mass transfer coefficient, k_f, calculated for helium and nitrogen at different superficial velocities, using Equation (4.28) (Wakao *et al.*, 1958).

Constant		**$Re^{1/2}$**		**$Sc^{1/3}$**		**D_{AB} (m^2 s^{-1})**		**External mass transfer coefficient, k_f (m s^{-1})**	
A	***B***	**He**	**N_2**	**He**	**N_2**	**He**	**N_2**	**He**	**N_2**
2	1.45	0.1662	0.4635	1.2056	0.6085	6.91×10^{-5}		0.1582	0.1664
2	1.45	0.1919	0.5352					0.1613	0.1707
2	1.45	0.2146	0.5983					0.1640	0.1746
2	1.45	0.2350	0.6555					0.1665	0.1781
2	1.45	0.2539	0.7080					0.1688	0.1813
2	1.45	0.2714	0.7569					0.1709	0.1842
2	1.45	0.2879	0.8028					0.1729	0.1870

Table 4.32: The external mass transfer coefficient, k_f, calculated for helium and nitrogen at different superficial velocities, using Equation (4.31) (Do, 1998).

Constant		**$Re^{0.6}$**		**$Sc^{1/3}$**		**D_{AB} ($m^2 s^{-1}$)**		**External mass transfer coefficient, k_f ($m s^{-1}$)**	
A	***B***	**He**	**N_2**	**He**	**N_2**	**He**	**N_2**	**He**	**N_2**
2	1.1	0.1161	0.3974	1.2056	0.6085	6.91×10^{-5}		0.1488	0.1565
2	1.1	0.1380	0.4723					0.1508	0.1600
2	1.1	0.1577	0.5399					0.1526	0.1631
2	1.1	0.1759	0.6024					0.1542	0.1660
2	1.1	0.1930	0.6607					0.1558	0.1687
2	1.1	0.2091	0.7158					0.1573	0.1712
2	1.1	0.2244	0.7683					0.1587	0.1736

4.2.1.1 Calculation of external mass transfer resistance, ξ_e

The external mass transfer resistance, ξ_e, for Case 1 has not been presented, because when it was considered, it was obvious that with an adsorption equilibrium constant, $K_a = 0$, then the value would be very small and much less than the other cases considered.

Category 1: **Cases 2b and 2c (linear method): External mass transfer coefficient expression from Wakao *et al.* (1958).** As described in Appendix 7, for **Case 2b**, external mass transfer resistance, ξ_e in Guangsuo *et al.* (2000) is given as:

$$\xi_e = \left(\frac{1-\varepsilon_b}{\varepsilon_b}\varepsilon\right)\frac{R^2\varepsilon}{a(a+2)}\left(1+\frac{\rho_P K_A}{\varepsilon}\right)^2\frac{(a+2)}{k_f R} \tag{4.32}$$

From Figures 4.6 and 4.7, when the external mass transfer coefficient, ξ_e, is not negligible, for the 2nd central moment method then recall Equation (A7.4), and that the intercept of the linear plot corresponds to the total resistance, ξ_1, that is:

$$\xi_1 = \xi_i + \xi_e + \xi_a \tag{4.33}$$

As mention in Chapter 3 (Section 3.8.5), the adsorption resistance, ξ_a, is negligible for a particle radius ≥ 0.50 mm (Schneider and Smith, 1968a). Therefore, ξ_a in Equation (4.33) is ignored and the intercept is the sum of the external mass transfer resistance, ξ_e, and intraparticle diffusion resistance, ξ_i.

For **Case 2c** with ξ_e (Schneider and Smith, 1968a), the only difference between Cases 2c and 2b in the calculation of ξ_e, is that the different values for the adsorption equilibrium constants, K_A^c and K_A are used (i.e. K_A in Equation (4.32) was replaced by K_A^c). Nevertheless, the ξ_e results calculated for Case 2c are similar to Case 2b, with ≤ 1% difference, and hence they are not shown.

For a fictitious bed (200 mm) packed with γ-alumina beads, the results of ξ_e for Case 2b with He and N_2 tracer (0.25 ml sample loop) are summarised in Tables 4.33 and 4.34, and the second central moment, μ_2', is obtained from **Cat. A and Cat. B**. The resistance ratios of ξ_e : ξ_i are also calculated.

Table 4.33: The results of ξ_e for γ-alumina beads with He and N_2 tracer (0.25 ml sample) packed in a **fictitious bed** (200 mm), and the second central moment, μ_2', was obtained from **Cat. A**.

Case 2b: γ-alumina beads (0.25 ml sample loop)										
Interstitial velocity term, $1/u_i^2$ (cm^{-2} s^2)	**$\Delta\mu_2'/(2L/u_i)$ (s)**		**Intercept: $\xi_1 = \xi_e + \xi_i$ (s)**		**External mass transfer resistance, ξ_e (s)**		**ξ_e / ξ_1 (%)**		**ξ_i / ξ_1 (%)**	
	He	**N_2**	**He**	**N_2**	**He**	**N_2**	**He**	**N_2**	**He**	**N_2**
1.76884	3.343	3.703	0.1373	0.1170	0.0013	0.0014	0.98	1.21	99.02	98.79
0.99497	1.947	1.777			0.0013	0.0014	0.95	1.18	99.05	98.82
0.63678	1.261	1.525			0.0013	0.0014	0.93	1.16	99.07	98.84
0.44221	0.939	1.304			0.0013	0.0013	0.91	1.15	99.09	98.85
0.32489	0.749	0.868			0.0012	0.0013	0.90	1.13	99.10	98.87
0.24874	0.573	0.658			0.0012	0.0013	0.88	1.12	99.12	98.88
0.19654	0.496	0.548			0.0012	0.0013	0.87	1.10	99.13	98.90

Table 4.34: The results of ξ_e for γ-alumina beads with He and N_2 tracer (0.25 ml sample) packed in a **fictitious bed** (200 mm), and the second central moment, μ_2', was obtained from **Cat. B.**

Case 2b: γ-alumina beads (0.25 ml sample loop)										
Interstitial velocity term, $1/u_i^2$ (cm^{-2} s^2)	**$\Delta\mu_2'/(2L/u_i)$ (s)**		**Intercept: $\xi_1 = \xi_e + \xi_i$ (s)**		**External mass transfer resistance, ξ_e (s)**		**ξ_e / ξ_1 (%)**		**ξ_i / ξ_1 (%)**	
	He	**N_2**	**He**	**N_2**	**He**	**N_2**	**He**	**N_2**	**He**	**N_2**
1.76884	3.561	4.273	0.2198	0.1494	0.0014	0.0014	0.62	0.96	99.38	99.04
0.99497	2.305	1.999			0.0013	0.0014	0.60	0.94	99.40	99.06
0.63678	1.461	1.582			0.0013	0.0014	0.59	0.92	99.41	99.08
0.44221	1.167	1.704			0.0013	0.0014	0.58	0.91	99.42	99.09
0.32489	0.667	0.631			0.0013	0.0013	0.57	0.90	99.43	99.10
0.24874	0.810	0.620			0.0012	0.0013	0.56	0.89	99.44	99.11

0.19654	0.726	0.635			0.0012	0.0013	0.55	0.88	99.45	99.12

Category 1: **Case 5 (non-linear method): External mass transfer coefficient expression from Wakao *et al.* (1958).** As described in Appendix 9, the external mass transfer resistance, ξ_f, in Garcá-Ochoa and Santos (1994), and Santos *et al.* (1996) is:

$$\xi_f = \frac{(1-\varepsilon_b)\varepsilon}{\varepsilon_b}(1+K_a)^2 \frac{R^2\varepsilon}{a(a+2)} \frac{(a+2)}{k_f R} \tag{4.34}$$

and the total resistance, ξ_1, was obtained from the G value of the non-linear curve plot in Figure 4.9 as:

$$\xi_1 = \frac{G(1+\xi_0)^2}{2} = \xi_f + \xi_M \tag{4.35}$$

where the resistance parameter, ξ_0, is given in Equation (4.19).

For a fictitious bed (200 mm) with γ-alumina beads, the results for ξ_f for Case 5 with He and N_2 tracer (0.25 ml sample loop) are summarised in Tables 4.35 and 4.36, and the second central moment, μ_2', was obtained from **Cat. A and Cat. B**. The resistance distributions of ξ_f and ξ_M were also calculated.

Table 4.35: Values of ξ_f for γ-alumina beads with He and N_2 tracer (0.25 ml sample) packed in a **fictitious bed** (200 mm), and the second central moment, μ_2', was obtained from **Cat. A**.

Case 5: γ-alumina beads (0.25 ml sample loop)										
Interstitial velocity, u_i (cm s^{-1})	**HETP: $\mu_2' L/(\mu_1)^2$ (cm)**		**ξ_1 from *G* value: $\xi_1 = \xi_f + \xi_M$ (s)**		**External mass transfer resistance, ξ_f (s)**		**ξ_f / ξ_1 (%)**		**ξ_M / ξ_1 (%)**	
	He	**N_2**	**He**	**N_2**	**He**	**N_2**	**He**	**N_2**	**He**	**N_2**
0.7519	1.360	1.449	0.1261	0.2576	0.0007	0.0005	0.53	0.19	99.47	99.81
1.0025	1.029	0.928			0.0007	0.0005	0.52	0.19	99.48	99.81
1.2532	0.873	0.825			0.0006	0.0005	0.51	0.18	99.49	99.82
1.5038	0.751	0.736			0.0006	0.0005	0.50	0.18	99.50	99.82
1.7544	0.686	0.609			0.0006	0.0005	0.49	0.18	99.51	99.82
2.0050	0.620	0.530			0.0006	0.0005	0.48	0.18	99.52	99.82
2.2557	0.582	0.501			0.0006	0.0005	0.47	0.18	99.53	99.82

Table 4.36: Values of ξ_f for γ-alumina beads with He and N_2 tracer (0.25 ml sample) packed in a **fictitious bed** (200 mm), and the second central moment, μ_2', was obtained from **Cat. B.**

Case 5: γ-alumina beads (0.25 ml sample loop)										
Interstitial velocity, u_i (cm s^{-1})	**HETP: $\mu_2' L/(\mu_1)^2$ (cm)**		**ξ_1 from *G* value: $\xi_1 = \xi_f + \xi_M$ (s)**		**External mass transfer resistance, ξ_f (s)**		**ξ_f / ξ_1 (%)**		**ξ_M / ξ_1 (%)**	
	He	**N_2**	**He**	**N_2**	**He**	**N_2**	**He**	**N_2**	**He**	**N_2**
0.7519	1.449	1.672	0.4639	0.3913	0.0007	0.0005	0.14	0.13	99.86	99.87
1.0025	1.218	1.044			0.0007	0.0005	0.14	0.12	99.86	99.88
1.2532	1.011	0.855			0.0006	0.0005	0.14	0.12	99.86	99.88
1.5038	0.935	0.961			0.0006	0.0005	0.14	0.12	99.86	99.88
1.7544	0.611	0.443			0.0006	0.0005	0.13	0.12	99.87	99.88
2.0050	0.876	0.505			0.0006	0.0005	0.13	0.12	99.87	99.88
2.2557	0.852	0.579			0.0006	0.0005	0.13	0.12	99.87	99.88

Category 2: **Case 3b (linear method): External mass transfer coefficient expression from Do (1998).** As described in Chapter 3 (Section 3.8.5), the external mass transfer resistance, ξ_e, for Case 3b was calculated from:

$$\xi_e = \left(\frac{1-\varepsilon_b}{\varepsilon_b}\varepsilon\right)\frac{R^2\varepsilon}{a(a+2)}\left(1+\frac{(1-\varepsilon)K_H}{\varepsilon}\right)^2\frac{(a+2)}{k_f R} \tag{4.36}$$

The resistance parameter, ξ_e, in Case 3b was based on Do (1998) and Armatas *et al.* (2005). The total resistance, ξ_1, was obtained from the intercept of the linear plot in Figure 4.7, that is:

$$\xi_1 = \xi_i + \xi_e \tag{4.37}$$

For Case 3b, the moment results of the fictitious γ-alumina beads bed are used in the ξ_e calculation, and the corresponding results are shown in Tables 4.37 and 4.38, and the second central moment, μ_2', was obtained from **Cat. A and Cat. B**. The resistance distributions ξ_e and ξ_i were also calculated.

Table 4.37: Values of ξ_e for γ-alumina beads with He and N_2 tracer (0.25 ml sample) packed in a **fictitious bed** (200 mm), and the second central moment, μ_2', was obtained from **Cat. A**.

Case 3b: γ-alumina beads (0.25 ml sample loop)										
Superficial velocity term, $1/u_0^2$ (cm^{-2} s^2)	**$\Delta\mu_2'/(2L/u_i)$ (s)**		**Intercept: $\xi_1 = \xi_e + \xi_i$ (s)**		**External mass transfer resistance, ξ_e (s)**		**ξ_e / ξ_1 (%)**		**ξ_i / ξ_1 (%)**	
	He	**N_2**	**He**	**N_2**	**He**	**N_2**	**He**	**N_2**	**He**	**N_2**
8.94847	1.486	1.647	0.06955	0.0520	0.0006	0.0007	0.91	1.28	99.09	98.72
5.03352	0.865	0.790			0.0006	0.0007	0.89	1.27	99.11	98.73
3.22145	0.560	0.678			0.0006	0.0007	0.88	1.25	99.12	98.75
2.23712	0.417	0.580			0.0006	0.0006	0.86	1.24	99.14	98.76
1.64360	0.333	0.386			0.0006	0.0006	0.85	1.23	99.15	98.77
1.25838	0.255	0.293			0.0006	0.0006	0.83	1.21	99.17	98.79
0.99427	0.220	0.244			0.0006	0.0006	0.82	1.20	99.18	98.80

Table 4.38: Values of ξ_e for γ-alumina beads with He and N_2 tracer (0.25 ml sample) packed in a **fictitious bed** (200 mm), and the second central moment, μ_2', was obtained from **Cat. B.**

Case 3b: γ-alumina beads (0.25 ml sample loop)										
Superficial velocity term, $1/u_0^2$ (cm^{-2} s^2)	**$\Delta\mu_2'/(2L/u_i)$ (s)**		**Intercept: $\xi_1 = \xi_e + \xi_i$ (s)**		**External mass transfer resistance, ξ_e (s)**		**ξ_e / ξ_1 (%)**		**ξ_i / ξ_1 (%)**	
	He	**N_2**	**He**	**N_2**	**He**	**N_2**	**He**	**N_2**	**He**	**N_2**
8.94847	1.583	1.900	0.0977	0.0664	0.0006	0.0007	0.66	1.02	99.34	98.98
5.03352	1.025	0.889			0.0006	0.0007	0.64	1.01	99.36	98.99
3.22145	0.649	0.703			0.0006	0.0007	0.63	0.99	99.37	99.01
2.23712	0.519	0.757			0.0006	0.0007	0.62	0.98	99.38	99.02
1.64360	0.297	0.281			0.0006	0.0006	0.61	0.97	99.39	99.03
1.25838	0.360	0.276			0.0006	0.0006	0.60	0.96	99.40	99.04
0.99427	0.323	0.282			0.0006	0.0006	0.59	0.96	99.41	99.04

Category 2: **Case 6 (non-linear method): External mass transfer coefficient expression from Do (1998).** For Case 6, the equation for external mass transfer resistance, ξ_f, is the same as Equation (A8.17), which is:

$$\xi_f = \frac{(1-\varepsilon_b)\varepsilon}{\varepsilon_b}\left(1+\frac{(1-\varepsilon)K_H}{\varepsilon}\right)^2 \frac{R^2\varepsilon}{a(a+2)}\frac{(a+2)}{k_f R} \tag{4.38}$$

The total resistance, ξ_1, is calculated by:

$$\xi_1 = \frac{G\varepsilon_b(1+\xi_0)^2}{2} = \xi_f + \xi_M \tag{4.39}$$

where the resistance parameter, ξ_0 is given in Equation (4.22).

The differences between Cases 5 and 6 are:

(a) When ξ_f was calculated different values of adsorption equilibrium constant, K_H and K_a were used;

(b) The theoretical external mass transfer coefficient expression used in Case 5 is adopted from Wakao *et al*. (1958) (Equation (4.28)); whereas for Case 6, theoretical expression given by Do (1998) was used (Equation (4.31)).

The differences between Cases 3b and 6 are:

(i) K_H in the former is calculated using moment analysis results from experimental response curve (i.e. $(\mu_1)_{inert}$), whereas the latter uses a theoretical expression (i.e. $(\mu_1)_0$).

(ii) The total resistance, ξ_1 for Case 3b was obtained from the intercept of the linear plot in Figure 4.7; whereas for Case 6, ξ_1 was obtained from the G value of the non-linear curve plot in Figure 4.10.

For Case 6, the moment results of the fictitious γ-alumina beads bed are used in the ξ_f calculation, and the corresponding results are shown in Tables 4.39 and 4.40, and the second central moment, μ_2', was obtained from **Cat. A and Cat. B**. The resistance distributions ξ_f and ξ_M were also calculated.

Table 4.39: Values of ξ_f for γ-alumina beads with He and N_2 tracer (0.25 ml sample) packed in a **fictitious bed** (200 mm), and the second central moment, μ_2', was obtained from **Cat. A**.

Case 6: γ-alumina beads (0.25 ml sample loop)										
Superficial velocity, u_0 (cm s^{-1})	**HETP: $\mu_2' L/(\mu_1)^2$ (cm)**		**ξ_1 from *G* value: $\xi_1 = \xi_f + \xi_M$ (s)**		**External mass transfer resistance, ξ_f (s)**		**ξ_f / ξ_1 (%)**		**ξ_M / ξ_1 (%)**	
	He	**N_2**	**He**	**N_2**	**He**	**N_2**	**He**	**N_2**	**He**	**N_2**
0.33429	1.360	1.449	0.1548	0.3720	0.0007	0.0020	0.57	0.39	99.43	99.61
0.44572	1.029	0.928			0.0007	0.0019	0.55	0.38	99.45	99.62
0.55715	0.873	0.825			0.0007	0.0019	0.54	0.38	99.46	99.62
0.66858	0.751	0.736			0.0007	0.0019	0.53	0.37	99.47	99.63
0.78001	0.686	0.609			0.0007	0.0019	0.52	0.37	99.48	99.63
0.89144	0.620	0.530			0.0007	0.0018	0.52	0.36	99.48	99.64
1.00287	0.582	0.501			0.0006	0.0018	0.51	0.36	99.49	99.64

Table 4.40: Values of ξ_f for γ-alumina beads with He and N_2 tracer (0.25 ml sample) packed in a **fictitious bed** (200 mm), and the second central moment, μ_2', was obtained from **Cat. B.**

Case 6: γ-alumina beads (0.25 ml sample loop)										
Superficial velocity, u_0 (cm s^{-1})	**HETP: $\mu_2' L/(\mu_1)^2$ (cm)**		**ξ_1 from *G* value: $\xi_1 = \xi_f + \xi_M$ (s)**		**External mass transfer resistance, ξ_f (s)**		**ξ_f / ξ_1 (%)**		**ξ_M / ξ_1 (%)**	
	He	**N_2**	**He**	**N_2**	**He**	**N_2**	**He**	**N_2**	**He**	**N_2**
0.33429	1.449	1.672	0.1654	0.5635	0.0007	0.0020	0.53	0.26	99.47	99.74
0.44572	1.218	1.044			0.0007	0.0020	0.52	0.25	99.48	99.75
0.55715	1.011	0.855			0.0007	0.0019	0.51	0.25	99.49	99.75
0.66858	0.935	0.961			0.0007	0.0019	0.50	0.25	99.50	99.75
0.78001	0.611	0.443			0.0007	0.0019	0.49	0.24	99.51	99.76
0.89144	0.876	0.505			0.0007	0.0019	0.48	0.24	99.52	99.76
1.00287	0.852	0.579			0.0006	0.0019	0.48	0.24	99.52	99.76

4.2.2 Calculation of effective diffusivity, D_{eff}

Using the information obtained on moments, different methods are now explored to calculate the effective diffusivity. These are:

Case 1: **2nd central moment method without K_a and ξ_e.** In Equation (A6.7), by matching moments, the intraparticle diffusion resistance, ξ_i, was evaluated from the intercept by plotting $\mu_2'/(2L/u_i)$ *versus* $1/u_i^2$ as shown in Figure 4.6. The external mass transfer resistance, ξ_e, is excluded, and D_{eff} was obtained from ξ_i as:

$$Intercept = \xi_i = \frac{(1-\varepsilon_b)}{\varepsilon_b}\frac{\varepsilon^2 R^2}{a(a+2)}\frac{1}{D_{eff}} \tag{4.40}$$

For a sphere, the particle shape factor a = 3.

For a fictitious γ-alumina beads bed, the D_{eff} results for Case 1 with He and N_2 tracer (0.25 ml sample loop) are summarised in Tables 4.41 and 4.42, and the second central moment, μ_2', was obtained from **Cat. A and Cat. B**.

Table 4.41: Effective diffusivity, D_{eff}, (He and N_2 tracer) for a **200 mm fictitious bed** with γ-alumina beads **(K_a = 0)**, and the 2nd central moment was obtained from **Cat. A**.

Case 1: γ-alumina beads (0.25 ml sample loop)						
Interstitial velocity term, $1/u_i^2$ (cm^{-2} s^2)	**$\mu_2'/(2L/u_i)$ (s)**		**Intraparticle diffusion resistance, ξ_i (s)**		**Effective diffusivity, D_{eff} (cm^2 s^{-1})**	
	He	**N_2**	**He**	**N_2**	**He**	**N_2**
1.76884	3.343	3.703	**0.1373**	**0.1170**	**5.36×10^{-4}**	**6.29×10^{-4}**
0.99497	1.947	1.777				
0.63678	1.261	1.525				
0.44221	0.939	1.304	**RSQ**			
0.32489	0.749	0.868				
0.24874	0.573	0.658	**0.9989**	**0.9539**		
0.19654	0.496	0.548				

Table 4.42: Effective diffusivity, D_{eff}, (He and N_2 tracer) for a **200 mm fictitious bed** with γ-alumina beads **(K_a = 0)**, and the 2nd central moment was obtained from **Cat. B**.

Case 1: γ-alumina beads (0.25 ml sample loop)						
Interstitial velocity term, $1/u_i^2$ (cm^{-2} s^2)	**$\mu_2'/(2L/u_i)$ (s)**		**Intraparticle diffusion resistance, ξ_i (s)**		**Effective diffusivity, D_{eff} (cm^2 s^{-1})**	
	He	**N_2**	**He**	**N_2**	**He**	**N_2**
1.76884	3.561	4.273	**0.2875**	**0.1494**	**2.56×10^{-4}**	**4.93×10^{-4}**
0.99497	2.305	1.999				
0.63678	1.461	1.582				
0.44221	1.167	1.704	**RSQ**			
0.32489	0.667	0.631				
0.24874	0.810	0.620	**0.9870**	**0.9451**		
0.19654	0.726	0.635				

Cases 2a: **2nd central moment method with K_A but without ξ_e.** In Equation (A7.13), by matching moments, ξ_i was evaluated from the intercept by plotting $\mu_2'/(2L/u_i)$ *versus* $1/u_i^2$ as shown in Figure 4.6. The external mass transfer resistance, ξ_e, was excluded and D_{eff} was obtained from ξ_i:

$$Intercept = \xi_i = \left(\frac{1-\varepsilon_b}{\varepsilon_b}\varepsilon\right)\frac{R^2\varepsilon}{a(a+2)}\left(1+\frac{\rho_P K_A}{\varepsilon}\right)^2\frac{1}{D_{eff}} \tag{4.41}$$

For a fictitious bed packed with γ-alumina beads, the D_{eff} results for Case 2a with He and N_2 tracer (0.25 ml sample loop) are summarised in Tables 4.43 and 4.44, and the second central moment, μ_2', was obtained from **Cat. A and Cat. B**.

Case 2b: **2nd central moment method with K_A and ξ_e.** D_{eff} was calculated in a similar manner to Case 2a, except that the external mass transfer resistance, ξ_e, in Equation (4.32) is now included. Hence, Equation (4.41) becomes:

$$Intercept = \xi_i + \xi_e = \left(\frac{1-\varepsilon_b}{\varepsilon_b}\varepsilon\right)\frac{R^2\varepsilon}{a(a+2)}\left(1+\frac{\rho_P K_A}{\varepsilon}\right)^2\left(\frac{1}{D_{eff}}+\frac{5}{k_f R}\right) \tag{4.42}$$

Hence, the ξ_e results from Tables 4.33 and 4.34 were used in the D_{eff} calculations for Case 2b, and these are summarised in the same table as Case 2a.

Table 4.43: Effective diffusivity, D_{eff}, (He and N_2 tracer) for a **200 mm fictitious bed** packed with γ-alumina beads **($(K_A)_{He/N2}$ = 0.3923 cm^3 g^{-1})**, and the 2nd central moment was obtained from **Cat. A**.

Cases 2a and 2b: γ-alumina beads (0.25 ml sample loop)						
Interstitial velocity term, $1/u_i^2$ (cm^{-2} s^2)	**$\mu_2'/(2L/u_i)$ (s)**		**Intraparticle diffusion resistance, ξ_i (s)**		**Case 2a: D_{eff} without ξ_e (cm^2 s^{-1})**	
	He	**N_2**	**He**	**N_2**	**He**	**N_2**
1.76884	3.343	3.703	**0.1373**	**0.1170**	**1.63 ×10^{-3}**	**1.91 ×10^{-3}**
0.99497	1.947	1.777				
0.63678	1.261	1.525				
0.44221	0.939	1.304	**RSQ**		**Case 2b: D_{eff} with ξ_e (cm^2 s^{-1})**	
0.32489	0.749	0.868				
0.24874	0.573	0.658	**0.9989**	**0.9539**	**1.64 ×10^{-3}**	**1.93 ×10^{-3}**
0.19654	0.496	0.548				

Table 4.44: Effective diffusivity, D_{eff}, (He and N_2 tracer) for a **200 mm fictitious bed** packed with γ-alumina beads **($(K_A)_{He/N2}$ = 0.3989 cm^3 g^{-1})**, and the 2nd central moment was obtained from **Cat. B**.

Cases 2a and 2b: γ-alumina beads (0.25 ml sample loop)						
Interstitial velocity term, $1/u_i^2$ (cm^{-2} s^2)	**$\mu_2'/(2L/u_i)$ (s)**		**Intraparticle diffusion resistance, ξ_i (s)**		**Case 2a: D_{eff} without ξ_e (cm^2 s^{-1})**	
	He	**N_2**	**He**	**N_2**	**He**	**N_2**
1.76884	3.561	4.273	**0.2198**	**0.1494**	**1.03 ×10^{-3}**	**1.52 ×10^{-3}**
0.99497	2.305	1.999				
0.63678	1.461	1.582				
0.44221	1.167	1.704	**RSQ**		**Case 2b: D_{eff} with ξ_e (cm^2 s^{-1})**	
0.32489	0.667	0.631				
0.24874	0.810	0.620	**0.9628**	**0.9451**	**1.04 ×10^{-3}**	**1.53 ×10^{-3}**
0.19654	0.726	0.635				

Case 2c: **2nd central moment method with K_A^c and ξ_e.** In Equation (A7.13), by matching moments, ξ_i was evaluated from the intercept by plotting $\mu_2'/(2L/u_i)$ *versus* $1/u_i^2$ as shown in Figure 4.7. D_{eff} was calculated in a similar manner to Cases 2a and 2b, and the external mass transfer resistance, ξ_e, from Equation (4.32) is included:

$$Intercept = \xi_i + \xi_e = \left(\frac{1-\varepsilon_b}{\varepsilon_b}\varepsilon\right)\frac{R^2\varepsilon}{a(a+2)}\left(1+\frac{\rho_P K_A^c}{\varepsilon}\right)^2\left(\frac{1}{D_{eff}}+\frac{5}{k_f R}\right) \quad (4.43)$$

For the fictitious bed packed with γ-alumina beads, the D_{eff} results for Case 2c with He and N_2 tracer (0.25 ml sample loop) are shown in Tables 4.45 and 4.46, and the second central moment, μ_2', was obtained from **Cat. A and Cat. B**.

Table 4.45: Effective diffusivity, D_{eff}, (He and N_2 tracer) for a **200 mm fictitious bed** packed with γ-alumina beads **($(K_A^c)_{He}$ = 0.1221 cm^3 g^{-1}, $(K_A^c)_{N2}$ = 0.2706 cm^3 g^{-1}),** and the 2nd central moment was obtained from **Cat. A**.

Case 2c: γ-alumina beads (0.25 ml sample loop)						
Interstitial velocity term, $1/u_i^2$ (cm^{-2} s^2)	**$\mu_2'/(2L/u_i)$ (s)**		**Intraparticle diffusion resistance, ξ_i (s)**		**Effective diffusivity, D_{eff} with ξ_e (cm^2 s^{-1})**	
	He	**N_2**	**He**	**N_2**	**He**	**N_2**
1.76884	3.343	3.703	**0.1351**	**0.1170**	**8.30×10^{-4}**	**1.45×10^{-3}**
0.99497	1.947	1.777				
0.63678	1.261	1.525				
0.44221	0.939	1.304	**RSQ**			
0.32489	0.749	0.868				
0.24874	0.573	0.658	**0.9997**	**0.9539**		
0.19654	0.496	0.548				

Table 4.46: Effective diffusivity, D_{eff}, (He and N_2 tracer) for a **200 mm fictitious bed** packed with γ-alumina beads **($(K_A^c)_{He}$ = 0.1221 cm^3 g^{-1}, $(K_A^c)_{N2}$ = 0.2755 cm^3 g^{-1})**, and the 2nd central moment was obtained from **Cat. B**.

Case 2c: γ-alumina beads (0.25 ml sample loop)						
Interstitial velocity term, $1/u_i^2$ (cm^{-2} s^2)	**$\mu_2'/(2L/u_i)$ (s)**		**Intraparticle diffusion resistance, ξ_i (s)**		**Effective diffusivity, D_{eff} with ξ_e (cm^2 s^{-1})**	
	He	**N_2**	**He**	**N_2**	**He**	**N_2**
1.76884	3.561	4.273	**0.2198**	**0.1494**	**5.09×10^{-4}**	**1.15×10^{-3}**
0.99497	2.305	1.999				
0.63678	1.461	1.582				
0.44221	1.167	1.704	**RSQ**			
0.32489	0.667	0.631				
0.24874	0.810	0.620	**0.9628**	**0.9451**		
0.19654	0.726	0.635				

Cases 3a: **New 2nd central moment method with K_H but without ξ_e.** In Equation (3.111), by moment matching, ξ_i, was evaluated from the intercept by plotting $\mu_2'/(2L/u_0)$ *versus* $1/u_0^2$ as shown in Figure 4.7. The external mass transfer resistance, ξ_e, was excluded and D_{eff} was calculated from:

$$\frac{Intercept}{\varepsilon_b} = \xi_i = \left(\frac{1-\varepsilon_b}{\varepsilon_b}\varepsilon\right)\frac{R^2}{a(a+2)}\left(1+\frac{(1-\varepsilon)K_H}{\varepsilon}\right)^2\frac{1}{D_{eff}} \tag{4.44}$$

Case 3b: **New 2nd central moment method with K_H and ξ_e.** In this case, D_{eff} is calculated by adding the external mass transfer resistance results from Tables 4.37 and 4.38. Hence, Equation (4.44) becomes:

$$\frac{Intercept}{\varepsilon_b} = \xi_i + \xi_e = \left(\frac{1-\varepsilon_b}{\varepsilon_b}\varepsilon\right)\frac{R^2\varepsilon}{a(a+2)}\left(1+\frac{(1-\varepsilon)K_H}{\varepsilon}\right)^2\left(\frac{1}{\varepsilon D_{eff}}+\frac{5}{k_f R}\right) \tag{4.45}$$

For a fictitious bed packed with γ-alumina beads, the D_{eff} results for Cases 3a and 3b with He and N_2 tracer (0.25 ml sample loop) are shown in Tables 4.47 and 4.48, and the second central moment, μ_2', was obtained from **Cat. A and Cat. B**.

Table 4.47: Effective diffusivity, D_{eff}, (He and N_2 tracer) for a **200 mm fictitious bed** packed with γ-alumina beads **($(K_H)_{He/N2}$ = 1.0887)**, and the 2nd central moment was obtained from **Cat. A**.

Cases 3a and 3b: γ-alumina beads (0.25 ml sample loop)						
Superficial velocity term, $1/u_0^2$ (cm^{-2} s^2)	**$\mu_2'/(2L/u_0)$ (s)**		**Intraparticle diffusion resistance, ξ_i (s)**		**Case 3a: D_{eff} without ξ_e (cm^2 s^{-1})**	
	He	**N_2**	**He**	**N_2**	**He**	**N_2**
8.94847	1.486	1.647	**0.0696**	**0.0520**	**1.43×10^{-3}**	**1.91×10^{-3}**
5.03352	0.865	0.790				
3.22145	0.560	0.678				
2.23712	0.417	0.580	**RSQ**		**Case 3b: D_{eff} with ξ_e (cm^2 s^{-1})**	
1.64360	0.333	0.386				
1.25838	0.255	0.293	**0.9971**	**0.9539**	**1.44×10^{-3}**	**1.93×10^{-3}**
0.99427	0.220	0.244				

Table 4.48: Effective diffusivity, D_{eff}, (He and N_2 tracer) for a **200 mm fictitious bed** packed with γ-alumina beads **($(K_H)_{He/N2}$ = 1.1070)**, and the 2nd central moment was obtained from **Cat. B**.

Cases 3a and 3b: γ-alumina beads (0.25 ml sample loop)						
Superficial velocity term, $1/u_0^2$ (cm^{-2} s^2)	**$\mu_2'/(2L/u_0)$ (s)**		**Intraparticle diffusion resistance, ξ_i (s)**		**Case 3a: D_{eff} without ξ_e (cm^2 s^{-1})**	
	He	**N_2**	**He**	**N_2**	**He**	**N_2**
8.94847	1.583	1.900	**0.0977**	**0.0664**	**1.03×10^{-3}**	**1.52×10^{-3}**
5.03352	1.025	0.889				
3.22145	0.649	0.703				
2.23712	0.519	0.757	**RSQ**		**Case 3b: D_{eff} with ξ_e (cm^2 s^{-1})**	
1.64360	0.297	0.281				
1.25838	0.360	0.276	**0.9628**	**0.9451**	**1.04×10^{-3}**	**1.53×10^{-3}**
0.99427	0.323	0.282				

Case 4: **HETP method with K_H but without ξ_f (linear).** In Equation (A8.31), by moment matching, intraparticle diffusion resistance, ξ_M, was evaluated from the slope by plotting $\mu_2' L/(\mu_1)^2$ *versus* u_0 as shown in Figure 4.11. The external mass transfer resistance, ξ_f, was excluded and D_{eff} was calculated from:

$$\frac{slope \times \varepsilon_b (1+\xi_0)^2}{2} = \xi_M = \frac{(1-\varepsilon_b)}{\varepsilon_b}\left(1+\frac{(1-\varepsilon)K_H}{\varepsilon}\right)^2 \frac{R^2\varepsilon}{a(a+2)D_{eff}} \qquad (4.46)$$

For a fictitious bed packed with γ-alumina beads, the D_{eff} results for Case 4 with He and N_2 tracer (0.25 ml sample loop) are shown in Tables 4.49 and 4.50, and the second central moment, μ_2', was obtained from **Cat. A and Cat. B**.

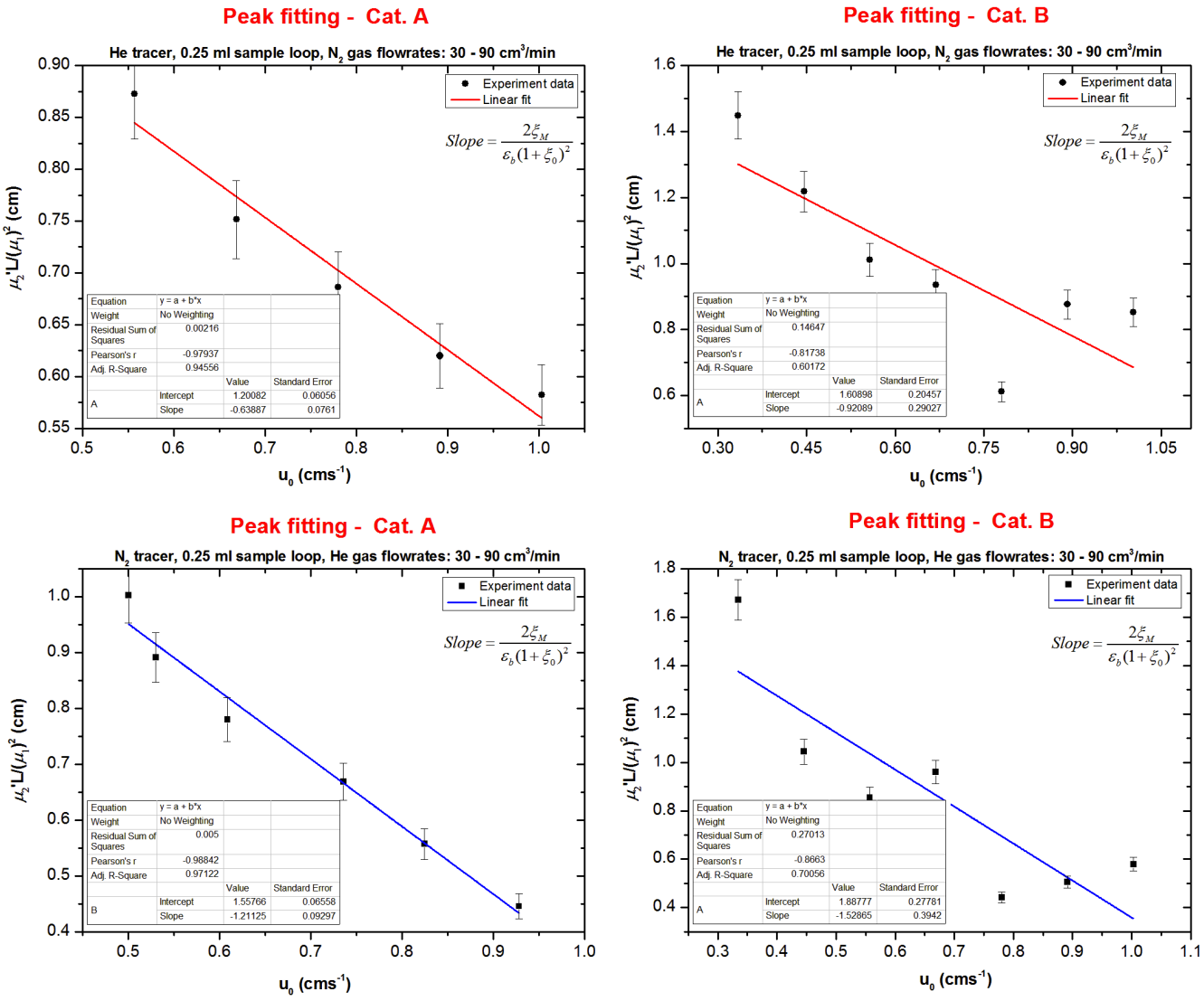

Figure 4.11: The intraparticle diffusion resistance, ξ_M, for a fictitious bed of γ-alumina beads (200 mm) with He and N_2 tracer (0.25 ml). This is calculated from the slope of the linear plot (**Case 4**).

Table 4.49: Effective diffusivity, D_{eff}, (He and N_2 tracer) for a **200 mm fictitious bed** packed with γ-alumina beads **($(K_H)_{He}$ = 0.3389, $(K_H)_{N2}$ = 1.4470),** and the 2nd central moment was obtained from **Cat. A**.

Case 4: γ-alumina beads (0.25 ml sample loop)						
Superficial velocity, u_0 (cm s^{-1})	**$\mu_2' L/(\mu_1)^2$ (cm)**		**Intraparticle diffusion resistance, ξ_M (s)**		**Effective diffusivity, D_{eff} (cm^2 s^{-1})**	
	He	**N_2**	**He**	**N_2**	**He**	**N_2**
0.33429	1.360	1.449	**0.5205**	**1.0989**	**2.14×10^{-4}**	**2.64×10^{-4}**
0.44572	1.029	0.928				
0.55715	0.873	0.825				
0.66858	0.751	0.736	**RSQ**			
0.78001	0.686	0.609				
0.89144	0.620	0.530	**0.9592**	**0.9770**		
1.00287	0.582	0.501				

Table 4.50: Effective diffusivity, D_{eff}, (He and N_2 tracer) for a **200 mm fictitious bed** packed with γ-alumina beads **($(K_H)_{He}$ = 0.3389, $(K_H)_{N2}$ = 1.4654)**, and the 2nd central moment was obtained from **Cat. B**.

Case 4: γ-alumina beads (0.25 ml sample loop)						
Superficial velocity, u_0 (cm s^{-1})	**$\mu_2' L/(\mu_1)^2$ (cm)**		**Intraparticle diffusion resistance, ξ_M (s)**		**Effective diffusivity, D_{eff} (cm^2 s^{-1})**	
	He	**N_2**	**He**	**N_2**	**He**	**N_2**
0.33429	1.449	1.672	**0.7503**	**2.0983**	**1.49×10^{-4}**	**1.40×10^{-4}**
0.44572	1.218	1.044				
0.55715	1.011	0.855				
0.66858	0.935	0.961	**RSQ**			
0.78001	0.611	0.443				
0.89144	0.876	0.505	**0.6681**	**0.7285**		
1.00287	0.852	0.579				

Case 5: **HETP method with K_a and ξ_f (non-linear).** In Equation (A9.11), by moment matching, D_{eff} is evaluated non-linearly from the value of G by plotting $\mu_2' L/(\mu_1)^2$ *versus* u_i as shown in Figure 4.9. The external mass transfer resistance, ξ_f, was included and D_{eff} was calculated from:

$$G = \frac{2}{15}\frac{\varepsilon_b R^2}{(1-\varepsilon_b)}\frac{1}{\left(1+1/\xi_0\right)^2}\left(\frac{1}{D_{eff}}\right) \tag{4.47}$$

The resistance parameter, ξ_0, was calculated according to Equation (4.19).

Using moment results for a fictitious bed of γ-alumina beads, and using external mass transfer resistance, ξ_f, from Tables 4.35 and 4.36, the D_{eff} results for Case 5 with He and N_2 tracer (0.25 ml sample loop) are presented in Tables 4.51 and 4.52. The second central moment, μ_2', was obtained from **Cat. A and Cat. B**.

Table 4.51: Effective diffusivity, D_{eff}, (He and N_2 tracer) for a **200 mm fictitious bed** packed with γ-alumina beads **($(K_a)_{He}$ = 0.2311, $(K_a)_{N2}$ = 0.03),** and the 2nd central moment was obtained from **Cat. A**.

Case 5: γ-alumina beads (0.25 ml sample loop)						
Interstitial velocity, u_i (cm s^{-1})	**$\mu_2' L/(\mu_1)^2$ (cm)**		**Intraparticle diffusion resistance, ξ_M (s)**		**Effective diffusivity, D_{eff} with ξ_f (cm^2 s^{-1})**	
	He	**N_2**	**He**	**N_2**	**He**	**N_2**
0.7519	1.360	1.449	**0.1255**	**0.2571**	**8.89×10^{-4}**	**3.04×10^{-4}**
1.0025	1.029	0.928				
1.2532	0.873	0.825				
1.5038	0.751	0.736	**RSQ**			
1.7544	0.686	0.609				
2.0050	0.620	0.530	**0.9985**	**0.9652**		
2.2557	0.582	0.501				

Table 4.52: Effective diffusivity, D_{eff}, (He and N_2 tracers) for a **200 mm fictitious bed** packed with γ-alumina beads **($(K_a)_{He}$ = 0.2311, $(K_a)_{N2}$ = 0.0333)**, and the 2nd central moment was obtained from **Cat. B**.

Case 5: γ-alumina beads (0.25 ml sample loop)						
Interstitial velocity, u_i (cm s^{-1})	**$\mu_2' L/(\mu_1)^2$ (cm)**		**Intraparticle diffusion resistance, ξ_M (s)**		**Effective diffusivity, D_{eff} with ξ_f (cm^2 s^{-1})**	
	He	**N_2**	**He**	**N_2**	**He**	**N_2**
0.7519	1.449	1.672	**0.4632**	**0.3908**	**2.41×10^{-4}**	**2.01×10^{-4}**
1.0025	1.218	1.044				
1.2532	1.011	0.855				
1.5038	0.935	0.961	**RSQ**			
1.7544	0.611	0.443				
2.0050	0.876	0.505	**0.7805**	**0.8493**		
2.2557	0.852	0.579				

Case 6: **New HETP approach with K_H and ξ_f (non-linear).** In Equation (3.120), instead of using the linearization method in the HETP method shown in Armatas *et al*. (2005), in this thesis, D_{eff} is evaluated non-linearly from G, by plotting $\mu_2' L/(\mu_1)^2$ *versus* u_0 as shown in Figure 4.10. The external mass transfer resistance, ξ_f, was included:

$$G = \frac{2}{15}\frac{R^2}{(1-\varepsilon_b)}\frac{1}{\left(1+1/\xi_0\right)^2}\left(\frac{1}{D_{eff}}+\frac{5}{k_f R}\right) \tag{4.48}$$

and the resistance parameter, ξ_0, was calculated according to Equation (4.22).

Using moment results for a fictitious bed of γ-alumina beads, and using external mass transfer resistance, ξ_f, from Tables 4.39 and 4.40, then D_{eff} results for Case 6 with He and N_2 tracer (0.25 ml sample loop) are presented in Tables 4.53 and 4.54. The second central moment, μ_2', was obtained from **Cat. A and Cat. B**.

Table 4.53: Effective diffusivity, D_{eff}, (He and N_2 tracer) calculated for a **200 mm fictitious bed** packed with γ-alumina beads **($(K_H)_{He}$ = 0.3389, $(K_H)_{N2}$ = 1.4470),** and the 2nd central moment was obtained from **Cat. A**.

Case 6: γ-alumina beads (0.25 ml sample loop)						
Superficial velocity, u_0 (cm s^{-1})	**$\mu_2'L/(\mu_1)^2$ (cm)**		**Intraparticle diffusion resistance, ξ_M (s)**		**Effective diffusivity, D_{eff} with ξ_f (cm^2 s^{-1})**	
	He	**N_2**	**He**	**N_2**	**He**	**N_2**
0.33429	1.360	1.449	**0.1255**	**0.5049**	**8.94×10^{-4}**	**5.75×10^{-4}**
0.44572	1.029	0.928				
0.55715	0.873	0.825				
0.66858	0.751	0.736	**RSQ**			
0.78001	0.686	0.609				
0.89144	0.620	0.530	**0.9985**	**0.9652**		
1.00287	0.582	0.501				

Table 4.54: Effective diffusivity, D_{eff}, (He and N_2 tracer) for a **200 mm fictitious bed** packed with γ-alumina beads **($(K_H)_{He}$ = 0.3389, $(K_H)_{N2}$ = 1.4654)**, and the 2nd central moment was obtained from **Cat. B**.

Case 6: γ-alumina beads (0.25 ml sample loop)						
Superficial velocity, u_0 (cm s^{-1})	**$\mu_2'L/(\mu_1)^2$ (cm)**		**Intraparticle diffusion resistance, ξ_M (s)**		**Effective diffusivity, D_{eff} with ξ_f (cm^2 s^{-1})**	
	He	**N_2**	**He**	**N_2**	**He**	**N_2**
0.33429	1.449	1.672	**0.1341**	**0.7715**	**8.32×10^{-4}**	**3.81×10^{-4}**
0.44572	1.218	1.044				
0.55715	1.011	0.855				
0.66858	0.935	0.961	**RSQ**			
0.78001	0.611	0.443				
0.89144	0.876	0.505	**0.7652**	**0.8493**		
1.00287	0.852	0.579				

4.2.3 Calculation of the tortuosity factor, τ

The tortuosity factor of the γ-alumina beads, τ is obtained using the parallel pore model shown earlier in Equations (3.9) and (3.10), which are:

$$D_C = \frac{1}{D_{AB}} + \frac{1}{D_K} \tag{4.49}$$

$$\frac{D_{eff}}{D_C} = \frac{\varepsilon}{\tau_p} \tag{4.50}$$

Example calculations for molecular diffusivity, D_{AB}, and Knudsen diffusivity, D_K, were summarised in Appendix 10. The tortuosity factor for cases discussed in Section 4.2.2 with 0.25 ml sample loop (He and N_2 tracer) and with μ_2' obtained from Cat. A and Cat. B are presented in Table 4.55.

Table 4.55: Tortuosity factor calculated using different methods for a fictitious bed of γ-alumina beads using the 0.25 ml sample loop (He and N_2 tracer), and μ_2' was obtained from Cat. A and Cat. B.

Tortuosity factor, τ for γ-alumina beads: 0.25 ml sample loop				
	He as tracer		**N_2 as tracer**	
	Cat. A	**Cat. B**	**Cat. A**	**Cat. B**
Case 1	38.62	80.87	12.84	16.40
Case 2a	12.72	20.07	4.23	5.33
Case 2b	12.50	19.85	4.14	5.23
Case 2c	24.84	40.56	5.52	6.99
Case 3a	14.49	20.07	4.23	5.33
Case 3b	14.25	19.83	4.13	5.22
Case 4	96.59	139.23	30.55	57.62
Case 5	23.18	85.86	26.55	40.13
Case 6	23.16	24.76	13.99	21.14

4.2.4 Summary of values for effective diffusivity D_{eff} and tortuosity factor τ

The D_{eff} values and apparent tortuosity factors calculated for the γ-alumina beads using different methods are presented in Tables 4.41 to 4.54 and in Tables 4.56 and 4.57.

From these comparative results, the following additional observations are made:

For D_{eff} values:

(a) There is a significant difference between Case 4 and the other cases, as the effective diffusivity is around 5 – 10 times smaller.

(b) Cases 2 and 3, produce similar results, which are comparable with values in the literature (see Table 4.58).

(c) In general, Cat. A and B produce slight different values, but they are of a similar order of magnitude in each case studied, except for some cases when the linear or non-linear fit was not good (i.e. low RSQ value).

For τ values:

(d) There is a significant difference between Case 4 and the other cases, where the tortuosity factor is around 5 – 10 times bigger.

(e) Cases 2 and 3 produce similar results which are comparable with literature data (see Table 4.58), and generally speaking, the results using the second central moment calculated by Cat. A and Cat. B produce slight different values for the tortuosity factor.

Table 4.56: Average values of effective diffusivity, D_{eff}, and the tortuosity factor, τ (He and N_2 tracer), for a fictitious bed of γ-alumina beads with the 2nd central moment, $\mu_2^{'}$ obtained from **Cat. A**.

Fictitious γ-alumina beads packed bed: 200 mm (Cat. A)						
	D_{eff} ($cm^2\ s^{-1}$, helium as tracer)	***RSQ* *(Helium as tracer)***	**Tortuosity factor, τ (Helium as tracer)**	**D_{eff} ($cm^2\ s^{-1}$, nitrogen as tracer)**	***RSQ* *(Nitrogen as tracer)***	**Tortuosity factor, τ (Nitrogen as tracer)**
Case 1	$5.18 \times 10^{-4} \pm 7.33 \times 10^{-5}$	*0.9934 ± 0.0082*	40.79 ± 6.1079	$7.44 \times 10^{-4} \pm 2.57 \times 10^{-4}$	*0.9616 ± 0.0118*	12.08 ± 3.5760
Case 2a	$1.35 \times 10^{-3} \pm 3.18 \times 10^{-4}$	*0.9934 ± 0.0082*	16.46 ± 4.5955	$1.92 \times 10^{-3} \pm 6.90 \times 10^{-4}$	*0.9616 ± 0.0118*	4.88 ± 1.9169
Case 2b	$1.36 \times 10^{-3} \pm 3.22 \times 10^{-4}$	*0.9934 ± 0.0082*	16.34 ± 4.5935	$1.94 \times 10^{-3} \pm 7.04 \times 10^{-4}$	*0.9616 ± 0.0118*	4.83 ± 1.9215
Case 2c	$7.51 \times 10^{-4} \pm 1.02 \times 10^{-4}$	*0.9934 ± 0.0082*	28.14 ± 4.2178	$1.81 \times 10^{-3} \pm 8.28 \times 10^{-4}$	*0.9710 ± 0.0121*	5.38 ± 2.0905
Case 3a	$1.28 \times 10^{-3} \pm 2.69 \times 10^{-4}$	*0.9934 ± 0.0082*	17.05 ± 4.1717	$1.92 \times 10^{-3} \pm 6.90 \times 10^{-4}$	*0.9616 ± 0.0118*	4.88 ± 1.9170
Case 3b	$1.29 \times 10^{-3} \pm 2.72 \times 10^{-4}$	*0.9934 ± 0.0082*	16.93 ± 4.1720	$1.94 \times 10^{-3} \pm 7.06 \times 10^{-4}$	*0.9616 ± 0.0118*	4.83 ± 1.9169
Case 4	$1.89 \times 10^{-4} \pm 2.08 \times 10^{-5}$	*0.9581 ± 0.0063*	111.00 ± 12.6088	$2.64 \times 10^{-4} \pm 2.53 \times 10^{-5}$	*0.9792 ± 0.0045*	30.88 ± 3.0178
Case 5	$1.06 \times 10^{-3} \pm 4.77 \times 10^{-4}$	*0.9752 ± 0.0323*	23.69 ± 9.6266	$3.46 \times 10^{-4} \pm 7.08 \times 10^{-5}$	*0.9853 ± 0.0145*	24.22 ± 4.3705
Case 6	$1.38 \times 10^{-3} \pm 9.38 \times 10^{-4}$	*0.9947 ± 0.0052*	22.82 ± 12.1660	$3.10 \times 10^{-3} \pm 3.55 \times 10^{-3}$	*0.9825 ± 0.0137*	9.49 ± 6.0107

Table 4.57: Average values of effective diffusivity, D_{eff}, and the tortuosity factor, τ (He and N_2 tracer), for a fictitious bed of γ-alumina beads with the 2nd central moment, $\mu_2^{'}$ obtained from **Cat. B**.

Fictitious γ-alumina beads packed bed: 200 mm (Cat. B)						
	D_{eff} ($cm^2\ s^{-1}$, helium as tracer)	***RSQ (Helium as tracer)***	**Tortuosity factor, τ (Helium as tracer)**	**D_{eff} ($cm^2\ s^{-1}$, nitrogen as tracer)**	***RSQ (Nitrogen as tracer)***	**Tortuosity factor, τ (Nitrogen as tracer)**
Case 1	$4.66 \times 10^{-4} \pm 2.08 \times 10^{-4}$	*0.9783 ± 0.0128*	53.70 ± 21.7412	$3.31 \times 10^{-4} \pm 1.15 \times 10^{-4}$	*0.9257 ± 0.0162*	27.12 ± 7.6947
Case 2a	$1.36 \times 10^{-3} \pm 2.43 \times 10^{-4}$	*0.9783 ± 0.0128*	15.73 ± 3.1147	$9.58 \times 10^{-4} \pm 4.28 \times 10^{-4}$	*0.8958 ± 0.0571*	10.45 ± 4.7468
Case 2b	$1.38 \times 10^{-3} \pm 2.45 \times 10^{-4}$	*0.9783 ± 0.0128*	15.61 ± 3.1193	$1.02 \times 10^{-3} \pm 3.71 \times 10^{-4}$	*0.8958 ± 0.0571*	8.94 ± 2.8806
Case 2c	$7.96 \times 10^{-4} \pm 2.34 \times 10^{-4}$	*0.9598 ± 0.0026*	28.58 ± 8.9836	$9.31 \times 10^{-4} \pm 1.89 \times 10^{-4}$	*0.8958 ± 0.0571*	9.07 ± 1.9592
Case 3a	$1.36 \times 10^{-3} \pm 2.43 \times 10^{-4}$	*0.9598 ± 0.0026*	15.72 ± 3.1157	$8.93 \times 10^{-4} \pm 4.47 \times 10^{-4}$	*0.9257 ± 0.0162*	11.21 ± 4.4062
Case 3b	$1.38 \times 10^{-3} \pm 2.45 \times 10^{-4}$	*0.9598 ± 0.0026*	15.60 ± 3.1193	$8.98 \times 10^{-4} \pm 4.51 \times 10^{-4}$	*0.9257 ± 0.0162*	11.16 ± 4.4089
Case 4	$1.33 \times 10^{-4} \pm 1.23 \times 10^{-5}$	*0.7740 ± 0.0783*	156.31 ± 13.8970	$1.59 \times 10^{-4} \pm 4.34 \times 10^{-5}$	*0.7428 ± 0.1188*	54.30 ± 13.0920
Case 5	$8.64 \times 10^{-4} \pm 9.16 \times 10^{-4}$	*0.8047 ± 0.0264*	67.80 ± 42.1211	$4.14 \times 10^{-4} \pm 3.20 \times 10^{-4}$	*0.7929 ± 0.0738*	31.90 ± 16.1528
Case 6	$1.06 \times 10^{-3} \pm 8.20 \times 10^{-4}$	*0.7997 ± 0.0315*	47.44 ± 43.1665	$6.23 \times 10^{-4} \pm 3.81 \times 10^{-4}$	*0.7769 ± 0.0963*	17.64 ± 7.6967

Table 4.58: Examples of effective diffusivity, D_{eff}, and the tortuosity factor, τ, found in the literature.

	Sample studied	**Tracer-Carrier gas system**	**Adsorption equilibrium constant**	**Method (correlation)**	**Effective diffusivity, D_{eff} ($cm^2\ s^{-1}$)**	**Particle porosity, ε**	**Tortuosity factor, τ**
Case 1: Baiker *et al*. (1982)	Commercial catalyst	Ar – He	$K_a = 0$	2nd central moment (linear)	0.002 – 0.028	0.407 – 0.627	4.29 – 5.03 (parallel pore model)
Case 1: Tang *et al.* (1987)	γ-alumina silica alumina	N_2 – H_2	$K_a = 0$	2nd central moment (linear)	0.0122 – 0.0384	0.592 – 0.672	N/A
Case 2a: Guangsuo *et al*. (2000)	Sulfur-tolerant (metal oxides)	He – N_2 N_2 – He	$K_A \neq 0$ (with unit: $cm^3\ g^{-1}$ and weak adsorption)	2nd central moment (linear)	7.36×10^{-4} – 2.619×10^{-3}	N/A	6 – 8.15 (parallel pore model)
Case 2c: Schneider and Smith (1968)	Silica oxides	C_2H_6, C_3H_8, n-C_4H_{10}	$K_A^c \neq 0$ (with unit: $cm^3\ g^{-1}$ and strong adsorption)	2nd central moment (linear)	2.39×10^{-3} – 6.36×10^{-3}	0.486	0.42 – 1.20
Case 4: Armatas *et al*. (2005)	Silica oxides	He – N_2	$K_H \neq 0$ (dimensionless and weak adsorption)	HETP (linear)	1.306×10^{-3} – 2.176×10^{-3}	0.59 – 0.66	9.10 – 11.12 (parallel pore model)
Case 5: Garcı́a-Ochoa and Santos (1994)	Silica alumina	N_2 and Ar (tracer)	$K_a \neq 0$ (dimensionless and weak adsorption)	HETP (non-linear)	0.02 – 0.0245	0.52 – 0.535	4.1 – 6.5 (parallel pore model)
Case 5: Santos *et al*. (1996)	De-NOx catalyst	Ar, O_2 and N_2 (tracer)	$K_a \neq 0$ (dimensionless and weak adsorption)	HETP (non-linear)	6×10^{-3} – 9.4×10^{-3}	0.616	2.62 – 3.61 (parallel pore model)

4.3 Concluding remarks

In this chapter, a variety of different methods were explored, which enable the effective diffusivity, and the apparent tortuosity of the pellets to be calculated from experimental techniques based on the chromatographic method. From these calculations, the following general concluding remarks are formed.

Axial dispersion coefficients

(a) **Glass beads:** The performance of experiments with the glass beads was useful, as in the comparative RTD plots (with data for the γ-alumina beads), it was very clear that the effect of intraparticle diffusion in the pores of the γ-alumina beads was very significant, and therefore at the range of conditions tested easily measurable.

(b) From the experiments on glass beads and also the γ-alumina beads, moment results for a fictitious bed (200 mm) without entrance and exit effect were obtained. These moments were calculated from the moment difference between 400 and 200 mm 'real' columns.

(c) From a comparison of the areas of the response, with sample loops 0.1, 0.25 and 0.5 ml in volume, the signals from the 0.25 and 0.5 ml sample loops were more accurate. To avoid repetition, the results from the 0.25 ml sample loop were presented and discussed in more detail.

(d) Values of axial dispersion, D_{ax}, depend on the method of analysis used. There were small variations between some of the methods. In conclusion methods based on **Cases 2a, 2b, 2c, 3a, 3b and 6 with N_2 tracer** are preferred for glass beads, as these produce results which are closer to expected values from the literature and correlations in the literature, and the linear correlation i.e. R^2 value is close to 1. Besides, the D_{ax} that used the experimental second central moment, μ_2', calculated by

Cat. A was better than **Cat. B,** because: (i) the R^2 values are high, (ii) the standard error is small.

(e) **γ-alumina beads:** From this series of experiments values of axial dispersion, D_{ax} depend on the method of analysis used. There were some small variations between some of the methods. Comparing values with the results from the glass beads experiment and correlations in the literature, then the results from **Cases 1, 2a, 2b, 2c, 3a, 3b and 6** with **both tracers** and the second central moment, μ_2', calculated by **Cat. A,** look more reliable.

Effective diffusivity values

(f) **γ-alumina beads:** From the interpretation of RTD data, there were some significant variations between some of the methods. If the preferred method(s) from the glass beads experiments are used, then the results with **Cases 2a, 2b, 2c, 3a, 3b and 6 with N_2 tracer** and the second central moment, μ_2' calculated by **Cat. A,** look more reliable.

External mass transfer coefficients

(g) **γ-alumina beads:** From the analysis performed, it was clear that the contribution of external mass transfer resistance was small (≤ 1%) relative to the intraparticle resistance term.

Apparent tortuosity values

(h) **γ-alumina beads:** Depending on the method selected to determine the effective diffusivity, and hence its value, there were some significant variations in the value of tortuosity calculated. If the preferred method(s) from the effective diffusivity analysis is used, then the results with **Cases 2a, 2b, 2c, 3a, 3b and 6 with N_2 tracer** and the second central moment, μ_2' calculated by **Cat. A,** look more reliable.

General remarks

(i) **Descriptions in the literature:** In general, these were difficult and time consuming to follow and understand, as key calculation steps were sometimes inadequately explained, and in some cases there were mistakes in the units quoted, which were difficult to resolve. Authors have also used slightly different ways in which they approach the problem, and also in the units that they assign in the expressions. For example, the Adsorption Equilibrium Constant, has units in some papers, but is dimensionless in others. All of these problems make it very difficult to follow the explanations offered.

(j) **In this thesis**: by applying different methods to the same set of experimental data, and by also performing experiments on glass beads of the same diameter as the γ-alumina beads, a useful comparison has been obtained between the different methods. Also, the shortcomings of certain methods have been more clearly identified.

(k) **Short and long column experiments:** these results were useful, as besides highlighting the importance of recognizing the existence of column, inlet and outlet effects (mentioned in (b)), they also provide valuable experimental data to be gained, when the convolution theorem was applied to calculate the moment results for a fictitious bed (200 mm) without entrance and exit effect.

4.4 Conclusions and Recommendations

In general, the effective diffusivity (D_{eff}) values calculated using moments results from the fictitious bed (i.e. without entrance and exit effects) proposed by this thesis are more accurate than the methods used in literature. The mathematical models used in Guangsuo *et al* (2000) (i.e. Case 2), Schneider and Smith (1968) (i.e. Case 2c) and the new combination models proposed in this thesis (i.e. Cases 3 and 6) are more reliable because of the high RSQ values. For N_2 tracer, with second central moment, $\mu_2^{'}$ obtained by Category A for the fictitious bed, D_{eff} values were between 1.8 – 3.1 $\times 10^{-3}$ cm^2 s^{-1}, and an apparent tortuosity factor (τ) between 5 – 9.5 was recommended for the γ-alumina bead.

The Péclet number calculated for 200 and 400 mm column using dimensionless second central moment results (σ_θ^2) at the corresponding carrier gas flowrates are larger than 100, which justified the peak fitting method used in Chapter 3 for pulse response curves – peak fitting with a Gaussian area function (Hayes and Mmbaga, 2012).

References

Armatas, G., Petrakis, D. & Pomonis, P., 2005. Estimation of diffusion parameters in functionalized silicas with modulated porosity: Part I: Chromatographic studies. *Journal of Chromatography A,* 1074, pp. 53-59.

Baiker, A., New, M. & Richarz, W., 1982. Determination of intraparticle diffusion coefficients in catalyst pellets: a comparative study of measuring methods. *Chemical Engineering Science,* 37, pp. 643-656.

Do, D.D., 1998. *Adsorption Analysis: Equilibria and Kinetics.* Imperial College Press.

Garc á-Ochoa, F. & Santos, A., 1994. Effective diffusivity under inert and reaction conditions. *Chemical Engineering Science,* 49, pp. 3091-3102.

Guangsuo, Y., Jianguo, Y. & Zunhong, Y., 2000. The measurement of effective diffusivity for sulfur-tolerant methanation catalyst. *Chemical Engineering Journal,* 78, pp. 141-146.

Hayes, R.E. & Kolaczkowski, S.T., 1997. *Introduction to catalytic combustion.* Gordon and Breach.

Hayes, R.E. & Mmbaga, J., 2012. *Introduction to Chemical Reactor Analysis.* CRC Press.

Ruthven, D.M., 1984. *Principles of Adsorption and Adsorption Processes.* John Wiley & Sons Inc.

Santos, A., Bahamonde, A., Avila, P. & Garcia-Ochoa, F., 1996. Measurement of the effective diffusivity for a vanadia-tungsta-titania/sepiolite catalyst for SCR of NO_x. *Applied Catalysis B: Environmental,* 8, pp. 299-314.

Schneider, P. & Smith, J., 1968. Adsorption rate constants from chromatography. *AIChE Journal,* 14, pp. 762-771.

Tang, G.H.Y., Trimm, D.L. & Wainwright, M.S., 1987. Effective diffusivity in cylindrical catalyst pellets. *Chemical engineering in Australia,* 12, pp. 9-12.

Wakao, N., Oshima, T. & Yagi, S., 1958. Mass transfer from packed beds of particles to a fluid. *Chemical Engineering of Japan,* 22, pp. 780-785.

5 Measurement of effective diffusivity in a monolith using the chromatographic technique

5.1 Introduction

Starý *et al*. (2006) carried out chromatographic experiments using two different column lengths (500 and 1000 mm), and they used washcoated monoliths and ceramic blank monoliths. To interpret their results, they applied convolution theorem to produce results for a fictitious 500 mm long bed.

As described in Chapter 1, the interest in how the chromatographic technique could be applied to measure the effective diffusivity in washcoated monoliths was the motivation for the work in this thesis.

In the literature much work has been done on the measurement of effective diffusivity in pellets, but there have been very few studies performed on monoliths. The reason being that measurements on monoliths are difficult; because the layer of washcoat is very thin e.g. 20 to 100 μm (e.g. Sideris (1998) and Holder (2008)).

In a review paper by Kolaczkowski (2003), it was proposed that the viability of using the chromatographic technique should be explored further, as a method of measuring the effective diffusivity in catalytic monoliths. It was proposed that a number of monoliths could be mounted inside a single tube, such that the channels in the monoliths were aligned along the axis of the tube, see Figure 5.1.

This suggestion led to the work described in Starý *et al.* (2006), in which the chromatographic technique was used to measure the effective diffusivity in catalytic monoliths. However, they did not align the monoliths as suggested in Kolaczkowski (2003), instead they packed cut sections of monolith in a random manner (see Figure 5.2).

Unfortunately, there is a lack of information in Starý *et al.* (2006), to check exactly how the data was interpreted, and the extent of experimental errors in their method. At the University of Bath, Yap (2011) tried the chromatographic technique (using the configuration in Figure 5.1), but did not find it easy to apply it to a monolith, without encountering significant experimental errors. Therefore in this chapter, it was decided to have a closer look at the technique described in Starý *et al.* (2006).

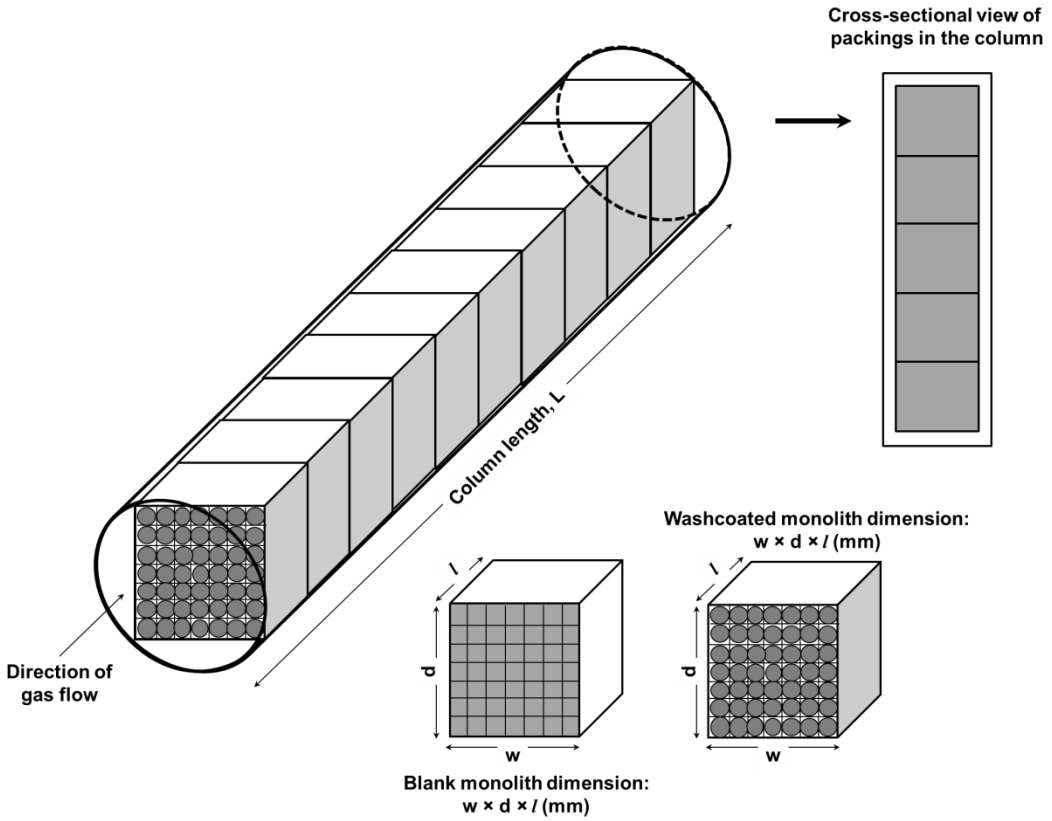

Figure 5.1 (copy of Figure 1.10): Schematic illustrating the positioning of monoliths for a chromatographic experiment (adapted from Kolaczkowski (2003)).

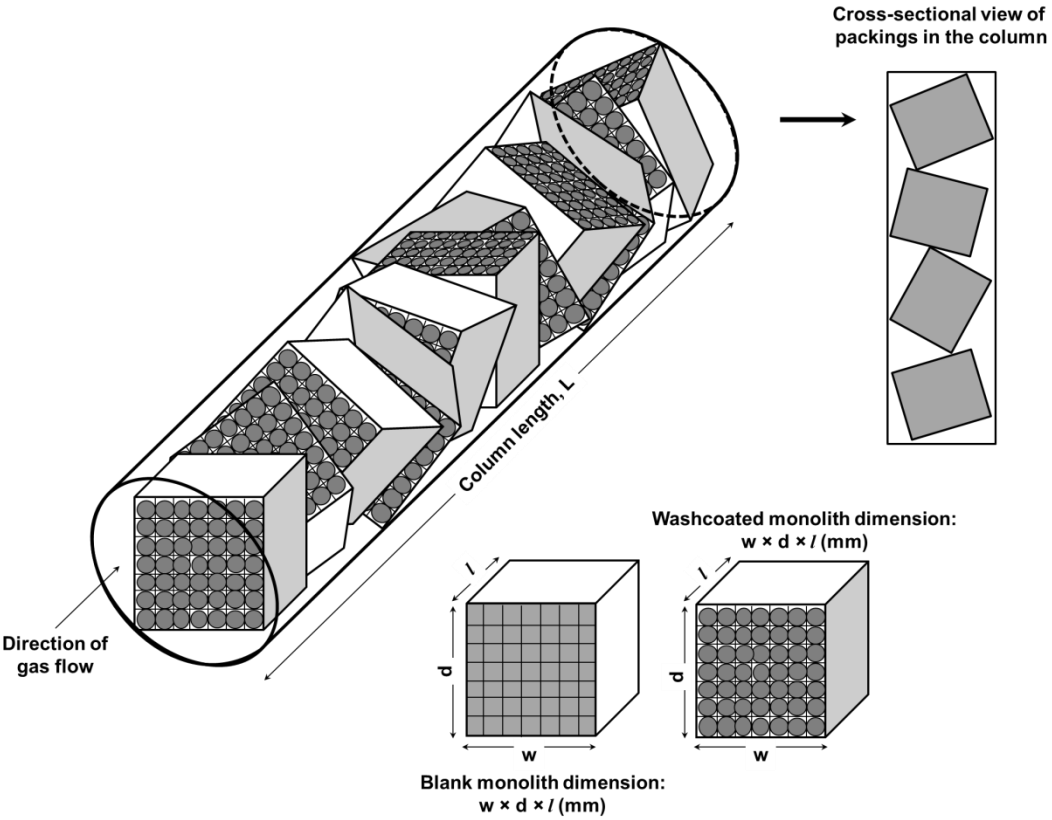

Figure 5.2 (copy of Figure 1.11): Schematic illustrating the positioning of monoliths for a chromatographic experiment (based on description in Staráý *et al.* (2006)).

5.2 Experiment set-up

In order to explore Stary's method, in this thesis, experiments were prepared at almost the same conditions. A picture of monoliths packed inside the 500 and 1000 mm columns is shown in Figure 5.3.

The monolith experiments started with the configuration proposed by Stary *et al*. (2006), where instead of packing the monoliths uniformly, monoliths were packed randomly in the column (see Figure 5.4).

Then, as shown in Figure 5.1, the monoliths alignment suggested in Kolaczkowski (2003) was used, where monoliths were aligned uniformly as shown in Figure 5.5, i.e. the empty channels of monoliths were aligned together as a long monolith section inside the column.

Table 5.1 compares the material properties and experimental conditions used in this chapter with the information presented in Stary *et al*. (2006).

Table 5.1: Comparison of material properties and experimental conditions.

	Staý *et al.* (2006)	**This thesis**
Monolith	Commerical ceramic and washcoated	Commerical ceramic and washcoated
Cell density	400 cpsi	400 cpsi
Wall thickness blank monolith	140 μm	175 μm
Average washcoat thickness	~ 60 μm	105 μm
Washcoat pore diameter	10 nm	11 nm
Packing particle	Cubic shape: 4.3 mm × 5.9 mm × 3.0 mm	Cubic shape: 5.96 × 4.70 × 5.26 mm (blank)
		Cubic shape: 5.87 × 4.76 × 5.05 mm (washcoated)
Column length	Short: 500 mm	Short: 500 mm
	Long: 1000 mm	Long: 1000 mm
Column i.d.	8 mm (column to particle ratio: 1.4)	7 mm (column to particle ratio: 1.18)
Tracer gas	He and Ar	He or N_2
Carrier gas	N_2	N_2 or He
Tracer gas sample loop	0.273 ml	0.1, 0.25 and 0.5 ml
Superficial carrier gas velocity	0.9947 – 6.6315 cm s^{-1}	1.2992 – 3.8977 cm s^{-1}
Temperature and pressure	296 K and 1.013 bar (a)	295 K and 1.013 bar (a)
Detector type	Thermal conductivity detector on Gas Chromatograph	Second Electron Multiplier (SEM) detector on Mass Spectrometer

Based on data in Chapter 2, the packed bed porosities for the SPSC column used for the monolith experiments is shown in Table 5.2.

The skeletal and bulk densities of the blank and washcoated monoliths were obtained from Chapter 2 and used for the calculation of bed porosities in this chapter.

Table 5.2: Single Pellet String Column (SPSC) configuration and bed porosity for the blank and washcoated monolith experiments.

		Column length	**Channel direction**	**Number of monoliths packed**	**Bed porosity, ε_L**
1	**Blank monolith**	500 mm	Aligned	95	0.5849
		1000 mm		190	
2	**Washcoated monolith**	500 mm	Aligned	95	0.5579
		1000 mm		190	
3	**Blank monolith**	500 mm	Random	100	0.5718
		1000 mm		196	
4	**Washcoated monolith**	500 mm	Random	103	0.5207
		1000 mm		200	0.5346
5	**Blank monolith**	1000 mm	Random **(repacked)**	198	0.5675
6	**Washcoated monolith**	1000 mm	Random **(repacked)**	197	0.5416

Stará *et al*. (2006) stated that the monoliths were packed in an **identical manner** in their SPSC. However, from their paper, the total number of cube shaped sections in the 500 and 1000 mm columns was different, and is similar to the difference of randomly packed monoliths (i.e. without following any packing pattern) in this thesis, as shown in Table 5.2 (e.g. see data in rows 3 and 4).

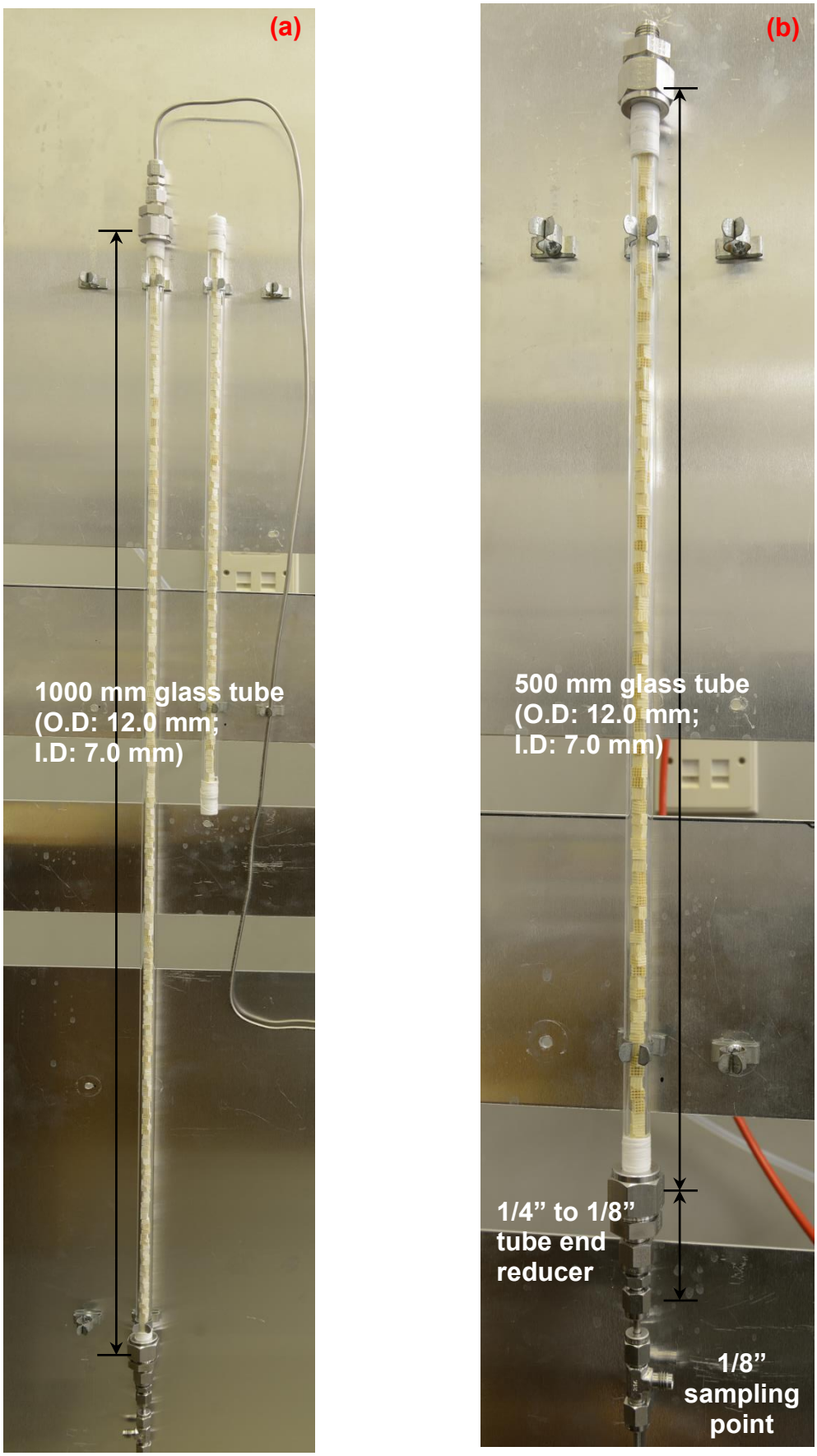

Figure 5.3: Prototype II design: column packed with monoliths: (a) 1000 mm; (b) 500 mm.

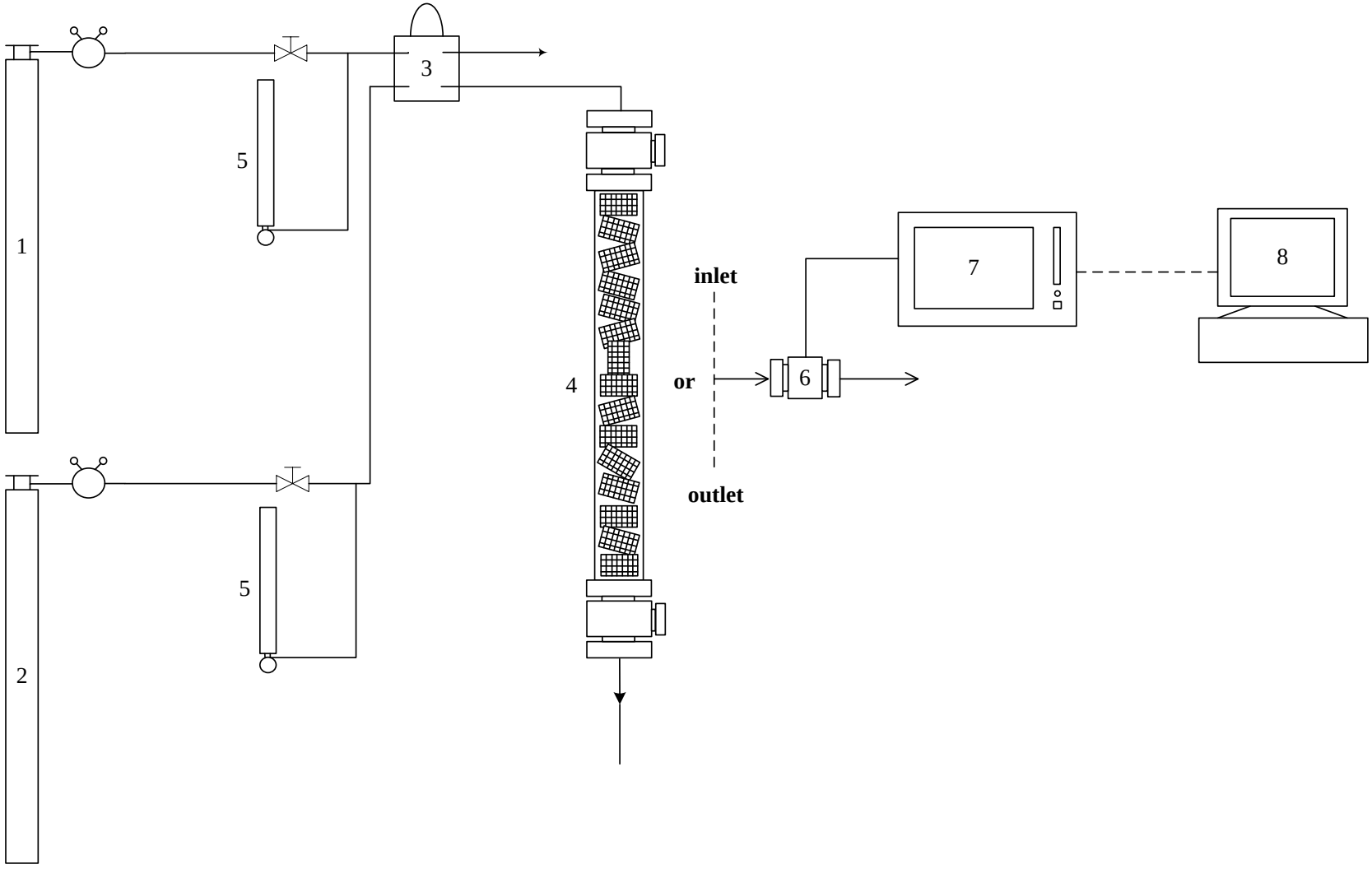

Figure 5.4: Schematic showing the chromatographic experimental set-up for monoliths (same configuration as in Stará *et al*. (2006)): (1) tracer gas cylinder; (2) carrier gas cylinder; (3) VALCO six-port injection valve; (4) column packed with monoliths; (5) MPB long series 1200 BVL flowmeter; (6) sampling probe; (7) Hiden HPR-20 QIC gas analyzer; (8) a PC with software package MASsoft Pro for data analysis.

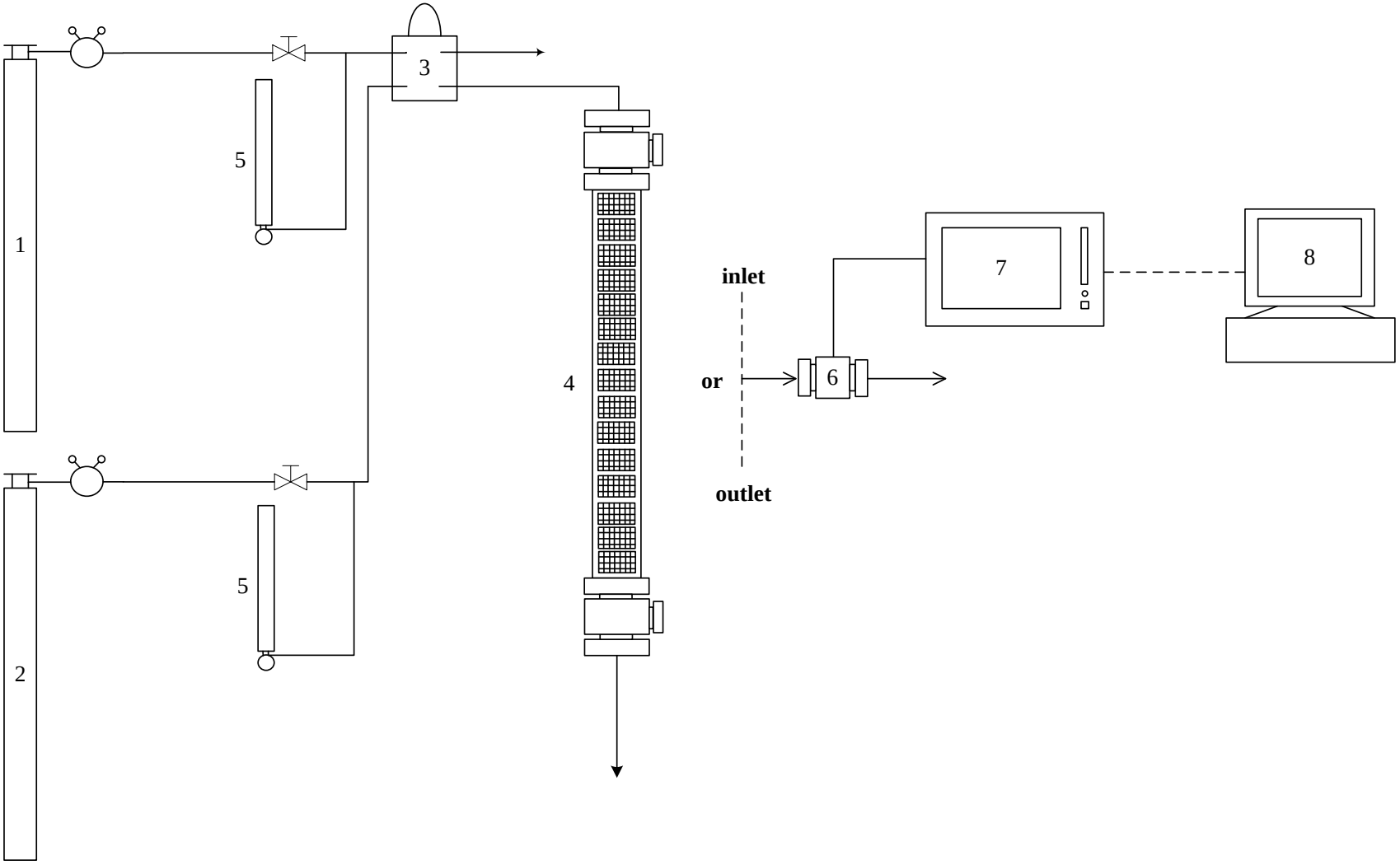

Figure 5.5: Schematic showing the chromatographic experimental set-up for monoliths (same configuration as in Kolaczkowski (2003)): (1) tracer gas cylinder; (2) carrier gas cylinder; (3) VALCO six-port injection valve; (4) column packed with monoliths; (5) MPB long series 1200 BVL flowmeter; (6) sampling probe; (7) Hiden HPR-20 QIC gas analyzer; (8) a PC with software package MASsoft Pro for data analysis.

5.3 Experiment response curves for monoliths

5.3.1 Experimental response curve for randomly packed monoliths

For the 500 and 1000 mm columns, the response curves for blank and washcoated monoliths using helium as a tracer gas (0.25 ml) at nitrogen gas flowrates: 30, 60 and 90 cm^3/min are shown in Figures 5.6 to 5.8, in addition, the number of monoliths packed in the SPSC column are:

- 1000 mm column: (a) washcoated monoliths counted: 200; (b) blank monoliths counted: 196.
- 500 mm column: (a) washcoated monoliths counted: 103; (b) blank monoliths counted: 100.

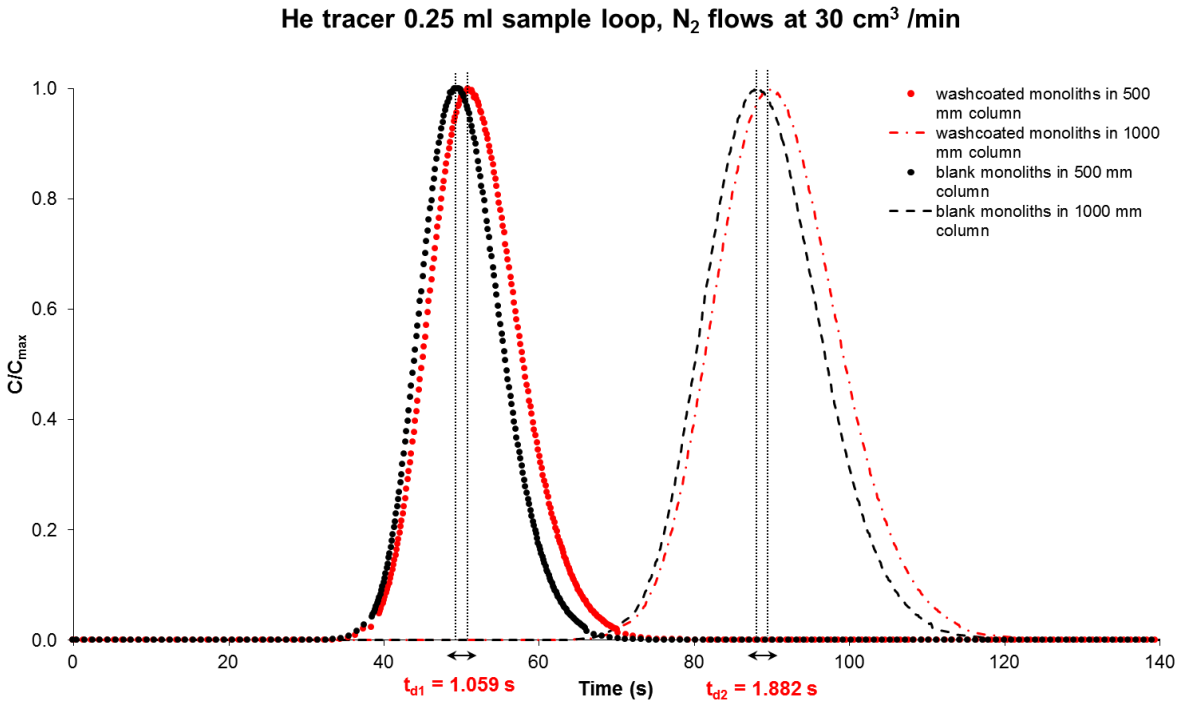

Figure 5.6: Experimental response curves for the SPSC columns **(500 and 1000 mm)** with carrier gas flowrate = **30 cm^3/min**.

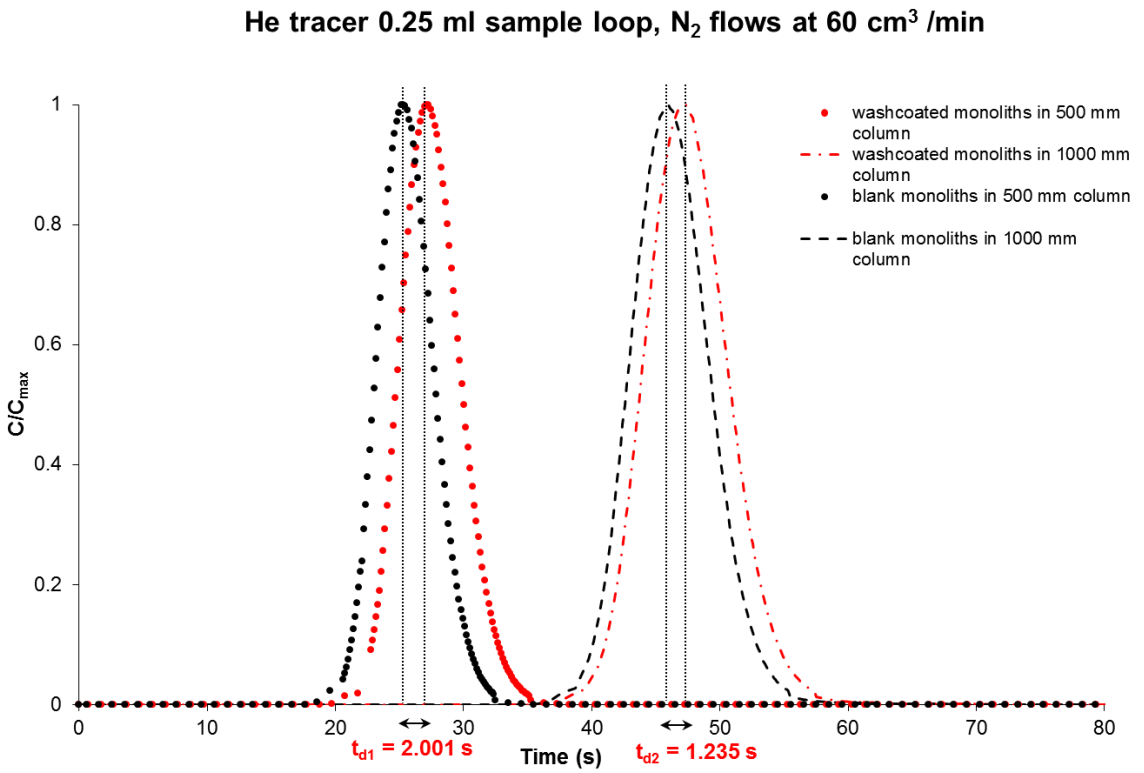

Figure 5.7: Experimental response curves for the SPSC columns **(500 and 1000 mm)** with carrier gas flowrate = **60 cm^3/min**.

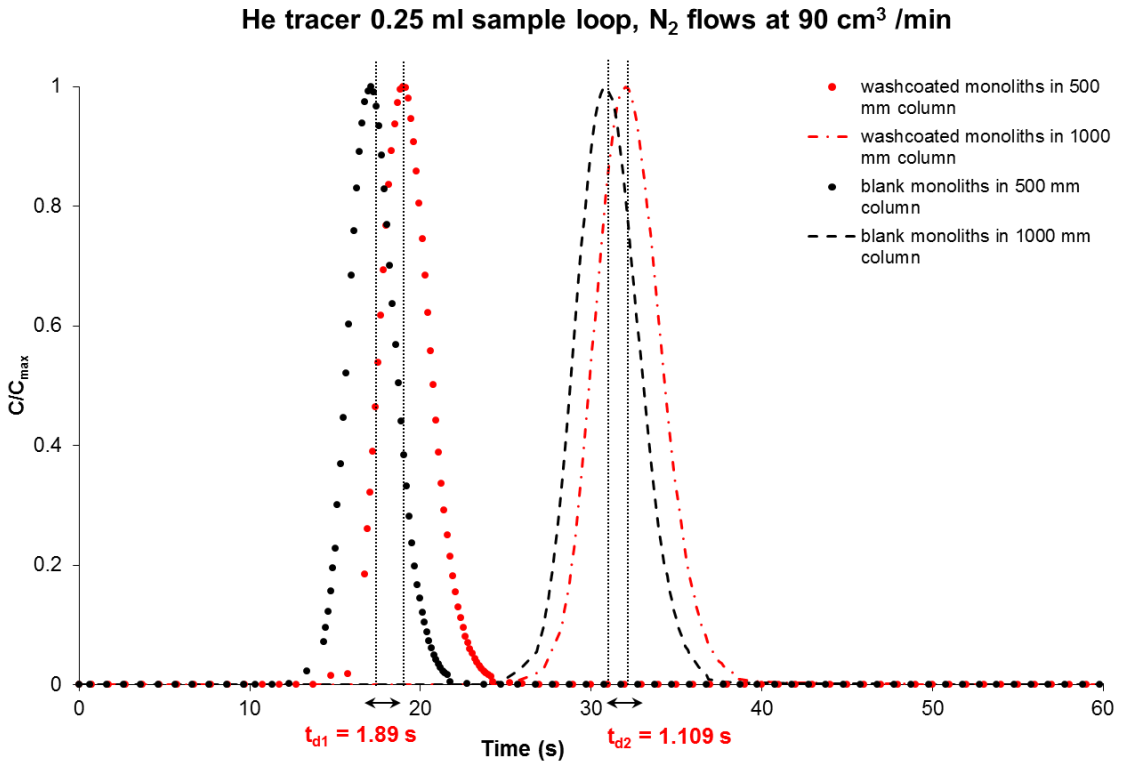

Figure 5.8: Experimental response curves for the SPSC columns **(500 and 1000 mm)** with carrier gas flowrate = **90 cm^3/min**.

5.3.1.1 Experimental response curves obtained with monoliths repacked randomly in SPSC column

To investigate the small difference in peak elution time between the blank and washcoated monolith in Figures 5.6 to 5.8, monoliths were repacked in the SPSC column.

Consequently, the number of monoliths recounted in the 1000 mm column was: (i) washcoated monoliths: 197; (ii) blank monoliths: 198.

Figures 5.9 to 5.11 show the pulse response curves for washcoated monolith repacked in the 1000 mm column. The response curves for the blank monolith in the 1000 mm column are almost the same as for the washcoated monoliths and hence they were not shown.

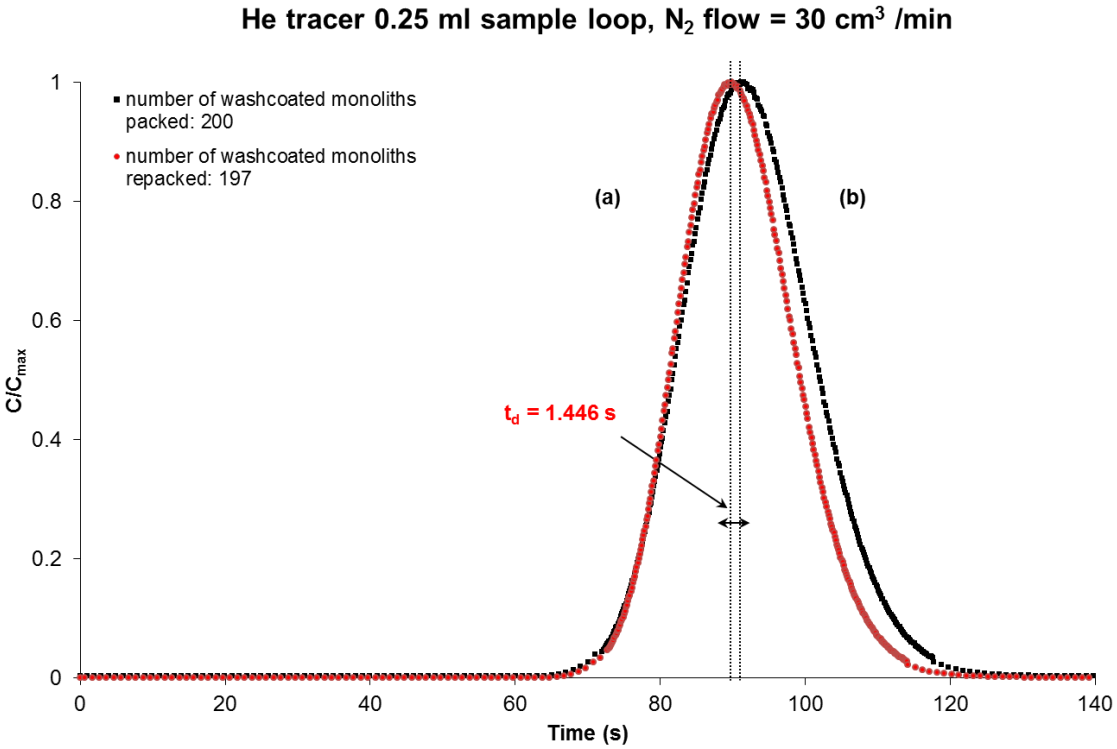

Figure 5.9: Experimental response curves (1000 mm column) with **re-packed** washcoated monoliths: (a) the red dotted line: 197; (b) the black dotted line: 200.

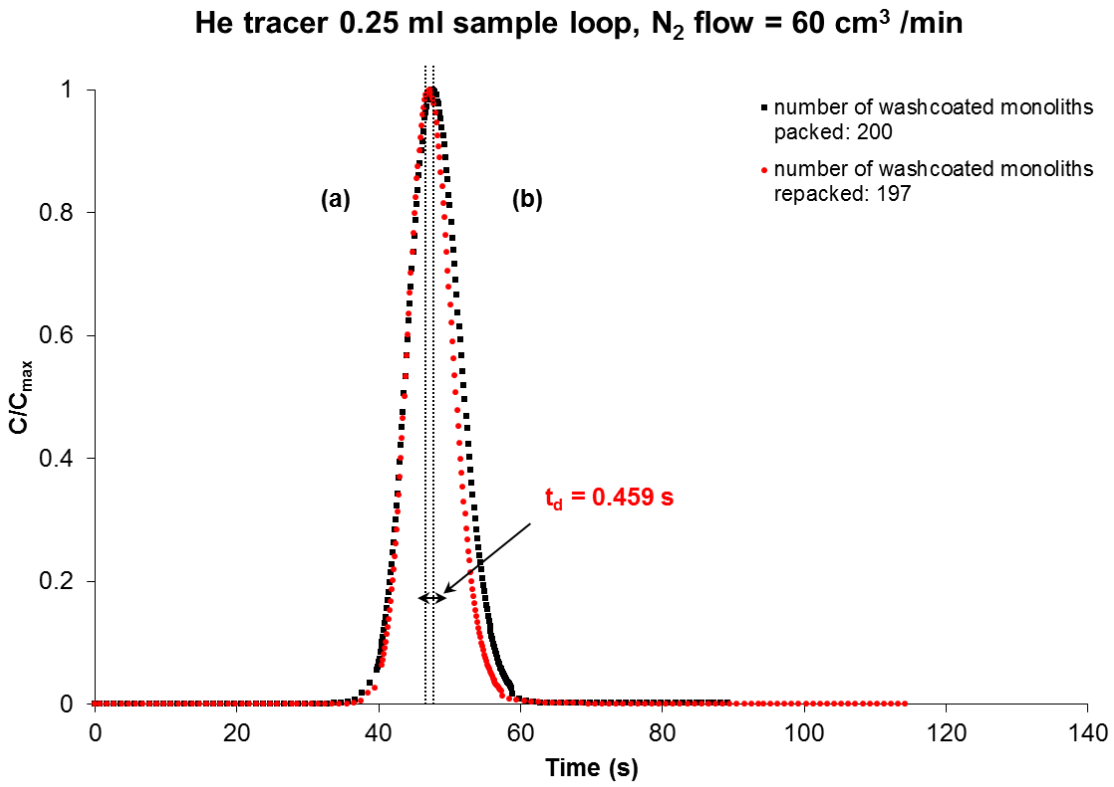

Figure 5.10: Experimental response curves (1000 mm column) with **re-packed** washcoated monoliths: (a) the red dotted line: 197; (b) the black dotted line: 200.

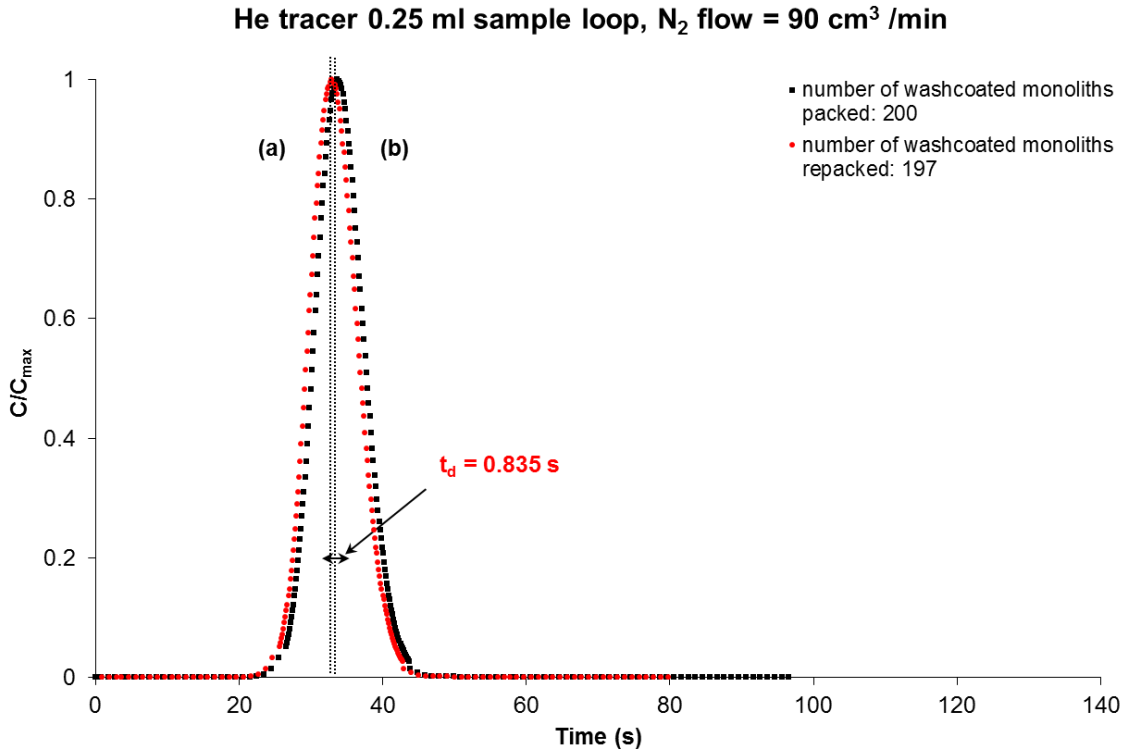

Figure 5.11: Experimental response curves (1000 mm column) with **re-packed** washcoated monoliths: (a) the red dotted line: 197; (b) the black dotted line: 200.

From Figures 5.9 to 5.11, when the SPSC column was re-packed with washcoated monolith, a total number of 197 monoliths were used. The difference in peak elution time between the packed (N_{WS} = 200) and the re-packed (N_{WS} = 197) for washcoated monoliths was ≤ 1.5 s at carrier gas flowrates of 30, 60 and 90 cm^3/min. The difference in the number of monoliths packed inside the SPSC column was between 1 ~ 3 monoliths, compared with: $N_{diff} = \pm 2$ in Star*ý et al.* (2006) for the 1000 mm column.

This now starts to explain the difference in peak elution time between the blank and the washcoated monolith in Figures 5.6 to 5.8 (i.e. t_d = 1 ~ 2 s). The randomness in the packing could have created this effect. The experimental error band is 1.5 s for both blank and washcoated monolith. Therefore, it would be very inappropriate to use these experimental response curves to calculate D_{eff}, because the error would be significant.

When convolution theorem is applied in Stará *et al*. (2006), from the response plot of the washcoated monolith in Stará *et al*. (2006), the time difference between the shorter column response (500 mm) and the response for the fictitious column (500 mm) is ≈ 2 s, and for the blank monolith ≈ 3 s. From convolution theorem, the first moment, μ_1, and the second central moment, $\mu_2^{'}$, of the whole system can be represented as the sum of individuial first moments and second central moments.

Hence, the first moment μ_1, for the response of a fictitious column (500 mm) is:

$$(\mu_1)_{fictitious} = (\mu_1)_{1000} - (\mu_1)_{500} \tag{5.1}$$

and the second central moment, $\mu_2^{'}$ is:

$$(\mu_2^{'})_{fictitious} = (\mu_2^{'})_{1000} - (\mu_2^{'})_{500} \tag{5.2}$$

Making use of the data in Figure 5.7 (at carrier gas flowrate 60 cm^3/min), from Equations (5.1) and (5.2), the responses of the fictitious column (500 mm) for the blank and washcoated monolith experiments (in this thesis) are shown in Figures 5.12 and 5.13. In addition, at flowrates of 30 and 90 cm^3/min, the mean residence time, μ_1 for the **fictitious** column packed with the blank and washcoated monoliths were also calculated:

<u>At 30 cm^3/min:</u>

$(\mu_1)_{washcoated} = 38.987$ s $\qquad\qquad$ $(\mu_1)_{blank} = 38.884$ s

<u>At 90 cm^3/min:</u>

$(\mu_1)_{washcoated} = 13.799$ s $\qquad\qquad$ $(\mu_1)_{blank} = 13.108$ s

These results now clearly show that there is no real distinquishable difference between washcoated and blank monoliths. Besides, the second central moments, $\mu_2^{'}$ for the fictitious monoliths packed bed would also be the same. Therefore, the effective diffusiivty, D_{eff} (if there is a value) would be the same for both blank and washcoated monoliths. However, the results reported by Stará *et al.* (2006) for blank and washcoated monoliths were:

- For blank monolith: $7.5 \times 10^{-3} - 8.6 \times 10^{-3}$ cm^2 s^{-1};
- For washcoated monoliths: $1.71 \times 10^{-3} - 2.99 \times 10^{-3}$ cm^2 s^{-1}.

Under the circumstances described, these are surprising values.

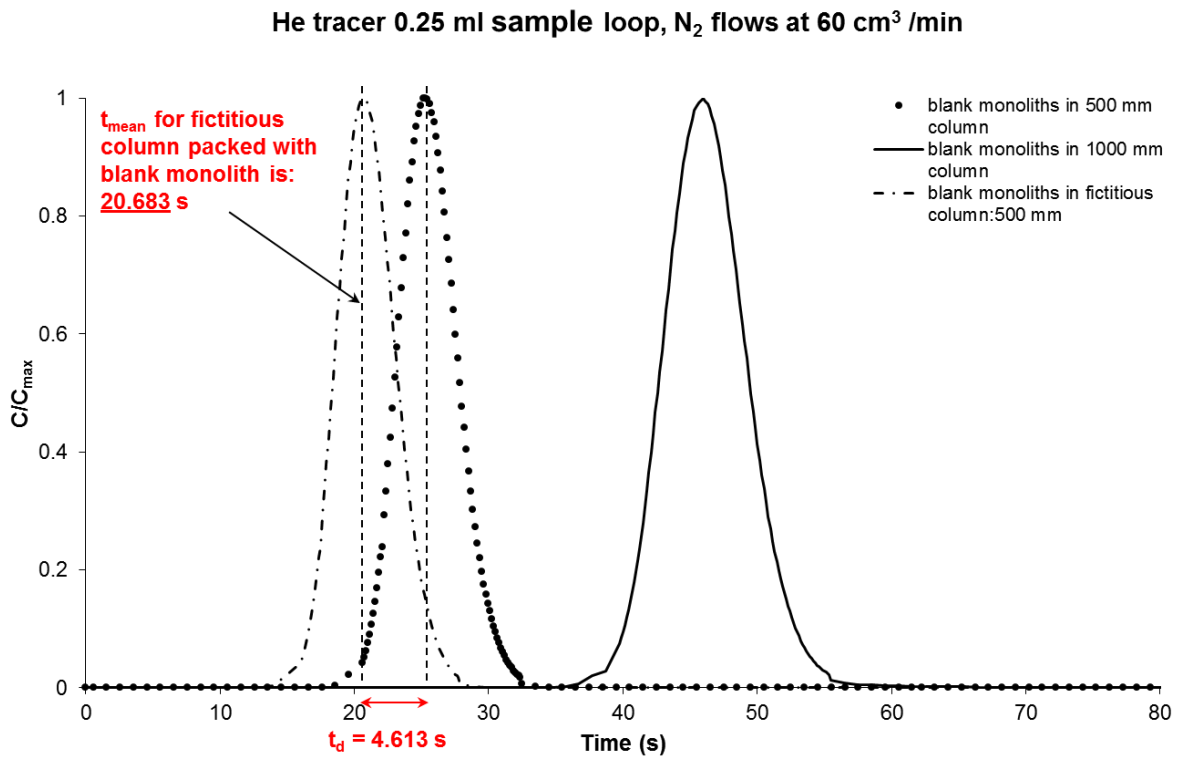

Figure 5.12: Response curve for a fictitious bed (L_c = 500 mm) packed with blank monoliths, with 0.25 ml (He tracer) sample loop at carrier gas flowrate 60 cm^3/min.

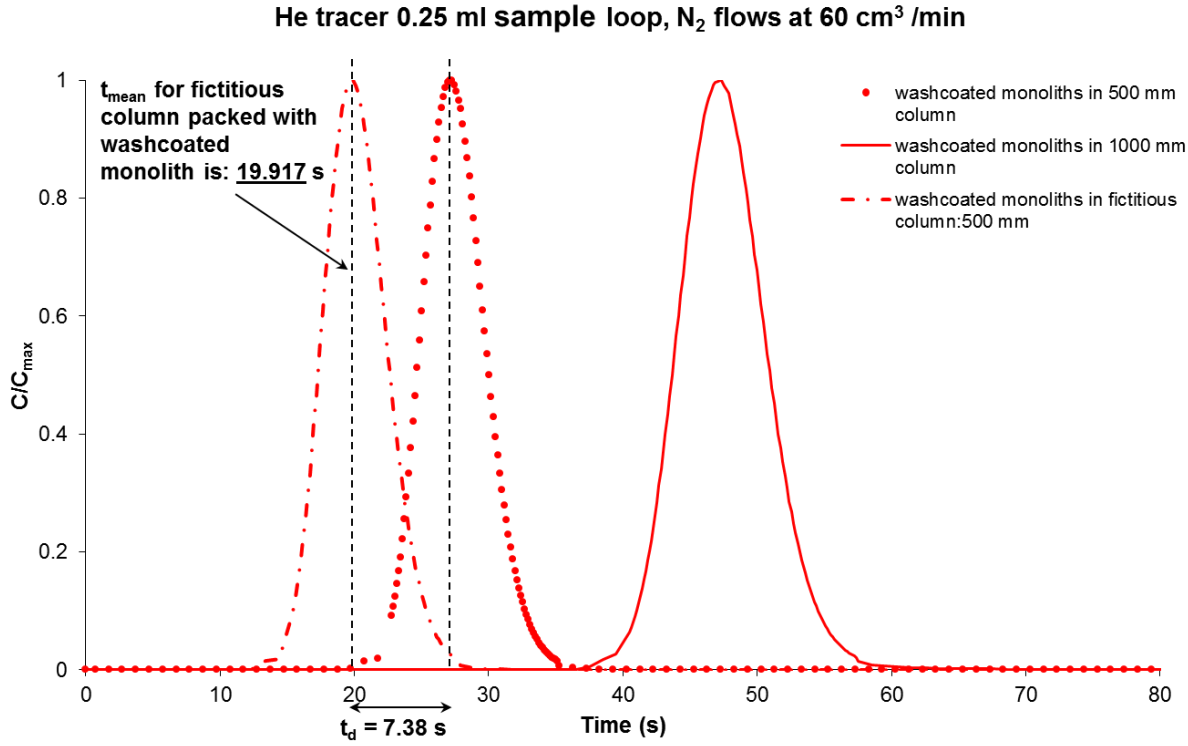

Figure 5.13: Response curve for a fictitious bed (L_c = 500 mm) packed with washcoated monoliths, with 0.25 ml (He tracer) sample loop at carrier gas flowrate 60 cm^3/min.

5.3.2 Experimental response curve for uniformly packed monolith experiments

Figures 5.14 to 5.16 show the response curves for blank and washcoated monoliths aligned uniformly in the direction of gas flow in the 500 and 1000 mm columns.

Looking closely at Figures 5.14 to 5.16, there is very little difference between the experimental response curves for the blank and the washcoated monoliths. This is because when monoliths are aligned in the direction of gas flow, the radial dispersion and mixing effects are reduced. Whereas in Staý *et al.* (2006)'s case, for randomly packed monoliths, the dispersion effects are more dominant and probably contribute to the small difference in peak elution time between the blank and washcoated monoliths.

Likewise, very little noticeable change in peak elution time was observed at different carrier gas flowrates, sample loop volumes and tracers. Therefore, the difference between the diffusivity of blank and washcoated monoliths is difficult to quantify. Hence, in conclusion, at this set of experimental conditions, it is difficult to use the chromatographic technique to measure the effective diffusivity of the γ-alumina washcoat layer.

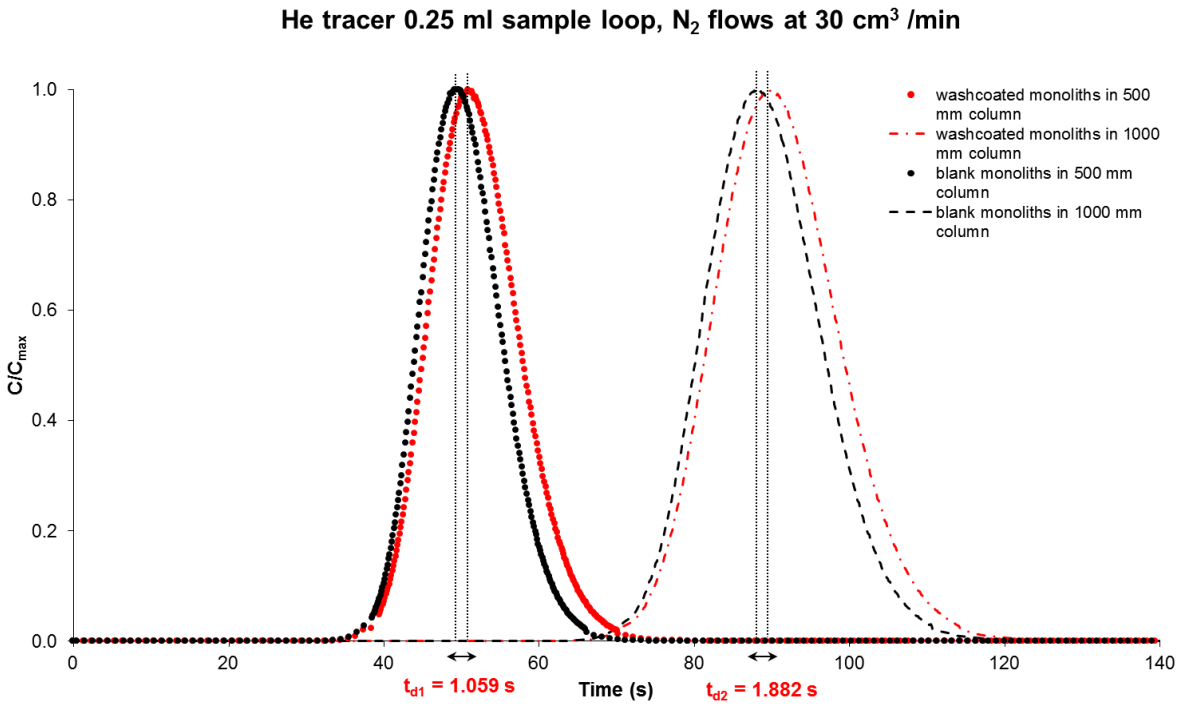

(a) Random placed (as in Stark *et al.* (2006)).

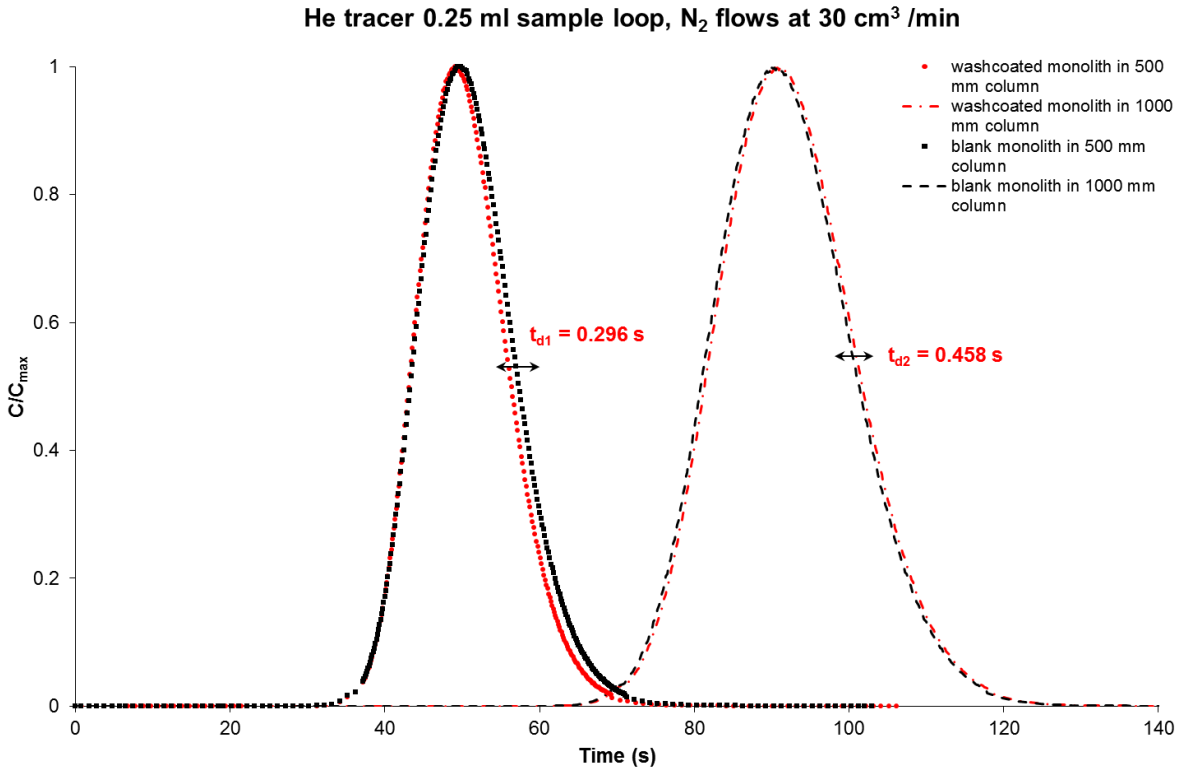

(b) Channel aligned (as in Kolaczkowski (2003)).

Figure 5.14: Response curves at 30 cm^3/min for (a) random packed columns, (b) channel aligned columns.

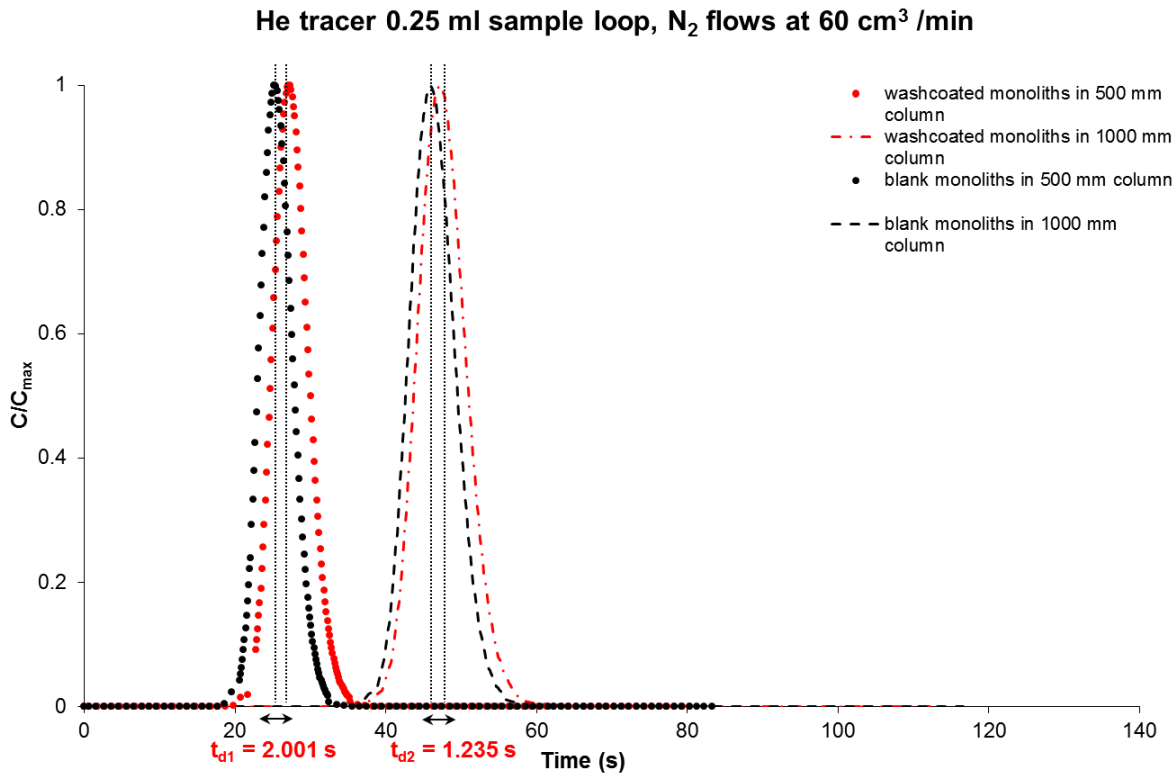

(a) Random placed (as in Staý *et al.* (2006)).

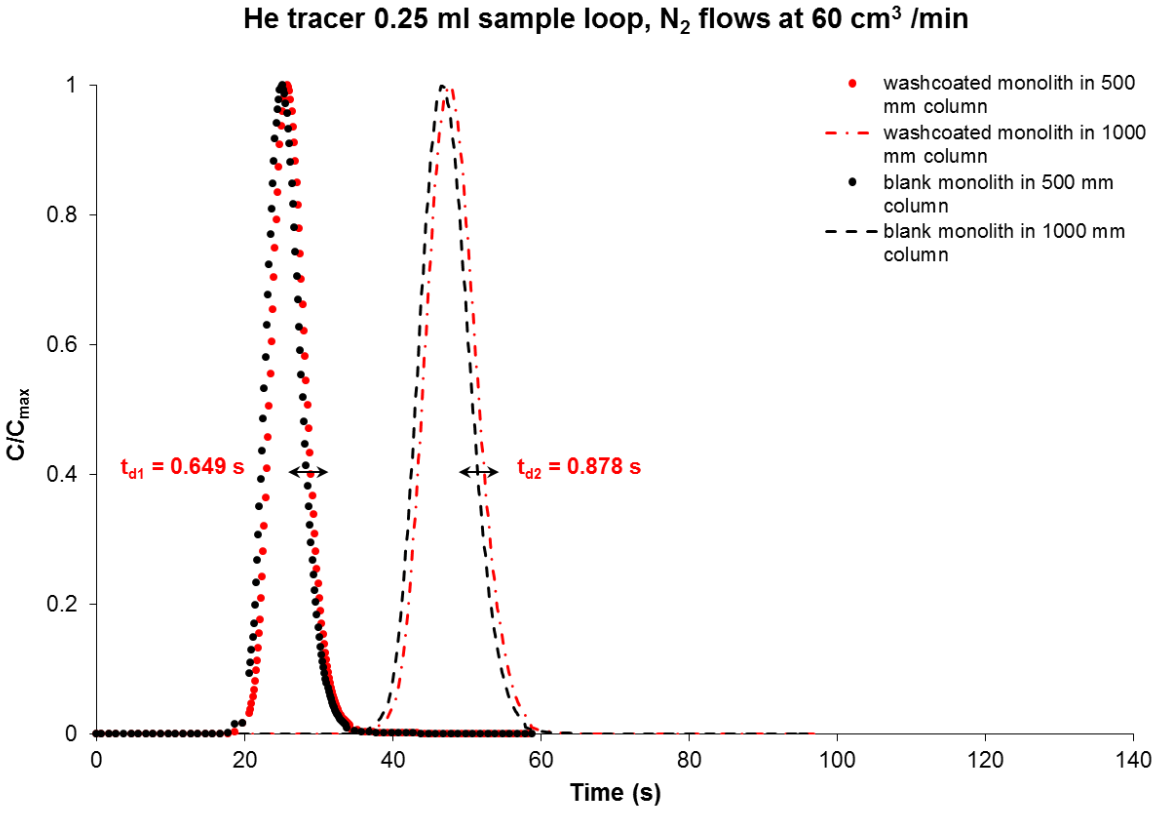

(b) Channel aligned (as in Kolaczkowski (2003)).

Figure 5.15: Response curves at 60 cm^3/min for (a) random packed columns, (b) channel aligned columns.

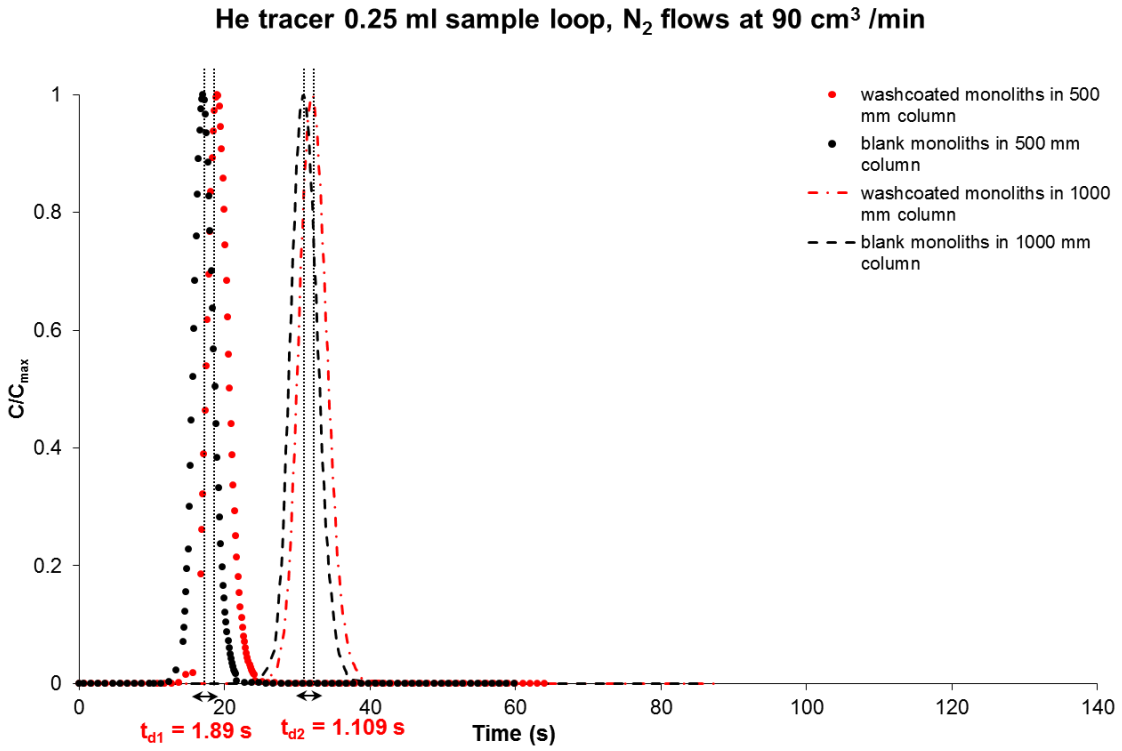

(a) Random placed (as in Staý *et al.* (2006)).

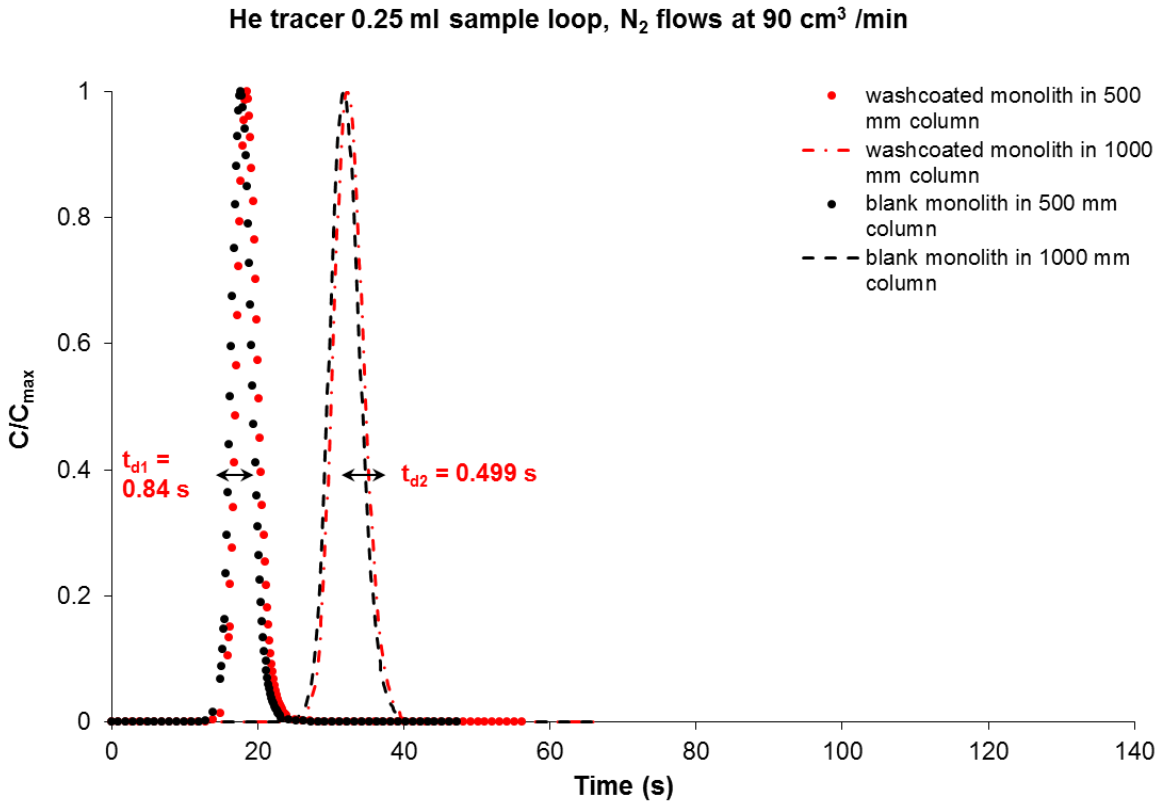

(b) Channel aligned (as in Kolaczkowski (2003)).

Figure 5.16: Response curves at 90 cm^3/min for (a) random packed columns, (b) channel aligned columns.

5.4 Conclusion

Measuring the effective diffusivity for monoliths using the chromatographic method and the monolith configuration as proposed by Starý *et al*. (2006) is difficult to implement for the following key reasons:

- **Blank monolith/washcoated monolith:** experiment response curves from the blank monolith experiments are almost the same as the washcoated experiments, with only a 1 – 2 s difference in the mean residence time. This could occur from a combination of experimental errors, variations in packing, variations in RTD because of washcoat volume etc.

- **Convolution theorem:** the convolution method used in Starý *et al*. (2006) was tried. The difference between the response curves of a fictitious column (500 mm) packed with blank monoliths and a fictitious column packed with washcoated monolith is negligible.

References

Holder, R., 2008. *A Global Reaction Mechanism for Transient Simulations of Three-Way Catalytic Converters.* Cuvillier Verlag.

Kolaczkowski, S.T., 2003. Measurement of effective diffusivity in catalyst-coated monoliths. *Catalysis Today*, 83, pp. 85-95.

Sideris, M., 1998. *Methods for monitoring and diagnosing the efficiency of catalytic converters: a patent-oriented survey.* Elsevier Science.

Starý, T., Solcová, O., Schneider, P. & Marek, M., 2006. Effective diffusivities and pore-transport characteristics of washcoated ceramic monolith for automotive catalytic converter. *Chemical Engineering Science*, 61, pp. 5934-5943.

Yap, Y. 2011. *On-line and on-engine catalyst characterisation – effective diffusion and reaction mechanisms.* Phd, University of Bath.

6 Conclusions and Recommendations

6.1 Conclusions

Experimental 1st moments

(a) These were relatively easy to evaluate from the RTD data, and the method using the proprietary package known as OriginPro 8.6 to calculate peak area and the 1st moment, μ_1, with a Gaussian area function was preferred, as it was: reliable, easier to use, and the package had other useful features (e.g. a user-defined equation for non-curve fitting in Chapter 4).

(b) From experiments on a combination of short (200 mm) and long (400 mm) columns, it was clear that 'column inlet' and 'column exit' effects, did affect the results.

Experimental 2nd central moments

(c) Similar to 1st moment, using peak fitting method, the 2nd central moment, μ_2' or the variance for pulse response curves were calculated. Generally speaking, both Cat. A and Cat. B produce similar results. However, for effective diffusivity and tortuosity factor calculations, the 2nd central moment, μ_2' calculated using Cat. A was preferred.

Convolution method

(d) Applying the convolution method to the RTDs determined with the 200 mm and 400 mm long columns, the 1st and second 2nd central moments for a fictitious 200 mm long bed (without entrance and exit effects) could be evaluated.

Material balance equations (Column and Particle Models)

(e) The material balance equations from Kubń and Kučera model (Kubń, 1965; Kučera 1965) were used in this thesis for calculating the adsorption equilibrium constant and effective diffusivity. Different intraparticle material balance models were investigated and discussed in this thesis. It is important to perform such calculations on a fictitious bed.

Equilibrium constants

(f) A variety of different methods were explored, and the methods based on Guangsuo *et al*. (2000) i.e. Cases 2a and 2b were preferred. This is because: (i) the intraparticle material balance was checked and the units balance; (ii) the first moment for the inert run, $(\mu_1)_{inert}$, is evaluated from the experimental curve rather than calculating it from a theoretical expression, $(\mu_1)_0$; (iii) the results for the adsorption equilibrium constants are small and compared well with literature data for weak adsorption gases – i.e. inert gas.

Axial dispersion coefficients

(g) The performance of experiments with the glass beads was useful, as in comparative RTD plots (with data for the γ-alumina beads), it was very clear that the effect of intraparticle diffusion in the pores of the γ-alumina beads was very significant, and therefore at the range of conditions tested easily measurable.

(h) Values of axial dispersion, D_{ax} depend on the method of analysis used. There were slight variations between some of the methods. In conclusion methods based on the results of experiments with the glass beads, and also with experiments on the γ-alumina beads **(Cases 1, 2a, 2b, 2c, 3a, 3b and 6)** were preferred.

Effective diffusivity values

(i) Although different methods were used to interpret the RTD data, there were some significant variations between some of the methods. The results with **N_2 tracer** and second central moment obtained from **Cat. A** look more reliable and agree with literature values. The preferred method(s) were: (i) 2nd central moment method: **Cases 2a, 2b, 2c, 3a and 3b;** (ii) HETP method: **Case 6**.

External mass transfer coefficients

(j) γ-alumina beads: From the analysis performed, it was clear that the contribution of external mass transfer resistance was small (≤ 1%) relative to the intraparticle resistance term (≥ 98%).

Apparent tortuosity values

(k) Depending on the method selected to determine the effective diffusivity there were some significant variations in the value of tortuosity calculated. If the preferred method(s) from the effective diffusivity analysis are used, then a value between **5 to 9.5 (base on N_2 as tracer)** could be assigned depending on the method used.

RTD experiments on monoliths

(l) When samples of monolith are inserted into the column, with the channels aligned along the direction of gas flow, then from chromatographic experiments performed on washcoated monoliths, and also blank uncoated monoliths, then over the range of conditions tested, it is difficult to distinguish any significant delay in the 1st moment as a result of intraphase diffusion into the γ-alumina layer.

(m) When the samples of monolith were inserted into the column in a random manner as in Stark *et al*. (2006), then from chromatographic experiments performed on washcoated monoliths, and also blank uncoated monoliths, then over the range of conditions tested, there is a delay in the 1st moment, but this occurs as a result of axial dispersions rather than intraphase diffusion into the γ-alumina layer.

(n) Based on observations (d) and (l), and a lack of explanatory information/data in Starý *et al*. (2006), it is concluded that the technique as described in Starý *et al*. (2006) would not be suitable for the measurement of effective diffusivity in washcoated (with γ-alumina) monoliths (where washcoat layer thickness is 20 to 100 μm).

Descriptions in the literature

(o) In general, these were very difficult and time consuming to follow and understand, as key calculation steps are sometimes inadequately explained, and in some cases there are mistakes in the units quoted, which were difficult to resolve. Authors have also used slightly different ways in which they approach the problem, and also in the units that they assign to some of the values in the expressions. For example, the Adsorption Equilibrium Constant, has units in some papers, but is dimensionless in others. All of these problems made it very difficult to follow the explanations offered, when a deeper level of understanding was required so that the techniques could be tried with confidence.

Overview of analysis in this thesis

(p) By applying different methods to the same set of experimental data, and by also performing experiments on glass beads and also on γ-alumina beads (of same diameter), a useful comparison has been obtained between the different methods. Also, the shortcomings of certain methods have been more clearly identified.

6.2 Recommendations

There are a number of areas in which this work could be taken further, and the following suggestions are made:

(a) Experiments could be performed on monoliths which have thicker washcoated layers, so as to establish at what thickness of washcoat, the RTD signal could be used to interpret effective diffusivity and tortuosity in the washcoat. These would be best done on monoliths where the channels are aligned along the axis of the tube (i.e. direction of gas flow) so as to minimize axial dispersion effects.

(b) Convolution theorem solved by numerical method. However, this would require the following steps:

(i) Interpolate the response curve for the 200 and 400 mm long columns with a simple function (e.g. cubic spline) and apply Laplace transform.

(ii) Using the deconvoluted function of the fictitious column obtained from mass balance equations (in Laplace form), which depends on a range of parameters.

(iii) By fitting certain parameters (i.e. the diffusion time is included for each fitting), use the least square method to minimise the difference between the deconvoluted results from experiments and from mass balance to find the optimum values for diffusion time. Inverse the diffusion time from Laplace to time domain using numerical technique (e.g. MATLAB code: algorithm of De-Hoog) to obtain D_{eff}.

(iv) The effective diffusivity results from convolution by numerical method, could then be used to compare the results obtained using the convolution principles described in this thesis.

Appendix

Appendix 1: Numerical integration: Simpson's rule

Simpson's rule can be used for numerical integration of curves. For high-order polynomial functions or complicated curves, different rules from Simpson's formula can be applied depending on the shape of the response curves. For instance, Figure A1.1 shows cases when trapezoidal rule and Simpson's three-point rule are applied to the response curves. Aside from using the trapezoidal rule with finer segmentation, another way to improve the estimation accuracy is to use higher order polynomials. For example, Figure A1.2 shows Simpson's four-point rule. In addition, following the same principle, there will be more divisions on *x*-axis of the response curves for Simpson's three-eighths rule and five-point rule and hence more accurate answers can be obtained (Fogler, 2004). However, even with more intervals on the *X*-axis (e.g. Figure 3.14), there are still some areas which the trapezoidal rule could not cover.

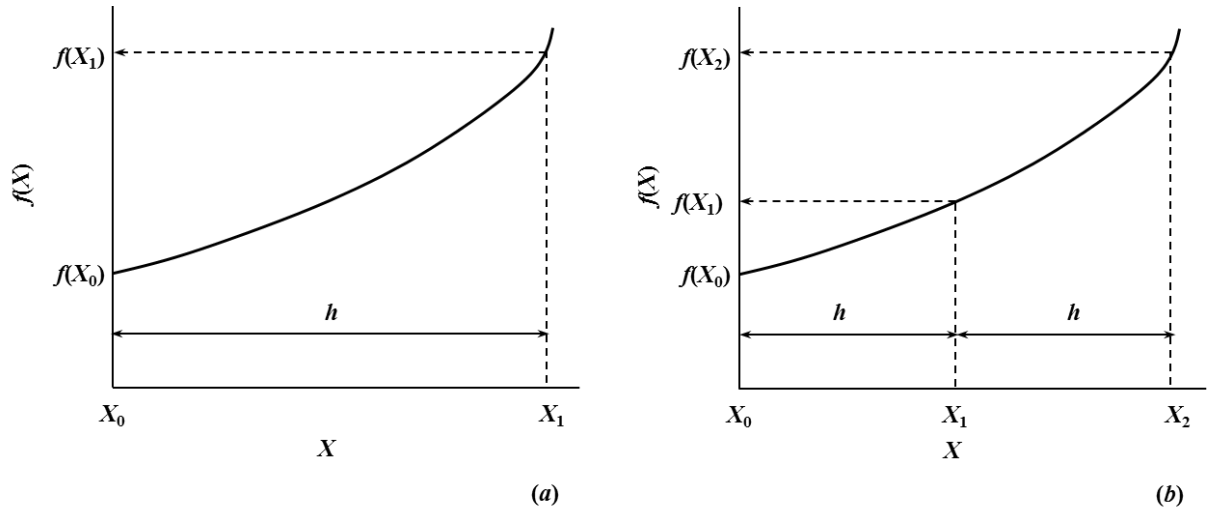

Figure A1.1: Graphical representations of Simpson's formula: (a) Trapezoidal rule; (b) Simpson's three-point rule (Fogler, 2004).

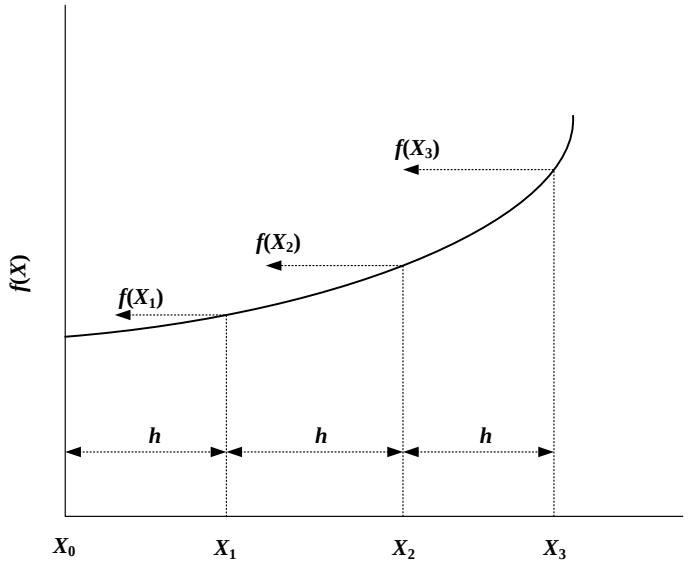

Figure A1.2: Simpson's four-point rule illustration (Fogler, 2004).

1. For $N + 1$ points, where $(N/3)$ is an integer:

$$\int_{X_0}^{X_N} f(X)dX = \frac{3h}{8}\left[f_0 + 3f_1 + 3f_2 + 2f_3 + 3f_4 + 3f_5 + 2f_6 + ... + 3f_{N-1} + f_N \right] \qquad \text{(A1.1)}$$

Where $h = \dfrac{X_N - X_0}{N}$

2. For $N + 1$ points, where N is even:

$$\int_{X_0}^{X_N} f(X)dX = \frac{h}{3}\left[f_0 + 4f_1 + 2f_2 + 4f_3 + 2f_4 + ... + 4f_{N-1} + f_N \right] \qquad \text{(A1.2)}$$

Where $h = \dfrac{X_N - X_0}{N}$

References

Fogler, H.S., 2004. *Elements of Chemical Reaction Engineering*. Pearson Education.

Appendix 2: The choice of SEM (Secondary Electron Multiplier) over Faraday detector

The difference between the Faraday detector and the Secondary Electron Multiplier (SEM) detector is their sensitivity. The SEM detector offers the ability to detect very low partial pressure of evolved gas between 1×10^{-13} torr to 1×10^{-7} torr, whereas the detectable range for Faraday detector is between 1×10^{-10} torr to 1×10^{-5} torr.

The response peaks recorded by Faraday detector and SEM detector are shown in Figures A2.1 and A2.2. Both of these peaks are recorded using the Prototype II design. The similarities and differences are summarised as follows:

1. Both peaks are recorded at column outlet with the same experimental conditions:
   (a) He (carrier) – N_2 (tracer) gas system is used;
   (b) carrier gas flowrate is 35 cm^3/min;
   (c) tracer gas sample loop 0.25 ml;
   (d) 295.15 K and 1.013 bar.
2. No of data points shown in MID scans:
   (a) 658 scans for SEM;
   (b) 23 scans for Faraday.
3. Maximum peak heights are different:
   (a) 1.60×10^{-7} torr for Faraday;
   (b) 1.05×10^{-7} torr for SEM.
4. Tracer gas retention or elution time is different:
   (a) 59 seconds for Faraday;
   (b) 106.8 seconds for SEM.

In this thesis, the SEM detector is selected rather than Faraday detector, not only because it gives more data points for the response peak, but also the peak shape is more symmetric and gaussian than the Faraday detector, which eventually leads to a better R-square value in peak fitting.

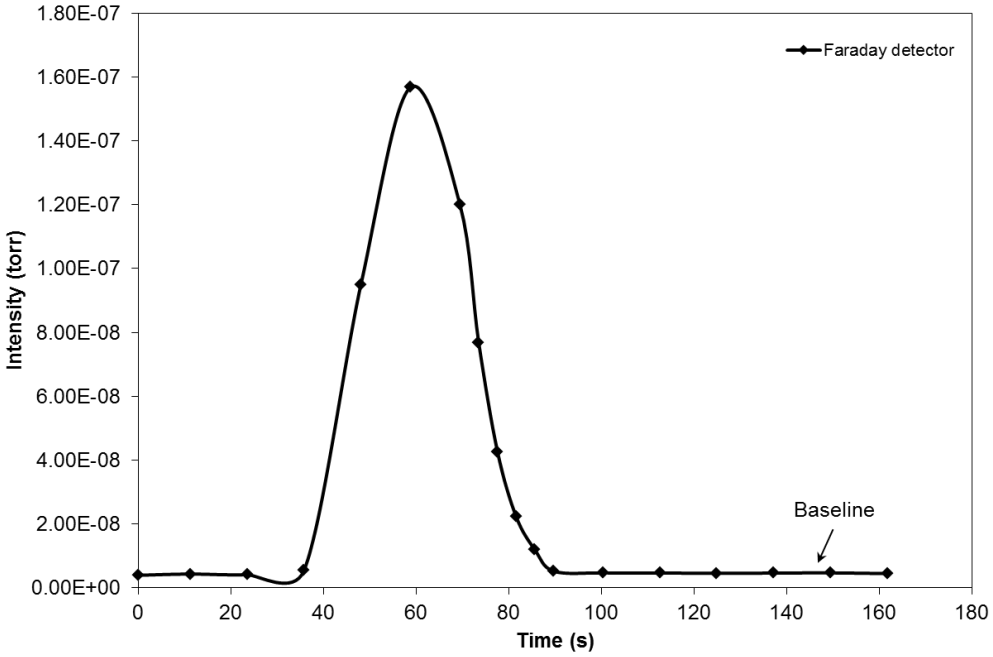

Figure A2.1: The response curve (to a Dirac pulse input) is recorded using the Faraday detector.

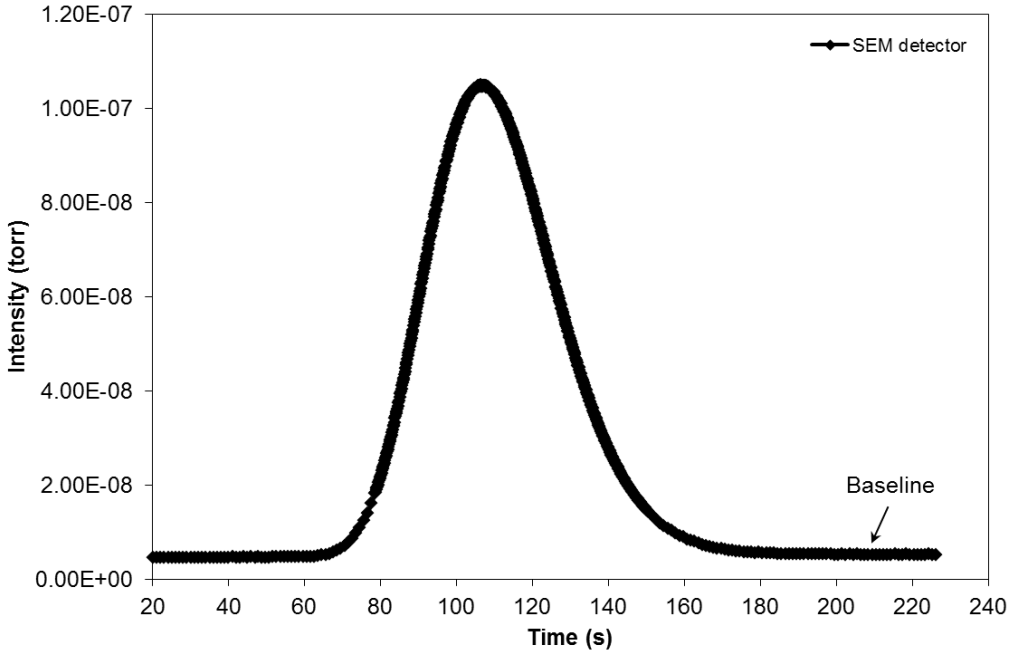

Figure A2.2: The response curve (to a Dirac pulse input) is recorded using the SEM detector.

Appendix 3: Moment calculations by integrating the area of the experimental response peak

Normalization: from *C*-curve *C*(*t*) to *E*-curve *E*(*t*):

$$E(t) = \frac{C(t)}{\int_0^\infty C(t)dt} \tag{A3.1}$$

Area under *E*(*t*) curve:

$$\int_0^\infty E(t)dt = 1 \tag{A3.2}$$

First moment:

$$\mu_1 = t_m = \int_0^\infty tE(t)dt \tag{A3.3}$$

Second central moment:

$$\mu_2^{'} = \int_0^\infty \left(t - t_m\right)^2 E(t)dt = \int_0^\infty t^2 E(t)d(t) - 2t_m \underbrace{\int_0^\infty tE(t)d(t)}_{t_m} + t_m^2 \underbrace{\int_0^\infty E(t)d(t)}_{1}$$
$$\Rightarrow \mu_2^{'} = \int_0^\infty t^2 E(t)dt - t_m^2 \tag{A3.4}$$

A3.1 The area under *I*-curve with time interval h_1 = 4 s

Figure A3.1 shows the experimental response peak (recorded by MID scan) plotted in terms of vacuum pressure (unit: torr) *versus* time. In the following section, the vacuum pressure are referred to as the intensity data *I*(*t*). To perform numerical integration of the peak area, 18 data points were chosen with an equivalent time interval h_1 = 4 s. The values of the data points are summarised in Table A3.1.

Table A3.1: The intensity data *I* as function of time *t* with time interval h_1 = 4 s.

Time (s)	**36.47**	**40.48**	**44.48**	**48.51**	**52.53**	**56.58**	**60.62**	**64.66**	**68.7**
***I*(*t*) (torr)**	6.03×10^{-12}	1.08×10^{-10}	8.55×10^{-10}	2.83×10^{-9}	7.53×10^{-9}	1.33×10^{-8}	1.73×10^{-8}	1.72×10^{-8}	1.40×10^{-8}
Time (s)	**72.74**	**76.77**	**80.79**	**84.79**	**88.89**	**92.59**	**96.59**	**100.6**	**104.6**
***I*(*t*) (torr)**	9.63×10^{-9}	5.73×10^{-9}	3.13×10^{-9}	1.53×10^{-9}	5.89×10^{-10}	2.77×10^{-10}	1.17×10^{-10}	4.99×10^{-11}	2.25×10^{-11}

The area under the *I*-curve is divided into two regions: 36.47 to 92.59 s, and 92.59 to 104.6 s. There are 18 data points on the response curve and the time interval h_1 between every data point is 4 s. Therefore, the area under the *I*-curve can be found using numerical integration (Equations (A1.1) and (A1.2)) for *N*+1 points.

$$\int_{36.47}^{104.6} I(t)dt = \int_{36.47}^{92.59} I(t)dt + \int_{92.59}^{104.6} I(t)dt \tag{A3.5}$$

$$\int_{36.47}^{92.59} I(t)dt = \frac{(92.59-36.47)}{14}\left[\begin{array}{l} 6.03\times10^{-12} + 4\times1.08\times10^{-10} + 2\times8.55\times10^{-10} + \\ .....+ 4\times5.89\times10^{-10} + 2.77\times10^{-10} \end{array}\right] \tag{A3.6}$$

$$\int_{36.47}^{92.59} I(t)dt = 3.7590\times10^{-7}\ \text{torr s} \tag{A3.7}$$

$$\int_{92.59}^{104.6} I(t)dt = \frac{3}{8}\frac{(104.6-92.59)}{3}\left[\begin{array}{l} 2.77\times10^{-10} + 3\times1.17\times10^{-10} + \\ 3\times4.99\times10^{-11} + 2.25\times10^{-11} \end{array}\right] \tag{A3.8}$$

$$\int_{92.59}^{104.6} I(t)dt = 1.2013\times10^{-9}\ \text{torr s} \tag{A3.9}$$

$$\int_{36.47}^{104.6} I(t)dt = \underline{3.7710\times10^{-7}}\ \text{torr s} \tag{A3.10}$$

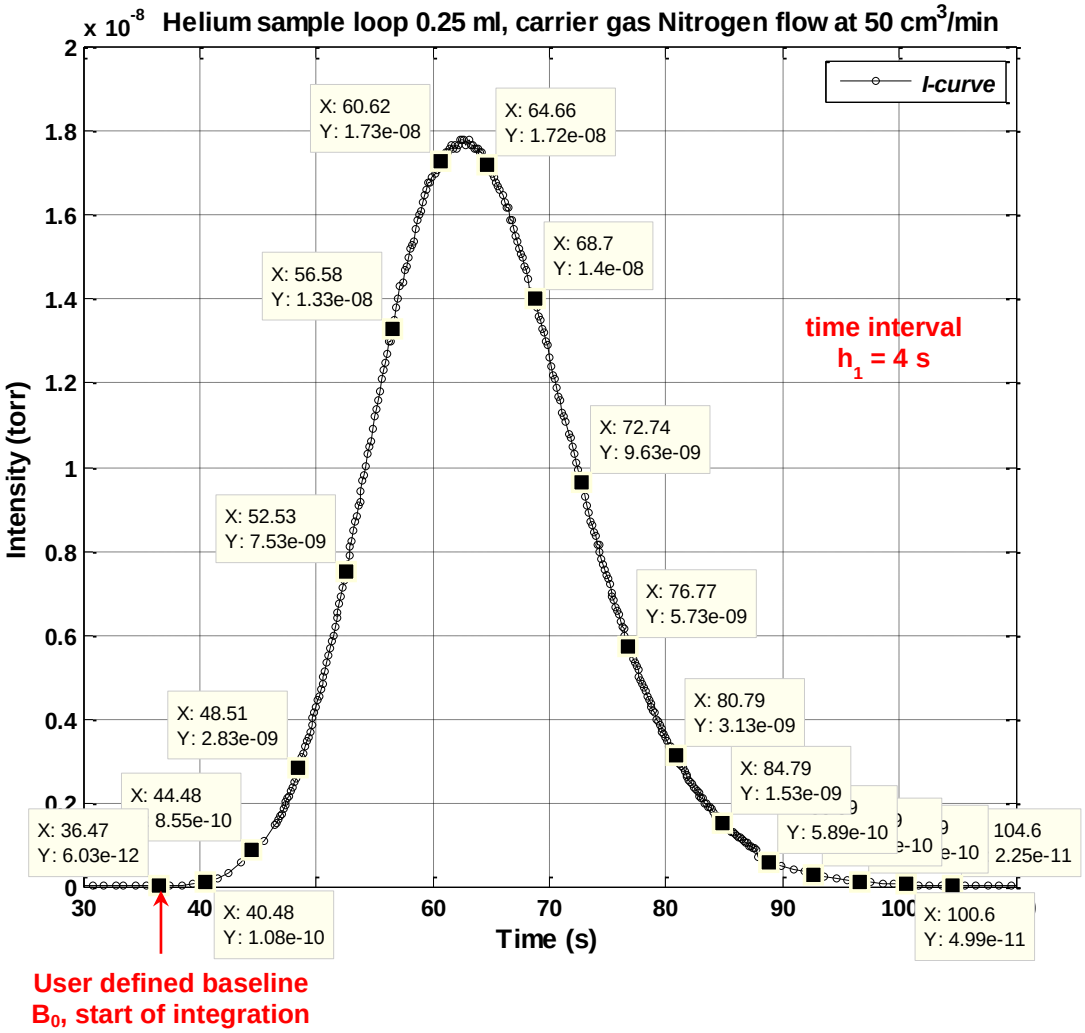

Figure A3.1: Pulse response curve recorded at the bottom sampling point with numerical integration performed with 18 data points and time interval h_1 = 4 s.

A3.2 The normalization curve: *E*-curve with time interval h_1 = 4 s

The experimental *E*-curve is obtained by normalizing the *I*-curve using Equation (A3.1):

$$E(t) = \frac{I(t)}{\int_{36.47}^{104.6} I(t)dt} = \frac{I(t)}{3.7710 \times 10^{-7}\, torr \cdot s} \tag{A3.11}$$

and the results are summarised in Table A3.2.

Table A3.2: Normalization process from $I(t)$ to $E(t)$ with time interval h_1 = 4 s.

Time (s)	**36.47**	**40.48**	**44.48**	**48.51**	**52.53**	**56.58**	**60.62**	**64.66**	**68.7**
***I*(*t*) (torr)**	6.03×10^{-12}	1.08×10^{-10}	8.55×10^{-10}	2.83×10^{-9}	7.53×10^{-9}	1.33×10^{-8}	1.73×10^{-8}	1.72×10^{-8}	1.40×10^{-8}
***E*(*t*) (s^{-1})**	1.60×10^{-5}	2.86×10^{-4}	2.27×10^{-3}	7.50×10^{-3}	2.00×10^{-2}	3.53×10^{-2}	4.59×10^{-2}	4.56×10^{-2}	3.71×10^{-2}
Time (s)	**72.74**	**76.77**	**80.79**	**84.79**	**88.89**	**92.59**	**96.59**	**100.6**	**104.6**
***I*(*t*) (torr)**	9.63×10^{-9}	5.73×10^{-9}	3.13×10^{-9}	1.53×10^{-9}	5.89×10^{-10}	2.77×10^{-10}	1.17×10^{-10}	4.99×10^{-11}	2.25×10^{-11}
***E*(*t*) (s^{-1})**	2.55×10^{-2}	1.52×10^{-2}	8.30×10^{-3}	4.06×10^{-3}	1.56×10^{-3}	7.35×10^{-4}	3.10×10^{-4}	1.32×10^{-4}	5.97×10^{-5}

The area of the $E(t)$ curve is equal to unity using Equation (A3.2) and the plot of E-curve is shown in Figure A3.2.

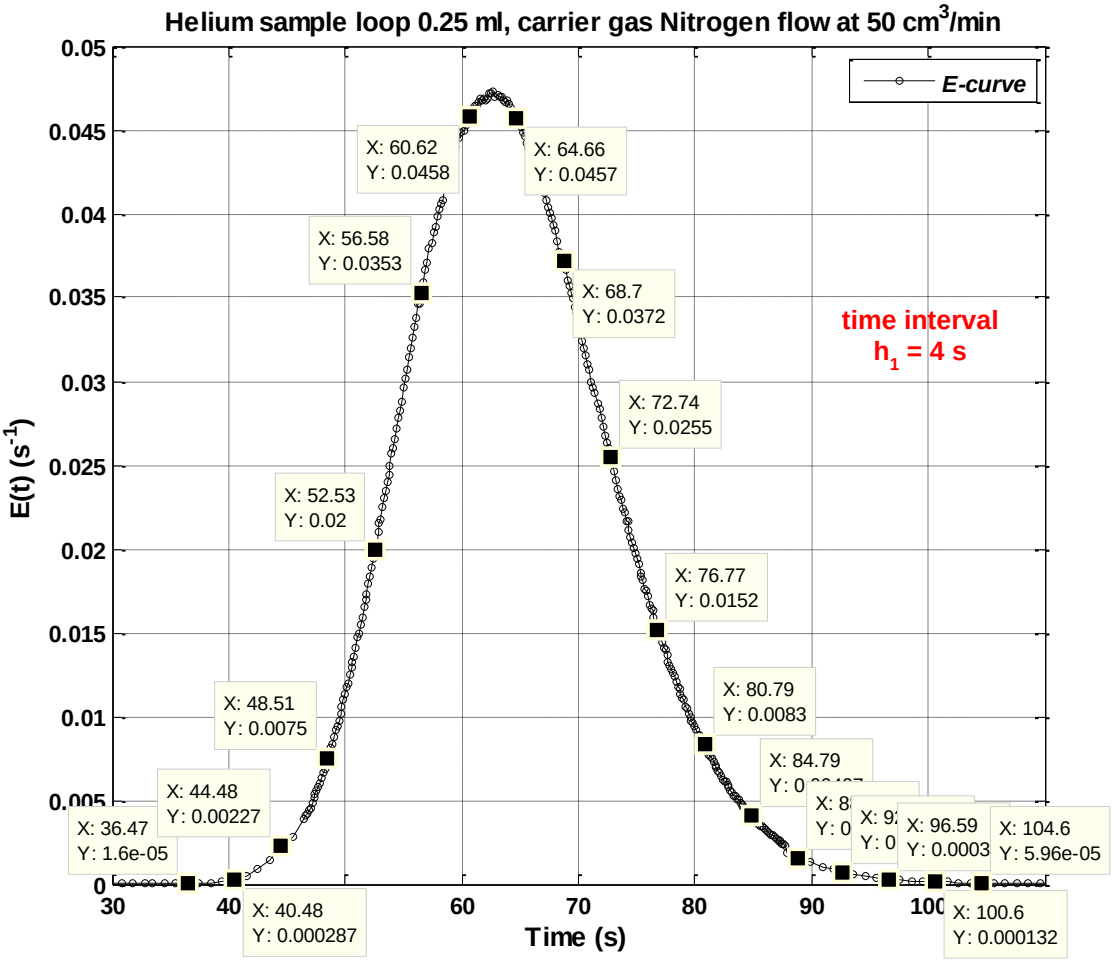

Figure A3.2: Normalization of the pulse response curve $I(t)$ to E-curve $E(t)$: the data points shown have a time interval h_1 = 4 s.

$$\int_{36.47}^{104.6} E(t)dt = \int_{36.47}^{92.59} E(t)dt + \int_{92.59}^{104.6} E(t)dt \tag{A3.12}$$

$$\int_{36.47}^{92.59} E(t)dt = \frac{(92.59-36.47)}{\frac{14}{3}} \begin{bmatrix} 1.60\times10^{-5} + 4\times2.86\times10^{-4} + 2\times2.27\times10^{-3} + \\ .....+ 4\times1.56\times10^{-3} + 7.35\times10^{-4} \end{bmatrix} \tag{A3.13}$$

$$\int_{36.47}^{92.59} E(t)dt = 9.9681\times10^{-1} \tag{A3.14}$$

$$\int_{92.59}^{104.6} E(t)dt = \frac{3}{8}\frac{(104.6-92.59)}{3} \begin{bmatrix} 7.35\times10^{-4} + 3\times3.10\times10^{-4} + \\ 3\times1.32\times10^{-4} + 5.97\times10^{-5} \end{bmatrix} \tag{A3.15}$$

$$\int_{92.59}^{104.6} E(t)dt = 3.1856 \times 10^{-3} \tag{A3.16}$$

$$\int_{36.47}^{104.6} E(t)dt = \underline{9.9999\times10^{-1}} \approx 1 \tag{A3.17}$$

A3.3 The area under $tE(t)$ curve with time interval h_1 = 4 s: first absolute moment μ_1 or mean residence time t_m

The first moment μ_1 is calculated by evaluating the experimental peaks using Equation (A3.3), which corresponds to the area under the $tE(t)$ curve. The data points on the $tE(t)$ curve are summarised in Table A3.3 and the graphical representation is shown in Figure A3.3.

Table A3.3: data used for calculating first moment μ_1 or mean residence time t_m with time interval h_1 = 4 s.

Time (s)	**36.47**	**40.48**	**44.48**	**48.51**	**52.53**	**56.58**	**60.62**	**64.66**	**68.7**
***E*(*t*) (s^{-1})**	1.60×10^{-5}	2.86×10^{-4}	2.27×10^{-3}	7.50×10^{-3}	2.00×10^{-2}	3.53×10^{-2}	4.59×10^{-2}	4.56×10^{-2}	3.71×10^{-2}
***tE*(*t*)**	5.83×10^{-4}	1.16×10^{-2}	1.01×10^{-1}	3.64×10^{-1}	1.05	2.00	2.78	2.95	2.55
Time (s)	**72.74**	**76.77**	**80.79**	**84.79**	**88.89**	**92.59**	**96.59**	**100.6**	**104.6**
***E*(*t*) (s^{-1})**	2.55×10^{-2}	1.52×10^{-2}	8.30×10^{-3}	4.06×10^{-3}	1.56×10^{-3}	7.35×10^{-4}	3.10×10^{-4}	1.32×10^{-4}	5.97×10^{-5}
***tE*(*t*)**	1.86	1.17	6.71×10^{-1}	3.44×10^{-1}	1.39×10^{-1}	6.80×10^{-2}	3.00×10^{-2}	1.33×10^{-2}	6.24×10^{-3}

The first moment μ_1 is calculated according to Equation (A3.3):

$$\int_{36.47}^{104.6} tE(t)dt = \int_{36.47}^{92.59} tE(t)dt + \int_{92.59}^{104.6} tE(t)dt \tag{A3.18}$$

$$\int_{36.47}^{92.59} tE(t)dt = \frac{(92.59-36.47)}{\frac{14}{3}}\left[\begin{array}{l} 5.83\times10^{-4}+4\times1.16\times10^{-2}+2\times1.01\times10^{-1}+ \\ .....+4\times1.39\times10^{-1}+6.80\times10^{-2} \end{array}\right] \quad \text{(A3.19)}$$

$$\int_{36.47}^{92.59} tE(t)dt = 64.14 \text{ s} \quad \text{(A3.20)}$$

$$\int_{92.59}^{104.6} tE(t)dt = \frac{3}{8}\frac{(104.6-92.59)}{3}\left[\begin{array}{l} 6.80\times10^{-2}+3\times3.00\times10^{-2}+ \\ 3\times1.33\times10^{-2}+6.24\times10^{-3} \end{array}\right] \quad \text{(A3.21)}$$

$$\int_{92.59}^{104.6} tE(t)dt = 3.064\times10^{-1} \text{ s} \quad \text{(A3.22)}$$

$$\int_{36.47}^{104.6} tE(t)dt = \underline{64.446} \text{ s} \quad \text{(A3.23)}$$

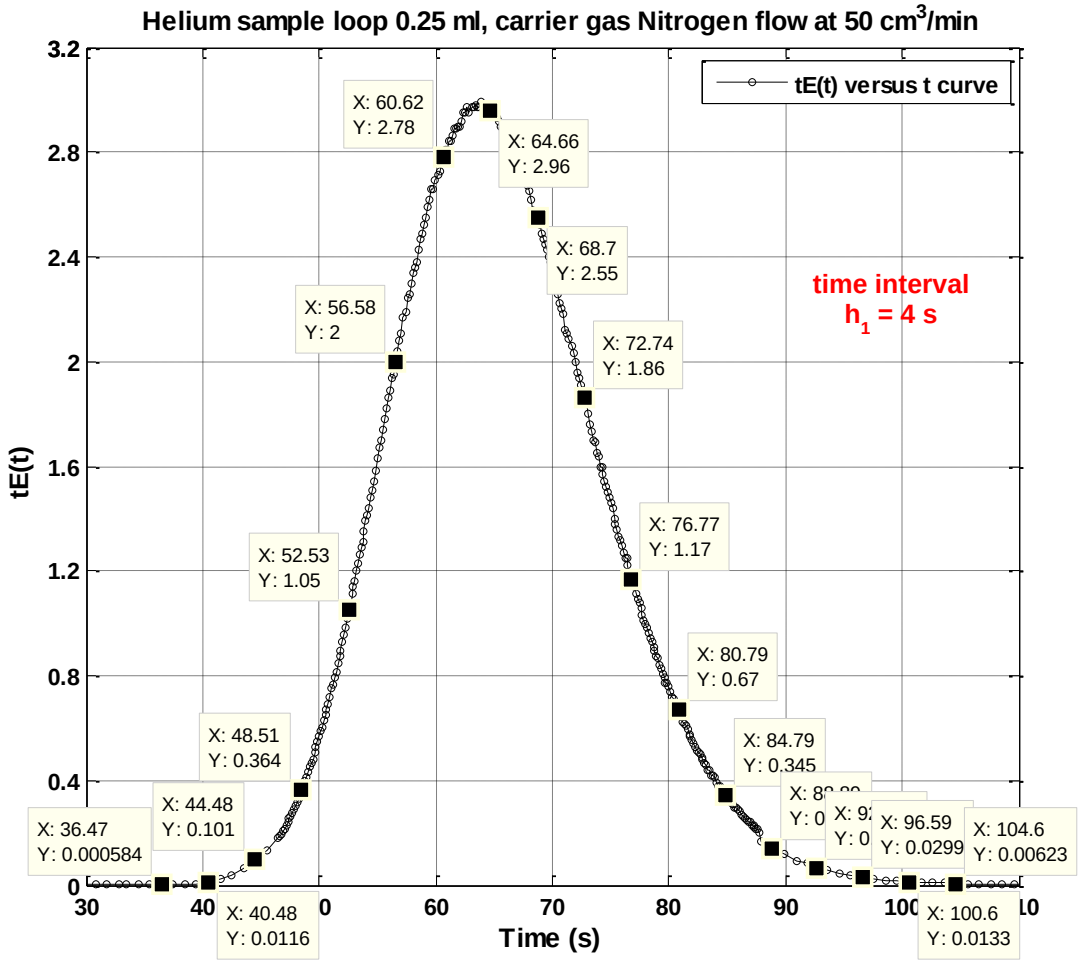

Figure A3.3: The area under the $tE(t)$ curve with the time interval h_1 = 4 s between each data point.

A3.4 The area under $(t\text{-}t_m^2)E(t)$ curve and $t^2E(t)$ curve minus t_m^2 with time interval h_1 = 4 s: second central moment μ_2' or variance σ^2

From Equation (A3.4), there are two methods to calculate the second central moment:

(1) the second central moment μ_2' is equal to the area under the $(t - t_m)^2 E(t)$ curve;

(2) the second central moment μ_2' is equal to the area of the $t^2 E(t)$ curve deducting t_m^2.

The corresponding data points results on $(t - t_m)^2 E(t)$ and $t^2 E(t)$ curves are summarised in Table A3.4 and the curve plots are shown in Figure A3.4 and Figure A3.5.

Table A3.4: Data used to calculate the second central moment μ_2' or the variance σ^2 with time interval h_1 = 4 s.

Time (s)	**36.47**	**40.48**	**44.48**	**48.51**	**52.53**	**56.58**	**60.62**	**64.66**	**68.7**
$(t-t_m)^2E(t)$ (s)	1.25×10^{-2}	1.65×10^{-1}	9.04×10^{-1}	1.91	2.84	2.18	6.72×10^{-1}	2.09×10^{-2}	6.72×10^{-1}
$t^2E(t)$ (s)	2.13×10^{-2}	4.69×10^{-1}	4.49	17.7	55.1	113	169	191	175
Time (s)	**72.74**	**76.77**	**80.79**	**84.79**	**88.89**	**92.59**	**96.59**	**100.6**	**104.6**
$(t-t_m)^2E(t)$ (s)	1.76	2.31	2.22	1.68	9.33×10^{-1}	5.82×10^{-1}	3.21×10^{-1}	1.73×10^{-1}	9.62×10^{-2}
$t^2E(t)$ (s)	135	89.6	54.2	29.2	12.3	6.30	2.89	1.34	6.53×10^{-1}

Method 1: area under $(t - t_m)^2 E(t)$ curve

$$\int_{36.47}^{104.6}(t-t_m)^2 E(t)dt = \int_{36.47}^{92.59}(t-t_m)^2 E(t)dt + \int_{92.59}^{104.6}(t-t_m)^2 E(t)dt \tag{A3.24}$$

$$\int_{36.47}^{92.59}(t-t_m)^2 E(t)dt = \frac{(92.59-36.47)}{3}\left[\begin{array}{l} 1.25\times10^{-2} + 4\times1.65\times10^{-1} + \\ 2\times9.04\times10^{-1} + ... + 4\times9.33\times10^{-1} \\ +5.82\times10^{-1} \end{array}\right] \tag{A3.25}$$

$$\int_{36.47}^{92.59}(t-t_m)^2 E(t)dt = 73.999 \text{ s}^2 \tag{A3.26}$$

$$\int_{92.59}^{104.6}(t-t_m)^2 E(t)dt = \frac{3}{8}\frac{(104.6-92.59)}{3}\left[\begin{array}{l} 5.82\times10^{-1} + 3\times3.21\times10^{-1} \\ +3\times1.73\times10^{-1} + 9.62\times10^{-2} \end{array}\right] \tag{A3.27}$$

$$\int_{92.59}^{104.6}(t-t_m)^2 E(t)dt = 3.2407 \text{ s}^2 \tag{A3.28}$$

$$\int_{36.47}^{104.6}(t-t_m)^2 E(t)dt = \underline{77.24} \text{ s}^2 \tag{A3.29}$$

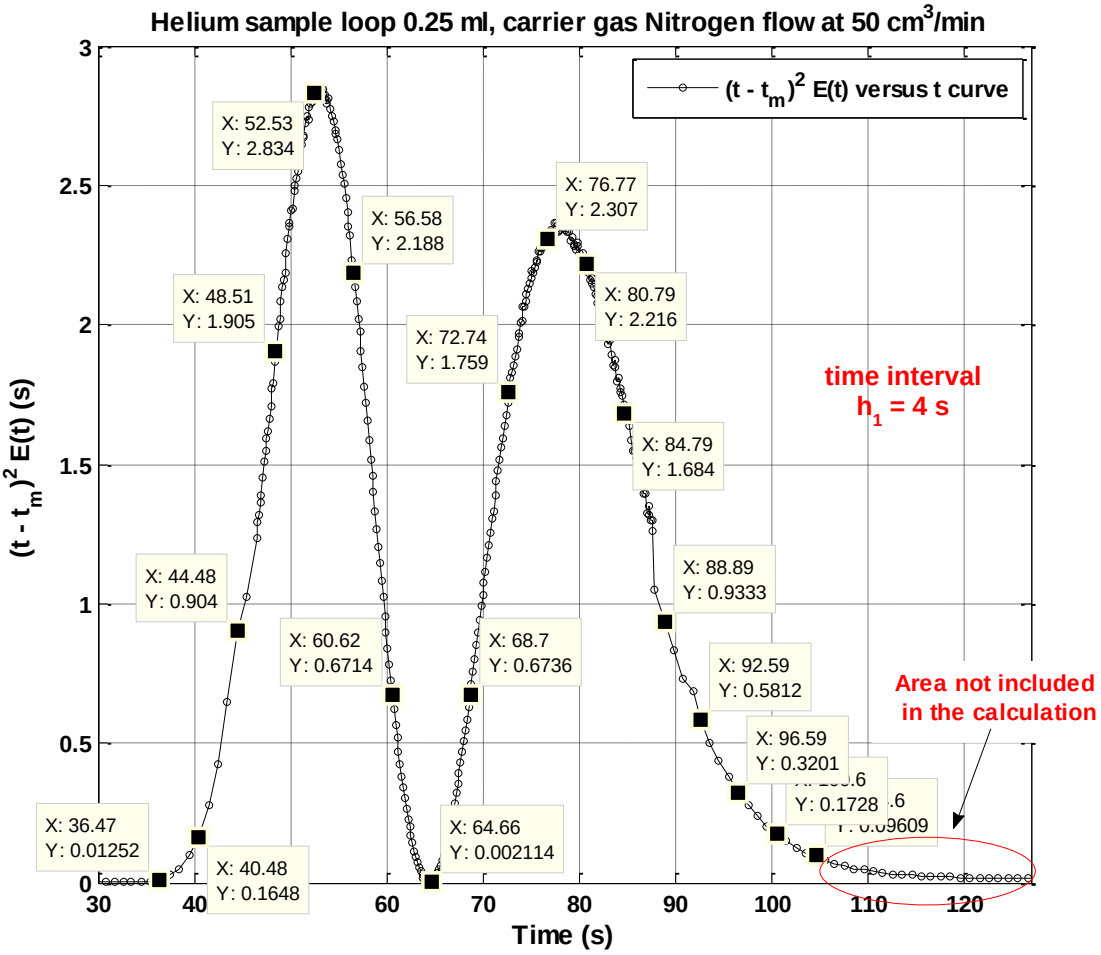

Figure A3.4: The second central moment $\mu_2^{'}$ or known as the variance σ^2 is equal to the area under the $(t - t_m)^2 E(t)$ curve with the time interval $h_1 = 4$ s between each data point.

Method 2: area under $t^2E(t)$ curve deducting t_m^2

$$\int_{36.47}^{104.6} t^2E(t)dt = \int_{36.47}^{92.59} t^2E(t)dt + \int_{92.59}^{104.6} t^2E(t)dt \tag{A3.30}$$

$$\int_{36.47}^{92.59} t^2E(t)dt = \frac{(92.59-36.47)}{14}\left[\begin{array}{l} 2.13\times10^{-2} + 4\times4.69\times10^{-1} + 2\times4.49 + \\ .....+ 4\times12.3 + 6.3 \end{array}\right] \tag{A3.31}$$

$$\int_{36.47}^{92.59} t^2E(t)dt = 4201 \text{ s}^2 \tag{A3.32}$$

$$\int_{92.59}^{104.6} t^2E(t)dt = \frac{3}{8}\frac{(104.6-92.59)}{3}\left[6.3 + 2\times2.89 + 3\times1.34 + 6.53\times10^{-1}\right] \tag{A3.33}$$

$$\int_{92.59}^{104.6} t^2E(t)dt = 29.502 \text{ s}^2 \tag{A3.34}$$

$$\int_{36.47}^{104.6} t^2E(t)dt = \underline{4230.502} \text{ s}^2 \tag{A3.35}$$

Therefore, the second central moment μ_2' or the variance σ^2 is equal to:

$$\mu_2' = \sigma^2 = \int_{36.47}^{104.6} t^2 E(t)dt \; - t_m{}^2 = 4230.502 - 64.446^2 = \underline{77.231}\ \text{s}^2 \qquad \text{(A3.36)}$$

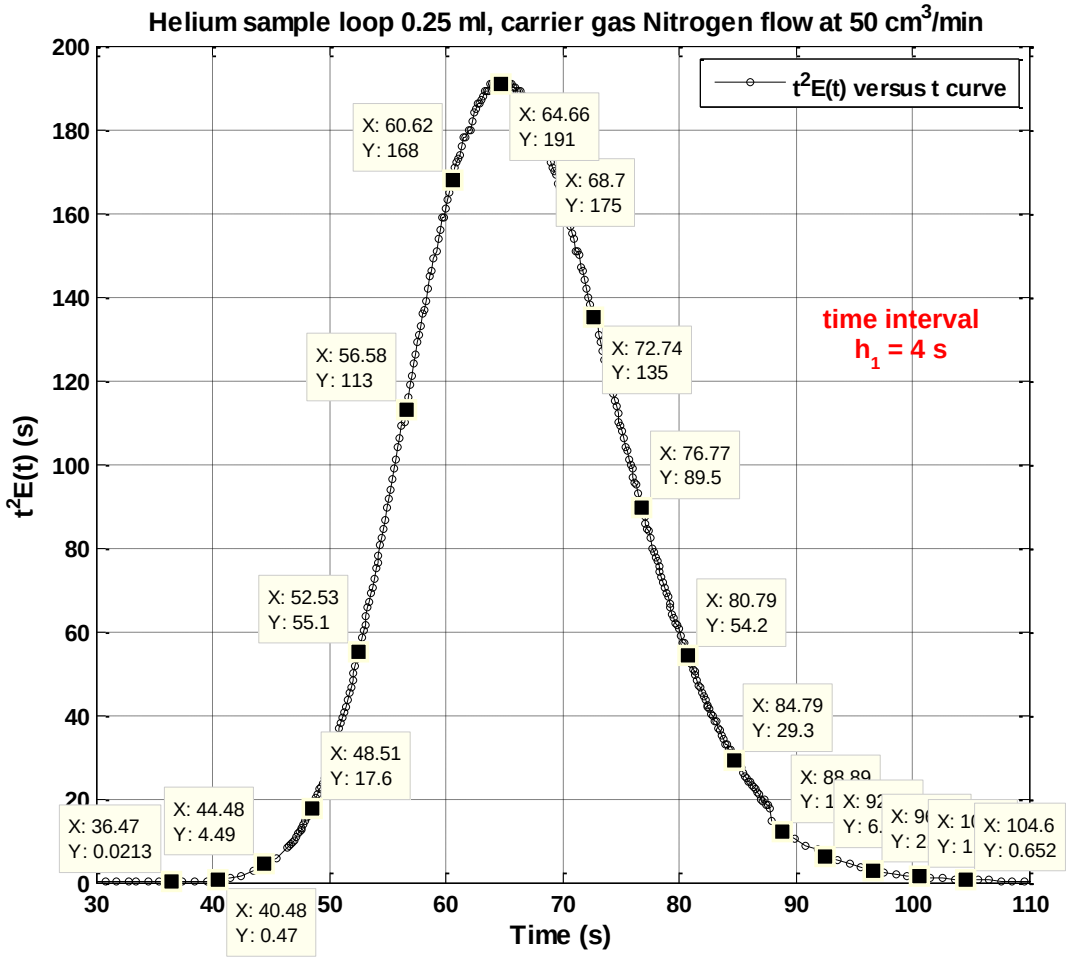

Figure A3.5: The second central moment μ_2' or known as the variance σ^2 is equal to the area under the $t^2E(t)$ curve (with time interval h_1 = 4 s) deducting $t_m{}^2$.

A3.5 The area under *I*-curve with equivalent time interval h_2 = 5 s

From peak area calculations using time interval h_1 = 4 s, there are some areas which numerical integration could not cover. Therefore, a time interval h_2 = 5 s is used and areas under $I(t)$, $E(t)$, $tE(t)$, $(t - t_m)^2E(t)$ and $t^2E(t)$ are recalculated. The located points on curves (18 data points) are summarised from Table A3.5 to Table A3.8. The corresponding graphs are presented in Figure A3.6 to Figure A3.10.

Table A3.5: Trace intensity data I as function of time t with time interval h_2 = 5 s.

Time (s)	**34.47**	**39.48**	**44.48**	**49.45**	**54.53**	**59.49**	**64.5**	**69.51**	**74.47**
***I*(*t*) (torr)**	1.33×10^{-12}	5.85×10^{-11}	8.55×10^{-10}	3.67×10^{-9}	1.05×10^{-8}	1.66×10^{-8}	1.72×10^{-8}	1.32×10^{-8}	7.81×10^{-9}
Time (s)	**79.44**	**84.52**	**89.89**	**94.59**	**99.6**	**104.6**	**109.6**	**114.6**	**119.6**
***I*(*t*) (torr)**	3.83×10^{-9}	1.63×10^{-9}	4.86×10^{-10}	1.81×10^{-10}	6.16×10^{-11}	2.25×10^{-11}	8.42×10^{-12}	4.16×10^{-12}	2.23×10^{-12}

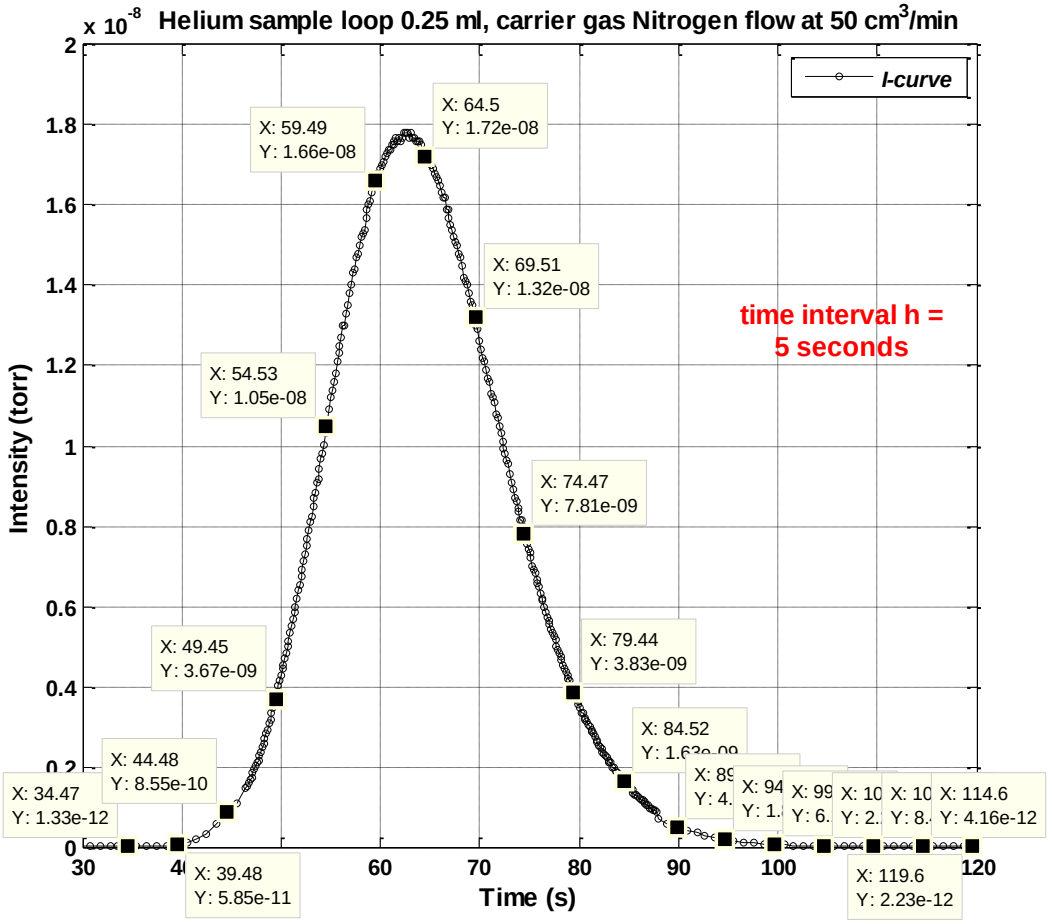

Figure A3.6: Experimental pulse response curve recorded at the bottom sampling point with time interval h_2 = 5 s between every consecutive data point.

The area of the *I*-curve with time interval h_2 = 5 s is:

$$\int_{34.47}^{119.6} I(t)dt = \int_{34.47}^{104.6} I(t)dt + \int_{104.6}^{119.6} I(t)dt \tag{A3.37}$$

$$\int_{34.47}^{104.6} I(t)dt = \frac{(104.6-34.47)}{3}\left[\begin{array}{l} 1.33\times10^{-12} + 4\times5.85\times10^{-11} + 2\times8.55\times10^{-11} + \\ .....+ 4\times6.16\times10^{-11} + 2.25\times10^{-11} \end{array}\right] \tag{A3.38}$$

$$\int_{34.47}^{104.6} I(t)dt = 3.8071\times10^{-7}\,\text{torr s} \tag{A3.39}$$

$$\int_{104.6}^{119.6} I(t)dt = \frac{3}{8}\frac{(119.6-104.6)}{3}\left[\begin{array}{l} 2.25\times10^{-11} + 3\times8.42\times10^{-12} + \\ 3\times4.16\times10^{-12} + 2.23\times10^{-12} \end{array}\right] \tag{A3.40}$$

$$\int_{104.6}^{119.6} I(t)dt = 1.1713\ \times\ 10^{-10}\,\text{torr s} \tag{A3.41}$$

$$\int_{36.47}^{104.6} I(t)dt = \underline{3.8082\times10^{-7}}\ \text{torr s} \tag{A3.42}$$

A3.6 The normalization curve: *E*-curve with time interval h_2 = 5 s

Table A3.6 summarised the data points located on the $I(t)$ curve that are converted into $E(t)$ using Equation (A3.3). The graphic representation of the *E*-curve is shown in Figure A3.7.

Table A3.6: Normalization from $I(t)$ to $E(t)$ with time interval h_2 = 5 s.

Time (s)	**34.47**	**39.48**	**44.48**	**49.45**	**54.53**	**59.49**	**64.5**	**69.51**	**74.47**
***I*(*t*) (torr)**	1.33×10^{-12}	5.85×10^{-11}	8.55×10^{-10}	3.67×10^{-9}	1.05×10^{-8}	1.66×10^{-8}	1.72×10^{-8}	1.32×10^{-8}	7.81×10^{-9}
***E*(*t*) (s^{-1})**	3.49×10^{-6}	1.54×10^{-4}	2.25×10^{-3}	9.64×10^{-3}	2.76×10^{-2}	4.36×10^{-2}	4.52×10^{-2}	3.47×10^{-2}	2.05×10^{-2}
Time (s)	**79.44**	**84.52**	**89.89**	**94.59**	**99.6**	**104.6**	**109.6**	**114.6**	**119.6**
***I*(*t*) (torr)**	3.83×10^{-9}	1.63×10^{-9}	4.86×10^{-10}	1.81×10^{-10}	6.16×10^{-11}	2.25×10^{-11}	8.42×10^{-12}	4.16×10^{-12}	2.23×10^{-12}
***E*(*t*) (s^{-1})**	1.01×10^{-2}	4.28×10^{-3}	1.28×10^{-3}	4.75×10^{-4}	1.62×10^{-4}	5.91×10^{-5}	2.21×10^{-5}	1.09×10^{-5}	5.86×10^{-6}

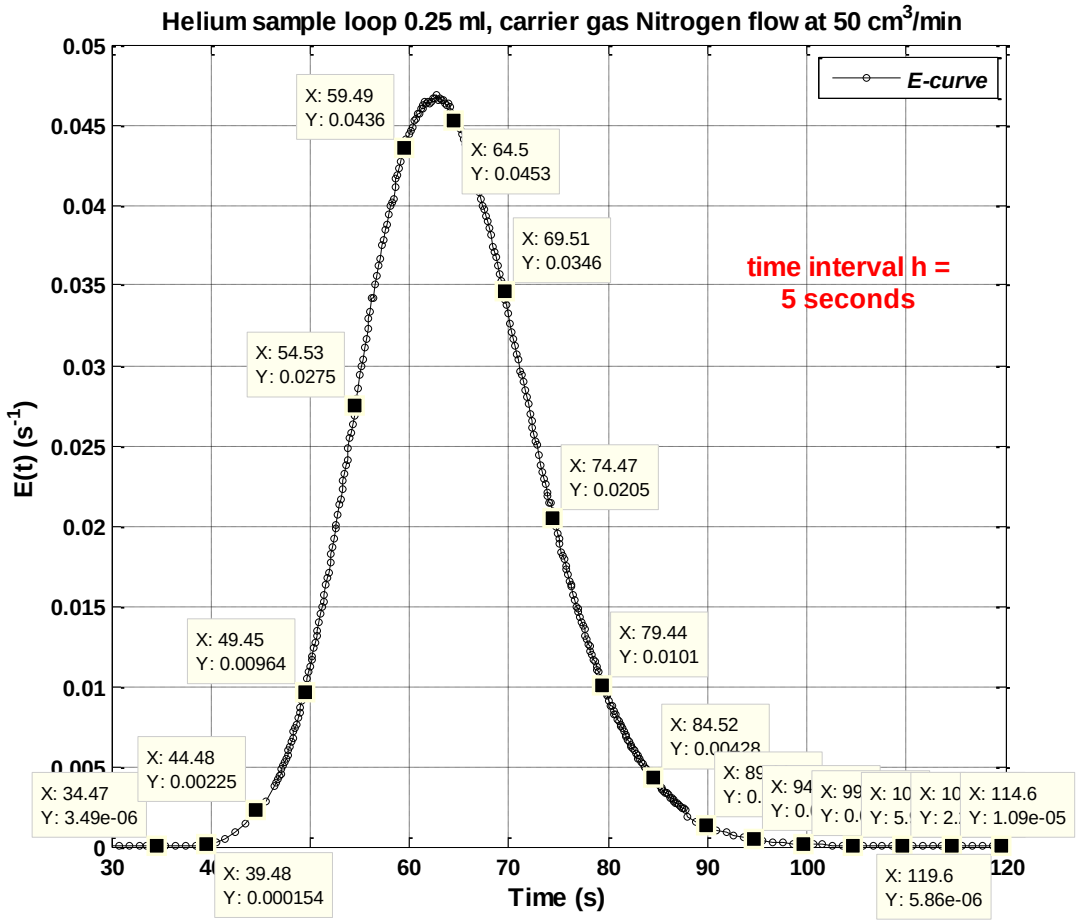

Figure A3.7: Normalization of pulse response curve $I(t)$ into $E(t)$: data points shown have equivalent time interval h_2 = 5 s.

Using Equation (A3.2), the area of the $E(t)$ curve is calculated from:

$$\int_{34.47}^{119.6} E(t)dt = \int_{34.47}^{104.6} E(t)dt + \int_{104.6}^{119.6} E(t)dt \tag{A3.43}$$

$$\int_{34.47}^{104.6} E(t)dt = \frac{(104.6-34.47)}{14}\left[\begin{array}{l} 3.49\times10^{-6} + 4\times1.54\times10^{-4} + 2\times2.25\times10^{-3} + \\ .....+ 4\times1.62\times10^{-4} + 5.91\times10^{-5} \end{array}\right] \tag{A3.44}$$

$$\int_{34.47}^{104.6} E(t)dt = 9.9970\times10^{-1} \tag{A3.45}$$

$$\int_{104.6}^{119.6} E(t)dt = \frac{3}{8}\frac{(119.6-104.6)}{3}\left[\begin{array}{l} 5.91\times10^{-5} + 3\times2.21\times10^{-5} + \\ 3\times1.09\times10^{-5} + 5.86\times10^{-6} \end{array}\right] \tag{A3.46}$$

$$\int_{104.6}^{119.6} E(t)dt = 3.0758\times10^{-4} \tag{A3.47}$$

$$\int_{34.47}^{119.6} E(t)dt = \underline{1} \tag{A3.48}$$

A3.7 The area under $tE(t)$ curve with time interval h_2 = 5 s: first moment μ_1 or mean residence time t_m

The data points used in $tE(t)$ curve are summarised in Table A3.7 and the corresponding plot is presented in Figure A3.8.

Table A3.7: Data points with time interval h_2 = 5 s used for first moment μ_1 or mean residence time t_m calculation.

Time (s)	**34.47**	**39.48**	**44.48**	**49.45**	**54.53**	**59.49**	**64.5**	**69.51**	**74.47**
***E*(*t*) (s^{-1})**	3.49×10^{-6}	1.54×10^{-4}	2.25×10^{-3}	9.64×10^{-3}	2.76×10^{-2}	4.36×10^{-2}	4.52×10^{-2}	3.47×10^{-2}	2.05×10^{-2}
***tE*(*t*)**	1.20×10^{-4}	6.06×10^{-3}	9.99×10^{-2}	4.77×10^{-1}	1.50	2.59	2.91	2.41	1.53
Time (s)	**79.44**	**84.52**	**89.89**	**94.59**	**99.6**	**104.6**	**109.6**	**114.6**	**119.6**
***E*(*t*) (s^{-1})**	1.01×10^{-2}	4.28×10^{-3}	1.28×10^{-3}	4.75×10^{-4}	1.62×10^{-4}	5.91×10^{-5}	2.21×10^{-5}	1.09×10^{-5}	5.86×10^{-6}
***tE*(*t*)**	7.99×10^{-1}	3.62×10^{-1}	1.15×10^{-1}	4.50×10^{-2}	1.61×10^{-2}	6.18×10^{-3}	2.42×10^{-3}	1.25×10^{-3}	7.00×10^{-4}

The first moment μ_1 is calculated according to Equation (A3.3):

$$\int_{34.47}^{119.6} tE(t)dt = \int_{34.47}^{104.6} tE(t)dt + \int_{104.6}^{119.6} tE(t)dt \tag{A3.49}$$

$$\int_{34.47}^{104.6} tE(t)dt = \frac{(104.6-34.47)}{3}\left[\frac{1}{14}\begin{matrix}1.20\times10^{-4}+4\times6.06\times10^{-3}+2\times9.99\times10^{-2}+\\.....+4\times1.61\times10^{-2}+6.18\times10^{-3}\end{matrix}\right] \tag{A3.50}$$

$$\int_{34.47}^{104.6} tE(t)dt = 64.398 \text{ s} \tag{A3.51}$$

$$\int_{104.6}^{119.6} tE(t)dt = \frac{3}{8}\frac{(119.6-104.6)}{3}\left[\begin{matrix}6.18\times10^{-3}+3\times2.42\times10^{-3}+\\3\times1.25\times10^{-3}+7.00\times10^{-4}\end{matrix}\right] \tag{A3.52}$$

$$\int_{104.6}^{119.6} tE(t)dt = 3.3573\times10^{-2} \text{ s} \tag{A3.53}$$

$$\int_{104.6}^{119.6} tE(t)dt = \underline{64.431} \text{ s} \tag{A3.54}$$

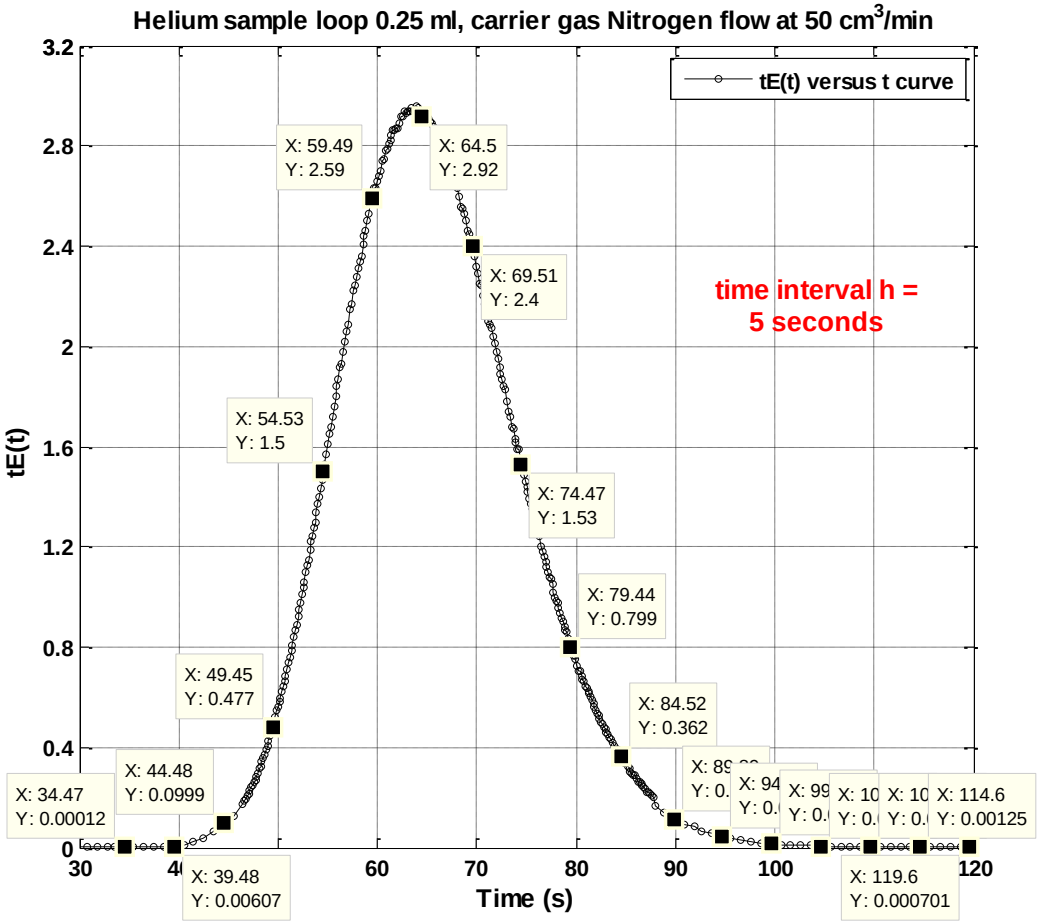

Figure A3.8: The area under the $tE(t)$ curve is the first moment, μ_1, and time interval h_2 = 5 s is applied to the curve.

A3.8 Second central moment μ_2' or variance σ^2 with equivalent time interval h_2 = 5 s between consecutive data points

The results of $(t - t_m)^2 E(t)$ and $t^2 E(t)$ are tabulated in Table A3.8 and the corresponding plots are presented in Figure A3.9 and Figure A3.10.

Table A3.8: Data used for calculating the second central moment μ_2' or the variance σ^2 with time interval h_2 = 5 s.

Time (s)	**34.47**	**39.48**	**44.48**	**49.45**	**54.53**	**59.49**	**64.5**	**69.51**	**74.47**
$(t-t_m)^2E(t)$ (s)	3.14×10^{-3}	9.56×10^{-2}	8.94×10^{-1}	2.16	2.70	1.06	2.15×10^{-4}	8.94×10^{-1}	2.07
$t^2E(t)$ (s)	4.15×10^{-3}	2.39×10^{-1}	4.44	23.6	81.99	154.3	187.9	167.5	113.7
Time (s)	**79.44**	**84.52**	**89.89**	**94.59**	**99.6**	**104.6**	**109.6**	**114.6**	**119.6**
$(t-t_m)^2E(t)$ (s)	2.27	1.73	8.27×10^{-1}	4.32×10^{-1}	2.00×10^{-1}	9.53×10^{-2}	4.51×10^{-2}	2.75×10^{-2}	1.78×10^{-2}
$t^2E(t)$ (s)	63.5	30.6	10.3	4.25	1.60	6.46×10^{-1}	2.66×10^{-1}	1.43×10^{-1}	8.38×10^{-2}

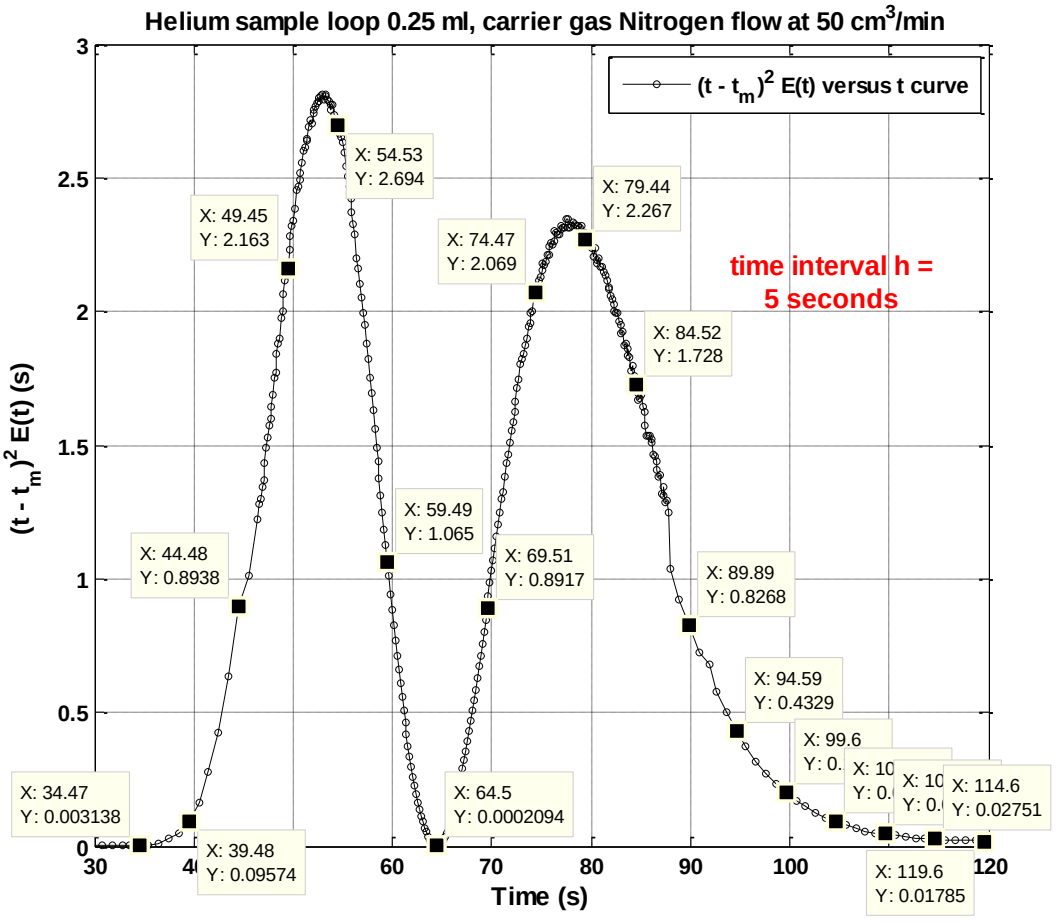

Figure A3.9: The area under the $(t-t_m)^2\,E(t)$ curve is the second central moment, μ_2' or known as variance, σ^2: equivalent time interval h_2 = 5s is used between each data point.

Method 1 (Cat. A): area under $(t - t_m)^2 E(t)$ curve

$$\int_{34.47}^{119.6}\left(t-t_m\right)^2 E(t)dt=\int_{34.47}^{104.6}\left(t-t_m\right)^2 E(t)dt+\int_{104.6}^{119.6}\left(t-t_m\right)^2 E(t)dt \tag{A3.55}$$

$$\int_{34.47}^{104.6}\left(t-t_m\right)^2 E(t)dt=\frac{\left(104.6-34.47\right)}{\frac{14}{3}}\begin{bmatrix}3.14\times10^{-3}+4\times9.56\times10^{-2}+2\times8.94\times10^{-1}\\+\ .....+4\times2.00\times10^{-1}+9.53\times10^{-2}\end{bmatrix} \tag{A3.56}$$

$$\int_{34.47}^{104.6}\left(t-t_m\right)^2 E(t)dt=76.448\ \mathrm{s}^2 \tag{A3.57}$$

$$\int_{104.6}^{119.6}\left(t-t_m\right)^2 E(t)dt=\frac{3}{8}\frac{\left(119.6-104.6\right)}{3}\begin{bmatrix}9.53\times10^{-2}+3\times4.51\times10^{-2}+\\3\times2.75\times10^{-2}+1.78\times10^{-2}\end{bmatrix} \tag{A3.58}$$

$$\int_{104.6}^{119.6}\left(t-t_m\right)^2 E(t)dt=6.2057\times10^{-1}\mathrm{s}^2 \tag{A3.59}$$

$$\int_{34.47}^{119.6}\left(t-t_m\right)^2 E(t)dt=\underline{77.069}\ \mathrm{s}^2 \tag{A3.60}$$

Method 2 (Cat. B): area under $t^2E(t)$ curve deducting $t_m{}^2$

$$\int_{34.47}^{119.6}t^2E(t)dt=\int_{34.47}^{104.6}t^2E(t)dt+\int_{104.6}^{119.6}t^2E(t)dt \tag{A3.61}$$

$$\int_{34.47}^{104.6}t^2E(t)dt=\frac{\left(104.6-34.47\right)}{\frac{14}{3}}\begin{bmatrix}4.15\times10^{-3}+4\times2.39\times10^{-1}+2\times4.44+\\.....+4\times1.60\ +6.46\times10^{-1}\end{bmatrix} \tag{A3.62}$$

$$\int_{34.47}^{104.6}t^2E(t)dt=4224.8\ s^2 \tag{A3.63}$$

$$\int_{104.6}^{119.6}t^2E(t)dt=\frac{3}{8}\frac{\left(119.6-104.6\right)}{3}\begin{bmatrix}6.46\times10^{-1}+3\times2.66\times10^{-1}+\\3\times1.43\times10^{-1}+8.38\times10^{-2}\end{bmatrix} \tag{A3.64}$$

$$\int_{104.6}^{119.6}t^2E(t)dt=3.6701\ \mathrm{s}^2 \tag{A3.65}$$

$$\int_{34.47}^{119.6}t^2E(t)dt=\underline{4228.4\ s^2} \tag{A3.66}$$

Therefore, the second central moment $\mu_2{}'$ or the variance σ^2 is equal to:

$$\mu_2{}'=\sigma^2=\int_{36.47}^{104.6}t^2E(t)dt\ -t_m{}^2=4228.4-64.431^2=\underline{77.092}\ \mathrm{s}^2 \tag{A3.67}$$

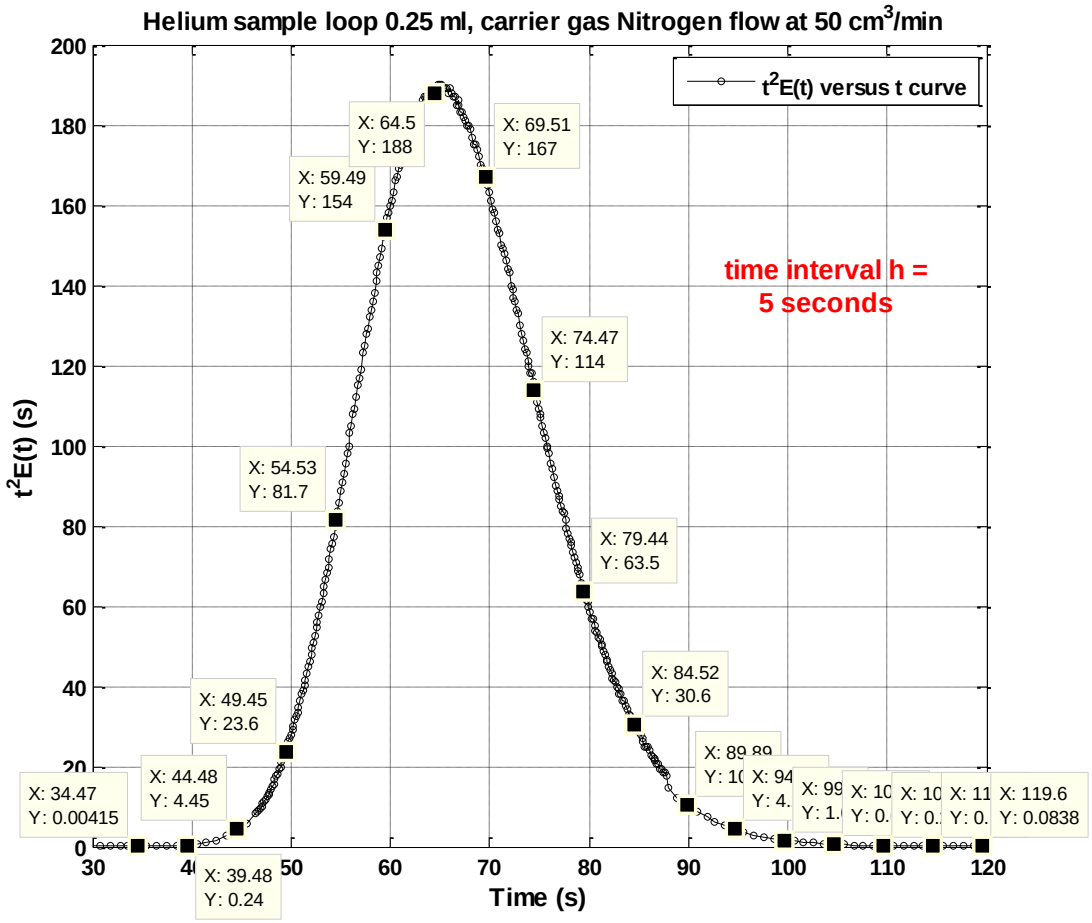

Figure A3.10: The area under the $t^2E(t)$ curve deducting $t_m{}^2$ is the second central moment $\mu_2{}'$ or known as the variance σ^2: the time interval h_2 between each data point is 5 s.

References

Fogler, H.S., 2004. *Elements of Chemical Reaction Engineering*. Pearson Education.

Appendix 4: Moment calculations using peaking fitting with a Gaussian area function

The experiment response peaks generated from MID scans have a relatively stable baseline concentration (in torr) at the peak-beginning and peak-end because the baseline is calibrated. Therefore, in OriginPro, the "Peak and Baseline" option is chosen rather than the others. The steps involved in analysing a pulse response curve are explained below:

1. Open OriginPro 8.6;
2. Import the experimental data from Excel into OriginPro, define X, Y-axis, Long name, Units and etc;
3. Select the data that needs to be analysed, then on the OriginPro panel window → Go to the "Analysis" option;
4. Under the "Analysis" panel → Choose "Peak and Baseline" → Click "Peak Analyzer" → Click "Open Dialog" button;
5. A "Peak analyser" window jumps out → On the "Goal" section → Choose "Fit Peaks (Pro)" → Click "Next" button;
6. On the "Baseline Mode" section → Select "Constant" and choose options between "Minimum" to "Median" if you want to use the system-found baseline, or you can choose "Custom" to define the baseline yourself → When finish, click "Next" button;
7. On the "Baseline Treatment" section → Choose "Fix Baseline Parameters" if you want the curve fitting baseline fixed, or choose "Auto Subtract Baseline" to subtract baseline value define in step 6 → Click "Next" button to continue;
8. On the "Find Peaks" section → Uncheck the box "Enable Auto Find" → Click "Peaks Info" → Click "Add" → Locate "Peak Centre" and "Peak Height" (i.e. X and Y values in the preview graph) by using the "Data cursor" on the side bar → Enter the values for "Peak Centre" and "Peak Height" → When finish, Click "Next";
9. On the "Fit Peaks" section → Click "Fit Control" → Tick the boxes for "y0" (i.e. Base value) and "xc_1" or "xc_2" (i.e. Peak centre; the second peak centre xc_2 occurs when analysing $(t - t_m)^2 E(t)$ curve) depend on the number of peaks in the response curve. Alternatively, by clicking the "Fix or release baseline parameters" and "Fix or release all peak centres" to let the system tick the corresponding boxes automatically → click on "Fit until converged", a number of convergence values will appear in the message box. In this section, the default method for peak fitting is

Gaussian area function. However, it can be changed under the "Peak Type" column → Click "OK" and "Finish" to go to the report sheet;

10. To save the current analysis method for later uses → Click the button on "Dialog Theme" → Choose "Save as" and enter a theme name, this would save lots of time when analysing a response curve using the similar method.

The peak fitting examples shown in this section used the exact same experimental response curve that was used for Simpson's rule in Appendix 3. The experimental conditions were:

(a) Helium tracer sample loop volume = 0.25 ml ;

(b) Nitrogen carrier gas flowrate = 50 cm^3/min;

(c) Maximum intake pressure for the SEM detector is maintained at 1.8 $\times 10^{-6}$ torr.

A4.1 Peak fitting with system-found baseline and without baseline subtraction

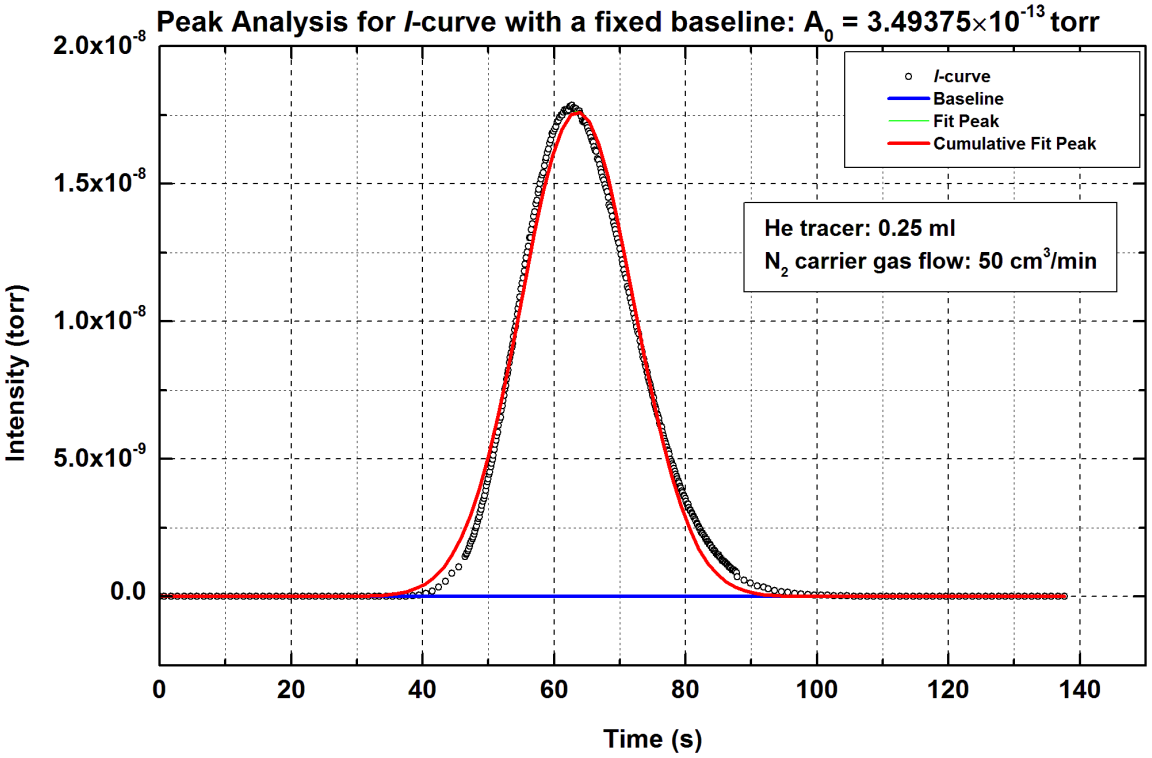

Figure A4.1: The experimental response peak (known as *I*-curve), with a fixed system-found baseline $A_0 = 3.49375 \times 10^{-12}$ torr (Blue line).

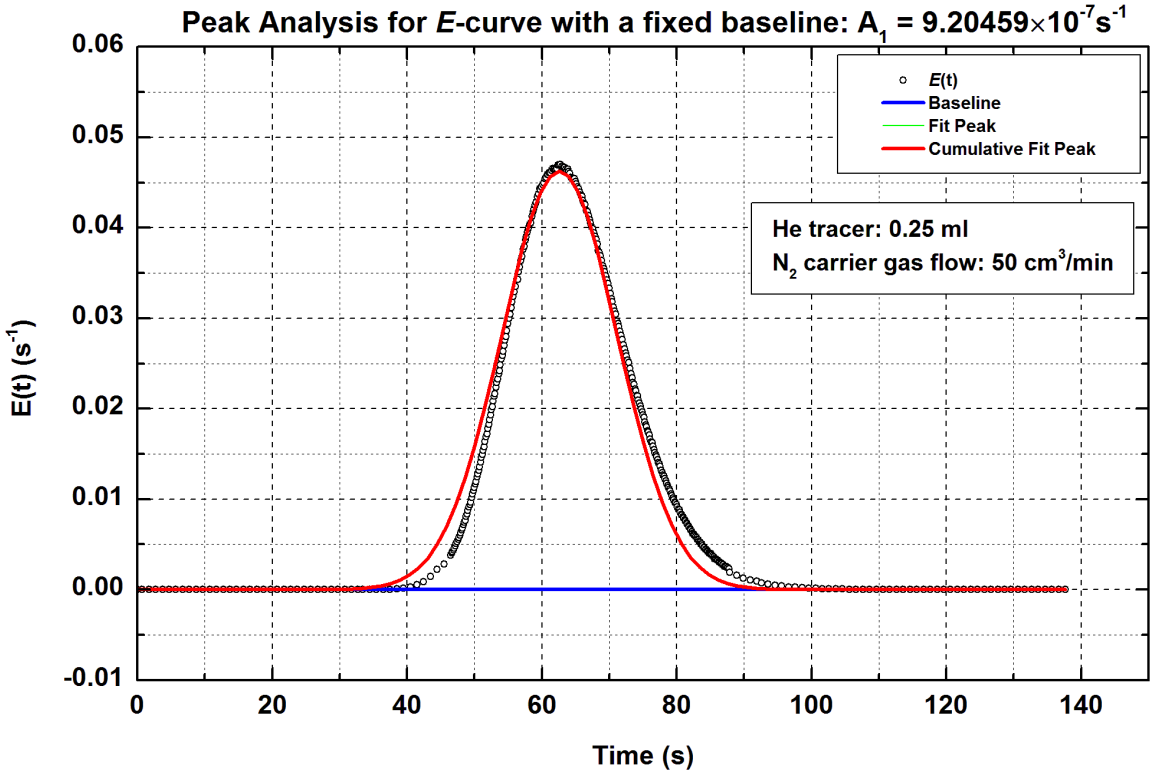

Figure A4.2: The normalization curve, or the age-distribution curve – *E*-curve, with a fixed system found baseline: $A_1 = 9.20459 \times 10^{-7}\ s^{-1}$.

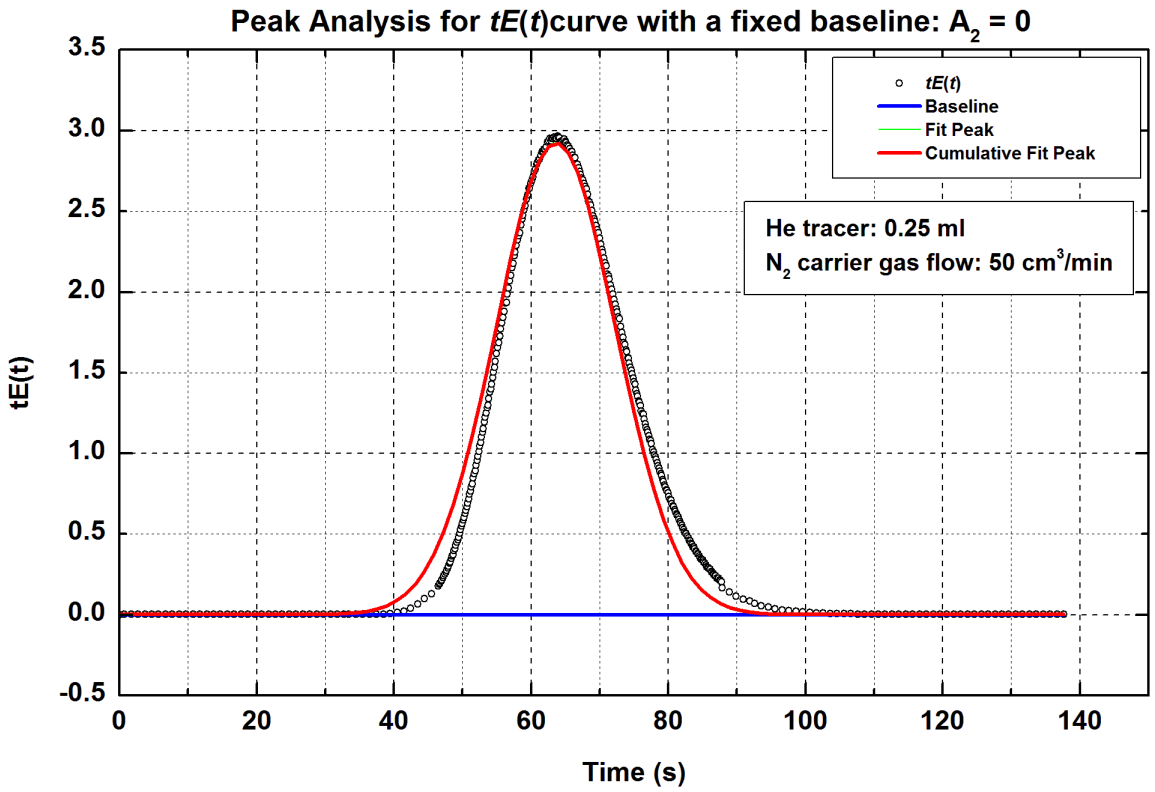

Figure A4.3: The area under the $tE(t)$ curve is the first moment, or the mean residence time μ_1, with a fixed system found baseline: $A_2 = 0$.

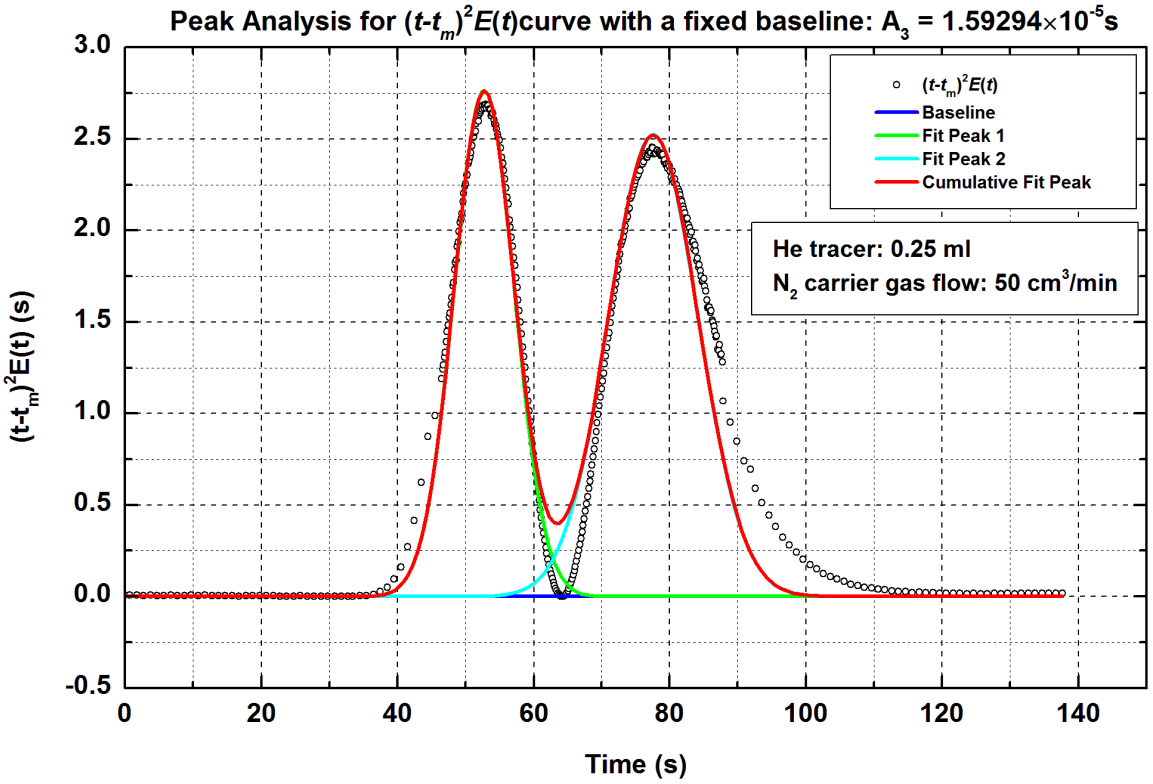

Figure A4.4: The area under the $(t - t_m)^2E(t)$ curve is the second central moment μ_2', or known as the variance σ^2, which defines the spread of a pulse response curve, with a fixed system found baseline: $A_3 = 1.59294 \times 10^{-5}$ s.

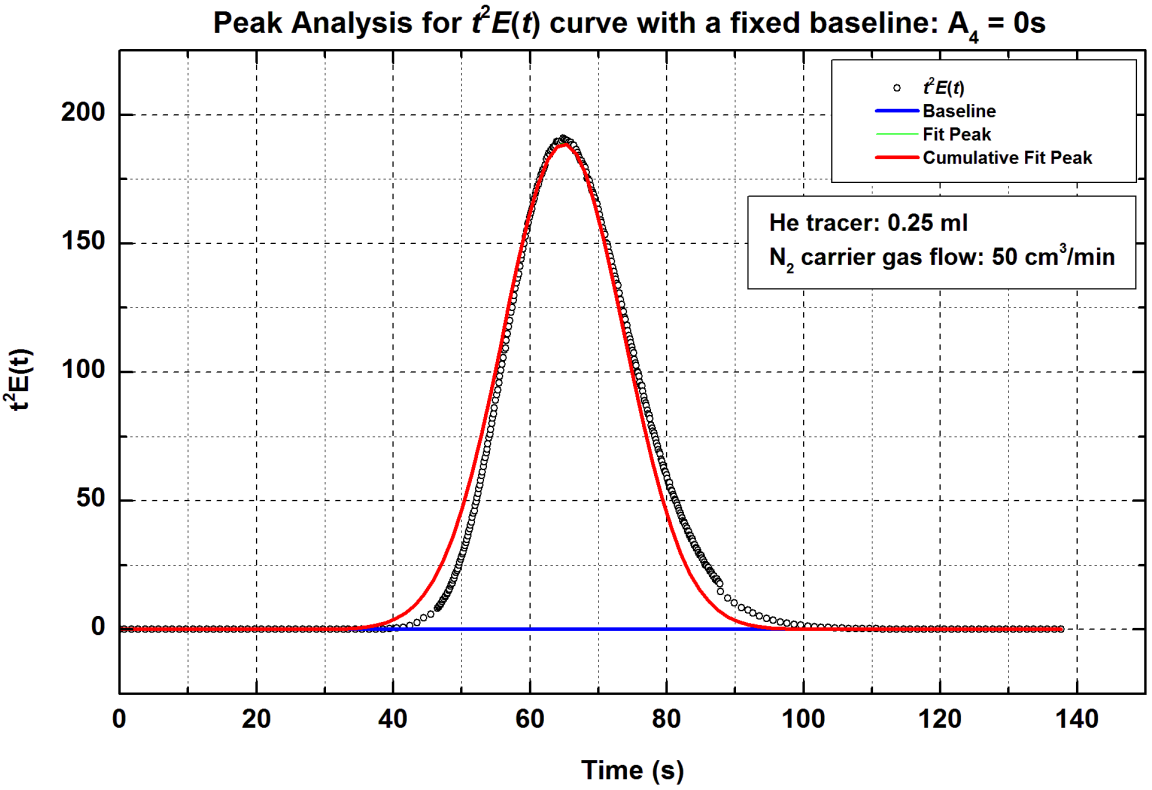

Figure A4.5: The area under curve the $t^2E(t)$ minus t_m^2 is the second central moment μ_2', or known as the variance σ^2, which defines the spread of a pulse response curve; with a fixed system found baseline: $A_4 = 0$ s.

Table A4.1: Summary of the results generated from peak fitting curves with a **system-found** baseline and **without** baseline subtraction.

***I*-curve**	**Value**		**Standard error**	
Baseline, A_0 (torr)	3.49375×10^{-13}		0	
Gaussian Fit Peak Area (torr.s)	3.79566×10^{-7}		1.4395×10^{-9}	
***E*-curve**	**Value**		**Standard error**	
Baseline, A_1 (s^{-1})	9.20459×10^{-7}		0	
Gaussian Fit Peak Area	0.9971		0.00622	
***tE*(*t*) curve**	**Value**		**Standard error**	
Baseline, A_2	0		0	
Gaussian Fit Peak Area (s)	64.15739		0.4444	
$(t - t_m)^2E(t)$ curve	**Value**		**Standard error**	
Baseline, A_3 (s)	1.59294×10^{-5}		0	
Gaussian Fit Peak Area (s^2)	**Peak 1**	**Peak 2**	**Peak 1**	**Peak 2**
	30.67725	41.64936	0.42872	0.50165
$t^2E(t)$ curve	**Value**		**Standard error**	
Baseline, A_4 (s)	0		0	
Gaussian Fit Peak Area (s^2)	4203.2858		52.5047	

A4.2 Peak fitting with system found baseline and with baseline subtraction

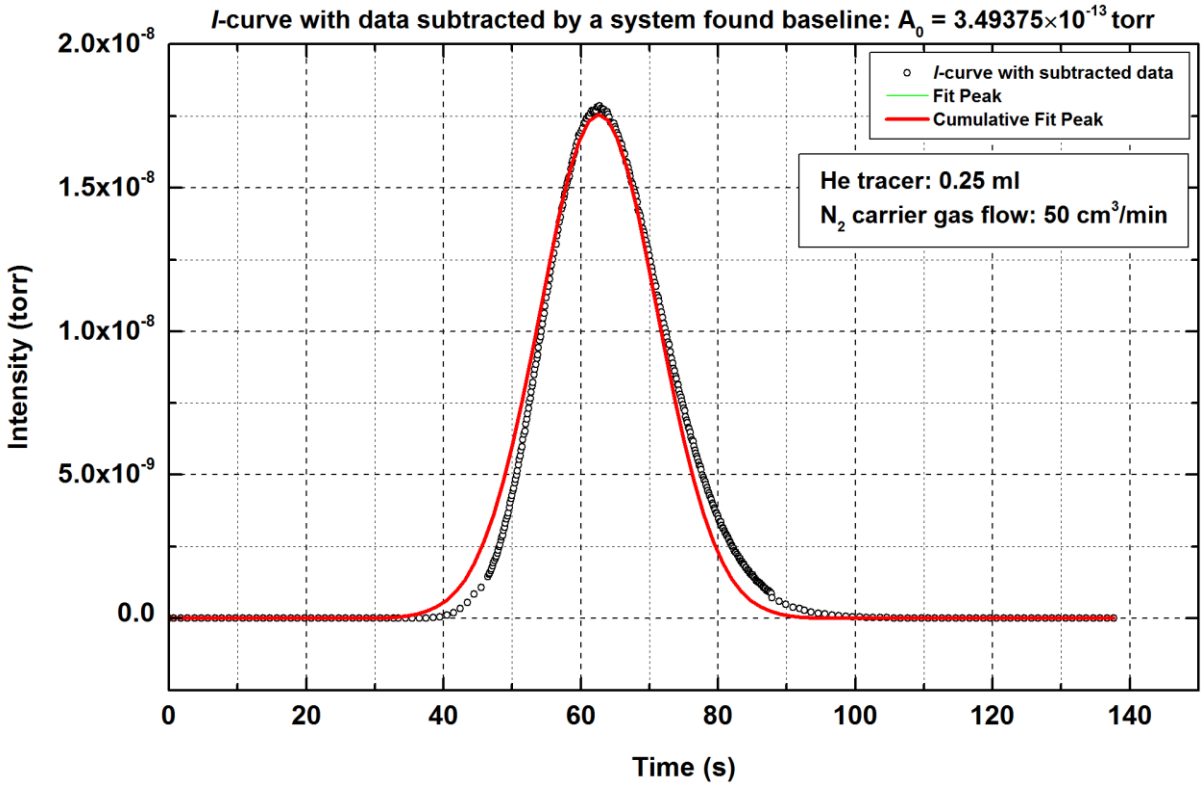

Figure A4.6: Experimental response peak or *I*-curve (Black dotted line) with each data point subtracted by a system-found baseline: $A_0 = 3.49375\times10^{-12}$ torr.

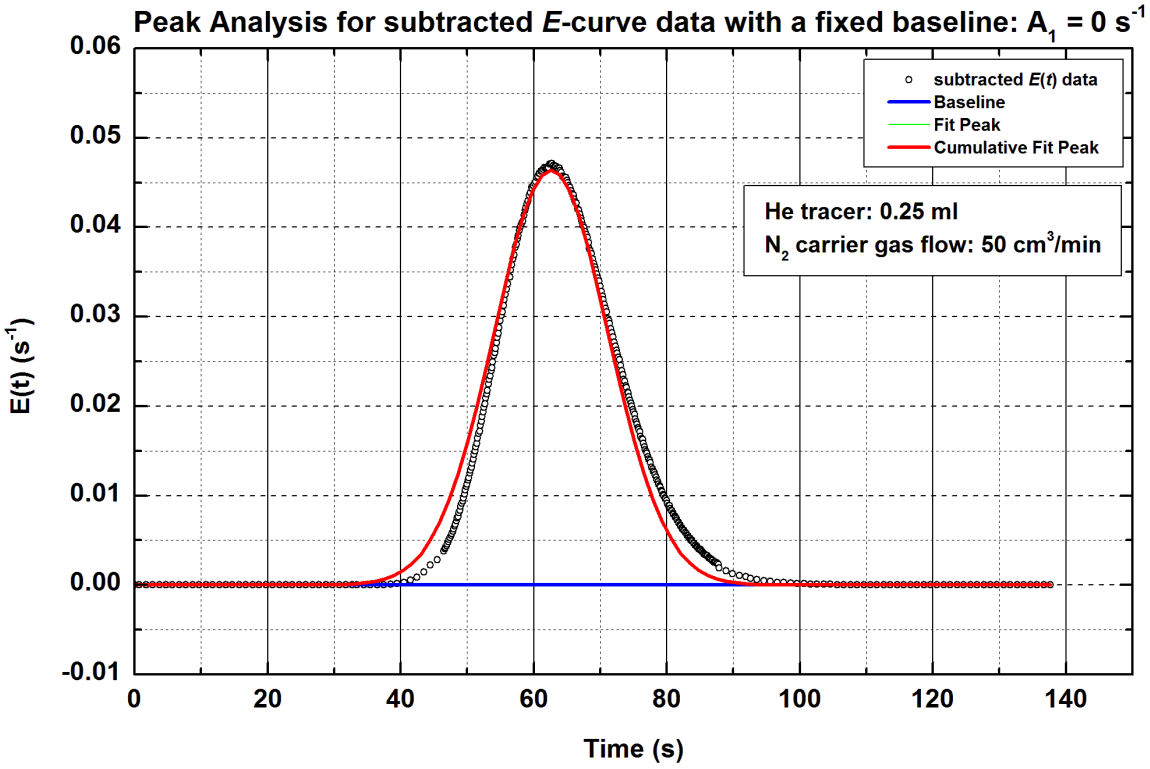

Figure A4.7: The normalization curve, or the age-distribution *E*-curve with subtracted data; with a fixed system found baseline: $A_1 = 0\ s^{-1}$.

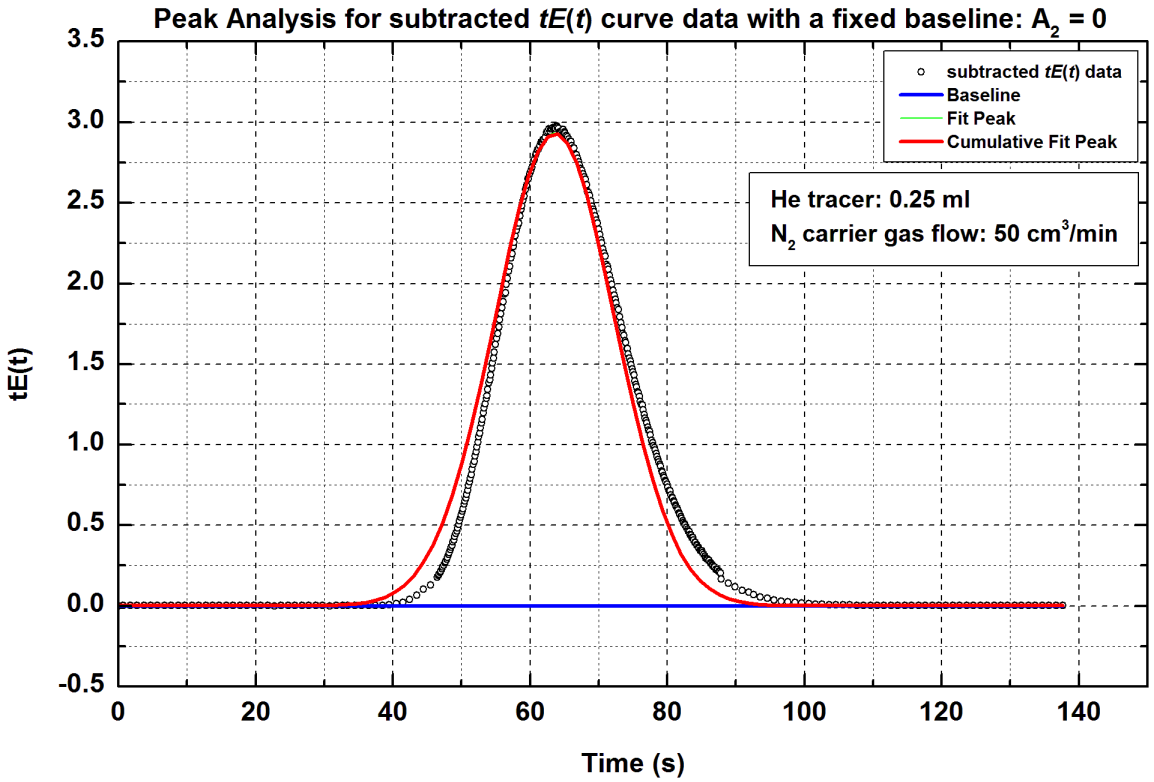

Figure A4.8: The area under the $tE(t)$ curve with subtracted data is the first moment, or the mean residence time μ_1, with a fixed system found baseline: $A_2 = 0$.

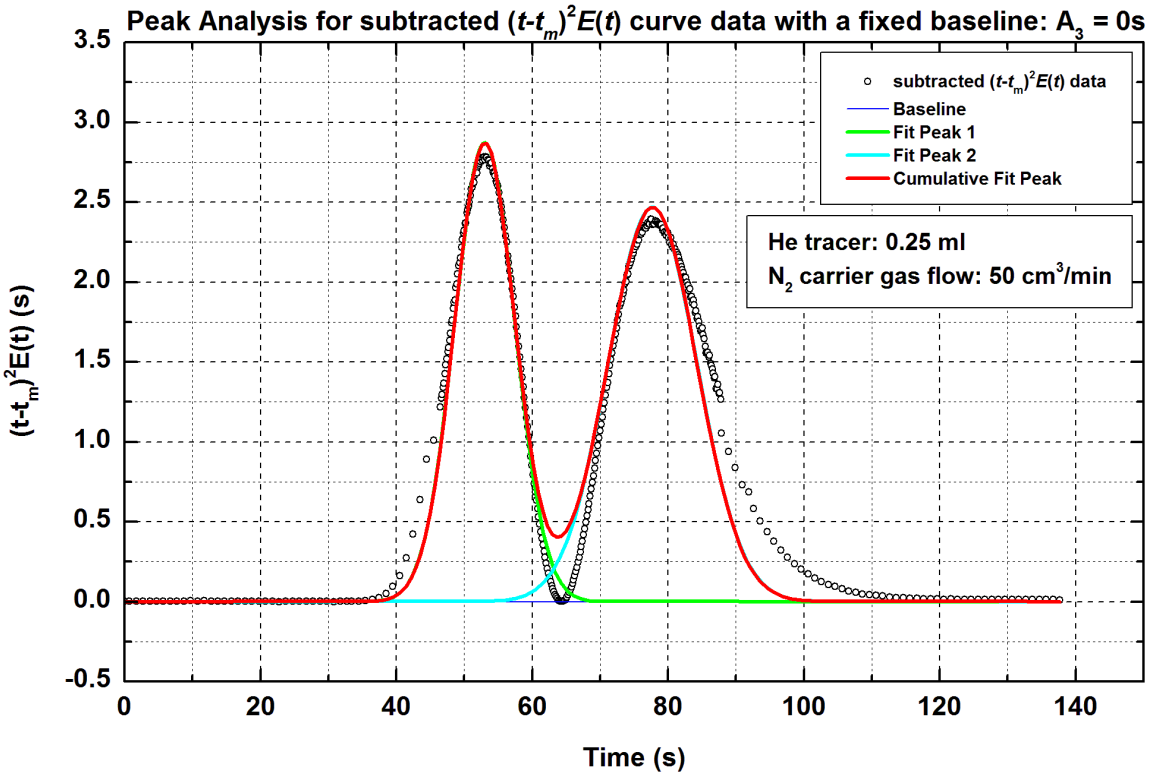

Figure A4.9: The area under the $(t - t_m)^2E(t)$ curve with subtracted data is the second central moment μ_2', or known as the variance σ^2, which defines the spread of a pulse response curve; with a fixed system found baseline: $A_3 = 0$ s.

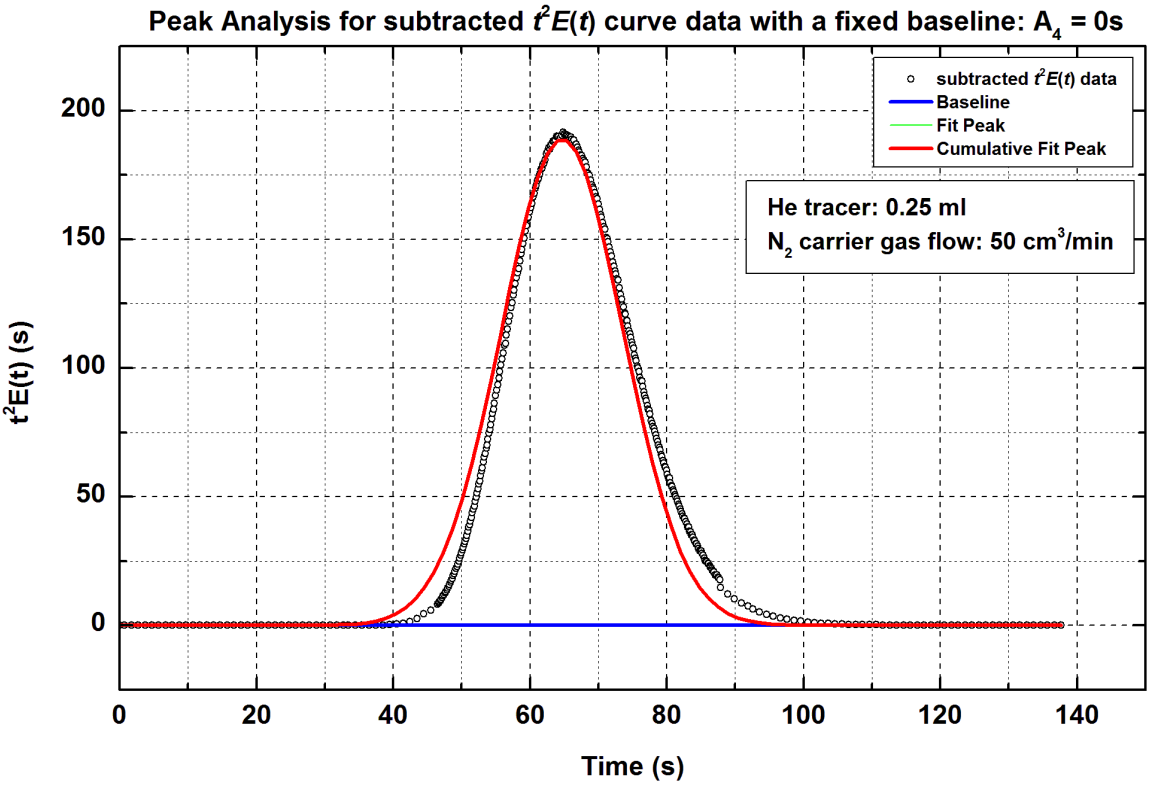

Figure A4.10: The area under the $t^2E(t)$ curve with subtracted data deducting the value of t_m^2 is the second central moment μ_2', or known as the variance σ^2, which defines the spread of a pulse response curve; with a fixed system found baseline: $A_4 = 0$ s.

Table A4.2: Summary of the results generated from peak fitting curves with a **system-found** baseline and **with** baseline subtraction.

***I*-curve**	**Value**		**Standard error**	
Baseline, A_0 (torr)	0		0	
Gaussian Fit Peak Area (torr.s)	3.78466×10^{-7}		2.35907×10^{-9}	
***E*-curve**	**Value**		**Standard error**	
Baseline, A_1 (s^{-1})	0		0	
Gaussian Fit Peak Area	1		0.00623	
***tE*(*t*) curve**	**Value**		**Standard error**	
Baseline, A_2	0		0	
Gaussian Fit Peak Area (s)	64.34115		0.44564	
$(t - t_m)^2E(t)$ curve	**Value**		**Standard error**	
Baseline, A_3 (s)	0		0	
Gaussian Fit Peak Area (s^2)	**Peak 1**	**Peak 2**	**Peak 1**	**Peak 2**
	31.88909	40.31499	0.42615	0.50304
$t^2E(t)$ curve	**Value**		**Standard error**	
Baseline, A_4 (s)	0		0	
Gaussian Fit Peak Area (s^2)	4218.93534		30.62134	

A4.3 Peak fitting with user-defined baseline and without baseline subtraction

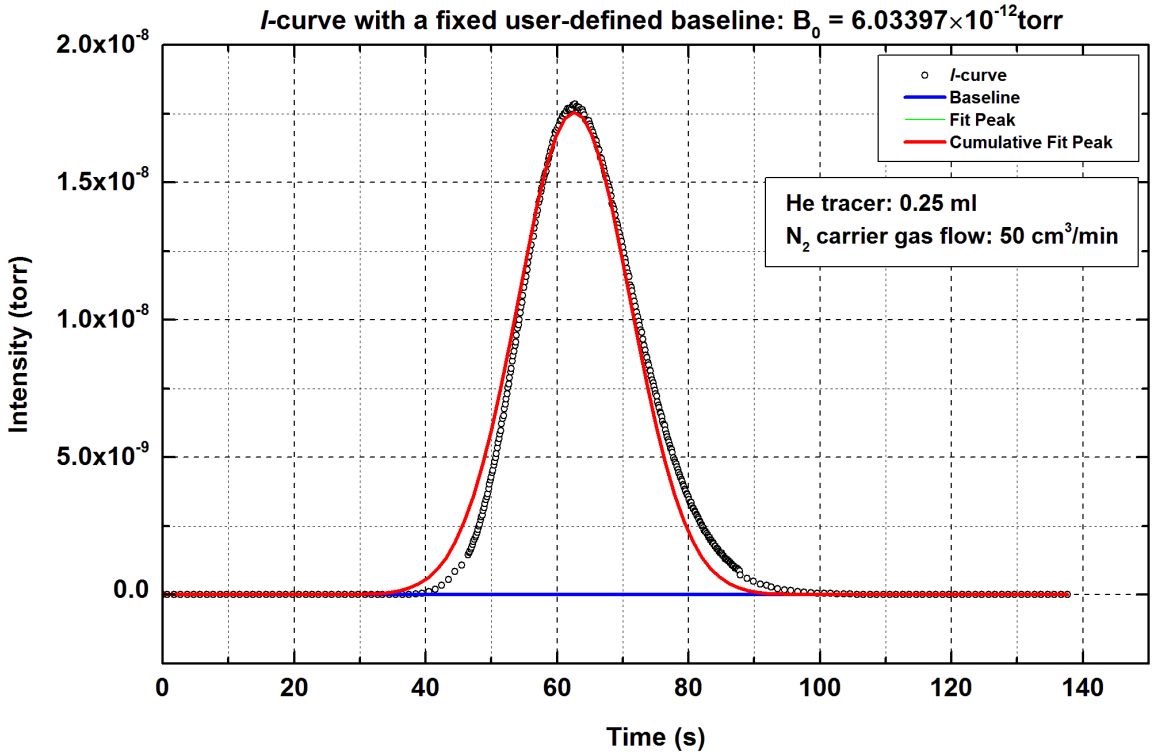

Figure A4.11: *I*-curve with a fixed user-defined baseline: $B_0 = 6.03397\times10^{-12}$ torr (this baseline constant is the same as the value used in numerical integration in Figure A3.1)

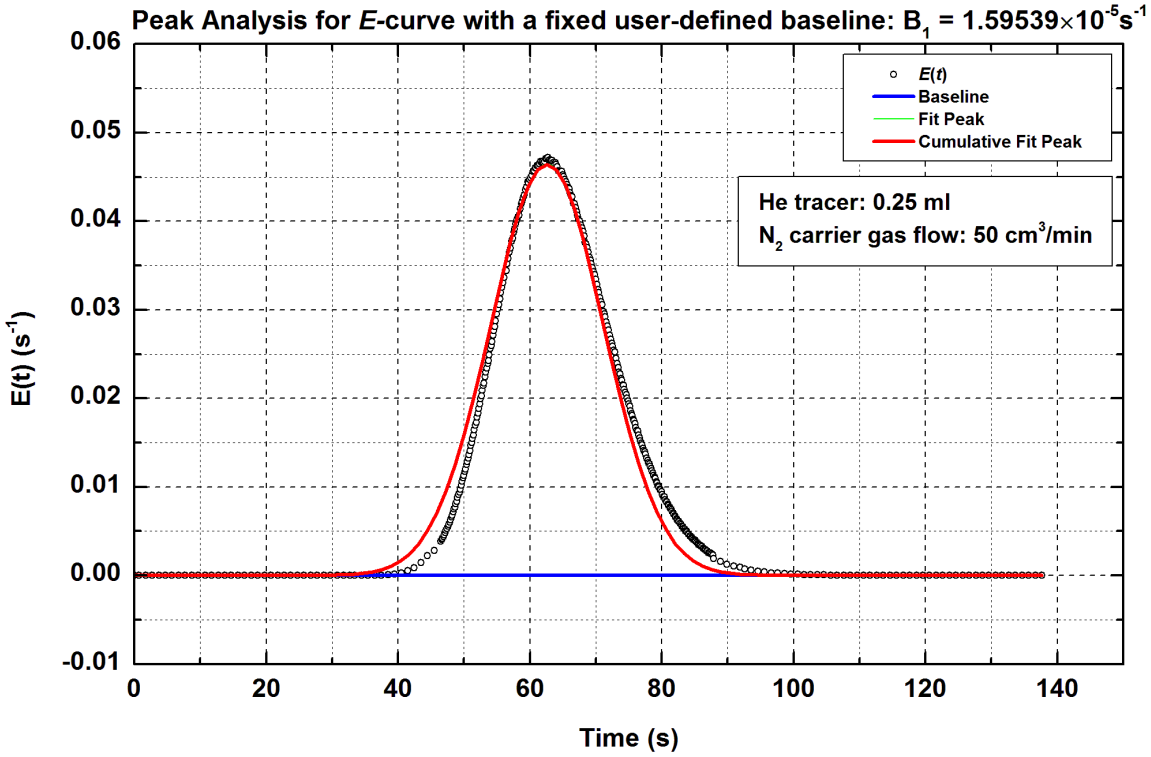

Figure A4.12: The normalization curve, or the age-distribution *E*-curve, with a fixed user-defined baseline: $B_1 = 1.59539 \times 10^{-5}\ s^{-1}$.

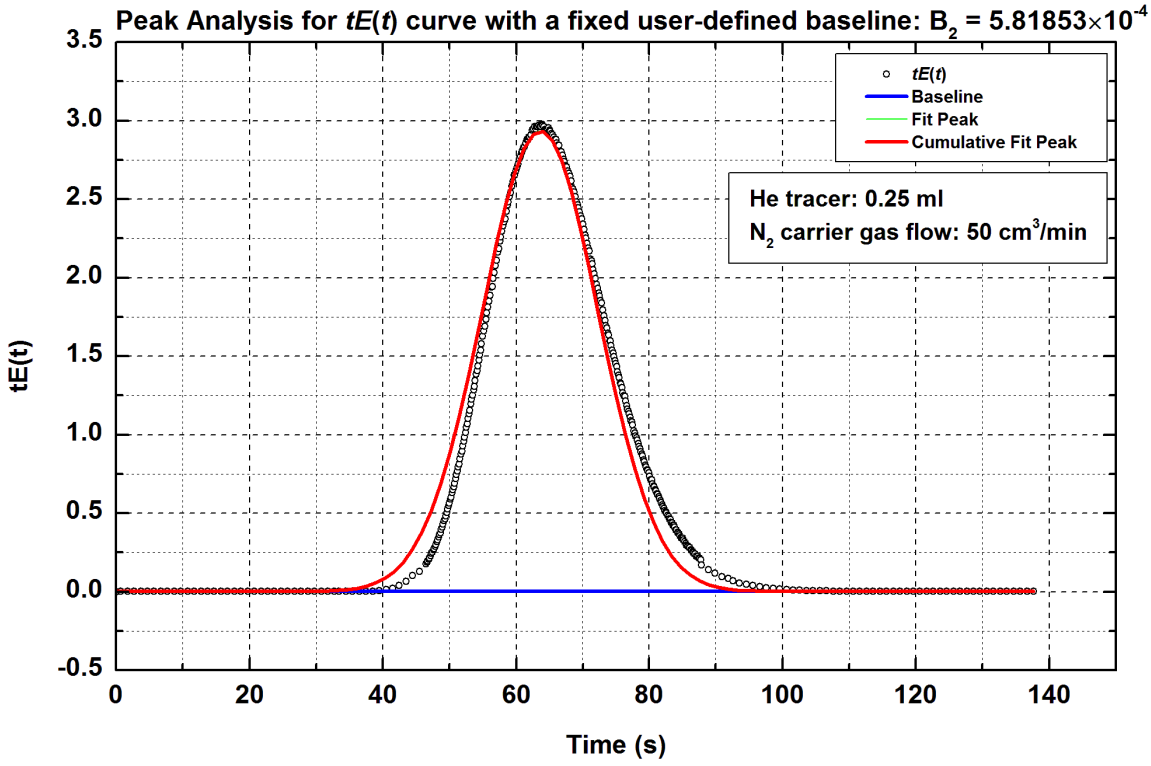

Figure A4.13: The area under the $tE(t)$ curve is the first moment or the mean residence time μ_1, with a fixed user-defined baseline: $B_2 = 5.81853 \times 10^{-4}$.

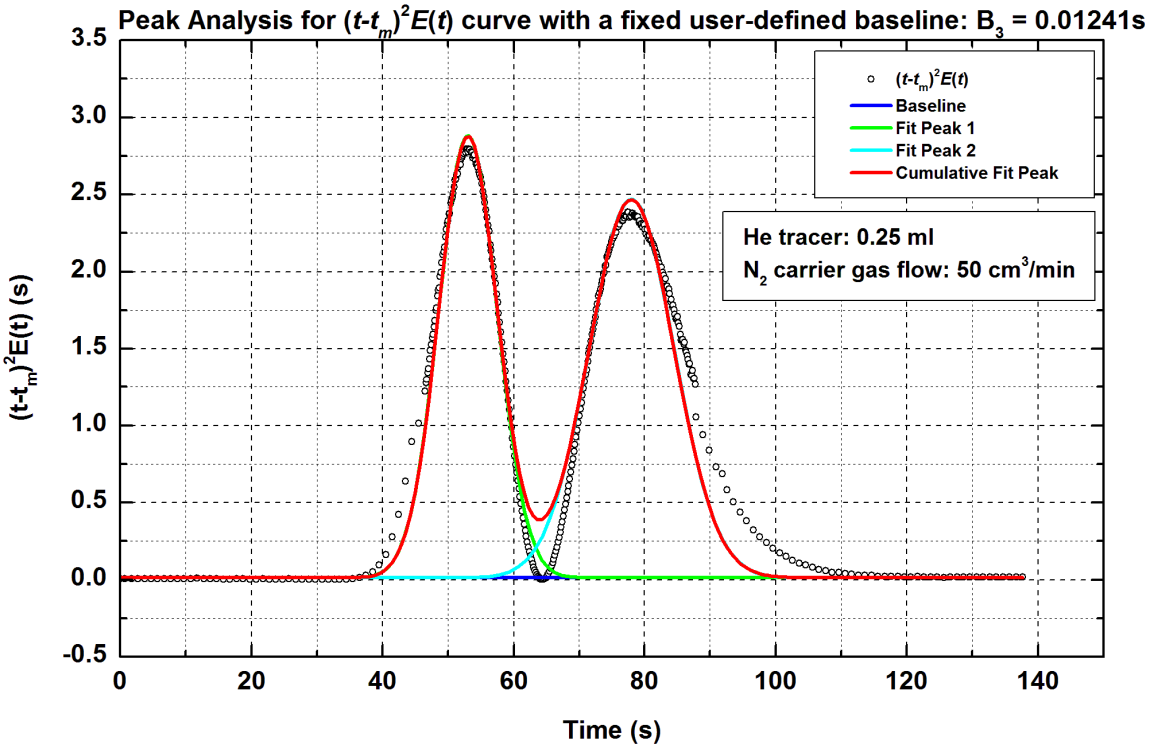

Figure A4.14: The area under the $(t - t_m)^2E(t)$ curve is the second central moment μ_2', or known as the variance σ^2, which defines the spread of a pulse response curve; with a fixed user-defined baseline: B_3 = 0.01241 s.

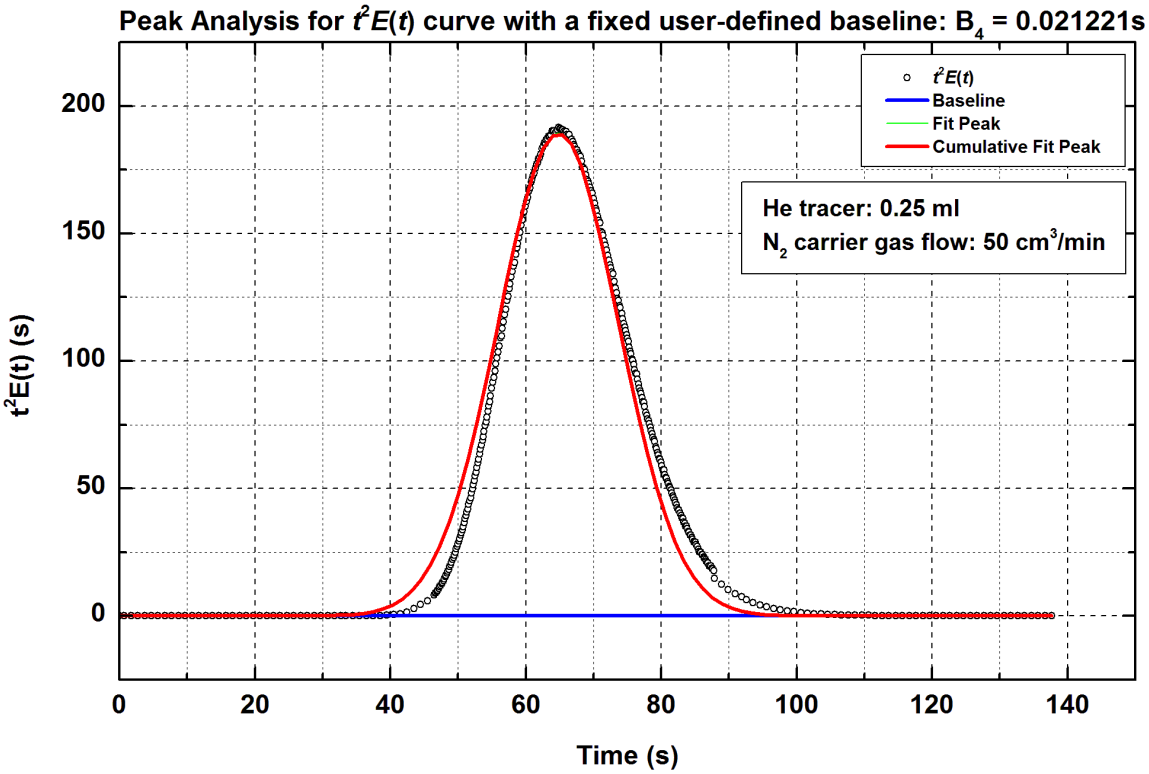

Figure A4.15: The area under the $t^2E(t)$ curve deducting the value of t_m^2 is the second central moment μ_2', or known as the variance σ^2, which defines the spread of a pulse response curve; with a fixed user-defined baseline: B_4 = 0.021221 s.

Table A4.3: Summary of the results generated from peak fitting curves with a **user-defined** baseline and **without** baseline subtraction.

***I*-curve**	**Value**		**Standard error**	
Baseline, B_0 (torr) [(a)]	6.03397×10^{-12}		0	
Gaussian Fit Peak Area (torr.s)	3.78214×10^{-7}		2.35665×10^{-9}	
***E*-curve**	**Value**		**Standard error**	
Baseline, B_1 (s^{-1})	1.59539×10^{-5}		0	
Gaussian Fit Peak Area	1		0.00623	
***tE*(*t*) curve**	**Value**		**Standard error**	
Baseline, B_2	5.81853×10^{-4}		0	
Gaussian Fit Peak Area (s)	64.36071		0.44577	
$(t-t_m)^2E(t)$ curve	**Value**		**Standard error**	
Baseline, B_3 (s)	0.01241		0	
Gaussian Fit Peak Area (s^2)	**Peak 1**	**Peak 2**	**Peak 1**	**Peak 2**
	31.91625	39.98747	0.37791	0.44811
$t^2E(t)$ curve	**Value**		**Standard error**	
Baseline, B_4 (s)	0.02122		0	
Gaussian Fit Peak Area (s^2)	4221.85067		28.83572	

Note: (*a*): The user defined baseline B_0 is the same constant used for numerical integration of peak area shown in Figure A3.1.

A4.4 Peak fitting with user-defined baseline and with baseline subtraction

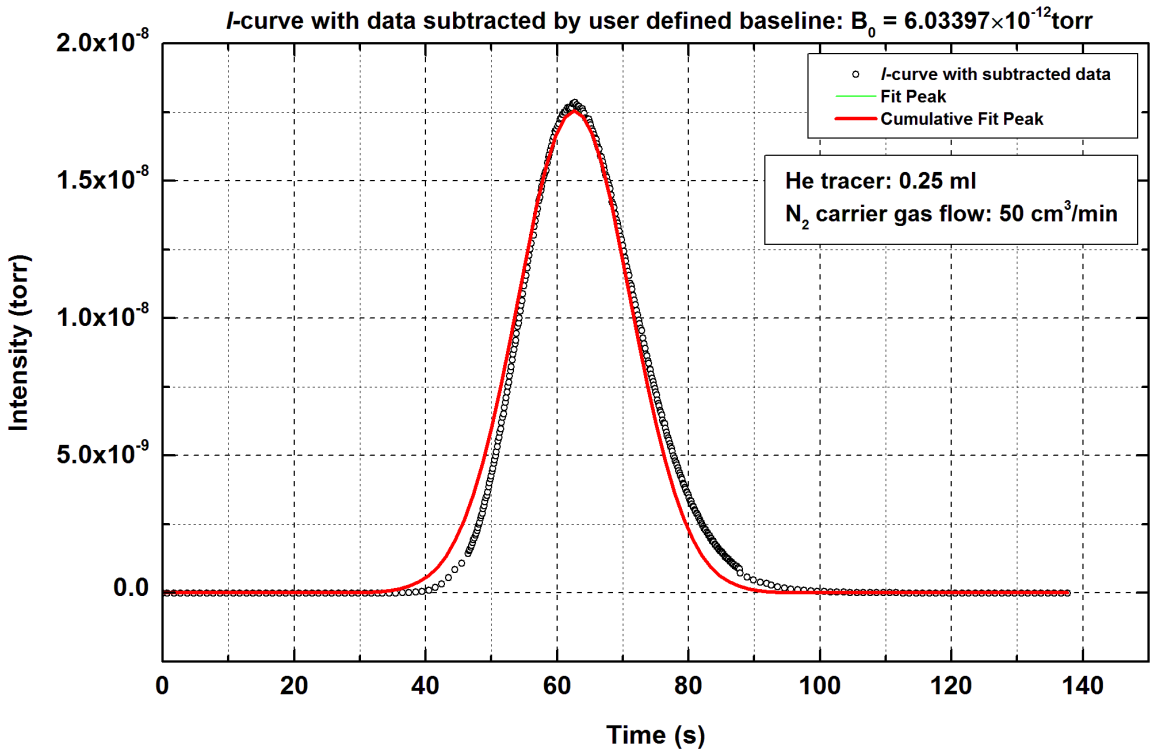

Figure A4.16: Experimental response peak or *I*-curve (Black dotted line) with each data point subtracted by a user-defined baseline: $B_0 = 6.03397\times10^{-12}$ torr.

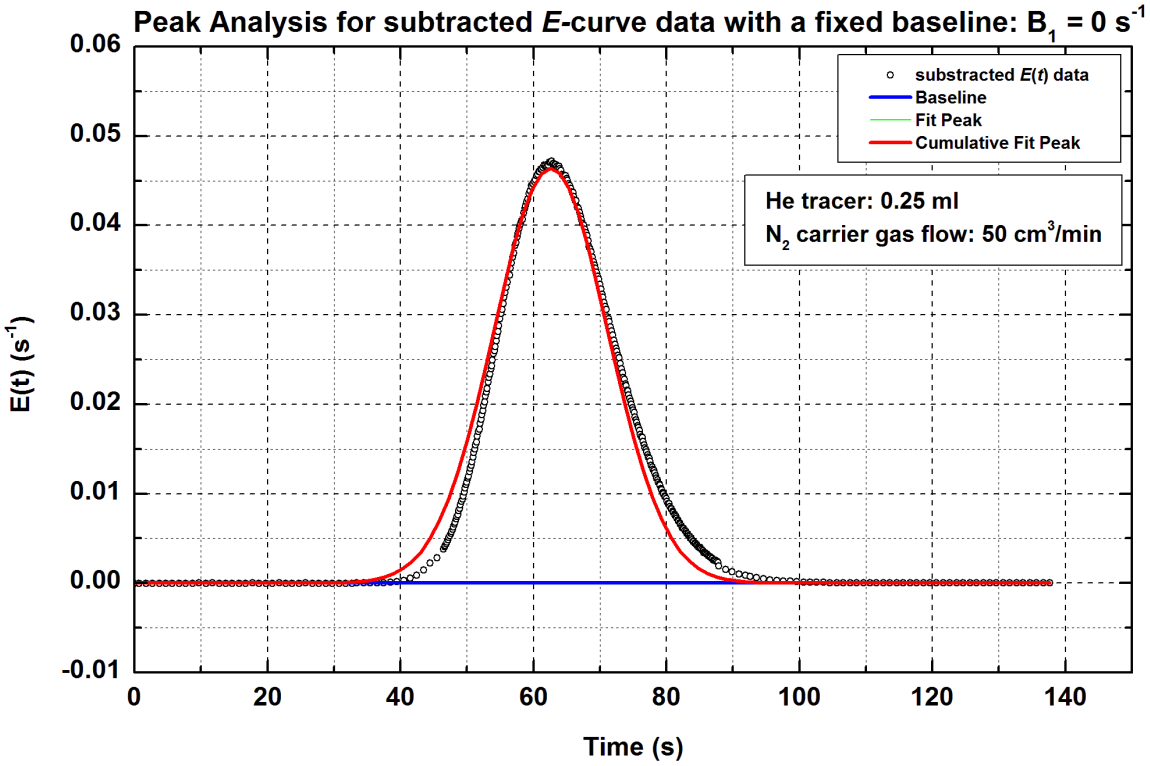

Figure A4.17: The normalization curve or the age-distribution curve – *E*-curve with subtracted data; with a user-defined baseline: $B_1 = 0\ s^{-1}$.

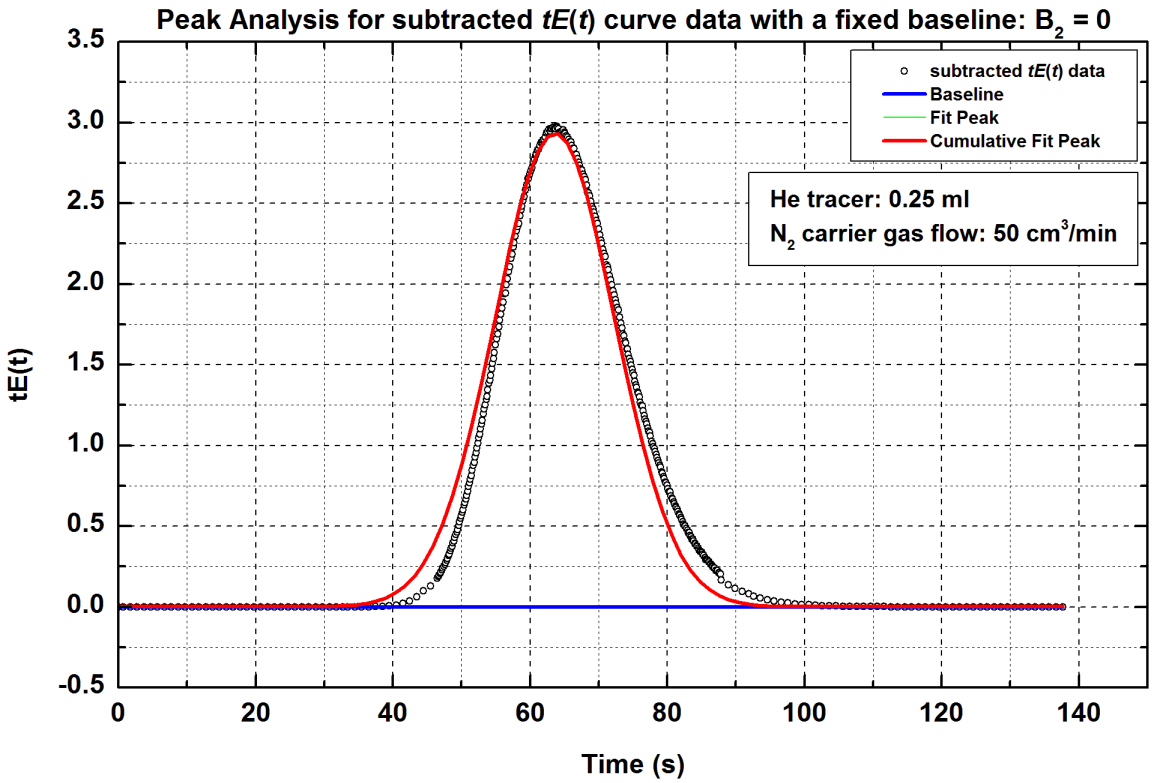

Figure A4.18: The area under the $tE(t)$ curve with subtracted data is the first moment or the mean residence time μ_1, with a user-defined baseline: $B_2 = 0$.

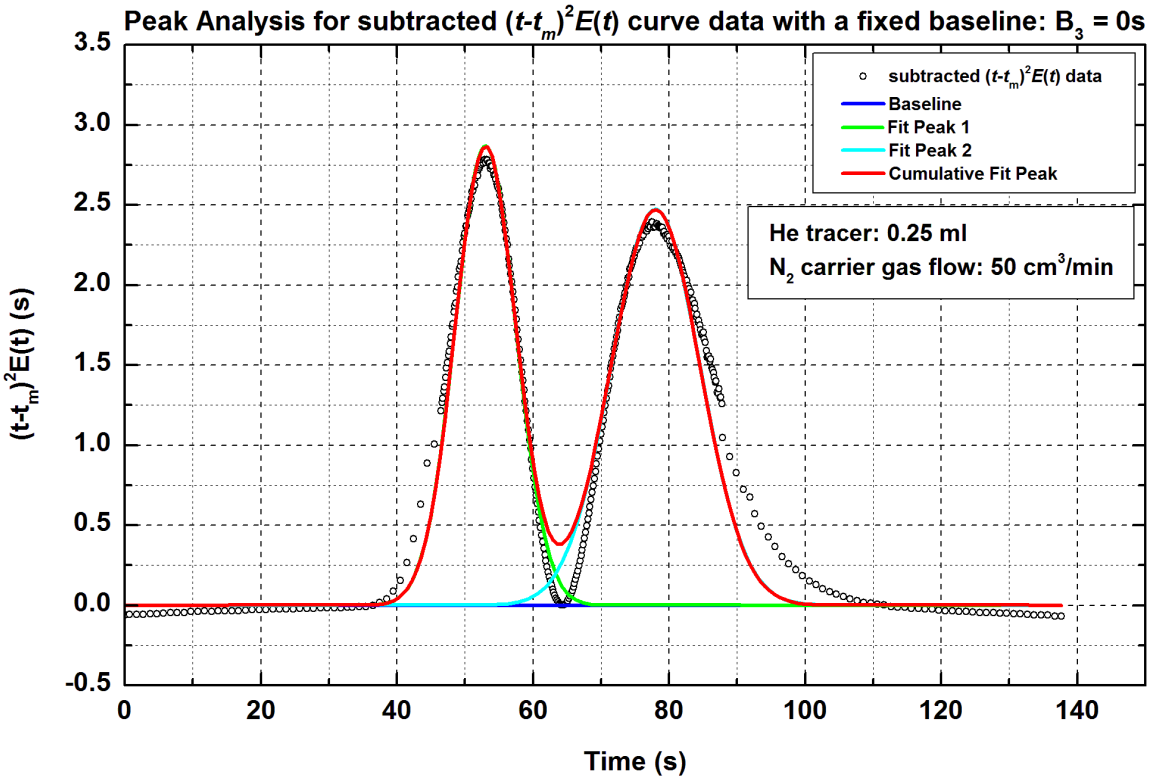

Figure A4.19: The area under the $(t - t_m)^2E(t)$ curve with subtracted data is the second central moment μ_2', or known as the variance σ^2, which defines the spread of a pulse response curve; with a user-defined baseline: $B_3 = 0$ s.

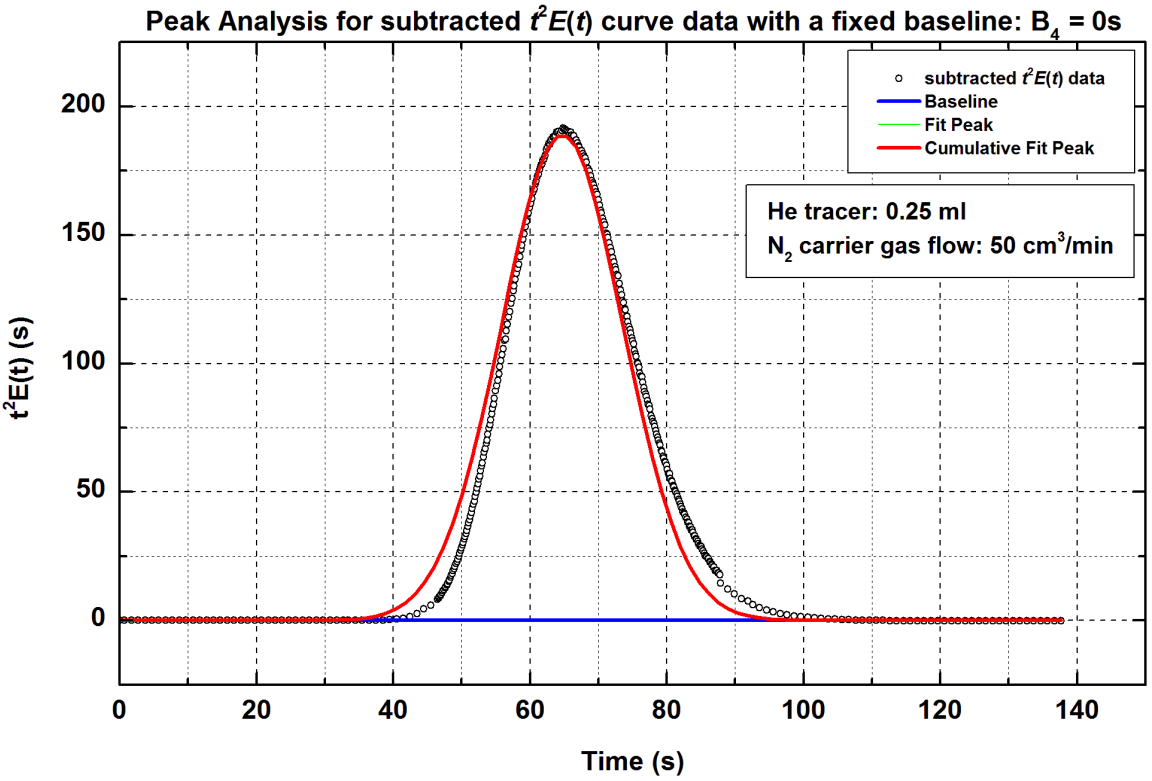

Figure A4.20: The area under the $t^2E(t)$ curve with subtracted data deducting t_m^2 is the second central moment μ_2', or known as the variance σ^2, which defines the spread of a pulse response curve; with a user-defined baseline: $B_4 = 0$ s.

Table A4.4: Summary of the results generated from peak fitting curves with a **user-defined** baseline and **with** baseline subtraction.

***I*-curve**	**Value**		**Standard error**	
Baseline, B_0 (torr)	0		0	
Gaussian Fit Peak Area (torr.s)	3.78214×10^{-7}		2.35665×10^{-9}	
***E*-curve**	**Value**		**Standard error**	
Baseline, B_1 (s^{-1})	0		0	
Gaussian Fit Peak Area	1		0.00623	
***tE*(*t*) curve**	**Value**		**Standard error**	
Baseline, B_2	0		0	
Gaussian Fit Peak Area (s)	64.34019		0.44514	
$(t - t_m)^2E(t)$ curve	**Value**		**Standard error**	
Baseline, B_3 (s)	0		0	
Gaussian Fit Peak Area (s^2)	**Peak 1**	**Peak 2**	**Peak 1**	**Peak 2**
	31.96613	40.3975	0.37463	0.44486
$t^2E(t)$ curve	**Value**		**Standard error**	
Baseline, B_4 (s)	0		0	
Gaussian Fit Peak Area (s^2)	4218.69524		30.56218	

Appendix 5: Moments analysis results for γ-alumina beads experiments

From Tables A5.1 to A5.30, the first moments for blank runs, $(\mu_1)_0$ were calculated according to Equations (3.59), and the $(\mu_1)_0$ results of the fictitious bed (200 mm) from Tables A5.31 to A5.42, were used for Cases 2c, 4 and 6 to calculate the adsorption equilibrium constant. The effect of using, or not using $t_0/2$ in the $(\mu_1)_0$ term is very small because changes in the K values are negligible.

A5.1 Moment analysis results for 400 mm (real) column packed with γ-alumina beads (Simpson's rule)

Table A5.1: Moment analysis results (γ-alumina beads experiment) in a 400 mm column with 0.1 ml He tracer pulse, and the 2nd central moment is obtained using Simpson's rule.

N_2 (carrier) - He (tracer)	**γ-alumina beads (0.1 ml sample loop)**					
	Flowrate (cm^3/min)	**1st moment, μ_1 (s)**	**2nd central moment, μ_2' (s^2)**	**$(\mu_1)_0$ for blank run (Equation (3.59))(s)**	**$(\mu_1)_0$ for blank run (Equation (3.60))(s)**	**Injection time, t_0 (s)**
bot01	30	110.180	338.010	89.76327218	89.86327218	0.20
bot03	40	83.006	143.900	67.32245413	67.39745413	0.15
bot06	50	66.148	77.175	53.85796331	53.91796331	0.12
bot08	60	56.876	48.091	44.88163609	44.93163609	0.10
bot10	70	49.360	32.071	38.46997379	38.51283093	0.09
bot13	80	42.334	20.422	33.66122707	33.69872707	0.08
bot16	90	39.152	17.062	29.92109073	29.95442406	0.07

Note: **'bot':** it's a file created in MID scans from mass spectrometer for each chromatographic experiment run. It has no meaning itself but just a file name which represents the data collected from the experimental response peak.

Table A5.2: Moment analysis results (γ-alumina beads experiment) in a 400 mm column with 0.1 ml N_2 tracer pulse, and the 2nd central moment is obtained using Simpson's rule.

He (carrier) - N_2 (tracer)	γ-alumina beads (0.1 ml sample loop)					
	Flowrate (cm^3/min)	1st moment, μ_1 (s)	2nd central moment, μ_2' (s^2)	$(\mu_1)_0$ for blank run (Equation (3.59))(s)	$(\mu_1)_0$ for blank run (Equation (3.60))(s)	Injection time, t_0 (s)
bot01	30	116.300	438.130	89.76327218	89.86327218	0.20
bot03	40	86.533	170.440	67.32245413	67.39745413	0.15
bot05	50	75.970	116.110	53.85796331	53.91796331	0.12
bot07	60	66.502	73.410	44.88163609	44.93163609	0.10
bot09	70	55.702	42.545	38.46997379	38.51283093	0.09
bot12	80	48.227	28.224	33.66122707	33.69872707	0.08
bot14	90	43.559	20.079	29.92109073	29.95442406	0.07

Table A5.3: Moment analysis results (γ-alumina beads experiment) in a 400 mm column with 0.25 ml He tracer pulse, and the 2nd central moment is obtained using Simpson's rule.

N_2 (carrier) - He (tracer)	γ-alumina beads (0.25 ml sample loop)					
	Flowrate (cm^3/min)	1st moment, μ_1 (s)	2nd central moment, μ_2' (s^2)	$(\mu_1)_0$ for blank run (Equation (3.59))(s)	$(\mu_1)_0$ for blank run (Equation (3.60))(s)	Injection time, t_0 (s)
bot01	30	110.020	314.120	89.76327218	90.01327218	0.50
bot03	40	83.805	149.000	67.32245413	67.50995413	0.38
bot06	50	66.426	72.699	53.85796331	54.00796331	0.30
bot08	60	56.397	50.991	44.88163609	45.00663609	0.25
bot10	70	49.289	31.437	38.46997379	38.57711665	0.21
bot13	80	42.537	21.360	33.66122707	33.75497707	0.19
bot16	90	38.511	15.521	29.92109073	30.00442406	0.17

Table A5.4: Moment analysis results (γ-alumina beads experiment) in a 400 mm column with 0.25 ml N_2 tracer pulse, and the 2nd central moment is obtained using Simpson's rule.

He (carrier) - N_2 (tracer)	γ-alumina beads (0.25 ml sample loop)					
	Flowrate (cm^3/min)	**1st moment, μ_1 (s)**	**2nd central moment, μ_2' (s^2)**	**$(\mu_1)_0$ for blank run (Equation (3.59))(s)**	**$(\mu_1)_0$ for blank run (Equation (3.60))(s)**	**Injection time, t_0 (s)**
bot01	30	114.320	396.270	89.76327218	90.01327218	0.50
bot03	40	85.398	152.040	67.32245413	67.50995413	0.38
bot05	50	75.266	101.450	53.85796331	54.00796331	0.30
bot07	60	66.998	70.238	44.88163609	45.00663609	0.25
bot09	70	55.634	42.130	38.46997379	38.57711665	0.21
bot12	80	48.892	27.939	33.66122707	33.75497707	0.19
bot14	90	43.766	20.593	29.92109073	30.00442406	0.17

Table A5.5: Moment analysis results (γ-alumina beads experiment) in a 400 mm column with 0.5 ml He tracer pulse, and the 2nd central moment is obtained using Simpson's rule.

N_2 (carrier) - He (tracer)	γ-alumina beads (0.5 ml sample loop)					
	Flowrate (cm^3/min)	**1st moment, μ_1 (s)**	**2nd central moment, μ_2' (s^2)**	**$(\mu_1)_0$ for blank run (Equation (3.59))(s)**	**$(\mu_1)_0$ for blank run (Equation (3.60))(s)**	**Injection time, t_0 (s)**
bot01	30	112.400	340.930	89.76327218	90.26327218	1.00
bot03	40	82.974	146.590	67.32245413	67.69745413	0.75
bot06	50	66.936	75.940	53.85796331	54.15796331	0.60
bot08	60	56.854	47.308	44.88163609	45.13163609	0.50
bot10	70	50.327	34.349	38.46997379	38.68425950	0.43
bot13	80	42.905	23.048	33.66122707	33.84872707	0.38
bot16	90	39.344	17.281	29.92109073	30.08775739	0.33

Table A5.6: Moment analysis results (γ-alumina beads experiment) in a 400 mm column with 0.5 ml N_2 tracer pulse, and the 2nd central moment is obtained using Simpson's rule.

He (carrier) - N_2 (tracer)	**γ-alumina beads (0.5 ml sample loop)**					
	Flowrate (cm^3/min)	**1st moment, μ_1 (s)**	**2nd central moment, μ_2' (s^2)**	**$(\mu_1)_0$ for blank run (Equation (3.59))(s)**	**$(\mu_1)_0$ for blank run (Equation (3.60))(s)**	**Injection time, t_0 (s)**
bot01	30	115.580	366.920	89.76327218	90.26327218	1.00
bot03	40	85.921	138.260	67.32245413	67.69745413	0.75
bot05	50	75.012	98.842	53.85796331	54.15796331	0.60
bot07	60	66.683	67.615	44.88163609	45.13163609	0.50
bot09	70	55.872	41.437	38.46997379	38.68425950	0.43
bot12	80	48.662	27.181	33.66122707	33.84872707	0.38
bot14	90	43.765	19.691	29.92109073	30.08775739	0.33

A5.2 Moment analysis results for 400 mm (real) column packed with γ-alumina beads (2^{nd} central moments are calculated by Cat. A):

Table A5.7: Moment analysis results (γ-alumina beads experiment) in a 400 mm column with 0.1 ml He tracer pulse, and the 2^{nd} central moment is obtained using **Cat. A**.

N_2(carrier) - He(tracer)	γ-alumina beads (0.1 ml sample loop)					
	Flowrate (cm^3/min)	1^{st} moment, μ_1 (s)	2^{nd} central moment, μ_2' (s^2)	$(\mu_1)_0$ for blank run (Equation (3.59))(s)	$(\mu_1)_0$ for blank run (Equation (3.60))(s)	Injection time, t_0 (s)
bot01	30	104.72323	293.33781	89.76327218	89.86327218	0.20
bot03	40	79.99072	131.05125	67.32245413	67.39745413	0.15
bot06	50	64.02926	70.06103	53.85796331	53.91796331	0.12
bot08	60	55.00931	44.24247	44.88163609	44.93163609	0.10
bot10	70	47.84691	30.28910	38.46997379	38.51283093	0.09
bot13	80	41.19657	18.28492	33.66122707	33.69872707	0.08
bot16	90	38.03590	14.91005	29.92109073	29.95442406	0.07

Table A5.8: Moment analysis results (γ-alumina beads experiment) in a 400 mm column with 0.1 ml N_2 tracer pulse, and the 2^{nd} central moment is obtained using **Cat. A**.

He(carrier) - N_2(tracer)	γ-alumina beads (0.1 ml sample loop)					
	Flowrate (cm^3/min)	1^{st} moment, μ_1 (s)	2^{nd} central moment, μ_2' (s^2)	$(\mu_1)_0$ for blank run (Equation (3.59))(s)	$(\mu_1)_0$ for blank run (Equation (3.60))(s)	Injection time, t_0 (s)
bot01	30	113.70199	555.58414	89.76327218	89.86327218	0.20
bot03	40	84.62016	146.36236	67.32245413	67.39745413	0.15
bot05	50	74.61935	98.01658	53.85796331	53.91796331	0.12
bot07	60	65.78593	66.81683	44.88163609	44.93163609	0.10
bot09	70	55.12268	40.00784	38.46997379	38.51283093	0.09
bot12	80	47.46371	26.03568	33.66122707	33.69872707	0.08
bot14	90	43.07355	19.25943	29.92109073	29.95442406	0.07

Table A5.9: Moment analysis results (γ-alumina beads experiment) in a 400 mm column with 0.25 ml He tracer pulse, and the 2nd central moment is obtained using **Cat. A**.

N_2(carrier) - He(tracer)	γ-alumina beads (0.25 ml sample loop)					
	Flowrate (cm^3/min)	**1st moment, μ_1 (s)**	**2nd central moment, μ_2' (s^2)**	**$(\mu_1)_0$ for blank run (Equation (3.59))(s)**	**$(\mu_1)_0$ for blank run (Equation (3.60))(s)**	**Injection time, t_0 (s)**
bot01	30	105.82143	310.52664	89.76327218	90.01327218	0.50
bot03	40	80.45573	138.24945	67.32245413	67.50995413	0.38
bot06	50	64.34115	72.20408	53.85796331	54.00796331	0.30
bot08	60	54.83164	45.35157	44.88163609	45.00663609	0.25
bot10	70	47.85306	30.79586	38.46997379	38.57711665	0.21
bot13	80	41.16452	20.16187	33.66122707	33.75497707	0.19
bot16	90	37.48024	15.51946	29.92109073	30.00442406	0.17

Table A5.10: Moment analysis results (γ-alumina beads experiment) in a 400 mm column with 0.25 ml N_2 tracer pulse, and the 2nd central moment is obtained using **Cat. A**.

He(carrier) - N_2(tracer)	γ-alumina beads (0.25 ml sample loop)					
	Flowrate (cm^3/min)	**1st moment, μ_1 (s)**	**2nd central moment, μ_2' (s^2)**	**$(\mu_1)_0$ for blank run (Equation (3.59))(s)**	**$(\mu_1)_0$ for blank run (Equation (3.60))(s)**	**Injection time, t_0 (s)**
bot01	30	111.92176	362.25254	89.76327218	90.01327218	0.50
bot03	40	84.18536	140.93407	67.32245413	67.50995413	0.38
bot05	50	74.22703	96.71883	53.85796331	54.00796331	0.30
bot07	60	65.91742	68.08020	44.88163609	45.00663609	0.25
bot09	70	54.93655	39.74568	38.46997379	38.57711665	0.21
bot12	80	48.16616	26.81245	33.66122707	33.75497707	0.19
bot14	90	43.08123	19.64441	29.92109073	30.00442406	0.17

Table A5.11: Moment analysis results (γ-alumina beads experiment) in a 400 mm column with 0.5 ml He tracer pulse, and the 2nd central moment is obtained using **Cat. A**.

N_2(carrier) - He(tracer)	γ-alumina beads (0.5 ml sample loop)					
	Flowrate (cm^3/min)	1st moment, μ_1 (s)	2nd central moment, μ_2' (s^2)	$(\mu_1)_0$ for blank run (Equation (3.59))(s)	$(\mu_1)_0$ for blank run (Equation (3.60))(s)	Injection time, t_0 (s)
bot01	30	107.36374	327.35918	89.76327218	90.26327218	1.00
bot03	40	80.22380	140.35775	67.32245413	67.69745413	0.75
bot06	50	64.48135	74.74857	53.85796331	54.15796331	0.60
bot08	60	55.13468	47.37953	44.88163609	45.13163609	0.50
bot10	70	48.23150	31.92637	38.46997379	38.68425950	0.43
bot13	80	41.42653	20.93585	33.66122707	33.84872707	0.38
bot16	90	38.03820	16.44464	29.92109073	30.08775739	0.33

Table A5.12: Moment analysis results (γ-alumina beads experiment) in a 400 mm column with 0.5 ml N_2 tracer pulse, and the 2nd central moment is obtained using **Cat. A**.

He(carrier) - N_2(tracer)	γ-alumina beads (0.5 ml sample loop)					
	Flowrate (cm^3/min)	1st moment, μ_1 (s)	2nd central moment, μ_2' (s^2)	$(\mu_1)_0$ for blank run (Equation (3.59))(s)	$(\mu_1)_0$ for blank run (Equation (3.60))(s)	Injection time, t_0 (s)
bot01	30	113.59566	348.89357	89.76327218	90.26327218	1.00
bot03	40	85.03001	143.90664	67.32245413	67.69745413	0.75
bot05	50	73.99991	96.41275	53.85796331	54.15796331	0.60
bot07	60	65.64624	67.53836	44.88163609	45.13163609	0.50
bot09	70	54.78793	39.99446	38.46997379	38.68425950	0.43
bot12	80	48.13273	27.24789	33.66122707	33.84872707	0.38
bot14	90	42.96398	19.64440	29.92109073	30.08775739	0.33

A5.3 Moment analysis results for 200 mm (real) column packed with γ-alumina beads (2nd central moment are calculated by Cat. A)

Table A5.13: Moment analysis results (γ-alumina beads experiment) in a 200 mm column with 0.1 ml He tracer pulse, and the 2nd central moment is obtained using **Cat. A**.

N_2(carrier) - He(tracer)	γ-alumina beads (0.1 ml sample loop)					
	Flowrate (cm^3/min)	1st moment, μ_1 (s)	2nd central moment, μ_2' (s^2)	$(\mu_1)_0$ for blank run (Equation (3.59))(s)	$(\mu_1)_0$ for blank run (Equation (3.60))(s)	Injection time, t_0 (s)
bot01	30	53.91372	128.34718	46.35628621	46.45628621	0.20
bot03	40	41.42950	56.79720	34.76721466	34.84221466	0.15
bot06	50	33.74820	29.94805	27.81377172	27.87377172	0.12
bot08	60	28.91111	19.26437	23.17814310	23.22814310	0.10
bot10	70	25.44974	12.89297	19.86697980	19.90983695	0.09
bot13	80	21.91116	8.12368	17.38360733	17.42110733	0.08
bot16	90	19.86439	6.23206	15.45209540	15.48542874	0.07

Table A5.14: Moment analysis results (γ-alumina beads experiment) in a 200 mm column with 0.1 ml N_2 tracer pulse, and the 2nd central moment is obtained using **Cat. A**.

He(carrier) - N_2(tracer)	γ-alumina beads (0.1 ml sample loop)					
	Flowrate (cm^3/min)	1st moment, μ_1 (s)	2nd central moment, μ_2' (s^2)	$(\mu_1)_0$ for blank run (Equation (3.59))(s)	$(\mu_1)_0$ for blank run (Equation (3.60))(s)	Injection time, t_0 (s)
bot01	30	59.24971	167.88328	46.35628621	46.45628621	0.20
bot03	40	45.11066	70.87815	34.76721466	34.84221466	0.15
bot05	50	39.72687	47.99389	27.81377172	27.87377172	0.12
bot07	60	35.18555	33.58383	23.17814310	23.22814310	0.10
bot09	70	29.40691	19.91147	19.86697980	19.90983695	0.09
bot12	80	25.86264	13.50330	17.38360733	17.42110733	0.08
bot14	90	23.22486	9.85798	15.45209540	15.48542874	0.07

Table A5.15: Moment analysis results (γ-alumina beads experiment) in a 200 mm column with 0.25 ml He tracer pulse, and the 2nd central moment is obtained using **Cat. A**.

N_2(carrier) - He(tracer)	γ-alumina beads (0.25 ml sample loop)					
	Flowrate (cm^3/min)	**1st moment, μ_1 (s)**	**2nd central moment, μ_2' (s^2)**	**$(\mu_1)_0$ for blank run (Equation (3.59))(s)**	**$(\mu_1)_0$ for blank run (Equation (3.60))(s)**	**Injection time, t_0 (s)**
bot01	30	54.68801	132.69421	46.35628621	46.45628621	0.50
bot03	40	41.59702	60.58020	34.76721466	34.84221466	0.38
bot06	50	33.97254	31.96704	27.81377172	27.87377172	0.30
bot08	60	29.05359	20.38360	23.17814310	23.22814310	0.25
bot10	70	25.54571	13.72542	19.86697980	19.90983695	0.21
bot13	80	21.96249	8.73318	17.38360733	17.42110733	0.19
bot16	90	20.10529	6.72825	15.45209540	15.48542874	0.17

Table A5.16: Moment analysis results (γ-alumina beads experiment) in a 200 mm column with 0.25 ml N_2 tracer pulse, and the 2nd central moment is obtained using **Cat. A**.

He(carrier) - N_2(tracer)	γ-alumina beads (0.25 ml sample loop)					
	Flowrate (cm^3/min)	**1st moment, μ_1 (s)**	**2nd central moment, μ_2' (s^2)**	**$(\mu_1)_0$ for blank run (Equation (3.59))(s)**	**$(\mu_1)_0$ for blank run (Equation (3.60))(s)**	**Injection time, t_0 (s)**
bot01	30	59.77943	165.23611	46.35628621	46.45628621	0.50
bot03	40	45.09890	70.04798	34.76721466	34.84221466	0.38
bot05	50	39.86844	48.04881	27.81377172	27.87377172	0.30
bot07	60	35.20971	33.39560	23.17814310	23.22814310	0.25
bot09	70	29.43729	19.95473	19.86697980	19.90983695	0.21
bot12	80	25.91928	13.68506	17.38360733	17.42110733	0.19
bot14	90	23.37371	9.92197	15.45209540	15.48542874	0.17

Table A5.17: Moment analysis results (γ-alumina beads experiment) in a 200 mm column with 0.5 ml He tracer pulse, and the 2nd central moment is obtained using **Cat. A**.

N_2(carrier) - He(tracer)	γ-alumina beads (0.5 ml sample loop)					
	Flowrate (cm^3/min)	**1st moment, μ_1 (s)**	**2nd central moment, μ_2' (s^2)**	**$(\mu_1)_0$ for blank run (Equation (3.59))(s)**	**$(\mu_1)_0$ for blank run (Equation (3.60))(s)**	**Injection time, t_0 (s)**
bot01	30	56.22629	144.01388	46.35628621	46.45628621	1.00
bot03	40	41.58749	59.93298	34.76721466	34.84221466	0.75
bot06	50	34.22596	32.61297	27.81377172	27.87377172	0.60
bot08	60	29.25567	20.58674	23.17814310	23.22814310	0.50
bot10	70	25.63625	13.48900	19.86697980	19.90983695	0.43
bot13	80	21.96088	8.75786	17.38360733	17.42110733	0.38
bot16	90	20.32728	6.90020	15.45209540	15.48542874	0.33

Table A5.18: Moment analysis results (γ-alumina beads experiment) in a 200 mm column with 0.5 ml N_2 tracer pulse, and the 2nd central moment is obtained using **Cat. A**.

He(carrier) - N_2(tracer)	γ-alumina beads (0.5 ml sample loop)					
	Flowrate (cm^3/min)	**1st moment, μ_1 (s)**	**2nd central moment, μ_2' (s^2)**	**$(\mu_1)_0$ for blank run (Equation (3.59))(s)**	**$(\mu_1)_0$ for blank run (Equation (3.60))(s)**	**Injection time, t_0 (s)**
bot01	30	59.47346	160.32530	46.35628621	46.45628621	1.00
bot03	40	45.07293	69.86156	34.76721466	34.84221466	0.75
bot05	50	39.56584	48.00840	27.81377172	27.87377172	0.60
bot07	60	34.88589	32.83445	23.17814310	23.22814310	0.50
bot09	70	29.29810	19.93547	19.86697980	19.90983695	0.43
bot12	80	25.91209	13.41441	17.38360733	17.42110733	0.38
bot14	90	23.22144	9.91754	15.45209540	15.48542874	0.33

A5.4 Moment analysis results for 400 mm (real) column packed with γ-alumina beads (2^{nd} central moments are calculated by Cat. B)

Table A5.19: Moment analysis results (γ-alumina beads experiment) in a 400 mm column with 0.1 ml He tracer pulse, and the 2^{nd} central moment is obtained using **Cat. B**.

N_2(carrier) - He(tracer)	γ-alumina beads (0.1 ml sample loop)					
	Flowrate (cm^3/min)	1^{st} moment, μ_1 (s)	2^{nd} central moment, μ_2' (s^2)	$(\mu_1)_0$ for blank run (Equation (3.59))(s)	$(\mu_1)_0$ for blank run (Equation (3.60))(s)	Injection time, t_0 (s)
bot01	30	104.72323	328.93014	89.76327218	89.86327218	0.20
bot03	40	79.99072	136.26824	67.32245413	67.39745413	0.15
bot06	50	64.02926	74.00700	53.85796331	53.91796331	0.12
bot08	60	55.00931	44.19986	44.88163609	44.93163609	0.10
bot10	70	47.84691	26.97776	38.46997379	38.51283093	0.09
bot13	80	41.19657	20.72130	33.66122707	33.69872707	0.08
bot16	90	38.03590	14.40800	29.92109073	29.95442406	0.07

Table A5.20: Moment analysis results (γ-alumina beads experiment) in a 400 mm column with 0.1 ml N_2 tracer pulse, and the 2^{nd} central moment is obtained using **Cat. B**.

He(carrier) - N_2(tracer)	γ-alumina beads (0.1 ml sample loop)					
	Flowrate (cm^3/min)	1^{st} moment, μ_1 (s)	2^{nd} central moment, μ_2' (s^2)	$(\mu_1)_0$ for blank run (Equation (3.59))(s)	$(\mu_1)_0$ for blank run (Equation (3.60))(s)	Injection time, t_0 (s)
bot01	30	113.70199	351.38436	89.76327218	89.86327218	0.20
bot03	40	84.62016	172.03026	67.32245413	67.39745413	0.15
bot05	50	74.61935	115.76555	53.85796331	53.91796331	0.12
bot07	60	65.78593	54.51066	44.88163609	44.93163609	0.10
bot09	70	55.12268	41.57554	38.46997379	38.51283093	0.09
bot12	80	47.46371	24.56363	33.66122707	33.69872707	0.08
bot14	90	43.07355	18.76922	29.92109073	29.95442406	0.07

Table A5.21: Moment analysis results (γ-alumina beads experiment) in a 400 mm column with 0.25 ml He tracer pulse, and the 2nd central moment is obtained using **Cat. B**.

N_2(carrier) - He(tracer)	γ-alumina beads (0.25 ml sample loop)					
	Flowrate (cm^3/min)	**1st moment, μ_1 (s)**	**2nd central moment, μ_2' (s^2)**	**$(\mu_1)_0$ for blank run (Equation (3.59))(s)**	**$(\mu_1)_0$ for blank run (Equation (3.60))(s)**	**Injection time, t_0 (s)**
bot01	30	105.82143	329.83670	89.76327218	90.01327218	0.50
bot03	40	80.45573	155.39183	67.32245413	67.50095413	0.38
bot06	50	64.34115	79.15176	53.85796331	54.00796331	0.30
bot08	60	54.83164	53.52091	44.88163609	45.00663609	0.25
bot10	70	47.85306	29.06857	38.46997379	38.57711665	0.21
bot13	80	41.16452	24.98300	33.66122707	33.75497707	0.19
bot16	90	37.48024	19.58944	29.92109073	30.00442406	0.17

Table A5.22: Moment analysis results (γ-alumina beads experiment) in a 400 mm column with 0.25 ml N_2 tracer pulse, and the 2nd central moment is obtained using **Cat. B**.

He(carrier) - N_2(tracer)	γ-alumina beads (0.25 ml sample loop)					
	Flowrate (cm^3/min)	**1st moment, μ_1 (s)**	**2nd central moment, μ_2' (s^2)**	**$(\mu_1)_0$ for blank run (Equation (3.59))(s)**	**$(\mu_1)_0$ for blank run (Equation (3.60))(s)**	**Injection time, t_0 (s)**
bot01	30	111.92176	401.41558	89.76327218	90.01327218	0.50
bot03	40	84.18536	147.18904	67.32245413	67.50095413	0.38
bot05	50	74.22703	91.48699	53.85796331	54.00796331	0.30
bot07	60	65.91742	76.20125	44.88163609	45.00663609	0.25
bot09	70	54.93655	33.29065	38.46997379	38.57711665	0.21
bot12	80	48.16616	24.16686	33.66122707	33.75497707	0.19
bot14	90	43.08123	22.41293	29.92109073	30.00442406	0.17

Table A5.23: Moment analysis results (γ-alumina beads experiment) in a 400 mm column with 0.5 ml He tracer pulse, and the 2nd central moment is obtained using **Cat. B**.

N_2(carrier) - He(tracer)	γ-alumina beads (0.5 ml sample loop)					
	Flowrate (cm^3/min)	**1st moment, μ_1 (s)**	**2nd central moment, μ_2' (s^2)**	**$(\mu_1)_0$ for blank run (Equation (3.59))(s)**	**$(\mu_1)_0$ for blank run (Equation (3.60))(s)**	**Injection time, t_0 (s)**
bot01	30	107.36374	405.90452	89.76327218	90.26327218	1.00
bot03	40	80.22380	150.25410	67.32245413	67.69745413	0.75
bot06	50	64.48135	93.34431	53.85796331	54.15796331	0.60
bot08	60	55.13468	55.54956	44.88163609	45.13163609	0.50
bot10	70	48.23150	38.94379	38.46997379	38.68425950	0.43
bot13	80	41.42653	25.29524	33.66122707	33.84872707	0.38
bot16	90	38.03820	20.83433	29.92109073	30.08775739	0.33

Table A5.24: Moment analysis results (γ-alumina beads experiment) in a 400 mm column with 0.5 ml N_2 tracer pulse, and the 2nd central moment is obtained using **Cat. B**.

He(carrier) - N_2(tracer)	γ-alumina beads (0.5 ml sample loop)					
	Flowrate (cm^3/min)	**1st moment, μ_1 (s)**	**2nd central moment, μ_2' (s^2)**	**$(\mu_1)_0$ for blank run (Equation (3.59))(s)**	**$(\mu_1)_0$ for blank run (Equation (3.60))(s)**	**Injection time, t_0 (s)**
bot01	30	113.59566	363.62092	89.76327218	90.26327218	1.00
bot03	40	85.03001	127.15248	67.32245413	67.69745413	0.75
bot05	50	73.99991	102.89521	53.85796331	54.15796331	0.60
bot07	60	65.64624	76.65664	44.88163609	45.13163609	0.50
bot09	70	54.78793	37.80125	38.46997379	38.68425950	0.43
bot12	80	48.13273	27.08626	33.66122707	33.84872707	0.38
bot14	90	42.96398	23.37033	29.92109073	30.08775739	0.33

A5.5 Moment analysis results for 200 mm (real) column packed with γ-alumina beads (2nd central moments are calculated by Cat. B)

Table A5.25: Moment analysis results (γ-alumina beads experiment) in a 200 mm column with 0.1 ml He tracer pulse, and the 2nd central moment is obtained using **Cat. B**.

N_2(carrier) - He(tracer)	γ-alumina beads (0.1 ml sample loop)					
	Flowrate (cm^3/min)	1st moment, μ_1 (s)	2nd central moment, μ_2' (s^2)	$(\mu_1)_0$ for blank run (Equation (3.59))(s)	$(\mu_1)_0$ for blank run (Equation (3.60))(s)	Injection time, t_0 (s)
bot01	30	53.91372	159.29728	46.35628621	46.45628621	0.20
bot03	40	41.42950	69.88848	34.76721466	34.84221466	0.15
bot06	50	33.74820	29.93864	27.81377172	27.87377172	0.12
bot08	60	28.91111	21.73889	23.17814310	23.22814310	0.10
bot10	70	25.44974	9.17028	19.86697980	19.90983695	0.09
bot13	80	21.91116	7.96614	17.38360733	17.42110733	0.08
bot16	90	19.86439	5.82178	15.45209540	15.48542874	0.07

Table A5.26: Moment analysis results (γ-alumina beads experiment) in a 200 mm column with 0.1 ml N_2 tracer pulse, and the 2nd central moment is obtained using **Cat. B**.

He(carrier) - N_2(tracer)	γ-alumina beads (0.1 ml sample loop)					
	Flowrate (cm^3/min)	1st moment, μ_1 (s)	2nd central moment, μ_2' (s^2)	$(\mu_1)_0$ for blank run (Equation (3.59))(s)	$(\mu_1)_0$ for blank run (Equation (3.60))(s)	Injection time, t_0 (s)
bot01	30	59.24971	158.36152	46.35628621	46.45628621	0.20
bot03	40	45.11066	72.73002	34.76721466	34.84221466	0.15
bot05	50	39.72687	45.13587	27.81377172	27.87377172	0.12
bot07	60	35.18555	39.27325	23.17814310	23.22814310	0.10
bot09	70	29.40691	20.41325	19.86697980	19.90983695	0.09
bot12	80	25.86264	13.72554	17.38360733	17.42110733	0.08
bot14	90	23.22486	10.14621	15.45209540	15.48542874	0.07

Table A5.27: Moment analysis results (γ-alumina beads experiment) in a 200 mm column with 0.25 ml He tracer pulse, and the 2nd central moment is obtained using **Cat. B**.

N_2(carrier) - He(tracer)	γ-alumina beads (0.25 ml sample loop)					
	Flowrate (cm^3/min)	**1st moment, μ_1 (s)**	**2nd central moment, μ_2' (s^2)**	**$(\mu_1)_0$ for blank run (Equation (3.59))(s)**	**$(\mu_1)_0$ for blank run (Equation (3.60))(s)**	**Injection time, t_0 (s)**
bot01	30	54.68801	140.40800	46.35628621	46.45628621	0.50
bot03	40	41.59702	63.42976	34.76721466	34.84221466	0.38
bot06	50	33.97254	32.98712	27.81377172	27.87377172	0.30
bot08	60	29.05359	22.46901	23.17814310	23.22814310	0.25
bot10	70	25.54571	13.85511	19.86697980	19.90983695	0.21
bot13	80	21.96249	8.83004	17.38360733	17.42110733	0.19
bot16	90	20.10529	6.72212	15.45209540	15.48542874	0.17

Table A5.28: Moment analysis results (γ-alumina beads experiment) in a 200 mm column with 0.25 ml N_2 tracer pulse, and the 2nd central moment is obtained using **Cat. B**.

He(carrier) - N_2(tracer)	γ-alumina beads (0.25 ml sample loop)					
	Flowrate (cm^3/min)	**1st moment, μ_1 (s)**	**2nd central moment, μ_2' (s^2)**	**$(\mu_1)_0$ for blank run (Equation (3.59))(s)**	**$(\mu_1)_0$ for blank run (Equation (3.60))(s)**	**Injection time, t_0 (s)**
bot01	30	59.77943	174.09917	46.35628621	46.45628621	0.50
bot03	40	45.09890	67.41435	34.76721466	34.84221466	0.38
bot05	50	39.86844	40.99351	27.81377172	27.87377172	0.30
bot07	60	35.20971	30.88613	23.17814310	23.22814310	0.25
bot09	70	29.43729	18.90405	19.86697980	19.90983695	0.21
bot12	80	25.91928	14.93577	17.38360733	17.42110733	0.19
bot14	90	23.37371	11.15961	15.45209540	15.48542874	0.17

Table A5.29: Moment analysis results (γ-alumina beads experiment) in a 200 mm column with 0.5 ml He tracer pulse, and the 2nd central moment is obtained using **Cat. B**.

N_2(carrier) - He(tracer)	γ-alumina beads (0.5 ml sample loop)					
	Flowrate (cm^3/min)	**1st moment, μ_1 (s)**	**2nd central moment, μ_2' (s^2)**	**$(\mu_1)_0$ for blank run (Equation (3.59))(s)**	**$(\mu_1)_0$ for blank run (Equation (3.60))(s)**	**Injection time, t_0 (s)**
bot01	30	56.22629	148.45984	46.35628621	46.45628621	1.00
bot03	40	41.58749	70.83306	34.76721466	34.84221466	0.75
bot06	50	34.22596	34.40702	27.81377172	27.87377172	0.60
bot08	60	29.25567	22.73512	23.17814310	23.22814310	0.50
bot10	70	25.63625	15.36959	19.86697980	19.90983695	0.43
bot13	80	21.96088	10.75919	17.38360733	17.42110733	0.38
bot16	90	20.32728	8.70305	15.45209540	15.48542874	0.33

Table A5.30: Moment analysis results (γ-alumina beads experiment) in a 200 mm column with 0.5 ml N_2 tracer pulse, and the 2nd central moment is obtained using **Cat. B**.

He(carrier) - N_2(tracer)	γ-alumina beads (0.5 ml sample loop)					
	Flowrate (cm^3/min)	**1st moment, μ_1 (s)**	**2nd central moment, μ_2' (s^2)**	**$(\mu_1)_0$ for blank run (Equation (3.59))(s)**	**$(\mu_1)_0$ for blank run (Equation (3.60))(s)**	**Injection time, t_0 (s)**
bot01	30	59.47346	151.50987	46.35628621	46.45628621	1.00
bot03	40	45.07293	63.91676	34.76721466	34.84221466	0.75
bot05	50	39.56584	49.01703	27.81377172	27.87377172	0.60
bot07	60	34.88589	33.97448	23.17814310	23.22814310	0.50
bot09	70	29.29810	25.11356	19.86697980	19.90983695	0.43
bot12	80	25.91209	15.82181	17.38360733	17.42110733	0.38
bot14	90	23.22144	7.65070	15.45209540	15.48542874	0.33

A5.6 Moment analysis results for a fictitious bed; 200 mm, packed with γ-alumina beads (2nd central moments are calculated by Cat. A)

According to Equations (3.57) and (3.58), the results for the moments of a fictitious bed (200 mm) packed with γ-alumina beads, were calculated by taking the difference between the moments of the 400 mm (real) column and the moments of the 200 mm (real) column.

Table A5.31: Moment analysis results (γ-alumina beads experiment) in a 200 mm **fictitious bed** with 0.1 ml He tracer pulse, and the 2nd central moment is obtained using **Cat. A**.

N_2(carrier) - He(tracer)	γ-alumina beads (0.1 ml sample loop)					
	Flowrate (cm^3/min)	1st moment, μ_1 (s)	2nd central moment, μ_2' (s^2)	$(\mu_1)_0$ for blank run (Equation (3.59))(s)	$(\mu_1)_0$ for blank run (Equation (3.60))(s)	Injection time, t_0 (s)
bot01	30	50.80951	164.99063	46.35628621	46.45628621	0.20
bot03	40	38.56122	74.25405	34.76721466	34.84221466	0.15
bot06	50	30.28106	40.11298	27.81377172	27.87377172	0.12
bot08	60	26.09820	24.97810	23.17814310	23.22814310	0.10
bot10	70	22.39717	17.39613	19.86697980	19.90983695	0.09
bot13	80	19.28541	10.16124	17.38360733	17.42110733	0.08
bot16	90	18.17151	8.67799	15.45209540	15.48542874	0.07

Table A5.32: Moment analysis results (γ-alumina beads experiment) in a 200 mm **fictitious bed** with 0.1 ml N_2 tracer pulse, and the 2nd central moment is obtained using **Cat. A**.

He(carrier) - N_2(tracer)	γ-alumina beads (0.1 ml sample loop)					
	Flowrate (cm^3/min)	1st moment, μ_1 (s)	2nd central moment, μ_2' (s^2)	$(\mu_1)_0$ for blank run (Equation (3.59))(s)	$(\mu_1)_0$ for blank run (Equation (3.60))(s)	Injection time, t_0 (s)
bot01	30	54.45228	387.70086	46.35628621	46.45628621	0.20
bot03	40	39.50950	75.48421	34.76721466	34.84221466	0.15
bot05	50	34.89248	50.02269	27.81377172	27.87377172	0.12
bot07	60	30.60038	33.23300	23.17814310	23.22814310	0.10
bot09	70	25.71577	20.09637	19.86697980	19.90983695	0.09
bot12	80	21.60107	12.53238	17.38360733	17.42110733	0.08
bot14	90	19.84869	9.40145	15.45209540	15.48542874	0.07

Table A5.33: Moment analysis results (γ-alumina beads experiment) in a 200 mm **fictitious bed** with 0.25 ml He tracer pulse, and the 2nd central moment is obtained using **Cat. A**.

N_2(carrier) - He(tracer)	**γ-alumina beads (0.25 ml sample loop)**					
	Flowrate (cm^3/min)	**1st moment, μ_1 (s)**	**2nd central moment, μ_2' (s^2)**	**$(\mu_1)_0$ for blank run (Equation (3.59))(s)**	**$(\mu_1)_0$ for blank run (Equation (3.60))(s)**	**Injection time, t_0 (s)**
bot01	30	51.13342	177.83243	46.35628621	46.45628621	0.50
bot03	40	38.85871	77.66925	34.76721466	34.84221466	0.38
bot06	50	30.36861	40.23704	27.81377172	27.87377172	0.30
bot08	60	25.77805	24.96797	23.17814310	23.22814310	0.25
bot10	70	22.30735	17.07044	19.86697980	19.90983695	0.21
bot13	80	19.20203	11.42869	17.38360733	17.42110733	0.19
bot16	90	17.37495	8.79121	15.45209540	15.48542874	0.17

Table A5.34: Moment analysis results (γ-alumina beads experiment) in a 200 mm **fictitious bed** with 0.25 ml N_2 tracer pulse, and the 2nd central moment is obtained using **Cat. A**.

He(carrier) - N_2(tracer)	**γ-alumina beads (0.25 ml sample loop)**					
	Flowrate (cm^3/min)	**1st moment, μ_1 (s)**	**2nd central moment, μ_2' (s^2)**	**$(\mu_1)_0$ for blank run (Equation (3.59))(s)**	**$(\mu_1)_0$ for blank run (Equation (3.60))(s)**	**Injection time, t_0 (s)**
bot01	30	52.14233	197.01643	46.35628621	46.45628621	0.50
bot03	40	39.08646	70.88609	34.76721466	34.84221466	0.38
bot05	50	34.35859	48.67002	27.81377172	27.87377172	0.30
bot07	60	30.70771	34.68460	23.17814310	23.22814310	0.25
bot09	70	25.49926	19.79095	19.86697980	19.90983695	0.21
bot12	80	22.24688	13.12739	17.38360733	17.42110733	0.19
bot14	90	19.70752	9.72244	15.45209540	15.48542874	0.17

Table A5.35: Moment analysis results (γ-alumina beads experiment) in a 200 mm **fictitious bed** with 0.5 ml He tracer pulse, and the 2nd central moment is obtained using **Cat. A**.

N_2(carrier) - He(tracer)	γ-alumina beads (0.5 ml sample loop)					
	Flowrate (cm^3/min)	1st moment, μ_1 (s)	2nd central moment, μ_2' (s^2)	$(\mu_1)_0$ for blank run (Equation (3.59))(s)	$(\mu_1)_0$ for blank run (Equation (3.60))(s)	Injection time, t_0 (s)
bot01	30	51.13745	183.34530	46.35628621	46.45628621	1.00
bot03	40	38.63631	80.42477	34.76721466	34.84221466	0.75
bot06	50	30.25539	42.13560	27.81377172	27.87377172	0.60
bot08	60	25.87901	26.79279	23.17814310	23.22814310	0.50
bot10	70	22.59525	18.43737	19.86697980	19.90983695	0.43
bot13	80	19.46565	12.17799	17.38360733	17.42110733	0.38
bot16	90	17.71092	9.54444	15.45209540	15.48542874	0.33

Table A5.36: Moment analysis results (γ-alumina beads experiment) in a 200 mm **fictitious bed** with 0.5 ml N_2 tracer pulse, and the 2nd central moment is obtained using **Cat. A**.

He(carrier) - N_2(tracer)	γ-alumina beads (0.5 ml sample loop)					
	Flowrate (cm^3/min)	1st moment, μ_1 (s)	2nd central moment, μ_2' (s^2)	$(\mu_1)_0$ for blank run (Equation (3.59))(s)	$(\mu_1)_0$ for blank run (Equation (3.60))(s)	Injection time, t_0 (s)
bot01	30	54.12220	188.56827	46.35628621	46.45628621	1.00
bot03	40	39.95708	74.04508	34.76721466	34.84221466	0.75
bot05	50	34.43407	48.40435	27.81377172	27.87377172	0.60
bot07	60	30.76035	34.70391	23.17814310	23.22814310	0.50
bot09	70	25.48983	20.05899	19.86697980	19.90983695	0.43
bot12	80	22.22064	13.83348	17.38360733	17.42110733	0.38
bot14	90	19.74254	9.72686	15.45209540	15.48542874	0.33

A5.7 Moment analysis results for a fictitious bed; 200 mm, packed with γ-alumina beads (2nd central moments are calculated by Cat. B)

Table A5.37: Moment analysis results (γ-alumina beads experiment) in a 200 mm **fictitious bed** with 0.1 ml He tracer pulse, and the 2nd central moment is obtained using **Cat. B**.

N_2(carrier) - He(tracer)	γ-alumina beads (0.1 ml sample loop)					
	Flowrate (cm^3/min)	1st moment, μ_1 (s)	2nd central moment, μ_2' (s^2)	$(\mu_1)_0$ for blank run (Equation (3.59))(s)	$(\mu_1)_0$ for blank run (Equation (3.60))(s)	Injection time, t_0 (s)
bot01	30	50.80951	169.63286	46.35628621	46.45628621	0.20
bot03	40	38.56122	66.37976	34.76721466	34.84221466	0.15
bot06	50	30.28106	44.06836	27.81377172	27.87377172	0.12
bot08	60	26.09820	22.46097	23.17814310	23.22814310	0.10
bot10	70	22.39717	17.80748	19.86697980	19.90983695	0.09
bot13	80	19.28541	12.75516	17.38360733	17.42110733	0.08
bot16	90	18.17151	8.58622	15.45209540	15.48542874	0.07

Table A5.38: Moment analysis results (γ-alumina beads experiment) in a 200 mm **fictitious bed** with 0.1 ml N_2 tracer pulse, and the 2nd central moment is obtained using **Cat. B**.

He(carrier) - N_2(tracer)	γ-alumina beads (0.1 ml sample loop)					
	Flowrate (cm^3/min)	1st moment, μ_1 (s)	2nd central moment, μ_2' (s^2)	$(\mu_1)_0$ for blank run (Equation (3.59))(s)	$(\mu_1)_0$ for blank run (Equation (3.60))(s)	Injection time, t_0 (s)
bot01	30	54.45228	193.02284	46.35628621	46.45628621	0.20
bot03	40	39.50950	99.30024	34.76721466	34.84221466	0.15
bot05	50	34.89248	70.62968	27.81377172	27.87377172	0.12
bot07	60	30.44928	27.84387	23.17814310	23.22814310	0.10
bot09	70	25.71577	21.16229	19.86697980	19.90983695	0.09
bot12	80	21.60107	10.83809	17.38360733	17.42110733	0.08
bot14	90	19.84869	8.62301	15.45209540	15.48542874	0.07

Table A5.39: Moment analysis results (γ-alumina beads experiment) in a 200 mm **fictitious bed** with 0.25 ml He tracer pulse, and the 2nd central moment is obtained using **Cat. B**.

N_2(carrier) - He(tracer)	γ-alumina beads (0.25 ml sample loop)					
	Flowrate (cm^3/min)	1st moment, μ_1 (s)	2nd central moment, μ_2' (s^2)	$(\mu_1)_0$ for blank run (Equation (3.59))(s)	$(\mu_1)_0$ for blank run (Equation (3.60))(s)	Injection time, t_0 (s)
bot01	30	51.13342	189.42870	46.35628621	46.45628621	0.50
bot03	40	38.85871	91.96207	34.76721466	34.84221466	0.38
bot06	50	30.36364	46.61890	27.81377172	27.87377172	0.30
bot08	60	25.77805	31.05190	23.17814310	23.22814310	0.25
bot10	70	22.30735	15.21346	19.86697980	19.90983695	0.21
bot13	80	19.20203	16.15296	17.38360733	17.42110733	0.19
bot16	90	17.37495	12.86732	15.45209540	15.48542874	0.17

Table A5.40: Moment analysis results (γ-alumina beads experiment) in a 200 mm **fictitious bed** with 0.25 ml N_2 tracer pulse, and the 2nd central moment is obtained using **Cat. B**.

He(carrier) - N_2(tracer)	γ-alumina beads (0.25 ml sample loop)					
	Flowrate (cm^3/min)	1st moment, μ_1 (s)	2nd central moment, μ_2' (s^2)	$(\mu_1)_0$ for blank run (Equation (3.59))(s)	$(\mu_1)_0$ for blank run (Equation (3.60))(s)	Injection time, t_0 (s)
bot01	30	52.14233	227.31641	46.35628621	46.45628621	0.50
bot03	40	39.08646	79.77469	34.76721466	34.84221466	0.38
bot05	50	34.35859	50.49348	27.81377172	27.87377172	0.30
bot07	60	30.70771	45.31512	23.17814310	23.22814310	0.25
bot09	70	25.49926	14.38660	19.86697980	19.90983695	0.21
bot12	80	22.13461	12.37308	17.38360733	17.42110733	0.19
bot14	90	19.70752	11.25332	15.45209540	15.48542874	0.17

Table A5.41: Moment analysis results (γ-alumina beads experiment) in a 200 mm **fictitious bed** with 0.5 ml He tracer pulse, and the 2nd central moment is obtained using **Cat. B**.

N_2(carrier) - He(tracer)	γ-alumina beads (0.5 ml sample loop)					
	Flowrate (cm^3/min)	1st moment, μ_1 (s)	2nd central moment, μ_2' (s^2)	$(\mu_1)_0$ for blank run (Equation (3.59))(s)	$(\mu_1)_0$ for blank run (Equation (3.60))(s)	Injection time, t_0 (s)
bot01	30	51.13745	257.44468	46.35628621	46.45628621	1.00
bot03	40	38.63631	79.42104	34.76721466	34.84221466	0.75
bot06	50	30.25539	58.93729	27.81377172	27.87377172	0.60
bot08	60	25.87901	32.81444	23.17814310	23.22814310	0.50
bot10	70	22.59525	23.57420	19.86697980	19.90983695	0.43
bot13	80	19.46565	14.53605	17.38360733	17.42110733	0.38
bot16	90	17.71092	12.13128	15.45209540	15.48542874	0.33

Table A5.42: Moment analysis results (γ-alumina beads experiment) in a 200 mm **fictitious bed** with 0.5 ml N_2 tracer pulse, and the 2nd central moment is obtained using **Cat. B**.

He(carrier) - N_2(tracer)	γ-alumina beads (0.5 ml sample loop)					
	Flowrate (cm^3/min)	1st moment, μ_1 (s)	2nd central moment, μ_2' (s^2)	$(\mu_1)_0$ for blank run (Equation (3.59))(s)	$(\mu_1)_0$ for blank run (Equation (3.60))(s)	Injection time, t_0 (s)
bot01	30	54.12220	212.11105	46.35628621	46.45628621	1.00
bot03	40	39.95708	63.23572	34.76721466	34.84221466	0.75
bot05	50	34.43407	53.87818	27.81377172	27.87377172	0.60
bot07	60	30.76035	42.68216	23.17814310	23.22814310	0.50
bot09	70	25.35626	17.15087	19.86697980	19.90983695	0.43
bot12	80	22.09955	15.03071	17.38360733	17.42110733	0.38
bot14	90	19.84585	13.45988	15.45209540	15.48542874	0.33

Appendix 6: <u>Case 1:</u> Theoretical moment expressions and resistance parameters for non-adsorbable tracer (Baiker *et al*., 1982; Tang *et al*., 1987)

From **Column Model** and **Particle Model 1**, assuming that when k_{ads} = 0 and K_a = 0, the theoretical moment expressions and resistance parameters shown in Baiker *et al*. (1982) and Tang *et al*. (1987) (Equations (A6.1) to (A6.6), were deduced from the material balance of tracer gas in the column free space (Equation (3.68)), and the material balance of tracer gas in the porous adsorbent particles (Equation (3.75)) (Suzuki and Smith, 1971).

The Kubń and Kučera (Kubń, 1965; Kučera, 1965) model in Equations (3.68) and (3.75), was initially used to describe the dispersion of an adsorbable tracer gas pulse in a packed-bed of porous adsorbent carried by an inert gas. It was shown later that the model can also be applied for the evaluation of gas chromatographic pulse response measurements with a non-adsorbable tracer (Baiker *et al*., 1982). For a Dirac input signal of a **non-adsorbable** tracer, the first absolute moment μ_1 and second central moment $\mu_2^{'}$ of the effluent peak from the bed (Baiker *et al*., 1982; Tang *et al*., 1987) are:

$$\mu_1 = \frac{L}{u_i}(1+\xi_0) \tag{A6.1}$$

$$\mu_2^{'} = \frac{2L}{u_i}\left(\xi_1 + \frac{D_{ax}}{\varepsilon_b}(1+\xi_0)^2\left(\frac{1}{u_i^2}\right)\right) \tag{A6.2}$$

$$\xi_0 = \frac{(1-\varepsilon_b)\varepsilon}{\varepsilon_b} \tag{A6.3}$$

$$\xi_1 = \xi_i + \xi_e \tag{A6.4}$$

$$\xi_e = \frac{(1-\varepsilon_b)}{\varepsilon_b}\frac{\varepsilon^2 R^2}{a(a+2)}\frac{(a+2)}{k_f R} \tag{A6.5}$$

$$\xi_i = \frac{(1-\varepsilon_b)}{\varepsilon_b}\frac{\varepsilon^2 R^2}{a(a+2)}\frac{1}{D_{eff}} \tag{A6.6}$$

Where u_i is the interstitial carrier gas velocity and it is equal to superficial velocity, u_0 divided by bed porosity, ε_b.

Parameters ξ_e and ξ_i represent the contribution of the external mass transfer resistance and the intraparticle diffusion resistance respectively. k_f is the external mass transfer coefficient and D_{eff} is the intraparticle diffusion coefficient.

For the evaluation of effective diffusivity, D_{eff}, it was assumed that external mass transfer limitation is negligible. With this assumption ($\xi_e = 0$), the axial intercept ξ_1 in Equation (A6.4) only comprises the intraparticle diffusion resistance ξ_i, and D_{eff} is obtained from the intercept by plotting $\mu_2'/(2L/u_i)$ as a function of $1/u_i^2$ (Baiker *et al*., 1982; Tang *et al*., 1987):

$$\frac{\mu_2'}{2L/u_i} = \xi_i + \frac{D_{ax}}{\varepsilon_b}\left(1+\frac{(1-\varepsilon_b)\varepsilon}{\varepsilon_b}\right)^2\left(\frac{1}{u_i^2}\right) \qquad \text{(A6.7)}$$

where:

$$\xi_1 = \xi_i = \frac{(1-\varepsilon_b)}{\varepsilon_b}\frac{\varepsilon^2 R^2}{a(a+2)}\frac{1}{D_{eff}} \qquad \text{(A6.8)}$$

In this thesis, the experimental first moments and second central moments (μ_1 and μ_2') for the 'real' columns (400 and 200 mm), were obtained from moment analysis using experimental response curves at carrier gas flowrates in the range: 30 – 90 cm^3/min. Then, the moment differences (i.e. the moment results for the fictitious bed: 200 mm), were used for D_{eff} calculation.

References

Baiker, A., New, M. & Richarz, W., 1982. Determination of intraparticle diffusion coefficients in catalyst pellets: a comparative study of measuring methods. *Chemical Engineering Science,* 37**,** 643-656.

Kubń, M., 1965. Beitrag zur theorie der chromatographie. *Collection of Czechoslovak Chemical Communications* 30**,** 1104-1118.

Kučera, E., 1965. Contribution of the theory of chromatography: Linear non-equilibrium elution chromatography. *Journal of Chromatography* 19**,** 23-248.

Suzuki, M. & Smith, J., 1971. Kinetic studies by chromatography. *Chemical Engineering Science,* 26**,** 221-235.

Tang, G.H.Y., Trimm, D.L. & Wainwright, M.S., 1987. Effective diffusivity in cylindrical catalyst pellets. *Chemical engineering in Australia,* 12**,** 9-12.

Appendix 7: Case 2: Theoretical moment expressions and resistance parameters for adsorbable tracer with no reaction (Guangsuo *et al*., 2000)

In Schneider and Smith (1968) and Guangsuo *et al*. (2000), theoretical moment expressions and resistance parameters (from Equations (A7.1) to (A7.7)) were derived from intraparticle material balance of tracer gas *A* (Equation (3.85)) and material balance of tracer gas *A* in the column free space (Equation (3.68)), and these are summarised as follows:

$$\mu_1' = \frac{L}{u_i}(1+\xi_0) + \frac{t_0}{2} + \mu_{1d}' \tag{A7.1}$$

$$\mu_2 = \frac{2L}{u_i}\left[\xi_1 + \frac{(D_{ax}/\varepsilon)(1+\xi_0)^2}{u_i^2}\right] + \frac{t_0^2}{12} + \mu_{2d} \tag{A7.2}$$

where $t_0/2$ and $t_0^2/12$ are for a square-wave pulse (Schneider, 1986), hence, for a Dirac pulse used in this thesis, these terms are equal to zero. The resistance parameters are:

$$\xi_0 = \frac{1-\varepsilon_b}{\varepsilon_b}\varepsilon\left(1+\frac{\rho_P K_A}{\varepsilon}\right) \tag{A7.3}$$

$$\xi_1 = \xi_a + \xi_i + \xi_e \tag{A7.4}$$

$$\xi_a = \left(\frac{1-\varepsilon_b}{\varepsilon_b}\varepsilon\right)\frac{\rho_P K_A^2}{\varepsilon k_{ads}} \tag{A7.5}$$

$$\xi_i = \left(\frac{1-\varepsilon_b}{\varepsilon_b}\varepsilon\right)\frac{R^2\varepsilon}{a(a+2)}\left(1+\frac{\rho_P K_A}{\varepsilon}\right)^2\frac{1}{D_{eff}} \tag{A7.6}$$

$$\xi_e = \left(\frac{1-\varepsilon_b}{\varepsilon_b}\varepsilon\right)\frac{R^2\varepsilon}{a(a+2)}\left(1+\frac{\rho_P K_A}{\varepsilon}\right)^2\frac{(a+2)}{k_f R} \tag{A7.7}$$

where ξ_a, ξ_i and ξ_e are the adsorption resistance, intraparticle diffusion resistance and external mass transfer resistance. For the adsorption resistance ξ_a shown in Equation (A7.5), there should be a square sign on the adsorption equilibrium constant i.e. K_A^2 in Guangsuo *et al*. (2000), as this was confirmed in Schneider and Smith (1968).

For an inert run, when the adsorption equilibrium constant $K_A = 0$, Equation (A7.3) becomes:

$$\xi_0 = \frac{1-\varepsilon_b}{\varepsilon_b}\varepsilon \tag{A7.8}$$

Then substituting Equation (A7.8) into Equation (A7.1) yields:

$$\left(\mu_1^{'}\right)_{inert} = \frac{L}{u_i}\left[1+\frac{(1-\varepsilon_b)}{\varepsilon_b}\varepsilon\right]+\frac{t_0}{2}+\mu_{1d}^{'} \tag{A7.9}$$

For an adsorption run, the adsorption equilibrium constant $K_A \neq 0$, Equation (A7.2) becomes:

$$\left(\mu_1^{'}\right)_{ads} = \frac{L}{u_i}\left[1+\frac{(1-\varepsilon_b)\varepsilon}{\varepsilon_b}\left(1+\frac{(1-\varepsilon)K_A}{\varepsilon}\right)\right]+\frac{t_0}{2}+\mu_{1d}^{'} \tag{A7.10}$$

The adsorption equilibrium constant, K_A, is evaluated from the linear regression plot of the difference in first moment $\Delta\mu_1^{'}$ as a function of velocity u:

$$\Delta\mu_1^{'} = \left(\mu_1^{'}\right)_{ads} - \left(\mu_1^{'}\right)_{inert} = \frac{L}{u_i}\frac{\left(1-\varepsilon_b\right)}{\varepsilon_b}\rho_p K_A \tag{A7.11}$$

$(\mu_1^{'})_{\text{ads}}$ and $(\mu_1^{'})_{\text{ads}}$ in Equation (A7.11) are: for example, for calculating adsorption equilibrium constant K_A for He(tracer) – N_2 (carrier) system, $(\mu_1^{'})_{\text{ads}}$ in this case will be the first moment for helium calculated from the experimental response curves, $(\mu_1^{'})_{\text{inert}}$ will be the first moment for nitrogen. Then vice versa for calculating K_A for N_2 (tracer) – He (carrier) system. The experimental first moments used for K_A calculation are obtained from moment analysis from experimental response curves at carrier gas flowrates in the range: 30 – 90 cm^3/min.

As mentioned in Guangsuo *et al*. (2000), the adsorption resistance term ξ_a is negligible because of the discussions in Schneider and Smith (1968), which means that the whole process is diffusion limited. In other words, according to Suzuki and Smith (1971), adsorption resistance is only important when the whole process is reaction limited (i.e. Figure 1.3 in Chapter 1, for rapid mass transfer or low diffusion time, when the surface reaction rate constant k_r is not zero), which is not applicable to this thesis because non-reacting gases are used.

In Guangsuo *et al*. (2000), the second central moment $(\mu_2^{'})_{ads}$ for adsorption run was corrected with a second central moment obtained with the packed-bed replaced by a short blank tube, known as $(\mu_2^{'})_{blank}$:

$$\left(\mu_2\right)_{blank} = \frac{t_0^2}{12}+\mu_{2d} \tag{A7.12}$$

where $(\mu_2)_{\text{blank}}$ accounts for the unnecessary dispersions and back mixing in the empty space of the fitting and lines, and $\mu_{2\text{d}}$ is the second central moment for the 'dead' volume.

The short blank tube experiment was not performed in this thesis because that convolution theorem was applied for two columns with different lengths, and the moments results of the fictitious bed (without column end effects) were used (i.e. the first moments and second central moments difference between the long and short column, see Chapter 3 Section 3.7.3).

Therefore, the second central moment expression $\mu_2^{'}$ from Guangsuo *et al*. (2000) is (subtracting Equation (A7.12) from Equation (A7.2)):

$$\frac{\mu_2^{'}}{2L/u_i} = \xi_i + \frac{(D_{ax}/\varepsilon_b)\left(1+\xi_0\right)^2}{u_i^2} \tag{A7.13}$$

D_{eff} is obtained from the intercept by the linearization method. Besides, Equation (A7.13) can be rewritten as:

$$\frac{\mu_2^{'}}{2L/u_0} = \varepsilon_b\xi_i + \frac{\varepsilon_b^2 D_{ax}\left(1+\xi_0\right)^2}{u_0^2} \tag{A7.14}$$

In this thesis, the experimental second central moments, $\mu_2^{'}$ (and first moment, μ_1), for the 'real' columns (400 and 200 mm), were obtained from moment analysis from experimental response curves at carrier gas flowrates range: 30 – 90 cm^3/min. Then, the moment differences (i.e. the moment results for the fictitious bed: 200 mm), were used for D_{eff} calculation.

References

Guangsuo, Y., Jianguo, Y. & Zunhong, Y., 2000. The measurement of effective diffusivity for sulfur-tolerant methanation catalyst. *Chemical Engineering Journal,* 78**,** 141-146.

Schneider, P. & Smith, J., 1968. Adsorption rate constants from chromatography. *AIChE Journal,* 14**,** 762-771.

Schneider, P., 1986. Determination of effective diffusion coefficients for porous packings with an impermeable centre from peak moments. *Chemical Engineering Science,* 41**,** 1759-1764.

Appendix 8: Case 4: Theoretical moment expressions and resistance parameters for adsorbable tracer with no reaction (Armatas *et al*., 2005)

Armatas *et al*. (2005) adapted the moment expressions and resistance parameters from Do (1998). Comparing this with Case 1, Case 2 and Case 5, the general material balance (tracer gas in column free space) and the intraparticle material balance are quite different from the material balance equations derived in the Kubń and Kučera model. These differences are explained as follows.

According to Figure 3.2, the mass balance equation describing the concentration distribution along the column accounts for the rate of hold-up in the column (accumulation), the axial dispersion, the convection term and the rate of mass transfer into the particles is (Do, 1998):

$$\underset{\text{axial dispersion term}}{D_{ax}\frac{\partial^2 C}{\partial x^2}} - \underset{\text{convection term}}{\frac{\partial}{\partial x}(u_0 C)} - \underset{\text{mass transfer into the partcle}}{\varphi \times J\big|_R} = \underset{\text{accumulation}}{\varepsilon_b \frac{\partial C}{\partial t}} \tag{A8.1}$$

where:
- u_0 is the superficial carrier gas velocity, m s^{-1};
- $J|_R$ is the mass transfer rate into the particle per unit interfacial surface area, mol m^{-2} s^{-1};
- φ is the interfacial area per unit bed volume, m^{-1}.

Superficial carrier gas velocity, u_0, is equal to the interstitial carrier gas velocity, u_i, multiplied by bed porosity, ε_b.

The interfacial area per unit bed volume for a spherical particle with radius R is (Do, 1998):

$$\varphi = \frac{3(1-\varepsilon_b)}{R} \tag{A8.2}$$

The boundary conditions are:

$$x = 0; \quad C = C_0(t) \tag{A8.3}$$

$$x = L; \quad \frac{\partial C}{\partial x} = 0 \tag{A8.4}$$

$$x = 0; \quad D_{ax}\ \frac{\partial C}{\partial x} = u_0 \left(C - C_0(t)\right) \tag{A8.5}$$

From Fick's law of diffusion, the flux into the particle $J|_R$ in Equation (A8.1) takes the form (in this case, the concentration of tracer gas A in the porous structure of particle is higher than the concentration in the bulk phase, hence the negative sign becomes positive):

$$J\big|_R = \varepsilon D_p \left.\frac{\partial C_s}{\partial r}\right|_R \tag{A8.6}$$

where D_p is the pore diffusivity and C_s is the concentration of tracer in the porous particle. Hence, Equation (A8.1) becomes:

$$D_{ax}\frac{\partial^2 C}{\partial x^2} - u_0\frac{\partial C}{\partial x} - \varepsilon_b\frac{\partial C}{\partial t} - \frac{a(1-\varepsilon_b)\varepsilon}{R}D_p\frac{\partial C_s}{\partial r} = 0 \tag{A8.7}$$

In Do (1998), the pore diffusivity D_p is related to effective diffusivity, D_{eff}, as:

$$D_p = \frac{D_e}{\varepsilon} \tag{A8.8}$$

Therefore, Equation (A8.7) becomes:

$$\frac{D_{ax}}{\varepsilon_b}\frac{\partial^2 C}{\partial x^2} - \frac{u_0}{\varepsilon_b}\frac{\partial C}{\partial x} - \frac{\partial C}{\partial t} - \frac{3}{R}\frac{(1-\varepsilon_b)}{\varepsilon_b}D_e\frac{\partial C_s}{\partial r} = 0 \tag{A8.9}$$

Hence, Equation (A8.9) is the same as Equation (3.68), and the material balance of tracer in the column free space shown in Do (1998) is the same as Schneider and Smith (1968).

According to Do (1998), for pore diffusion with linear adsorption kinetics, the material balance equation describing the tracer concentration within the particle has the following form (Do, 1998):

$$\frac{\varepsilon D_p}{r^2}\frac{\partial}{\partial r}\left(r^2\frac{\partial C_s}{\partial r}\right) - \varepsilon\frac{\partial C_s}{\partial t} - (1-\varepsilon)\frac{\partial C_\mu}{\partial t} = 0 \tag{A8.10}$$

Equation (A8.10) can be rewritten as:

$$D_e\left(\frac{\partial^2 C_s}{\partial r^2} + \frac{2}{r}\frac{\partial C_s}{\partial r}\right) - \varepsilon\frac{\partial C_s}{\partial t} - (1-\varepsilon)\frac{\partial C_\mu}{\partial t} = 0 \tag{A8.11}$$

For a sphere, the shape factor $a = 3$. Hence, substitutnig this into Equation (A8.11) yields:

$$D_e\left(\frac{\partial^2 C_s}{\partial r^2} + \frac{(a-1)}{r}\frac{\partial C_s}{\partial r}\right) - \varepsilon\frac{\partial C_s}{\partial t} - (1-\varepsilon)\frac{\partial C_\mu}{\partial t} = 0 \tag{A8.12}$$

From the intraparticle material balance of tracer gas *A* in Equation (A8.12), Do (1998) has interpreted that the adsorbed tracer concentration profile C_μ is closely correlated to the non-porous adsorbent surface, $(1 - \varepsilon)$, because of the units that defined (e.g. the units for C_μ: mol cm^{-3}_{solid}; and the units for $(1 - \varepsilon)$ are: cm^{-3}_{solid} / $cm^{-3}_{particle}$. For details, see Chapter 3 Section 3.8.4).

In Particle Model 1 (Equations (3.75) and (3.76)), the consumption term (dn_A/dt) is correlated with the particle porosity, ε, because a dimensionless adsorption equilibrium constant, K_a is used (Suzuki and Smith, 1971).

In Particle Model 2, the consumption term dw/dt is correlated with the apparent density of the adsorbent, ρ_p, because the adsorption equilibrium constant, K_A for this model has unit: $cm^3\ g^{-1}$. (i.e. apparent density of the adsorbent particles, ρ_p, is the mass of adsorbent over the total volume of the adsorbent including the pore voids).

By applying the method of Laplace transforms, the solution for the exit concentration $\bar{C}(L, s)$ in the Laplace domain is obtained. From Equation (3.47), the theoretical moment expressions are (Do, 1998):

$$\mu_1 = \frac{L\varepsilon_b}{u_0}(1+\xi_0) + \frac{t_0}{2} \tag{A8.13}$$

$$\mu_2^{'} = \frac{2L\varepsilon_b}{u_0}(\xi_d + \xi_f + \xi_M) + \frac{t_0^2}{12} \tag{A8.14}$$

The parameters ξ_0, ξ_d, ξ_f and ξ_M are defined as:

$$\xi_0 = \frac{(1-\varepsilon_b)\varepsilon}{\varepsilon_b}\left(1+\frac{(1-\varepsilon)K_H}{\varepsilon}\right) \tag{A8.15}$$

$$\xi_d = \frac{D_{ax}}{\varepsilon_b}(1+\xi_0)^2\left(\frac{\varepsilon_b}{u_0}\right)^2 \tag{A8.16}$$

$$\xi_f = \frac{(1-\varepsilon_b)}{\varepsilon_b}\left(1+\frac{(1-\varepsilon)K_H}{\varepsilon}\right)^2 \frac{R\varepsilon^2}{ak_f} \tag{A8.17}$$

$$\xi_M = \frac{(1-\varepsilon_b)}{\varepsilon_b}\left(1+\frac{(1-\varepsilon)K_H}{\varepsilon}\right)^2 \frac{R^2\varepsilon^2}{a(a+2)D_{eff}} \tag{A8.18}$$

D_{eff} is determined from the second central moment $\mu_2^{'}$. Hence rearranging Equation (A8.14) into the following form (Do, 1998):

$$\frac{\left(\mu_2^{'} - t_0^2/12\right)}{2\left(\frac{L}{u_0/\varepsilon_b}\right)} = \xi_f + \xi_M + \left(\frac{D_{ax}}{\varepsilon_b}\right)(1+\xi_0)^2\left(\frac{\varepsilon_b}{u_0}\right)^2 \tag{A8.19}$$

The RHS of Equation (A8.19) has three dispersion forces: pore diffusion, external mass transfer resistance and axial dispersion. As discussed in Section 3.4 on RTD, these forces affect the spread of the response peak curve in an additive manner. The axial dispersion resistance term ξ_d depends on the velocity. The pore diffusional resistance term ξ_M is

independent of velocity, because the flow variation outside the particle does not affect the internal resistance. The film resistance term ξ_f depends on the velocity through the external mass transfer coefficient k_f.

The axial dispersion term is obtained by plotting the LHS of Equation (A8.19) against $(\varepsilon_b/u)^2$, the intercept of this plot is equal to $\xi_f + \xi_M$. The intercept is corresponding to infinite velocity at which the contribution of film resistance is negligible. Therefore, the intercept is just ξ_M (Do, 1998), and the diffusion coefficient can be calculated from Equation (A8.18) as:

$$D_{eff} = \frac{(1-\varepsilon_b)\varepsilon}{\varepsilon_b}\left[1+\frac{(1-\varepsilon)K_H}{\varepsilon}\right]\frac{R^2\varepsilon}{15\xi_m} \tag{A8.20}$$

A8.1 Adsorption equilibrium constant, K_H

By matching the theoretical moments as shown in Equations (A8.13) and (A8.14) with the corresponding experimental moments, the diffusion parameter ξ_M can be extracted. To assure the reliability of the parameter extracted, the use of an inert tracer as well as an adsorbing tracer is used. Experiments are carried out for both tracers at different flow carrier gas flowrates.

The adsorption equilibrium constant K_H is zero for an inert tracer because no adsorption is happening. Therefore, the first normalised moment for an inert tracer has the following form:

$$\left(\mu_1\right)_0 = \frac{L\varepsilon_b}{u_0}\left[1+\frac{\left(1-\varepsilon_b\right)\varepsilon}{\varepsilon_b}\right]+\frac{t_0}{2} \tag{A8.21}$$

where t_0 is the injection time of the tracer gas. Kaplan (1958) stated that the first normalised moment for an inert tracer is (where $t_0/2$ is negligible):

$$\left(\mu_1\right)_0 = \frac{L\varepsilon_b}{u_0}\left[1+\frac{\left(1-\varepsilon_b\right)\varepsilon}{\varepsilon_b}\right] \tag{A8.22}$$

At the same flowrate, the first normalised moment for the adsorbing tracer is given by Equation (A8.13). Taking the difference between the first moment for adsorbing tracer and that for the inert:

$$\frac{\mu_1-\left(\mu_1\right)_0}{\left[\dfrac{\left(1-\varepsilon_b\right)(1-\varepsilon)}{\varepsilon_b}\right]} = K_H\,\frac{L\varepsilon_b}{u_0} \tag{A8.23}$$

Equation (A8.23) means that a plot of LHS against $\varepsilon_b L/u_0$ would yield a straight line and the slope of this line is equal to the adsorption equilibrium constant K_H. This demonstrates how using the inert gas and the variation of flows in the experiment can help to obtain K_H. It is important to validate the linearity of the isotherm correlations experimentally by carrying out experimental runs at different concentration of adsorbate (tracer gas) in the pulse, in other words, using different sample loops for injecting the tracer sample. In this thesis, sample loops of 0.1 ml, 0.25 ml and 0.5 ml were used. If the same results are obtained, and the chromatographic curve is symmetrical, then the assumption of isotherm linearity is justified.

In this thesis, it was shown that the chromatographic curves are symmetrical, and also a proportional relationship is found in peak heights corresponding to different sample loops used.

A8.2 The expression for the chromatographic response

The chromatography response is characterised by the first normalised moment and the second central moment. The chromatographic response is measured as the ratio of second central moment (the spread) to the square of the first normalised moment (Do, 1998; Armatas *et al*., (2005)):

$$\frac{\mu_2^{'}}{(\mu_1)^2} = \frac{2}{L}\left[\frac{D_{ax}}{u_0} + \frac{(\xi_M + \xi_f)}{(1+\xi_0)^2}\left(\frac{u_0}{\varepsilon_b}\right)\right] \tag{A8.24}$$

For a given system, the degree of spread $\mu_2^{'}/(\mu_1)^2$ is a function of velocity that for a specific particle size, length and porosity. The axial dispersion in terms of velocity are given by the following expression (Do, 1998):

$$D_{ax} = \varepsilon_b\left(\gamma_1 D_M + \gamma_2 2R\frac{u_0}{\varepsilon_b}\right) \tag{A8.25}$$

where D_M is the molecular diffusivity or known as the bulk diffusivity, D_{AB}, and:

$$\gamma_1 = 0.45 + 0.55\varepsilon; \qquad \gamma_2 \approx 0.5 \tag{A8.26}$$

The parameter ξ_f is related to the film mass transfer coefficient, which is a function of velocity. For a packed column, the external mass transfer coefficient k_f can be calculated from the following correlation:

$$\frac{k_f(2R_p)}{D_{AB}} = 2 + 1.1\left(\frac{u2R_p\rho}{\mu}\right)^{0.6}\left(\frac{\nu}{D_{AB}}\right)^{\frac{1}{3}} \tag{A8.27}$$

where D_{AB} is the bulk or molecular diffusivity, ρ is the density of the fluid, R_p is the particle radius, μ and ν is the dynamic and kinematic viscosity of the fluid respectively.

Substituting Equation (A8.25) into Equation (A8.24) yields:

$$\frac{\mu_2^{'}}{(\mu_1)^2} = \frac{2}{L}\left[2\gamma_2 R + \frac{\varepsilon_b\gamma_1 D_M}{u} + \frac{(\xi_M + \xi_f)}{(1+\xi_0)^2}\left(\frac{u_0}{\varepsilon_b}\right)\right] \tag{A8.28}$$

The degree of spread of a chromatographic response *versus* velocity is shown in Figure A8.1. The contribution of the axial dispersion effect towards a smaller spread occurs when the velocity is increased. However, this will lead to an increase in the pore and film diffusional resistances and hence an increase in the degree of spread. Therefore, an optimal velocity is found when the chromatographic operation is optimal when the function in the RHS of Equation (A8.28) has a minimum. The optimal velocity is:

$$u_0 \approx \frac{\varepsilon_b(1+\xi_0)\sqrt{\gamma_1 D_M}}{\sqrt{\xi_M + \xi_f}} \tag{A8.29}$$

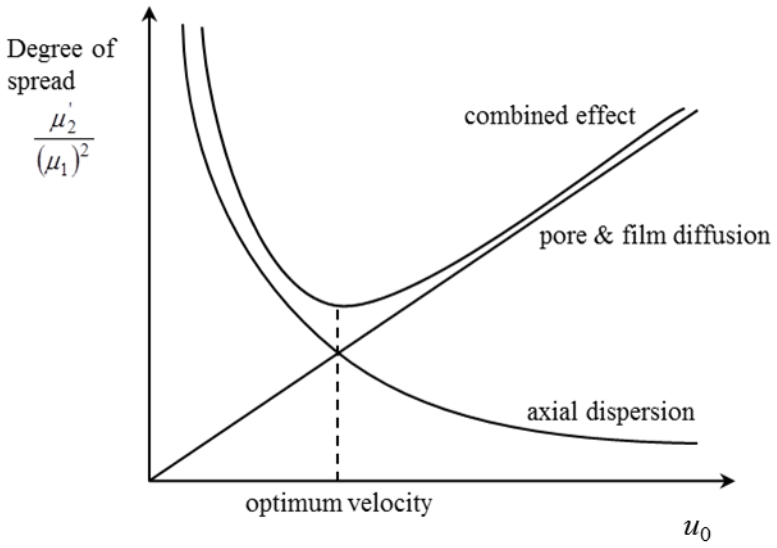

Figure A8.1: Plot of degree of spread $\mu_2^{'}/\mu_1$ against velocity u_0 (adapted and redrawn from Do (1998))

An equivalent term commonly used in the chromatographic literature is the "Height Equivalent to a Theoretical Plate" (HETP). The degree of spread of a chromatographic response is expressed as:

$$\mathrm{HETP} = \frac{\mu_2^{'} L}{\left(\mu_1\right)^2} \tag{A8.30}$$

According to Equation (A8.24) defined in Do (1998), the expression for the chromatographic response are (Armatas *et al*., 2005):

$$\mathrm{HETP} = \frac{\mu_2^{'} L}{\left(\mu_1\right)^2} = 2\left[\frac{D_{ax}}{u_0} + \frac{\left(\xi_M + \xi_f\right)}{\left(1+\xi_0\right)^2}\left(\frac{u_0}{\varepsilon_b}\right)\right] \tag{A8.31}$$

For D_{eff} calculation in Armatas *et al*. (2005), D_{ax} and ξ_f in Equation (A8.31) is ignored, therefore, the HETP expression becomes:

$$\mathrm{HETP} = \frac{\mu_2^{'} L}{\left(\mu_1\right)^2} = \frac{2\xi_M}{\left(1+\xi_0\right)^2}\left(\frac{u_0}{\varepsilon_b}\right) \tag{A8.32}$$

References

Armatas, G., Petrakis, D. & Pomonis, P., 2005. Estimation of diffusion parameters in functionalized silicas with modulated porosity: Part I: Chromatographic studies. *Journal of Chromatography A,* 1074**,** 53-59.

Kaplan, W., 1958. *Ordinary differential equations*. Addison-Wesley, London.

Do, D.D., 1998. *Adsorption analysis: Equilibria and kinetics*. Imperial College Press.

Schneider, P. & Smith, J., 1968. Adsorption rate constants from chromatography. *AIChE Journal,* 14**,** 762-771.

Appendix 9: <u>Case 5:</u> Theoretical moment expressions and resistance parameters for adsorbable tracer with no reaction (García-Ochoa and Santos, 1994; Santos *et al*., 1996)

When the adsorption equilibrium constant $K_a \neq 0$, the theoretical moments expressions and resistance parameters shown in García-Ochoa and Santos (1994) and Santos *et al.* (1996), (Equations (A9.2) to (A9.8)), were deduced from the material balance equations in **Column Model** and **Particle Model 1** (Suzuki and Smith, 1971):

$$\mu_1 = \mu_1^{'} - \mu_0 - \frac{\tau_0}{2} \tag{A9.1}$$

As stated in García-Ochoa and Santos (1994), $\mu_1^{'}$ is the experimental value of the absolute first moment, τ_0 is the injection time, and μ_0 is the first moment evaluated by injecting the tracer in the packed-bed column replaced with a void tube of negligible volume. In this thesis, the void tube experiment was not performed because of the use of convolution theorem for the calculation of a fictitious column (200 mm), which allow for the dispersion in the lines (i.e. delay time, τ_d, see Chapter 3 Sections 3.5.2 and 3.7.3). Besides, the term (τ_0/2), is proved to be negligible in Appendix 5.

Therefore, the theoretical first moment and second central moment are:

$$\mu_1 = \frac{L}{u_i}\left[1 + \frac{(1-\varepsilon_b)\varepsilon}{\varepsilon_b}(1+K_a)\right] \tag{A9.2}$$

$$\mu_2^{'} = \frac{2L}{u_i}\left[\xi_d + \xi_f + \xi_M\right] \tag{A9.3}$$

However, García-Ochoa and Santos (1994) and Santos *et al.* (1996) only presented the theoretical moment expressions in Equations (A9.2) and (A9.3), without given the resistance parameters. As a results, in this thesis, based on information given in Suzuki and Smith (1971), the resistance parameters should be similar to Equations (A6.1) to (A6.6) shown in Baiker *et al*. (1982) and Tang *et al*. (1987) but with an adsorption equilibrium constant K_a:

$$\xi_0 = \frac{(1-\varepsilon_b)\varepsilon}{\varepsilon_b}(1+K_a) \tag{A9.4}$$

$$\xi_d = \frac{D_{ax}}{\varepsilon_b}(1+\xi_0)^2\left(\frac{1}{u_i^2}\right) \tag{A9.5}$$

$$\xi_a = \frac{(1-\varepsilon_b)\varepsilon}{\varepsilon_b}\left(\frac{K_a^2}{\varepsilon k_{ads}}\right) \tag{A9.6}$$

$$\xi_f = \frac{(1-\varepsilon_b)\varepsilon}{\varepsilon_b}(1+K_a)^2\frac{R^2\varepsilon}{a(a+2)}\frac{(a+2)}{k_f R} \tag{A9.7}$$

$$\xi_M = \frac{(1-\varepsilon_b)\varepsilon}{\varepsilon_b}(1+K_a)^2\frac{R^2\varepsilon}{a(a+2)}\frac{1}{D_{eff}} \tag{A9.8}$$

The adsorption resistance ξ_a is negligible because the whole process is diffusion controlled (or diffusion limited).

The adsorption equilibrium constant K_a, was evaluated linearly by plotting μ_1 as a function of L/u_i in Equation (A9.2).

The HETP can then be calculated as:

$$\text{HETP} = \frac{\left(\mu_2 - \mu_1^2\right)L}{\mu_1^2} = \frac{\sigma^2 L}{\mu_1^2} \tag{A9.9}$$

Therefore, by substituting Equations (A9.4) to (A9.8) into Equation (A9.9) yields:

$$\text{HETP} = \frac{\mu_2^{'}L}{\left(\mu_1\right)^2} = 2\left[\frac{D_{ax}}{\varepsilon_b u_i} + \frac{\left(\xi_M + \xi_f\right)}{\left(1+\xi_0\right)^2}u_i\right] \tag{A9.10}$$

The HETP expression (Equation (A9.10)) in Garc á-Ochoa and Santos (1994) is incorrect. A bed porosity, ε_b was missing in the aixal dispersion term. A corrected from of the derivation has been given in this thesis i.e. Equation (A9.10). This expression was checked and derived from Equations (A9.2) to (A9.5). Besides, the HETP expression in Equation (A9.10) is different from the HETP expression (Equation (A8.31)) shown in Armatas *et al*. (2005). This is because:

(1) For the particle models, the difference in units for the adsorbed tracer concentration in the particle pores (C_μ compared to n_A and w), leads to different consumption terms in the intraparticle material balance.

(2) In Garc á-Ochoa and Santos (1994) and Armatas *et al*. (2005), the intraparticle phase in the former was based on **Particle Model 1** (Suzuki and Smith, 1971), whereas the latter used **Particle Model 3** (adapted from Do (1998)).

By substituting Equations (A9.4), (A9.7) and (A9.8) into Equation (A9.10), this yields (Garc á-Ochoa and Santos, 1994):

$$\mathrm{HETP} = \frac{\mu_2' L}{(\mu_1)^2} = 2\frac{D_{ax}}{\varepsilon_b u_i} + \left[\frac{\frac{2}{15}\frac{\varepsilon_b}{(1-\varepsilon_b)} R^2}{\left(1+\frac{1}{\xi_0}\right)^2} \left(\frac{1}{D_{eff}} + \frac{5}{k_f R} \right) \right] u_i \qquad \text{(A9.11)}$$

As described in Garc á-Ochoa and Santos (1994) and Santos *et al.* (1996), the correlation between HETP and intersititial velocity, u_i in Equation (A9.11) is similar to that found by Van Deemter *et al*. (1956):

$$\mathrm{HETP} = \frac{A}{u_i} + B + G u_i \qquad \text{(A9.12)}$$

From Equation (A9.12), the axial dispersion coefficient can be estimated according to:

$$\frac{D_{ax}}{\varepsilon_b} = \frac{b_1 + b_2 u_i}{2} \qquad \text{(A9.13)}$$

Therefore, the coefficient G in Equation (A9.12) is given by:

$$G = \frac{\frac{2}{15}\frac{\varepsilon_b}{(1-\varepsilon_b)} R^2}{\left(1+\frac{1}{\xi_0}\right)^2} \left(\frac{1}{D_{eff}} + \frac{5}{k_f R} \right) \qquad \text{(A9.14)}$$

G values are obtained by using non-linear curve fitting with HETP plotted as a function of u_i, and for the D_{eff} calculation, from the G value in Equation (A9.14), it was possible to estimate k_f value using the model proposed by Wakao *et al*. (1958):

$$\frac{2k_f R}{D_{AB}} = 2.00 + 1.45\,\mathrm{Re_p}^{1/2}\,\mathrm{Sc}^{1/3} \qquad \text{For } \mathrm{Re_p} < 100 \qquad \text{(A9.15)}$$

where $\mathrm{Re_p}$ is the particle Reynolds number and Sc is the particle Schmidt number. The velocity used for particle Reynolds number is the superficial velocity, u_0, and not the interstitial velocity, u_i. The values calculated for external mass transfer term, k_f, in Equation (A9.15) proposed by Wakao *et al*. (1958) is almost the same as the values for k_M using Equation (A8.27) proposed by Do (1998), with 6 – 9 per cent difference. But the values of k_f and k_M are so small that they make no real difference to the D_{eff} values calculated (≤ 1%, see Chapter 4 Section 4.2.1).

References

Garc á-Ochoa, F. & Santos, A., 1994. Effective diffusivity under inert and reaction conditions. *Chemical Engineering Science,* 49**,** 3091-3102.

Santos, A., Bahamonde, A., Avila, P. & Garcia-Ochoa, F., 1996. Measurement of the effective diffusivity for a vanadia-tungsta-titania/sepiolite catalyst for SCR of NO_x. *Applied Catalysis B: Environmental,* 8**,** 299-314.

Suzuki, M. & Smith, J., 1971. Kinetic studies by chromatography. *Chemical Engineering Science,* 26**,** 221-235.

Wakao, N., Oshima, T. & Yagi, S., 1958. Mass transfer from packed beds of particles to a fluid. *Chemical Engineering of Japan,* 22**,** 780-785.

Van Deemter, J., Zuiderweg, F. & Klinkenberg, A., 1956. Longitudinal diffusion and resistance to mass transfer as causes of nonideality in chromatography. *Chemical Engineering Science,* 5**,** 271-289.

Appendix 10: Example of calculations of bulk diffusivity D_{AB}, Knudsen diffusivity D_K and composite diffusivity D_C

1. D_{AB}, bulk diffusion coefficient from the empirical correlations

As mentioned in Cussler (2009), diffusion coefficient for a binary gas system from the empirical correlations is defined by Fuller *et al.* (1966) as:

$$D_{AB} = 10^{-3} \frac{T^{1.75}\left(1/\tilde{M}_1 + 1/\tilde{M}_2\right)^{\frac{1}{2}}}{P\left[\left(\sum_i V_{i1}\right)^{1/3} + \left(\sum_i V_{i2}\right)^{1/3}\right]^2} \tag{A10.1}$$

where:
- D_{AB} is the diffusion coefficient, $cm^2\ s^{-1}$;
- T is the absolute temperature, K;
- P is in atmospheres, bar;
- $\tilde{M}_1$ and $\tilde{M}_2$ are the molecular weight of the gases 1 and 2;
- V_{i1} and V_{i1} are the diffusion volumes of gas molecules.

A similar expression for the empirical correlations can be found in Hayes and Kolaczkowski (1997) as:

$$D_{AB} = \frac{1.013\times10^{-2} T^{1.75}\left(\frac{1}{M_A} + \frac{1}{M_B}\right)^{\frac{1}{2}}}{P\left[\left(\sum v_i\right)_A^{1/3} + \left(\sum v_i\right)_B^{1/3}\right]^2} \tag{A10.2}$$

Equation (A10.2) and (A10.1) are effectively the same except that, the units in Equation (A10.2) for D_{AB} and P are: $m^2\ s^{-1}$ and Pascal respectively.

Therefore, the relevant data used for calculating the molecular diffusion coefficient, D_{AB}, for the He (tracer) – N_2 (carrier) and N_2 (tracer) – He (carrier) gas systems used in this thesis is summarised in Table A10.1.

Table A10.1: Data used for calculating the diffusion coefficients for binary gas systems.

Diffusion volumes		Molar mass		Temperature (K)		Pressure (Pa)	
He	N_2	He	N_2	He	N_2	He	N_2
2.67	18.5	4.0026	28.0134	295.15		101325	

Hence, the bulk diffusivity, D_{AB} for the tracer-carrier gas system in this thesis is:

$$D_{AB} = \frac{1.013\times10^{-2}\times(295.15)^{1.75}\times\left(\frac{1}{4.0026}+\frac{1}{28.0134}\right)^{\frac{1}{2}}}{101325\times[(2.67)^{1/3}+(18.5)^{1/3}]^2} = 6.91\times10^{-5}\ \text{m}^2\text{s}^{-1} \qquad \text{(A10.3)}$$

From Reid *et al*. (1987), the literature data for bulk diffusivity from experiment at low pressure and 298 K is 0.696 $cm^2\ s^{-1}$. Therefore, the empirical expression from Fuller *et al*. (1966) is considered to be a good estimation for bulk diffusion coefficient, D_{AB}.

2. D_K, Knudsen diffusion coefficient

The γ-alumina bead pore diameter from analysis in Chapter 2 of this thesis is in the mesoporous range i.e. 8.2 – 12 nm. The manufacturer provided data is 8.8 nm. Hence, pore diameter 8.8 nm is used to calculate Knudsen diffusivity D_K and according to Equation (3.7):

Knudsen diffusivity for helium tracer gas, $(D_K)_{He}$:

$$\left(D_K\right)_{He} = 3.67\times10^{-6}\ \text{m}^2\text{s}^{-1} \qquad \text{(A10.4)}$$

Knudsen diffusivity for nitrogen tracer gas, $(D_K)_{N2}$:

$$\left(D_K\right)_{N_2} = 1.39\times10^{-6}\ \text{m}^2\text{s}^{-1} \qquad \text{(A10.5)}$$

The composite diffusivity D_c in Equation (3.8) has a simplified form, according to Evans *et al*. (1961) and Hayes and Kolaczkowski (2000), for diffusion coefficients in the mesopores:

$$\frac{1}{D_\mu} = \frac{1}{D_b} + \frac{1}{\left(D_K\right)_\mu} \qquad \text{(A10.6)}$$

Where subscript μ stands for mesopores, D_b is the bulk diffusivity and $(D_K)_\mu$ is the Knudsen diffusivity for mesopores.

Hence, substitute Equations (A10.3), (A10.4) and (A10.5) into Equation (A10.6):

Composite diffusivity for helium tracer gas, $(D_C)_{He}$:

$$\left(D_C\right)_{He} = 3.48\times10^{-6}\ \mathrm{m^2 s^{-1}} \tag{A10.7}$$

Composite diffusivity for nitrogen tracer gas, $(D_C)_{N2}$:

$$\left(D_C\right)_{N_2} = 1.36\times10^{-6}\ \mathrm{m^2 s^{-1}} \tag{A10.8}$$

References

Cussler, E.L., 2009. *Diffusion: mass transfer in fluid systems.* Cambridge university press.

Evans, R., Watson, G. & Mason, E., 1961. Gaseous diffusion in porous media at uniform pressure. *The Journal of chemical physics,* 35**,** 2076.

Fuller, E.N., Schettler, P.D. & Giddings, J.C., 1966. New method for prediction of binary gas-phase diffusion coefficients. *Industrial & Engineering Chemistry,* 58**,** 18-27.

Hayes, R.E. & Kolaczkowski, S.T., 2000. Evaluating the effective diffusivity of methane in the washcoat of a honeycomb monolith. *Applied Catalysis B: Environmental,* 25**,** 93-104.

Reid, R.C., Prausnitz, J.M. & Poling, B.E., 1987. *The Properties of Gases & Liquids.* New York: McGraw-Hill.